Monitoring the Microstructural Evolution of Solid Oxide Fuel Cell Anodes

Joshua James Bailey

Supervisors: Prof P. R. Shearing, Prof D. J. Brett & Prof A. Atkinson

Submitted in part fulfilment of the requirements for the degree of Doctor of Philosophy

2019

Electrochemical Innovation Lab

Department of Chemical Engineering

University College London

Declaration

I, *Joshua James Bailey*, confirm that the work presented in this thesis is my own. Where information has been derived from other sources, I confirm that this has been indicated in the thesis.

.....

Signature

.....

Date

Acknowledgements

First and foremost, I would like to thank my primary UCL supervisor, Paul Shearing, without whom this PhD thesis would not have been possible. His unwavering support, enthusiasm, wisdom and kind direction have not only been motivating and enabling in terms of research but have also inspired me to pursue my own interests in sustainability and education. Together with Dan Brett, they have created a research group with excellent facilities and even more excellent researchers. Paul's ability to juggle a million things at once and perform them all so well, along with Dan's ability to provide helpful advice while bringing a smile to everyone's face, have made the Electrochemical Innovation Lab a brilliant place to work. I have been spoilt in terms of supervision, what with the insightful input and modelling expertise from my Imperial College supervisors, Alan Atkinson and Xin Wang, respectively. I must thank David McPhail and Stephen Skinner for their roles as the Imperial heads of the Centre of Doctoral Training in Advanced Characterisation of Materials; both were welcoming and supportive during my time in the CDT. Moreover, Neil Curson, as the UCL head, has been a consistent source of support and friendship throughout the 4 years and I would like to extend my sincerest gratitude for the time he has taken to help me along the way.

No PhD would be complete without the many and various interactions with fellow PhD students and PDRAs, ranging from technical guidance and research conversations to taking a break and enjoying the company of many wonderful characters. Researchers who had a positive impact on my studies but are no longer with the group are: Leon Brown – who first inspired me to join the EIL and helped set me up in the very beginning; Donal Finegan – who was a constant source of enjoyable chats, helpful discussions and funny quirks; Quentin Meyer – whose bright outlook and keen research eye were both encouraging; Bernhard Tjaden – whose determination and humour were always found in equal measure; Dami Taiwo – who never forgot to be kind and helpful; and Tan Pathan for all the laughs along the way.

There is a whole host of current PhDs and PDRAs to whom I am very grateful, for all sorts of reasons. I would like to take this opportunity to thank Tom Heenan who was my SOFC buddy from the start and from whom I have learnt many things about engineering and with whom I have been fortunate to work. On moving from Chemistry to Chemical Engineering, I was very lucky to receive lots of guidance from both our ex-lab manager, Jason Millichamp, and our current lab manager, Toby Neville, without whom I doubt I would have been able to produce any results! I have also been very lucky to share great times with and receive useful research advice from Sam Cooper at Imperial College, whose modelling expertise and ability to explain it have been invaluable. On this note, both Xuekun Lu and Matt Kok have also provided tonnes of guidance and collaborative support when it comes to computational matters and to both I am grateful for their good character and willingness to share their knowledge. I would also like to especially thank Francesco Iacoviello for his patience, friendship and eternally upbeat demeanour; he has made working with X-rays a joy for many people over the years.

For productive and interesting collaborations, I would like to extend thanks to: Quentin Meyer, Donal Finegan, Tom Heenan, Xuekun Lu, Sofia Marchesini, Vidal Bharath, Tom Johnson and Jason Cho. Thanks to each of you, I have been exposed to many different fields and had to tackle all sorts of research questions that have given me a much broader PhD experience. For other advice and help along the way, I'd also like to thank the old guard, including: Rhodri Jervis, James Robinson, Erik Engebretsen, Vidal Bharath, Patrick Cullen and Rema Abdulaziz. Not only did you provide direction, but you also made going to the pub much more interesting! It has also been great to work with Dina Ibrahim, who never fails to inject laughter into the day; Fabiola Valdés-Lopez and Jon Morgado for putting up with my bad Spanish, Nivedita Kulkarni and Daniela Ledwoch for their friendly chats and Sohrab Daemi, whose understanding and patience as my desk neighbour have been gratefully received!

To the newer guard, it would be remiss not to thank the many wonderful people for creating such a stimulating and lively atmosphere in the lab and office. So big love to:

Lara Rasha, Jennifer Hack, Ralf Ziesche, Drasti Patel, Zahra Rana, Max Meier, Gyen Angel, James Dodwell and Martin Pham. You guys all bring so many new strengths to the lab and have made the last few years an absolute pleasure. I'd also like to thank the CDT-ACM administrators (Claire Smithson and Hafiza Bibi) for all their hard work and my colleagues from the CDT-ACM: Sofia Marchesini, Nadir Basma, Mohamed Koronfel, Jon Rackham, Martin Hart, Lizzie Norris, Shiny Mathew, Tim Ellis, Daphné Lubert-Perquel, Jingyi Chen and Oscar Williams, for making all of the extra activities, including the great trips to Snowdonia and Girona, really good fun, and for creating positive cohort atmospheres which will hopefully endure for many more years.

A special thanks to everyone involved in UCell, past and present, for making public engagement and talking about fuel cells so entertaining and enjoyable, and for the many friends I've made along the way while establishing PPL PWR. A huge thanks again to Tom Heenan, Francesco Iacoviello and Xuekun Lu for their time and efforts at SLS for beamtime experiments; I hope the wonderful Bentley ride made up for all the long nights! Thanks again also to Donal Finegan for allowing me to help out blowing up batteries outside Oxford, and to Andy Clare and Adam Bone at Ceres Power for being so welcoming and making the internship there a truly engaging and interesting experience.

And last, but certainly not least, I must make a vain attempt at expressing the full extent of my gratitude to my close friends and loved ones. Bernardo Maza Stern has been irreplaceable during my write-up and has been both a great friend and a great leader in taking PPL PWR forward this year. To Michael Foley and Luke Vancliffe-Davis, thank you also for your help and constant friendship over the years. My family (and second family!) have both been incredibly sympathetic and supportive throughout the PhD and for this I would like to thank them dearly. Most of all, I would like to recognise the sacrifices that my partner, Ciara, has made, not least during these final months, along with the many moments of kindness and generosity she has shared to keep me going. Her love, support, understanding (and food!) have long been the bedrock of everything I do, and for that I will happily continue to thank her for many years to come.

Abstract

As the global energy landscape evolves in the face of climate change, the uptake of intermittent renewables is gaining ground. Electrochemical devices for energy generation and storage are therefore becoming increasingly prevalent. Solid oxide fuel cells represent an energy conversion device with high efficiency and fuel versatility but continue to suffer from cost and durability issues, hindering commercial viability. Establishing electrode microstructure-property relationships provides insight into both initial and long-term performance and thus far, full comprehension of degradation phenomena has remained elusive. Building on 2D stereological approaches, recent advances in tomographic techniques such as focused-ion beam-scanning electron microscopy and X-ray nano-computed tomography have allowed for 3D investigations of electrode microstructures. However, the former methodology is inherently destructive and with the latter, reliable contrast for typical SOFC electrode materials has not been easily accessible. In this thesis, an examination of these tomographic modalities is conducted, with focused-ion beam scanning electron microscropy slice-and-view applied to both *virgin* and *aged* Ni-YSZ anodes to virtually reconstruct their microstructures. A laser-preparation technique for the fabrication of geometrically optimised samples for X-ray nano-computed tomography is developed, and facilitates access to a larger sampled volume, thus providing more representative characterisation of the entire anode. Prepared samples are exposed to *ex-situ* annealing in a lab-based furnace wherein 900 °C is identified as the appropriate temperature for monitoring appreciable microstructual evolution within the first 12 hours of annealing. An *in-situ* laser-heating set-up at a synchrotron beamline illustrates the very early-stage microstructural reorganisation inherent to high-temperature operation. Significant attention is directed throughout towards the extraction of reliable metrics, sampling a representative volume element and capturing evolution by digital volume correlation techniques. The expectation is that the developed methodology will provide insight into the necessary fabrication and operational parameters for maximising solid oxide fuel cell performance and durability.

Impact Statement

The main academic impact of the work included in this thesis is the provision of a methodology that can be utilised to conduct 4D imaging of SOFC materials in order to gain an improved understanding of microstructural evolution therein. Additionally, this work illustrates the nature of the information derivable from such studies, both in a lab-based setting and with a synchrotron source. By comparison of FIB-SEM and X-ray tomographies, this work serves to provide insight for future research of different anode or cathode materials, in terms of how best to apply these techniques. Metrics development on both a global and local scale is provided, alongside in-depth representative volume element analysis to test the validity of the extracted properties.

In an industrial context, an internship as part of the CDT-ACM with Ceres Power Ltd. allowed for these tomographic modalities to be employed on real materials with a view to tackling genuine engineering challenges facing SOFC technologies today. The hope is that the workflow developed here will provide a route to further useful discoveries in the endeavour to fabricate and run high-performance and highly durable SOFCs.

From a public engagement point-of-view, the focus of this thesis and the authored papers herein have generated ample material for discussion with the wider public, in the form of Talks, Workshops, Demonstrations and Festival Stalls as part of UCell – UCL Fuel Cells and PPL PWR.

Contents

List of Figures

List of Tables

Nomenclature

Abbreviations

3YSZ 3 mol% Yttria-Stabilised Zirconia
8YSZ 8 mol% Yttria-Stabilised Zirconia
AC Alternating Current
AFC Alkaline Fuel Cell
AFL Anode Functional Layer
ANOVA Analysis of Variance
AOI Area of Interest
ASC Anode-supported Cell
ASL Anode Support Layer
ASR Area-specific Resistance
BET Brunauer-Emmet-Teller method
BSE Back-scattered Electron
CA Cellular Automata
CAES Compressed Air Energy Storage
CCD Charge-coupled Device
CGO Gadolinia-Doped Ceria
cPSD Continuous Particle Size Distribution
CT Computed Tomography
CVD Chemical Vapour Deposition
DVC Digital Volume Correlation
EIS Electrochemical Impedance Spectroscopy
EPA Environmental Protection Agency
FBP Filtered-back Projection algorithms
FC-HES Fuel Cell-Hydrogen Energy Storage
FEM Finite Element Method
FFT Fast Fourier Transform
FIB Focused-ion beam
FOV Field-Of-View
FZP Fresnel-Zone Plate
GHG Greenhouse Gas emissions
HEI Health Effects Institute
HHV Higher Heating Value
HOR Hydrogen Oxidation Reaction
HRES High-Resolution mode
HT High-Temperature
IEA International Energy Agency
IPCC Intergovernmental Panel on Climate Change
IR Infra-red
IT Intermediate-Temperature
LBM Lattice-Boltzmann Method
LEL Lower Explosive Limit
LFOV Large Field-Of-View mode
LHV Lower Heating Value
LMIS Liquid Metal-Ion Source
LSCF Lanthanum Strontium Cobalt Ferrite
LSGM Lanthanum Strontium Gallium Manganite
LSM Lanthanum Strontium Manganite
MCFC Molten Carbonate Fuel Cell
MEA Membrane Electrode Assembly
MIEC Mixed-ionic-electronic-conductor
MIP Mercury Intrusion Porosimetry
MT Micro-tubular
Mtoe Mega Tonnes of Oil Equivalent
NIR Near Infra-red
OECD Organisation for Economic Co-operation and Development
ORR Oxygen Reduction Reaction
PAFC Phosphoric Acid Fuel Cell
PVC Passive Voltage Contrast
PEMFC Polymer Electrolyte Membrane Fuel Cell
PHS Pumped Hydro Storage
PM Particulate Matter
PSD Particle Size Distribution
PSI Paul Scherrer Institut
PV Photovoltaic
RF Radio-Frequency
RVE Representative Volume Element
S/C Steam-to-Carbon ratio
SDG Sustainable Development Goals
SE Secondary Electron
SEM Scanning Electron Microscopy
SHE Standard Hydrogen Electrode
SLS Swiss Light Source
SOFC Solid Oxide Fuel Cell
SSCTP Standard State Conditions of Temperature and Pressure
TEC Thermal Expansion Co-efficient
TPB Triple-Phase Boundary
TPR Temperature-Programmed Reduction
UK United Kingdom
UNFCCC United Nations Framework Convention on Climate Change
US United States
VOI Volume Of Interest
VSIA Volume-Specific Interfacial Area
VSSA Volume-Specific Surface Area
WD Working Distance
WDX Wavelength-Dispersive X-ray spectroscopy
WHO World Health Organisation
XANES X-ray Absorption Near-Edge Structure spectroscopy
XAS X-ray Absorption Spectroscopy
XPS X-ray photoemission Spectroscopy
XRD X-ray Diffraction
YSZ Yttria-Stabilised Zirconia

Greek Symbols

α Transfer (or symmetry) coefficient [-]
δ Constrictivity Factor [-]
δ_{SE} Secondary electron yield [-]
δ_{BSE} Back-scattered electron yield [-]
ΔE Excess Photon Energy [J]
$\Delta E/E$ Spectral Bandwidth [%]
ΔG_{act} Activation Energy [$Jmol^{-1}$]
ΔG_{rxn} Gibbs Free Energy [$Jmol^{-1}$]
ε Porosity [%]
η Overpotential [V]
η_{act} Activation Overpotential [V]
η_{mass} Mass Transport Overpotential [V]
η_{ohm} Ohmic Overpotential [V]
η_i Efficiency (type i) (%)
η_{visc} Viscosity [Pa·s]
θ Driving force [varies]
λ Stoichiometric factor [-] or Wavelength [nm]
μ Chemical Potential [$Jmol^{-1}$]
μ_{ec} Electrochemical Potential [$Jmol^{-1}$]
μ_i Chemical Potential of species i [$Jmol^{-1}$]
μ_i^o Reference Chemical Potential of species i [$Jmol^{-1}$]
$\mu(x,y)$ Mass Attenuation Coefficient [cm^2g^{-1}]
v_{fuel} Rate of fuel supply [mol/s]
φ_i Electrical Potential of Species i [V]
φ_s Sphericity [-]
ρ Mass density [gcm^{-3}]
σ Conductivity [Scm^{-1}]
σ_{ion} Ionic Conductivity [Scm^{-1}]
τ Tortuosity factor [-]
Γ_i Transport Rate [cm^2/s]
Γ_i^{eff} Effective Transport Rate [cm^2/s]

Parameters

a_i Activity of species i [-]
A Cross-sectional Area [cm^2]
A_p Surface area of a particle [μm^2]
c Molar Carrier Concentration [$molcm^{-3}$]
C_i Correlation value [-]
d Interplanar Spacing [nm]
$D_{s,ion}$ Solid-phase Ionic Diffusivity [cm^2/s]
D_{ij} Bulk Gas Diffusivity [cm^2/s]
D_{ij}^{eff} Effective Gas Diffusivity [cm^2/s]
$D_{s,0}$ Solid-phase Attempt Frequency [cm^2/s]
D_{obj} Diameter of scanned object [µm]
E Reversible Cell Potential (or Electrical Potential Difference) [V]
E^o Reversible Cell Potential at standard-state conditions [V]
E_{ii} Strain component in i direction [-]
F Faraday's Constant [$Cmol^{-1}$]
H Enthalpy [J]
G Gibbers Free Energy [J]
i Current [A]
$I(x,y)$ Transmitted Intensity [-]
j Current Density [Acm^{-2}]
j_o Exchange Current Density [Acm^{-2}]
k_B Boltzmann constant [$m^2kgs^{-2}K^{-1}$]
$k_{s,Cap}$ Reciprocal time constant for nickel coarsening [s^{-1}]
l Length of particle [µm]
l_o Initial length of particle [µm]
L Length of conductor [cm]
L_e Pore length [µm]
L_{eucl} Euclidean distance between two plane edges of porous medium [µm]
n Number of electrons transported [-]
n_i Number of atoms/molecules of species i [-]
N_i Number of voxels of species i [-]
Ns_i Number of voxels at surface of species i [-]
N Total number of voxels [-]
p Pressure [Pa]
pH_2 Partial Pressure of Hydrogen [Pa]
pH_2O Partial Pressure of Water (Vapour) [Pa]
pO_2 Partial Pressure of Oxygen [Pa]
P Number of projections [-]
q Heat Transferred [J]
Q Charge [C]
Q_{vol} Volume flow rate [cm^3/s]
$\langle r^2(t)\rangle_i$ Mean-square displacement of species i [cm^2]
r Capillary radius [µm]
R Universal Gas Constant [$J^{-1}K^{-1}mol^{-1}$] or Resistance [Ω]
R_{ct} Charge Transfer Resistance [Ω]
R_{max} Maximum Resistance [Ω]
R_o Initial Resistance [Ω]
S Entropy [$J^{-1}K^{-1}mol^{-1}$]
S_{path} Number of points per ray path [-]
t Time [s]
T Temperature [K]
T_o Reference Temperature [K]
u Carrier Mobility [$cm^2V^{-1}s^{-1}$]
U Internal Energy [J]
V Volume [m^3] or Voltage [V]
V_i Volume Fraction [-]
V_p Volume of a particle [μm^3]
w Work done [J]
$[X]$ Concentration of species X in the bulk [$moldm^{-3}$]
$[X]_o$ Concentration of species X at the electrode interface [$moldm^{-3}$]
z Charge Number [-]
Z Atomic Number [-]

Indices

ads Adsorbed
elec Electric
g Gas phase
ion Ionic
m Melting
rev Reversible
rxn Reaction

Chapter 1: Motivation & Introduction

Motivation

The latest synthesis report from the Intergovernmental Panel on Climate Change (IPCC) summarises findings from their Fifth Assessment Report and makes for startling reading [1]. The report states that “warming of the climate system is unequivocal”, “human influence on the climate system is clear” and that “recent anthropogenic emissions of greenhouse gases are the highest in history”. The Earth’s warming is producing devasting impacts across the globe: ocean acidification; sea-ice diminution; increases in extreme weather; sea level rise; species extinction; food and freshwater insecurity, among others. Sustained greenhouse gas emissions (GHG) will very likely cause further warming, exacerbating these problems and increasing “the likelihood of severe, pervasive and irreversible impacts for people and ecosystems”. Given this indictment of our current situation, the urgent need for action in terms of the mitigation of climate change and our adaptation in the face of rising global temperatures is clear and profound. An element of the remedial strategy centres on changing our energy landscape: including generation and harnessing, storage and distribution, as well as use and efficiency, which must entail substantial reductions in GHG emissions. Decades-long international co-operation culminated in 2016 in the adoption of the Paris Climate Agreement, signed in 2018 by 195 United Nations Framework Convention on Climate Change (UNFCCC) state parties, in a bid to hold “the increase of the global average temperatures to well below 2 °C above pre-industrial levels” [2]. Key elements of this agreement were that contributions should be nationally determined and take account of various sustainable development goals (SDG) [3], as well as requiring countries to report regularly on their emissions.

According to the Climate & Clean Air Coalition, short-lived climate pollutants, such as black carbon (soot), are “responsible for a significant fraction of near-term climate change” [4] and that measures to reduce the production of these environmental contaminants could provide “win-win results for the climate, air quality [and] public health”. The World Health Organisation (WHO) has stated that, where there is air pollution monitoring, the proportion of urban dwellers who are exposed to air quality levels that exceed WHO limits is “more than 80%” [5]. Moreover, poorer demographics disproportionately experience the negative effects of poor air quality, with “7 million deaths attributable to the joint effects of household and ambient air pollution in 2016”, ~94% of whom were in low- and middle-income countries [6]. In the State of Global Air report, produced by the Health Effects Institute (HEI), particulate matter measuring 2.5 μm or less in aerodynamic diameter (PM2.5) was shown to contribute significantly to disease and disability through chronic lung disease, lung cancer, heart disease and stroke, and therefore was “the 6th-highest risk factor for early death” in 2016 [7]. Clearly, due to the presence of various deleterious components in polluted air, there is a pressing need to curtail activities that emit these pollutants, with the purpose of mitigating the global and local crises of climate change and in public health. With global population set to rise to almost 10 billion by 2050 [8] and with growing urbanisation and resource demands, the pressure to overcome this challenge is likely to increase.

Based on 2015 figures gathered by the International Energy Agency (IEA), the total primary energy supply of the world was approximately 13,643 Mtoe (mega tonnes of oil equivalent) where a single ‘toe’ represents 42 gigajoules [9]. The major contributors of this energy were: primary and secondary oil (32%), coal (28%) and natural gas (22%) - all finite fossil fuels with their high associated GHG emissions on burning. In the same year, according to the US Environmental Protection Agency (EPA), approximately 32,294 million metric tonnes of CO_2 were emitted by the combustion of fossil fuels globally [10]. Taking the US as an example, “76% of total U.S. anthropogenic GHG emissions (based on global warming potential) and about 94% of total U.S. anthropogenic CO_2 emissions” were produced from the combustion of fossil fuels for

energy in 2016, illustrating that a large majority of human contributions to global warming comes from burning fossil fuels.

Although several renewable energy sources are available and are currently in use across the world, biofuels and waste constitute roughly 10% of total energy production, while hydropower represents only 2-3%, and all other renewables (including solar, geothermal and wind) constitute a mere 2-3% combined [9]. On the other hand, renewables experienced their fastest growth in history during the 2000-2012 period and accounted for the second largest increment in energy consumption last year (2017) [11]; our energy landscape appears to be changing at a previously unseen rate. In 2008, the UK wrote into law that the Secretary of State must ensure that "the net UK carbon account for the year 2050 is at least 80% lower than the 1990 baseline" [12] . This has already begun to translate into a low-carbon, more decentralised approach to energy generation [13].

For millennia, the most renewable energy source for human exploitation has been solid biomass, such as wood, grass, charcoal, crops, and dried manure. In the modern era, solid biofuel, mainly in the form of wood or charcoal for residential cooking and heating, remains the main renewable energy resource, representing 62.4% of global renewables supply in 2016 [9]. However, in Organisation for Economic Co-operation and Development (OECD) countries, this figure is much lower (35.4%) and non-biofuel sources constitute a greater proportion of the renewable energy supply (46.5%, 2017) than they do globally (30.5%, 2016). With regards to electricity generation in OECD countries, the full complement of renewable sources constitutes approximately one-quarter of energy production, outstripping the use of nuclear power. Although this is mainly hydroelectric in nature, a substantial percentage of this is produced by Wind (25%) and Solar PV (10%) with both newer renewable technologies showing dramatic growth rates between 1990 and 2017, as shown in Figure 1.

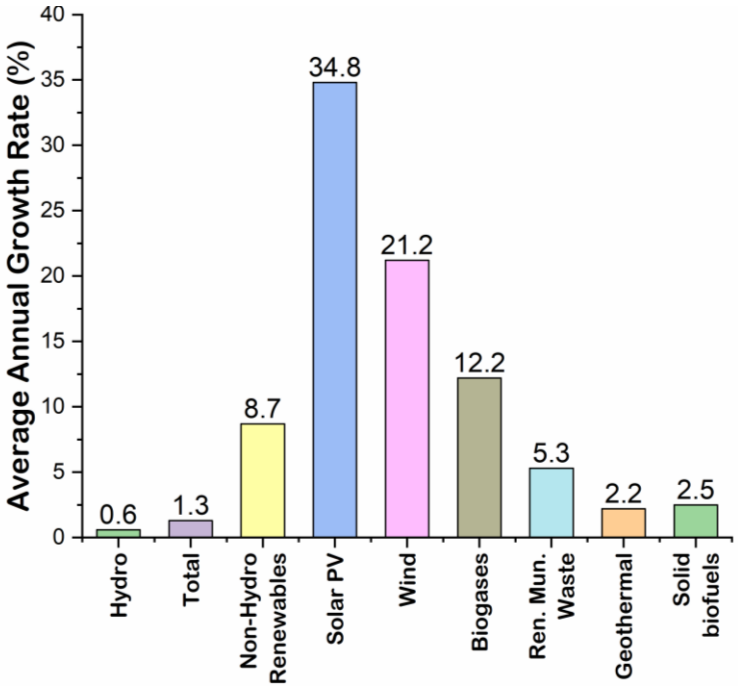

Figure 1: Annual growth rates of electricity production between 1990 & 2017 in OECD countries, from [14]

This huge growth in Solar PV and Wind (37.3% and 23.6%, 1990-2016 WORLD; 38.4% and 20.7%, 1990-2017 OECD), represents a shift towards low-carbon energy production techniques that are inherently intermittent in nature. During last year (2017), Wind "provided more than half of renewables growth, while solar contributed more than a third" [11], while the use of hydroelectric power in Europe declined substantially. As the trend towards these newer renewable technologies continues, energy generation will likely become more dependent on the time of day, the season and the local weather environment. As our electricity consumption often does not favourably match the peaks and troughs of supply by Wind and Solar PV, the impetus behind developing energy storage systems in a variety of forms becomes increasingly clear.

In the past, the issues of network load stability have often been addressed by the use of fossil-fuel based primary power in peak-load power stations, or they have required energy storage in the form of lead-acid batteries [14]. However, these batteries often cannot withstand the requisite high cycling rates, nor do they have high volumetric energy density and alternative technologies for energy storage are under development. The main forms can be broadly categorised as mechanical, chemical or thermal and include: pumped hydro storage (PHS), flywheel energy storage, battery storage, energy

storage using flow batteries, fuel cell-hydrogen energy storage (FC–HES), energy storage in supercapacitors, thermal energy storage and compressed air energy storage (CAES), amongst others. Although PHS is the most prevalent for high-power applications, and is highly efficient, it does require the appropriate geography for having different water elevations. Similarly, CAES often requires particular geological formations to facilitate the containment of the air mass. Flow batteries are a promising field for grid-scale energy storage, with inherent advantages such as the decoupling of energy and power, as well as potential for storing large quantities of energy. However, issues of cycle durability, corrosivity and cost need to be addressed before flow batteries are adopted widely [15].

Although storage by electrolysing water to create renewable hydrogen (under the umbrella of FC-HES) is currently being considered for a near-future hydrogen economy [16], there are still cost and infrastructure challenges that need to be overcome. As interim technologies, high- and intermediate-temperature solid oxide fuel cells (SOFC) are thought to provide a great alternative to FC-HES. Given that SOFCs operate at high temperatures and can run on natural gas, amongst other hydrocarbon-based fuels, they hold great promise for attending to the critical challenges of today by simply making use of existing natural gas infrastructure to deliver low-emission, highly efficient combined heat and power (CHP). This thesis focuses on the SOFC as an alternative energy conversion device that is likely to be a key player in mitigating the local and global issues discussed above.

Introduction

1.1 Fuel Cells

1.1.1 Introduction to Fuel Cells

Fuel cells are electrochemical cells that convert chemical energy from fuels into useful electrical energy, producing heat as a by-product which may, in some cases, be harnessed. Like all full electrochemical cells, a fuel cell comprises two electrodes: the anode where oxidation occurs; and the cathode where reduction takes place. These electrodes are separated by an electrolyte or "membrane", which acts not just as a barrier to reactant cross-over, but also as an electronic insulator and an ionic conductor. On the introduction of fuel at the anode, and oxidant at the cathode, redox processes give rise to the production of ions and electrons, the latter of which cannot readily traverse the electrolyte. Instead, electrons flow through an external circuit, performing work, and counterbalance the transport of ions through the electrolyte, maintaining charge neutrality. Compared with internal combustion engines, fuel cells generally have no moving parts and so are not susceptible to the normal wear of engines. More importantly, they are not constrained by the Carnot Cycle, which limits the efficiency of heat engines as determined by Equation *1-1*, and thus have higher reversible thermodynamic efficiencies up to temperatures of approximately 700 °C [17].

$$Efficiency = \frac{T_{upper} - T_{lower}}{T_{upper}} \qquad 1\text{-}1$$

To meet the electrical requirements of most applications, multiple cells are stacked in series or parallel and thus require interconnect materials that provide electrical connection and housing for reactant and product channels. A simple schematic of a generic planar fuel cell repeating unit, inclusive of the membrane-electrode assembly (MEA), is shown in Figure 2. Crucially, the nature of the redox processes occurring within the fuel cell depend on the type of fuel cell, which is likely to be one of five main types: phosphoric acid fuel cell (PAFC), polymer electrolyte membrane fuel cell (PEMFC), alkaline fuel cell (AFC), molten carbonate fuel cell (MCFC) or solid oxide fuel cell (SOFC), each named after their membrane material. Although the redox reactions involved in

each case are relatively simple, they are facilitated by a complex, bespoke device, for which material selection must meet several constraints and whose physical design must be highly engineered for optimal performance.

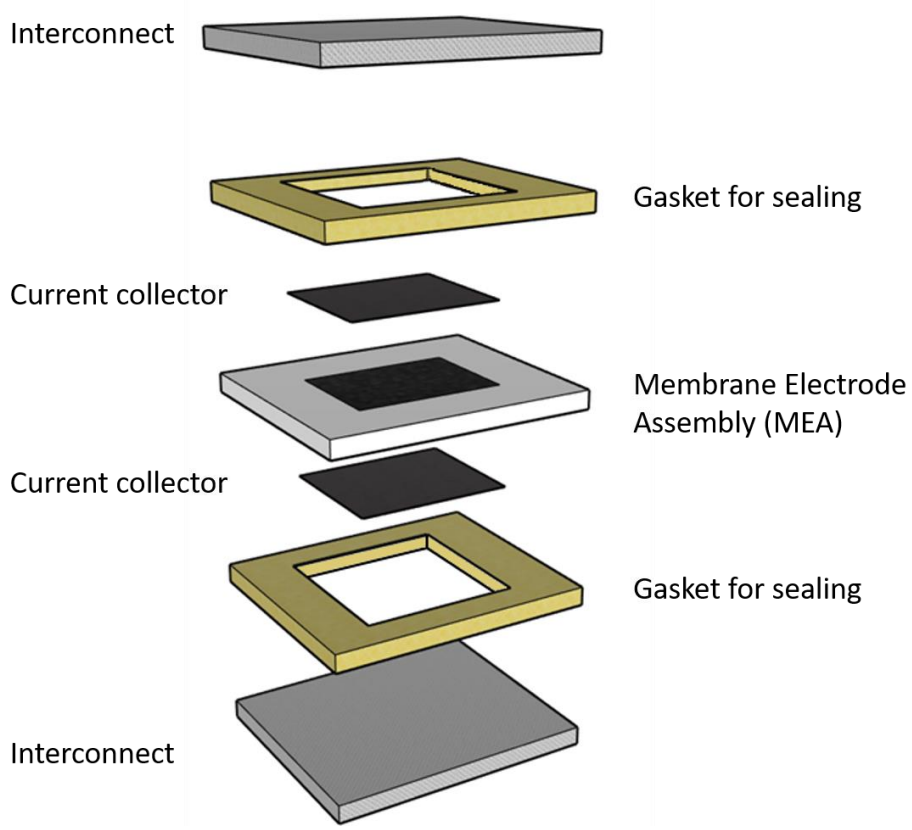

Figure 2: Schematic of a generic fuel cell repeating unit

The work in this thesis is solely devoted to the study of SOFCs which correspond to intermediate- or high-temperature fuel cells, typically running at temperatures of approximately 500-750 or 750-1000 °C, respectively [18]. In this work, the high-temperature (HT) variant is the subject matter of choice.

1.1.2 Solid Oxide Fuel Cells

Solid oxide fuel cells (SOFC) belong to a class of electrochemical devices that can be used to convert a range of fuels plus an oxidant, typically air or pure oxygen, into electricity and heat. SOFC stacks run at high temperatures, as their oxide-ion conducting electrolytes must be heated sufficiently to yield ionic conductivities associated with minimal losses and thus adequate efficiency levels. The mode of operation of an SOFC is similar to that of other fuel cell types, except that the mobile species in the electrolyte is a negatively charged oxide ion, O^{2-} (Figure 3).

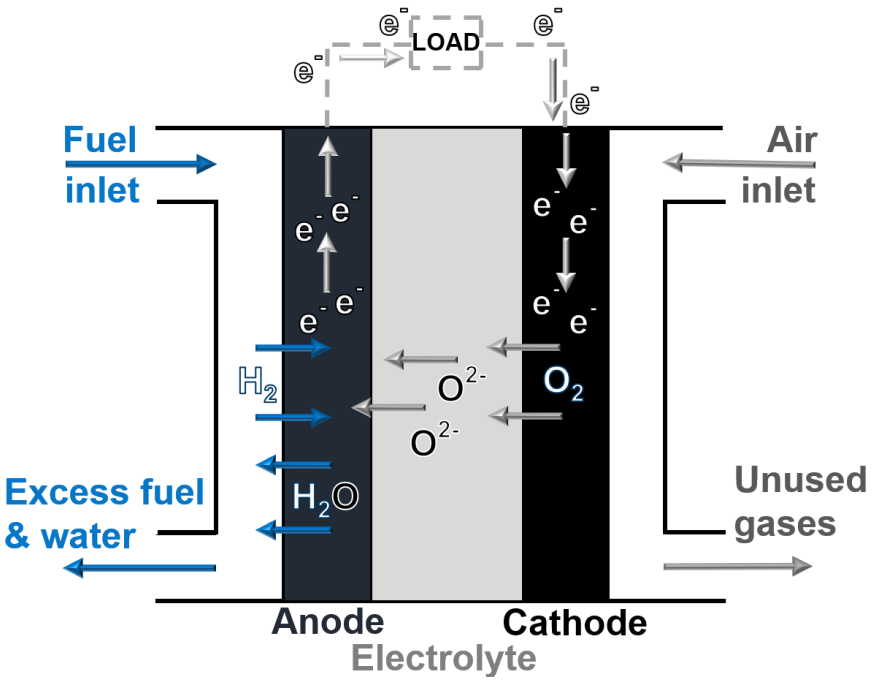

Figure 3: Schematic of the mode of operation of an SOFC

If hydrogen is used as the fuel and oxygen as the oxidant, the processes inside each cell correspond to the hydrogen oxidation reaction (HOR) at the anode (Equation *1-2*) and the oxygen reduction reaction (ORR) at the cathode (Equation *1-3*). The resultant oxide ions at the cathode permeate through the solid oxide electrolyte, as a result of the gradient in oxygen chemical potential and combine with the protons created from oxidation of H_2 at the anode. The electrons that are produced at the anode are effectively forced to travel around the external circuit, performing useful work in the process. The sole chemical by-product of this reaction is water in the form of steam (Equation *1-4*).

$$H_{2(g)} \rightarrow 2H^+ + 2e^- \qquad 1\text{-}2$$

$$\frac{1}{2}O_{2(g)} + 2e^- \rightarrow O^{2-} \qquad 1\text{-}3$$

$$H_{2(g)} + \frac{1}{2}O_{2(g)} \rightarrow H_2O_{(g)} \qquad 1\text{-}4$$

The cell potential under standard state conditions of temperature and pressure (SSCTP) is determined by the individual electrode potentials of the two redox processes listed above. Relative to the standard hydrogen electrode (SHE), the reaction in Equation *1-3* has an electrode potential equal to +1.23 V, where Equation *1-2* is approximately the SHE itself and is said to have an electrode potential of zero, yielding a theoretical

maximum cell potential of +1.23 V, but only under the conditions of SSCTP with unit activity of each of the reactants and products. Here, activity may be understood in relation to either the concentration of partial pressures of substances present, with any non-ideality being represented by an activity other than unity. Deviations from this 'ideal' cell potential are discussed in **Section 1.3**.

On the micro- and nanoscale, these electrocatalytic half-reactions are surmised to occur at or near the triple-phase boundary (TPB) [19], which is the interface between an electron-conducting metallic phase (e.g. nickel, Ni), an ion-conducting ceramic phase (e.g. yttria-stabilised zirconia, YSZ) and the porous phase containing gases (Figure 4). For these TPBs to be active sites for the aforementioned redox processes, each must be appropriately percolated to either the current collector/manifold (metal and pores) or electrolyte (ceramic).

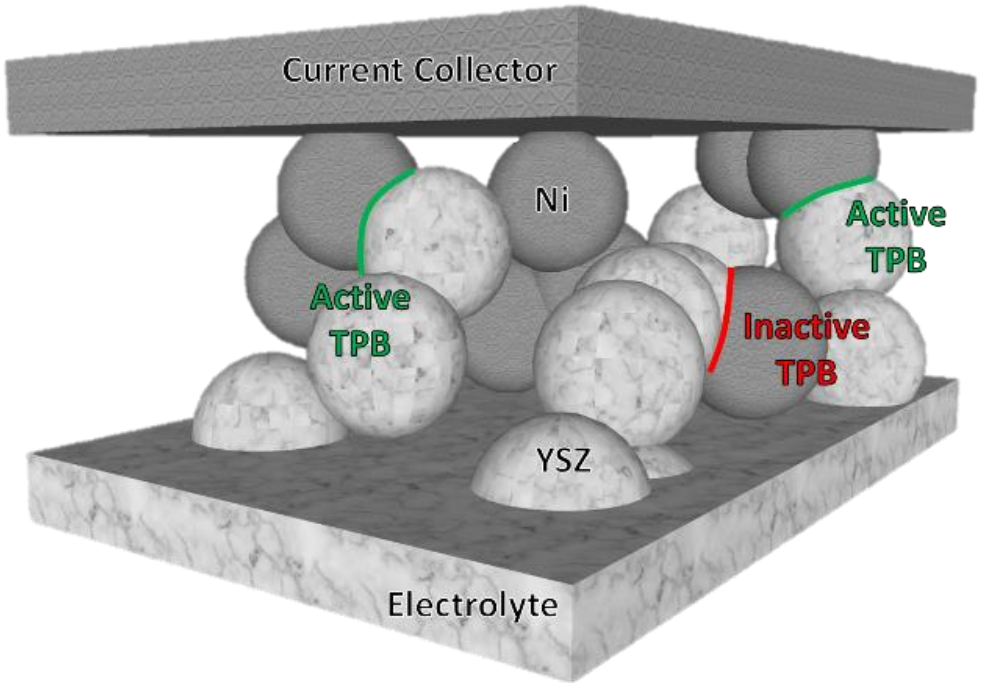

Figure 4: Schematic illustrating active and inactive TPBs in a typical Ni-YSZ SOFC anode

There are two main SOFC design geometries that are researched and commercialised; the tubular (sometimes flattened or micro-sized) and planar layouts. The two designs are shown in Figure 5. A single cell, with a theoretical maximum voltage of 1.23 V in ambient conditions (practically closer to 1.05 V, due in part to high temperature operation) is insufficient for any modern applications and hence single cells

are connected in series and/or parallel by virtue of cell-to-cell connectors and/or interconnect materials [20]. However, the different design types require different interconnections and sealing due to their geometries.

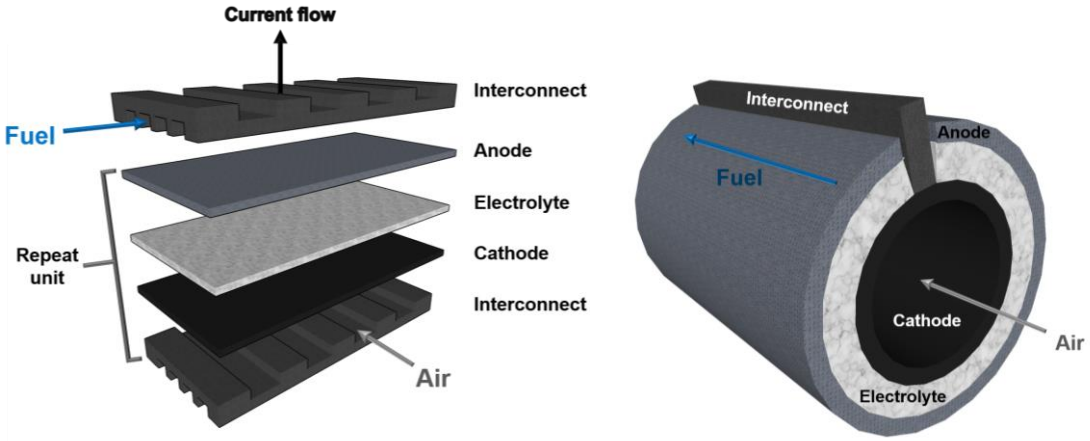

Figure 5: Schematic planar and tubular solid oxide fuel cells

Strengths of the tubular design are its seal-less system (which does, however, pose problems in the planar analogue) and the fact that, by being axially symmetric, it is more resilient to thermal cycling. It is said to be seal-less as it has one open end and the oxidant and fuel are otherwise separated by the presence of a dense electrolyte and interconnect [21]. Being more thermally resilient allows for much faster start-up as the temperature can be raised more rapidly. However, a great advantage of the planar design is the low component volume and shorter, more direct pathway for electron flow.

Up until the turn of the 21st century, research centred on SOFC devices which typically operated at the upper end of the HT-regime (850 – 1000 °C), with more efficient internal reforming of hydrocarbon fuels, and increased overall efficiency from combining their output of high grade heat with a gas turbine [22]. At higher temperatures, the kinetics of the HOR and ORR are improved, and this co-generation of heat and power affords high efficiency, which both compensate for modest thermodynamic losses in cell potential (see **Section 1.3**). However, the high temperatures do pose serious materials constraints and limit durability, so attention has more recently been diverted towards intermediate-temperature (IT-)SOFCs with the aim of reducing cost, expanding the potential material pool and reducing the degradation of cell and stack. Nevertheless, on lowering the temperature, the ionic conductivity of the solid electrolyte drops

dramatically, requiring a remediation strategy to ensure that an adequate power density can still be reached. For this reason, the choice of which component of an SOFC serves as the mechanical support is vitally important.

Although it is theoretically possible to fabricate a support based on: either of the two electrodes; the electrolyte; an inactive porous insulator; or the interconnect (as shown in Figure 6), modern electrolytes are often kept to a minimum thickness, whilst still maintaining the other desirable characteristics noted above. The resultant cells are either cathode-supported or anode-supported cells, with a thin electrolyte providing a shorter ionic conduction path to offset the drop in conductivity at lower temperatures.

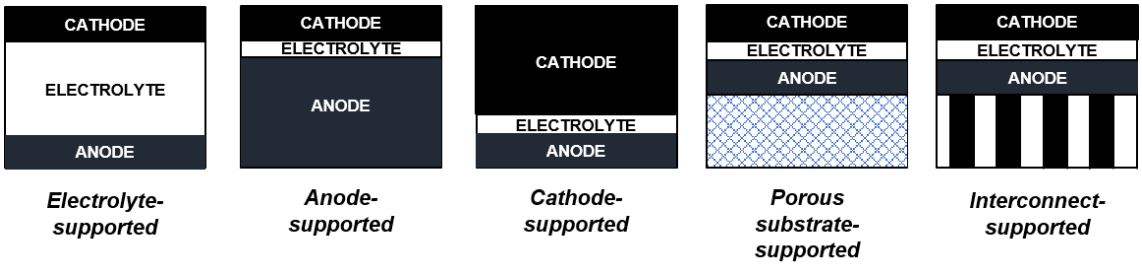

Figure 6: Schematic diagram of different SOFC geometries, from [28]

Throughout the historical development of SOFC stacks, a variety of different supports have been used, taking into account various technical and economic aspects such as mechanical strength, ease and cost of manufacture and resultant peak power densities. Early tubular SOFCs by Siemens-Westinghouse were electrolyte-supported, before switching to cathode-supported designs [20]. However, with the advent of co-extrusion methods, amongst other fabrication techniques [23], which allowed for the manufacture of both the anode and electrolyte in the same step, anode-supported tubular assemblies, with better mechanical integrity, rose in popularity. Anode-supported assemblies also work well as planar stacks giving rise to high power densities, since the ORR is less electrochemically favoured than the HOR at typical operating temperatures. Since these anode-supported cells can be run at lower temperatures (with a thin electrolyte), oxidation-resistant alloys can be incorporated as interconnect materials [21].

Another design was devised in the early 1990s by Kendall *et al.* called the micro-tubular solid oxide fuel cell (MT-SOFC) [24], which tends to have macroscale characteristic lengths of millimetres. A significant gain from scaling down is the potential

for more rapid start-up and an increase in volumetric output power density. The micro-tubular design was afforded by the successful development of thin extruded YSZ tube supports, although anode-supported MT-SOFCs are now more common. Their large-scale applications often involve the harnessing of the heat generated, typically using a Stirling engine and they have better thermal cycling resilience and greater portability [24]. Fabricating tubular SOFCs of both length scales is typically more complex than for the planar design, although extrusion is a conventional route. It is worth noting that, as with other electrochemical technologies, each application has a certain set of requirements that may be met by different manifestations of the same technology; here, we focus only on planar SOFCs, but both macro- and micro-sized tubular SOFCs also have multiple applications.

1.1.2.1 Materials

Numerous constraints are placed upon the selection of materials for the main three components of SOFCs (anode, electrolyte, cathode), principally due to their high operating temperature. For instance, modern electrode materials must comprise both electronic and ionic conductors in order to maximise the degree to which the TPB extends from the electrode-electrolyte interface into the electrode. This optimisation of the active reaction region may be realised by use of a composite material, or by using materials classed as mixed-ionic-electronic conductors (MIECs) [25][26].

Importantly, the electrolyte employed in the middle of an SOFC must provide an ionic pathway but at the same time, must not allow the ready flow of electrons, as this would ‘short-circuit’ the cell. The following sections highlight some key properties required of candidate SOFC materials and underline the significance of a long-standing material combination selected for use in HT-SOFCs.

There are several roles that a successful oxide-ion-conducting electrolyte must fulfil in a high-performance SOFC. Firstly, it must have high oxide-ion conductivity, preferably greater than 0.1 Scm^{-1} [27] in both reducing and oxidising environments. At the same time, the material must possess negligible electronic conductivity to prevent short-circuiting and thus inherent voltage losses. Secondly, to prevent reactant

cross-over, the selected material must be fully dense, such that no porosity percolates from one side to the other and its thermal expansion coefficient (TEC) must closely match that of its adjacent components. Finally, the candidate must display good thermal and chemical stability with regards to both the fuel and oxidant gases [28]. If possible, it is also advantageous to have a cheap fabrication route for access to relatively thin membranes in electrode-supported assemblies. Studies have shown that an optimal thickness for the electrolyte in an anode-supported assembly is in the region of 8 – 15 μm [29] for operation around 800 °C with hydrogen, at typical current densities.

In both IT- and HT-regimes, the higher temperatures allow for the use of a solid ceramic electrolyte whose ionic conductivity is enabled by an oxide-ion/vacancy hopping mechanism [30][31]. This process is thermally activated, and hence ionic conductivity in these ceramics increases with temperature. SOFCs benefit from the fact that there are no corrosive liquids nor solutions involved in the system, such that the electrolyte need not be regularly replaced. There is little upkeep required due to a lack of moving parts; the solid barrier between oxidant and fuel inhibits combustion and reactant mixing (at least in most planar set-ups) and the electrolyte may be used to impart sufficient mechanical stability for long-term operation.

The most prominent example of an electrolyte material that has been successfully employed in HT-SOFCs is yttria-stabilised zirconia – either as an 8 mol% (8YSZ) or a 3 mol% (3YSZ) compound [32]. Pure zirconia, or zirconium (IV) oxide, can be found in 3 polymorphs: monoclinic-ZrO_2 below 1443 K; tetragonal-ZrO_2 between 1443 and 2543 K; and in a cubic form above 2643 K. By doping the material with yttria, or yttrium (III) oxide (Y_2O_3), the cubic polymorph may be stabilised down to room temperature which adopts the fluorite structure [33]. Due to the discrepancy in oxidation state between the aliovalent Y^{3+} and native Zr^{4+}, the ceramic material contains vital oxygen anion vacancies. These vacancies are theorised to impart relatively high ionic conductivity (0.1 - 0.18 Scm^{-1} at 1000 °C and 0.03 - 0.05 Scm^{-1} at 800 °C [27][34]) to the lattice. The greatest oxide-ion conductivity is seen when the doping cation is closest in ionic radius to the native cation [28], which is Sc^{3+} in the case of the zirconia-based electrolytes [35].

However, the low cost and wide availability of yttrium over scandium makes the former more economically sound, and scandium's long term stability is less understood [34].

Introducing increasing amounts of yttria does not increase the electrolyte's ionic conductivity (σ_{ion}) indefinitely; there is an upper limit. This occurs as a result of the play-off between carrier concentration (c) and carrier mobility (u) as delineated in Equation *1-5* [17].

$$\sigma = (|z|F)cu \qquad 1\text{-}5$$

To begin with, the carrier concentration is increased with doping, but due to complex defects arising from interactions between oxide vacancies and dopant cations, and possibly Y_2O_3 segregation and accumulation at grain boundaries [36][37], the average mobility decreases after a certain point. This can be seen in the graph below of log(σT) versus $\%Y_2O_3$:

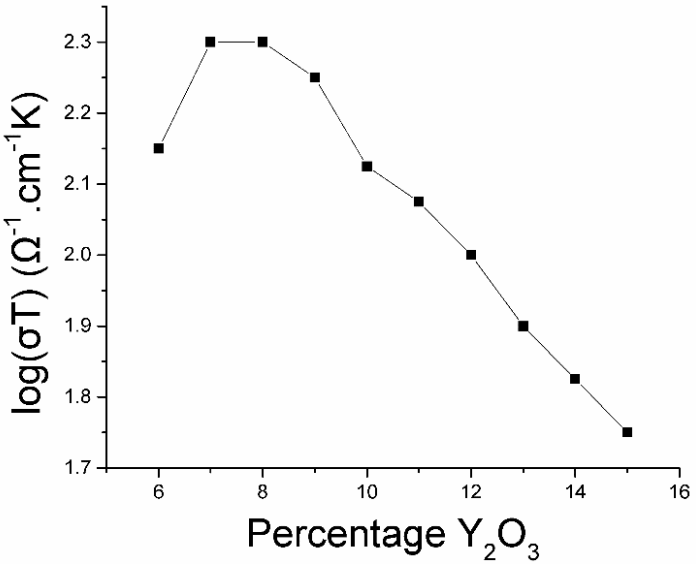

Figure 7: YSZ conductivity versus $\%Y_2O_3$ (molar basis) from [17]

The mobility of an ion is related to the solid's diffusivity for that ion ($D_{s,ion}$) by Equation *1-6*, such that its conductivity can be written as Equation *1-7*:

$$u = \frac{|z|FD_{s,ion}}{RT} \qquad 1\text{-}6$$

$$\sigma = \frac{c(|z|F)^2 D_{s,ion}}{RT} \qquad 1\text{-}7$$

Due to the "hopping mechanism" which affords the conductivity in yttria-stabilised zirconia, oxide-ion mobility in YSZ shows an Arrhenius-type dependence on temperature, characterized by $D_{s,O^{2-}}$:

$$D_{s,O^{2-}} = D_{s,0} exp(-\frac{\Delta G_{act}}{RT}) \qquad 1\text{-}8$$

where $D_{s.0}$ represents the attempt frequency and ΔG_{act} is the activation energy

By substituting the solid's diffusivity for the oxide ion (Equation *1-8*) into the equation for its conductivity (Equation *1-7*), a more complete expression is given for the conductivity of oxide ions in SOFC electrolytes (Equation *1-9*):

$$\sigma_{O^{2-}} = \frac{c(|z|F)^2 D_{s,0} exp(-\frac{\Delta G_{act}}{RT})}{RT} \quad 1\text{-}9$$

Steele developed an approach accounting for both thickness and ionic conductivity for a range of materials so as to gauge the appropriate temperature of operation for a given desired power density [18]. This method assumed an area-specific resistance (resistance multiplied by cross-sectional area) of 0.15 Ωcm^2 as sufficiently low to give acceptable performance, and materials constraints at the time granted an electrolyte thickness only as small as 15 μm, giving a specific ion conductivity threshold of 10^{-2} Scm^{-1}. Figure 8 displays his findings based on this model which highlight that 8YSZ requires a higher temperature (>700 °C) to give reasonable performance compared with gadolinia-doped ceria (CGO) (>500 °C).

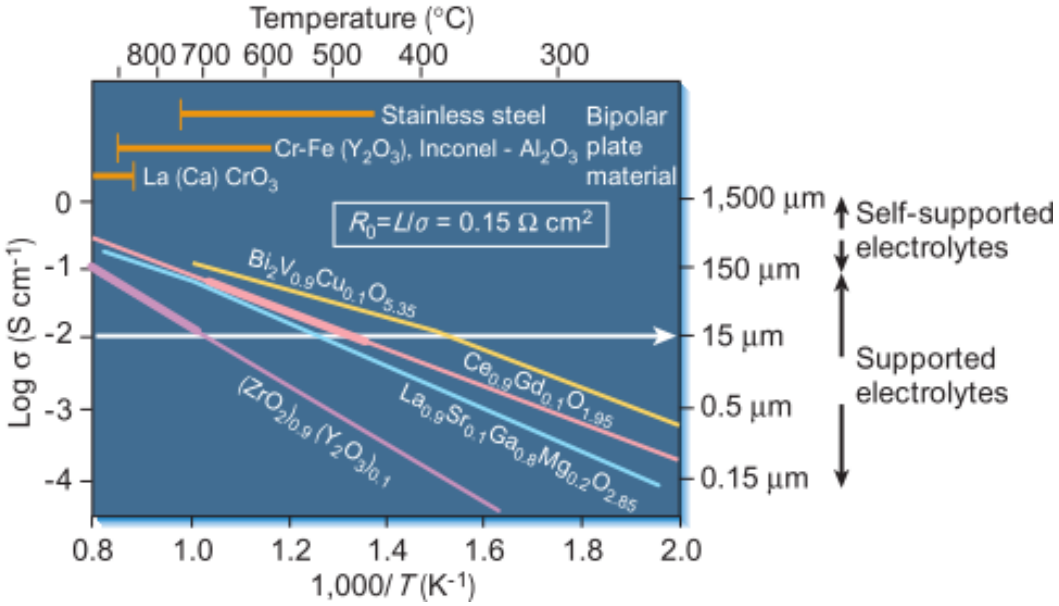

Figure 8: Plot of suitable electrolyte materials at various temperatures, reproduced with permission from [18]

Ceria (CeO_2) doped with divalent alkaline earth or trivalent rare earth cations [28] is also seen widely in IT-SOFC analogues. Pure ceria adopts the fluorite structure and

again there is substantial oxide-ion conductivity as a result of the aliovalent dopants inducing oxide vacancies. Samarium (III) and gadolinium (III) are the most suitable aliovalent dopants due to the matching of their ionic radii to that of the host ions. Although gadolinium-doped ceria (CGO) is the most popular choice for IT-SOFCs, it does suffer from a variety of issues, such as becoming a mixed conductor in the reducing environment of the anode since the low pO_2 atmosphere and high temperatures allow for reduction of some cerium (IV) to cerium (III). This reduction gives rise to an increase in electronic conduction, thus defining the operating temperature regime applicable to these IT-SOFCs as below ~600 °C. Aside from this increase in electronic conductivity, there is also a mechanical issue due to lattice volume expansion that occurs due to the reduction in charge density. A possible solution to these issues comes in the form of a thin protective layer of YSZ so as not to expose the CGO to the harshly reducing atmosphere [27]. Other materials with potential in IT-SOFCs are lanthanum strontium gallium manganite, $La_{0.9}Sr_{0.1}Ga_{0.8}Mg_{0.2}O_3$ (LSGM) and doped bismites (Bi_2O_3).

The cathode in HT-SOFCs must also display several properties to perform successfully in the cell and effectively promote the ORR, as described in Equation *1-10*:

$$\frac{1}{2}O_{2(gas)} + 2e^-_{(cathode)} \rightarrow O^{2-}_{(electolyte)} \qquad 1\text{-}10$$

As the ORR occurs close to the TPBs in the cathode, the electrode must be porous as well as catalytic for the reduction of oxygen molecules, able to conduct oxide ions, and, crucially, suitably conductive to electrons. Consequently, typical cathodes either constitute porous composites of electron- and ion-conducting materials or porous single materials known as mixed-ionic-electronic-conductors (MIEC) (Figure 9). In MIEC materials, the standard nomenclature of triple-phase boundary becomes redundant, and the entire interface between the solid material and the pore space is rendered electrochemically active.

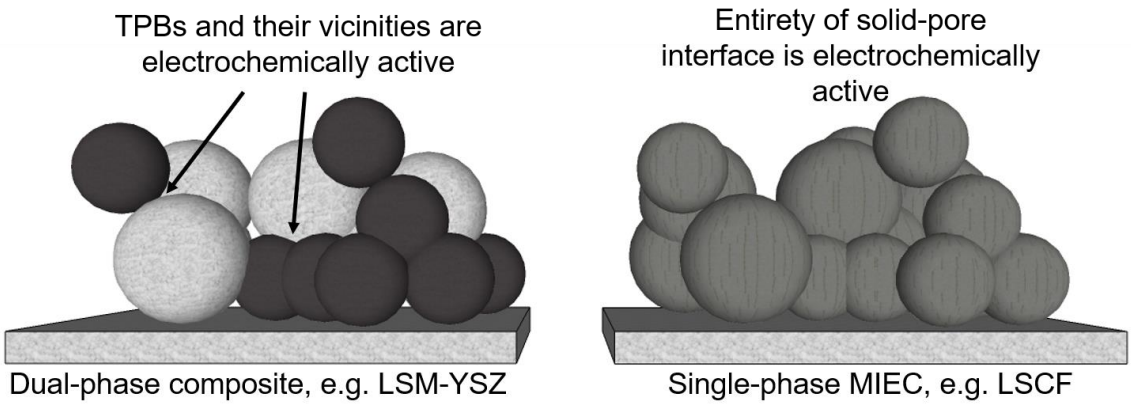

Figure 9: Schematic of two approaches to producing porous cathode materials

Other than high ORR catalytic activity, and an electronic conductivity of preferably > 100 Scm^{-1} [38], the cathode must be chemically stable in a highly oxidising (and potentially reducing) atmosphere and have a TEC compatible with its adjacent components. The most common material family that meets these demands is the doped lanthanum manganites ($La_{1-x}A_xMnO_{3\pm\delta}$), usually combined with YSZ to give the requisite microstructural and conductivity profiles. Typical dopants include Sr^{2+} and Ca^{2+}, giving rise to conductivity by oxygen non-stoichiometry (surplus or deficiency). As a result of the similar ionic radius of Sr^{2+} and La^{3+} (1.44 versus 1.36 Å [39]), strontium-doped lanthanum manganite (LSM), often with a stoichiometry of $(La_{0.8}Sr_{0.2})_{0.95}MnO_{3-\delta}$, is the archetypal HT-SOFC cathode material. LSM belongs to the perovskite family and has an electronic conductivity of approximately 200 – 300 Scm^{-1} at typical operating temperatures [27]. Alternatively, a typical single-phase MIEC cathode material family employed is the lanthanum strontium cobalt ferrites (LSCF) which has high electronic conductivity (> 200 Scm^{-1}) and good ionic conductivity (0.2 Scm^{-1}) [27].

A major degradation pathway followed by SOFC cathodes is the progressively worsening poisoning by volatile chromium species when Cr-containing alloys are employed as interconnect materials [40], typically leading to the formation of Cr_2O_3 at the cathode/electrolyte interface. This performance-limiting phenomenon associated with metallic interconnects is an example of a disadvantage associated with replacing traditional $LaCrO_3$ interconnects with chromium metal alloys when temperatures are lowered. Nevertheless, the substantial advantages offered, such as higher electrical

conductivity, higher mechanical stability and lack of oxygen permeation mean that overcoming chromium volatization is of vital significance to the community developing IT-SOFCs.

Another issue subject to research efforts has been a degree of incompatibility between YSZ and LSM that gives rise to unwanted product formation, such as the appearance of $La_2Zr_2O_7$ or $SrZrO_3$ at interfaces and grain boundaries. Unfortunately, these phases are electronically insulating so can not only block ORR activity but also hinder electronic conductivity in the cathode. Possible solutions are either to maintain low fabrication temperatures or to ensure that an appropriate amount of Sr ($0 < x < 30$ mol%) is substituted to minimise the production of either of the insulating phases. Several reviews provide further understanding of the role of SOFC cathode materials and their degradation pathways [40][41][42][43].

The anode is where the HOR takes place, as characterised by Equation *1-11*, and must meet several criteria to deliver high electrochemical performance.

$$H_{2(gas)} \rightarrow \ 2H^{+}_{(anode)} + \ 2e^{-}{}_{(anode)} \quad 1\text{-}11$$

As in the cathode, the anode must be porous to provide a route for mass transfer of both reactants and products, in and out of the cell. A dual-phase composite approach is most common, typically constituting a composite of metallic and ceramic components. The anode must have high electronic conductivity, sufficient electrocatalytic activity for the HOR, be chemically stable in a highly reducing environment and be appropriately matched in TEC with adjacent components to minimise mechanical issues [44].

Historically, several different metallic materials have been investigated for SOFCs, initially in single-phase form, in an attempt to meet the above requirements. Metals were possible candidates since the anode is predominantly in a highly reducing atmosphere [45] whereas for the cathode, metals are effectively ruled out due to the highly oxidising environment. Above all, the surface of the chosen material or a component therein was required to have a high catalytic activity for the HOR, which although not completely characterised, is now thought to involve the physisorption of hydrogen (Equation *1-12*), its dissociative chemisorption giving two separately-bound

hydrogen atoms on the nickel surface (Equation*1-13*), followed by charge transfer which releases the resultant protons (Equation *1-14*) [17]. Moreover, the candidate material had to be amenable to hydrocarbon-reforming to allow the SOFC to run on natural gas, amongst other carbon fuels.

$$H_{2\,(pore)} \rightarrow H_{2\,(electrode)} \qquad 1\text{-}12$$

$$H_{2\,(electrode)} \rightarrow 2H_{ads} \qquad 1\text{-}13$$

$$Ni - H \rightarrow Ni + e^{-} + H^{+} \qquad 1\text{-}14$$

Selection was limited primarily to nickel, cobalt and the noble metals (e.g. Pt, Ru) since the material had to be stable to oxidation in the more oxidising conditions of H_2O/H_2 found towards the fuel outlet or when fuel is interrupted [46]. Nickel was found to have the highest electrochemical activity towards the HOR when studied against platinum, graphite and other transition metal catalysts [47]. Nickel also catalyses the reforming of methane, though coking (carbon deposition) causes significant anode degradation (see **Section 1.5.1**) and loss of fuel cell performance unless conditions are optimised to inhibit it [48][49]. Nickel is also cheaper and more abundant than platinum with a slightly higher electronic conductivity and hence nickel presented a sensible alternative to the expensive platinum found in low-temperature PEM fuel cells. Nevertheless, both mechanical and micro-structural problems arose from the selection of nickel, not least because of its high TEC of 16.9 x 10^{-6} K^{-1} [50], relative to approximately 10.5 x 10^{-6} K^{-1} for YSZ [44][51]. The morphological changes associated with holding nickel metal at high temperatures also degrade electrochemical performance and represent a primary focus of this thesis.

To give mechanical stability to the porous structure and mitigate the mismatch in TEC, the most commonly employed material as a HT-SOFC anode is a cermet (ceramic-metallic) material comprising a combination of nickel metal and YSZ ceramic, originally introduced by Spacil [52]. The ceramic network helps to inhibit the natural tendency for metallic nickel to coarsen at elevated temperatures by allowing the nickel to partially wet the hard, percolating ceramic surface, though the adhesion is less than ideal. Additionally, the presence of YSZ leads to a greater electrochemically active region

as the TPBs, instead of occupying only part of the 2D pseudo-planar interface between electrode and electrolyte, extend into the electrode in a 3D active region. In a bulk sense, the inclusion of YSZ in the anode allows access to a material with a TEC more aligned with that of the pure YSZ electrolyte. During fabrication, the TEC of a NiO-YSZ composite is much more aligned with that of the YSZ electrolyte (~12.3 x 10^{-6} K^{-1} for 52% NiO [50] versus 10.5 x 10^{-6} K^{-1} [51]) and moreover the approximate average for a 40 vol% Ni-YSZ cermet is 11.5 x 10^{-6} K^{-1} value (50 - 1000 °C [50]), which is far below the pure Ni value of ~17 x 10^{-6} K^{-1} (Figure 10).

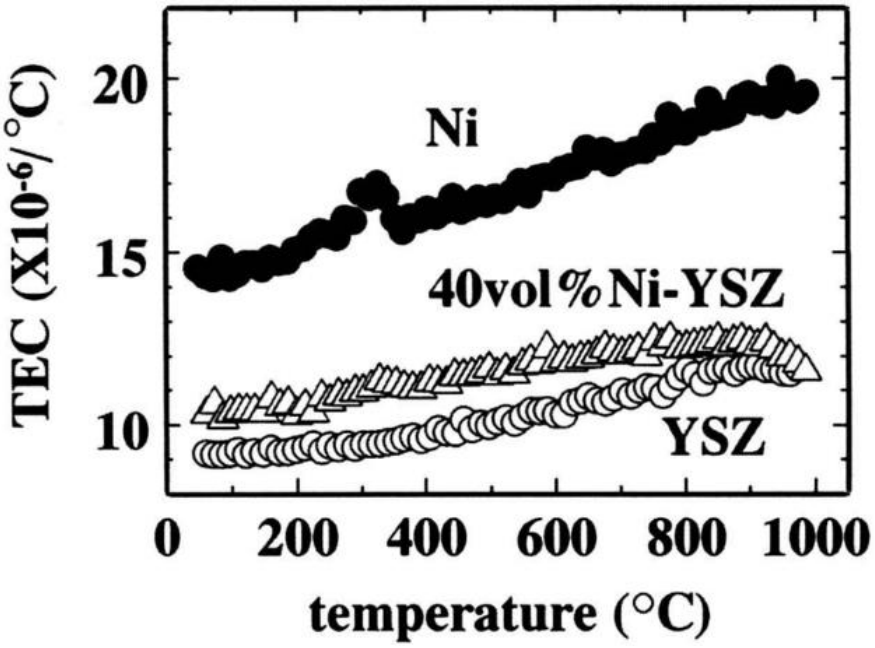

Figure 10: TEC of pure YSZ, pure Ni and 40 vol% Ni-YSZ composite, reproduced with permission from [50]

The majority of HT-SOFCs have therefore been developed with porous Ni/YSZ anodes, and in the case of IT-SOFCs, often a composite of Ni and gadolinia-doped ceria (Ni-CGO) is used along with a CGO electrolyte which has a sufficiently high ionic conductivity at lower temperatures. Nonetheless, these IT-SOFC materials do suffer other challenges, such as appreciable n-type electronic conductivity and lattice expansion in reducing conditions above approximately 600 °C [28] due to the partial reduction of Ce^{4+} to Ce^{3+}. In this thesis, solely the archetypal HT-SOFC anode material, Ni-YSZ, is investigated.

The modern anode usually comprises two distinct layers in an anode-supported assembly to account for different key performance criteria; a thin anode functional layer

(AFL) that is directly adjacent to the YSZ electrolyte and a thicker, coarser anode support layer (ASL) (Figure 11) that effectively behaves as the current collector and interim gas diffusion network. The fine microstructure of the AFL provides a high density of TPB lengths, thus maximising electrochemical activity, and the ASL contains larger particles that act as the mechanical support for the cell whilst providing a rigid skeleton to a porous network for facile migration of reactant and product species.

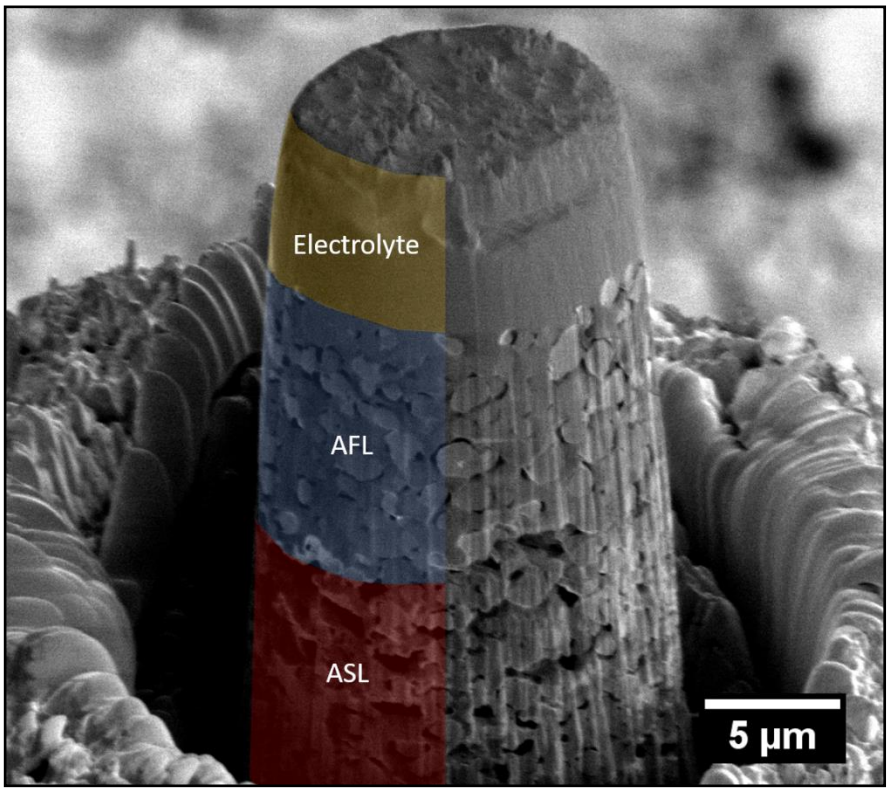

Figure 11: SEM micrograph of an SOFC electrolyte/anode pillar illustrating the various layers of an SOFC half-cell (electrolyte, AFL and ASL)

The Ni/YSZ anode contains two inter-penetrating solid networks, the metallic nickel phase which is electronically-conducting but ionically-insulating and the ceramic YSZ phase which even at high temperatures only conducts ions (O^{2-}). As a result, the proportions of each phase play a pivotal role in the charge transport processes across the electrode thickness; the compositional balance between nickel and YSZ impacts the anode's conductivities and the depth of the active region with respect to its interface with the electrolyte. Literature investigations into the impact of Ni/YSZ ratio, particle size and anode thickness are explored in **Chapter 2**.

One of the great advantages of SOFCs over other fuel cell types is their fuel versatility and if a hydrocarbon fuel such as natural gas (predominantly methane) is used,

the anode material must also be: catalytic towards hydrocarbon reforming (Equations *1-15 – 1-17*); have reasonable sulfur tolerance; and be resistant to coking (Equations *1-18 – 1-20*).

Desirable Reactions:

Reforming: $CH_4 + H_2O \rightarrow CO + 3H_2;$ *1-15*

Water-gas shift: $CO + H_2O \rightarrow CO_2 + H_2;$ *1-16*

Overall: $CH_4 + 2H_2O \rightarrow CO_2 + 4H_2$ *1-17*

Undesirable Reactions:

Cracking: $CH_4 \rightarrow 2H_2 + C;$ *1-18*

Reduction: $2CO \rightarrow CO_2 + C;$ *1-19*

Boudouard reaction: $CO + H_2 \rightarrow H_2O + C$ *1-20*

Nickel catalyses both reforming of hydrocarbons and carbon deposition reactions, but the balance depends on a variety of factors, including temperature, Ni/YSZ ratio and steam-to-carbon ratio [53]. Carbon deposition is explored in **Section 1.5.1.** but for the purposes of this thesis, operation is limited to hydrogen only, to avoid convolution of multiple degradation mechanisms.

1.1.2.2 Fabrication

For traditional electrolyte-supported HT-SOFCs, fabrication typically constitutes a mixture of NiO and 8YSZ powders in an aqueous slurry, slip-cast or screen-printed onto a pre-sintered dense electrolyte. For the common electrode-supported assemblies, the YSZ electrolyte is applied using thin film techniques onto die-pressed or tape-caste NiO-YSZ anodes, followed by the addition of the other electrode. These thin film processes can involve a range of complex techniques, including: chemical vapour deposition (CVD) [54]; electrochemical vapour deposition (EVD) [55][56]; physical vapour deposition (RF-/Magnetron-sputtering) [57]; spray pyrolysis [58]; pulsed laser deposition [59]; or the sol-gel method [60]. Similarly, more traditional processing routes for ceramic powders such as screen-printing, tape-casting, slurry coating, tape calendaring or electrophoretic deposition are often used. For a comprehensive review and examples of the wide range of fabrication procedures used, see [61].

If powder processing techniques are followed, the necessary sintering step of the initial NiO-YSZ “green body” usually entails heat treatments of 1350-1400 °C [62][63], resulting in the desired densification but some initial nickel coarsening. The following step is a reduction in hydrogen or forming gas at approximately 800 °C [64] to convert nickel oxide to nickel, thus imparting desirable porosity to the cermet for gas transport and endowing the anode with electrochemically active sites for the HOR.

Other than the IT-SOFC alternative material set (Ni-CGO cermet/CGO electrolyte), other materials with very low to no metal content have also been candidates. Such materials include lanthanum chromites (also used as an interconnect material), strontium titanates and fluorite-structure ceria materials without interspersed metal particles, due to their MIEC properties. However, only the traditional HT-SOFC materials, Ni-YSZ/YSZ, are the focus of this thesis.

1.2 Performance

1.2.1 Efficiency

The overall cell efficiency, $\eta_{overall}$, for an SOFC (or any other fuel cell) is given by the product of its reversible/thermodynamic efficiency, $\eta_{reversible}$, its voltage/practical efficiency, $\eta_{voltage}$, and its fuel utilisation efficiency, η_{fuel}, as given by Equation *1-21* [18]:

$$\eta_{overall} = \eta_{reversible} \times \eta_{voltage} \times \eta_{fuel} \quad 1\text{-}21$$

In this section, a brief overview of the nature of these efficiencies is given before a more in-depth examination of the thermodynamics and kinetics that affect fuel cell performance.

1.2.2 Reversible Efficiency

The reversible efficiency is associated with the theoretical maximum potential for useful work that can be thermodynamically derived from the chemical reactions occurring in the full cell. This may be summarised as the quotient of the amount of useful energy extracted and the total energy evolved by the process [17], as shown in Equation *1-22*:

$$\eta_{reversible} = \frac{useful\ energy}{total\ energy} \quad 1\text{-}22$$

In the case of a fuel cell (stack), the useful energy extracted may be interpreted in different ways, but for the purposes of understanding its electrical output, the useful

energy output is the electrical work performed and the total energy available is given by the total energy involved in the reaction of the fuel and oxidant.

1.2.3 Voltage Efficiency

The voltage efficiency of a fuel cell is the deviation from the theoretical efficiency categorised by thermodynamics. Specifically, the voltage efficiency accounts for the irreversible kinetic effects that lead to losses in voltage, relative to that expected from $\eta_{reversible}$, due to unavoidable processes which occur during operation. These losses are often characterised by their cause and point of cell operation. Three distinct losses are typically discussed: activation losses, which dominate at the low current density, ohmic losses, which tend to result in a linear drop in voltage at intermediate current densities and mass transport/concentration losses which are associated with drawing high current densities (Figure 12). Each of these losses or "polarisations", are discussed in **Section 1.4**.

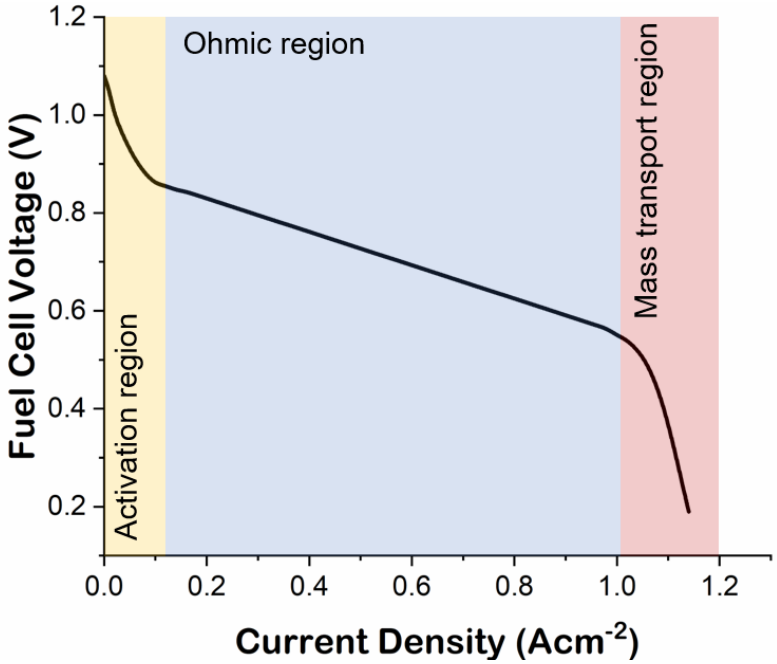

Figure 12: Generic fuel cell current density-voltage (j-V) curve

1.2.4 Fuel Efficiency

This aspect of the overall cell efficiency represents the portion of the actual fuel supplied that takes part in the electrochemical reaction (HOR), accounting for the fact that some unspent fuel is exhausted. It also incorporates any fuel that undergoes side reactions which do not produce useful electrical energy [17]. The implications of fuel utilisation are discussed in **Section 1.4.4**.

1.3 Thermodynamics

1.3.1 Standard-state Reversible Voltage

Thermodynamics explains the relationship between the energy available from the combination of fuel and oxidant, and the current that can be drawn from the redox processes involved. A brief treatment explaining the underpinnings of this relationship is given here. The 1st Law of Thermodynamics (Equation *1-23*) relates the internal energy, *U*, to heat transfer and work done. The 2nd Law (Equation *1-24*) connects entropy with heat and temperature.

$$dU = dq - dw \qquad 1\text{-}23$$

where q *is the heat transferred to the system and* w *is the work done by the system*

$$dS = \frac{dq_{rev}}{T} \qquad 1\text{-}24$$

where S *is entropy (level of disorder) and* T *is temperature*

Equation *1-23* can be developed to include both mechanical and electrical work:

$$dU = dq - pdV - w_{elec} \qquad 1\text{-}25$$

where p *is pressure and* V *is volume*

Importantly for fuel cells, entropy can be thought of as a measure of the amount of thermal energy that cannot be harnessed as work. This gives a new equation for the change in internal energy of the system, Equation *1-26*.

$$dU = TdS - pdV - w_{elec} \qquad 1\text{-}26$$

The enthalpy (*H*) of a system describes the energy needed to bring it about (internal energy, *U*, and make space for it, *pV*) a change in enthalpy is given by:

$$dH = dU + Vdp + pdV \qquad 1\text{-}27$$

$$dH = TdS + Vdp - w_{elec} \qquad 1\text{-}28$$

The Gibbs free energy (*G*), defines a system in terms of its enthalpy and entropy (*G* = *H* – *TS*), and the change in Gibbs energy can be described by changes in temperature and pressure:

$$dG = dH - TdS - SdT = Vdp - SdT - w_{elec} \qquad 1\text{-}29$$

Thus, at fixed temperature and pressure, this provides a direct link between the Gibbs free energy change of a system and the total available energy in the form of electrical work:

$$dG = -w_{elec} \qquad 1\text{-}30$$

The Gibbs free energy change describes the amount of useful energy available in a system to perform non-expansion (electrical) work. w_{elec} can be written as the product of charge (Q) that moves across an electrical potential difference (E):

$$dG = -QE \qquad 1\text{-}31$$

The amount of charge in the electrochemical cell reaction of a fuel cell depends on the number of electrons transported (n), and the charge can be described in molar terms by use of Faraday's constant (F = 96485 $Cmol^{-1}$), that is, the amount of charge per mole of electrons:

$$dG = -nFE \qquad 1\text{-}32$$

This means, as an alternative to finding the difference in electrode potentials (**Section 1.1.2**), the Gibbs energy change associated with the electrochemical combination of H_2 and O_2 (2-electron process) can be used to calculate the maximum theoretical cell voltage:

$$H_2 + \frac{1}{2}O_2 \rightarrow H_2O \text{ (1-4)} \quad \Delta G_{rxn} = -237 \text{ kJmol}^{-1}$$

$$-237000\ Jmol^{-1} = -(2) * 96485\ Cmol^{-1} * E$$

$$E = +1.23\ V$$

However, it should be noted that this value for the Gibbs energy change is to produce liquid water, as opposed to gaseous water (steam) which is more appropriate for SOFCs. The production of steam is accompanied by a slightly less negative Gibbs free energy change (-229 $kJmol^{-1}$), giving a theoretical maximum E = +1.18 V.

When assessing the reversible efficiency, $\eta_{reversible}$, it is important to state the selection of the appropriate enthalpy of reaction, again depending on the physical state of the product water. There is more heat recoverable if the product is liquid water, giving

a higher heating value (HHV) of ΔH_{HHV} = -286 kJmol^{-1}, as opposed to the lower heating value (LHV) of ΔH_{LHV} = -241 kJmol^{-1} which is associated with steam production. For a more equitable calculation of the efficiency of a fuel cell, the HHV should be employed, acknowledging that there is more recoverable heat from the hydrogen fuel than perhaps is amenable to SOFC operation [17].

As a result, the maximum theoretical efficiency of an SOFC, at SSCTP, with no irreversible losses and full fuel utilisation is:

$$\eta_{reversible} = \frac{-229\ kJmol^{-1}}{-286\ kJmol^{-1}} = 80\%$$

This calculation is theoretical as no SOFC can run at 298 K, and in fact, many alterations to this reversible voltage need to be made to account for non-standard-state conditions.

1.3.2 Non-standard Temperature and Pressure

It is important to assess the impact of temperature on the cell voltage, as SOFC operation tends to be between 500 and 1000 °C and cells are never run at SSCTP, as the ionic conductivity of the electrolyte is too low at 25 °C. At fixed pressure, the dependence of Gibbs free energy change on temperature is defined as in Equation *1-33*:

$$\left(\frac{d(dG)}{dT}\right)_p = -dS \quad 1\text{-}33$$

Using Equation *1-34*, this gives the reversible cell voltage as a function of temperature:

$$\left(\frac{dE}{dT}\right)_p = \frac{dS}{nF} \quad 1\text{-}34$$

Given a fixed dS_{rxn} of -44.34 Jmol^{-1}K^{-1} for the production of steam [17], it can be shown that for every 100 °C of temperature increase, the reversible cell voltage drops by ~23 mV giving a reversible cell voltage of ~1.00 V for an SOFC running on H_2 at 800 °C.

The same process can be applied to inspect the impact of non-standard pressure on the reversible cell voltage; instead of entropy change, it is volume change that represents the dependence of cell voltage on pressure, as shown in Equation *1-35*:

$$\left(\frac{d(dG)}{dp}\right)_T = dV \quad 1\text{-}35$$

Using Equation *1-36* and the ideal gas law, this gives the reversible cell voltage as a function of pressure:

$$\left(\frac{dE}{dp}\right)_T = -\frac{dV}{nF} = -\frac{dn_g RT}{nFp} \qquad 1\text{-}36$$

where dn_g *is the change in number of moles of gas*

Given a fixed $dn_g RT$ of -4460.46 J for the production of steam at 800 °C, it can be shown that an increase from 1 to 3 atm corresponds to an increase in cell voltage by ~21 mV, such that increasing pressure has the opposite effect on the reversible voltage to increasing temperature.

1.3.3 Reversible Voltage at non-standard concentration

Most importantly, the concentration of reactant and product species plays a role in determining the reversible cell potential. Defining the chemical potential as the Gibbs energy change accompanying an infinitesimal change in the quantity of a species *i* (Equation 1-37):

$$\mu_i = \left(\frac{dG}{dn_i}\right)_{T,p,n_{j\neq i}} \qquad 1\text{-}37$$

The chemical potential of a species *i* is given by Equation *1-38*:

$$\mu_i = \mu_i^0 + RT ln a_i \qquad 1\text{-}38$$

where μ_i^0 *is the reference chemical potential of species* i *and* a_i *is its activity*

By combination of Equations *1-37* and *1-38*:

$$dG = \sum_i \mu_i \, dn_i = \sum_i (\mu_i^0 + RT ln a_i) \, dn_i$$

$$dG = dG^0 + RT ln \prod_i a_i \qquad 1\text{-}39$$

Using Equation *1-39* to link the change in Gibbs energy to the cell potential yields the Nernst Equation (Equation *1-40*), which gives Equation *1-41* for the H_2-O_2 reaction of interest:

$$E = E^0 - \frac{RT}{nF} ln \prod_i \frac{a_{products}^{v_i}}{a_{reactants}^{v_i}} \qquad 1\text{-}40$$

$$E = E^0 - \frac{RT}{nF} ln \frac{a_{H_2O}}{a_{H_2} a_{O_2}^{0.5}} \qquad 1\text{-}41$$

The Nernst equation accounts for both concentration (activity) and pressure, but it does not fully account for temperature. Equation *1-42* considers all these parameters at once:

$$E = E^0 + \frac{dS}{nF}(T - T_0) - \frac{RT}{nF} ln \prod_i \frac{a_{products}^{v_i}}{a_{reactants}^{v_i}} \qquad 1\text{-}42$$

1.4 Kinetics

Fundamentally, electrochemical reactions involve the transfer of electrons between an electrode and an adjacent chemical species, a thermodynamically favourable process for fuel cell reactions, whose kinetics must be understood to assess the irreversible losses implicit in current generation. The full cell reaction involving the combination of hydrogen and oxygen gases takes place at two separate interfaces in the fuel cell, with the HOR occurring at the anode and the ORR taking place at the cathode. Both of these half-cell reactions are thermodynamically favourable, but also entail an energy penalty or activation barrier, as illustrated in Figure 13.

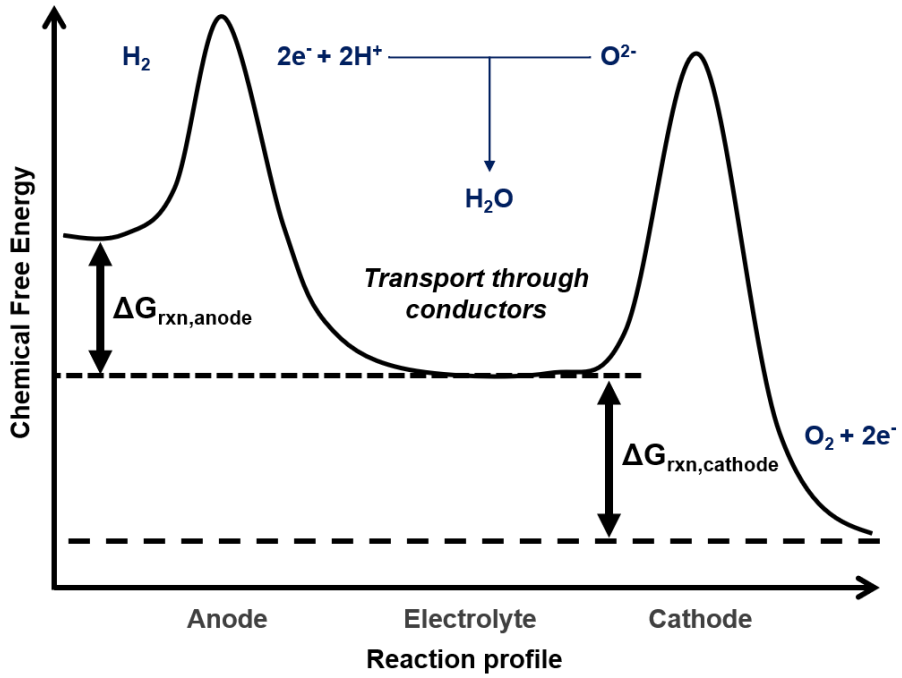

Figure 13: Reaction profile schematic for the combination of H_2 and O_2, from [17]

The thermodynamics of the process explain the ΔG_{rxn} terms in Figure 13, whereas the kinetics address the activation energy of the two half-cell reactions, as well as the transport of charge through conductors and the transfer of mass through the porous electrodes.

1.4.1 Activation Overpotential

The activation barriers to the HOR and ORR represent irreversible losses that occur when current is drawn. These losses are known as polarisations or polarisation losses, and if given as the corresponding voltages, as overpotentials. For the purposes of comparison between cells of different size, current, *i*, is often normalised per area and

given as the current density, *j*. Taking the HOR as an example, the electrochemical reaction consists of several elementary steps involving diffusion, adsorption and charge transfer. If the latter is taken as rate-limiting, an empirically-determined equation has been shown to model the relationship between *j* and overpotential, *η*, known as the Butler-Volmer equation (Equation *1-43*):

$$j = j_0\left(\frac{[A]_0}{[A]} exp\left(\frac{(1-\alpha)F\eta}{RT}\right) - \frac{[B]_0}{[B]} exp\left(-\frac{\alpha F\eta}{RT}\right)\right) \qquad 1\text{-}43$$

where j_0 *is the exchange current density,* α *is the transfer (symmetry) coefficient,* $[X]_0$ *&* [X] *are the concentration of* X *at the electrode interface & in the bulk, respectively*

The exchange current density is proportional to the rate of reaction at dynamic equilibrium, that is, when overpotential is zero. At this point, the forward and backward reaction rates and therefore current densities are equal in magnitude and opposite in sign. However, as current is drawn from the fuel cell, and the system moves away from equilibrium, irreversible losses in the form of activation overpotential are unavoidable. The relationship between absolute current density and overpotential for a generic electrode is shown in Figure 14, illustrating the effect of exchange current density on the behaviour.

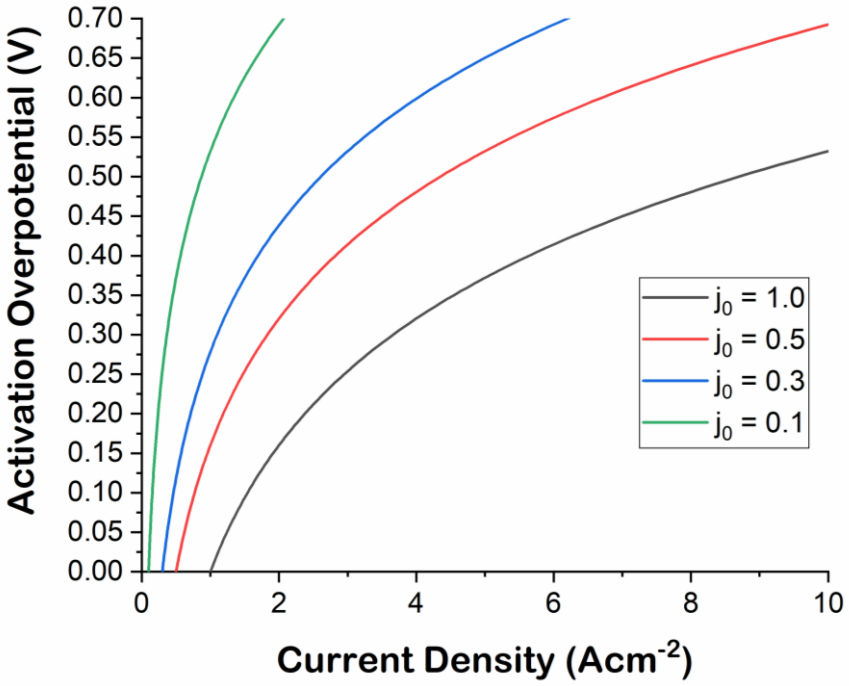

Figure 14: Plot of activation overpotential, given different exchange current densities, for a generic electrode (based on part of Butler-Volmer equation)

The total output current density (*j*) is the net result of the two individual contributions of the forward and backward reactions (Equation *1-43*), as shown in Figure 15. Disturbing the system from equilibrium results in net current flow and a penalty in the form of an overpotential (voltage loss), versus the reversible cell voltage.

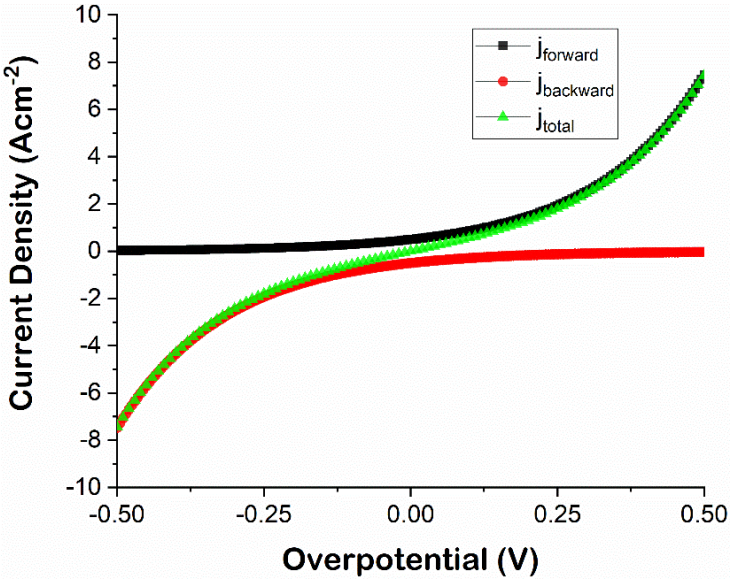

Figure 15: Plot of total, forward and backward current density versus activation overpotential

The *α* term is known as the symmetry factor or transfer coefficient, broadly representing the effect of changing the potential on the energy profile for the reaction. If the energy profile is symmetrical about the transition state (*α* = 0.5), the forward and backward activation energy barriers are affected equally by a potential change. If 0 < *α* < 0.5 or 0.5 < *α* < 1.0, however, the forward and backward reactions are affected unequally.

At high overpotentials, the Butler-Volmer equation can be approximated by the first term (Equation *1-44*). Taking the natural logarithm gives a linear equation that can be used to access the exchange current density, j_0, and the transfer coefficient, *α*, as shown in Equation *1-45*:

$$j_{tot} = j_0\left(\frac{[A]_0}{[A]} exp\left(\frac{(1-\alpha)F\eta}{RT}\right)\right) \quad 1\text{-}44$$

$$ln j_{tot} = ln\frac{j_o[A]_0}{[A]} + \left(\frac{(1-\alpha)F\eta}{RT}\right) \quad 1\text{-}45$$

At each electrode interface, with no current flowing, a dynamic equilibrium is established by the balancing of the chemical potential profile and its electrical

counterpart. The unequal forward and backward activation barriers means that initially there is a build-up of electronic charge – this accumulation proceeds until the resultant electrical potential difference across the reaction interface exactly counterbalances the chemical potential difference between reactants and products [17]. It is useful to be able to quantify these energy differences in combination, which is performed by the "electrochemical potential", as defined in Equation *1-46*:

$$\mu_{ec} = \mu_i + z_i F \varphi_i = \mu_i^0 + RT ln a_i + z_i F \varphi_i \qquad 1\text{-}46$$

where μ_{ec} *is the electrochemical potential and* φ_i *is the electrical potential of species* i

At equilibrium, the electrochemical potential is zero and the chemical and electrical potentials are equal in magnitude and opposite in sign. When the activation energy of forward reaction (oxidation of H_2 for the HOR and reduction of O_2 for the ORR) is lowered, it is equivalent to a sacrifice in the electrical potential difference at that interface (also known as a Galvani potential). As a result, current flows at the expense of a proportion of the Galvani potentials at both the anode and cathode, the latter of which tending to be greater than the former.

This activation overpotential, can be observed as a voltage loss with respect to the reversible fuel cell voltage. Due to the exponential nature of this activation, the current density-voltage (*j-V*) curve of a fuel cell includes an exponential contribution from η_{act} that manifests as a large contribution to overall overpotential at low current densities, and much less significant at medium and high current densities. Consequently, the first section of the *j-V* is known as the activation region, where this type of overpotential dominates (see Figure 12).

The activation losses arise from both the cathode and anode, although the oxygen reduction reaction (ORR) usually dominates. Key parameters that determine the exchange current density, j_0, include the concentration of the reactants, the activation energy of the reaction, and the number of possible sites at which the electrochemical reaction can occur, all of which can be optimised to increase j_0. Hence it is of utmost importance to make a good selection of catalyst to speed up these reactions, as well as designing the reaction zones appropriately to maximise surface area and reaction

efficiency. In terms of microstructure, this activation polarisation is directly affected by the distribution and activity of the TPBs, which is a key metric of interest when observing electrode microstructure and linking it to electrochemical behaviour.

1.4.2 Ohmic losses

At intermediate current loads, losses can be primarily ascribed to ohmic (resistive) losses that are associated with electrical resistance from various parts of each cell. The majority of this comes from the hindrance to charge transfer in the solid electrolyte, principally because it is more difficult for a relatively large and massive oxide ion to move through the ceramic lattice than for electrons to move through the metallic conduction band structure in electronically conducting media. There exists a loss in cell voltage (ohmic overpotential) as a result of the intrinsic resistance found in the components of the fuel cell, which increases with current density.

The current density is determined by the conductivity of and potential difference across a medium (Equation *1-47*). For an ideal uniform conductor of cross-sectional area, *A*, and length, *L*, the resistance can be estimated to be inversely proportional to the conductivity of the medium (Equation *1-48*):

$$j = \sigma \frac{dV}{dx} = \sigma \frac{V}{L} \qquad 1\text{-}47$$

$$V = \frac{jL}{\sigma} = \frac{iL}{A\sigma} = iR \qquad 1\text{-}48$$

$$R = \frac{L}{A\sigma} \qquad 1\text{-}49$$

Since this is the major contribution to η_{ohm}, anode-supported assemblies have been developed to have very thin electrolytes, on the order of 10 – 15 μm, to minimise the *L* term.

There are other contributions to the ohmic or series resistance which include: the electrode materials and their microstructures; the contacting interfaces between components; and the current-collecting interconnect materials and wires used to attach the cell to an external load. These losses can be minimised by selecting high electronic conductivity electrode materials with fully percolated electronic conducting networks, using interconnect materials which retain high electronic conductivity in both oxidising

and reducing atmospheres along with appropriately wiring and compressing the assembly to achieve minimal contact resistances. Nevertheless, ohmic losses are unavoidable and are the dominant contribution to overpotential in the intermediate region of current density (see Figure 12).

1.4.3 Concentration Overpotential

At higher current load density, the reactant gas at an electrode is depleted so quickly, and the product gas so abundant, that near the TPB, the reactant is not replenished fast enough, nor the product expelled quickly enough, for the requisite electrochemical process. This has the effect of introducing a mass transfer polarisation loss that can be seen at high current densities (right side of Figure 12), as the electrochemical reaction occurring at the catalyst in both electrodes may be affected by unsuitable concentrations of reactants and products. Furthermore, if the microstructure of the bulk electrode or the design of the flow field is such that the gaseous species cannot reach or escape from the active areas, this may represent another overpotential.

Using “fixed film electrodes” comprised of a porous ceramic support atop a redox-activated nickel thin film attached to a ceramic electrolyte, Nakagawa *et al.* identified the polarisation contribution from the thickness of the porous ceramic support, separate from the polarisation attributable to the nickel thin film [65]. It was clearly identified that the mass transport limitation manifests as a low frequency arc in electrochemical impedance spectroscopy (EIS), which involves probing the impedance response of the system by small AC perturbation signals. The higher frequency arc was attributed to the reaction occurring at the electrode/electrolyte interface and the high-frequency X-axis intercept represented the ohmic polarisation. Moreover, at low pH_2, it was shown that at high current densities, a sharp drop in potential is observed, highlighting that mass transfer effects are a convolution of microstructure and the prevalence of reactant and product species.

The consumption of the reactant and accumulation of the product at the TPB has two notable effects on cell performance, jointly termed the mass transport or concentration loss. Firstly, there is a Nernstian contribution as one would expect from Equation *1-40*,

such that the reversible fuel cell voltage is diminished by a lack of reactant and/or predominance of product. Furthermore, there is a concomitant increase in activation loss as the reaction rate is also dependent on these concentrations. Eventually the rate of diffusion of species matches their consumption/accumulation and a steady state is reached. The diffusion of the gaseous species cannot be treated simply by kinetic theory but must also take into account the porosity and tortuosity of the surrounding electrode. The porosity (ε) is defined as the ratio of the pore volume to the total volume and the tortuosity factor (τ) describes the relative difficulty of passing through a porous body with a convoluted pathway with respect to a simple rectilinear journey. As the predominant mass transport mechanism in the porous electrodes is diffusion, it is important to understand the electrode microstructure in terms of its porosity and tortuosity in order to establish the effective diffusivity of the reactant and product gases. Often, at high temperatures, a key equation (Equation *1-50*) for understanding the impact of porosity and tortuosity factor on gas diffusion is given by:

$$D_{ij}^{eff} = {}^{\varepsilon}/_{\tau} D_{ij} \qquad 1\text{-}50$$

where D_{ij}^{eff} *is the effective gas diffusivity,* ε *is the porosity,* τ *is the tortuosity factor and* D_{ij} *is the bulk gas diffusivity*

If a steady-state is reached, the diffusive fluxes across the electrode will match the consumption/production rates of the electrochemical reaction. However, if the fuel cell arrives at a state where the concentration of reactants falls to zero, this will be when the fuel cell delivers its maximum current, known as its limiting current, at which point, mass transport losses are maximised. This corresponds to the point furthest to the right on a *j-V* curve, where current density is maximised but at the expense of almost all of the voltage. The deviation from the linear ohmic polarisation is characterised by the mass transport efficiency, η_{mass}. As a result, the optimal operating point of a fuel cell, from an efficiency perspective, is not at maximum current density, but rather at maximum power density, where the best trade-off between current density and voltage is found.

1.4.4 Fuel Utilisation

Other than the reversible thermodynamic and irreversible kinetic constraints on the practical cell voltage when running a fuel cell, there is also an effective fuel utilisation efficiency to account for. This factor represents the fact that not all the fuel provided is used in the electrochemical reaction of interest; some exits the cell without reaction, and some may react but by a different route, without creating usable current. The fuel utilisation efficiency is the quotient of the fuel used to generate electricity and the total fuel supplied, as shown in Equation *1-51*:

$$\eta_{fuel} = \frac{i/nF}{\nu_{fuel}} \qquad 1\text{-}51$$

where ν_{fuel} is the rate of fuel supply

Fuel cells are usually run in one of two modes, either with constant stoichiometry or constant flow rate. At constant flow rate, the same amount of fuel is supplied, regardless of the current drawn, meaning that the efficiency is low at low current densities and approaches a maximum towards the maximum current density, from which its magnitude had been chosen. In the constant stoichiometry regime, the cell fuel supply reacts to the current drawn and the system is provided with a fixed excess. The ratio of the supply versus that which is required is known as the stoichiometric factor (λ) and under this regime, the fuel utilisation is independent of current density and thus the efficiency can be re-written as Equation *1-52*:

$$\eta_{fuel} = \frac{1}{\lambda} \qquad 1\text{-}52$$

1.5 Degradation Processes

Several degradation processes during the operation of SOFCs affect their performance, exacerbating the activation, ohmic and mass transfer losses discussed above, limiting their maximum power densities. Whether in the electrodes, electrolyte, interconnects or sealing materials, a vast number of chemical and physical processes curtail the durability of single cells and stacks alike. Here, a brief overview of the multiple degradation routes that plague the anode are explored.

During the lifecycle of a single SOFC Ni-YSZ anode, there are many potential instances where deleterious materials or processes may be introduced. The raw materials during fabrication may pose issues if their impurities are above certain critical thresholds, and the purity of fuel gases also plays an important role, particularly when running on carbonaceous fuels.

During operation, a typical SOFC anode will experience a variety of phenomena linked to thermal or load cycling that results from the start-up/shut-down as well as varying current demands. If the fuel supply is interrupted, or high current densities are drawn and pH_2O is elevated, nickel metal may undergo oxidation. This process and the subsequent reduction constitute a redox cycle which can cause microstructural degradation to the anode. Moreover, short- and longer-term irreversible microstructural changes can occur, separate from redox cycling, as a result of coarsening mechanisms which impact the connectivity and percolation of the cermet. The chemical, thermal and redox degradation phenomena are discussed briefly in this section, and the nature of the microstructural issues are introduced. **Chapter 2** then provides an in-depth literature review of the monitoring of microstructural evolution in cermet anodes.

1.5.1 Chemical

The two main routes by which impurities are introduced to a cermet anode are through the raw materials processed in its fabrication or by the accumulation of unwanted species from the incoming fuel. Of this latter type, two principal contamination mechanisms that have been identified are sulfur deposition and coking. Moreover, there is the potential for unwanted behaviours between cell components that are present by design, such as yttria segregation [66] towards grain boundaries in Ni-YSZ anodes.

Foreign phases found in the raw materials used to fabricate SOFC anodes may migrate, during production or operation, to the active interfaces that enable electrochemical reactions. Studies of a Ni-YSZ interface between a nickel wire and a polished piece of YSZ showed that after 200-300 h of heating in a reducing atmosphere at 1000 °C, a ridge of impurities formed [67]. The rim of this ridge contained mainly Si, Al, Na, Mn and K, as did other areas of contact. Impurities were also found on the nickel

wire, away from the contact area, suggesting the source of the contamination was in part from the raw nickel material. Nevertheless, SiO_2 was also shown to enrich the YSZ surface, particularly at grain boundaries where an enrichment of Y_2O_3 was also seen (by X-ray photoelectron spectroscopy (XPS)), suggesting impurities from both constituents play a role. Moreover, a different morphology, of hills and valleys, was observed at the contact area, whereas smooth structures were seen outside of this area.

Later work focused on the effects of raw material impurities on the microstructure of real Ni-YSZ electrodes, as opposed to a model system [68]. Two types of NiO were used, with different purity levels, and a durability test was performed of 1500 h at 850 °C with an anodic load of 0.3 Acm^{-2}. The anode polarisation was seen to increase abruptly after several hundred hours in the anodes with the higher percentage impurities. Moreover, larger nickel agglomerates were also observed in these anodes. These investigations showed not only that impurities can affect surface areas and triple-phase boundaries, thus influencing activation polarisation, but that they may impact microstructural changes, such as nickel agglomeration (see **Section 1.5.4**) and thus affect all aspects of performance loss.

One of the major advantages of SOFCs is their fuel versatility, including their ability to run on carbonaceous fuels with external or even internal reforming capability. However, when introducing such fuels, both impurities and the fuel itself can present issues for the continuing performance of the cell/stack.

A common impurity in hydrocarbon fuels is sulfur, in one or more forms, e.g. hydrogen sulfide (H_2S), CH_3SH (methanethiol) or COS (carbonyl sulfide). SOFCs running on natural gas, for example, are exposed to sulfur-containing compounds unless efforts are made to remove them. It has been shown that the tolerance of Ni-YSZ anodes to H_2S is low, but temperature-dependent: ohmic polarisation and anodic polarisation were seen to increase with 0.05, 0.5 and 2 ppm of H_2S at 750, 950 and 1000 °C, respectively [69]. Although the degree of poisoning was correlated with the total S content of the fuel, it was also shown that the performance was recoverable given the removal of the impurity from the fuel.

Carbon deposition has been observed under a variety of operating conditions when SOFCs are run on carbonaceous fuels. One of the most common fuels, aside from hydrogen, is natural gas. Ni/YSZ anodes have been shown to be deactivated by coking when running on natural gas, due to competing reactions, such as the Boudouard reaction (Equation *1-20*), with the desirable reforming reactions (see **Section 1.1.2.1**) [70].

Unfortunately, Ni catalyses the Boudouard reaction, and gives rise to coking, inhibiting electrochemical oxidation due to a loss in exposed surface area. Research has shown that increasing the steam-to-carbon (S/C) ratio can help suppress this degradation route, alongside the addition of specific alkali additives [71]. Other possible solutions include the use of direct electrochemical oxidation of dry methane [72] on ceria-based materials, which also benefits from the other aforementioned advantages associated with running SOFCs at intermediate temperatures. A comprehensive review of SOFC anode material selection, including the incorporation of copper to suppress coking, is found in [73].

1.5.2 Thermal

As in any elevated-temperature device made of multiple materials, the interaction of these materials at interfaces, as well as their intrinsic response to changes in temperature, are key to understanding their stability in operation. In traditional Ni-YSZ-based SOFCs, there is a fundamental mismatch between the TEC of nickel and that of YSZ. Fortunately, the use of a composite Ni-YSZ anode mitigates, to some extent, the TEC mismatch associated with the bulk anode and bulk electrolyte. Nevertheless, there remains a difference in behaviour which is particularly exacerbated by high heating ramp rates.

An increase in anode overpotential of approximately a factor of 2 was shown to result from 12 thermal cycles (25 - 1000 °C) in a classical Ni-YSZ cermet [74]. Later experiments have shown that often the greatest degradation in performance is caused by initial thermal cycles, e.g. in [75], anode overpotential increased by ~9% over the first two cycles (<100 - 1000 °C) but then remained constant for the subsequent seven cycles.

Macroscopic changes as a result of thermal cycling have also been observed, including bowing and delamination. In a recent study by Heenan *et al.*, various ramp rates from 3 to 30 °C/min were used to inspect, by X-ray micro-computed tomography (X-ray micro-CT), the impact of thermal shock on the anode-electrolyte interface [76]. The authors found a thermally-induced concaving of the electrolyte and identified tensile crack propagation as a result, demonstrating that the residual impact of TEC differences can have a deleterious impact on anode microstructure.

1.5.3 Redox

Due to the volumetric change inherent in the oxidation of Ni (+70%)/reduction of NiO (-42%), when an SOFC anode is exposed to significant change in pO_2, severe microstructural changes can result. Often the original state of the anode is not recovered subsequent to a single redox cycle, and stresses may build up in the anode or other components [77]. Recent work by Song *et al.* has used focused-ion beam-scanning electron microscopy (FIB-SEM) tomography (see **Chapter 3**) alongside EIS to investigate the changes associated with multiple redox cycles on electrochemical performance, mechanical stability and microstructural change [78]. This work highlighted previous observations of electrolyte cracking [79], but also investigated the influence of redox phenomena on the changes in nickel particle size and introduction/elimination of porosity. It had previously been shown that anode polarisation increased as a function of redox cycles due to hysteresis in the redox behaviour [80], but this FIB-SEM study also correlated this with a drop in TPB density from ~4.6 to ~1.1 μm^{-2} after 20 cycles. Moreover, Ni-YSZ interfacial area was seen to decrease, similar to the de-wetting behaviour expected from longer-term annealing, and the mechanical strength (hardness and elastic modulus) were also seen to diminish with every 5 redox cycles.

1.5.4 Microstructural

Although several phenomena can induce microstructural changes in Ni-YSZ cermet anodes, including thermal cycling, redox cycling and the inclusion of contaminants in raw materials and fuels, microstructural evolution in this thesis centres on the changes that occur in the anode simply upon sustained annealing at high

temperature. This approach derives from the recognition that nickel coarsening / nickel agglomeration appears to be a degradation pathway of great significance, seen in the various studies explored in **Chapter 2.**

Microstructural evolution of Ni-YSZ anodes manifests in several ways. The three important networks (electronic, ionic and porous) may evolve in different ways and to differing extents, depending on the conditions of temperature, humidity and operation time. Evidence has shown that multiple mechanisms with disparate time constants affect the particle size, connectivity, surface area and TPB. In particular, the coarsening of the lower-melting-point solid (Ni) has been shown to diminish not only the preponderance of active TPBs, but also lead to morphological changes in the pore network. Moreover, studies have shown that even nickel network percolation may be adversely affected [81] by coarsening, such that this single phenomenon can degrade performance in terms of TPB density (activation loss), pore morphology (mass transfer loss) and even electronic conductivity (ohmic loss).

This chapter has highlighted the urgent need to curb local air pollution and mitigate the serious impacts of anthropogenic climate change. It has underlined the potential for SOFC technology to provide at least an interim solution by providing a CHP solution that produces fewer emissions with greater energy efficiency. In **Chapter 2**, an in-depth literature review of previous work carried out to inspect microstructural evolution in SOFC cermet anodes will be presented, as context for the work in this thesis. A principal aim is to develop a robust method to monitor the microstructural evolution which occurs at various points in time in traditional Ni-YSZ anodes, purely as a result of their operation at high temperatures in a reducing atmosphere. To this end, **Chapter 3** sets out the specific objectives of this study and highlights the experimental and computational techniques employed within. **Chapters 4 – 7** present both results and discussion thereof, based on experiments to fulfil these aims. The final chapter, **Chapter 8**, provides several conclusions from the experiments conducted and suggests appropriate future work to further develop the understanding drawn from this thesis.

Chapter 2: Literature Review

This chapter focuses on published studies in the area of porous cermet (Ni-YSZ, Ni-CGO) anode microstructure, with a view to understanding which techniques, metrics and analyses are amenable to understanding the complex microstructure-property relationships key to developing high-performance, durable and commercially viable SOFCs. The chapter is divided into three main sections: earlier and fundamental 2D imaging and physical techniques; more recent 3D techniques including FIB-SEM and X-ray nano-computed tomography and their advantages and drawbacks; and finally, the state-of-the-art 4D imaging modalities that highlight previously unseen complex 3D phenomena occurring in the same sample over time.

2.1 2D imaging and Physical Methods

Early work used various physical and 2D imaging techniques to probe the effects of several fabrication and operational parameters on the phenomena involved in porous cermet anode microstructure and its evolution.

2.1.1 Fabrication Parameters

2.1.1.1 Nickel content

Dees *et al.* investigated the importance of nickel content in the archetypal SOFC cermet anode [52], composed of nickel and YSZ [82]. It was found that conductivity increased by 3 orders of magnitude at 30 vol% nickel (approximately the percolation threshold [83]), whereby conduction switched from ionic (ceramic phase) to electronic (metallic phase). This finding had implications for the choice of Ni:YSZ ratio for SOFC anodes thereafter; although limiting the proportion of nickel reduces the TEC mismatch between the electrode and electrolyte, if the nickel content is much below 30 vol%, percolation is likely lost and ohmic polarisation increases dramatically.

Kawada *et al.* used a current interruption technique to study the effect of nickel content on ohmic polarisation resistance and again saw a drastic increase at about 30 vol% nickel [84], supporting the work by Dees *et al*.. Further confirmation of this was provided by Aruna *et al.* who showed that by a solution combustion synthesis route, cermets with less than 30 vol% Ni had low conductivity, and those above 30 vol% Ni

displayed metallic characteristics, with much higher conductivity [85]. By the use of random resistor networks, Sunde's model also predicted "an almost abrupt rise in total conductivity at an electrode particle volume-fraction of 0.3" [86].

Work by C.-H. Lee *et al.* investigated the impact of varying Ni content for equisized NiO/YSZ-based anodes and investigated their properties by EIS [87] (see **Chapter 3**). The total resistance was shown to be minimised with a Ni content of between 45 and 55 vol% of solids, with the authors proposing the greatest likelihood of percolated metallic and ceramic channels occurring with similar proportions of the two components (when their particle sizes are similar). Increasing the Ni loading was shown to increase the rise in electrode reaction resistance over time (Figure 16), explained by an increasing tendency to sinter. Work by Huebner *et al.* corroborated that 45 vol% Ni gave the lowest initial overpotential by EIS investigation [88].

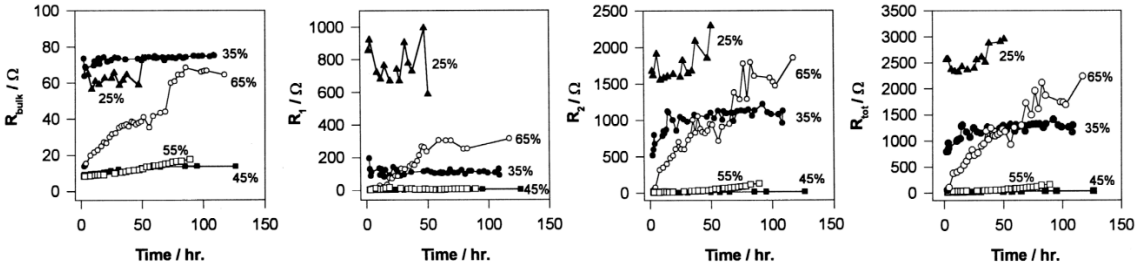

Figure 16: Resistance changes during operation at 1000 °C, with different Ni solid vol%, reproduced with permission from [87]

J.-H. Lee *et al.* focused on how changing the proportion of metal impacts contiguity and interfacial areas [89]. Using the Archimedes method for measuring density [90], it was observed that as the NiO content was increased, the resultant porosity after reduction decreased relative to the corresponding theoretical value, attributable to greater nickel coarsening. The occurrence of coarsening during reduction was supported by the observation of an increase in average particle size from 3 – 5 μm NiO to an average of 10 μm nickel particles. However, coarsening and densification are not the same phenomena (although may occur together), and the Archimedes method employed may not have satisfactorily represented real porosities due to isolated pores. Their analysis nonetheless revealed that as the nickel content is increased, the average nickel grain size after heating to 1000 °C increases, possibly indicating that agglomeration is

favoured by higher contact probability – a fact that corresponds well with the way particles are known to grow *via* neck creation, supporting previous work [87]. Nickel particle growth was shown to be greater than that for YSZ, although the ceramic appeared to show a similar growth trend with increasing proportion, even at a temperature of 1400 °C, which is modest versus its melting point (2690 °C). The authors suggested Ni grew during reduction at 1000 °C and during sintering at 1400 °C whereas only the latter contributed to the bulk of ceramic grain growth. The study showed that microstructure is highly dependent on nickel coarsening; the movement of nickel gives rise to complex pore shapes which control the increase in pore perimeter more than the increase in pore size. Intraphase contiguity was shown to correlate well with phase content whereas Ni-YSZ contiguity peaked at 40 Ni vol% which is lower than expected (50 vol%) due to the impact of nickel coarsening. However, it was seen that the Ni-YSZ interfacial area showed a maximum at 50 Ni vol%, and at only 35 Ni vol% for the Ni-pore interfacial area. The authors proposed that at low nickel content, growth preferentially occurs to increase Ni-pore interfacial area as the vast ceramic network is rather “rugged”. As the proportion of Ni and YSZ becomes more similar, the nickel increases its grain size due to increasing its interfacial contact with YSZ and finally, with little YSZ and little pore volume at high nickel content, both interfaces drop as neither can constrain nickel coarsening. One issue with this interpretation is that it does not account for the surface energies involved, and that there is a preference for Ni-pore interface, over the unfavourable Ni-YSZ (de-wetting) interface. Moreover, this analysis depends solely on 2D information, such that contiguity and percolation in the third dimension have not been considered.

By varying the nickel content between 50 vol% and 100 vol%, Jiang *et al*. showed that the surface morphology of a cermet with more nickel (70 vol%) was much more noticeably transformed by sintering as compared to one with a lower content (50 vol%) [91]. Dramatic outward growth of nickel particles was observed for the former but not for the latter, even after 2000 h. The inhibiting role of the ceramic network was clear. Moreover, work by Fukui *et al.* showed that morphology was also key, and affected the

optimum NiO:YSZ starting ratio [62]. By varying the proportion of 8YSZ in an initial NiO/YSZ cermet, Ni-YSZ microstructures of different heterogeneity after reduction were achieved. High performance could be realised while retaining low anode polarisation and a stable cell voltage across 7200 h by utilising a spray pyrolysis method, with a 25 mol% proportion of 8YSZ (versus NiO), despite being lower than the typical proportion in SOFCs.

2.1.1.2 Particle Size Distributions

C.-H. Lee *et al.* studied the anodic properties of two distinctly different particle size systems; one with very coarse Ni and fine YSZ, and one with equally coarse metal and ceramic particles [87]. In the former case, YSZ particles tended to encase the Ni(O) particles and this led to poor anodic performance when examined by EIS. On the other hand, the cell fabricated from similarly sized powders performed much better and was shown to have reduced resistances due to an improved nickel network. However, nickel sintering and degradation in performance was more severe in the latter electrode as coarsening is less hindered by the ceramic microstructure and hence active TPB sites diminish significantly with operation.

Itoh *et al.* investigated the impact of including two YSZ powders of different coarseness on the extent of microstructural change in SOFC anodes during sintering and reduction [92]. Comparison with materials containing only one coarseness of YSZ, the mix of fine and coarse ceramic gave a much-improved stability in terms of anodic overpotential over 5000 h, and SEM analysis suggested that the fine particles effectively bridged the larger YSZ particles and fixed the Ni particles in place.

Brown *et al*. showed that the activation energy of electrode polarisation resistance increases with increasing coarseness, demonstrating the impetus to produce finer-grained anodes, and that new arcs in the impedance spectrum appear for coarse anodes (2-3 µm feature size), with respect to finer analogues (0.5-1 µm) [19] (Figure 17). Faes *et al.* corroborated these differences in degradation based on particle size; the fine microstructure evolved much faster in the initial 240 h and then began to plateau, compared with a much slower evolution for a coarse grained anode [93].

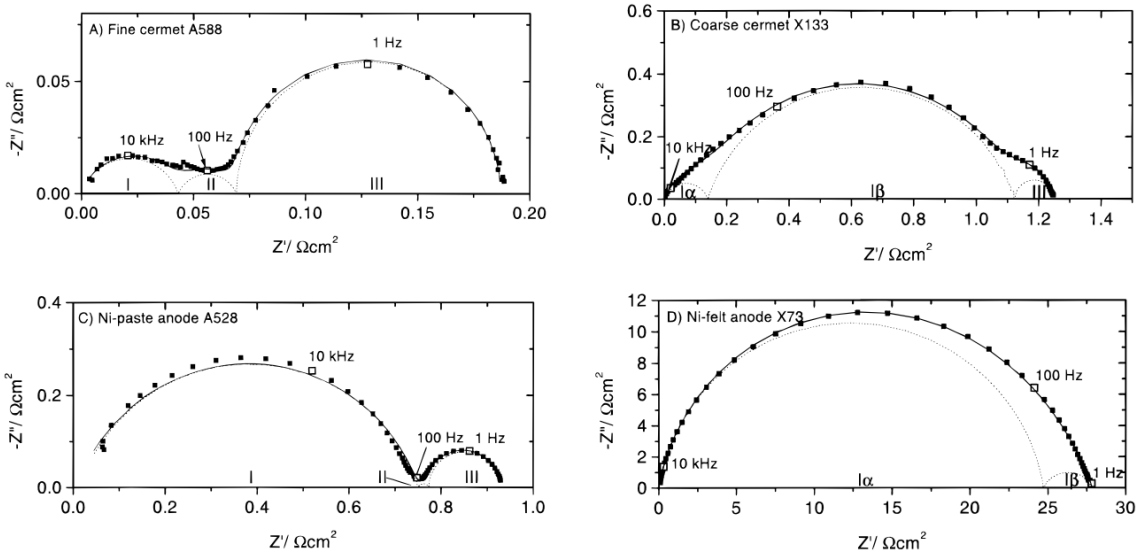

Figure 17: EIS spectra demonstrating the new impedance arc (Iβ) appearing when switching from fine- to coarser-grained cermet, reproduced with permission from [19]

2.1.1.3 Preparation Temperature

Kawada *et al.* also investigated the effect on electrochemical performance of changing the temperature at which the cermet component materials were pre-calcined and at which the electrode assembly was sintered before operation [84]. It was observed that a higher sintering temperature was required to increase interfacial conductivity and reduce associated activation overpotential, and that after sintering at the relatively low temperature of 1200 °C, exchange current density decreased and ohmic resistance increased. Large ohmic resistances in the ceramic phase were avoided with higher sintering temperatures, possibly due to a more continuous nickel network forming on YSZ composed of larger particles. Moreover, it was proposed that by forming a more rigid ceramic network at higher sintering temperature, the reaction zone extended further from the electrode-electrolyte plane into the electrode itself, as the grain boundary impedance of YSZ was lowered. A pre-calcination step was particularly favourable before a high sintering temperature. High pre-calcination temperature reduced the difference in activation overpotential between initial testing and the measurements taken when impedances had reached a constant value (after 1 h). The authors suggest that the initial degradation rate when operating the cells is dependent upon the initial (YSZ) microstructure surrounding the nickel particles, and that pre-calcination affects the morphology of this protecting network.

Suzue *et al.* reconstructed artificial 3D microstructures from 2D 2-point correlation functions extracted from confocal laser micrographs [94]. The anode overpotential for their reconstructed anodes is calculated by the Lattice Boltzmann Method (LBM) [95][96] and the dependence on sintering temperature was examined. As the sintering temperature was increased from 1300 to 1400 °C, polarisation resistance (and hence anode overpotential) decreased (almost linearly) and with the same trend as was shown experimentally by Primdahl *et al.* [97].

2.1.1.4 Reduction

Temperature-programmed reduction (TPR) investigations of Ni-YSZ anodes were conducted by Shirakawa *et al*. to study the link between NiO reducibility and ease of nickel agglomeration [98]. More aggregation of nickel was observed after reduction at a higher temperature, and it was noted that “metal atoms move and aggregate easily over the absolute temperature of about two-thirds of its melting point” which for nickel is approximately 1150 K (877 °C) [T_m (Ni) = 1728 K (1455 °C)]. By TPR, it was found that the reduction temperature depended upon the sintering temperature and that the interaction between the metallic and ceramic phases resulted in an increase in reduction temperature relative to pure NiO. A decrease in the dominance of this interaction is seen with increasing sintering temperature which is said to be due to greater nickel agglomeration and thus greater “bulk NiO” structure.

The investigation of pure Ni versus the traditional cermet microstructure by Jiang *et al.* clearly indicated that the presence of zirconia particles inhibited the sintering of NiO particles, even prior to reduction [91]. However, during reduction, a clear increase in nickel particle size is seen, despite the volume reduction expected on converting NiO to Ni. This corroborates the work by J.-H. Lee *et al.* which shows an increasing discrepancy between practical and theoretical porosity after reduction [89].

2.1.2 Anode Fundamentals

2.1.2.1 Electrode Thickness

Tanner *et al.* investigated the effect of using a composite electrode and how the inclusion of ceramic particles within the electrode expands the active volume contributing

to charge transfer [99]. Their two-dimensional model predicted that the effective charge-transfer resistance decreases quickly with increasing electrode thickness, and by a greater degree for a lower intrinsic electrode-electrolyte resistivity. The work surmised that the benefit of decreasing porosity (by inclusion of more active sites in a given volume) should be weighed against the negative effects attributable to concentration polarisation; when porosity falls below about 20%, effective R_{ct} climbs rapidly for all electrode thicknesses. Strictly in terms of initial performance, this work illustrated that finer microstructures give rise to increased electrochemical performance, as the minimal effective charge transfer resistance can be reached with a thinner electrode and its absolute value is lower due to increased TPB density.

Brown *et al.* used the Risø geometry electrode assembly [100] to investigate the impact of cermet thickness on anode polarisation resistance [19]. When the electrode thickness reached approximately 10 µm, there was a substantial reduction in the polarisation resistance associated with the electrode microstructure. An apparent thermal activation was observed for this polarisation, and dependencies of this electrode polarisation on pH_2 and pH_2O were non-zero. Interestingly, an area-specific oxide-ion conductivity for the porous YSZ structure in their fine cermet was calculated to be 0.01 Scm^{-1} from extracted series resistances, which would give an area-specific polarisation resistance of 0.10 Ωcm^2 for the active thickness of 10 µm: the same value extracted from their EIS analysis for the anode polarisation resistance. The authors claim that “only minor contributions to the total current density are expected from TPB points with a specific oxide-ion transport resistance comparable with or higher than the specific electrode reaction resistance”.

2.1.2.2 Wetting/Interfacial Reactions

Work was carried out by Tsoga *et al.* investigating the wetting properties and interfacial reactions at high temperatures (up to 1500 °C) of Ni-YSZ systems [101]. Using the sessile drop technique [102], the contact angle between metal and ceramic was shown to be approximately 117°, indicative of a de-wetting interaction. However, it was later shown to be lowered in a TiO_2-doped system (103°), implying that better wetting

may be accessible *via* ceramic doping [103]. It was noted that poor adhesion between nickel and YSZ was observed. No reaction between the solids is observed just above the melting point of nickel in a reducing atmosphere but at the highest temperatures and without H_2 present, a chemical interaction region between the solids is indeed observed. Fortunately, however, this is far beyond standard SOFC operating temperatures and is therefore only relevant to fabrication parameters.

2.1.2.3 Triple-phase boundary

Misuzaki *et al.* produced nickel-pattern electrodes on 8YSZ, with line widths as small as 5 µm, in order to study the relationship between a measurable TPB length and electrode impedance behaviour [104]. After initial grain growth over the first 24 h, EIS gave a stable activation polarisation which was loosely shown to be linearly proportional to TPB length, hence implying that the reaction occurs near to the TPB. The same dependence of this value on pH_2 and pH_2O with patterned and compact electrodes suggested that the rate-determining step likely takes place on the nickel surface close to the TPB.

Nagakawa *et al.* used microlithography to produce fixed film electrodes, and investigated the effect of varying both the Ni film and the porous ceramic layer on the anode polarisation, to identify the extension of the active zone [65]. In their configuration, the three-phase line constituted the edge of cracks at the interface between the film and the electrolyte, in the otherwise solid film. For a given thickness of porous ceramic support, the thickness of the nickel film was varied between 0.8 and 12.9 µm, which had very little impact on the electrochemical behaviour of the electrode. The authors suggested that this result implies that the process that occurs at the electrode/electrolyte takes place within less than a micrometre. This correlates with the low ionic conductivity of nickel and suggests a maximum “width” of TPBs in percolated Ni-YSZ cermet anodes of approximately 800 nm.

Ioselevich *et al.* simulated the effect of nickel sintering on the active TPB length by means of a “correlated-percolation” model [105]. The authors noted that metallic particle coalescence may lead not only to loss of contacts, and therefore a shortening of

the active TPB, but also potentially an improvement in gas transport due to the opening of new pores. It was found that their proposed lattice model described rapid catastrophic degradation when adjacent ceramic particles were set to have little restraining effect on metal particle coalescence. Nevertheless, when a “hard blocking” regime was adopted, a gentler decline and stabilisation of active TPB sites was observed. Quantitatively, if the model is set to yield pores on coalescence, the maximum active TPB after initial degradation is allegedly achieved if the proportion of metal is greater than that for ceramic, and the porosity is low (0.45:0.35:0.2, metal:ceramic:pore). This model assumes this type of sintering dominates and may underestimate the impact of finer porosity on mass transport.

Nakagawa *et al.* devised an experiment to investigate the nature of the incursion of the TPB into the electrode, by varying the conductivity of the YSZ used in the cermet whilst keeping the electrolyte ceramic unchanged, effectively altering the active region depth [106]. By EIS, the anode polarisation was seen to decrease with increasing conductivity (or yttria content) of the YSZ used in the anode. At a given overpotential, greater anodic current was generated from YSZ with a higher ionic conductivity, with the Tafel slope remaining the same, suggesting no change in mechanism. The authors then separated the contribution from the YSZ where all TPBs are at the electrode/electrolyte interface (ZrO_2 is an insulator) from the exchange current densities given by the other cermets, inferring the difference between the proportion of active TPB on the 2D plane versus the 3D active zone. Their calculations showed that for 8YSZ, the ratio is approximately 2.5:1 for the 3D versus 2D active zone contributions.

Divisek *et al.* combined optical micrograph stereology with porosimetry to compare estimated TPB densities with apparent exchange current densities from electrochemical measurements [107]. Active ‘bonds’ (TPBs) were measured by the intercept-segment method [108] and stereological estimates gave a change from 1.8×10^9 to 4.4×10^8 per cm^3 in TPB density, alongside a reduction in exchange current density from ~21 to 4 $mAcm^2$ after 16 h of operation at 950 °C. This appears to be an approximately linear relationship between reaction sites and electrochemical

performance. However, since percolation information is unavailable, the estimation errors intrinsic to this stereological approach are high, approximated to be 30%. The required arbitrary correction to their stereological conversion exponent exposes the fact that information in the third dimension was crucially absent. Moreover, the work demonstrated that simply measuring the internal electrode surface area was unsatisfactory as an electrochemical performance metric.

Additionally, Brown *et al.* reiterated that there is likely a width to the TPB, such that a reaction zone is set up, dependent upon the electrode overpotential and corresponding limit to transport in one or more phases [19]. The authors suggest that this width is less than 1 μm on both Ni and YSZ, based on previous studies [109][110] and in line with Nakagawa's work [65][106]. The authors propose that at certain locations within particular microstructures, protons may "spill-over" onto the YSZ surface, or electrons may be forced to travel though a short YSZ pathway. This increases the importance of understanding surface/interfacial areas as well as the 1D triple-phase boundary lines.

2.1.3 Operating Parameters

2.1.3.1 Temperature

Iwata *et al.* used electrochemical methods, mercury intrusion porosimetry (MIP), and SEM to investigate the effects of temperature and time on the microstructure of a Ni-YSZ anode [4]. For a cell run at approximately 920 °C and at a fixed current density of 0.3 Acm^{-2}, anodic polarisation initially reduced, and then was found to increase monotonically after 70 h, whereas a cell run at over 1000 °C at the same current density exhibited a polarisation increase from start to finish (0 - 1000 h). This suggests more than one mechanism may be at play and the relationship between microstructural change and temperature is complex; an initial reorganisation of microstructure may be taking place as noted by Kawada *et al.* [84]. The degradation rate was greater for the cell run at higher temperature, potentially due to a greater sintering rate of the nickel in the cermet. MIP showed a slight increase in average pore radius by ~200 h of operation and a major positive shift in the pore sizes in the 10 to 200 nm range by ~1000 h, thought

to be those contributing to the majority of active TPBs. SEM micrographs showed increases in nickel particle sizes from the nanometre range to 1 - 10 µm. Interestingly, for the cell run at the lower temperature and shorter time, the Ni-YSZ volume-specific interfacial area increased compared with the virgin sample, whereas a clear decrease was observed for the cell operated at higher temperature and for over 1000 h. This increase in contact between the metal and ceramic at the lower of the two temperatures is at odds with the expected de-wetting behaviour of Ni upon YSZ.

Hagen *et al.* showed the importance of operational temperature on how other parameters impact degradation rate (see **Section 2.3.3.**). At lower temperatures, an increase in drawn current density has more of a deleterious effect on anode performance. In contrast with previous work, degradation rates were seen to be lower at higher temperatures, but this may be due to the dominant effect of current density, which is particularly pronounced at lower operating temperatures.

2.1.3.2 Time

Simwonis *et al.* undertook medium-term annealing studies on Ni/YSZ cermets and showed that prolonged annealing at 1000 °C (4000 h) in humid forming gas gave a 30% increase in average nickel particle size and a concomitant loss of electrical conductivity of 33%, measured by the four-point probe technique [114]. 2D optical images of polished surfaces were used in image analysis (using an average grain intercept method [108]) but achieving contrast between the solids was non-trivial.

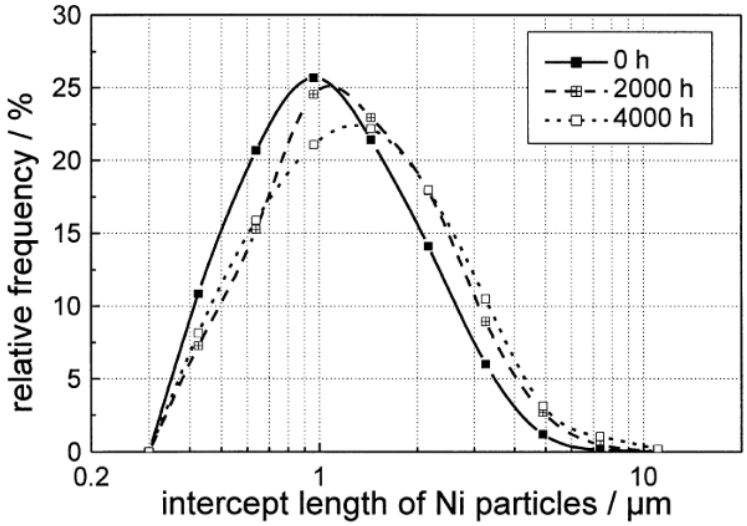

Figure 18: Intercept method plot for Nickel particle size change over time, reproduced with permission from [114]

Alongside particle growth, a small increase in apparent particle sphericity (circularity) was observed for nickel, and whilst the pores initially coarsen slightly, the ceramic phase was not seen to evolve substantially. Importantly, growth rates for nickel were seen to decrease with increasing time. Taking inspiration from work by Mizusaki [112], a model for the conductivity based on volume fractions was devised and applied to their annealing data. The model gave a conductivity of the same order of magnitude as that measured for their cermet, but this could not be used to examine the evolution of conductivity as the nickel volume fraction remained constant whilst conductivity fell with increasing annealing time. Instead, a contiguity theory was employed, which matched the evolution of conductivity over time, but with estimated absolute values which were about twice as high as by experiment. Moreover, the authors noted that particle size distribution (PSD) functions would be more useful than mean intercept lengths as inputs to their model.

Vassen *et al.* modelled this experimental work by proposing a two-particle model in which the observed coarsening is driven solely by the difference in diameter of adjacent particles and occurs only by surface diffusion [113]. Moreover, a mathematical term was developed to account for the limited space available for Ni grain growth which was linked to the pore volume obtained experimentally. The simulations were able to closely match the evolution of average particle size from the experiments of Simwonis *et al.* [114] but the extracted nickel surface diffusion coefficient estimates were low compared with literature precedents. This may be because the model was based on a simplified two-particle model, or perhaps more importantly, because connectivity and percolation could not be accounted for in their stereological approach. Nonetheless, the study promoted the use of sintering theory; using the difference in curvature of adjacent particles to model the difference in vacancy concentration below the surface and mathematically describe the vacancy and thus atomic self-diffusion flux.

By SEM analysis, Jiang *et al*. compared the microstructures of pure Ni with a cermet made from nickel and 3YSZ (3 mol% yttria) over medium-term sintering at 1000 °C [91]. YSZ particle size and distribution were not observed to change whereas

porosity and nickel particle size were seen to evolve, relative to the initial microstructure. The evolution of nickel particle size and porosity level was monitored over time and is reproduced in Figure 19.

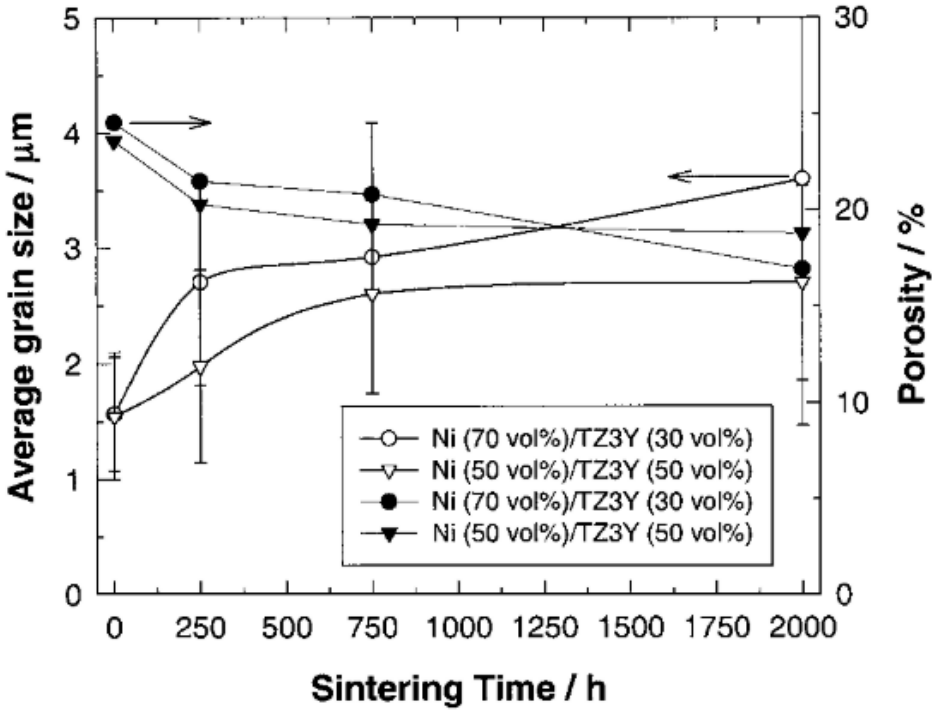

Figure 19: Plot of average Ni grain size and porosity against sintering time for two compositions of Ni/YSZ cermet, reproduced with permission from [91]

As aforementioned, there is stronger growth in Ni particle size for the cermet with a greater proportion of nickel. Moreover, there are clearly at least two regimes whereby growth rates are not constant throughout this sintering period; for the 70:30 Ni/3YSZ case, plateauing of nickel growth appears around 250 h, whereas for the 50:50 Ni/3YSZ cermet, the drop in growth rate appears to occur later, at approximately 750 h. A decrease in porosity with increasing sintering time was also noted, although this may be a surface effect. Unfortunately, the measurement technique was *via* scaled transparency paper, could not detect features below 200 nm, and was based on stereology from 2D images, which led to very wide error bars and diminished data reliability. Nonetheless, two time regimes are clearly observed and much faster growth is seen initially than at longer times or in similar experiments by Simwonis *et al*. [114].

In terms of time constant for degradation phenomena, work by Hagen *et al.* [115] corroborated the findings by Jiang *et al.,* in that there was clearly a faster rate of degradation in the first 300 h than for the entire 1500 h period, suggesting decay in the

driving force for change over time and/or a change in dominant degradation mechanism. However, their nickel grain growth analysis was only conducted post-mortem, so the coarsening rate could not be reliably gauged.

Faes *et al.* investigated Ni-YSZ half-cell anodes during medium-term stack testing, by employing stereological techniques on SEM images, with a focus on nickel agglomeration and the related drop in TPB density [93]. Their work incorporated a method to link nickel grain growth with the loss in TPB and *via* the Butler-Volmer equation, attempted to link this with cell voltage drop. An increase in Ni particle size was observed with time, using either stereological techniques (intercept method [108] or morphological operations [93]). The evolution of particle sizes is shown in Figure 20.

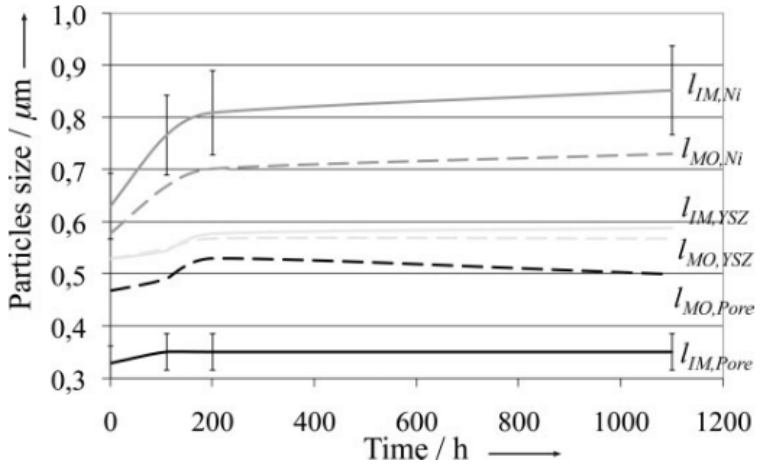

Figure 20: Plot of particle size evolution for an anode annealed at 800 °C, by intercept method (IM) or morphological operation (MO) method, reproduced with permission from [93]

One of the key results was that, as seen previously [115][116], nickel particle size was seen to markedly increase for the first 200 h before beginning to level out. To explain the Ni evolution profile, the authors noted that the results did not fit a simple Ostwald Ripening [117] or exponential growth law, but instead invoked a "charging capacitor" model that introduced a maximal size to the nickel particles, as a result of the physical constraints imposed by the ceramic backbone (Equation *2-1*).

$$R = (R_{max} - R_0)\left(1 - exp\left(-k_{s,Cap}t\right)\right) + R_0 \qquad 2\text{-}1$$

where $1/k_{s,Cap} = \tau$ *is the time constant for nickel coarsening*

The time constant extracted was approximately 160 h, possibly where the dominant effect stops being traditional coarsening and is instead hindered by the YSZ skeleton.

An equivalent “discharging capacitor” model is invoked for the length of the TPB, giving a time constant of approximately 120 h. The results from their experiments indicate an initial degradation highly dependent on Ni agglomeration in SOFC anodes, whereas longer-term performance loss may be more attributable to cathode degradation.

Tanasini *et al.* took EIS measurements after various operation times for Ni-YSZ/YSZ/LSM-YSZ single cells, at a constant current of 0.6 A and compared the results with morphological observations by SEM [118]. Firstly, an activation period of approximately 24 h is observed, which agrees with previous works [105][115]. Their analysis of average Ni particle size by the intercept method showed a clear increase, whose rate decreased with time, whilst the grain size of YSZ remained unchanged. The authors note, however, that the activation does not appear to be linked to the microstructural evolution in the anode (or cathode) as very little change is observed during this time. Their work identifies 800 h as being the point at which growth plateaus, which is longer than seen in previous works (200-250 h), except that for the 50:50 Ni/TZ3Y cermet in work by Jiang et al. [91]. Their electrochemical micro-model indicated that as the nickel phase coarsens with time, there is a small increase in the Ni vol% required for percolation, theoretically explaining the fall in connectivity and conductivity reported previously [81]. Their simulation results for the evolution of anode overpotential for various Ni phase fractions, as a function of time, showed the importance of ensuring the Ni content is high enough not just for initial electrochemical activity, but also far enough away from the percolation thresholds that coarsening does not result in significantly deleterious effects (Figure 21).

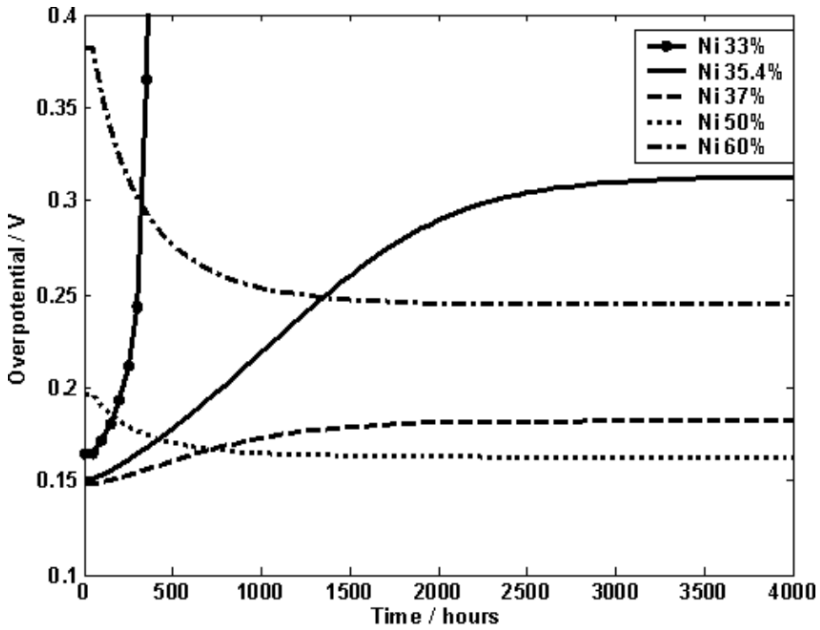

Figure 21: Plot illustrating the predicted changes in anodic overpotential with time, for various Ni vol% contents, reproduced with permission from [118]

2.1.3.3 Humidity

Brown *et al.* noted that, even across a range of Ni/YSZ microstructures, there is a clear decrease in anode polarisation resistance with increasing pH_2O, somewhat in contradiction with that fact that H_2O is a reaction product and its presence may be thought to hinder the hydrogen oxidation reaction. On the contrary, some authors have suggested that water may have an "auto-catalytic" effect on the HOR [119].

However, work by Jiang *et al.* suggested that water played some role in the Ni agglomeration phenomenon since the sintering of pure nickel in dry and moist (~3% H_2O) conditions gave different results; in the presence of moisture, the nickel particle growth was clearly greater [91]. The authors suggested that humidity may increase the surface self-diffusion coefficient of nickel.

Significant nickel loss was reported by Hagen *et al.*, but rather than due to introduced humidity, this was likely due to the product water from the cells which were run at 0.75 and 1.9 Acm^{-2} at 750 and 850 °C, respectively [115]. Up to 40% nickel loss was observed locally, with $Ni(OH)_2$ the suspected volatile species responsible for this phenomenon.

2.1.3.4 Current Density

Hagen *et al.* performed medium-term (1500 h) parametric studies of cell degradation, with current density as one of the parameters [115]. Cell voltage was

observed to drop with time, and although this was somewhat dominated by cathode degradation, it was shown that cell voltage behaved linearly at low and exponentially at high current densities (Figure 22).

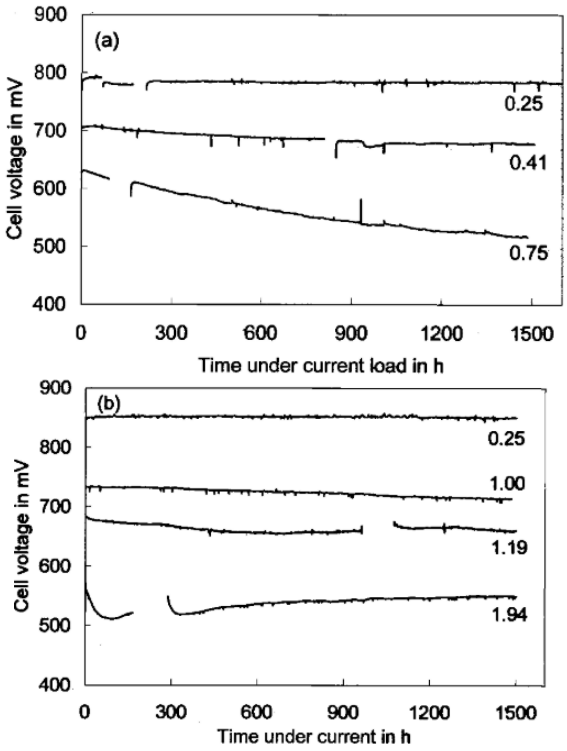

Figure 22: Plots of cell voltage against operation time, for a range of current densities a) at 750 °C and b) at 850 °C, reproduced with permission from [115]

An initial performance increase was observed in most cases, which may reflect early-stage improvements in anode microstructure, such as the opening of new pores and an increase in TPB density, as suggested by Ioselevich *et al.* [105], and/or activation processes in the cathode [120]. It was noted that generally, drawing more current increased degradation rate, except for the highest current density at 850 °C, where an overall increase in cell voltage was observed (Figure 22 b)). This was particularly true for the first 300 h, and from their results, it was clear that at least two regimes of cell degradation were at play, initial (<300 h) and longer-term (>300 h), with the former representing faster decay in performance. Furthermore, lower temperatures (Figure 22 a)) gave rise to a greater increase in degradation rate with increasing current density. This may suggest that the extra heat at higher temperatures compensates for the mechanism that links current density to degradation, perhaps by minimising temperature differentials near the conduction pathway. Surprisingly, the degradation rates at higher

temperatures were significantly smaller than at lower temperature. To investigate this, their results were re-framed in terms of cell polarisation, which is much higher at lower temperatures. Degradation rate showed a near exponential dependence on cell polarisation, and importantly was independent of temperature up to 300 h, suggesting cell polarisation is a more significant factor in cell voltage drop than current density or temperature during this initial regime (Figure 23).

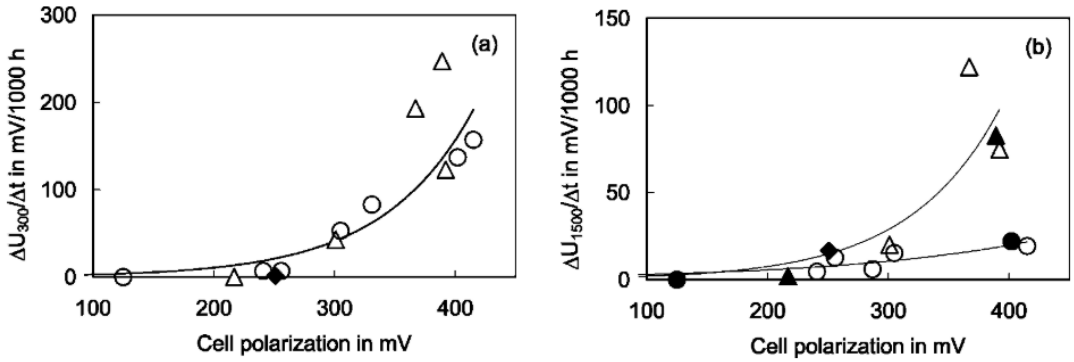

Figure 23: Plots of cell degradation rate vs. polarisation (triangles = 750 °C, circles = 850 °C, diamonds = 950 °C; for a) 300 h, b) 1500 h, reproduced with permission from [115]

It was only after this initial period that the degradation rates were seen to be temperature-dependent, being greater at lower temperatures. This behaviour is at odds with nickel coarsening, but since these tests account for total cell degradation, perhaps cathodic deactivation processes outweigh any anodic nickel coarsening effects. Using EIS, it was shown that the high degradation rate at low temperatures and high current density appeared to derive from increases in ohmic resistance, and to a greater degree than at higher temperature or lower current density. However, the authors noted that the results from EIS differ from their degradation rate measurements for the relative magnitude of losses for low current density at high and low temperatures, which weakens the reliability of the results. Nonetheless, deconvolution of the EIS analysis concluded that at low temperatures and high current density, it was likely that a cathode deactivation process resulted in most of the cell degradation, precluding this result from implying a link between nickel coarsening and high cell polarisation.

Nevertheless, nickel coarsening was observed by SEM, along with loss of Ni at the higher temperature of 850 °C. The average particle diameter shifted upwards after

operation, more so for the higher temperature. However, nickel loss in the higher temperature case confounds the particle size distribution (PSD) measurement. Furthermore, the method used (intercept length) is constrained by statistical errors and has only been applied in 2D. It does appear, however, that these changes are less detrimental to the performance of the cells examined than the changes occurring in the cathode.

Research by Xiao *et al.* corroborates the fact that cathode contributions to cell polarisation are more dominant than those coming from the anode, although the latter are not negligible [121], even when broadly normalising for electrode area disparity. As temperature was increased, the anode contribution increased, possibly due to decreasing electronic conduction in nickel dominating over increased kinetics for the HOR. It was also shown that the relative contribution from the anode increases on greater current density drawn, potentially as a result of poor kinetics for steam egress. A drawback of this study, however, was the asymmetrical placement of their reference electrode, which increased the error in the already approximate polarisation values.

2.2 3D imaging

More recent work employed 3D imaging techniques to gain greater insight into the degradation processes within Ni-based SOFC anodes, with an increasing focus on connectivity, percolation and transport properties. The first 3D insights of an SOFC anode were gained by using FIB-SEM slice-and-view tomography, to sequentially slice away the front face of a volume of interest (VOI) with a FIB, revealing the microstructure behind for imaging with an SEM (see **Section 3.2.4**). Concurrently, X-ray nano-computed tomography was utilised to inspect SOFC anodes in a non-destructive fashion by reconstructing 3D volumes from a series of 2D X-ray projections. The details of key investigations to-date that used these two tomographic techniques are given below.

2.2.1 Slice-and-view tomography (FIB-SEM)

2.2.1.1 Initial Studies

A breakthrough example of FIB-SEM slice-and-view tomography was conducted by Wilson *et al.* in which the first truly 3D information was extracted for an SOFC anode, including information about volume fractions, specific surface areas, and the connectivity and tortuosity of different phases [123]. The research not only provided means to validate the macro-homogeneous properties that are often estimated by a set of individual physical experiments, but also gave access to those that are experimentally difficult to determine. The study highlighted the need for the third dimension to calculate tortuosity as well as stressed the importance of accounting for percolation of the three networks when considering active TPBs. However, the sampled volume was relatively small (105.2 μm^3) (Figure 24) and the work represented only an initial snapshot of anode microstructure without capturing any evolution. Nonetheless, an active TPB density from the AFL of a state-of-the-art SOFC anode was calculated to be 4.28 μm^{-2}, which indicated the order of magnitude to be expected in these types of microstructure.

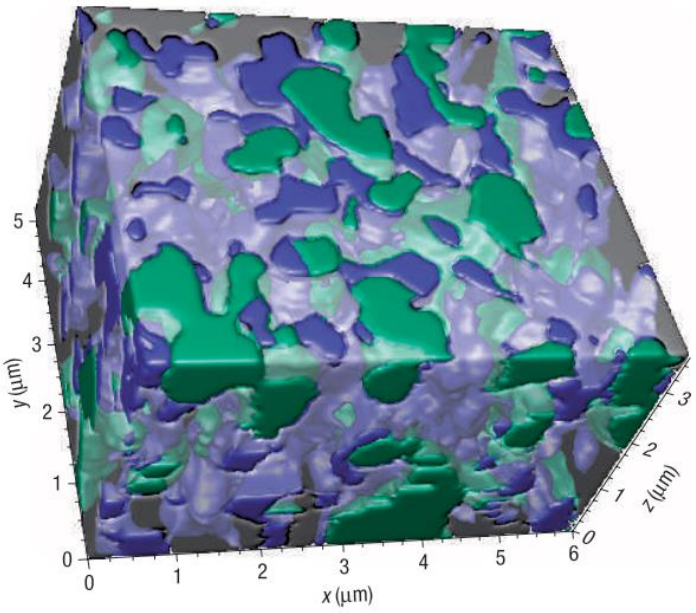

Figure 24: First 3D reconstruction of an SOFC anode showing all three phases – Ni (green), YSZ (translucent), Pore (blue), reproduced with permission from [123]

Similar work was conducted the following year by Gostovic *et al.*, performing FIB-SEM slice-and-view on a MIEC SOFC cathode material, lanthanum strontium cobalt ferrite (LSCF), measuring TPB lengths of a similar order of magnitude but demonstrating a

complex relationship with sintering temperature [122]. Wilson *et al.* also concurrently investigated the SOFC cathode material, $(La,Sr)CoO_3$.

2.2.1.2 Nickel content

Further work from Wilson *et al.* used the FIB-SEM technique to assess the effect of anode composition on TPB and electrochemical performance by varying the Ni content (40-70 wt% NiO) in the Ni-YSZ AFL of full cells. Based on EIS measurements, the compositions derived from 50 and 60 wt% NiO gave the best electrochemical performances, equating to approximately 35 - 45 vol% Ni. By performing FIB-SEM slice-and-view, these compositions were also found to have the highest TPB densities, although the variation in TPB density did not correspond well with the variation in polarisation resistance, suggesting more than one factor was at play. Unfortunately, this study relied upon stereological estimations and only inspected initial performance without tracking evolution. It did, however, allude to the fact that the models based on random packing spheres did not match well with real microstructural data [124], strengthening the call for tomographic investigations.

Matsui *et al.* investigated the effect cermet composition (Ni:YSZ = 50:50, 55:45, 68:32 vol%) had on the performance of Ni-YSZ cells [125], comparing the degraded microstructures (treatment at high humidities – see **Section 2.2.1.6**) with the Ni:YSZ = 50:50 vol% microstructure from previous work in the group [126]. Their work showed that the lower nickel content cermet was unable to withstand high fuel utilisations as well as that with higher nickel content; the time until degradation proved catastrophic was prolonged by the presence of more metal, likely due to nickel phase connectivity. On the other hand, these experiments were conducted under 40% humidity fuel stream, which is outside the normal operating parameters seen in commercial stacks, which reduces its relevance.

Vivet *et al.* provided one of the early investigations, by FIB-SEM slice-and-view, of the effect of the initial Ni content within a Ni-YSZ anode on important microstructural properties such as TPB_L and tortuosity [127]. They incorporated earlier work by Thydén *et al*. which reported on a passive voltage contrast (PVC) technique which can

identify the level of percolation of an electronically conducting phase [128]. Initial powders with 45, 51, 54, 56 and 61 wt% NiO were used to produce anodes which were reconstructed at volumes of approximately 350 - 1000 μm^3. The authors noted that the area fractions calculated from single 2D SEM images did not match the volume fractions extracted by metrics analysis of the 3D reconstructed volumes, adding weight to the constraints of stereology [129]. However, the PVC technique did provide percolating/non-percolating ratios for Ni that matched those extracted from FIB-SEM data well. A jump in conductivity, resultant from percolation, was again found at around 40 $\%vol_{solids}$ or ~26 %vol Ni. The experimentally-determined electrical conductivities were one order of magnitude smaller than those estimated from solving transport equations based on FIB-SEM data, although this may have been due to poor contacts or the chosen literature Ni conductivity value used in their simulations. However, the effective electronic conductivities showed the expected trend of increasing with Ni concentration but appeared to be highly anisotropic. By looking at the Ni volume fraction slice-by-slice, the authors noted that the direction in which this varied most, the conductivity was also measured to be lowest.

2.2.1.3 TPB & Anode Overpotential

Several studies used microstructures gathered by the slice-and-view approach as the input for a range of simulations [130] [131]. For example, Matsuzaki *et al.* applied the LBM to calculate the anode overpotential from 3D reconstructed data [130]. Their approach to measuring TPB was based upon finding the distance between the centroids of triangles whose corners were the midpoints of line segments adjacent to three different phases. *Via* this method, the authors estimated the proportion of connected TPB to be 60%. The output of their simulation gave values for the overall anode overpotential that matched experimental data reasonably well, although they stress that domain size (and thus the volume) captured by slice-and-view was particularly crucial in obtaining reliable results.

Based on interconnectivity algorithms (discussed in **Section 2.2.1.4**), Wilson *et al.* calculated the proportion of active TPBs [131] from their initial data set

[132]. 9.5% of the identified TPB was estimated to be inactive and 23.8% were inconclusive as they were connected to the lateral faces and thus their true percolation was unknown. Applying the same proportionality, the authors estimated a total of 11.6% inactive TPB, giving an active TPB density for the AFL of 3.7 μm^{-2} (~88% active).

Similar work was conducted by Shearing *et al.* but with the added improvement of a "lift-out" technique that maximised the accessible data quality [133]. By performing slice-and-view in an *ex-situ* manner, re-deposition of material is avoided, shadowing effects are removed, charging is reduced and Ni-YSZ solid phase contrast is maximised. The paper emphasised the merits of a dual-beam FIB-SEM system which overcomes the time-consuming and not fully automated sample stage movements between each milling and imaging step. The authors used a method for measuring the TPB density summarised by Golbert *et al.* [134] wherein all the pixels neighbouring a TPB edge are counted and divided by 4 to smooth out the otherwise very jagged total segment length. When percolation was accounted for, 51% of the measured TPBs were estimated to be active in one microstructure, and 45% in the other, both large reductions as compared with the ~88% Wilson *et al.* calculated [131]. This may be due to the larger (more representative) volumes investigated by this method, better matching the value found by Matsuzaki *et al.* (60%) which also investigated a large volume (~1000 μm^3) [130]. Alternatively, it could be due to a more heterogeneous microstructure being investigated in these latter cases, in comparison with that by Wilson *et al.*.

Iwai *et al.* took a methodological approach and applied two evaluation methods to computing the TPB density, namely the volume expansion and the centroid methods [126] (see **Section 3.4.2.1**). For the former method, the authors applied it to a well-defined, albeit simplified, geometry. The calculated values from the simulation matched the theoretical values very well and on application to their most representative 3D reconstructions, gave a TPB density of ~2.49 μm^{-2}. Similarly, the widely-used centroid method gave a TPB density of ~2.56 μm^{-2}, exhibiting less than 3% difference versus the volume expansion method, adding credibility to each of these methods.

Shearing *et al.* performed FIB-SEM tomography on a Ni-YSZ anode, analysing relatively small volumes (~50 μm^3), which gave high active TPB densities of 8.15 and 9.34 μm^{-2} [135]. Nonetheless, a complex model linking ionic and electronic potentials, Butler-Volmer kinetics and the diffusion of H_2 and H_2O led to a finite volume simulation that gave length-specific exchange current densities of 9.4 x 10^{-11}, 2.14 x 10^{-10} and 1.22 x 10^{-9} Aμm^{-1} at 800, 900 and 1000 °C, respectively, which compared favourably with data from EIS experiments. Furthermore, except at the highest temperatures and for the smallest samples, the data matched well previous work on patterned electrodes by Bieberle *et al*. [136].

Shikazono *et al.* took their group's research further by using a combination of the LBM method and equations for the electrochemical reaction at the TPB to compare their simulated anode overpotentials [137] with those from experimental data [125]. Moreover, three approaches to calculating TPB were compared: i) summation of TPB voxel edge segments; ii) connection length of midpoints of TPB voxel edge segments; iii) total distance between the centroids of the triangles defined by the adjacent midpoints of the TPB voxel edge segments, as shown in Figure 25.

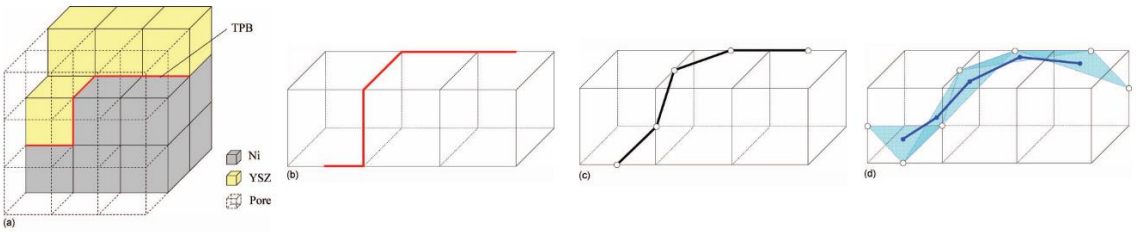

Figure 25: Schematic displaying different measurement approaches for a) voxelised TPB length, by b) summation of line segment; c) connection of adjacent mid-points; d) triangular centroid method, reproduced with permission from [137]

For a simple sphere overlap case, the authors showed that the triangular centroid method gives the smallest error but noted that the level of this error depends on the ratio between the resolution and feature size (in this case, sphere radius). For the anode microstructures investigated by FIB-SEM, their model showed good alignment with experiment for low humidity (1 - 2% H_2O) streams, but greater deviation at higher humidity. Moreover, there was a marked change in predicted anode overpotential when

the voxels were effectively coarsened above a certain size, reinforcing the need to match spatial resolution to feature size.

Kanno *et al.* reconstructed large volumes from the Ni-YSZ anode of an electrolyte-supported cell (ESC), ranging from ~2,500 to ~17,500 μm^3, focusing on analysing the impact of volume on TPB density and tortuosity factors [138]. Even at these large volumes, variations in extracted phase fractions were notable, peaking at 7% (proportionally) for YSZ, relative to the average value: a clear mark of the heterogeneity of these microstructures. Their extracted connectivity values were all above 90% and their total extracted TPB densities were all approximately 2.0 μm^{-2}, in line with previous studies. Tortuosity factor was shown to be broadly independent of cross-sectional area for the porous phase, but YSZ required at least 200-300 μm^2 in cross-sectional area and the values for nickel were the most volatile, even up to large considered volumes (Figure 26).

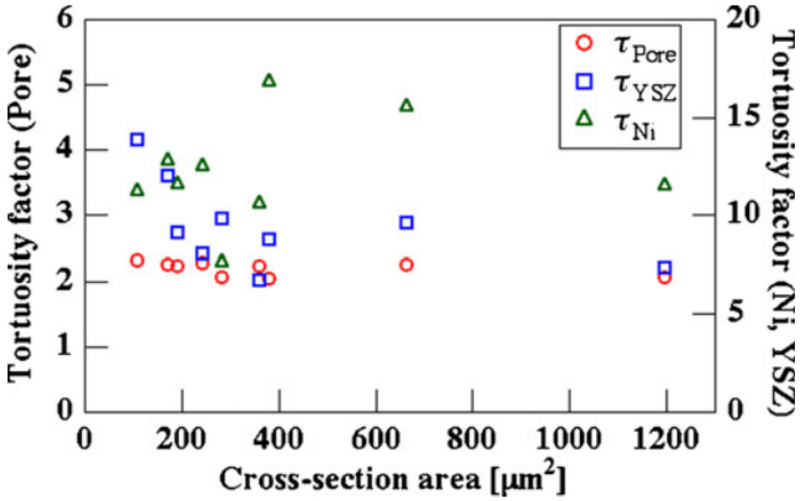

Figure 26: Variation in tortuosity factor for each phase for large reconstructed volumes of the Ni-YSZ anode of an ESC, reproduced with permission from [138]

The authors used the LBM developed in previous work [137] and the dusty gas model [139] to predict anodic polarisation from their 3D reconstructions. Due to the volume taken for their largest sample, the entire electrode thickness was modelled, and it was shown that the overpotential is slightly underestimated with smaller volumes. The simulated results fit the experimental data better, in terms of the steam concentration dependence of exchange current density, from Bieberle *et al.* [136] than from

de Boer *et al.* [140]. Nevertheless, significant discrepancy was still seen, thought to be due to the assumption of constant pressure in their diffusion model.

Kishimoto *et al.* used microstructural parameters extracted from FIB-SEM investigations to predict anode polarisation [141]. They adopted the “volume expansion method” to identify the total TPB density but failed to make the distinction between total and active TPB density. Nevertheless, their simulations corroborated that the thickness of the active region is approximately 10 µm and at lower humidities, their simulated anode overpotentials broadly matched those measured by experiment. However, at high humidity and/or low temperatures, the deviation between theory and practice widened greatly.

Holzer *et al.* further highlighted that although electrochemical reactions likely take place close to the TPB, there is a finite width to many different reaction steps, including surface adsorption of fuel on and desorption of fuel from the metal, formation of hydroxides on the ceramic, alongside charge transfer reactions [142]. Therefore, these properties should also be investigated when inspecting the structure-property relationships key to assessing SOFC electrochemical performance. Work by Joos *et al.* further reinforced the need for a representative volume for reliable metrics analysis [143].

2.2.1.4 Contiguity

Wilson *et al.* developed algorithms to describe whether each phase “network” is isolated within the volume, is dead-ended (enters from either current collector or electrolyte but does not reach the other side) or contiguous if it crossed the entire domain [131]. Their analysis showed that for the volume investigated, a single connected network of nickel constituted 68% of the total Ni volume, and 87.5% in the case of the pores, with overall contiguity in each case reaching 86 vol% and 96 vol%, respectively. The YSZ phase was 100% contiguous and represented the backbone of the system. The authors remarked that it was unusual that the smaller pore volume (vs nickel) had a more percolated network and cited the tendency to minimise interfacial energy by appearing on Ni-YSZ interfaces.

Vivet *et al.* utilised in-house software, based on a Hoshen-Kopelman algorithm [144] to inspect the level of connectivity of the three phases in a porous Ni-YSZ cermet [145]. This method establishes 'clusters' by grouping voxels of the same phase sharing faces (but excludes vertices or edges). If an identified cluster reached all six artificial boundaries (encapsulating the volume under analysis), said cluster was deemed to be percolating. In their ~1000 μm^3 volume, all three phases were shown to be primarily made up of percolated clusters, with the least percolated being the nickel network at 87.4%. Interestingly, their volume-specific surface area (VSSA) and volume-specific interfacial area (VSIA) calculations only included the percolating volumes, which is not yet common practice in the literature.

2.2.1.5 Tortuosity Factor

Wilson *et al.* solved the Laplace equation using finite element analysis to assess the tortuosity factor (discussed in detail in **Chapter 3**) in all directions for the gas phase [132]. The authors found a significant degree of anisotropy, considered to be an artefact of the small volume investigated.

Kishimoto *et al.* used the geometry acquired from slice-and-view tomography for a random-walk-based diffusion simulation [146] in order to quantify tortuosity factors [141]. The authors defined the effective transport rate as shown in Equation *2-2*:

$$\Gamma_i^{eff} = \frac{V_i}{\tau_i}\Gamma_i \qquad 2\text{-}2$$

where V_i *and* τ_i *are the phase fraction and tortuosity factor for phase* i*, respectively*

In this method, a large number of "random walkers" are distributed at random across a particular phase, and "walk" to an adjacent voxel if they are the same phase; they remain stationary if not. The mean square displacement of the random walkers is calculated as a function of time, and the transport rate can be correlated with its time derivative (Equation *2-3*):

$$\Gamma_i = V_i \frac{1}{6}\frac{d<r^2(t)>_i}{dt} \qquad 2\text{-}3$$

To access the tortuosity factor, this is compared with the transport rate that is obtained if the same process is allowed to run in free space, hence giving Equation *2-4*:

$$\tau_i = \frac{V_i}{V_i^{eff}} \frac{\frac{d<r^2(t)>_{bulk}}{dt}}{\frac{d<r^2(t)>_i}{dt}} \qquad 2\text{-}4$$

The study found that the tortuosity factors for the two solid phases were highly anisotropic (at the volumes investigated), and in their microstructure, the tortuosity factor was lowest and more isotropic for the pore phase for all 3 volumes sampled.

Vivet *et al.* completed similar work but used an implicit 3D finite difference method to evaluate the diffusive tortuosity factor [145]. Again, the diffusivity factor was defined in a similar way as in the work by Kishimoto *et al.* Here, an effective diffusion coefficient was calculated under steady-state conditions by solving Equation *2-5* and then the average convective flux over a cross-sectional area normal to the flux direction was calculated.

$$\vec{\nabla} \cdot \left(-D\vec{\nabla}\theta\right) = 0 \qquad 2\text{-}5$$

where θ corresponds to the driving force in each case for each form of transport (i.e. electronic potential for electronic conductance and concentration for mass diffusion).

Comparing this for the equivalent homogenous medium (i.e. phase fraction = 1) gave similar tortuosity factors in the X- and Y-directions but a higher value in the Z-direction. However, the final step in their calculation, to calculate “tortuosity” from “tortuosity factor” assumes the same cross-sectional area to all networks which was very improbable in the real anode microstructure investigated [147].

2.2.1.6 Humidity

Matsui *et al.* exposed Ni-YSZ cermets to highly humidified atmospheres (simulating high fuel utilisation and/or direct internal reforming conditions) and investigated the degraded microstructure by FIB-SEM tomography [125]. It was found that, regardless of the cermet composition, a parabolic relationship existed between interfacial conductivity and pO_2 such that a local maximum in conductivity was found at approximately 15 - 25% humidification of the incoming H_2 stream. A minimum in anode

overpotential was found for a 20% H_2O-80% H_2 atmosphere. When humidity was increased past 20%, degradation was much more severe than the gentle decline seen at 20% itself (Figure 27).

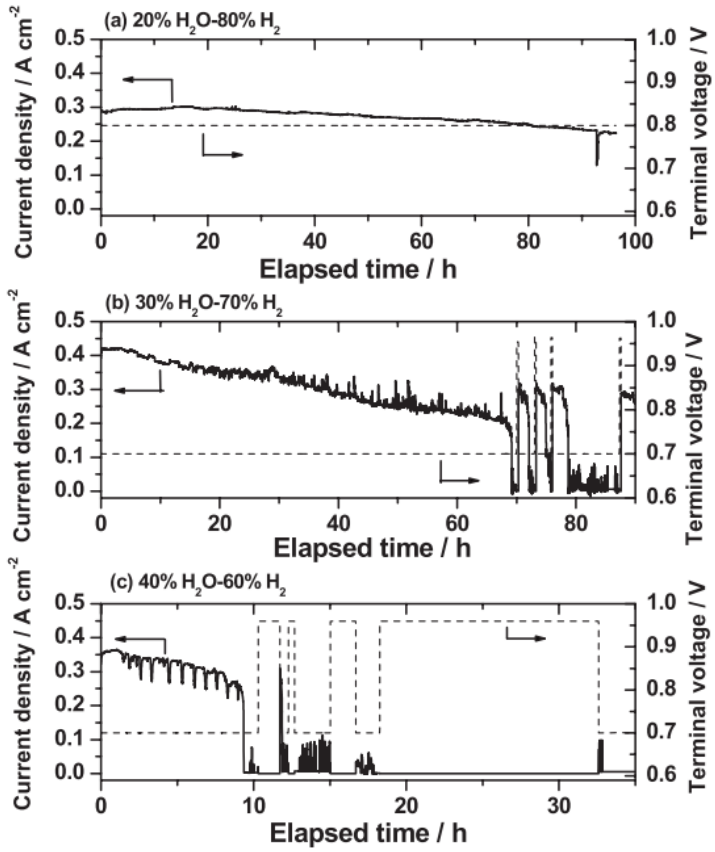

Figure 27: Time evolution of current density as a function of humidity, reproduced with permission from [125]

The authors noted that sudden deterioration of current density at 30% humidity could have been caused by a further increase in pH_2O due to the build-up of steam generated by electrochemical reaction, causing the inhibition of fuel diffusion and/or the deactivation of nickel. At 40% initial humidity, the degradation was irreversible and resulted from a marked increase in anodic polarisation after only 10 h, along with an increase in ohmic resistance, possibly due to partial oxidation of nickel. Further work on humidity is described in the next section, as both microstructural snapshots before and after humid treatments were gathered.

2.2.1.7 Microstructural Evolution

During the last decade, much research has focused on microstructural evolution in SOFC electrodes, such that FIB-SEM tomographies are taken of an untreated, and separately of a treated sample, for comparison. The extracted metrics are then used to

investigate the treatment's impact on microstructure and attempts are made to correlate this with electrochemical performance.

Holzer *et al.* undertook a comprehensive study focusing on Ni-CGO anodes, both in the reproducibility of microstructural analysis and monitoring the effect of annealing in dry and humid conditions on two compositions [148]. The foci were two underlying mechanisms behind the Ostwald ripening phenomenon [149] seen in nickel grain growth: the transportation of volatile nickel and the diffusion of vacancies driven by differences in surface curvature. For the former mechanism, the authors noted that $Ni(OH)_{2(g)}$ is the most volatile species in a gas mixture of H_2 and H_2O over a nickel surface at 950 °C and 1 atm. (Figure 28). Clearly, in dry conditions, volatilisation of either of the species shown is markedly lower.

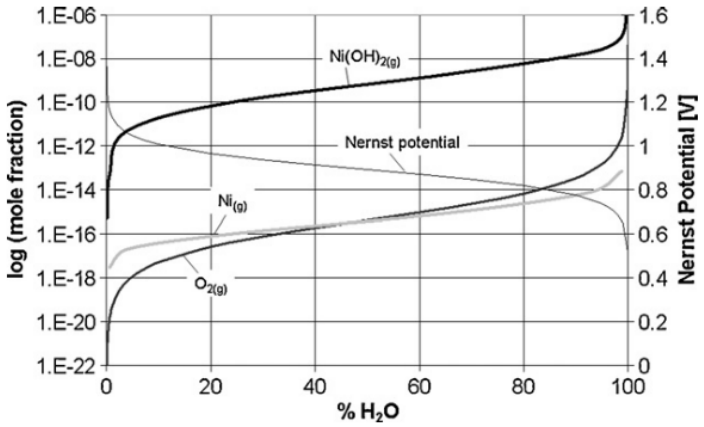

Figure 28: Thermodynamics for Ni at 950 °C & 1 atm, reproduced with permission from [148]

Referring back to work by Vassen *et al.* [113] (see **Section 2.1.3.2**), the latter mechanism is attributed to the different curvatures of adjacent particles. Assuming the vacancy theory of diffusion [150], differences in curvature between large and small particles yield different pressures in their matrices and hence different vacancy concentrations in the particles [113]. This discrepancy results in a flux of vacancies from the large to the small particle, or a diffusive flux of material from small to large particles.

The authors investigated the use of a discrete PSD, implementation of the intercept method [108] and the application of an in-house continuous PSD (cPSD) method [151] (**Section 3.4.1.3**) to evaluate the time-dependent changes of PSD throughout annealing. The cPSD approach was shown to work better than former

methods by precluding the need to identify individual objects and by avoiding any stereological estimations. When applied to the microstructural evolution of their Ni-CGO in dry H_2 atmospheres, the average nickel radii increased by 36% for their fine-grained layer and 25% for their coarser layer. Growth rates were seen to increase with time in dry conditions, but a very different trend was seen in humid conditions. As previously observed, nickel grain size increased very rapidly in the initial 150 - 200 h but remained constant between about 1000 and 2000 h (Figure 29). Significantly, the authors also note much greater evolution in the CGO and pore structures, suggesting that the formation of continuous CGO layers around nickel grains may contribute to the hindrance of further growth at long exposure times.

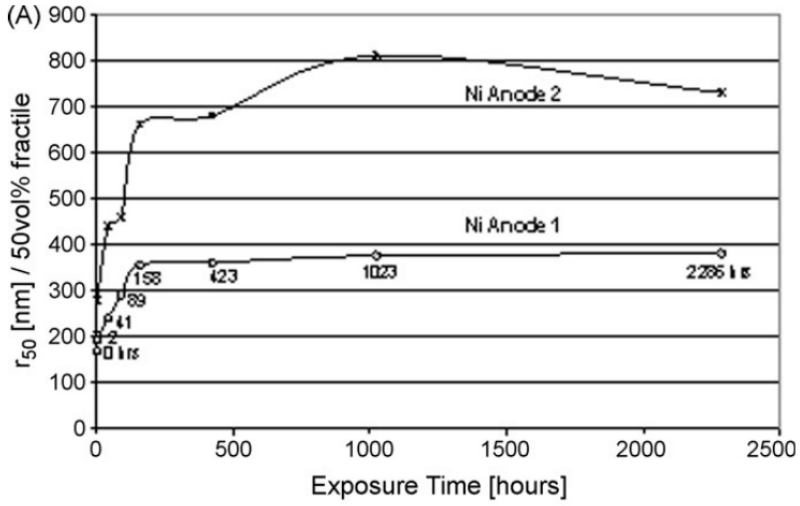

Figure 29: Evolution of Ni r50 with time under humid conditions, where Anode 1 has a finer microstructure than Anode 2, reproduced with permission from [148]

Under humid conditions, the microstructural changes were greater in Anode 2 (coarser microstructure); the gradient during the first 158 h is greater than for Anode 1. The CGO constituent in this coarser layer continued to evolve, even at times >1000 h. Again, this work emphasised that nickel growth rates are high initially when the inlet gas is wet, but plateau somewhere around the 150 - 200 h mark.

Further work by the same group focused on linking TPB density to the nickel grain size (by cPSD) and inspected the specific changes in TPB density and VSSAS/VSIAs linked to the nickel grain growth in their experiments on Ni-CGO anodes at 950 °C in humid H_2 [142]. For their coarsest layer, $VSSA_{Ni}$ was appreciably lower than that for the CGO and pore phases, as expected, but only 35% of this was exposed to pore and thus

readily accessible for surface reactions (Figure 30). Their analysis showed that the TPB density was not linearly correlated to the surface area of any specific phase, although the changes in volume fraction and VSSA of nickel had the strongest impact on it. However, there is a strong correlation between the $VSIA_{Pore-Ni}$ and TPB density, emphasizing it as a limiting microstructural factor for TPB formation.

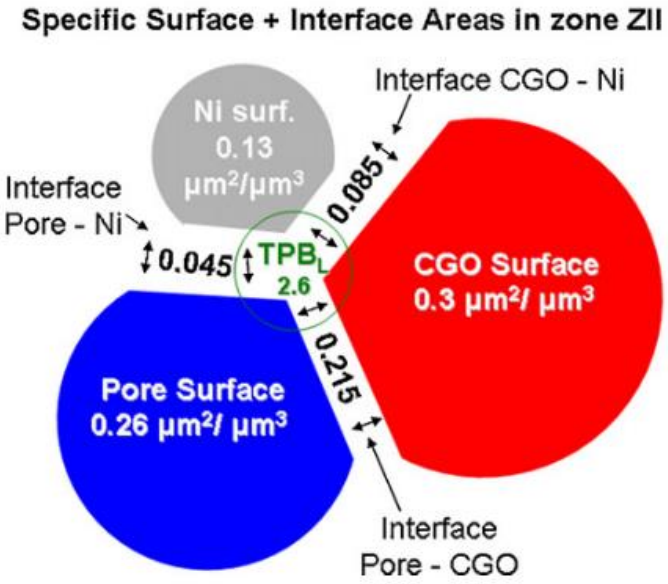

Figure 30: Metrics extraction from FIB-SEM reconstruction of 'virgin' Ni-CGO anode, from the ASL near the current collector (Zone ZII), reproduced with permission from [142] (N.B. the VSIA values presented are missing units of μm^{-1})

Unfortunately, only the 'virgin' sample in this study was investigated in 3D; the TPB information from the 'aged' samples was based on stereology so the quantification of the evolution of active TPB density was not possible. Their analyses nonetheless concluded that TPB length is strongly correlated with nickel grain growth, at least for an initial (~200 h) period, thereafter continuing to fall despite nickel grain growth almost halting; the authors explain the loss of TPB at longer times as a result of nickel loss [115] and/or a continuous CGO layer forming around nickel grains [91].

Cronin *et al.* investigated the microstructural evolution of a Ni-YSZ AFL by accelerated ageing at 1100 °C, providing geometrical input for an electrochemical model and comparing its results to EIS measurements made on full cells [152]. Their analysis showed there was no net nickel loss, $VSSA_{Pore}$ significantly decreased (-25%) and the $VSSA_{Ni}$ remained constant within experimental error, somewhat at odds with previous observations [142]. Total TPB density decreased, but the active TPB density dropped

considerably more, reducing the %Active TPB from 77% to 56%, based on linear apportioning of “unknown” lengths. This represents a dramatic change for only 100 h annealing but is testament to the degradation that can occur when applying an accelerated test at a higher temperature than usual.

Work by Matsui *et al.* on the $Ni(Sc_2O_3)_{0.10}(CeO_2)_{0.01}(ZrO_2)_{0.89}$ cermet anode of tubular SOFCs investigated both before and after long-term operation at 900 °C with humidified gas, linking voltage loss with microstructural evolution [153]. Some indication of Ni loss was observed in volume fraction changes from an area chosen downstream from the fuel inlet, likely to be high in humidity [115]. A large increase in isolated Ni volume was observed at longer times and %Active TPB was also seen to drop from initially 92%, to 78% at 6500 h. This study, however, did not quantify nickel grain growth, so the connection between active TPB loss and nickel coarsening unfortunately cannot be determined from their results.

Jiao *et al.* investigated the impact of sintering temperature (1400, 1450 and 1500 °C) on initial anode performance and its electrochemical performance degradation after 100 h of operation [154]. The intercept-length method [108] was used to quantify (only in 2D) the particle size after sintering, and both Ni and YSZ were found to increase, whilst pores remained constant, with increasing sintering temperature. During operation, percolation was seen to drop for Ni but remained the same for YSZ and pores. The authors found that the anode sintered at 1450 °C gave both the highest initial performance, as well as the lowest degradation rate and attributed this to producing a strengthened YSZ network capable of somewhat inhibiting nickel coarsening. Large-scale cracking was seen at the highest temperature, thought to be detrimental to percolation and active TPB density. Moreover, the authors stressed that both ohmic and polarisation resistance are affected by nickel coarsening’s deleterious effect on active TPB. The authors also underlined the importance of considering ex-solved Ni from NiO dissolved in the YSZ framework during sintering; the higher the sintering temperature, the greater the excess Ni ex-solved on reduction, the lower the stability of cubic YSZ. As a result, the conductivity of the YSZ decreases as a result of the presence of more

tetragonal phase [155] and thus the ohmic resistance attributable to the anode increases at the same time as the polarisation resistance.

Y.-H. Lee *et al.* investigated the effects of temperature (1000 vs 1100 vs 1200 °C) and humidity (10% vs 40% H_2O) on nickel agglomeration by performing slice-and-view on a "virgin" Ni-YSZ anode and then on individual anodes subsequent to each of the aforementioned treatments for 50 h [156]. EIS showed that polarisation and ohmic resistances increased in all cases (Figure 31), but most dramatically for the higher temperatures and higher humidities, matching a similar trend in nickel grain growth.

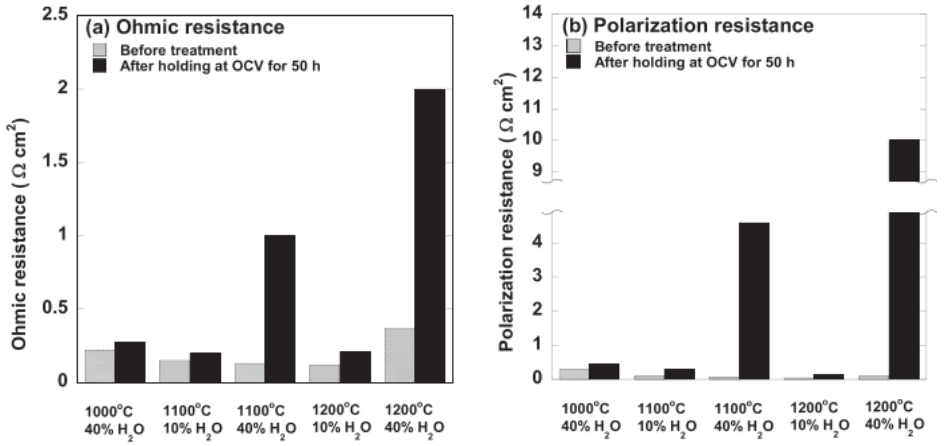

Figure 31: Anodic ohmic and polarisation resistances, before and after various high temperature treatments, reproduced with permission from [156]

The authors also noted qualitative changes to the nickel surface; in dry atmospheres, fine cracks were observed whereas with high humidity, significant crack formation was observed. This is likely to influence the percolation of various phases and hence cause a drop in active TPB and conductivity of electrons to the current collector. Using the line-intercept method [108], the PSD for each phase was extracted from the microstructural data, as shown in Figure 32. YSZ remains largely unchanged, whereas nickel and pore clearly coarsen. The trend in the magnitude of this effect matches the resistance changes measured by EIS.

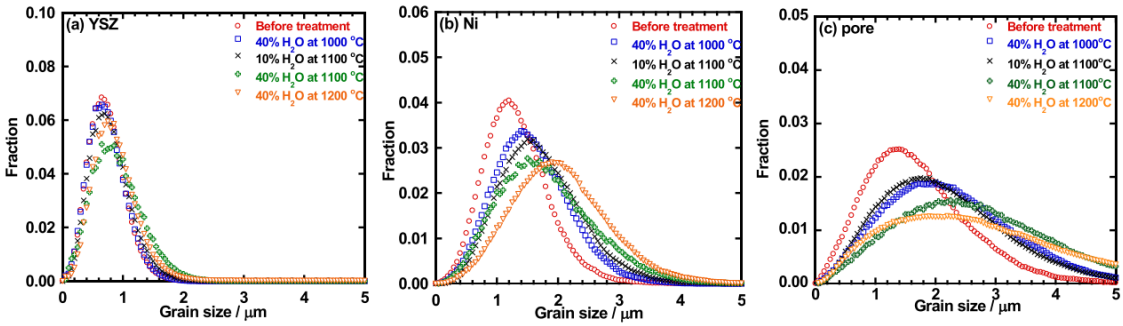

Figure 32: Plots of PSDs for each phase, reproduced with permission from [156]

The absolute TPB length dropped in the same order as the polarisation resistance, providing more evidence of the link between nickel coarsening, TPB loss and loss of electrochemical performance. However, although the initial active TPB proportion was 81% (c.f. that from work by Wilson *et al.* [132]), this proportion did not, in fact, show a clear monotonic drop but instead remained approximately stable. Significantly, this work also highlighted the possible encapsulating effect of the ceramic (here, YSZ) on restraining nickel grain growth, as seen in the work by Holzer *et al.* [148][142] in Ni-CGO anodes. The authors postulate a mechanism of Ni movement, as migrating ions, through NiO formed at TPBs, to coalesce into large particles but do not provide solid evidence of observing this.

2.2.2 X-ray computed tomography (XCT)

Despite many insights into understanding microstructural properties, along with their time evolution, one major drawback common to all FIB-SEM slice-and-view studies is the variation between different samples that is inherent in this type of tomography approach; by virtue of its destructive nature, there are resultant uncertainties caused by microstructural variations between different samples investigated in pre- and post-treatment steps. Fortunately, another tomographic route has been investigated concurrently, namely, X-ray nano-computed tomography (X-ray nano-CT). A clear advantage of X-ray nano-CT over FIB-SEM slice-and-view is that it is non-destructive, potentially lending itself to examining the same area of the same sample before and after a treatment of choice. However, juxtaposed with the high contrast between Ni and YSZ *via* low-voltage electron microscopy [128], X-ray nano-CT contrast for these solids has been less forthcoming and thus required synchrotron-source X-ray fluxes before the

development of careful sample preparation, parameter optimisation and post-processing expertise.

2.2.2.1 Lab-based experiments

Despite issues with contrast, the first investigations using X-ray nano-CT to examine the microstructure of SOFC electrodes were undertaken using lab-based instruments by Tkachuk *et al.* [157] and Izzo *et al.* [158], utilising the K_α emission line of a Cu anode (8.05 keV). A hollow anode-supported tubular SOFC was imaged with sub-50 nm pixel dimension but required 300 s per projection and only provided contrast between solids and pores as distinguishing Ni from YSZ was not possible. Nevertheless, the binary segmented image provided a real initial microstructure that was the basis of tortuosity simulations by solving the Laplace equation by the LBM [159]. From their analysis, the authors extracted a porosity of 30%, a mean pore size of 0.34 µm and proposed that a volume of only 8 μm^3 was necessary to be representative for porosity of this nature. Their analysis showed that tortuosity factor values required a larger representative volume element (RVE), and that their SOFC anode microstructure displayed anisotropy in these values. This work represented a promising start in the non-destructive investigation of SOFC electrodes with X-ray nano-computed tomography but suffered from long scan times, no solid-phase contrast and lack of a robust sample preparation technique.

Similar work was carried out by Shearing *et al.* in which the X-ray nano-CT and FIB-SEM approaches were compared on the same batch of sample [160]. In the X-ray nano-CT case, the FIB lift-out approach [161] was employed to ensure the sample fit within the X-ray field-of-view (FOV), though this work reiterated that there existed insufficiently uniform contrast between Ni and YSZ grains to give reliable three-phase segmentation.

2.2.2.2 Synchrotron-based experiments

2.2.2.2.1 Single Microstructure

To circumvent the solid-phase contrast issue, many researchers focused their attention on using brighter synchrotron sources whereby the greater flux not only leads to a higher signal-to-noise ratio, but the tune-ability of the X-ray energy also allows for

specific “K-edges” of constituent materials to be exploited. Specific beam energies can be chosen given the knowledge that an element of interest has a sharp gradient in its attenuation coefficient at a nearby energy, a technique often denoted X-ray absorption near-edge structure (XANES) spectroscopy that typically inspects the fine structure close to the absorption edge (usually ~ 20 eV above and below).

A good example of early X-ray absorption spectroscopy (XAS) imaging measurements on SOFC anodes was conducted by Shearing *et al.*, taking advantage of the discontinuity in X-ray absorption coefficient of Ni around 8.33 keV (K-edge) [162]. By imaging above and below this energy, all three phases (and hence the percolated triple phase boundary density) were identified. The study indicated the need for a large sample volume to provide microstructural data representative of the electrode and again a FIB lift-out sample preparation route was followed [133]. The study calculated phase fractions and active TPBs in two-directions for the full volume and sub-divisions thereof, showing that their SOFC electrode analogue contained heterogeneities at a scale of roughly a quarter of their entire sampled volume. This result illustrated the need for investigation of real state-of-the-art microstructures which benefit from well-developed manufacturing procedures that give a greater degree of microstructural homogeneity.

Similar studies were performed by Grew *et al.* on the real microstructure of an anode from a micro-tubular fuel cell, however analysis was only applied to very small sub-volume of ~14 μm^3 [163]. Thresholding of the below-edge and above-edge data (Figure 33) required visual inspection of each slice but avoided the need to rely on externally obtained information from other methods with their own inherent uncertainties. Their tortuosity calculations utilised the same LBM as used by Izzo *et al.* [159] but applied it to all three phases identified by XAS imaging. Contiguity of all three phases along with the two-phase and three-phase interfaces were examined, as well as using a combined LBM/ray-shooting approach for assessing particle/pore size distributions (PSDs). This ray-shooting method discretised the considered directions to 19 per voxel, and from each interfacial voxel, virtual rays were ‘launched’ normal to that interface and terminated when they reached another interface. The voxel length of the rays is calculated and used

in calculations of the PSD, about which more details are provided in [164]. Considerations were also made based on the constrictions identified by the tomographic data and their estimated role in Joule heating [165].

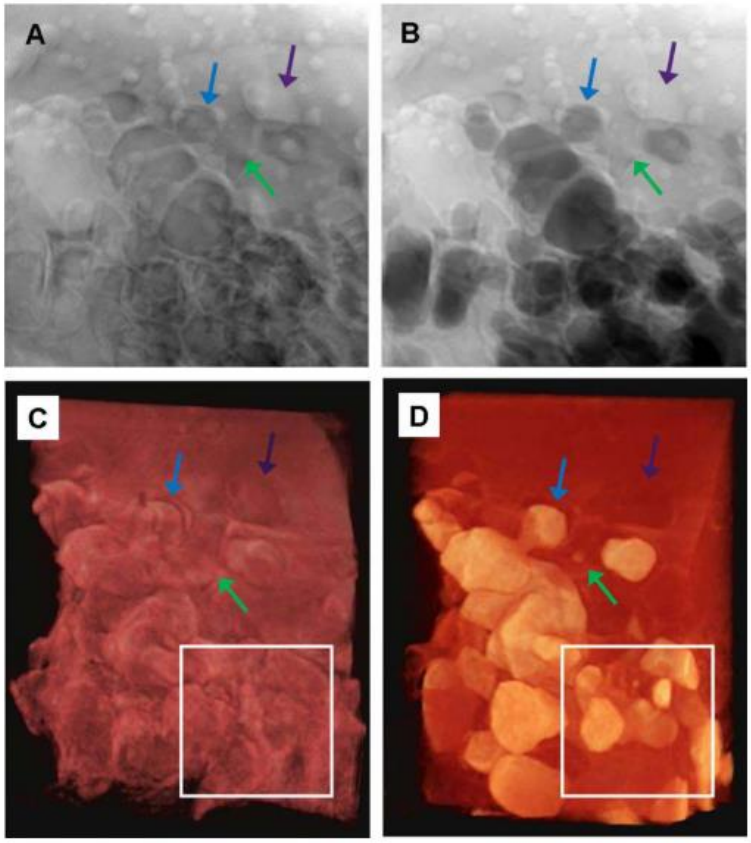

Figure 33: Radiographs at a) 16 eV below and b) 24 eV above the Ni K edge (8.333 keV) and 3D reconstructions from the same, reproduced with permission from [163]

Their PSD analysis identified that roughly 50% of the cumulative volume of the pore, Ni and YSZ phases constituted regions with diameters of 0.2, 0.5 and 1.0 µm – a relatively fine microstructure. An anomalously high value was found for the tortuosity factor for the pore phase in the Z-direction and the authors noted that the investigated volume was too small to be representative and probably suffered from boundary truncation effects. Nevertheless, the authors determined that even when the bulk resistivity difference between nickel (electronic) and YSZ (ionic) is accounted for, there was a clear microstructural factor that led to greater losses for ionic transport than electronic transport. Their %Active TPB was extremely low (3%), indicating that for this metric, the small volume studied was very likely not representative.

Guan *et al.* undertook similar studies at a synchrotron and applied an “expansion method” for RVE analysis of their reconstructed volumes [166]. The RVE analysis predicted that approximately 100 μm^3 were needed to represent the pore volume, larger than previous studies. The work developed a method to extract the connected porosity, similar to previous work on cement pastes [167], which showed that only 1% of the pore volume in their samples was unconnected. The authors extracted VSSAs and VSIAs, however, from their presented orthoslice, it appears that their segmentation may have suffered from the mis-allocation of YSZ-pore boundaries to the nickel phase, which is likely to have affected the reliability of these measurements.

These studies were expanded upon by examining larger volumes, first in a large-volume study of the AFL of an anode-supported button cell by Chen-Wiegart *et al*. wherein a total volume of ~25,000 μm^3 was imaged and ~3,600 μm^3 analysed [168]. Connectivities were seen to be in the region of 99%, the proportion of active TPB was roughly 95% and the absolutely active TPB density was 2.89 μm^{-2}, in line with previous studies [132][131][126]. Subsequently, a holo-tomographic investigation of an ASL was undertaken by Laurencin *et al*. [169] who reconstructed a volume of ~185,000 μm^3 at a voxel dimension of 60 nm (Figure 34), far surpassing the volumes in previous studies. The authors referred to previous works in which RVE sizes of 500 μm^3 [170] and 1000 μm^3 [171] had been identified as sufficient to describe overall electrode properties for finer microstructure. However, they also pointed out that this is less than the theoretical predictions by Metcalfe *et al.* [172], and that there was a need for greater volumes to describe the coarser ASL. The latter work predicted that a cubic volume with dimensions 14 times the mean particle diameter was necessary for representative analysis.

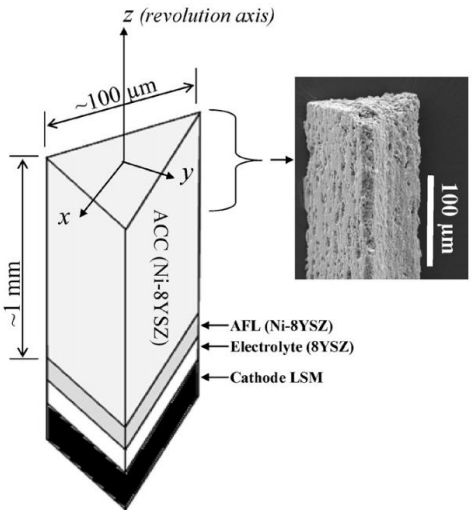

Figure 34: Schematic of large sample investigated by X-ray nano-CT and SEM micrograph of the same, reproduced with permission from [169]

Their analysis centred on extracting metrics to describe the porous network, including contiguity, phase fraction, tortuosity and mean pore radius. 96% of the pores in the reconstructed volume were shown to be percolated, broadly agreeing with work by Guan *et al.* (99%) [166], which had a similar level of porosity. Due to the large volume investigated, several separate 'sub-samples' could be extracted and used to extract a standard deviation for the porosity, shown to drop significantly at a volume dimension of ~14 µm (2,750 μm^3) but only falling within 'negligible dispersion' at 35 µm (~43,000 μm^3), according to the authors. It is important to note that both suggested volumes necessary to represent porosity are much larger than the volumes investigated or suggested hitherto. When estimating the pore VSSA, the authors noted the discrepancy between the real microstructure and the cubic voxel representation, calling upon a scaling factor of π/6 to account for this. The median value between their voxel-based value and the scaled value matched the VSSA determined experimentally by the Brunauer-Emmet-Teller (BET) method very well (within 5%). In applying RVE analysis to tortuosity factor, it was seen that a similarly large volume (>40,000 μm^3) was necessary, and with very large volumes, the discrepancies between directions are much reduced compared with previous investigations. A significant drawback of this work, however, was the lack of solid-phase contrast such that all analysis was limited to a single phase (pore).

Villanova *et al.* improved on this work on large volumes by inspecting the ASL and AFL with high energy (29 keV) synchrotron radiation utilising the same phase contrast technique, known as 3D nano-holotomography. This technique quantitatively exploits the phase shift that results when the coherent radiation from a synchrotron source interacts with the sample, and by taking X-ray nano-radiographs at multiple focus-to-sample distances, a 3D reconstruction of the attenuation coefficients of the sample materials can be generated (more information about which can be found in [173]). Compared with the previous study, resolution and contrast were improved. Given the high resolution (voxel dimension = 25 nm) and large imaged volumes (~100,000 μm^3) of both important layers (AFL and ASL), the solid-phase contrast is especially impressive, as seen in Figure 35.

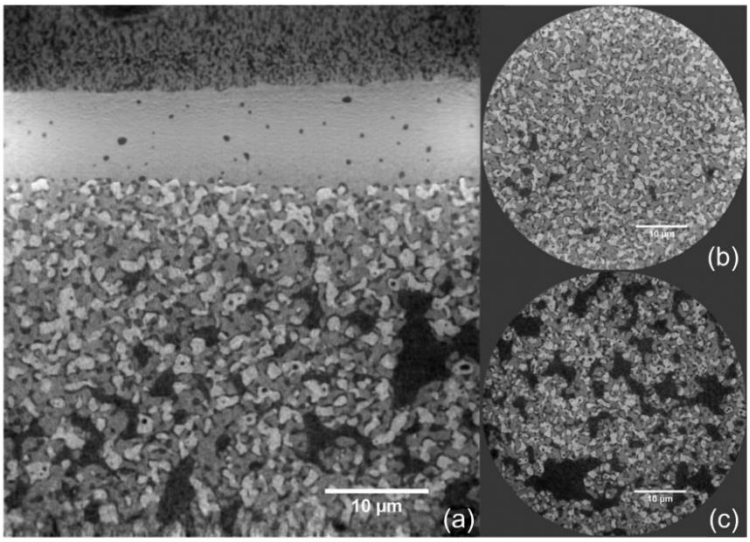

Figure 35: a) Longitudinal cross-section of holotomographic reconstruction of an anode-supported cell (ASC); transverse cross-sections of b) AFL; and c) ASL, reproduced with permission from [173]

The authors discovered that by infiltrating their ASCs with epoxy resin, the phase contrast could be improved, and the region boundaries made sharper. Their analysis showed that the Ni and YSZ particles were on average 30% smaller in the AFL than ASL and that the average pore diameter was ~3 times smaller, thus, they recommended an RVE dimension of ~13 µm for analysing the finer layer. Consideration was also given to the resolution required to adequately capture the microstructure, making reference to work by Joos *et al.* [174][175] that claimed 15 - 20 voxels are needed per characteristic diameter for accurate surface area measurements. By this analysis, Villanova *et al.*

stated that ~55 nm was required for appropriate assessment of the ASL and ~36 nm for the AFL, at least with the microstructure investigated.

Cronin *et al.* also inspected the entire active region of an SOFC, in this case the inner anode-electrolyte-cathode section, totalling ~38,500 μm^3 from which a ~3,650 μm^3 volume of the Ni-YSZ AFL was reconstructed [176]. The authors prepared the sample as a cylinder with diameter ≈ 35 μm and height ≈ 80 μm, using a focused-ion beam, before imaging with typical XAS imaging below and above the Ni K-edge. From their extracted metrics, a very high level of percolation was seen for all phases and the %Active TPB was 94%. It was also noted that there was relatively little Ni-pore interface, which the authors suggested may limit Ni coarsening processes during operation, and hence could be an advantageous metric of interest. Only the YSZ tortuosities were calculated, showing a low value of 1.26, consistent with a very well connected and easy-to-traverse path for O^{2-} ions. Their 1D model predicted anodic (and cathodic) polarisation resistance which matched very well with the EIS-extracted value. Importantly, this work showed that only ~15% of the cell polarisation resistance came from the anode, suggesting that its initial performance is good, and that focus should be on how it evolves and degrades.

2.2.2.2.2 Multiple Microstructures

While these researchers were implementing strategies to extract particular metrics, to develop simulations based on microstructural data, and to determine the representative volumes required, other researchers were investigating the impact of certain conditions by inspecting microstructures that had received treatments and contrasting them with those that had not. An early example is that by Nelson *et al.* wherein the researchers imaged central pieces from anode supports extracted from cells at various time intervals during operation at 720 °C under current load with *ex-situ* XAS imaging [177]. Their observations by X-ray nano-CT, and corroborated by SEM cross-sectional analysis, confirm that over 1130 and 1900 h, the Ni phase noticeably coarsens. However, this study was limited by the number of measurements, errors of a

similar magnitude to the changes examined, and not specifying the method by which the Ni “size” was established.

With more of a focus on thermal-cycling, Guan *et al.* also investigated the microstructural evolution of Ni-YSZ anodes by XAS imaging [178]. With increasing numbers of cycles, the Ni surface area diminished from an initial value of 1.65 (0 cycles) to 1.05 μm^{-1} (8 cycles), a drop of ~36%. Moreover, during the same treatments, Ni connectivity dropped from 98.3 to 90.6%. This study provided a measure of both the total and active TPB length over several time steps, as shown in Figure 36**.**

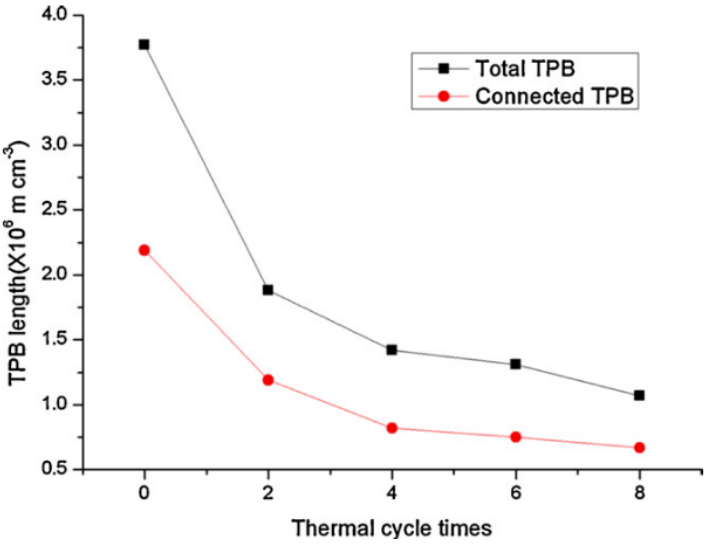

Figure 36: Plot of total and active TPB lengths as functions of the number of thermal cycles, reproduced with permission from [178]

These results displayed a roughly proportional relationship for total/active TPB degradation, and showed that by heating to 750 °C multiple times, TPB density is clearly degraded. However, it is not clear in this case to what extent the evolution is a result of the thermal gradients/changes involved in thermal cycling as opposed to the coarsening that accompanies being heated to this temperature. Later work by the same authors took a LBM approach to modeling the gas transport in these anodes, showing that thermal cycling induces a loss in pore connectivity and generates high concentration polarisation at TPB sites [95].

Further work by the research group of Chiu inspected the effect of annealing on Ni-YSZ anode microstructure but, importantly, took a statistically more rigorous approach, imaging 9 sub-samples in total, exploring the mechanism behind Ni particle

growth from the reconstructed volumes [179]. The authors used the evolution of PSDs, measured by the ray-shooting approach [163], along with a one-way layout analysis of variance (ANOVA [180]), to probe whether operation time could be used as a predictor for microstructural evolution. Moreover, the “dihedral angle” at TPB points between YSZ and pore surfaces were also investigated. A clear shift towards larger Ni diameter was seen with time, although at the longest times, the average Ni diameter was actually decreased. The authors suggest this may be due to the appearance of new small particles to reduce the complex curvature from the constrained microstructure, but this is less likely than a volatilisation effect that the authors predict not to be at play. Alternatively, it could be due to changes in the YSZ microstructure, as the authors note a gentle decline in characteristic YSZ size throughout operation. Their ANOVA analysis shows that there was less than a 2% chance that the observed Ni size changes were random: a much stronger statistical footing than most previous investigations. However, the YSZ size changes do not show this level of statistical significance (17%), so these changes may not require the above explanation. The active TPB length and contiguous Ni-YSZ contact area are shown to decrease exponentially, in line with previous studies suggesting Ostwald ripening [148] with a growth limit [93].

Accelerated AFL microstructural evolution was investigated by Yakal-Kremski *et al.*, using a mixture of FIB-SEM and X-ray nano-CT techniques, showing that isolated pore fraction increased significantly after 100 h annealing at 1100 °C and both the total and active TPB density decrease markedly [181]. The investigated volumes with X-ray nano-CT were notably larger than those sampled by FIB-SEM, emphasising the greater practical accessibility to statistically accurate metrics. Comparing X-ray nano-CT datasets, greater characteristic Ni feature size is seen after longer times, as well as a decrease in both specific surface areas for all phases and total and active TPB densities.

Kennouche *et al.* conducted accelerated annealing studies on Ni-YSZ anodes using synchrotron X-ray nano-CT to inspect different samples before and after annealing steps [182]. The work illustrated in-depth image processing techniques: correction for lateral shifts in the histograms across image stacks; brightness corrections along

horizontal and vertical axes; and stretching of the peaks in histograms to fit specific grayscale values, facilitating segmentation, as shown in Figure 37.

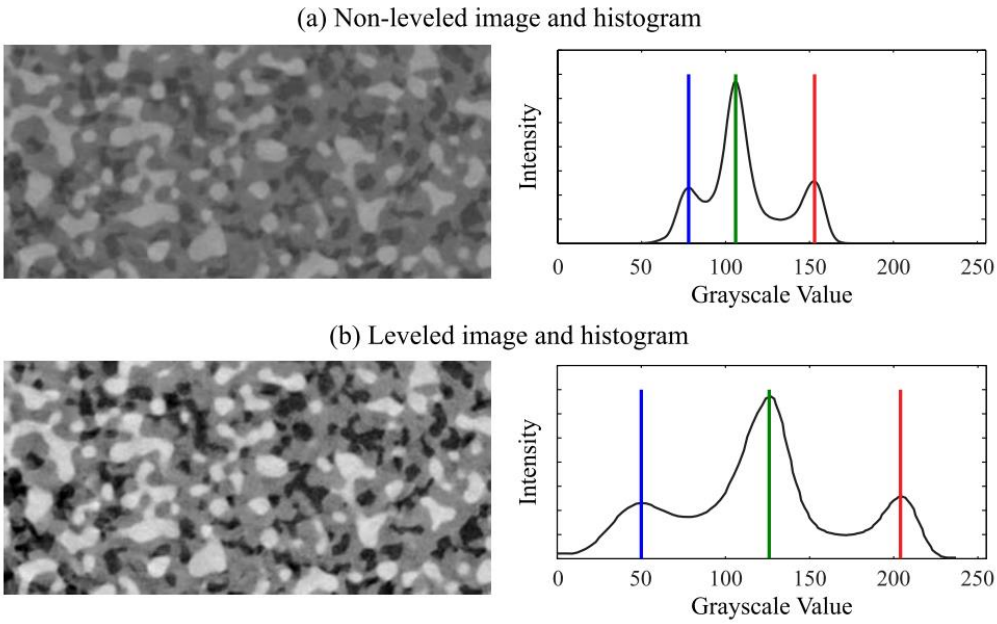

Figure 37: Example orthoslices, before and after image processing, to yield more segmentable dataset, reproduced with permission from [182]

For their initial studies with large sampled volumes (2500 – 6000 μm^3), the extracted volume fractions were within 3% error with respect to raw material compositions and the annealed samples clearly contained coarser nickel particles, with no nickel loss identified (1100 °C). The pore volume-specific surface area decreased over time, but that of Ni increased initially and then decreased for the highest temperature (1100 °C). Although $VSSA_{YSZ}$ did not change much for lower temperatures, it decreased notably at 1100 °C. PSDs extracted *via* an earlier method [148] displayed only significant coarsening for YSZ after annealing at the highest temperature for longer times, and was only significant for Ni for the highest temperature but even for shorter times. Most surprisingly, the nickel phase showed an increase in surface area between 20 and 100 h, which is at odds with general surface free energy minimisation considerations. TPB density, both active and total, decreased with increasing temperature and time, but maintained a similar proportionality throughout. Tortuosity factor values were generally isotropic but again, an increase was seen at intermediate temperatures and times, along with a drop in connectivity.

Further work from Kennouche *et al.* developed a coarsening model and a complementary electrochemical model to describe the effect of nickel evolution on anode charge-transfer polarisation [183]. The authors noted that early-stage changes seen in their previous study may have been due to non-equilibrated Ni and pore structures that result from NiO reduction and may not reflect long-term stability. Thus an initial 100 h (1100 °C) annealing step was completed before any analysis of microstructural evolution. Larger features were evident in the microstructures annealed at higher temperatures (up to 1200 °C), and again the authors confirmed no nickel loss and no significant Ni-YSZ sintering (pore volume loss). The PSDs extracted from the 3D reconstructions are shown in Figure 38 and display a general trend of increasing feature size with both temperature and time, with only the 1150 °C result for porosity bucking the trend.

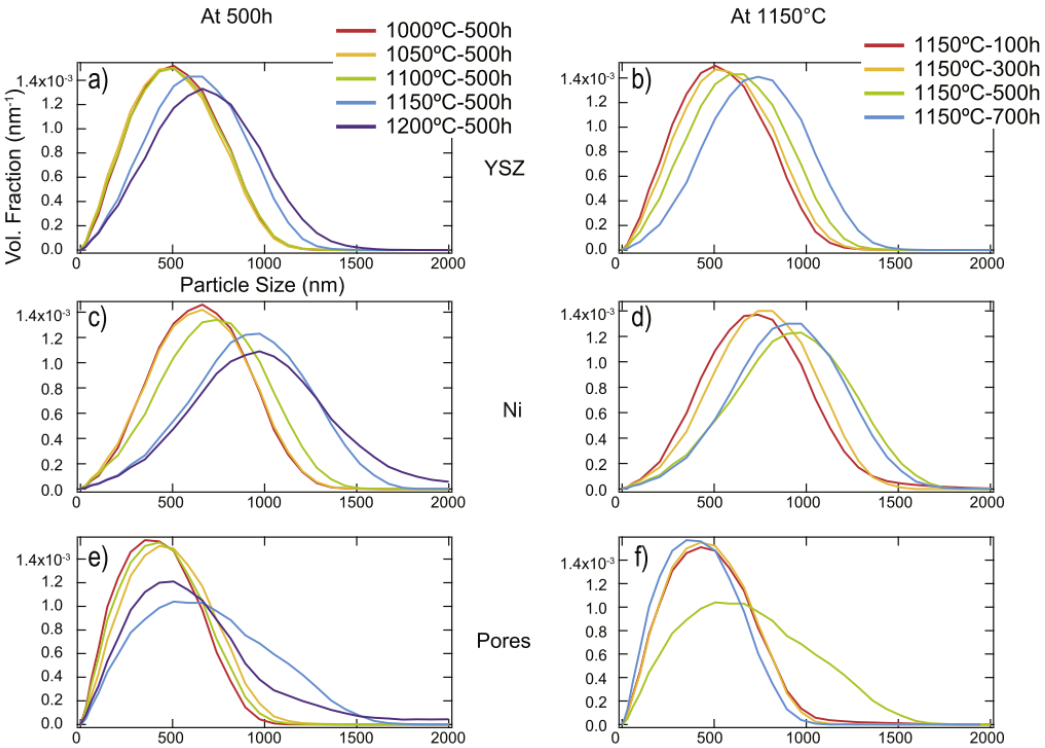

Figure 38: Plots of the PSDs for the three phases as they undergo annealing at different temperatures for different times, reproduced with permission from [183]

Unfortunately, the trends in power density measured by *i-V* curves did not follow the order of increasing ageing time and temperature, which the authors ascribed to sample-to-sample variations, possibly due to contributions from other cell components. Their EIS measurements were only marginally more in-line with these trends, showing

some complex behaviour. The authors admitted that there was insufficient data to provide a definitive exponent for their coarsening model, but they also state the n = 4 is a reasonable selection, giving the following equation:

$$l = l_0(1 + l_0^{-4} K_{D,0} t exp(\frac{-\Delta G_{act}}{k_B t})^{1/4} \qquad 2\text{-}6$$

where l_0 *is the initial length,* $K_{D,0}$ *is the pre-exponential factor for the thermally-activated process of surface diffusion,* t *is time and* k_B *is the Boltzmann constant*

The authors claimed the drop in anode polarisation predicted from this model and the TPB density from a model derived from it matched the experimentally measured polarisation resistance and TPB density, although there was considerable scatter in their results. Nonetheless, the study illustrated the potential to use multiple microstructural snapshots after various ageing regimes to link electrochemical performance to microstructural evolution.

2.3 4D imaging

2.3.1 X-ray computed tomography (XCT)

2.3.1.1 Synchrotron-based experiments

Very early work that attempted to leverage the non-destructive capability of the X-ray nano-CT technique by imaging the same sample before and after a defined treatment was work by Shearing *et al.* in which an SOFC cathode (LSCF) was imaged, *in-situ*, in a high-temperature environment on a synchrotron beamline, using XANES spectroscopy [184]. This involved the use of a bespoke IR-heated furnace and careful water-cooling to maintain nearby components at suitable temperatures. The sample was imaged and then heated *in-situ* at a rate of 50 °C/min to ~ 700 °C and allowed to equilibrate for 2 h, before re-imaging with the same parameters. The sampled volumes were approximately 330 μm^3 and a slight indication of sintering was detected between the tomograms. Although the data was two-phase and for an SOFC cathode material, this work presented a very clear pathway for monitoring microstructural evolution with high-resolution X-ray nano-CT conducted on the same sample and thus free of sample variation.

Although the main focus was Ni oxidation as opposed to Ni coarsening, insight into the latter process was drawn from research by Shearing *et al.* who investigated *ex-situ* heating of Ni-YSZ anodes in high pO_2, imaging after temperatures of 200 – 700 °C were achieved for 10-min periods in a furnace [185][186]. It was noted that unreduced NiO cores were seen in the centre of large Ni particles, attributed to high-temperature reduction and therefore concomitant nickel sintering which hinders gas access to the Ni/NiO interface required for the reaction. Although partial mechanical failure was observed for the final heating step, significant microstructural changes were observed as a result of this treatment (700 °C). A NiO film began to grow on the exterior of the nickel particles, with its own inherent porosity, blocking access to active Ni surface area for the HOR. This type of change should only occur when local pO_2 is high (oxygen ingress/high humidity), but it is worth bearing in mind that other microstructural changes occur within the anode that may compound the effects of interest in this thesis.

Further to previous research on different samples, Kennouche *et al.* conducted synchrotron-based X-ray nano-CT observation of microstructural evolution of Ni-YSZ anodes, inspecting the same microstructure between accelerated *ex-situ* annealing steps [187]. This study built upon previous work by fabricating a sample geometry amenable to elevated temperature annealing and providing means for nanometre-resolution image registration [188]. Mechanical polishing followed by several FIB milling steps were required to form a pillar with appropriate geometry for imaging, based on XANES spectroscopy. One sample was imaged, aged at 1050 °C for 24 h in forming gas, then re-imaged and this process was duplicated once. An example 2D orthoslice from the reconstructions from their unaligned pre- (0 h) and post- (48 h) annealing datasets is shown in Figure 39. The most remarkable features are the large nickel agglomerates seen on the exterior of the cylindrical sample volume, both in the AFL and ASL.

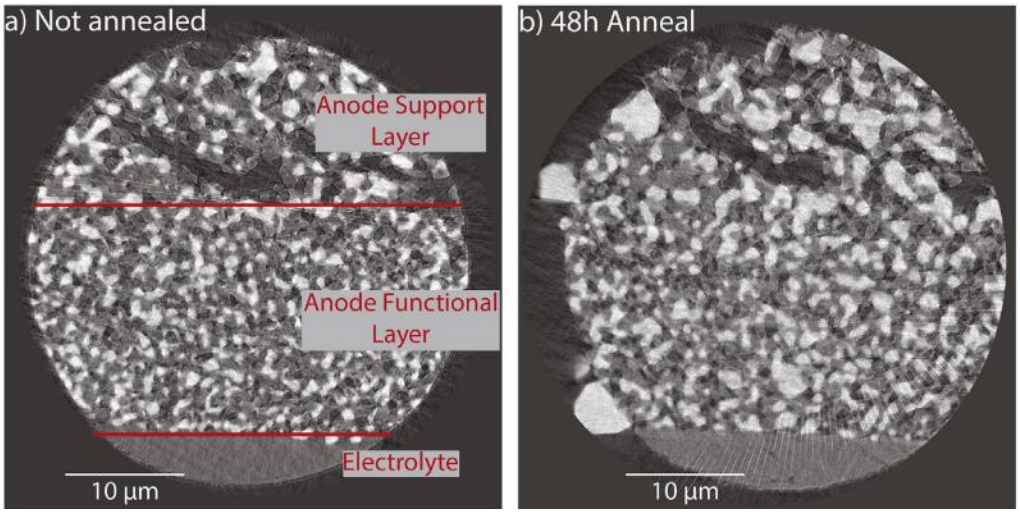

Figure 39: Orthoslices from reconstructions before and after annealing for 48 h at 1050 °C (black = pore, grey = YSZ and white = nickel), reproduced with permission from [187]

The agglomerates were deemed an “experimental artefact” as this type of interface is only present at the edge of an electrode layer, however it is possible that this underplays the importance of this observation. At the AFL-ASL interface and at the interface between internal nickel and cracks that form during operation, there is a good chance that the free space will become filled with nickel agglomerates; this phenomenon requires further investigation. A three-fold decrease in TPB length, elimination of small pores and nickel particles as well as the coalescence of separate nickel particles were all observed, along with an increase in pore phase tortuosity. Two other noteworthy observations are that the YSZ phase appears mobile at this temperature and that neck formation between nickel particles appears reversible and not easily explained by local surface energy minimisation effects. These observations are at odds with many previous studies and suggest complex processes at play during microstructural evolution of Ni-YSZ anodes.

Further work from the same research group investigated the effect of nickel content on the evolution of the cermet microstructure [189] concluding that increasing the metal/ceramic ratio accelerates the nickel coarsening rate, as suggested previously for Ni-CGO systems [142]. The appearance of external nickel agglomerates and the effect of reducing YSZ content are both stark examples of the importance of the ceramic backbone in mitigating the nickel agglomeration process. This study noted that significant

coarsening is observable after 12 h at 1050 °C, although it wasn't possible to obtain TPB densities due to the low image quality of the pore and YSZ phases.

2.3.1.2 Lab-based experiments

To avoid the hard-to-access and time-limited synchrotron sources, recent work has focused on achieving three-phase segmentation [190] using a lab-based source, by utilisation of long exposure times and small sample sizes. Access to reliable three-phase data from SOFC anodes in a laboratory setting gives way to conducting 4D (3D plus time) microstructural investigations without the restrictions implied by having limited beamtime at a synchrotron source. The first example of 4D nanotomography of electrochemical devices using a lab-based source was recently published by Heenan *et al.*, analysing the effect of redox cycling on commercially available SOFC anodes [191]. The necessary sample geometry was prepared by the methods outlined in this thesis (**Chapter 5**) and provided a robust platform from which to attain X-ray nano-CT tomograms of the same region between high-temperature treatments. The work provided 3-phase contrast, albeit by binning the data by 2, giving a voxel dimension of 126 nm and utilised a high-precision Class 4 laser for some of the sample heating. The resulting tomograms indicated a large increase in pore tortuosity as the pore volume was diminished on conversion of Ni to NiO (~70% volume increase [77]). This is particularly important when considering the issues inherent in a working stack; sealant damage, fuel interruption or particularly high pH_2O can result in major microstructural reorganisation that is often irreversible and has deleterious effects on electrochemical performance.

Further work by Heenan *et al.* used X-ray micro-CT, with a voxel dimension of ~400 nm, to characterise the large volumes of Ni-YSZ half-cells undergoing thermal cycling at various ramp rates [192]. The study employed the concept of "grayscale-fiducials" in order to ascertain a three-phase segmentation, after which several metrics including tortuosity factors, percolation percentages and TPB densities were extracted. It was noted that the pore tortuosity decreased significantly after the first thermal cycle to 750 °C (at 3 °C/min), possibly due to the mobility of nickel, which corroborates the speculation by Ioselevich *et al.* that new pores may be opened up during

initial reorganisation of microstructure [105][193]. Some evidence is presented to suggest that there is a slight fall in the number of small Ni particles with a concomitant rise in larger ones, whereas there is less suggestion of average particle size change for YSZ. It is noted that the nickel-YSZ interfacial area diminishes most, a phenomenon ascribed to the effects of Ni-YSZ thermal expansion mismatch by the authors. Comparisons of the first and last thermal cycles illustrate a retention of the general profile across the anode thickness for most metrics, but a clear diminution in TPB density and Ni-YSZ interfacial area (Figure 40).

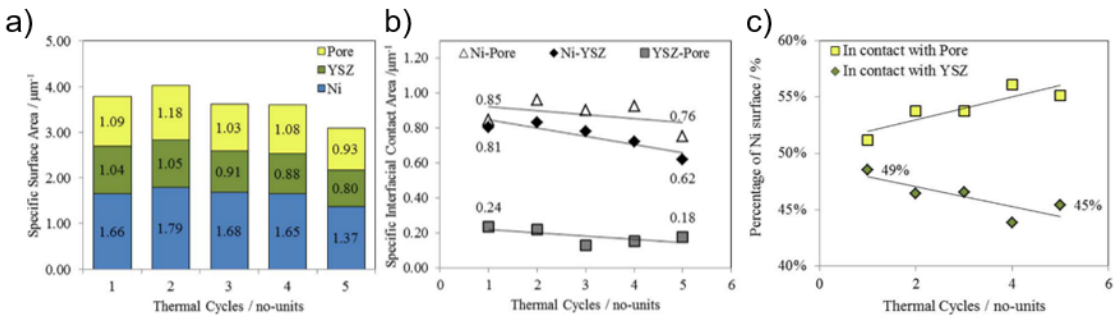

Figure 40: Plots displaying a) VSSA; b) VSIA; and c) % Ni surface in contact with pores vs YSZ, as a function of thermal cycling, reproduced with permission from [192]

2.3.2 Ptychography

X-ray ptychography is a recent technique, with the first reported use in 1996 [194] and more widespread use from 2007 [195]. It is a form of lensless diffraction microscopy with the potential to deliver wavelength-limited resolution by solving for the phase of X-rays scattered from a sample upon illumination by a collimated beam. The technique only measures the intensity of the scattered X-rays but must overlap collected data in real space to define a unique solution to the phase and amplitude of the image wave function [196]. A common X-ray ptychographic technique uses overlapping diffraction data gathered through a movable aperture and uses an iterative algorithm like that shown in Figure 41 to solve for the real space object.

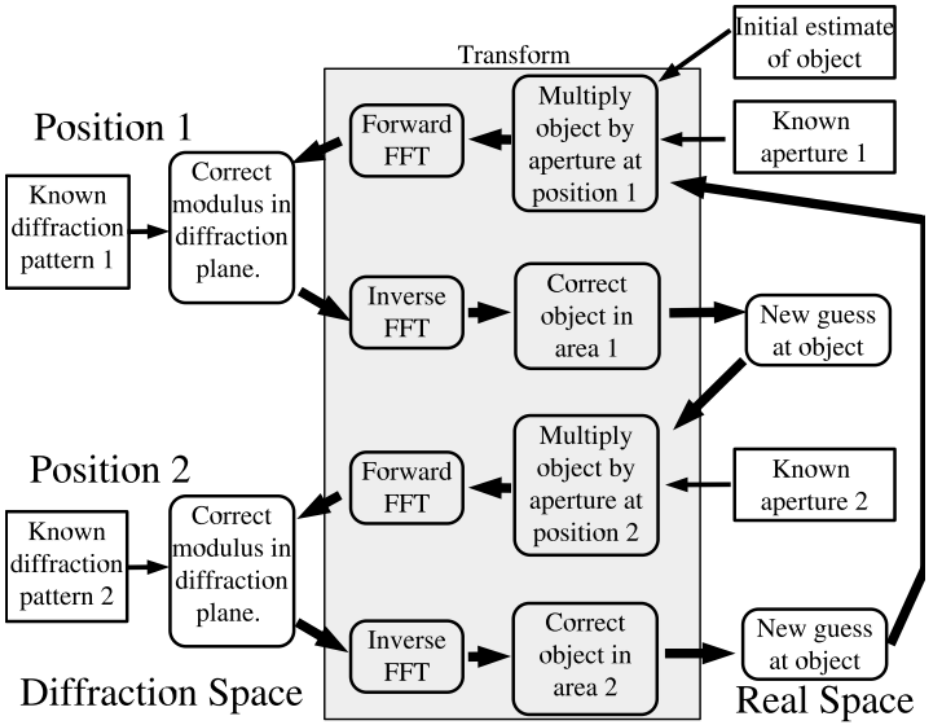

Figure 41: Schematic illustrating the basics of an iterative algorithm to solve for a real space object from overlapping diffraction moduli

Stockmar *et al.* applied 3D near-field ptychography to the study of the nanostructure of an SOFC, including a Ni-YSZ anode [197], and compared it with previous work using holotomography [198]. The inspected volume was over 100,000 μm^3 (example slices in Figure 42) with an effective voxel dimension of ~50 nm. This is similar to the voxel dimensions accessible for traditional X-ray nano-CT, but with a much larger sampling volume, almost certain to overcome limitations in representativeness for characteristic anode features. The authors employed a covariance function to measure specific surface areas and mean particle diameters; this involves a statistical correlation function that determines the probability that two voxels separated by a given distance belong to a certain phase. The large volume allowed multiple sub-volumes to be leveraged against one another for good statistics and many metrics for the AFL and ASL were extracted.

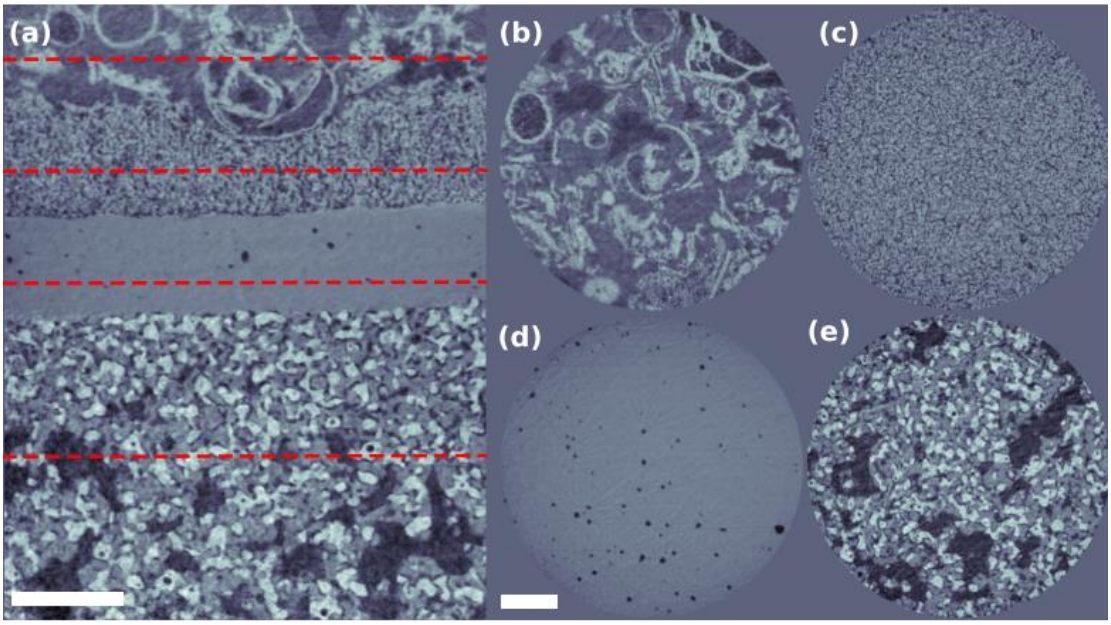

Figure 42: Tomographic reconstruction from ptychography: a) cross-sectional slice; transverse slices showing b) cathode current collector; c) cathode functional layer; d) electrolyte; and e) the anode substrate (scale bar is 10 µm), from [197]

The metrics extracted compared well with those from previous holotomographic calculations, with average deviations of 4%, 8%, 9% and 19% for volume fractions, VSSAs, mean particle diameters and TPBs, respectively.

De Angelis *et al.* performed *ex-situ* ptychographic imaging of a 17-µm-diameter pillar from a Ni-YSZ anode before and after undergoing reduction and oxidation, at a voxel dimension of 18.4 nm [199]. The image quality extracted was very high, allowing for facile segmentation. Registration was performed solely on the practically immobile YSZ phase and a range of metrics were extracted. Evidence was provided for cracking in the YSZ network, predominantly at grain boundaries, as a result of the volume change attributable to Ni oxidation, along with significant changes in nickel and pore morphology when comparing the reduced to the initial state. This result gives evidence that microstructural changes in SOFC anodes may give rise to small improvements in performance, at least in the short-term. It was seen that Ni connectivity only decreased marginally even though the size of Ni particles appreciably decreased, but pore connectivity showed an increase as isolated regions were connected by the microstructural change. Moreover, detachment of Ni from the YSZ skeleton is also noted, with a drop in $VSIA_{Ni\text{-}YSZ}$ of over 40%, along with a clear change of shape of the nickel particles. Interestingly, the total and active TPB densities increased across this redox

cycle, as did the proportion of active TPB, and the authors proposed that a redox cycle could be used as a remedial strategy for the lost TPB density attributable to Ni coarsening.

Further work from the same authors specifically inspected the impact of nickel coarsening by another *ex-situ* ptychographic nano-tomography study [200]. In this research, a 14-µm-diameter Ni-YSZ pillar was subjected to 3 and 8 h of annealing at 850 °C in a dry hydrogen atmosphere, imaged between each step. The authors pointed out that it was not clear if initial coarsening mechanisms were the same as those observed in long-term studies, warranting an inspection of the rapid microstructural evolution at short times. The high image quality achieved can be seen in Figure 43, wherein the green markers indicate the same feature in each tomograph, and the blue and red ones point out areas of coarsening.

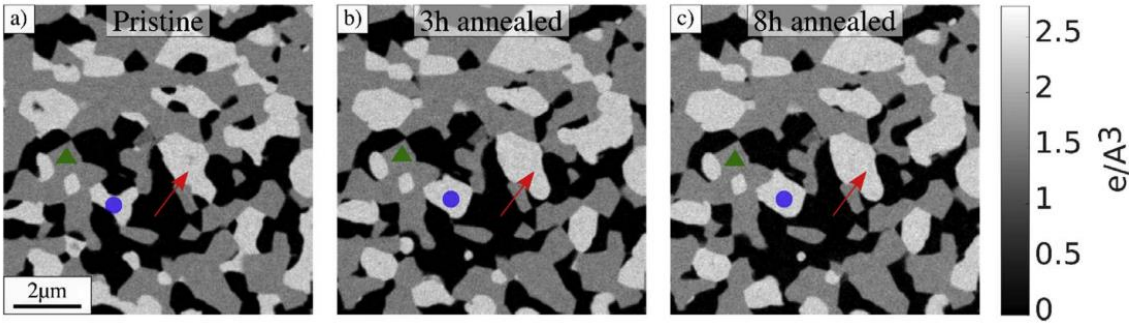

Figure 43: Orthoslices from ptychographic tomography of the "virgin" anode, where black is pore, grey is YSZ and white is nickel, reproduced with permission from [200]

After registration by an iterative close point method [201], typical metrics were extracted, as well as TPB tortuosity and TPB critical path radius (see [200] for definitions). The authors noted that the YSZ network did not noticeably change, the Ni particles coarsened and their sharp edges became more rounded, and that there was less change during the latter 5 h of annealing than during the former 3 h. Over the full annealing time, the total $VSSA_{Ni}$ fell by 15%, whereas those for pore and YSZ remained unchanged within segmentation error. There was a loss in Ni-YSZ surface area and a gain for pore-YSZ surface area, suggestive of a de-wetting regime and in accordance with, albeit to a lesser extent than, observations drawn from their previous work [199]. Even though the total TPB density dropped by 13%, active TPB density only dropped by

6%, yielding an increase of 7 %Active TPB. The PSD for pores moves marginally towards smaller sizes, whereas that for Ni clearly displays coarsening behaviour, with a greater number of larger particles. The TPB tortuosity for the nickel phase increased between the “virgin” and 3 h annealed state but remained unchanged after the following 5 h of annealing. The critical path diameter analysis showed that in the annealed states, the nickel phase involved in active TPBs had larger neck diameters, whereas the pore phase trend was reversed.

By inspecting only the isolated Ni particles, the authors concluded that the major mechanism behind Ni coarsening was that of Ni-Ni surface diffusion, as the volume attributable to these particles remained unchanged within segmentation errors. The fact that Ni evaporation and condensation were negligible is in line with the low humidity used in these experiments. Connectivity wise, disconnected particles from the pristine state remained disconnected in the 3 h annealed state, and new isolated particles were formed (an example of which is shown in Figure 44) often from the disappearance of bottlenecks measured to be 50 - 250 nm in diameter.

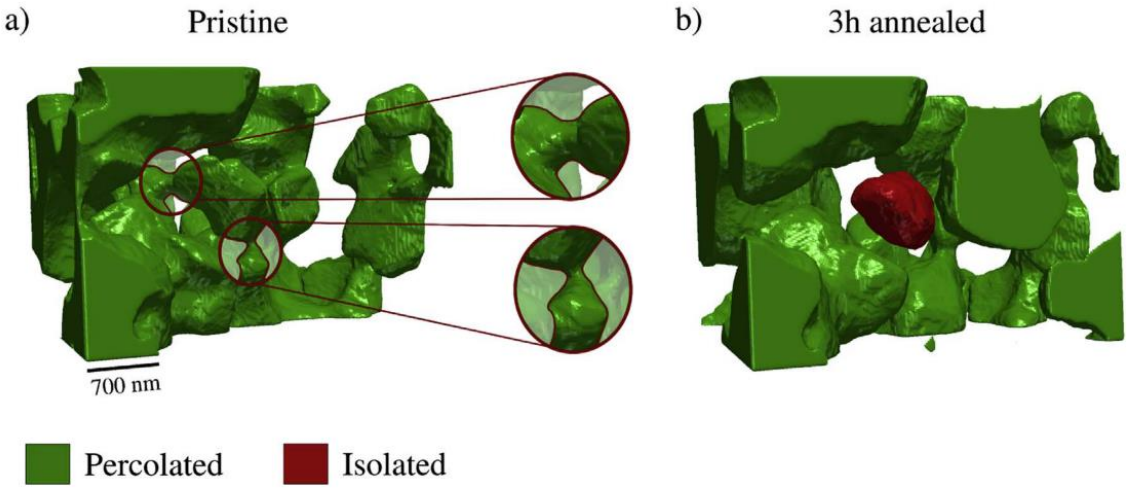

Figure 44: 3D volume renderings illustrating the disconnection of the Ni network, resulting in an isolated particle, reproduced from [200]

At the same time, the pore network connectivity increased, which is ascribed as the reason for the overall increase in % active TPB, as previously disconnected TPB lengths became active, in line with previous investigations [105][118][115][192]. This study reveals complex microstructural changes due simply to annealing in reducing atmospheres and highlights the importance of monitoring early-stage microstructural

evolution in SOFC anodes in order to better understand the complex degradation phenomena occurring in porous Ni-YSZ cermets.

2.4 Key Themes

From a survey of the literature, it is clear that the investigation of microstructural evolution of SOFC anodes has progressed immensely in the last three decades; it has evolved from stereological assessments from 2D images, through 3D imaging, to the recent advent of 4D approaches. Some key areas of interest lie in the understanding of each of the three networks, both in terms of their initial distribution and effect on performance as well as how their morphology evolves over time and affects durability.

The fundamentally important phenomenon of nickel coarsening or agglomeration has been justly identified as a key factor in the deterioration of the electrochemical performance of SOFC anodes. As the nickel metal is mobile at typical operating temperatures, its movement has impacts on: the pore connectivity and tortuosity, nickel conductivity and the prevalence and availability of triple-phase boundaries. Respectively, these have been shown to influence mass transport, ohmic loss and activation overpotential, although the complex microstructure-property relationships and how they interplay is still not well understood.

With an increasing focus on monitoring the same microstructure as it evolves after controlled high-temperature treatments, as well as considerations of RVE analysis with improved time and spatial resolutions, 4D tomography offers many advantages versus previous techniques for exploring the degradation mechanisms at play in Ni-YSZ anodes. The focus of the following chapters is the development of more accessible physical and metrological techniques to provide insight into the key parameters of interest when designing long-lasting, high performance SOFC cermets.

Chapter 3: Methodology

This chapter firstly provides an overview of the work undertaken as part of this thesis. The second section provides theoretical and experimental details of the different instrumentation utilised for sample preparation, experiment and/or characterisation. Subsequently, a detailed summary of the metrological approaches, or 'metrics', is provided, before a brief outline of simulations run on the microstructural data gathered by tomography.

3.1 Thesis Overview

Following on from work in the literature [132][128][133], the first aim was to gain clear insights into the evolution of SOFC anode microstructure attributable to long-term ageing. By using FIB-SEM slice-and-view tomography, the objective was to extract microstructural information from cermet anodes and develop metrics analysis to describe the changes observed after annealing. An advantage of this technique was the high attainable resolution [202] and high level of contrast between Ni and YSZ phases, afforded by using a low-voltage electron beam [128]. The disadvantages were the potential for acquisition artefacts which preclude access to an adequately large sampled volume and the statistical variations inherent in inspecting an aged sample which did not derive from the inspected virgin sample. The latter issue is an inherent part of this *destructive* technique, which cannot be overcome without changing imaging modality.

However, with a view to employing the *non-destructive* technique of X-ray nano-CT, the subsequent aim was to develop a robust method for producing samples that may be investigated with a lab-based instrument, albeit still relevant to synchrotron investigations. Hitherto, there were no lab-based X-ray nano-CT investigations that had achieved adequate contrast between Ni and 8YSZ to provide reliable segmentation. To achieve sufficient solid-phase contrast and to provide a robust structure and appropriate geometry, a micro-fabrication technique was developed. The chosen route was *via* laser micro-machining, coupled with FIB milling when required.

Once the preparation technique was properly established and optimised, the next objective was to follow the procedure to fabricate appropriately sized pillar samples that

could be annealed in the laboratory, before being imaged in the lab-based X-ray instrument. The annealing-imaging cycle was to be repeated several times and replicated at different temperatures to probe the evolution of anode microstructure as a function of time and temperature. Suitable metrics to capture subtle changes were required, as well as the use of digital volume correlation (DVC) [203] to monitor the changes over time.

The final aim of the work in this thesis was to perform an *in-situ* synchrotron experiment for the analysis of the *early-stage* reorganisation of microstructure, this time under direct heating by infra-red (IR) lasers. The rationale behind this portion of work was manifold. First, the *in-situ* set-up minimised the risk of sample failure between furnace and X-ray instrument and had the potential to improve the registration of consecutive tomograms. Secondly, the use of ultra-high brightness synchrotron radiation gave access to solid-phase contrast for larger sample volumes, improving the likelihood of capturing a RVE for analysis. Moreover, the high temporal resolution afforded by the high flux and specialist detectors allowed for the analysis of the *early-stage* reorganisation of microstructure, by taking full tomographies in less than a minute, over prolonged periods to inspect subtle changes. The experiment involved a forming gas environment to minimise oxidation, laser calibration to ensure reliable temperature measurement and very fast acquisition. The results were subject to varied metrics analysis and DVC calculations to probe the reorganisation of anode microstructure at very short times.

3.2 Instrumentation

3.2.1 Reduction & Annealing

The reduction of nickel (II) oxide, NiO, to yield metallic nickel, Ni, is often performed by exposure to hydrogen at elevated temperatures [204][205], accompanied by a reduction in volume of approximately 42% [77]. It has been shown that after initial incubation and induction periods, the reduction of NiO at a given pH_2 and temperature is linear with time, up to relatively high percentage conversion [204]. Due to the volume loss, a metallic film is unstable up to high conversion, but once it manages to form, it is

postulated that the rate-determining step in the reduction is the solid-state diffusion through the film, giving rise to growth with a parabolic dependence. In SOFC anodes, NiO is often reduced to Ni in a primary reduction step in many lab-based cell studies [85][206][207][208] or during the first cycle in stack testing [18] or real operation.

All lab-based reduction and annealing was conducted using a Carbolite GHA 12/300 tube furnace (Carbolite Gero, Sheffield, UK) under reducing conditions which was, in all cases, forming gas composed of nominally 4% H_2 / balance N_2 (certified to be 4.07% H_2 by BOC Limited, Guildford, UK). Samples for reduction were placed in an alumina (Al_2O_3) crucible and samples for annealing were held upright in a bespoke holder, which was CNC-machined from pyrophyllite (Ceramic Substrates & Components Ltd, Isle of Wight, UK). In each case, the samples were then placed inside an Alsint (Morgan Technical Ceramics, Stourport-on-Severn, UK) ceramic tube, positioning them squarely in the hot-zone of the furnace. The furnace tube was evacuated using a rotary pump, then filled with forming gas and the sample heated at a ramp rate of 5 °C/min to the required temperature, depending on the prescribed treatment. A K-type, Inconel-sheathed thermocouple (Omega Engineering, Manchester, UK) was used to monitor the temperature near the sample. After the reduction or annealing treatment, the furnace was switched off and the sample was allowed to passively cool under the reducing atmosphere.

3.2.2 Scanning Electron Microscopy (SEM)

SEM is a technique used to acquire images of the surface of samples by utilising the high accessible resolution afforded by electron beams. An electron gun is located at the top of a microscope column, and its emitted electrons are accelerated towards the sample, which is held under vacuum, usually at an acceleration voltage between 5 and 30 kV. The electron beam is first focused by a condenser lens to control the probe size and directed through an aperture to control brightness. The beam is then focused by an objective lens, focussing it to a spot on the specimen surface (Figure 45). An objective aperture is used to reduce the angle of convergence of the beam and to reduce aberrations by excluding electrons that have deviated significantly from the optical axis.

By using a range of scanning coils, the angle at which the beam enters the objective lens can be altered, controlling its lateral position. Thus, a focused spot can be rastered across the sample surface, providing spatially resolved information.

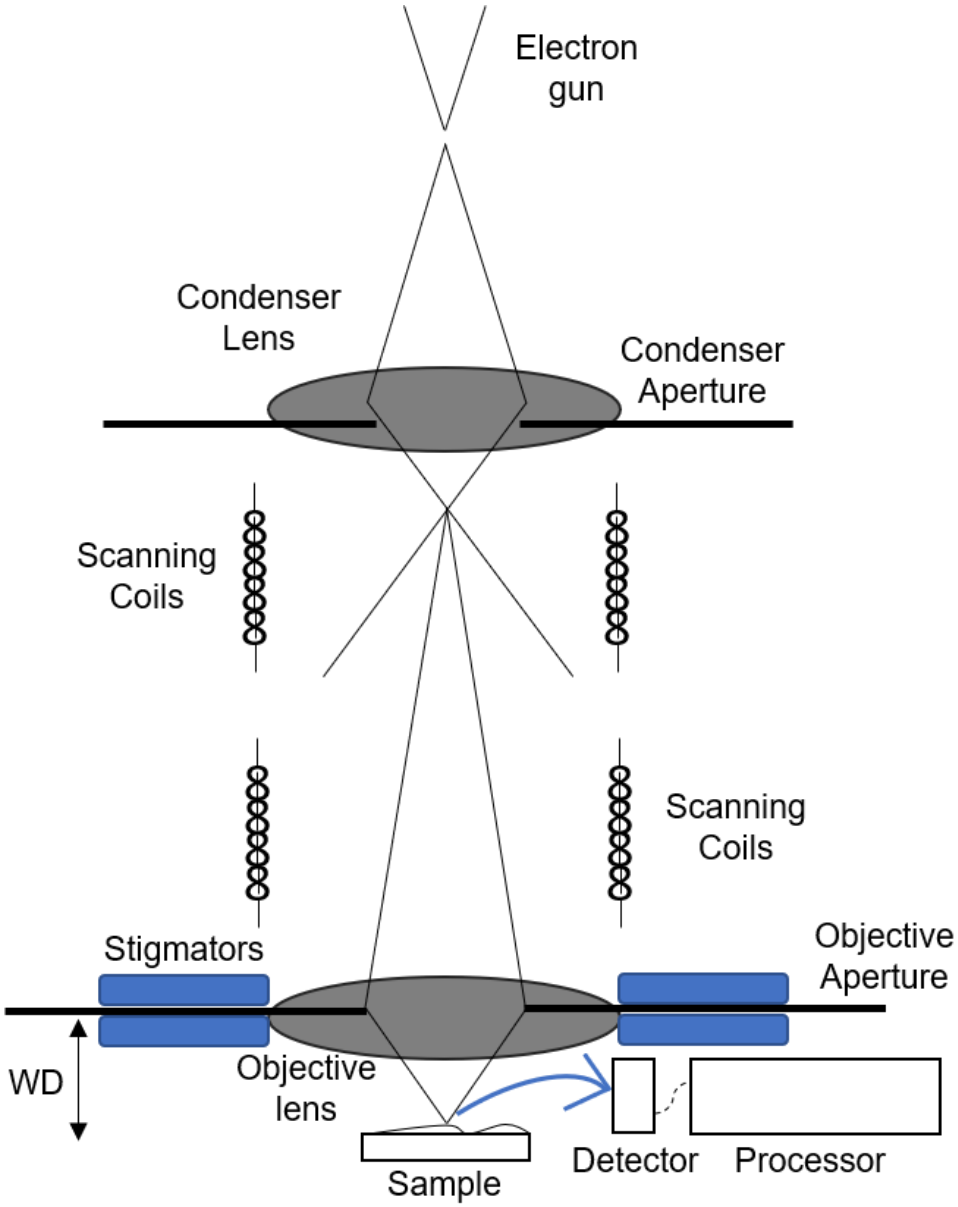

Figure 45: Schematic of an SEM instrument

Many beam-specimen interactions occur when electrons interact with the atoms on the surface of interest, requiring several different detectors to collect the appropriate signal. The principal interactions of interest in this thesis include: secondary electron (SE) emission, back-scattered electron (BSE) emission and the production of X-rays (Bremsstrahlung and Characteristic emissions). A summary of these interactions and their relative interaction volumes is presented in Figure 46.

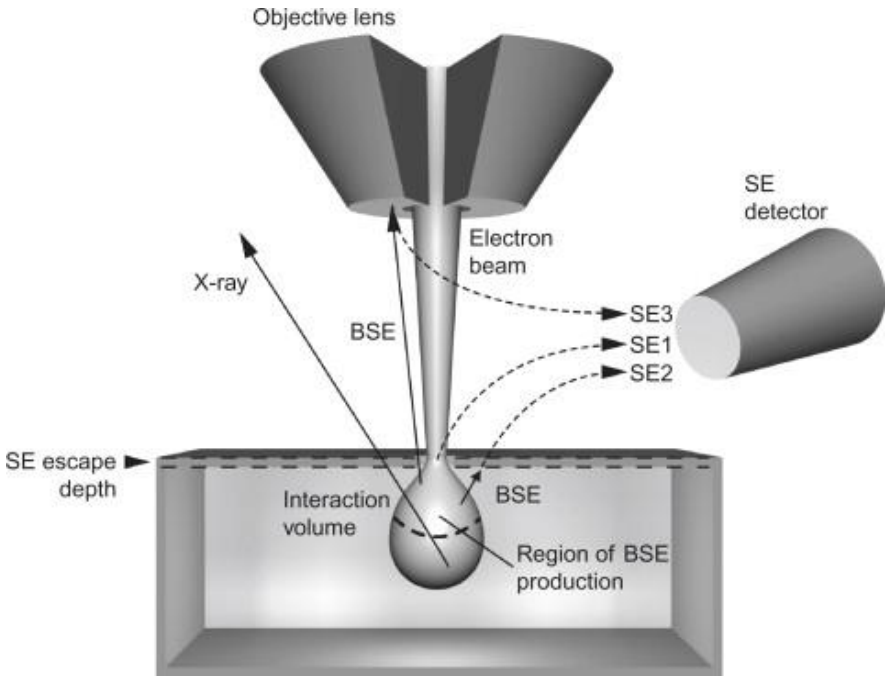

Figure 46: Schematic of interaction/sampling volumes for various SEM signals, reproduced from [210]

Secondary electrons (SE) come from the excitation of electrons from atomic shells and can be caused by the primary electron beam (SE1) or back-scattered electrons interacting with the sample (SE2) or with the pole piece (SE3), typically having an energy in the range of 0.1 – 50 eV. A typical SE yield for an incoming primary electron is 10% (δ_{SE} = 0.1), and varies very little with average atomic number, *Z*. Although the *interaction* depth for SEs may be on the order of 1 – 2 µm, only the SEs generated very close to the surface are able to escape, giving a much smaller *sampling* depth on the order of 10s of nanometres, with the sampling width only slightly wider than the probe width. SE imaging tends to be highly surface-sensitive, susceptible to morphology, and allows for high resolution images to be acquired which typically use a low-bias Everhart-Thornley detector [209].

Back-scattered electrons (BSE), however, are high energy electrons that result from the primary beam being deflected by a series of elastic and inelastic collisions, and then managing to escape the material's surface. BSEs typically travel quite far before leaving the sample and often have *sampling* volumes larger than the *interaction* volume of the primary electron beam. The backscattered electron yield (δ_{BSE}) for a solid elemental sample is a strong function of *Z* and ranges from 10 to 50% ($0.1 < \delta_{BSE} < 0.5$)

as *Z* varies from 5 to 80. Consequently, BSE imaging is routinely used where differences in *Z* are a key contrast mechanism. High-*Z* features are readily visible in BSE imaging, although the resultant spatial resolution is often lower than for SE imaging. BSEs are usually detected by a scintillator or solid-state detector at the bottom of the pole piece, below the objective lens. X-ray emission is discussed in **Section 3.2.3**.

In this work, multiple SEM instruments were used: Zeiss SEM EVO MA10 (Carl Zeiss, Oberkochen, Germany) [SEM_UCL]; Zeiss FIB-SEM XB1540 “Cross-Beam” [FIB-SEM_UCL] and Helios FIB-SEM NanoLab 600 (Thermo Fisher Scientific, US) [FIB-SEM_ICL]. The general procedure for preparing samples for SEM imaging is given here, and the specifics for each sample of interest is given in the “Samples” section of each corresponding chapter.

3.2.2.1 Epoxy Impregnation

On investigating electrode or electrode-electrolyte cross-sections by SEM, a small fragment of the sample is encapsulated using a low-viscosity epoxy resin, Struers EpoFix (Struers, Rotherham, UK), adding a hardener and placing under vacuum overnight in a desiccator. There are many advantages to impregnating a porous electrode sample with epoxy. Firstly, by filling the voids with a solid material, the electrode area of interest (AOI) becomes more amenable to surface flattening, during the subsequent grinding and polishing steps. This reduces artefacts due to complex morphological features on imaging, particularly in SE2 mode. Secondly, by replacing the air in the pore network with a solid resin, that volume becomes electron-transmitting under the electron beam, as opposed to an electron-transparent vacuum. Therefore, the microstructure ‘behind’ a particular AOI is obscured, and electrons are only emitted from the surface of interest, giving an image from a narrower plane. Later, a further advantage will be discussed in relation to FIB milling.

On the other hand, a possible disadvantage is that complete filling is rarely achieved, not least because isolated pores exist. Thus, the filling procedure may introduce an extra grayscale peak in the histogram of the image to be taken. Fortunately, as traditional epoxy-resin is carbonaceous and therefore low in average atomic number,

the unfilled and filled pores can often be co-segmented easily, as both lie towards the lower end of the grayscale histogram and away from the higher atomic number materials typical of SOFCs.

3.2.2.2 Cross-sectioning

In fuel cell electrodes, a multi-component, multi-layer structure is required for a working device and often cross-sectional imaging is the most efficient procedure for accessing information about individual lamellae and their interfaces. This can be achieved by orienting the sample perpendicularly to the macro-surfaces of the resin, held upright by a small metallic clip. The resulting puck, encapsulating the fixed sample, is subsequently ground with silicon carbide papers of increasing fineness, to achieve the desired low roughness surface for imaging. As electrons are charged species, there must be a conductive pathway from the point of beam impingement to 'ground' to avoid *"charging"*, a well-known phenomenon for insulating sub-samples that can cause large brightness variations and potentially sample movement. To ensure a surface to be imaged is adequately electron-conducting, often a thin conductive film is deposited on the macroscopic sample before SEM imaging. In this work, impregnated samples were gold-sputtered either with a Quorum SC7620 Sputter Coater (Quorum Emitech, Laughton, UK) at UCL or a K575X Sputter Coater (Quorum Emitech, Laughton, UK) at ICL. The coating time was 30 seconds in both cases with a deposition thickness of approximately 7 - 8 nm.

3.2.2.3 Imaging

Mounting of the samples in each of the instruments (SEM_UCL, FIB-SEM_UCL and FIB-SEM_ICL) was similar in that the smoothed puck was affixed to an aluminium stub by means of a sticky carbon pad and affixed to a carousel for imaging. In many cases, silver paint was used to ensure there was a conduction pathway from the top surface to the metallic substrate below. To achieve optimal imaging, the appropriate working distance (WD) of between 5 and 10 mm must be followed, depending on the instrument used. Similar to optical imaging, there is a trade-off between spatial resolution and FOV but there are some added corrections required when obtaining high quality

SEM micrographs. To overcome aberrations to the electron beam, apertures must be used, and thus aligning these components is key to achieving good images. Moreover, the electromagnetic lenses used to focus the beam can suffer from astigmatism, such that their magnetic field is not rotationally symmetric. Whilst imaging, it is vital to use a *stigmator* to apply opposing fields to correct for this defect. Finally, the choice of X-ray energy is key and will be discussed in relation to the specific imaging undertaken.

3.2.3 Energy-dispersive X-ray spectroscopy (EDX)

Electrons deflected by charged nuclei result in X-ray emission with a continuous spectrum; this radiation is known as Bremsstrahlung (or "braking radiation") and gives rise to the background signal in EDX spectroscopy. Of more utility, high energy primary electrons can also cause the ejection of any electron from an atomic orbital, raising the atom from its ground state to an excited state. The atom can relax by either releasing another electron (Auger electron) or by emitting a photon in the form of an X-ray. Since this X-ray radiation emitted from the sample atoms is characteristic of their electronic configuration, a suitable detector can provide chemical (elemental) information about the sample surface, based on its energy (or wavelength – known as wavelength-dispersive X-ray spectroscopy [WDX]).

In this work, an INCAx-act silicon drift detector (Oxford Instruments, UK) was used for all EDX spectroscopy acquisition, in conjunction with INCA Energy software for analysis. Typically, this is run with high primary beam voltage (at least 15 keV) to maximise the possible X-ray emission energies necessary for elemental identification. Moreover, good statistics are accessed by ensuring a sufficient dwell time for each scan, assessed by the relative abundance of features in the output elemental maps.

3.2.4 Focused-ion beams (FIB)

A standard FIB instrument comprises a liquid metal-ion source (LMIS), an ion column, a vacuum set-up and sample stage as well as detectors and a gas delivery system for deposition [210]. Often it is found hybridised with an SEM column in a so-called "dual-beam" or "cross-beam" instrument. Typically, the metal of choice is gallium due to its low melting point ($T_m \approx 303$ K), long source life, low surface free energy

and excellent electrical, mechanical and vacuum characteristics. Coils heat a reservoir of Ga which wets a tungsten needle with a narrow tip. An electric field is applied to the end of the tip such that the liquid Ga forms an even narrower point, often with a diameter as small as 2 – 5 nm. Once the cone tip is small enough, an extraction voltage pulls the Ga from the end of the tip, ionising it in the process, forming a beam of gallium ions. Liquid Ga from the reservoir replaces the Ga^+ ions lost, and a stable flux is established.

As in an SEM, the emitted charged species are accelerated down an (ion) column, and interact with both a condenser and objective lens to form the probe and focus the beam onto the sample surface, respectively [210]. Apertures are used to define the current (typically between 2 pA and 20 nA) and probe size, and cylindrical octupole lenses can be used to control the scan field and correct for astigmatism. When the gallium ions (or charged clusters) hit the sample surface, sputtered atoms, molecules, secondary electrons and secondary ions are emitted, the latter two of which are often detected by an electron multiplier at 45 ° to the beam direction. Additionally, a multi-channel plate, located directly above the sample, may also be used to form SE images. Thus, focused-ion beams can be used for imaging at low beam currents and milling at higher currents.

On collision with a solid surface, a Ga^+ ion sequentially strikes constituent atoms, resulting in a many-body problem with complex consequences. Fortunately, in the interaction of an ion with an atom, the collision between the ion and the electrons can be treated separately from that of the ion and the nucleus due to the large mass difference between the electron and the nucleus (ratio of 1:130,000) [211]. The collision between the ion and the electrons is inelastic and results in excitation and ionization of the constituent electrons in the atom, giving rise to the imaging capability of FIB systems. On the other hand, the nuclear collision is elastic, wherein kinetic energy and momentum are conserved and during which the incident ion recoils the target atom and is scattered at the same time. It is through this process that FIB systems can mill, as well as implant/reorganise the atomic structure of the specimen.

3.2.4.1 Sample Preparation

As was discussed by Wilson *et al.* [212], the use of epoxy impregnation of porous electrodes allows for more planar sectioning of the sample by the FIB as well as improving the image quality by mitigating the effects of charging at pore edges and signals derived from the material beneath the pore layer itself. Epoxy resins are commonly used in the preparation of porous samples for FIB-SEM slice-and-view as the presence of this carbonaceous phase provides a uniformly dark and distinct greyscale value on imaging [213] and limits mistakes due to the finite SEM depth-of-field during imaging [214]. The epoxy impregnation process is the same as that described in **Section 3.2.2.1** for SEM imaging. Gold-sputtering is used to minimise charging, unless contamination is to be strictly avoided.

3.2.4.2 Image Acquisition

Before milling around the VOI, often a protective layer of platinum is deposited on the top face of the VOI. This layer serves to protect this top face from accidental milling as well as to prevent erosion of the VOI during milling [215]. Moreover, it has been shown that by depositing a layer of Pt, which is inherently smoother than the surface topology, the FIB milling process gives rise to fewer "curtaining" effects [202][216]. Once the protective layer is deposited, high beam currents are used to mill away a "U-shaped" trench to allow for efficient SE2 egress to reduce issues with shadowing. Also, by providing a deep trench around the VOI, the redeposition of material upon milling is less likely to obscure the front face (Figure 47).

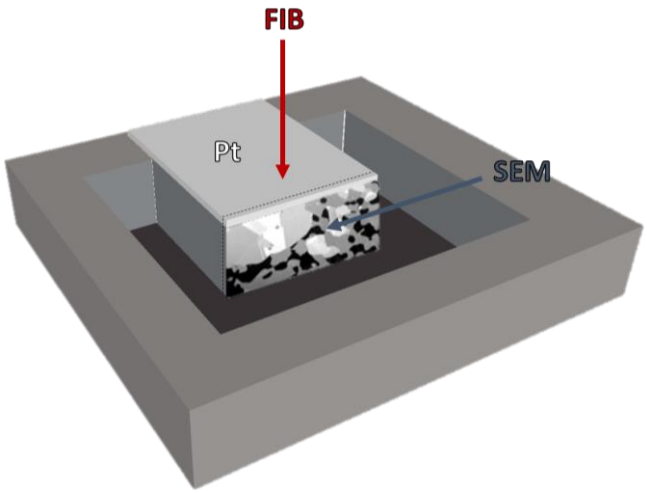

Figure 47: Schematic of the protective Pt layer and U-shaped trench surrounding the VOI

Depending on the desired spatial resolution and FOV, and whether cubic or merely cuboidal voxels are desired, a particular magnification and cut thickness will be chosen in the FIB software and slice-and-view will be performed over tens or hundreds of slices, yielding maximal contrast by using an appropriate beam voltage.

3.2.4.3 Data Processing and Analysis

Due to sample movement as well as the angle at which the SEM column collects SEs from the face of interest, the acquired image slices require an alignment step before they can be digitally stitched together to give a 3D representation of the real microstructure. This may be carried out in a number of different pieces of software, including open-access Fiji (National Institutes of Health, Maryland, USA), which was used in all FIB slice alignment in this thesis [217]. To denoise the data, it is common practice in the literature to apply a simple filter, such as a median filter to the raw data [218][219], or sometimes employ a bespoke technique to remove erroneous voxel allocations in segmented images [131].

Various approaches can be followed to segment (allocate each voxel to its respective phase) images gathered by FIB-SEM slice-and-view. Due to the high solid-phase contrast and high resolution, typically segmentation is reasonably straightforward by simple thresholding techniques. However, often there are minor complications introduced either by acquisition artefacts (unfilled pores, charging, streaking) or by the nature of finite boundaries in three-phase systems. In the SOFC anode, there are three distinct grayscale values for pore (low), YSZ (medium) and Ni (high) at low beam voltages. However, at the interface between Ni and pore phases, there is a finite thickness of voxels which have grayscale values similar to those associated with YSZ. To overcome this, morphological operations such as “opening” and “closing” can be used to effectively erode the erroneous YSZ voxels and dilate the other phases to fill the gaps (see **Chapter 4**).

3.2.5 X-ray computed tomography (X-ray CT)

3.2.5.1 Brief History

Ever since W.C. Roentgen published his seminal work in 1896 [220], X-ray radiography has played a very important role in diagnostic medicine, and more recently, in other fields of research. During this time, X-rays have routinely been used for direct imaging and for indirect, diffraction-based studies, predominantly in crystallography experiments (see **Section 3.2.6**). To gain more information from 2D projection images attained through radiography, several scientists have addressed the issue of retrieving information in the third dimension. First, H.A. Lorentz considered the case at a higher dimensional order [221] and subsequently J.K.A. Radon introduced an integral transform in arbitrary dimensions that provided practical access to 3D information from 2D projections in 1917 [222]. This work showed that the distribution of a material property in an object can be calculated if the integral values along a sufficient number of lines passing through the same layer are known [223].

Later, G. Frank demonstrated the equipment needed to form linear representations of an object being scanned [224] before significant contributions were made to practically use the mathematics involved to tackle problems in radioastronomy [225] and medical diagnostics [226][227]. A.M. Cormack then performed experiments in radiotherapy and published various theoretical foundations for utilising tomography in a range of medical applications [228]. R.N. Bracewell & A.C. Riddle subsequently introduced the filtered back-projection algorithm, in their case for radioastronomy, which was later used for converting acquired 2D images back into 3D reconstructions of an investigated object [229] (see **Section 3.2.5.6**).

The first practical implementation of computed tomography (CT) came about in the 1970s [230], followed by key work on the filtering functions necessary for CT reconstruction [231]. Over the following decades, a variety of developments were made, both in terms of geometry (including the introduction of spiral-CT) and in terms of improvements in 3D spatial resolution [223]. More recently, X-ray CT has been applied to materials science problems, at larger scales for industrial applications [224], and, with

the advent of micro-focus X-ray beams, at much smaller length-scales for a wide range of research questions [232][233][234].

3.2.5.2 X-ray Sources

The two main categories of X-ray sources relevant to this thesis are those generated from lab-based sources and those generated at large-scale synchrotron facilities.

3.2.5.2.1 Lab-based Sources

Lab-based sources are predominantly based on thermionic emission principles developed by Coolidge [235]; a cathode and an anode are positioned opposite to one another over a short distance, under a high vacuum [236]. The cathode is provided with a tungsten filament which is heated, thus controlling the number of thermal electrons emitted, independently of the potential difference between the electrodes. A potential difference is applied, and the resultant accelerated electron beam strikes a metal target in the anode, thus generating X-rays within the beam focus. The X-rays generated are polychromatic in nature, and from the divergent beam often a conical solid angle is selected [232].

There are three main mechanisms by which the X-rays are produced (Figure 48). Firstly, if the impinging electrons brush close to the nucleus and feel its positive attractive force, they effectively "brake" and give up some of their energy as radiation in the form of "*Bremsstrahlung*" ('braking radiation'). Secondly, the electrons may collide with inner-shell electrons, causing them to be ejected and ionising the atom in question. A hole is left in the electron's wake into which an outer-shell electron may drop, releasing its excess energy as radiation. Due to the quantisation of atoms' electronic levels, the ejected photon has a quantised energy equal to the difference between the binding energies of the electron in its initial and final states. This radiation is therefore classed as "Characteristic Radiation" and betrays the character of the atom from which it emanates. Finally, albeit a much rarer event, an electron may directly hit the nucleus, thereby giving up all its energy as *Bremsstrahlung*, thus defining the upper limit of the exiting photon's energy profile.

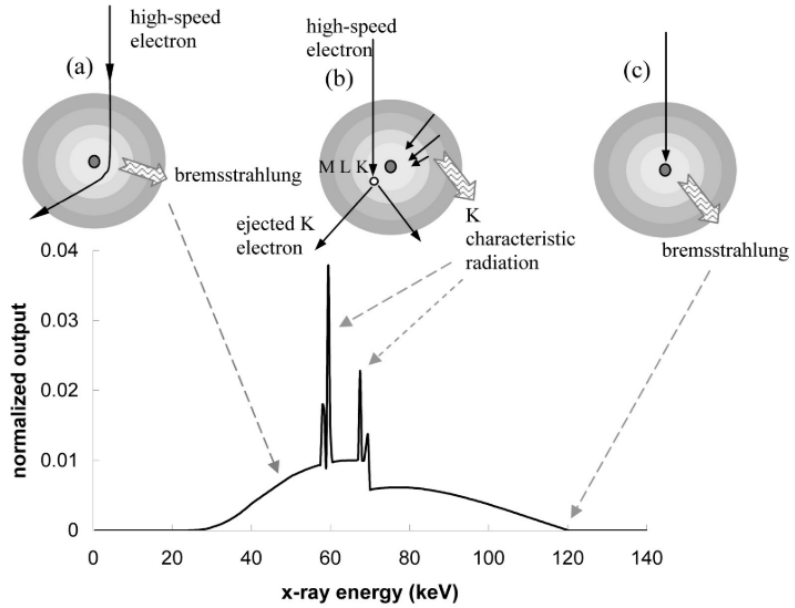

Figure 48: Schematic displaying the three mechanisms by which X-rays are produced by bombarding materials with electrons, reproduced from [237]

However, the generation efficiency at the anode is less than 1% as most of the energy is converted to heat, thus the excess generated heat must be removed rapidly [236]. The first lab-based X-ray generation sources were sealed tube types which needed forced cooling of the focused target face with flowing water. However, another way to mitigate this issue was to ensure the focus kept hitting a fresh, cooled face, leading to the development of movable anodes by using a range of methods for rotation. This gave birth to rotary anode X-ray sources which are the most popular sources used in lab-based instruments today.

In this context, an important metric when considering X-ray source performance is the “brilliance”, which is defined as the load per unit area of the focus. The rotary anode types can withstand much higher loads than the sealed tube type, and although they are more efficient with less focused probes, they can be micro-focused to achieve much higher brilliance than can be reached by the older sealed type. However, more consideration is needed for the design of the vacuum sealing around the moving shaft through the vacuum wall. Although the attainable flux has been increasing with time, the limiting values are still far lower than for synchrotron sources.

3.2.5.2.2 Synchrotron Sources

A synchrotron source is a large-scale facility that is designed to force high-speed charged particles around curved trajectories by use of applied magnetic fields in order to

emit electromagnetic radiation called synchrotron radiation [238]. This type of radiation was observed for the first time in 1947 [239]: since this time, it has been applied across many disciplines and can be utilised to investigate many different types of matter, in real space, reciprocal space, both as a function of energy or of time.

Electrons are first accelerated to high speeds by a linear accelerator, where their energy reaches the MeV range, and subsequently by a booster ring up to the GeV range. Subsequently, the electrons enter the main "storage" ring where powerful electromagnets are used to force them to travel in a circular path, at speeds close to the speed of light. As the beam bends, radiation is emitted tangentially, with well-defined characteristics, along a range of "beamlines" (see Figure 49). This involves a loss of energy, which is restored using radiofrequency electric fields.

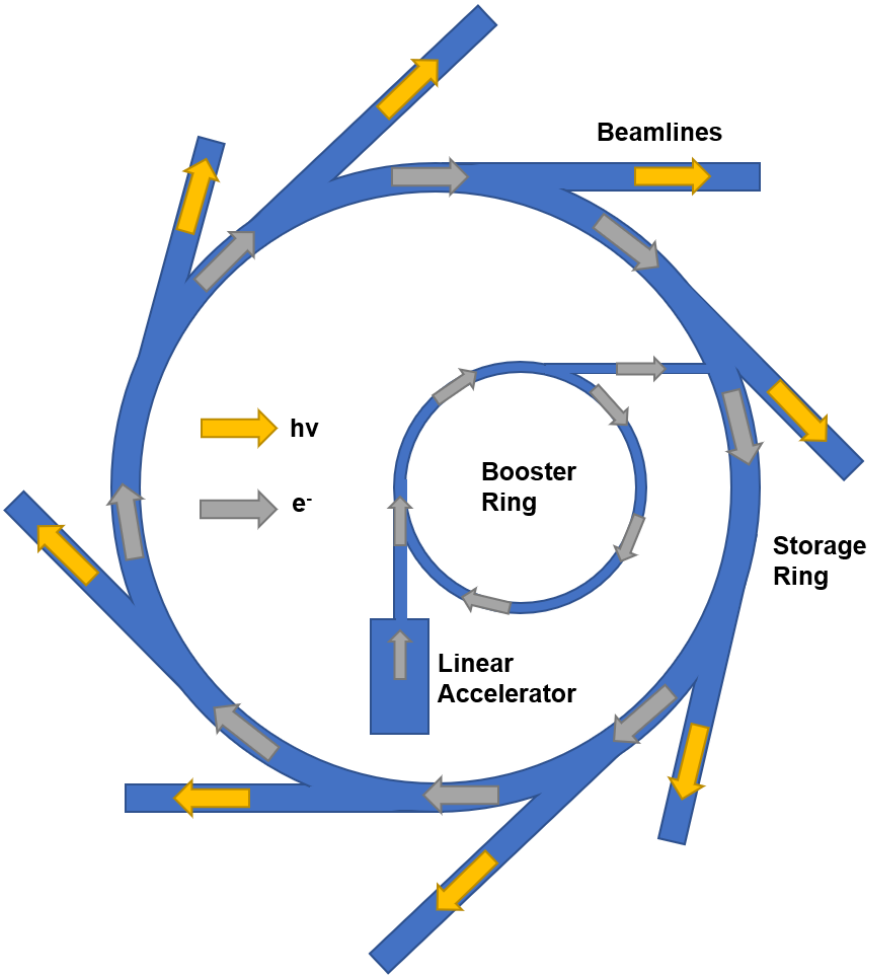

Figure 49: Schematic plan view of a typical synchrotron facility

Synchrotron facilities have gone through so-called "generations" from the first-generation sources used primarily for high-energy particle physics (1960s), through

the second-generation dedicated to synchrotron light (1970s) to the third-generation sources with advanced ways of optimising the applied magnetic fields that we see today. Crucially, this latest generation of synchrotron sources use “insertion devices” known as “wigglers” and “undulators” in straight sections of the storage ring. Both internally deflect the electron beam due to an alternating magnetic field; raise the critical electron energy; increase the intensity of the emitted radiation; and increase the spectral brightness [240]. “Fourth-generation” sources using free-electron lasers are currently under development.

Importantly, the emitted radiation has certain advantageous properties for use in studying condensed matter. These attributes include: very high intensity; a broad continuous spectral range; a high degree of polarisation; high brightness due to the small cross-section of the electron beam; a high degree of collimation; a pulsed time structure; and great stability in an ultra-high vacuum environment. Moreover, these characteristics are in all cases calculable and in many cases tuneable, which provides users great flexibility when designing experiments using synchrotron radiation.

An important metric when assessing synchrotron sources is their spectral brightness, defined as the number of photons emitted per second, in a unit source area, per unit of solid angle, in a spectral bandwidth, *ΔE/E,* of 0.1%. The huge increase in brightness over the years can be seen in Figure 50, which now stands at approximately one million times the brightness of the Sun for the latest synchrotron sources.

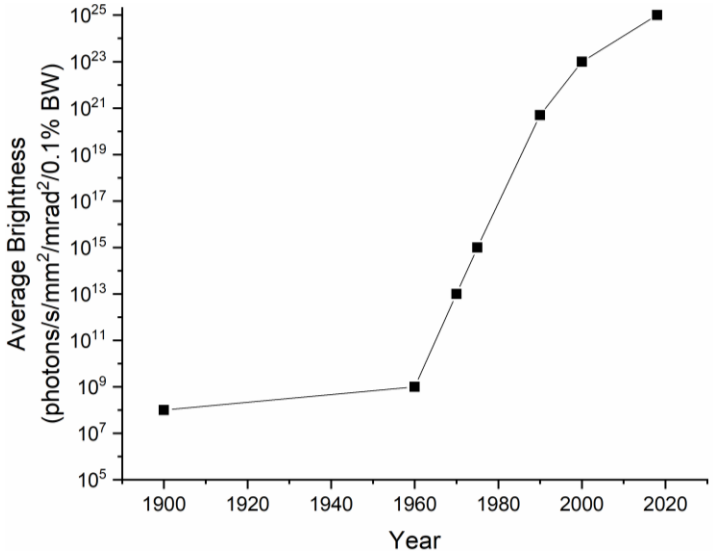

Figure 50: Plot illustrating the increase in spectral brightness with time

Another aspect that must be considered is their flux, defined as simply the number of photons per second, again for $\Delta E/E$=0.1%. A typical photon flux at the sample, emitted from a standard beam size and ring current, is of the order of 10^{10} photon/s [240]. This value is at least 10^3 times greater than for a lab-based source [232], with the concomitant effect of delivering a better signal-to-noise ratio for the same exposure time at a beamline than in a lab setting. Furthermore, within the optics array downstream from the radiation source, monochromators can be used to select a specific energy, with a very narrow energy bandwidth, or not used, if a 'white beam' is desired. If the former is chosen, beam hardening artefacts are reduced (see **Chapter 7**).

On operating at a beamline, it is important to consider several controllable parameters, including: what bandwidth is suitable for the application (white beam or monochromatic); which beam energy (if the latter); the exposure time; the number of projections; and how many reference images (without sample and blanked) to take. Once these acquisition decisions have been optimised, the gathered data is then subject to reconstruction algorithms, which are often part of a 'data pipeline' at the facilities and will likely utilise either analytic or iterative algorithms designed to reconstruct data from a parallel illumination set-up (see **Section 3.2.5.5**).

3.2.5.3 X-ray-matter Interactions

On collision with matter, X-rays interact with it in several ways, depending on the energy of the beam and the material. The most significant interaction for absorption-based imaging (including absorption X-ray computed tomography), is the photoelectric effect, whereby the incident radiation causes the photoemission of a previously bound electron. The photon is destroyed and any excess energy (difference between incident photon energy and the binding energy of the electron) is transferred to kinetic energy of the emitted photoelectron. It can be shown that the probability of emission is greater when the energies are well-matched, as described by Equation *3-1*, wherein $P_{P.E.}$ is the probability of photoemission and ΔE is the excess photon energy:

$$P_{P.E.} \propto \Delta E^{-3} \qquad 3\text{-}1$$

On the other hand, this probability has a direct proportionality with the atomic number, *Z,* of the atom from which the photoelectron emanates (Equation *3-2*):

$$P_{P.E.} \propto Z^3 \qquad 3\text{-}2$$

This effect is responsible for the majority of the electron-matter interactions that occur at low energy (< 20 keV) and for the purposes of this thesis, since the work in **Chapters 5** and **6** was conducted at 5.4 keV, the photoelectric effect accounts for almost the entirety of the X-ray absorption underpinning the contrast witnessed in the majority of the tomograms in this thesis. In the case of the synchrotron studies in **Chapter 7**, the hard X-ray energy of 17 keV is used, wherein there is a greater but not substantial contribution from other interactions.

At high energies, a second inelastic interaction becomes more prominent, namely Compton scattering. This type of interaction occurs to a negligible extent at low energies but as the X-ray energy approaches 20 keV, Compton scattering must be taken into consideration. This scattering occurs when the incident photon has a much greater energy than the electron binding energies and thus it is instead deflected or “scattered” with partial loss of its initial energy at some angle between 0 and 180 °. At the lower end of this higher energy regime, the photons tend to be preferentially back-scattered (> 90°) and at the upper end, forward-scattered (<90°). The probability of this type of interaction is dependent upon electron density.

A third interaction can also occur; an elastic scattering phenomenon called Rayleigh scattering which results in no ionisation nor transfer of photon energy to kinetic energy, such that the out-going radiation is of the same energy as the incident beam. The relative significance of each of these interactions as a function of energy is displayed in Figure 51.

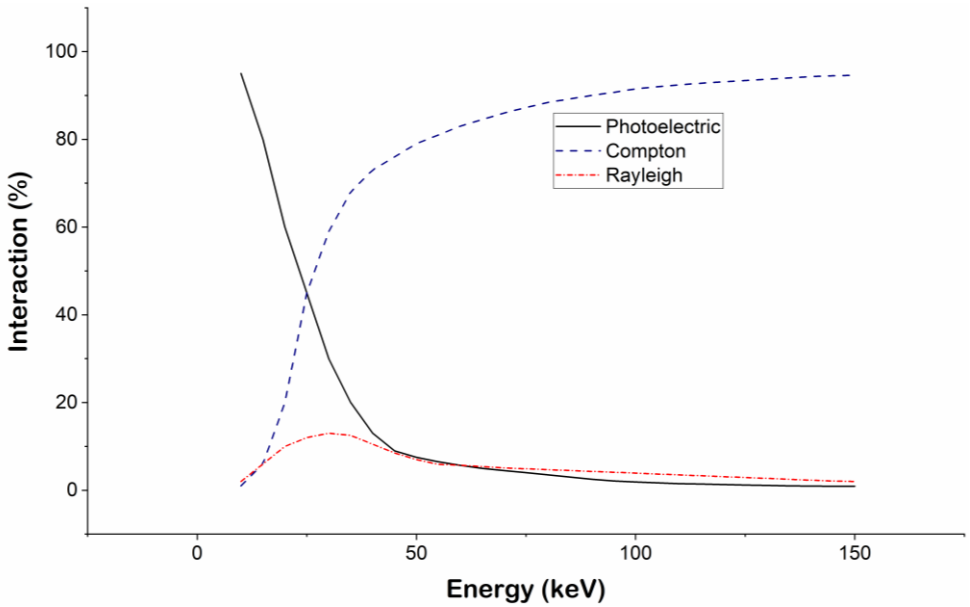

Figure 51: Plot displaying the proportion of different types of interaction as a function of energy, based on the water molecule

3.2.5.4 Tomography Theory

The word "tomography" derives from the Greek words for "to cut or section", 'tomos', and "to write", 'graphein' [241]. The concept behind tomographic imaging is a procedure for imaging sections of an object by reconstructing 2D slices and stitching them together to form a 3D representation. One can take an arbitrary object, O(x,y,z), which is effectively composed of n slices of equal thickness, Δz, which all lie parallel to the XY-plane [242] (Figure 52). Each of these slices cut through the object under investigation. The 2D reconstructed slice can be seen as a 2D function, *f(x,y)*, that may describe any material property of the objects contents; in X-ray CT, this is the position-dependent attenuation coefficient *μ(x,y)*.

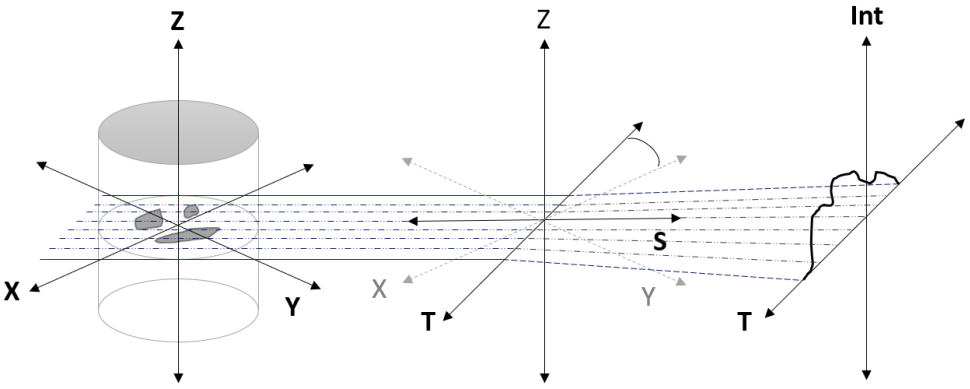

Figure 52: Schematic of scanning geometry of an object in x,y,z-coordinate system. A slice of the object (in XY-plane) is scanned through an angle, θ; the transmitted intensity is registered in the rotated coordinate system, T-S

The goal of the tomographic procedure is to reconstruct the 2D function (i.e. produce a slice) from the projections that are measured from the instrument. The approach is thus to ensure that the interaction between the X-ray beam and the material throughout its path is well understood, such that the projected values relate succinctly to the property of interest. The problem is therefore an inverse problem, how does one access the function f(x,y) given the projection information, g(s,t)? The answer lies in understanding the Radon transform [222].

In a simple, traditional, X-ray absorption tomography experiment, each 'slice' is effectively scanned through, θ, where 0 ° < θ < 180 ° with an X-ray beam, by incremental rotation of the sample. Using a detector, the transmitted intensity of X-rays at each position (*t*, Figure 52) is recorded and using reference imaging, the incident intensity is also known. Using the Beer-Lambert Law, the path integral of the attenuation coefficients across the beam path can be linked to the transmitted intensity, *I(x,y)*, (i.e. the recorded data) according to Equation *3-3*:

$$I(x,y) = I_0 exp[-\int_{path} \mu(x,y)ds] \quad 3\text{-}3$$

Similarly, the logarithm of the intensity ratio is proportional to the line integral of the attenuation function through the object, and if defined in terms of the angle of rotation, *θ*, and the *t* axis, this gives the so-called projection $P_\theta(t)$ [242]:

$$P_\theta(t) = ln\frac{I_0}{I(x,y)} = \int_{path} \mu(x,y)ds \quad 3\text{-}4$$

Collectively, the set of all the projections is called the Radon transform of *μ(x,y)* from which a 2D image of *μ(x,y)* can be reconstructed by the "Fourier slice theorem", which is to say that the Fourier transform (FT) of a projection of a property across line integrals, is a subset of the FT of the property itself. An example of an algorithm used to back-project from the acquisition of the line integrals is given in **Section 3.2.5.6**.

3.2.5.5 Geometries

For many decades, X-ray detection was limited to a 1D array such that the movement of the source or the detector was performed in order to obtain the 2D image required before a rotation could be made (translation-rotation principle [223]) (Figure

53 a)). With the advent of 2D detectors, and later optimised by the charge-coupled device (CCD) array, single 2D projections could be taken without the need for translation (Figure 53 b)). However, for laboratory sources with divergent beams from a (near-)point source, there is a geometric magnification of the sample, in addition to any other magnification due to optics used in the beam path. On the other hand, at a synchrotron source, due to the narrow solid angle of production of synchrotron radiation and the use of slits and collimating devices, the X-rays are almost fully parallel when impinging on the sample (Figure 53 c)). This means that there is effectively no geometric magnification and instead, complex X-ray optics are used to provide the requisite magnification.

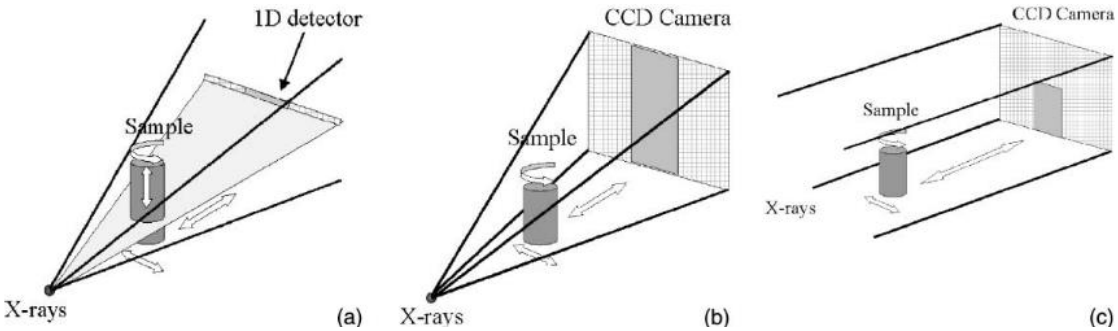

Figure 53: Schematic of a) Fan-beam geometry (1D detector); b) Cone-beam geometry (2D detector) c) Parallel geometry (synchrotron radiation, 2D detector), reproduced with permission from [232]

A common system utilised to achieve high-resolution tomography utilises wavelength-selective Fresnel zone-plates (FZP), which provide X-ray focussing by means of a diffraction-based lens composed of concentric rings with gradually smaller spacings towards the outer edge (Figure 54). This set-up, consisting of finely-tuned X-ray optics, may be combined with either high-brightness, highly collimated X-ray radiation produced at third-generation synchrotrons, or with a cone-beam lab-source, provided it is collimated by use of a capillary condenser lens and beamstops which yield a focused quasi-monochromatic beam.

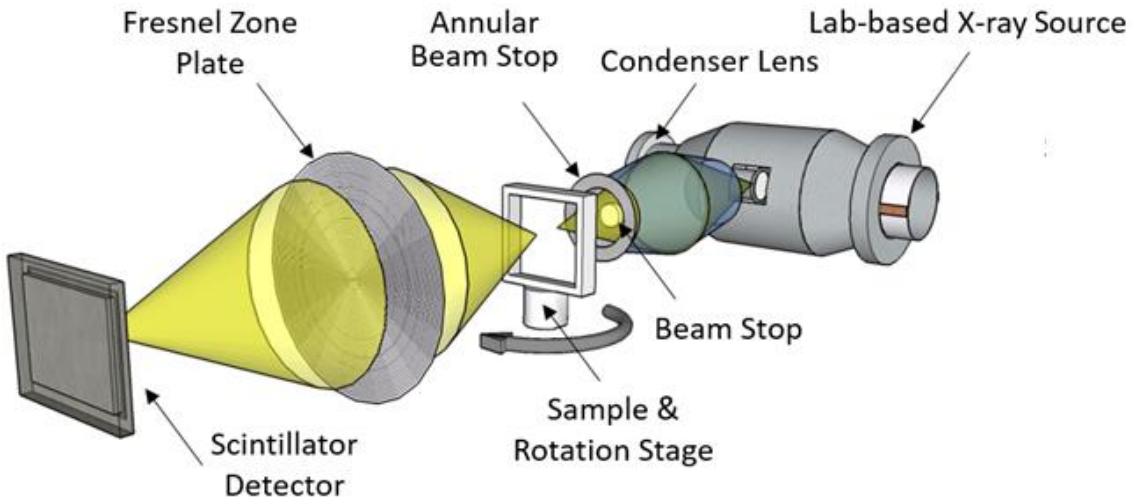

Figure 54: Schematic displaying a typical X-ray optical set-up used in a lab-based X ray nano-CT instrument (not to-scale), reproduced from [305]

3.2.5.6 Reconstruction

There are two main categories of mathematical algorithms that can be used for the reconstruction of a 3D object from a series of 2D images taken at angular increments: analytic reconstructions and iterative reconstructions [243]. Analytical reconstructions include matrix inversion techniques [244][245], algebraic methods [246] [247] [248], linear superposition techniques [227][249] and filtered back-projection algorithms (FBP) [229][231]. This latter technique has been the most prevalent for many decades and is the algorithm by which all tomographic data in this thesis was reconstructed. Below is an explanation of FBP algorithms, both schematically and mathematically.

Here, a schematic treatment is given for the FBP algorithm. It can be shown that the acquisition of 2D projection radiographs by exposure of 3D objects to X-ray radiation is mathematically analogous to performing a 2D Radon transform [222] on the linear attenuation coefficients of the constituent materials. In other words, the collected values represent the result of a forward projection, at the various incremental angles, of integrating over each of the X-ray paths from source to detector. This results in sinograms, like that shown in Figure 55, which contain all the projection data collected by the tomographic technique, as a function of angle (θ) and a dimension of the rotated co-ordinate system (t) (see Figure 52).

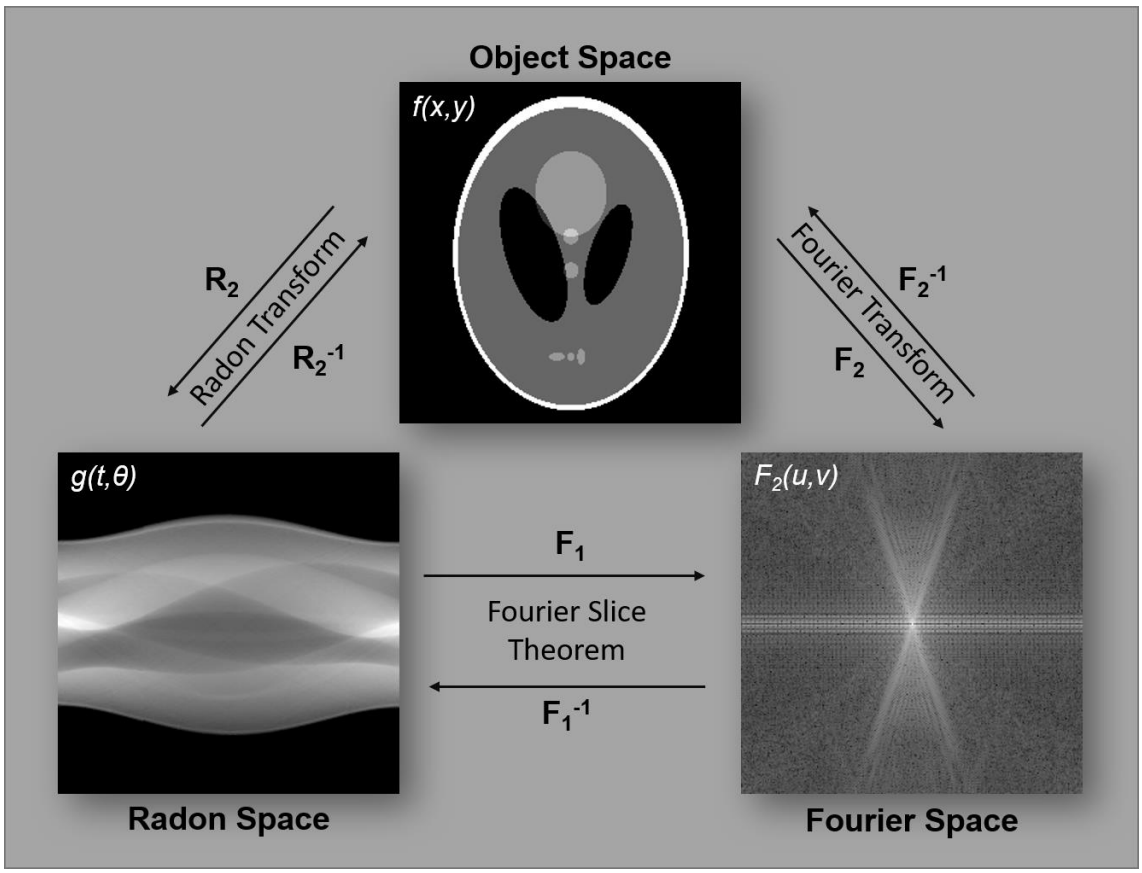

Figure 55: Schematic illustrating the steps required to invert the Radon transform which is an inherent part of X-ray transmissive projection imaging

To re-establish the 3D nature of the object, the aim is to establish the inverse Radon transform, which is accomplished by invoking the Fourier-slice theorem which states that the 1D Fourier transform of the projection of a two-dimensional function onto a one-dimensional line is equal to performing a two-dimensional Fourier transform on the same function and subsequently slicing it parallel to the projection line. Unfortunately, if this approach is taken on the as-generated sinogram, the result is blurry due to unavoidable noise within the acquisition. Hence the acquired data is often filtered (in Fourier space) by the application of a Fast Fourier Transform FFT, followed by a complex filter (predominantly composed of a ramp filter) [250][251] and returned to the spatial domain with an inverse FFT. Subsequently, the back-projection can be applied utilising the Fourier-slice theorem, returning a 3D projection of the object originally projected. A mathematical treatment is given in **Appendix 11.1**.

3.2.5.7 Experiment

3.2.5.7.1 Lab-based

For lab-based X-ray nano-CT, the Zeiss Xradia 810 Ultra instrument (Carl Zeiss, Pleasanton, USA) was used for all data acquisition. This machine uses a rotating anode (Cr) X-ray source, with a characteristic emission peak at 5.4 keV. The instrument is designed to convert the white beam from the source into a quasi-monochromatic beam, to effectively perform a full-field illumination of the sample. This is achieved by a combination of collimating devices and importantly by a wavelength-selective capillary condenser. The transmitted X-rays from the sample are re-focused by a Fresnel zone plate and are registered on a 1K scintillator-detector.

There are two imaging modes accessible on the instrument: large field-of-view (LFOV) and high resolution (HRES) modes, with dimensions of 65 and 16 µm, respectively. In binning 1 (that is, all pixel counts correspond directly to pixel grayscales in each radiograph), this results in voxel dimensions of 63 and 16 nm, respectively. Although a phase contrast imaging modality is available (Zernike phase contrast), this set-up is of little practical use for high attenuation materials such as the constituents of SOFC anodes due to its reduced flux.

After acquisition, reconstruction of 3D tomograms from the series of 2D radiograms was achieved in proprietary software, XRMReconstructor (Carl Zeiss). In all cases, the data was reconstructed using a standard FBP algorithm without further binning.

3.2.5.7.2 Synchrotron-based

All synchrotron X-ray nano-CT featured in this thesis was performed at the X02DA beamline (also known as TOMCAT) in the Swiss Light Source (SLS) at the Paul Scherrer Institut (PSI). This beamline offers fast, non-destructive, high resolution, high brilliance, high coherence X-ray capabilities and receives synchrotron light from a 2.9 Tesla superbend, giving rise to a critical energy of 11.1 keV [252]. The TOMCAT set-up may facilitate both white beam and monochromatic options, and the details of the configuration used are given in **Chapter 7**.

3.2.6 X-ray Diffraction (XRD)

X-ray diffraction (XRD) refers to the theory and practice of obtaining crystallographic information about a material of interest by the diffraction of imposed X-rays. Monitoring the diffraction direction and intensity sheds light on the internal atomic structure of crystalline matter [253]. Diffraction is the effect which follows the interaction of a wave with an object that has dimensions comparable to the wavelength of the wave. If light waves encounter a periodic array, waves emanate from the array at discrete angles, as long as their wavelength is comparable to the periodicity of the "diffraction grating" (here, atomic distances ≈ 0.1 nm). These angles are geometrically defined by the wavelength and the interplanar spacing between the atoms and the relationship is discussed below.

Typical metals used in lab-based X-ray sources for XRD include: Cu, Mo, Fe, Co and Cr, often giving rise to two characteristic K_α emissions and one characteristic K_β emission [253]. The K_β emission is often filtered out leaving K_α, which may or may not be distinguished as $K_{\alpha1}$ and $K_{\alpha2}$ lines.

It is the elastic *coherent* scattering of X-rays (also referred to as Rayleigh scattering) that gives rise to the important observations made through XRD, as any inelastic Compton scattering does not have a fixed relationship between the phase of the incident and emitted waves, which is vital for interference and thus observation of a diffraction pattern. Thus, when X-rays with wavelengths of 0.5–2.5 Å are incident upon crystalline materials, diffraction patterns are observable as this is the same scale as the distances between adjacent atoms *and* because the incident X-rays are coherently scattered from the electrons of the constituent atoms. Any incoherent scattering occurs simultaneously, but only contributes to the background of the diffraction pattern [253].

A lattice is an abstraction from the true crystalline structure of many materials but helps explain the direction and intensity of X-ray diffraction patterns; it is made up of a periodically repeating array of points, onto which a *basis* or *motif* (set of one or more atoms/ions/etc.) may be superimposed to yield the crystalline structure of a material. Myriad structures can be described by crystal groups whose symmetry properties are

the basis of the broad subject area of crystallography which is explored in numerous texts [254][255]. From this approach, systems of crystallographic planes were indexed by Miller [256], giving rise to [*h k l]* notation to denote the different planes responsible for observed X-ray diffraction patterns.

When a plane X-ray wave interacts with a periodic array of atoms, the atoms may be seen as point sources of scattered secondary wavelets, according to Huygen's principle [257]. Importantly, it is only when many atoms' scattering is in-phase that it is clearly observed by the experimenter, as although all the atoms in a crystal scatter incident X-rays, they do so in all directions and with an amplitude that depends on the scattering direction. Hence, the wave scattered by a single atom has an extremely weak electric field compared to that of the incident X-ray beam. Nevertheless, when the scattered waves from many atoms are in-phase and constructively interfere, the scattering intensity becomes considerably higher and thus observable on the detector. As it is only when the phase difference between exiting waves is equal to an integer multiple of the wavelength of the incident X-ray that the waves constructively interfere, there is a geometrical constraint on observing high intensity outward signals. This can be mathematically summarised in Bragg's law, which states that the condition for diffraction is given by Equation *3-5*:

$$n\lambda = 2dsin\theta \qquad 3\text{-}5$$

where n *is an integer,* λ *is wavelength,* d *is interplanar spacing and* θ *is incidence angle*

This mathematical relationship is best understood by the diagram given in Figure 56.

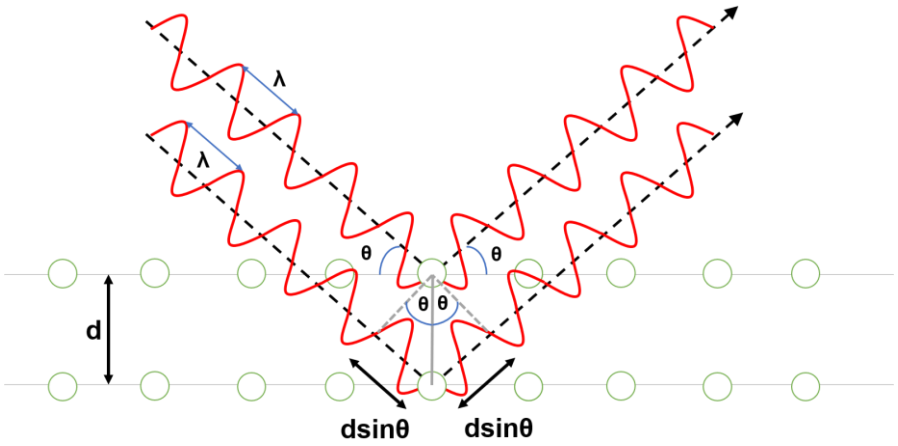

Figure 56: Diagram illustrating that the path difference between emitted waves from atoms on adjacent lattice planes is given by 2dsinθ

Experimentally, a diffractometer constitutes an X-ray radiation source, a sample stage and a detector which often scans through angles of *2θ*, collecting the emitted intensity. Using Bragg's equation, the interplanar spacing, *d*, can be determined and various peaks of specific intensity at particular angles can be used to characterise the presence or absence of specific crystalline compounds, amongst other properties. In this thesis, XRD acquisition was performed on a PANalytical X'Pert MPD (Malvern PANalytical, Malvern, UK) at Imperial College London, using Ni-filtered Cu K_α radiation at 40 keV and an X'Celerator multi-strip detector. The sample was ground *via* pestle and mortar and powder diffraction was performed covering *2θ* angles from 5° to 90° with a step-size of 0.033°, collecting a total of 2575 data points.

3.3 Software

3.3.1 Image Processing

3.3.1.1 Fiji (ImageJ)

Freeware from the National Institutes of Health, Fiji, (NIH, Maryland, USA), was used to visualise, process, align, and prepare figures from data acquired from various characterisation techniques used in this thesis [217]. The alignment of FIB-SEM data was carried out by use of the TurboReg and StackReg [258] plug-ins which apply a nonlinear least-squares optimization approach to minimise the mean square intensity difference between adjacent slices.

3.3.1.2 Avizo

For the purposes of visualisation, processing, filtering, registration, and 3D rendering, Avizo 9.4/9.5 (ThermoFisher Scientific, Oregon, USA) was used. This software successfully allows the import of proprietary filetypes such as '.txm' from the lab-based X-ray nano-CT instrument used in this work, as well as standard image formats such as .tif stacks. Filters such as "non-local means" [259] and "unsharp masking" [260] were employed to denoise and improve image segmentation and are discussed when implemented. The built-in registration module "Register Images" is also extensively used, which was applied after manually aligning 3D datasets close to their optimum alignment. More details can be found in the Avizo user guide [261].

3.3.1.3 Ilastik

To improve on the direct and indirect methods of segmentation using grayscale and grayscale gradient, respectively, a further freeware, Ilastik (Heidelberg, Germany), was implemented when appropriate [262]. In cases where edges between phases are ill-defined but there are sufficiently large features with internal texture, a user-introduced segmentation is performed on a small number of slices, and the software applies machine-learning algorithms to create a training field which is subsequently used to segment the entire volume. A good overview of the use of ML techniques, such as automated neural networks, is described in work by A. Kan [263]. In all work using Ilastik in this thesis, a conservative approach using the recommended kernel sizes (σ = 1.0 – 3.5 pixels) for a range of features, including intensities, edges and texture, was used alongside minimal user input in segmentation training (3-6 slices per dataset of hundreds of slices).

3.3.2 XRD Analysis

All XRD analysis was performed in X'Pert Highscore Plus (Malvern PANalytical, Malvern, UK) by making use of the in-built compound library and comparing acquired XRD patterns with those available in the literature. The results are shown in **Chapter 5**.

3.4 Metrics

3.4.1 Simple Metrics

Several standard length, areal and volumetric metrics are typically extracted from 3D FIB-SEM and X-ray nano-CT reconstructions, and the approaches to each metric of interest extracted in this thesis is detailed in this section.

3.4.1.1 Volumes

One of the most straightforward metrics commonly employed when assessing 3D data is the volume or phase fraction (V_i), which is calculated by summing all the allocated voxels from a specific phase and dividing this by the total number of voxels encompassed by the entire volume, as shown by Equation *3-6*:

$$V_i = \frac{N_i}{N} \qquad 3\text{-}6$$

where N_i *is the number of voxels of a specific phase* i *and* N *is the total number of voxels*

If *i* corresponds to the porous phase, this is often termed the porosity (***ε***) and this parameter is of high importance when considering fuel cell porous media as it is this phase which determines the transport properties of reactant and product gases. For the solid phases, it is important to note that volume fraction may be given in absolute terms, in accordance with Equation *3-6*, or sometimes a %Solids volume which uses solely the total solids volume as the denominator. Although the cuboidal voxelization of real non-cuboidal structures inherently involves a degree of error, for phase fraction, this is often a small error, given sufficiently large features, as the bulk of the material outweighs the influences of surfaces/interfaces.

3.4.1.2 Areas

Surface areas are reported in different ways, defined absolutely, specifically with regards to the volume of the same phase, or specifically with regards to the total volume under consideration. In the last case, the volume-specific surface area (VSSA) is given by Equation *3-7*:

$$VSSA = \frac{Ns_i}{N} \quad 3\text{-}7$$

where $\mathrm{Ns_i}$ is *the number of voxels at the surface of a specific phase* i

Again, an issue arises from the nature of voxelization of the real volume as the cuboidal voxels almost certainly do not correctly represent the morphology of any of the phase surfaces. This discretisation of surfaces is unavoidable and will incur sizeable errors unless the selected resolution (read: pixel dimension) is much smaller than the radius of curvature of any surface feature. In most cases, it is not possible to reliably quantify the incurred error, but many authors use a smoothing algorithm in order to address this issue [133][264][265]. However, although it is fair to say that real surfaces are not jagged like voxels, it is not clear what extent or type of smoothing is required to approach the true morphology. The most important aspect must be consistency across comparison such that fair analysis can take place, even if this does not fully represent the exact 3D microstructure under investigation. For this reason, all surfaces formulated in this thesis involve the same conservative smoothing step corresponding to a “Smoothing Extent” of 3 *via* a “Constrained Smoothing” module in Avizo [261].

3.4.1.3 Particle Size Distribution (PSD)

Characterising the size of 2D or 3D discrete particles is straightforward, involving volumes, areas, diameters and/or radii. However, the nature of the problem becomes more complex as the pores or particles effectively coalesce and give rise to a connected, sinuous network whose characteristics are less facile to define with single values. As a consequence, several methods exist as metrological devices to capture changes in particle or porous networks for a range of sample types, including chord distributions [266][267], intercept methods [81][93], Lattice-Boltzmann methods [268][269], and distance-transform-based approaches [270][151][271].

In this work, two approaches have been adopted. Firstly, for some datasets, a continuous particle size distribution (cPSD) approach, as part of the “Xlib” plug-in for Fiji, was used [151]. For other datasets, a different metrics extraction methodology was developed, based on a local thickness measurement. For the solid phases, the chosen algorithm retrieves the local feature size and determines the feature size distribution, while for the pore phase it similarly shows the local pore size as well as the global pore size distribution. Local thickness is determined by assigning each voxel in the phase of interest the radius of the largest sphere that can be drawn entirely in that phase and includes that voxel. Local thickness should not be confused with distance transform which similarly finds the largest sphere that can be *centred* on that voxel. To determine the local thickness, subsequent morphological opening operations are performed on the phase of interest with increasingly large structuring elements. After each successive iteration the voxels unaffected by the operation are assigned the radius of the structuring element [272].

3.4.2 Advanced Metrics

3.4.2.1 TPB

The length and density of the triple-phase boundary (TPB) can be measured in several different ways from 2D or 3D datasets. Stereological methods have been employed previously on 2D images, wherein the number of TPB points per unit area was mapped onto a virtual 3D volume [273][274][275] although this has the inherent drawback of a lack of connectivity and percolation information, and as a result, accessing

the proportion of active-to-total TPB length or density is not technically possible. Random sphere models have also been used to model the particulate microstructure in three dimensions. These models have been implemented to simulate the impact of grading the anode on percolation and active TPB length [276], the effect of electrode thickness [277] as well as particle size distributions [278], although unfortunately these model structures are not truly representative of real SOFC electrode microstructures.

With the advent of 3D methods to virtually reconstruct real microstructures, a range of algorithms have been developed to extract TPB length from segmented datasets. Iwai *et al*. investigated both a volume expansion and a centroid method to calculate total TPB lengths [126]. Pecho *et al.* used a simple indexing system whereby voxels located next to two unlike phases were identified as TPB voxels, forming a binary mask which is skeletonised to give a TPB length [279], subsequently removing any non-percolated lengths. Lu *et al.* excluded non-percolated regions first and then used a voxel expansion-contraction method to give the Euclidean length of the active TPB [280]. Cooper *et al.* included a built-in TPB density calculator in open-source software, TauFactor [281], which can be used to calculate the total TPB density, wherein the calculation uses the MATLAB language to label each phase with a prime number (2, 3 or 5) and select only the voxels which contain an edge which is part of 4 voxels whose computed product is a multiple of 30. This number of voxels is then divided by 4 and by the total volume to yield the total TPB density. Similarly, Golbert et al. [19] counted all the voxels neighbouring a TPB edge and divided this overall number by four. In this work, however, solely the algorithms developed by X. Lu *et al.* were used [280] (Figure 57), to calculate both the *active* and *total* TPB densities, and retain consistency across datasets.

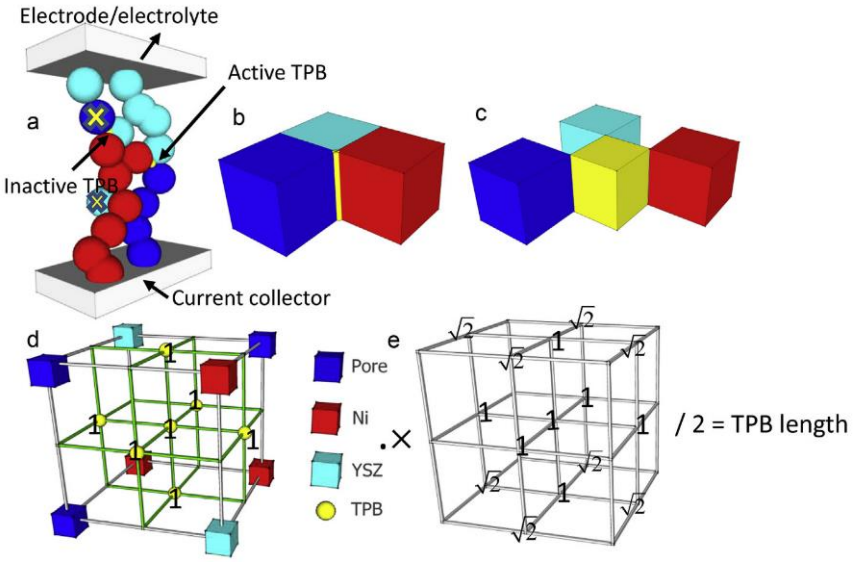

Figure 57: Volume expansion methodology for calculation of TPB length from 3D microstructural data, using MATLAB, reproduced from [280]

3.4.2.2 Shape

Changes in the shape and structure (such as elongation in a particular direction) of any of the three phases can be investigated in the following way. Chord length distributions are extracted from each phase as previously reported by Kok *et al.* [282]. Chords are straight lines drawn across a particular phase, wherein their length probes the feature size in that direction and the distribution of lengths across an entire domain, the so-called chord length distribution, measures the degree of anisotropy in the material. In **Chapter 6**, chords were applied to each phase, in each direction for a range of samples. These chord length distributions offer quantitative insight into the average *global* feature shape and possibly how different treatments affect this aspect.

3.4.2.3 RVE and Error Analysis

Due to inherent heterogeneity in porous electrode materials made *via* traditional slurry-based fabrication routes, it is important to assess the validity of sub-sectional datasets to determine whether they are representative of the macroscopic properties of the overall microstructure. The calculation of the RVE [283] can be performed in a number of ways, including a growing cuboid [281][284] approach; sampling multiple regions [162], or statistical correlation methods [285]. In this work, the MATLAB-based open-source software TauFactor was used to apply a cubic volume expansion method to investigate the RVE for both tortuosity factor and porosity. Solely this method was chosen due to its ease-of-use and to retain consistency in approach.

3.4.3 Digital Volume Correlation (DVC)

DVC is a technique used to measure displacements and, in turn, strains, across a sequence of tomographic volume images. First, a volume is sub-divided into smaller sub-volumes and algorithms are used to calculate the displacement of the pattern within each sub-volume from the reference to the deformed state. The result is a 3D matrix of vectors representing local sample displacements. Local strain values are obtained by numerical derivation of the displacement vector field [286] and many other metrics may be extracted based on this directional information. The approach is detailed below on a 1D basis for clarity and the mathematical treatment for 3D datasets is presented in **Appendix 11.2**.

3.4.3.1 One-dimensional shifts

The software computes the correct shift vector for each sub-volume by moving the initial (reference) sub-volume pattern around until it best matches the position of the pattern in the deformed volume. The quality of this match is described by the correlation value, *C(i)*, with a maximum of 1 for a perfect match.

For 1-dimension [286]:

$$C(i) = \sum_{i=x_0}^{x_0+N-1} A(i)B(i+dx) \qquad 3\text{-}8$$

where A is the reference image, B is the deformed image, x_0 *denotes the start position, N is the window size and dx is the current shift.*

By varying dx over a certain range, the desired outcome is that a peak is obtained, the maximum of which corresponds to the shift (dx) with the best match. Since images tend to experience some noise and potentially some overall changes in “brightness” may occur between reference and deformed images, a normalised form of the correlation value is normally used to account for intensity fluctuations, using the arithmetic means (Equations *3-9* and *3-10*) of the voxels in the two volumes (here, A & B):

$$< A > = \sum_i \frac{A(i)}{N} \quad 3\text{-}9, \qquad < B > = \sum_i \frac{B(i+dx)}{N} \quad 3\text{-}10$$

The normalised version for the 1D correlation value is thus given by Equation *3-11* [286]:

$$C_{norm}(i) = \frac{\sum_{i=x_0}^{x_0+N-1}(A(i)-<A>)(B(i+dx)-<B>)}{\sqrt{\sum_{i=x_0}^{x_0+N-1}(A(i)-<A>)^2}\sqrt{\sum_{i=x_0}^{x_0+N-1}(B(i+dx)-<B>)^2}} \qquad 3\text{-}118$$

3.4.3.2 Resolution & Precision

When selecting the appropriate sub-volume, there is competition between better spatial resolution (smaller sub-volume) and reduced influence from noise due to better correlation statistics (larger sub-volume). To overcome sampling issues, one can also choose to overlap sub-volumes. Overlap increases the spatial density of vectors without reducing the sub-volume size. Therefore, the displacement vectors still average the signal over the same region of space.

DVC can provide sub-pixel precision, since sub-pixel shifts will still affect the integrated intensities measured by pixels surrounding a feature. If so, the discrete correlation peak will show slight asymmetry. By fitting a Gaussian to this correlation function, the true position of the maximum can be restored with sub-pixel precision.

Digital volume correlation was performed on the raw grayscale images, given directly by reconstruction, using DaVis 10.0.4 software (LaVision Ltd., Germany). The software imports images in the RAW format (stack of grayscale images) and computes deformation vectors based on the change of gray-scale structures within the images. It can be performed on two volumes (reference and deformed) or on a longer sequence of image stacks. With this software, the minimum deformation between subsequent images must be at least 0.05 voxels to be reliably calculated and the internal structure must have some internal contrast pattern (ideally randomly distributed and 2-3 voxels in size).

There are several input parameters open to the user. Depending on the number of registered volumes, calculations can be made all relative to the first image or correlation can be purely assessed between each volume and its predecessor. The user then defines an FFT pre-shift window size which defines the size of the initial FFT correlation, yielding a predictor displacement field used for further DC correlation. The user selects several parameters for the DC correlation calculations, including:

- Window size, N, which the software uses to split undeformed and deformed images into N x N x N sub-volumes, defining the node spacing.
- Window shape, which defines the shape of these sub-volumes (cubical or spherical)
- Overlap, defining the overlap of the sub-volumes (50% or 75% are standard)

- Peak search, this defines the neighbourhood that is searched in order to find a match to the sub-volume of interest

- Binning, as with computed tomography data, this reduces the data size by finding the average of adjacent voxels

- Passes, refers to the number of iterations attempted, and works by applying its next calculation to a “de-warped” version of the deformed volume based on the previous calculation

When undertaking DVC calculations, the above parameters are chosen in accordance with the feature size and separation, accounting for the play-off between spatial resolution and computation time.

3.5 Simulation

3.5.1 Tortuosity (factor)

The concepts of tortuosity and tortuosity factor are crucial in discussing the structure-property relationships for porous media such as the cermet anode found in an SOFC. Unfortunately, there has historically been some confusion between the two parameters and a less-than-clear approach to nomenclature in the area. Epstein distinguished between systems in which all porous capillaries are sinuous but *parallel* with the situation of sinuous and non-parallel (variable cross-sectional area) networks more commonly present in real systems [147]. The paper explains that in the former case, the ratio of the average (same for all capillaries) pore length to the Euclidean distance between the two plane edges of the porous medium is defined as the tortuosity, τ (Equation *3-12*).

$$\tau = \frac{L_e}{L_{eucl}} \qquad 3\text{-}12$$

where L_e *is pore length &* L_{eucl} *is plane separation distance in the direction of flow*

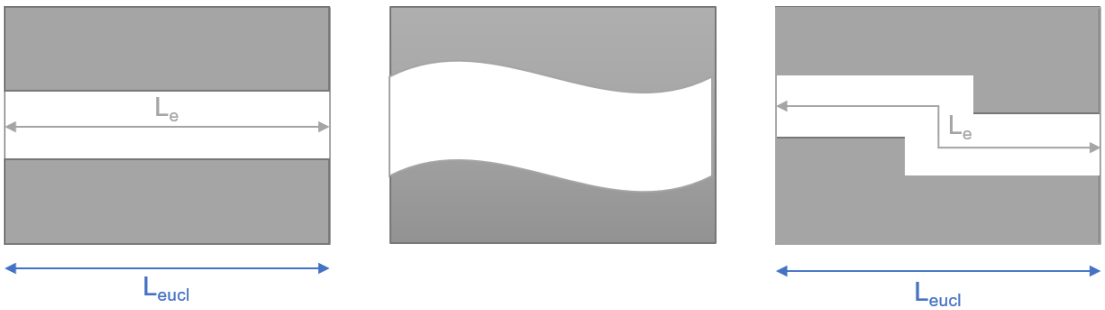

Figure 58: Diagram of pore length and Euclidean distance between two plane edges of a porous medium

Assuming an incompressible, Newtonian fluid in laminar flow, travelling through parallel porous capillaries, driven by a pressure difference, the Hagen-Poiseuille equation applies:

$$Q_{vol} = \frac{\Delta p \pi r^4}{8 \eta_{visc} L_e} \qquad 3\text{-}13$$

where Q_{vol} *is the volume flow rate,* Δp *is the pressure differential between the two planes,* r *is (constant) radius of the capillary,* η_{visc} *is the viscosity and* L *is the pore length.*

Taking into account the relationship between the axial velocity (in the direction of flow) and the superficial velocity (in absence of solids), Epstein re-derived the equation of the effective diffusivity in terms of the pore length and pore medium length [287], showing that this ratio appears raised to the second power:

$$D_{i,eff} = \frac{D_i \varepsilon}{(\frac{L_e}{L})^2} = \frac{D_i \varepsilon}{\tau^2} \qquad 3\text{-}14$$

where $D_{i,eff}$ *is the effective diffusivity of component* i *and* ε *is porosity*

The τ^2 term is known as the tortuosity factor and is a proportionality coefficient between the true diffusivity and the effective diffusivity due to the resistance presented by the presence of the porous medium. It is worth noting, however, that the power relationship between tortuosity factor and tortuosity is only strictly valid in the case where the pore capillary cross-sectional area is constant – in other words, deviations from pore wall parallelism cause a deviation from the squared mathematical relationship between the two parameters [147].

To estimate or calculate the tortuosity or tortuosity factor, several approaches have been taken. The simplest involves using an empirically determined relationship between porosity and tortuosity, such as the Bruggeman correlation (Equation *3-15*).

$$\frac{D_{A,eff}}{D_A} = \varepsilon^{(1+n)/n} \qquad 3\text{-}15$$

where n = 2 for spheres ($\tau^2 = \varepsilon^{-\frac{1}{2}}$) *and n = 1 for cylinders* ($\tau^2 = \varepsilon^{-1}$)

However, various comparisons between experiment and the Bruggeman correlation have led researchers to doubt its validity in many circumstances and other methods have been sought [288]. Geometrical and flux-based tortuosity factor approaches based on

3D microstructural data have been developed to overcome the limitations in the Bruggeman and similar correlations; a good review of these methods has been provided by Tjaden *et al*. [289]. For instance, to account for the deviation from the parallel capillary model, van Brakel and Heertjes and Holzer *et al.* included a constrictivity factor, δ, in their calculations, a crude inclusion of the variation in pore diameter [290][291]. Moreover, in the latter work, an important distinction was made between indirect tortuosity factor measurements derived from experiment and those determined based on geometries accessed by 3D reconstructed volumes. Aside from empirical and theoretical relationships, experimental procedures have also been utilised to extract tortuosity values, such as diffusion cell experiments [292] and electrochemical setups [116].

In the case of flux-based analysis of 3D reconstructions, e.g. from FIB-SEM slice-and-view or X-ray nano-CT data, it is important to consider what type of diffusive regime is followed; Fick's, Knudsen, viscous or indeed some combination thereof [293]. Moreover, it is vital to distinguish between algorithms which look for a singular shortest path based solely on *geometry* and those that imitate mass transfer mechanisms such as diffusion (so-called "flux-based" approaches) which may be voxel or mesh-based [289]. Some examples from the literature on establishing tortuosity factors from 3D reconstructions include: Wilson *et al.* [294] and Izzo *et al.* [158], who evaluated the tortuosity factors by solving Laplace equation with a finite element method (FEM) and a lattice Boltzmann method (LBM), respectively, and Gostovic *et al.* [122] and Smith *et al*. [274] who calculated tortuosity by tracking the pore centre locations and measuring the lengths of the path, comparing those with the Euclidean distance between planes. In this work, the most robust and reproducible method was followed, utilising open-source MATLAB software, TauFactor, whose underpinnings are well explained in the literature [295]. Hereafter, τ is used to denote tortuosity factor, and a square-root relationship with tortuosity is not assumed to be valid.

3.5.2 Cellular Automata (CA)

The details of the CA approach can be found in [296][297][298]. Here only a brief description is given. Space is discretised into cells (voxels) and each cell is assigned

both an internal state describing its nature (e.g. solid, pore, surface, interface) as well as its own internal energy with respect to a common reference energy. The system evolves by switching the state of the cells according to energy-based criteria or set of rules. The energy of a given cell depends on its interaction with neighbouring cells [299][297]. In CA, all the cells that are able to make a switch to a lower energy state are simultaneously permitted to switch their state (within one timestep). The relative excess energy of a cell, which drives the microstructural evolution, is calculated by quantifying its “structural imbalance”, which has been confirmed to be consistent with the Gibbs-Thomson equation for the excess energy of curved surfaces [299].

Two major matter transport mechanisms were considered in the literature simulations: surface transport and grain boundary migration. Surface transport is simulated with the assumption of fast diffusion, while the detachment/attachment of Ni atoms is the rate-determining step. Hence, thermodynamics are assumed to play a dominant role while transportation kinetics only play a marginal role. Consequently, the kinetics of different matter transport mechanisms are not required and this fast diffusion model was found to match the experimental results of nickel film de-wetting [300].

The algorithm used in the fast diffusion model is similar to that used in the evaporation-condensation model [297]. In brief, each surface matter voxel is given a chance to become a vacant voxel (in practical sense this means surface matter moves away from its current position). The probability of this matter voxel detachment (or erosion) is proportional to its relative free energy. In parallel, each vacant surface voxel may be eliminated by the attachment of a matter voxel. The probability of this vacant voxel elimination is proportional to the relative free energy of the vacant voxel. However, unlike the evaporation-condensation model which allows matter to be transported between disconnected particles, this fast diffusion model prohibits the transport between disconnected particles. In this work, only the surface transport mechanism is investigated as the crystallographic orientation of the grains is not collected by the lab-based X-ray nano-CT technique used to collect the data upon which the simulation was run.

Chapter 4: FIB-SEM slice-and-view of virgin & aged SOFC anodes

This chapter covers FIB-SEM slice-and-view tomographic investigations of ‘virgin’ and ‘aged’ Ni-YSZ samples supplied by a manufacturer. The first section details sample preparation, both pre-introduction to the instrument and under vacuum, immediately prior to milling. Secondly, data processing and analysis is presented, focusing on metrics extraction and RVE analysis. Finally, conclusions are drawn with respect to the tomographic technique and the observed microstructural evolution.

4.1 Samples

Two planar SOFC anodes, composed of nickel, 8YSZ and porosity in a nominally 1: 1: 1 volume ratio, were supplied by Forschungszentrum Jülich (Jülich, Germany), both comprising an approximately 550-µm-thick ASL and a roughly 5-µm-thick AFL. Both samples constituted anodes only, without electrolyte or cathode layers. One sample was effectively a ‘virgin’ anode; a reduced but otherwise untreated porous Ni-8YSZ cermet. The other sample was pre-conditioned by ageing for 1500 h at 1000 °C in 80 % humidity hydrogen while bearing a load of 0.5 A/cm^2. This treatment was performed at Forschungszentrum Jülich prior to receiving the sample.

Both samples were sectioned and epoxy-impregnated under vacuum until bubbling was deemed to have stopped (approximately 6 h), before being left under vacuum overnight. The coarse grinding process was performed using silicon carbide pads (Buehler, Illinois, USA), entailing the abrasion of the epoxy-filled sample with finer and finer papers (grades 320, 600, 1200, 2500 and 4000), interspersed with a cleaning sonication treatment for 2 min in isopropanol. The grinding stage was followed by a 15-min polishing step with 1 µm diamond paste on a lapping wheel. Separately, another fragment of each of the samples was prepared as above for separate SEM analysis. EDX was used, in unison with SEM imaging ([SEM_UCL]), to confirm the identity and distribution of the solid phases captured during slice-and-view.

4.2 FIB-SEM

4.2.1 Platinum deposition / Trench milling

After placing each sample under vacuum in the dual-beam instrument ([FIB-SEM_UCL]) in the London Centre for Nanotechnology (LCN) at University College London (UCL), two 500-nm layers of Pt were deposited (100 pA) atop the VOI of the ASL in each case. Subsequently, an approximately 15-µm-deep "U-shaped" trench (Figure 47) was milled away at high beam current (20 nA) to provide an adequately sized volume for any redeposited material to build-up without obscuring the VOI, as well as allowing the efficient egress of the electrons, hence reducing "shadowing" effects.

4.2.2 Slice-and-view

4.2.2.1 Virgin microstructure

After an initial polishing step to reveal the microstructure of interest to a suitable degree for subsequent segmentation, FIB-SEM slice-and-view was performed on both samples. For the *virgin* sample, milling was performed at a current of 200 pA, set to remove 32 nm in the Z-direction, with an XY-pixel dimension of 32 nm to give cubic voxels. SEM imaging was conducted at 2 kV, in accordance with the work by Thydén *et al.* [128] which showed that at low accelerating voltages, Ni/YSZ contrast can be enhanced due to a dominant contribution from a particular type of secondary electron signal (SE3). 98 usable slices were captured in total and used in subsequent image processing and analysis.

4.2.2.2 Aged microstructure

For the *aged* sample, milling was performed at a current of 200 pA, set to remove 45 nm in the Z-direction, with an XY-pixel dimension of 45 nm to give cubic voxels. Unfortunately, this Z-dimension was different with respect to that used for the *virgin* microstructure but was used as the FIB beam stability at the time did not support thinner slicing. SEM imaging was conducted at 2 kV for the reasons described above. 60 usable slices were captured in total and used in subsequent image processing and analysis. Further collection of slices was limited by the appearance of re-deposited material which managed to build-up sufficiently to obscure the face of interest.

4.2.3 Data Processing

4.2.3.1 Alignment

As noted in **Chapter 3**, unavoidable sample drift during the several hours of acquisition led to 2D micrographs which were not in full alignment and did not initially provide an adequate representation of the 3D microstructure of interest. To align the images, the TurboReg and StackReg [258] plug-ins for the freeware Fiji (US NIH, Maryland, USA) [301] were utilised in "Translation" mode (wherein the mapping is of the simple form $x = u + \Delta u$) to minimise this acquisition artefact. Visually, the result appeared a significant improvement on the previous, unaligned images.

4.2.3.2 Filtering

To remove any streaking caused by imperfect milling, a non-local means filter was applied in Avizo which works by comparing the neighbourhoods of all voxels in a given search window (set to be 19 pixels in dimension in this instance) with the neighbours of the voxel to be denoised. The similarity between the neighbours determines the weight with which the value of a voxel in the search window influences the new value of the voxel to be denoised. The final weights are determined by applying a Gaussian kernel to the similarity values [302].

4.2.3.3 Segmentation

Contrast between the solid phases was generally adequate for straightforward greyscale-based distinction (see Figure 59), although, a few obstacles had to be overcome for a high-fidelity segmentation.

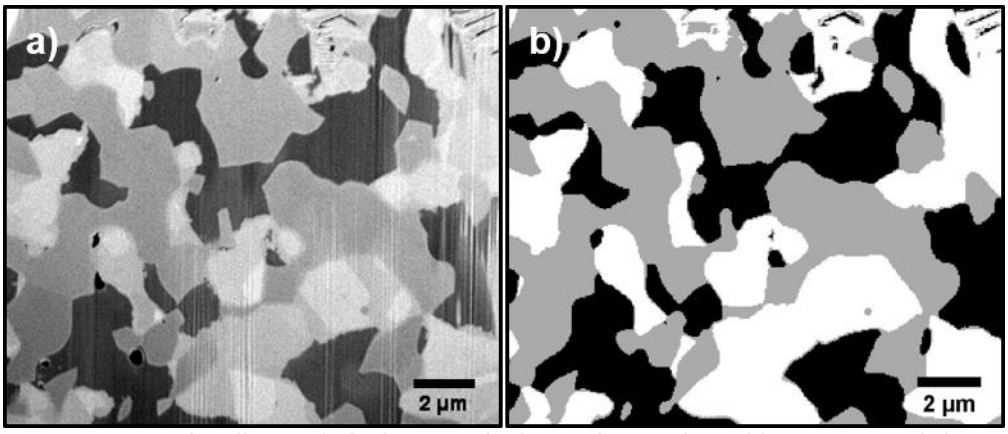

Figure 59: XY-orthoslices of virgin sample from a) raw data, b) segmented data

First, at the boundary between bright grey/white nickel and dark grey/black pore phases, the grayscale gradient is large but not infinite, leading to a narrow continuum

that generates false voxel allocations to the YSZ phase [135]. To overcome this mis-allocation, a 2-pixel erosion-dilation approach was used wherein the larger domains were unaffected, but single- or double-pixel-wide lines at the boundaries were effectively eradicated (). This approach works perfectly if all genuine features are larger than 2 pixels in thickness and remain after the erosion step, and all false allocations are 1 or 2 pixels in thickness and disappear during this step. In reality, this approach is an approximation, but observation of multiple slices shows it to give a much-improved boundary region, with far fewer misallocated pixels.

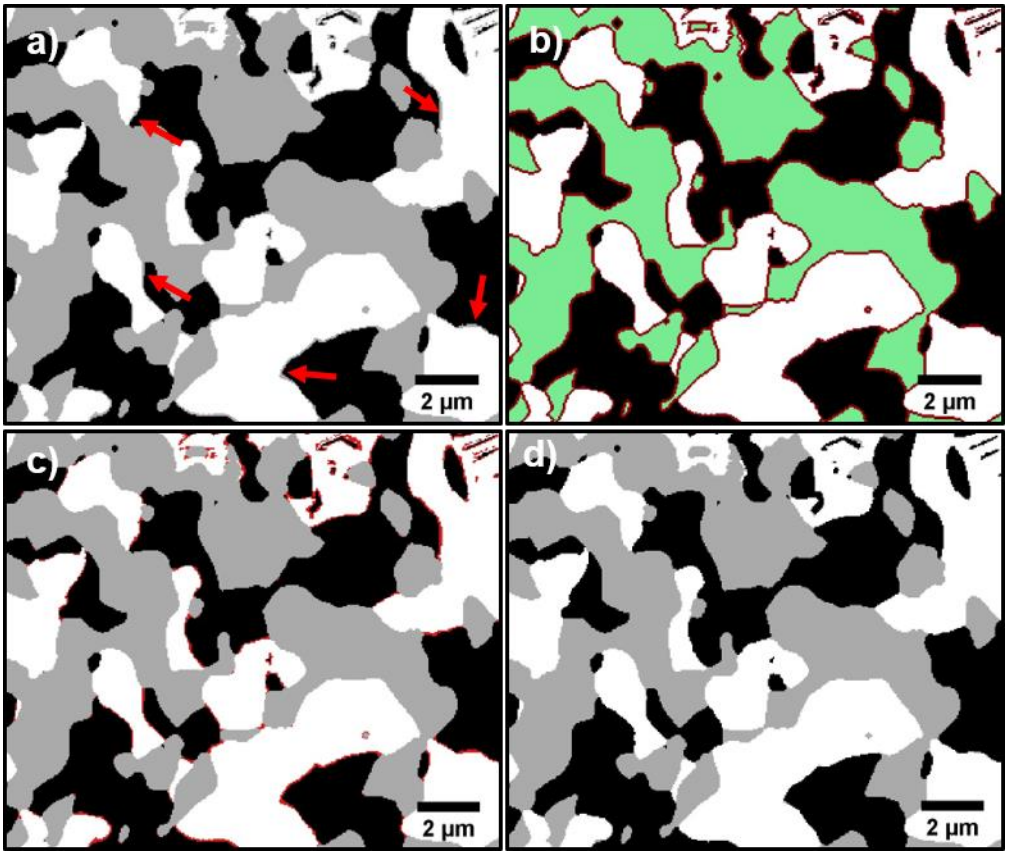

Figure 60: XY-orthoslices showing erosion-dilation method to eradicate false voxel allocations at Ni-pore interface, a) false YSZ allocation (see red arrows); b) shrinkage gives new (green) and old (red) YSZ domains; c) regrowth (2 pixel-dilation) leaves false voxels unallocated; d) reallocation to nickel gives corrected segmentation

Second, a small percentage of unfilled pores led to “bubble-like” artefacts whose outlines gave aberrantly high grayscale values but should nonetheless have been allocated to the pore phase. This issue was overcome by manual tweaking which required no more than 2 h of user input per sample. Third, the secondary electron coefficient is a function of the crystallographic orientation of the grain from which it exits and thus a certain amount of “channelling contrast” [303] was apparent, particularly in

the brightest nickel phase, at times making it difficult to distinguish the darker Ni grains from the YSZ backbone. Decisions were made, based on morphology and adjacent grain location to overcome this issue, however, it remains unclear, without direct slice-by-slice EDX data [126], if the segmentations are in *all* cases appropriate.

4.2.4 Data Analysis

4.2.4.1 Metrics

Volume/phase fractions (V_i), volume-specific surface/interfacial areas (VSSA/VSIAs) and total and active triple-phase boundaries (TPBs) were extracted from the 3D datasets. Flux-based tortuosity factor simulations were run on each of the three phases in each direction.

4.2.4.2 Representative Volume Element (RVE) Analysis

Since these SOFC electrode materials were made by traditional slurry-based methods, they likely contained inherent heterogeneity. It was therefore vital to assess the validity of sub-volumes used for analysis for whether they were representative of the global properties of the electrode microstructure. TauFactor software was used to apply a cubic volume expansion method to identify the RVE for both tortuosity factor and porosity (see **Section 3.4.2.3**). This approach involved taking incrementally larger cubic volumes from the dataset, starting from one with dimensions of 10% of the total volume and working in increments of 10% until the full volume was considered. The results are displayed graphically and the RVE is found when deviations are found to remain under a specified threshold. The effect of the variation of this tolerance level is discussed in **Section 4.3**.

4.3 Results & Discussion

4.3.1 Virgin sample

SEM-EDX analysis confirmed the presence of three phases, Ni, YSZ and an epoxy-filled porous region, here shown as black (Figure 61).

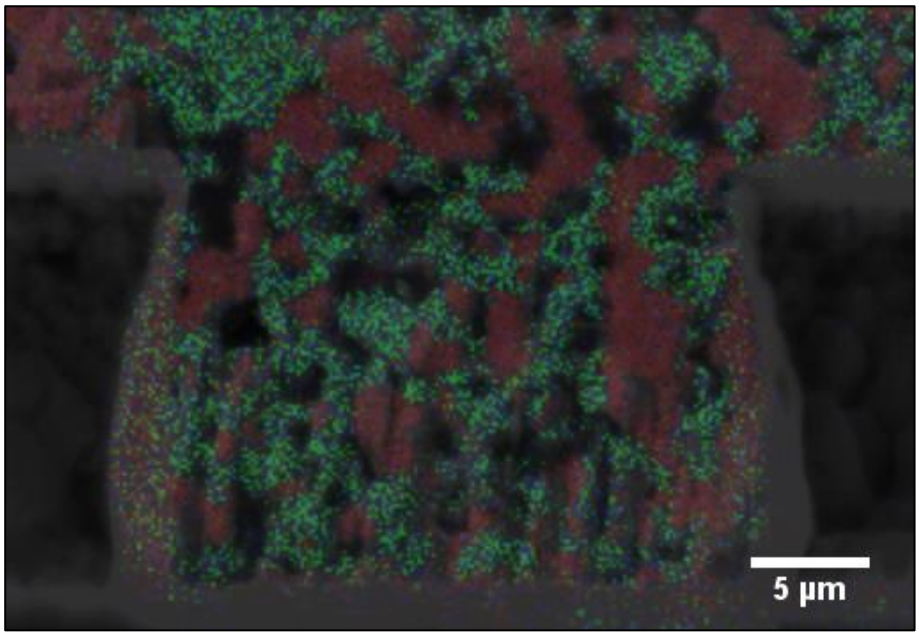

Figure 61: SEM-EDX micrograph of the virgin *sample, illustrating the distribution of the different phases: Ni in red, and Zr (green) & Y (blue) coincident*

The phases were clearly defined and showed that the solids were well-mixed and had feature sizes consistent with the SEM slices collected during the FIB-SEM slice-and-view tomography of the *virgin* sample.

4.3.1.1 Basic Metrics

Slice-and-view was performed on the *virgin* sample, yielding 139 slices in total, 98 consecutive slices of which were used to reconstruct a 3D representation of the virgin microstructure. The remaining 41 slices were excluded from analysis due to either redeposited material; obscuring the face of interest or shadowing effects that would make subsequent segmentation too difficult. The total volume analysed comprised 329 × 277 × 98 voxels, representing almost 300 µm^3. An example XY-orthoslice from the raw data, along with its corresponding processed slice (non-local means filter applied) and a segmented version are shown in Figure 62.

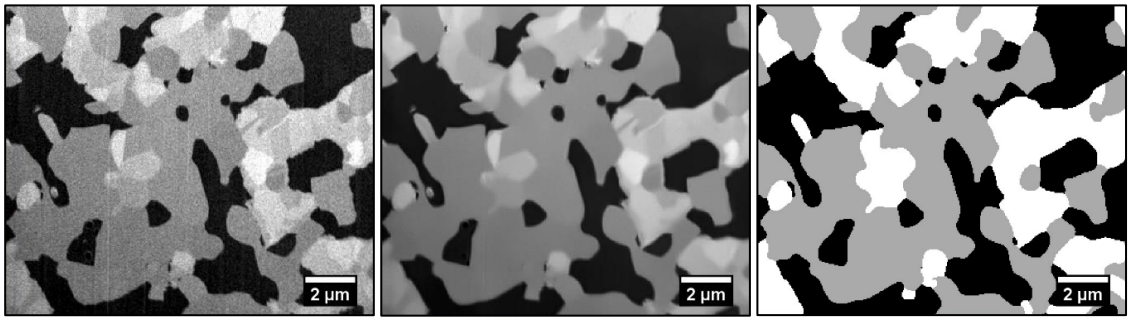

Figure 62: XY-orthoslice of a) raw; b) filtered; and c) segmented virgin microstructure (black = epoxy/pore; grey = YSZ; white = nickel)

The ternary segmentation, accounting for boundary misallocations, unfilled pores and channelling contrast due to the presence of multiple grain orientations, yielded the basic metrics given in Table 1.

Phase	Pore	Nickel	YSZ
Volume Fraction (%)	30.5	28.3	41.2
VSSA (μm^{-1})	0.8	0.6	0.9
VSIA (μm^{-1}) [P:N, N:Y, Y:P]	0.3	0.4	0.5
Total TPB Density (μm^{-2})	2.9		
Active TPB Density (μm^{-2})	2.4		
% Active TPB	81.1%		
Tortuosity Factor:			
X	8.5	23.5	3.5
Y	9.2	10.3	3.3
Z	2.3	2.0	1.7
Percolation (%)	98.4	75.8	99.6

Table 1: Basic metrics from ternary segmentation of virgin *ASL reconstruction*

The volume fractions deviated significantly from the manufacturer's specifications (33 % each), with YSZ representing the most abundant phase. This deviation may suggest that the volume investigated is not representative of the entire ASL. Although this is a *virgin* sample, the VSSA is lowest for nickel. However, the lowest VSIA is for the interface between pore and nickel, consistent with appreciable wetting of the ceramic surface. Combined with the visualisation of the microstructure, and the fact that YSZ is most abundant, the initially low surface area of nickel suggests the ceramic phase acts as the backbone with nickel particles residing on its surface. The low VSIA between pore and nickel suggests that although the metal is non-wetting on 8YSZ (117 ° at 1500 °C [101]), there is significant contact between the two solids before ageing. The total and active (appropriately percolated) TPB densities measured are of the same order of magnitude as many studies in the literature [132][130][133] for similar microstructures, and the proportion of active TPB is ~81%, a figure one might expect from a virgin microstructure [279]. 3D volume renderings of each of the three phases of the virgin sample are shown in Figure 63 for visualisation.

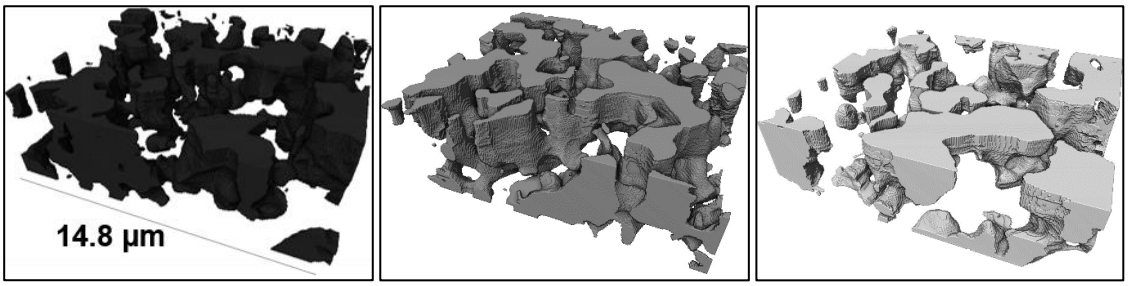

Figure 63: 3D volume renderings of virgin *a) pore; b) YSZ; and c) nickel microstructures*

The tortuosity factors extracted suggest some anisotropy; the Z-direction value is significantly lower than the X- and Y- values (which are self-similar) for all three phases. However, this is likely an artefact of the short Z-dimension (slice direction); in this direction, the cross-sectional area is larger than for the other two, and thus there is more likelihood of a more direct path between the front and back face, which are themselves closer together than in the other directions. This discrepancy indicates the importance of having large volumes, or if larger volumes are not accessible, at least approaching a more cubic volume.

4.3.1.2 Representative Volume Element (RVE) Analysis

RVE analysis was performed using an expanding volume window to investigate the deviation of porosity and tortuosity factor with sampled volume. The results of this analysis are shown in Figure 64.

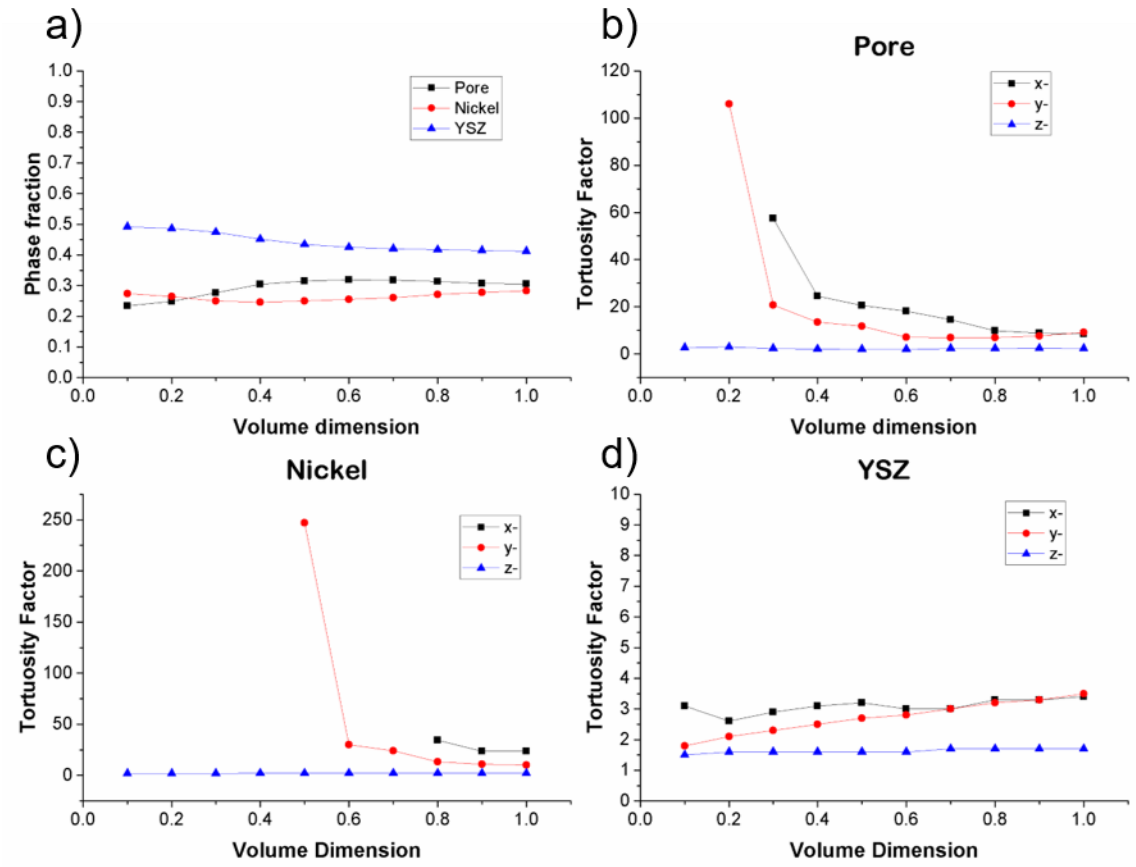

Figure 64: RVE Analysis of segmented virgin sample for phase fraction (a), and tortuosity factor (b-d)

With a ± 2% tolerance and using phase fraction as the metric of choice (Figure 64 a)) the analysis indicates that approximately 70% (volume dimension of 0.7) of the total sampled volume is sufficient to provide a representative figure for YSZ, but 90% is required for both pore and nickel, in line with the order of their absolute phase fraction values. However, previous work has shown that simply using the phase fraction as the metric of investigation for RVE analysis is often not sufficient [285]. Inspecting tortuosity factor instead, across all phases, the Z-direction deviation is far less than for the X- and Y-directions, beginning to plateau at x = 0.7. However, this is likely to be an artefact of the shorter Z-dimension, such that the 10% increments implicit in the RVE approach correspond to much minor changes in microstructure. In the pore phase, a representative volume is not reached in the X- and Y- directions. For nickel, the X-direction values converge sufficiently at x = 0.9, but the deviation is still too large at all volumes in the Y-direction. Finally, for the YSZ phase, neither the X- or Y- phases display an RVE at ± 2% tolerance. It is also worth noting that the nickel phase is non-percolating until 0.8

and 0.5 in the X- and Y-directions but does percolate in the entire volume range in the Z-direction; its anisotropy in connectivity adding weight to the value of a cubic volume.

4.3.2 Aged sample

4.3.2.1 Basic Metrics

Slice-and-view was performed on the *aged* sample, yielding 88 slices, of which 60 consecutive slices were used to reconstruct a 3D representation of the aged microstructure, due to the same issues encountered for the virgin sample. The total volume analysed comprised 99 × 134 × 60 voxels, representing almost 75 μm^3. An example XY-orthoslice from the raw data, along with two corresponding processed slices and a segmented version are shown in Figure 65.

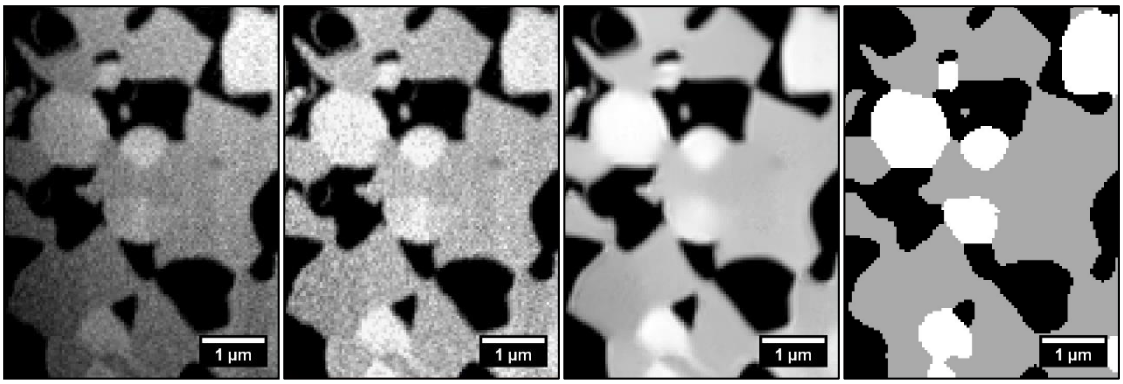

Figure 65: XY-orthoslice of a) raw, b) shading correction, c) filtered and d) segmented aged microstructure, (black = epoxy/pore; grey = YSZ; white = nickel)

The volume examined is smaller than for the *virgin* sample due to multiple complications, both with re-deposition of milled material and “walling” effects, whereby sample drift was sufficiently large that sequential slicing steps did not overlap and effectively gave rise to “walls” of material obscuring the face of interest. As a result, the useful volume reconstructed was approximately a quarter of that for the virgin microstructure, which is likely to further impact on representativeness. Qualitatively, however, the microstructure is notably different, with much more spherical nickel particles, whose circularity is clear from Figure 66.

In this case, the processing required an extra step; a shading correction to account for the gradient in grayscale (Figure 65 a)). After this ternary segmentation, accounting for boundary misallocations and unfilled pores (little channelling contrast was evident), the basic metrics given in Table 2 were extracted.

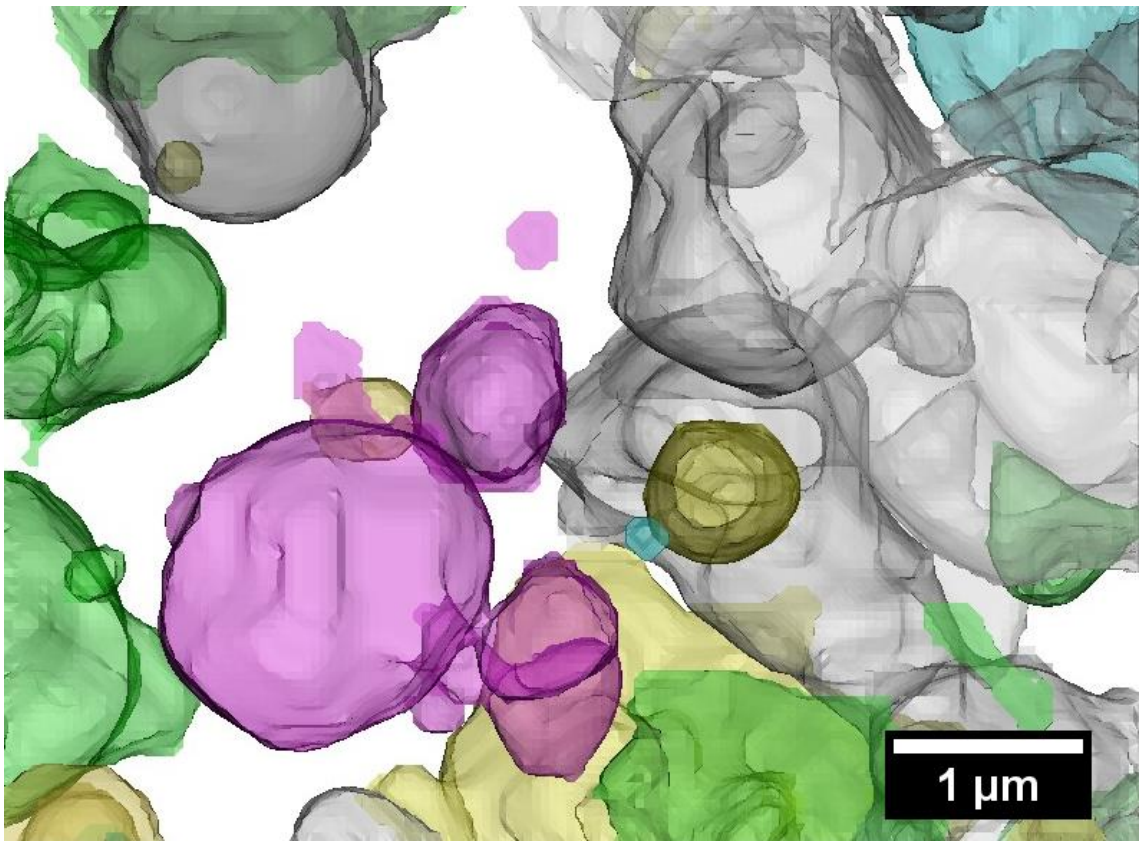

Figure 66: Volume rendering displaying the spheroidal nickel "particles"

Phase	Pore	Nickel	YSZ
Volume Fraction (%)	33.5	23.2	43.3
VSSA (μm^{-1})	1.8	1.1	1.9
VSIA (μm^{-1}) [P:N, N:Y, Y:P]	0.5	0.6	1.4
Total TPB Density (μm^{-2})	6.1		
Active TPB Density (μm^{-2})	2.5		
% Active TPB	41.6%		
Tortuosity Factor:			
X	2.9	∞	2.2
Y	3.1	∞	2.1
Z	4.4	∞	2.5
Percolation (%)	99.7	0.0	99.9

Table 2: Basic metrics extracted from ternary segmentation of aged ASL reconstruction

Again, the volume fractions deviated substantially from the 1: 1: 1 ratio specified by the manufacturer, which is thought to be due to representativeness issues. The VSSA of nickel is lowest, significantly lower than those for the pore and YSZ phases, which are the same within statistical error. This is consistent with nickel coarsening and correlates well with the visualisation of highly spherical nickel particles. Even though the VSIA for the pore-nickel interface is still lowest, there is little difference between it and the VSIA for nickel-YSZ interface; most noticeably, the VSIA for the pore-YSZ interface is significantly higher than the other two, consistent with de-wetting of nickel, coarsening

and therefore greatly increased exposure of the ceramic backbone to the pore space. The total and active TPB densities measured are of the same order of magnitude as many studies in the literature [132][130][133] for similar microstructures. The value for the total TPB density is higher than in the case of the *virgin* microstructure – but this is thought to be due to the small volume investigated artificially inflating the density. This supposition is supported by the fact that only ~42% of the total TPB is shown to be "active", which is much lower than the value for the *virgin* microstructure. Moreover, this proportional loss of active TPB density is in line with previous reductions, e.g. in the medium coarseness anode of work by Pecho *et al*. [279]. 3D volume renderings of each of the phases of the aged sample are shown in Figure 67.

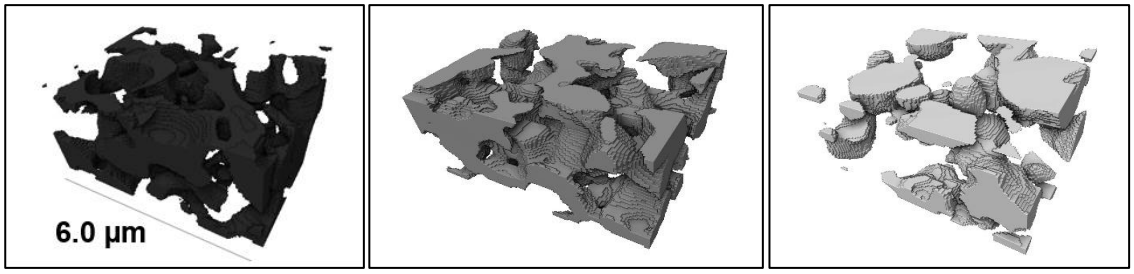

Figure 67: 3D volume renderings of aged *a) pore; b) YSZ; and c) nickel microstructures*

4.3.2.2 Representative Volume Element (RVE) Analysis

RVE analysis was performed using an expanding volume window to investigate the deviation of porosity and tortuosity factor with sampled volume. The results of this analysis are shown in Figure 68. Note that, due to a lack of percolation at all investigated sub-volume sizes, there are no available datapoints for the nickel phase (Figure 68 c)).

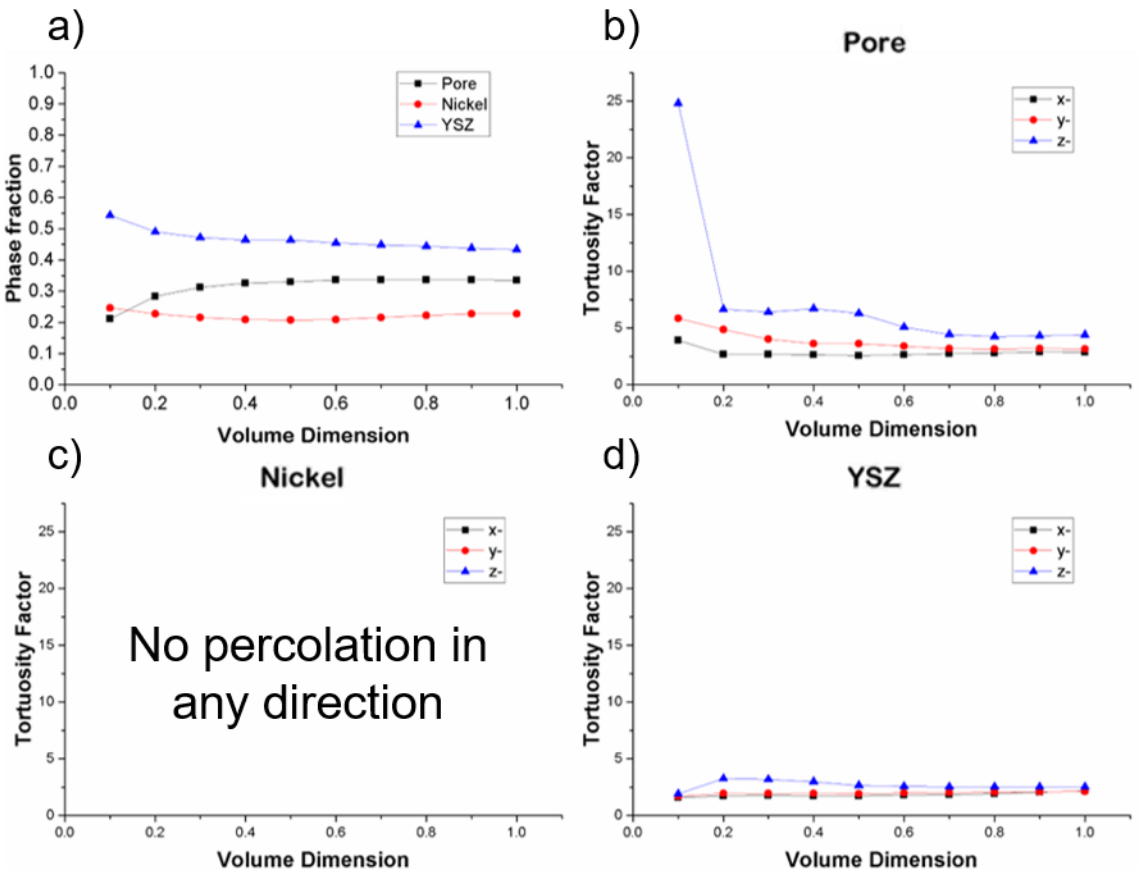

Figure 68: RVE Analysis of segmented aged sample for phase fraction (a), and tortuosity factor (b-d)

With a ± 2% tolerance and using phase fraction as the metric of choice (Figure 68 a)), the analysis indicates that approximately 90% (volume dimension of 0.9) of the total sampled volume is sufficient to provide a representative figure for Ni and YSZ, but only 50% is required for the pore phase, suggesting that differing levels of microstructural evolution for each phase may have an impact on the necessary size required for as a representative volume. Looking at tortuosity factor for the pore phase, an RVE is achieved at x = 0.9, 0.6 and 0.9 for X-, Y- and Z-directions, respectively. Nickel is found not to percolate across the entire volume range – a further indication of the disconnection brought about in the nickel network through nickel agglomeration, and consistent with previous work [81]. In the YSZ phase, an RVE is not achieved in the X-direction but is found to be at x = 0.9 and x = 0.6 in the Y- and Z-directions, respectively. The fact that the most abundant and percolating phase (YSZ) does not reach an RVE in one of the directions is likely to be due to the significantly shortened X-dimension for the analysed volume, as opposed to a significant change in the ceramic microstructure.

As tortuosity factor is more sensitive to volume, it is worth inspecting the RVE analysis under a relaxed criterion of 4% tolerance, the results of which are shown in Table 3.

			RVE	
Phase	**Direction**	**Sample**	**2% Tolerance**	**4% tolerance**
Pore	***X-***	*Virgin*	-	0.9
		Aged	0.9	0.8
	Y-	*Virgin*	-	-
		Aged	0.7	0.7
	Z-	*Virgin*	-	-
		Aged	0.9	0.7
Nickel	***X-***	*Virgin*	0.9	0.9
		Aged	-	-
	Y-	*Virgin*	-	-
		Aged	-	-
	Z-	*Virgin*	0.7	0.7
		Aged	-	-
YSZ	***X-***	*Virgin*	-	0.8
		Aged	-	-
	Y-	*Virgin*	-	-
		Aged	0.9	0.8
	Z-	*Virgin*	0.7	0.7
		Aged	0.6	0.6

Table 3: Tortuosity Factor RVE Analysis for both samples, with 2 and 4% tolerances

It is clear that relaxing the tolerance does not have a profound effect on the extracted RVE from each sample, phase and direction; only in two out of the ten cases where an RVE is not reliably identified at 2% tolerance, does the relaxation lead to a definable RVE (*Virgin*, pore, X-direction and *Virgin*, YSZ, X-direction). Equally, there are only three cases out of eight wherein the RVE lowers in value (and mostly by only 10%).

4.3.3 Comparisons between virgin *and* aged *samples*

4.3.3.1 Basic Metrics

There is satisfactory qualitative evidence for microstructural evolution, including the obvious visual changes. With regards to the changes in phase fraction, the most notable change is the loss of Ni (-17.0%, Table 4). Although humid H_2 has been shown sometimes to lead to a loss of Ni [304][115], it is difficult to tell if this is the case here due to the small volume of the aged microstructure investigated (its heterogeneity is likely not fully averaged out). On the other hand, the RVE analysis performed indicates that the phase fraction values level out below a 2% tolerance in all cases, for both virgin and aged microstructures, supporting the hypothesis that nickel has been lost. As YSZ has

been surmised to be immobile at typical SOFC operating temperatures (700 – 1000 °C), it is also interesting to note that the smallest change in volume fraction is for YSZ.

	Virgin	Aged	Change
Volume Fraction (%):			
Pore	30.5	33.5	+9.8%
Nickel	28.3	23.5	-17.0%
YSZ	41.2	43.3	+5.1%
VSSA (μm^{-1})			
Pore	0.8	1.8	+139.0%
Nickel	0.6	1.1	+69.8%
YSZ	0.9	1.9	+119.8%
VSIA (μm^{-1})			
Pore-Nickel	0.3	0.5	+92.9%
Nickel-YSZ	0.4	0.6	+69.4%
YSZ-Pore	0.5	1.4	+172.5%
Total TPB Density (μm^{-2})	2.9	6.1	+108.2%
Active TPB Density (μm^{-2})	2.4	2.5	+5.5%
% Active TPB	81.1	41.6	-48.1%
Pore Tortuosity Factor:			
X	8.5	2.9	-65.9%
Y	9.2	3.1	-66.3%
Z	2.3	4.4	+91.3%
Nickel Tortuosity Factor:			
X	23.5	∞	-
Y	10.3	∞	-
Z	2.0	∞	-
YSZ Tortuosity Factor:			
X	3.5	2.2	-37.1%
Y	3.3	2.1	-36.4%
Z	1.7	2.5	+47.1%
Percolation			
Pore	98.4%	99.7%	+1.4%
Nickel	75.8%	0%	-100.0%
YSZ	99.6%	99.9%	+0.3%

Table 4: Basic metrics comparison of ternary segmentations of virgin *and* aged *ASL*

However, contrary to the what might be expected from a coarsening of materials at high temperatures, all three phases appear to increase in VSSA. This is likely due to an artefact of the small volume investigated, as surface areas are particularly sensitive to the volume investigated. It is interesting to note that the increase in VSSA for the nickel phase is by far the lowest of the three phases. If the positive changes are assumed to be due to the small volume factor, and YSZ is thought to be broadly immobile and unchanging, the smaller increase in nickel VSSA may be indicative of a true surface area decrease. However, without further investigation at a larger sampled volume, this is only speculative (see **Section 4.4**) and cannot be taken as conclusive.

On comparing the VSIA values, despite all showing increases, the relative trend correlates well with the coarsening mechanism. The greatest increase is for the YSZ-pore interface, and the least is for the nickel-YSZ interface, coherent with a de-wetting of the metal from the ceramic, revealing more YSZ to porosity.

The TPB case is similar; the total TPB density increases markedly (by over 100%), which is likely an artefact of the small investigated volume. However, the active TPB density only increases marginally (+5.5%), and as such, may be representative of an actual decrease, masked by the small volume effect. More reliable evidence comes in the form of the %Active TPB (active TPB density / total TPB density), which is independent of volume. The %Active TPB drops from ~81% in the virgin microstructure to ~42% in the aged microstructure, a drop of almost half. This demonstrates the connection between microstructural change (nickel coarsening) and a property closely linked to electrochemical performance (active TPB density). This severe loss of active TPB would have deleterious effects on the electrochemical performance of the fuel cell, severely limiting reaction sites and causing a notable increase in anodic activation polarisation.

The starkest change, in terms of transport properties (tortuosity factor/percolation), is that the nickel phase changes from being percolating (75.8%) and having measurable tortuosity factors (albeit high values), to there being no percolation and thus infinite tortuosity factors in all directions. This change illustrates the sort of microstructural evolution that breaks down the electronically conductive network and leads to a loss in conductivity and an increase in ohmic polarisation during operation at high temperatures [81]. Although not quantitatively reliable, there are some qualitative changes apparent from the extracted metrics for tortuosity factor. Firstly, there may be an anisotropic evolution occurring during the annealing process. The changes in the X- and Y- directions are approximately the same whereas the change in the Z-direction, in both cases, is opposite in sign and greater in magnitude. This may be interpreted as a result of the way the annealing was conducted, the way in which evolution occurs with respect to gravity, or perhaps as a result of an anisotropic aspect of manufacture. This

could also be linked to the sampled volume dimensions; however, more investigation would be required to unpick the true nature of this anisotropy.

4.3.3.2 Representative Volume Element (RVE) Analysis

On average, it appears that the volumes inspected are likely large enough to be representative for phase fraction, but not for tortuosity factor. This is indicative of the requirement, for reliable analysis, to be metric- and direction-specific when defining a representative volume. Clearly changes can be observed in the microstructures, but the absolute values of the tortuosity factors extracted should be viewed with caution. Even without applying the same volume expansion method to the volume-specific surface and interfacial areas, nor the TPB densities, it is clear that the volumes are too small to extract reliable absolute values and should instead be illustrative of general relative trends.

4.4 Conclusions

The work in this chapter has shown that FIB-SEM slice-and-view tomography can be used to obtain segmentable data for SOFC anodes, distinguishing the three phases (Ni, YSZ and pores). At low acceleration voltage, the solid-phase contrast was shown to be high, and the accessible resolution *via* electron imaging provided high-level microstructural detail. By investigating a sample as-reduced and one that had undergone several hundreds of hours of high-temperature, humid annealing, a clear evolution in microstructure could be visualised. Clearly, the nickel phase becomes more spherical, as is expected due to coarsening driven by surface energy minimisation.

However, some limitations to this technique have been highlighted by this work. Firstly, the nickel phase displayed some internal contrast thought to be due to a channelling effect. Although this may be useful for investigations probing crystallographic orientation, it can present difficulties when performing reliable segmentation of material phases. Secondly, the volumes that were accessed by this approach appear to be too small to capture representative microstructural properties, as evidenced by RVE analysis. Due to the small volumes, the metrics analysis suffers poor reliability, and inferences had to be made based on the nature of the unrepresentativeness. For example, although the absolute values for the Total and Active TPB densities increased

after ageing, this was attributed to the small volume effect, and more attention was directed towards the fact that the proportion of active TPB significantly drops (81% to 42%), possibly representing approximately a doubling in the activation polarisation associated with the HOR at the TPB (if the relationship were linear).

Finally, even if larger volumes were gathered by overcoming re-deposition and walling issues, the nature of this technique is inherently destructive. As a result, it is impossible to escape differences between the *virgin* sample and the sample which served as the starting microstructure for the *aged* sample. This adds another degree of error, compounding this microstructural variation with acquisition, processing and analysis errors, and thus indicates that an analogous *non-destructive* technique could provide a more reliable monitoring system for Ni-YSZ anode microstructural evolution.

Chapter 5: Laser-preparation for X-ray nano-computed tomography

The majority of this chapter has been peer-reviewed and published in the Journal of Microscopy: Bailey, J.J., Heenan, T.M.M., Finegan, D.P., Lu, X., Daemi, S.R., Iacoviello, F., Backeberg, N.R., Taiwo, O.O., Brett, D.J.L., Atkinson, A., Shearing, P.R., Laser-preparation of geometrically optimised samples for X-ray nano-CT, Journal of microscopy 267 (3), 384-396, https://doi.org/10.1111/jmi.12577 (2017) [305].

This chapter explains the development of a laser-preparation technique that can be used to fabricate geometrically optimised samples to fit the FOV of a lab-based X-ray nano-CT instrument. The first sections discuss the samples that are investigated in this work, covering the rationale behind the selection of certain pillar diameters based on attenuation coefficients, transmission and signal-to-noise considerations. Next, an outline of the micro-machining techniques and procedures is given, followed by details of the investigated parametric array in terms of pillar diameter, exposure time, projection number and binning.

The results section presents a series of tomographs, the extraction of key metrics including surface areas, TPB densities and directional tortuosity factors, as well as RVE analysis used to assess the reliability of the deduced properties. Comparisons are drawn across sub-samples and with regards to the implementation of a common filter, to assess the level of error involved in this type of metrics analysis.

5.1 Samples

Two principal samples were used in this portion of work. Firstly, the same Ni-YSZ electrodes (*Sample 1*) that were used for the FIB-SEM tomography and characterisation work (see **Section 4.1**) were used in preliminary studies and secondly, a single large planar anode-supported half-cell, composed of nickel oxide, 8YSZ and porosity acted as a starting material for further sample provision (*Sample 2*). This second anode comprised an approximately 600-µm-thick ASL and an approximately 10-µm-thick AFL, both constituting a mixture of NiO and 8YSZ, attached to a dense ~7-µm-thick 8YSZ electrolyte, determined by SEM analysis (Figure 69). This half-cell did not contain any

cathode layers. Both samples were provided by Forschungszentrum Jülich (Jülich, Germany).

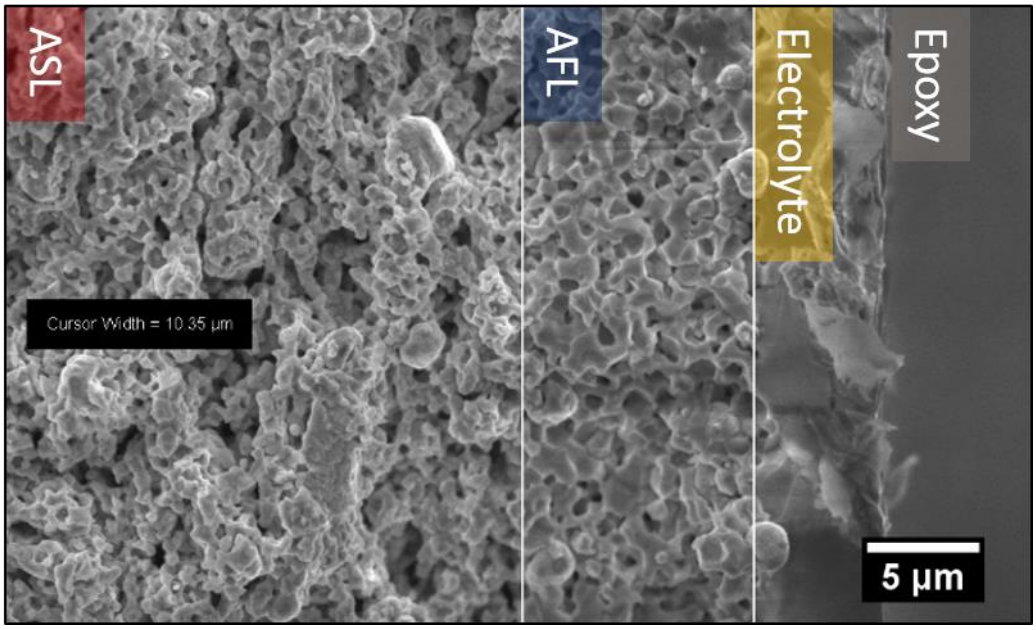

Figure 69: SEM Micrograph of anode cross-section – AFL thickness is indicated

For the first of the two samples, no reduction or cutting was required as the electrode was provided as a small (12 x 12 mm) porous composite of nickel and 8YSZ. To fabricate multiple sub-samples for various treatments from the second sample, both a sectioning and a reduction step were required before approaching the more intricate sample preparation. The large (36 x 36 mm) NiO/8YSZ half-cells were laser-cut into 9 smaller pieces (12 x 12 mm) at high power (1.2 W) using an A Series/Compact Laser Micromachining System (Oxford Lasers, Oxford, UK) with an embedded Class 4, 532-nm-wavelength laser. Subsequently, these pieces were reduced, in batches of 4-5 in an alumina crucible, in a tube furnace, under 300 ml/min flow of 4% H_2/balance N_2 at 800 °C for 4 h.

5.2 X-ray nano-computed tomography (X-ray nano-CT)

A common system used in high-resolution X-ray tomography utilises wavelength-selective Fresnel zone-plates (FZP) (see **Section 3.2.5.5**). These X-ray optics may be combined with either high-brightness, highly collimated X-ray radiation produced at third-generation synchrotrons, or with a cone-beam lab-source as long as it is coupled with a capillary condenser lens, giving a focused quasi-monochromatic beam. This latter set-up is found inside the Zeiss Xradia 810 Ultra (Carl Zeiss X-ray Microscopy,

Pleasanton, USA), the lab-based instrument used in this work, which produces X-rays with a characteristic peak at 5.4 keV (Cr anode), as described in **Chapter 3**. High-flux synchrotron sources are not readily accessible and come with time constraints, and thus a sample preparation technique, although still amenable to synchrotron radiation, was sought to produce samples amenable to lower flux lab-based sources.

Each of the nano-CT set-ups (lab-based and at synchrotrons) has a limited FOV, when operating with a specific optical component, which is often no more than tens or hundreds of micrometres in dimension when achieving nanometre-level spatial resolution. Particularly with highly attenuating materials, sample sizes that exceed the FOV dimensions often lead to severe imaging artefacts due to undersampling [306]. With the lab-based instrument used in this thesis, the FOV was either 16 or 65 µm, in HRES or LFOV mode, respectively (see Table 5). Although the former would give rise to a smaller voxel dimension and improved spatial resolution, the focusing efficiency is lower with respect to LFOV mode and thus the flux is considerably lower (<10×). As will be seen later in this chapter, flux (and hence signal-to-noise ratio), is crucial in establishing adequate contrast. Hence, there was a general need for samples to have dimensions on the order of 50 - 100 µm. This was not only to be appropriately X-ray transmissive such that adequate image data quality could be captured in the LFOV mode of the lab-based instrument, during a tomography lasting a reasonable length of time, but also to minimise artefacts intrinsic to region-of-interest (ROI) imaging.

X-ray source	Imaging Mode	FOV	Voxel Dimension	Relative Flux
Laboratory	HRES	16 x 16 µm	16 nm	Low
Laboratory	LFOV	65 x 65 µm	63 nm	Medium
Synchrotron	*Chapter 7**	400 x 300 µm	162.5 nm	Very High

*Table 5: Table of the relative merits of lab-based imaging modes & synchrotron set-up used in Chapter 7 (*higher resolution is possible)*

5.2.1 Sample Requirements

By fabricating samples on the micrometer scale, practical scanning times and sufficiently high signal-to-noise ratios for reliable post-acquisition analysis was thought to be achievable, even on lab-based instruments, reducing concomitant imaging artefacts. The issue of repeatedly accessing appropriate sample sizes and shapes, for

use in lab-based X-ray nano-CT acquisition systems, has plagued the community for some time [307], demanding a reproducible and cost-effective solution for the further exploitation of X-ray nano-CT imaging. Hitherto, crude and irreproducible forms of sample preparation have been pursued, mainly involving the mechanical fixation of sectioned sample pieces to small substrates such as steel dowels or pins. Unfortunately, this procedure has lent itself to low throughput, as it is non-trivial to fabricate a sample with the appropriate size and shape (Figure 70 shows an example with lithium-ion battery cathode materials from [305]). Moreover, this route also leads to an underuse of the X-ray FOV, reducing the effectiveness of these instruments in high-throughput studies. Sample preparation by purely FIB-milling has also been widely used [133][160][308] but is a lengthy procedure due to the time involved in milling from a macroscopic sample, and may involve Pt welds which are mechanically unstable [185].

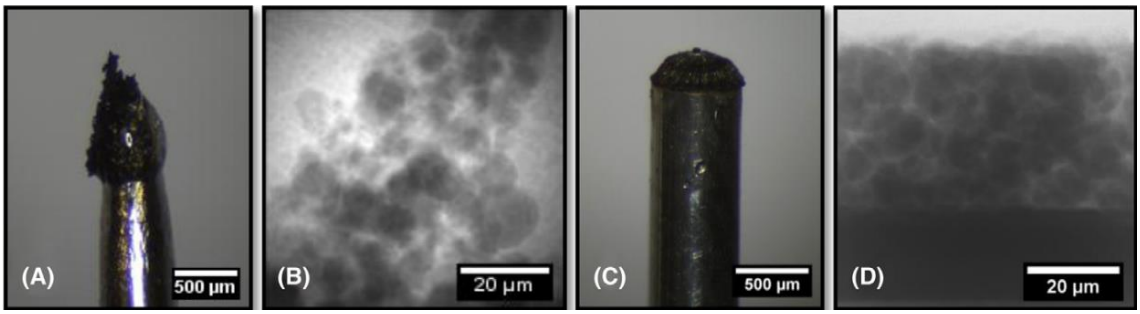

Figure 70: Example of FOV under-use via *mechanical preparation route (a,b) versus the laser preparation route (c,d), here for lithium-ion battery cathodes, reproduced from [305]*

Post-processing and segmentation of X-ray CT data inevitably introduces errors, however, their magnitude can often be reduced by improving the initial conditions associated with image acquisition. Good image quality derives from achieving the appropriate spatial resolution and an adequately high signal-to-noise ratio. The former is governed by selection of the appropriate imaging modality, with a corresponding voxel dimension that ensures the spatial resolution of the instrument appropriately matches the size of the sample features of interest. The latter is controlled by exposure time, projection number and by ensuring the sample fits the FOV. All these parameters are related and can be understood from the perspective of the “number of counts” per pixel of the detector over the full duration of the scan.

For a fixed exposure time and projection number, a smaller or less dense sample will lead to higher counts and higher signal-to-noise ratio, given all contributions to noise remain constant. Equally, for a fixed projection number and sample size and density, an increase in exposure time will increase the number of photons striking each detector pixel per unit time. Up to a point, by increasing the number of projections from a low number, keeping all else constant, the data quality may improve due to a greater number of counts per degree of rotation. In summary, if a suitable exposure time is chosen to avoid sample drift and impractical scan times, the only user-accessible adjustable parameters are size or density of the sample and the number of projections taken. The sample size and number of projections required for appropriately high quality data are interlinked, and given that the densities of the SOFC anode materials of interest were fixed, this rationale led to searching for the optimised sample thickness (with a concomitantly suitable number of projections) for gathering high-quality, segmentable data using a lab-based X-ray instrument.

It is worth clarifying that, as the FOV is fixed, any part of the sample outside of this area is not imaged, which can lead to further artefacts on reconstruction. Hence, control of sample size, particularly down to sizes smaller than the FOV, is essential. In some cases, this may be relaxed to slightly larger (for lowly attenuating materials) samples where oversampling projections can compensate for these artefacts [306]. However, the materials in SOFC anodes are highly attenuating metals and ceramics, and thus do require preparation that gives a sample with dimensions smaller than the FOV to obtain adequate transmission.

5.2.2 Attenuation Characteristics of SOFC anode materials

By consideration of the attenuating power of the individual phases within the composite material, the optimal thickness for pillars of SOFC anode materials can be evaluated. The degree to which a non-diverging monochromatic incident beam is attenuated is a form of the Beer-Lambert Law (see **Section 3.2.5.4**), giving Equations *5-1* and *5-2:*

$$I = I_0 exp[-\int(\frac{\mu(L)}{\rho}\rho)dL] \qquad 5\text{-}1$$

$$-ln|\frac{I}{I_0}| = \int(\frac{\mu(L)}{\rho}\rho)dL \qquad 5\text{-}2$$

where I *is the transmitted X-ray intensity,* I_0 *is the incident X-ray intensity,* μ/ρ *is the mass attenuation coefficient at a given energy,* ρ *is the mass density and* L *is the path length*

Equation *5-2* allows for the derivation of an "attenuation length", which is defined as the path length of material through which radiation permeates before reducing to 1/e of its original intensity. Attenuation length, *x*, can therefore be given by Equation *5-3*:

$$x = \frac{1}{\left(\frac{\mu(L)}{\rho}\right)\rho} \qquad 5\text{-}3$$

Thus, to enable readily accessible, high data quality collection, particularly with lab-based sources, very small samples are required. It is worth noting that at an X-ray energy of 5.4 keV (Cr anode source in the Zeiss Xradia 810 Ultra), the theoretical path length/pillar diameter for a typical SOFC anode sample consisting of 33% porosity must be smaller than or equal to ca. 30 μm to attain average transmission values above 5% and to provide sufficiently high signal-to-noise (for reliable segmentation) at practical exposure times (<100 s) [309]. This constraint relaxes with greater porosity and becomes more stringent with lower porosity, as shown in Figure 71, which displays the estimated transmission from pillars constituting various ratios of pore: nickel: 8YSZ.

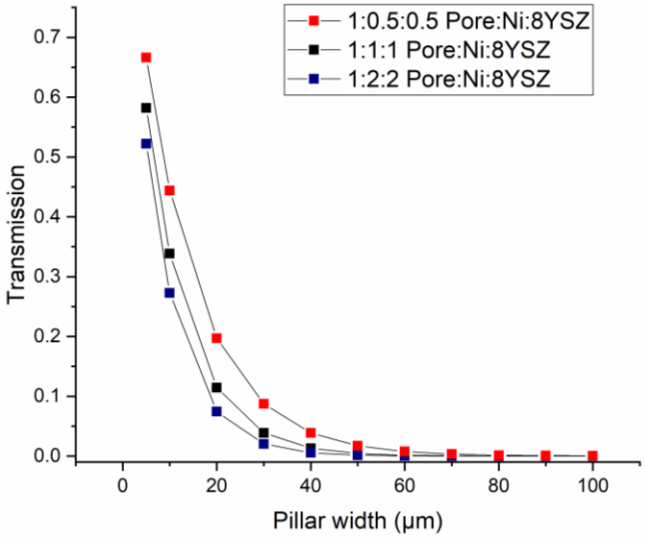

Figure 71: Plot of transmission (%) versus pillar width for ideal linear attenuation of 5.4 keV X-ray beam for various Pore: Ni: 8YSZ ratios

The following section summarises the development of a procedure to fabricate the optimal geometry samples by producing uniform cylinders and balancing the need for a representative volume with a small enough thickness to provide sufficient photon counts on the scintillator-detector given that exposure times are limited.

5.3 Preparation of X-ray nano-CT samples

5.3.1 Laser micro-machining

The A Series/Compact Laser Micromachining System (Oxford Lasers, Oxford, UK), with a 532-nm-wavelength diode laser, was used for all laser-preparation carried out in this thesis. The maximum pulse energy of the instrument is 1 mJ and the instrument normally operates at a power between 0.1 and 2.4 W with a beam pulse duration between 10 and 500 ns. Since this setup had been calibrated at 5000 Hz, all the work conducted in this project was carried out at this repetition frequency, thus giving the most reproducible spot energy, size and shape. In each preparation route, the laser power was adjusted accordingly.

Initially, work was carried out on *Sample 1*, with the aim of producing cylindrical pillars of sufficiently narrow width that Ni-YSZ solid phase contrast could be achieved on the lab-based X-ray nano-CT instrument. A key strategy to ensure the structural integrity of the resultant fine pillars was to produce a tiered geometry, thus reducing the potential stresses experienced at the base of the fine part of the pillar. This approach involved milling a coarse pillar approximately 1 mm in diameter from the planar sample, to produce the wide base of the final geometry. Two approaches were attempted with regards to sectioning this coarse disc from the original planar electrode (Figure 72); i) milling a large annulus about the central disc and removing the piece of interest by manipulation with sharp tweezers; ii) milling directly through the out-of-plane thickness of the electrode onto a sacrificial surface below.

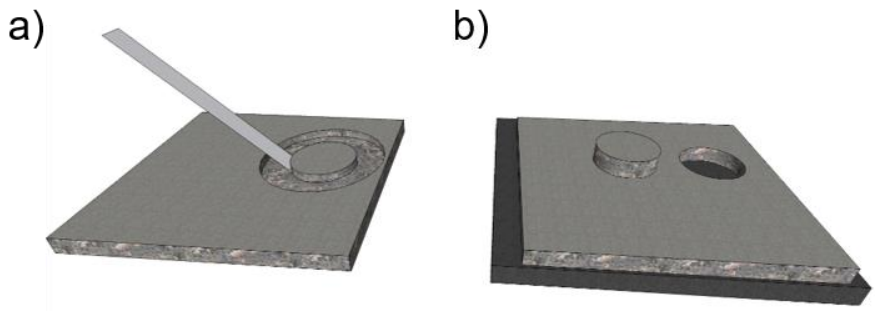

Figure 72: Schematic of the two options for sectioning a coarse circular disc from a planar anode: a) lever from milled annulus; b) mill straight through with sacrificial substrate

The first approach took less milling time, but the fragility of the small piece meant that its removal with tweezers often resulted in breakage of the sample. The second approach required more milling time and left more visual laser damage close to the cut edge. However, as this volume was to be removed later, and the duration of the laser-milling was not prohibitive, this second approach was adopted for all future preparation. Once removed, the coarse pillar was attached to an appropriate substrate: either to a stainless-steel dowel with fast-drying epoxy (Devcon, ITW, Illinois, USA) or to a macroscopic hollow alumina tube with Ceramabond 685-N cement (Aremco Products, New York, USA) if the sample was later to be subject to high-temperature heating.

The next step of the laser micro-machining procedure used the instrument's lateral chuck effectively as a lathe to laser-mill the coarse pillar down to smaller pillar widths, often about half the diameter of the original coarse pillar. The dowel had dimensions chosen to fit the chuck so, in the case of the Al_2O_3 tube, a dowel was epoxy-affixed inside the tube for this process and removed before any heat treatment. Subsequently, the rotary chuck mimicked the behaviour of a mechanical lathe by rotation and movement under a fixed laser beam, as configured in the instrument's software. In most cases, the sample end was 'faced-off' and a tiered structure was machined by first reducing the pillar diameter by approximately half, before machining a shorter section to the fine pillar diameter, as dictated by the sample in question. To better visualise the result of this procedure, an XZ-orthoslice and volume rendering of a tiered sample is provided in Figure 73, which was acquired using a Zeiss Xradia 520 Versa (Carl Zeiss

X-ray Microscopy, Pleasanton, USA), with a polychromatic beam whose average energy was tuned to 70 keV (NB. at this energy, Ni appears white).

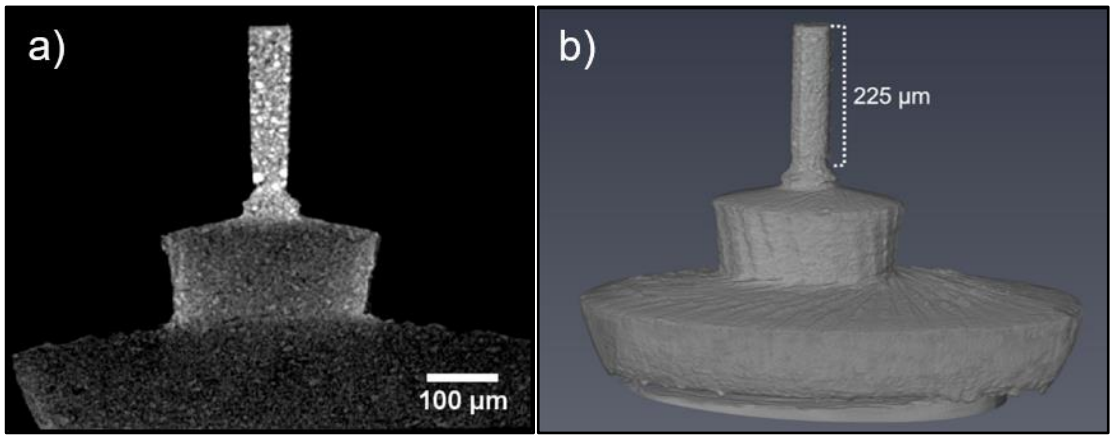

Figure 73: a) XZ-orthoslice from a tiered structure; b) 3D volume rendering of the same

This procedure is shown schematically in Figure 74, which was used to provide all the tiered structures to be placed in the X-ray instrument.

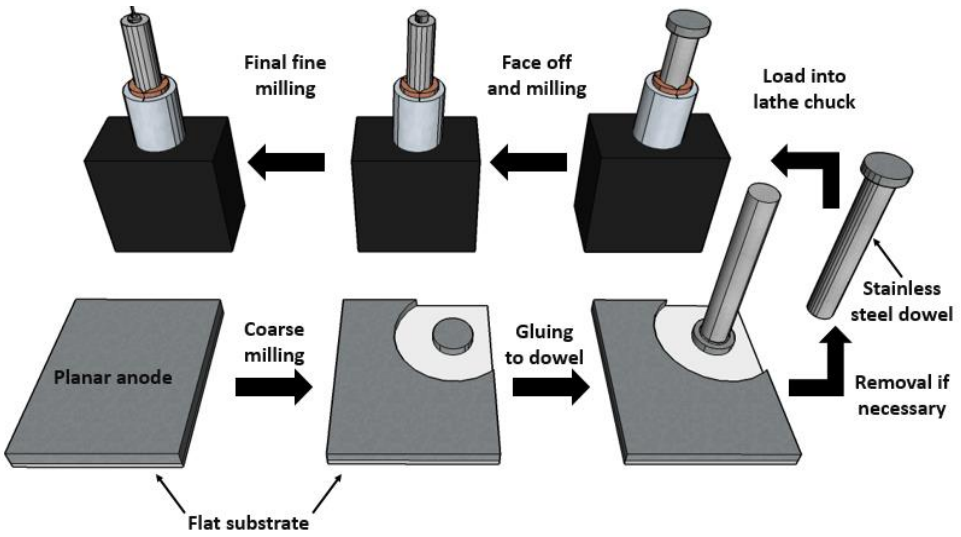

Figure 74: Workflow for laser micro-machining preparation of fine pillar from a planar electrode, following the original approach, reproduced from [305]

The minimum reliably attainable cylindrical pillar width from the A Series/Compact Laser Micromachining System was approximately 30 µm, due to its minimum spot size of 15 µm and the precision of its stage controllers. Consequently, to access pillar widths < 30 µm, an additional FIB milling step was followed. It is worth noting that on its own, FIB milling would take a prohibitively long time to administer sufficient milling from a macroscopically sized sample and it is only here, once the pillar is on the micrometre scale, that the focused-ion-milling process becomes short and facile for creating fine cylindrical pillars.

5.3.2 Focused-ion beam milling

When producing pillars with widths <30 µm, secondary FIB milling was carried out using the [FIB-SEM_UCL] at the LCN. Once the tiered structure had been produced and attached to a suitable substrate, the dowel or tube was affixed to a special SEM stub (angled at 36 ° to the horizontal) with sticky carbon tape before being Au-coated and placed under vacuum in the instrument. This allowed for facile alignment of the pillar with the FIB column, after which all machining was undertaken at a milling current of ~20 nA. Figure 77 displays the mounted stub, tiered laser structure and SEM micrographs of before and after FIB-milling.

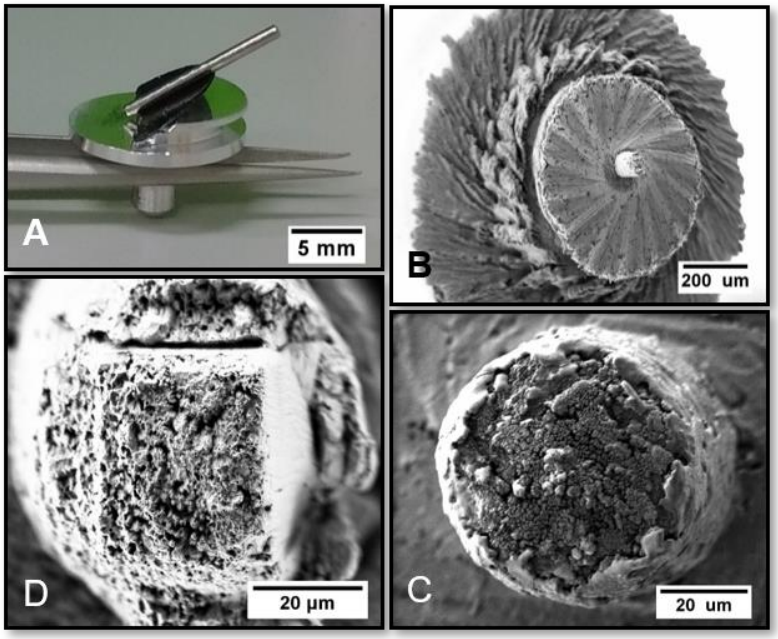

Figure 75: a) Photograph of Al stub with dowel attached, SEM micrographs of b) tiered structure at low magnification; c) pillar aligned before milling; d) example of pillar after FIB milling, reproduced from [305]

5.4 Sample Sizes

5.4.1 Preliminary Testing

Initial testing was performed on pillars that were laser micro-machined from the aged form of *Sample 1* (electrode only) to match the large FOV (65 µm). All the pillars in this section are labelled *P* for Preliminary; with a letter to denote sub-sample (*x* or *y*), and with a subscript to denote the relative projection number (*low*, *med*, or *high*).

Sample Px was milled to a diameter of 70 µm to minimise undersampling and inspect the degree to which oversampling may overcome artefacts due to the peripheral volume outside the FOV in this ROI scan. It was scanned with a medium (1401) and high

(2801) number of projections, as shown in Table 6. A slightly smaller pillar, *Sample Py*, was milled to 60 µm to fit entirely inside the FOV and scanned a total of three times, with a medium (1601) and low (901) number of projections. All these scans were conducted in LFOV mode and with a binning value of 2. The use of this binning effectively halves the spatial resolution by averaging the grayscale for every non-overlapping 2 × 2 pixel array on the detector but increases the signal-to-noise ratio by a factor of 4: a necessary requirement with thick, electron-dense samples. Additionally, another scan was conducted of *Sample Py* at low projection number but with binning 1, denoted $Py_{low,1}$.

Sample No.	Sample Type	Procedure	Pillar Width	Exp time	No. Proj	Bin	Mode
Px_{med}	Electrode only – aged	Laser only	70 µm	50 s	1401	2	LFOV
Px_{high}	Electrode only – aged	Laser only	70 µm	50 s	2801	2	LFOV
Py_{low}	Electrode only – aged	Laser only	60 µm	60 s	901	2	LFOV
Py_{med}	Electrode only – aged	Laser only	60 µm	60 s	1601	2	LFOV
$Py_{low,1}$	Electrode only – aged	Laser only	60 µm	120 s	901	1	LFOV

Table 6: Pillars and their corresponding XCT parameters from preliminary laser preparation

The first pillar (*Sample Px*) displayed obvious laser damage at the outer edges, particularly at the top of the fine pillar. It was for this reason that the other samples were 'faced-off' before fine milling was undertaken. The XZ-orthoslices shown in Figure 76 illustrate the nature of this laser-damaged region, measuring approximately 3-4 µm in thickness. The first observation from these scans was that the microstructural detail from the interior of the pillar was 'washed out', possibly due to the sheer thickness of the electron-dense pillar and/or the material outside the FOV during acquisition. However, the doubling of the projection number only very marginally improved this detail and so it may be that the thickness is the major contributing factor; signal-to-noise is not high enough to resolve these features (theoretical calculations predict a transmission of 1 - 2%). It is also clear that there is no contrast between metal and ceramic.

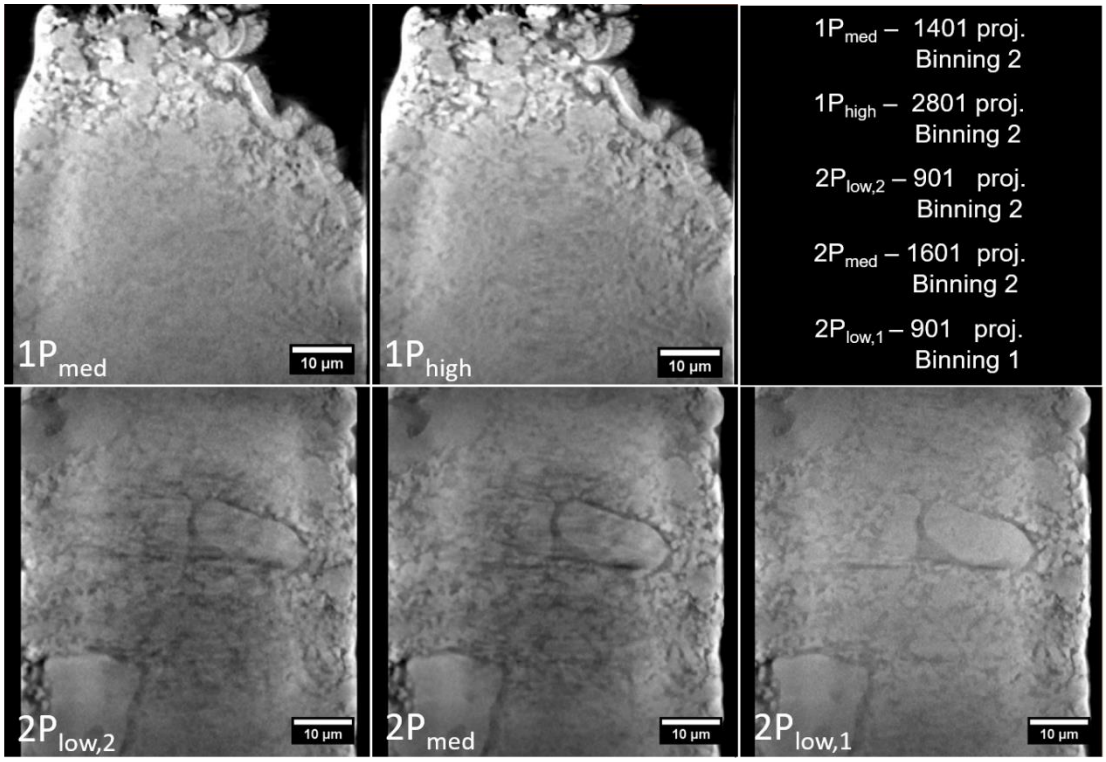

Figure 76: XZ-orthoslices from preliminary scans of relatively wide pillars

For the second pillar investigated (*Sample Py*), there is a noticeable improvement in the internal microstructure, by ensuring the sample is fully inside the FOV for the entire scan. However, there is a clear artefact in the central portion for both the 901- and 1601-projection scans. The latter is marginally less noisy, but the most significant change is seen on repeating the scan at Binning 1, with a doubling of the exposure time, where the central darkened region is absent. However, due to the 4-fold decrease in average pixel count on changing from Binning 2 to Binning 1, and a doubling in exposure time from 60 to 120 s, effectively the signal-to-noise ratio has dropped by half (longer exposure times are subject to temperature and stage drifts).

5.4.2 Comparison with mechanical methods

It is worth demonstrating the data quality and use of the FOV that is typical of manual/mechanical preparation. For this route, a small piece of the planar virgin sample was sectioned with a razor blade and by use of a light microscope, glued to the top of a stainless-steel pin. This approach was time-consuming and resulted in several erroneous scans. Eventually, a suitable sample was glued erect upon the pin and a digital photograph, radiograph and XZ-orthoslice from a tomogram taken can be seen in Figure 77.

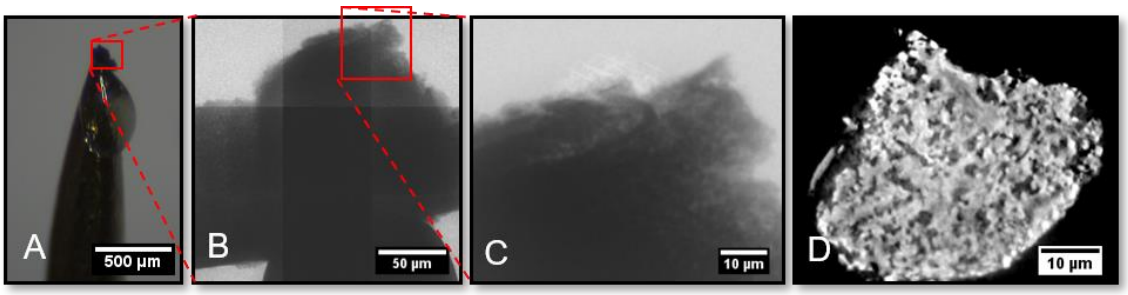

Figure 77: a) Digital photograph of mechanically mounted sample; b) Mosaic of radiographs showing scale; c) Single radiograph; d) XZ-orthoslice from tomogram

This image (Figure 77 d)) illustrates the non-uniform size and shape of a mechanically produced sample, which does not make the best use of the FOV. Moreover, variable contrast between phases results from differing path lengths as a function of the Y-dimension.

Given the theoretical approach to transmission and the experimental preliminary work, all samples henceforth were made to be smaller than the FOV (in the lateral direction) of the lower resolution mode of the X-ray nano-CT instrument (< 65 µm) and scanned in Binning 1 mode. The samples in the following sections are denoted using the number of the sample from which they were machined, either *1* or *2*, an upper-case letter denoting if the sample is virgin (*V*) or aged (*A*), a lower-case letter to denote the sub-sample (*a*,*b* or *c*), and a subscript "$_L$" for laser-prepared or "$_F$" for laser- and FIB-milled.

5.4.3 Sample 1

The first two sub-samples, *Sample 1Aa*$_L$ and *Sample 1Ab*$_L$**,** were machined by laser to 55 and 45 µm in diameter, respectively, maximising the potential for a representative volume element (RVE) to be analysed from them. These sub-samples came from the same aged planar sample that was investigated in **Chapter 4** and in the preliminary work and thus contained large nickel agglomerates (see Figure 65).

The next sub-sample, *Sample 1Va*$_L$, was also machined solely by laser, but to a smaller diameter (33 µm). In this case, the sample was taken from the virgin planar sample previously investigated and displayed a more homogeneous microstructure, which was thought to be more useful for future inspection of image quality as large features are often clear even in poor-quality images. The sample was subsequently FIB

milled to approximately 25 µm (giving a truncated-cone shape) and will hereafter be known as *Sample 1Va$_F$*.

Another sub-sample, *Sample 1Vb$_L$* was machined as a repeat of *Sample 1Va$_L$,* which gave a pillar of approximately 30 µm in diameter and the same virgin microstructure was observed. Similarly, a FIB milling step was undertaken, resulting in a cuboidal volume with X- and Y-dimensions of approximately 20 µm. This sample is denoted *Sample 1Vb$_F$*. The details of the sample pillars extracted from *Sample 1* are given in Table 6.

Sample No.	Sample Type	Procedure	Pillar Width
1Aa$_L$	Electrode only – aged	Laser only	55 µm
1Ab$_L$	Electrode only – aged	Laser only	45 µm
1Va$_L$	Electrode only – virgin	Laser only	33 µm
1Va$_F$	Electrode only – virgin	Laser + FIB	25 µm
1Vb$_L$	Electrode only – virgin	Laser only	30 µm
1Vb$_F$	Electrode only – virgin	Laser + FIB	20 µm

Figure 78: Pillars and their corresponding XCT parameters from Sample 1 *laser preparation*

5.4.4 Sample 2

Sample 2 comprised an ASL, AFL and the electrolyte, from reduced pieces of a supplied NiO-8YSZ|8YSZ sample. The first sub-sample, *Sample 2Va$_L$,* was laser-machined to 33 µm in width. The sample was subsequently FIB-milled to approximately 15 µm (giving a truncated-cone shape) and will hereafter be known as *Sample 2Va$_F$*. Due to the smaller diameter, microstructural details in the AFL could be observed

A second sub-sample, *Sample 2Vb$_F$* was prepared from the same batch of reduced samples, first by laser micromachining to approximately 50 µm and then FIB-milling to 14 µm in diameter. In this instance, no tomogram was generated of the larger laser-machined pillar. The details of the sample pillars extracted from *Sample 2* are given in Table 7.

Sample No.	Sample Type	Procedure	Pillar Width
2Va$_L$	Electrode & Electrolyte	Laser only	33 µm
2Va$_F$	Electrode & Electrolyte	Laser + FIB	18 µm
2Vb$_F$	Electrode & Electrolyte	Laser + FIB	14 µm

Table 7: Pillars and their corresponding XCT parameters from Sample 2 *laser preparation*

5.5 Acquisition

Each of the samples scanned in the X-ray nano-CT instrument in this section were scanned in LFOV mode and with parameters chosen subject to certain requirements and restraints. Firstly, the overall scan duration had to be kept below 36 h*, and preferably below 24 h, both due to the potential for significant sample drift and the normal time constraints of shared apparatus. Secondly, guidelines from the instrument manufacturers suggested a minimum average count number of 2000 through the VOI to ensure adequate image quality (signal-to-noise ratio), and at times this was increased, when time allowed, to augment the solid-phase contrast. Thirdly, the number of projections was varied, partly due to time constraints but partly to probe its significance in returning a segmentable tomogram; if fewer projections were sufficient, longer exposure times could be used to deliver improved contrast, for the same overall scan duration. The details of the scan parameters for each sub-sample are presented in Table 8.

Sample No.	Sample Type	Procedure	Pillar Width	Exp time	No. Proj	Bin	Scan Time
1Aa$_L$	Electrode only – aged	Laser only	55 µm	40 s	1601	2	18 h
1Ab$_L$	Electrode only – aged	Laser only	45 µm	70 s	1001	1	20 h
1Va$_L$	Electrode only – virgin	Laser only	33 µm	70 s	1741	1	34 h
1Va$_F$	Electrode only – virgin	Laser + FIB	25 µm	64 s	1601	1	29 h
1Vb$_L$	Electrode only – virgin	Laser only	30 µm	50 s	1401	1	20 h
1Vb$_F$	Electrode only – virgin	Laser + FIB	20 µm	72 s	1101	1	23 h
2Va$_L$	Electrode & Electrolyte	Laser only	33 µm	60 s	1501	1	26 h
2Va$_F$	Electrode & Electrolyte	Laser + FIB	18 µm	64 s	2201	1	40 h*
2Vb$_F$	Electrode & Electrolyte	Laser + FIB	14 µm	64 s	1101	1	20 h

Table 8: Pillars and their corresponding XCT parameters for Samples 1 *& 2, *blurred image*

It should be noted that there is a mathematical estimate of the number of projections required to return, to a good approximation, the 3D reconstruction of the property of interest with sufficient sampling [310]. This approach notes that a unique reconstruction of an object sampled in the spatial domain can be obtained if the object is sampled with a frequency greater than twice the highest frequency of the object detail, which is the Nyquist condition of the Shannon sampling theorem [311]. Thus, a number of projections, *P*, is required to meet this condition when sampling for a certain number

of points per projection line (ray path), S_{path}. If the diameter of the scanned object is D_{obj}, and the difference between two points of scanning is Δx, then [306]:

$$S_{path} = \frac{D_{obj}}{\Delta x} \qquad 5\text{-}4$$

Over a 360° scan, each point is scanned again after a path has been traversed equal to πd, thus for the points situated on the surface, this is equal to πD. The numbers of projections, *P*, must be represented by Equation *5-5* [306]:

$$P = \frac{\pi D_{obj}}{\Delta y} \qquad 5\text{-}5$$

To meet the Nyquist criterion of the Shannon theorem, $\Delta y \leq 2\Delta x$, gives Equation *5-6* [306]:

$$P \geq \frac{\pi}{2} S_{path} \qquad 5\text{-}6$$

This corresponds to only about 750 projections for a sample pillar with a diameter of 30 µm, FOV of 65 µm and the highest spatial frequency assumed to be the voxel dimension (~ 63 nm). This number of projections, with the flux of the current generation of lab-based X-ray nano-CT scanners is easily achievable and can be surpassed within reasonable scan times. A standard FBP algorithm in the commercially available Zeiss XMReconstructor software was used to reconstruct all 3D volumes from the acquired projection data. The resulting stacks of 2D slices were processed in commercially available Avizo software (ThermoFisher Scientific, Massachusetts, USA) as described in **Chapter 3**.

5.6 Results & Discussion

5.6.1 Tomograms

5.6.1.1 Sample 1

The internal microstructure is more observable in all *Sample 1* pillars than in the preliminary samples (*Px* and *Py)* (see Figure 79: XZ-orthoslices from *Sample 1* scans, black = pore, grey = nickel, and white = YSZ). There is a clear improvement both in image quality and in solid-phase contrast as the pillar width is decreased. In most cases, it is possible to extract a reliable binary segmentation (solids vs pores) from the tomograms but it is only in the case of the FIB-milled samples (*Samples 1Va$_F$* and

Sample 1Vb$_F$) that the nickel and YSZ phases are visibly distinguishable, and hence have the potential for ternary segmentation.

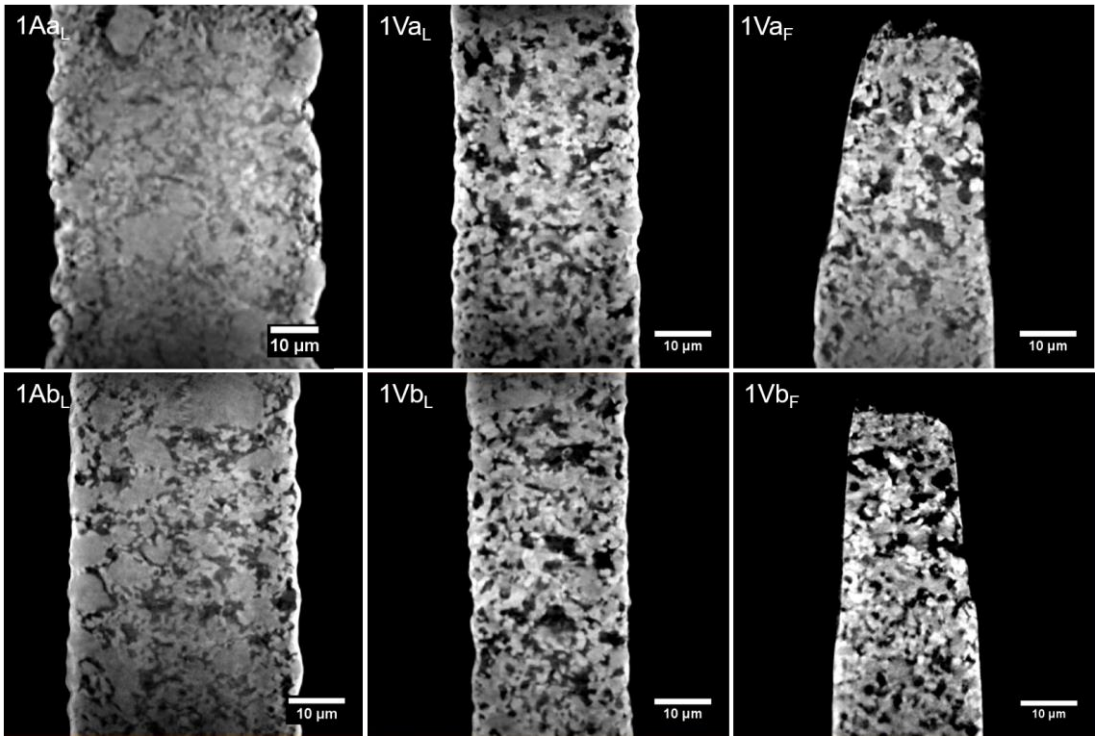

Figure 79: XZ-orthoslices from Sample 1 *scans, black = pore, grey = nickel, and white = YSZ*

Comparing *Samples 1Aa$_L$* and *1Ab$_L$*, the sharpness of particle edges improves and the potential for binary segmentation from the latter suffers from less uncertainty. This is due to a slightly reduced thickness, a decrease in voxel dimension from 126 to 63 nm and an increase in exposure time. To maintain the same scan time, fewer projections were used, appearing not to noticeably jeopardise image quality. For *Samples 1Va$_L$* and *1Vb$_L$*, solid-phase contrast starts to become apparent, and the small difference in diameter is compensated for by the higher exposure time for the former.

Applying the final FIB milling step, resulting in *Samples 1Va$_F$* and *1Vb$_F$*, not only shortened the path length and increased the signal-to-noise ratio due to greater counts on the detector for a given exposure time, but moreover, it removed the thin laser-affected region on the outer edges of the lasered pillars. This bright region (see Figure 79 a), b) d) and e)), is a dense layer apparently given by high-temperature laser sintering and attenuates the beam by a proportionally high degree given its density. Consequently, the solid-phase contrast for a pillar or 20 – 25 µm, imaged at exposure

times between 64 and 72 s, is adequate for attempts towards three-phase segmentation. It was observed that lowering the projections further to 1101, in accordance with theoretical estimates, maintained sufficient image quality for feature resolution, thus giving access to longer exposure times for reasonable overall scan durations.

5.6.1.2 Sample 2

The distinct layers of the half-cell are readily visible in the example XZ-orthoslices presented in Figure 80. The *Sample 2Va$_L$* orthoslice shows both the ASL and AFL, although the microstructure of the latter is not well-resolved. The solid-phase contrast level is low due to the pillar thickness (> 30 µm) but it is also clear that the signal-to-noise ratio is not as high at the upper and lower edges of the FOV, and the fine microstructure is washed out as a result.

For *Sample 2Va$_F$*, the pillar thickness is reduced and the AFL (where the anodic electrochemistry is all thought to occur) is placed in the centre of the FOV. From this orthoslice, the three layers are clearly distinguishable, with the 8YSZ electrolyte at the top, then the fine microstructure of the AFL below, and the coarser, more porous ASL beneath. The solid-phase contrast is vastly improved, but it is most notable for the slightly thinner pillar (*Sample 2Vb$_F$*) shown magnified in Figure 80 c).

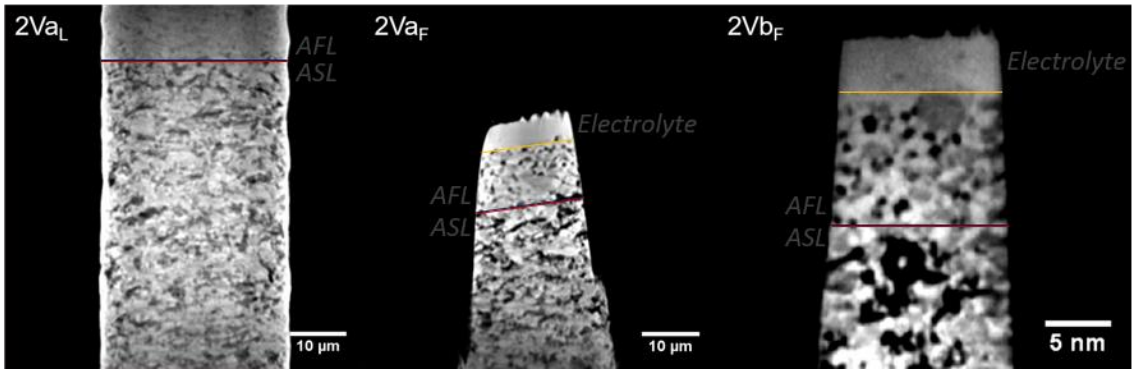

Figure 80: XZ-orthoslices from Sample 2 scans, black = pore, grey = nickel, and white = YSZ

5.6.2 Image processing

For each tomogram, the histogram was expanded across the entire 16-bit range from the portion of data containing the microstructural detail of interest; this process excluded some low grayscale exterior artefacts and darkened the pore regions to suitably account for the non-zero attenuation of air. If necessary, the volumes were transformed

to match the orthogonal axes of the software, to include as much volume as possible in the following rigid sub-volume process. These volumes were resampled using Lanczos interpolation [312][261].

From the fully adjusted tomograms, cuboidal sub-volumes were extracted to preclude the erroneous allocation of air as pore space. The volume of greatest solid-phase contrast was central to the pillar, both due to imperfect beam profile compensation and because this was away from the thicker non-FIB-milled base. In each case, the largest cuboid was extracted from these regions in Avizo, and analysis was performed on the result.

For *Sample 1Va$_F$* and *1Vb$_F$,* it can be seen from Figure 79 that there may be a thin AFL present (4 - 5 µm), but the finer microstructure does not lend itself to adequate resolution of features nor solid-phase contrast at this pillar thickness. The extracted cuboid therefore wholly contained the ASL.

For *Sample 2Va$_F$* and *2Vb$_F$*, however, the fine microstructure of the AFL is visible (Figure 80). High solid-phase contrast, particularly in the case of *Sample 2B$_F$*, renders three-phase segmentation viable. The cuboidal volumes were therefore extracted from the denser AFL layers for these samples.

5.6.3 Image Analysis

5.6.3.1 Sample 1 (No electrolyte)

5.6.3.1.1 Sample 1Va$_F$

Primarily, *Sample 1Va$_F$* was segmented from the extracted raw sub-volume, comprising 260 × 269 × 387 voxels, with a voxel dimension of 63.1 nm, giving a total sampled volume of approximately 6,800 µm^3, substantially greater than the volumes afforded by the FIB-SEM slice-and-view technique employed in **Chapter 4**. The segmentation was performed using a combination of grayscale and watershed thresholding, firstly without image filtering, in Avizo. As in the FIB-SEM case, manual adjustment at boundaries using erosion and dilation morphological operations was used to improve the fidelity of the segmentation.

Phase fractions, total and active TPB densities and VSSA/VSIAs were calculated; the latter excluding the exterior voxels (which represent arbitrarily truncated features). This information is displayed in Table 9 and representative images of raw and segmented slices, 3D segmented volume and a 3D map of the active TPBs are shown in Figure 81**.**

Phase	Volume (μm^3)	Phase Fraction (%)	VSSA (μm^{-1})	Interface	VSIA (μm^{-1})	ρ_{TPB} (μm^{-2})
Pore	2263	33.3	0.9	**Pore-Nickel**	0.5	**Active: 1.9**
Nickel	2327	34.2	1.2	**Nickel-YSZ**	0.6	
YSZ	2213	32.5	1.0	**YSZ-Pore**	0.4	
Total	6802	100.0	-	**Pore-Nickel-YSZ**	-	**Total: 2.2**

Table 9: Estimated Sample 1Va_F *volume, area and length metrics (unfiltered)*

It is notable that the phase fractions are much closer to the 1: 1: 1 volume ratio supplied by the manufacturer. This is indicative of the importance of having a representative volume element, such that the extracted metrics better represent the global average for the electrode. Although the VSSAs and VSIAs are similar in magnitude to those extracted from the FIB-SEM data (see **Section 4.3.1.1**) the trend is different. Most significantly, the nickel surface area is much higher based on the X-ray nano-CT than the FIB-SEM tomographic data (1.2 μm^{-1} versus 0.6 μm^{-1}). Given that the small volume analysed by FIB-SEM gave a Ni content that was lower than expected (28.3%) may at least partly explain not accounting for the roughness of the nickel phase; it is thought that the nickel microstructure from FIB-SEM tomography was not representative from RVE analysis. The Total and Active TPB densities are lower than those extracted from the FIB-SEM data (Total: 2.2 versus 2.9 and Active: 1.9 versus 2.4) however the %Active TPB density is broadly the same (~86% versus ~81%), suggesting the true proportion of active TPBs (albeit within the ASL) is around 80 - 90%, in line with various literature precedents [132][131]. It should be noted, however, that the ASL is not connected to the electrolyte, so these are only theoretical in nature and it is more relevant to ascertain the level of percolation for the TPB lengths in the AFL.

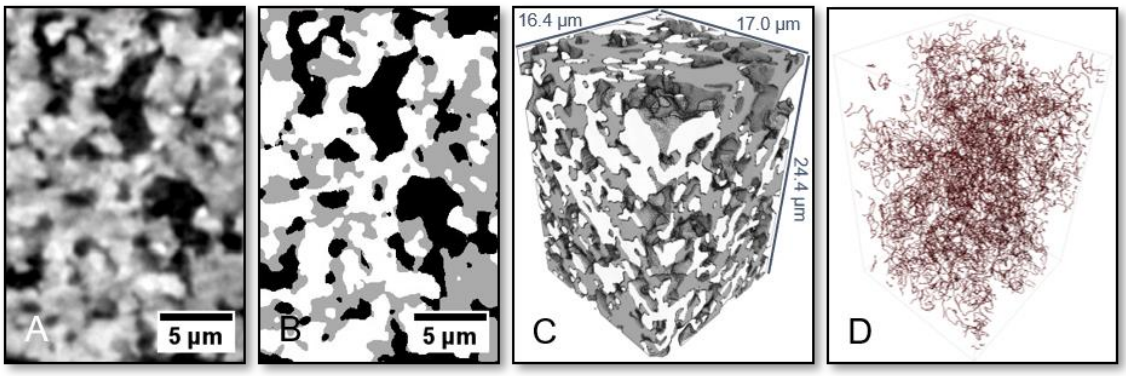

Figure 81: Raw slice from Sample 1Va$_F$*; b) Corresponding segmented image; c) 3D volume rendering (transparent = pore, grey = nickel, white = YSZ); d) 3D Active TPB map*

In order to probe segmentation error, this analysis was repeated by duplicating the procedure but with an intermediate filtering step, by use of an in-built Avizo "Unsharp Masking" filter that is used to sharpen edges without dramatically increasing noise [313]. The results of the application of similar processing and segmentation are given below (Table 10), which were extracted from a similar volume of 270 × 270 × 405 voxels, totalling approximately 7,400 µm^3.

Phase	Volume (µm^3)	Phase Fraction (%)	VSSA (µm^{-1})	Interface	VSIA (µm^{-1})	ρ_{TPB} (µm^{-2})
Pore	2341	31.5	0.9	**Pore-Nickel**	0.5	**Active: 2.4**
Nickel	2582	34.8	1.2	**Nickel-YSZ**	0.8	
YSZ	2497	33.7	1.2	**YSZ-Pore**	0.4	
Total	7420	100.0	-	**Pore-Nickel-YSZ**	-	**Total: 2.7**

Table 10: Estimated Sample 1Va$_F$ *volume, area and length metrics (filtered)*

The phase fractions from the raw and filtered processing differ by a maximum of ~6%, and on average by 3.6%. The question of whether this is negligible depends on the context in which these phase fractions are utilised; any changes in phase fraction due to microstructural evolution of less than 6 % would certainly be unsubstantiated by this method, but this is considerably lower than the proportional changes seen in literature reporting nickel loss [115], and therefore volumetric changes. However, the VSSA/VSIA comparisons display different behaviour. In terms of VSSA, the pore and nickel phases are within the same degree of error as the volume fractions (0% for pore and 5.8% for nickel). On the contrary, the VSSA$_{YSZ}$ is markedly different, 1.2 versus 1.0 µm^{-1} for the filtered and raw segmentations, respectively. This highlights that the filtering step can have a singular effect on a particular phase; here it appears that the edge enhancement

has afforded a greater delineation of fine YSZ microstructural details. This is also seen in the VSIAs, with very little change in the pore-nickel interface, but substantially greater surface area for the other two interfaces involving YSZ.

The TPB densities extracted from the filtered segmentation are higher than for the unfiltered analogue, and more closely match the absolute values extracted from FIB-SEM analysis of the virgin sample (Total: 2.7 versus 2.9 and Active: 2.4 versus 2.4), whereas the proportion of active TPB has been raised to a slightly higher value of ~90% (versus ~81%). Again, by picking up the finer YSZ details, it is possible that this filtered segmentation approach, of a larger volume, better represents the true connectivity of the triple-phase boundaries in the ASL of this virgin microstructure.

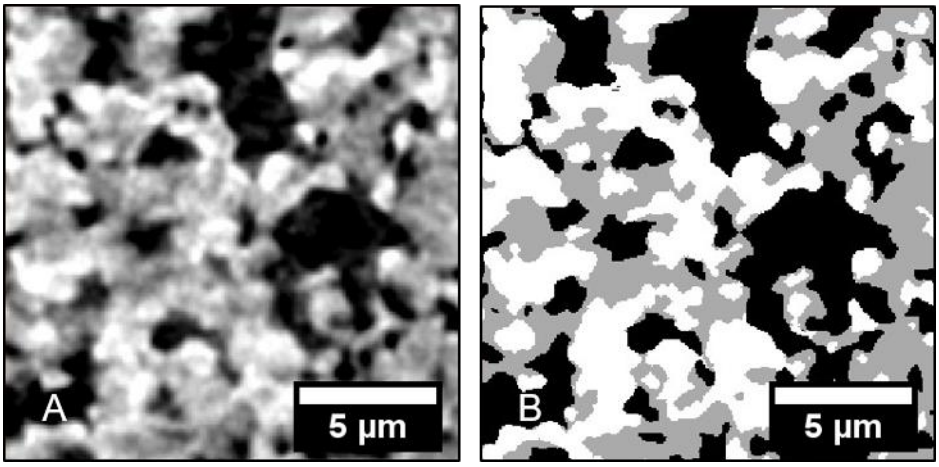

Figure 82: a) Filtered slice from Sample 1Va$_F$*; b) Corresponding segmented image showing the three phases: transparent = pore, grey = nickel, white = YSZ*

For both segmentations (with and without filter), tortuosity factors for the pore, nickel and YSZ phases in the X-, Y- and Z-directions were calculated using TauFactor [314]. The tortuosity factor values are presented in Table 11 and Table 12. RVE analysis using both the pore phase fraction and pore tortuosity factor as representative microstructural parameters was performed once, for the unfiltered data, as calculations showed that these values differed insignificantly for the filtered volume (<4 % difference) and thus only small changes were envisaged.

Phase	Direction			Standard Deviation
	X-	***Y-***	***Z-***	**(*Anisotropy*)**
Pore	4.4	5.1	6.3	1.0 (18% of average)
Nickel	3.7	2.9	3.9	0.5 (15% of average)
YSZ	4.0	4.3	4.1	0.01 (2% of average)

Table 11: Tortuosity Factor values from Sample 1Va$_F$ *raw segmentation*

Phase	Direction			Standard Deviation
	X-	***Y-***	***Z-***	**(*Anisotropy*)**
Pore	4.6	5.1	6.9	1.2 (22% of average)
Nickel	3.7	3.2	3.8	0.3 (9% of average)
YSZ	3.9	4.4	4.2	0.3 (6% of average)

Table 12: Tortuosity Factor values from Sample $1Va_F$ *filtered segmentation*

For the raw (unfiltered) segmentation, the tortuosity values found for the X-, Y- and Z-directions were 4.4, 5.1 and 6.3, respectively. These values are similar to those observed in the literature [138], suggesting the investigated microstructure is representative of the type of ASL microstructure seen in other anodes. The filtered segmentation gave very similar results to the unfiltered dataset, for each direction and each phase, likely as the Unsharp Masking filter only appreciably affects boundaries and therefore only a minimal number of bottlenecks might be affected by the filtering step. As a measure of anisotropy, the standard deviations for each phase and each segmentation route were calculated. It appears, regardless of the use of a filter or not, the pore phase displays the greatest anisotropy, with the Z-direction having the highest value. This may be a result of the way in which the majority of the pore network is formed, during reduction of NiO to Ni. Perhaps the uniqueness of the Z-direction in terms of gravity has some role to play in the fabrication process. Nonetheless, the X- and Y- tortuosity factors are broadly the same, representing reasonably homogeneous ink manufacture.

Representative flux volumes for the pore phase are shown in Figure 83, highlighting bottleneck areas where gas flow may be constrained; this approach can help identify specific problem areas, which may be inspected for changes upon evolving the microstructure.

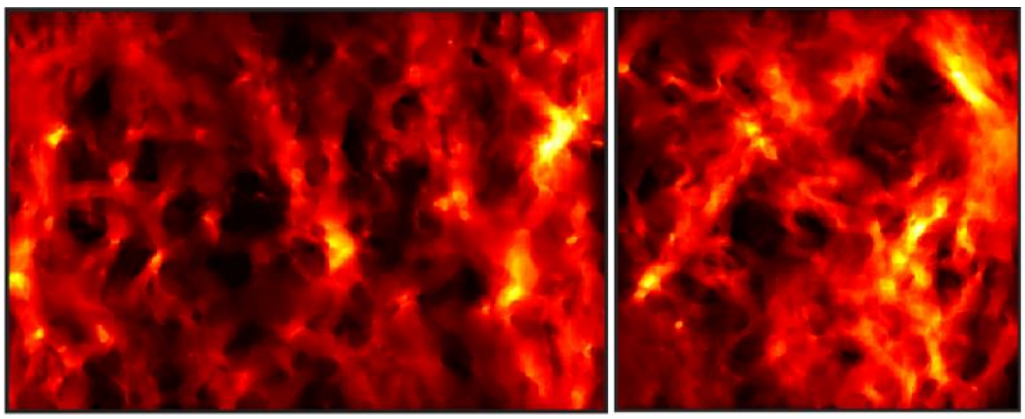

Figure 83: 2D a) X-; and b) Y-projected Flux Maps for Pore phase of (filtered) Sample $1Va_F$

Using a tolerance of 4% (see **Chapter 4**), the RVE analysis of porosity for the unfiltered volume shows that a volume dimension, *x = 0.7*, is required to be representative of the pore volume, representing a total volume of ~4,800 µm^3. For tortuosity factor, *x = 0.7, 0.9 and 0.8* for the X-, Y- and Z-directions, respectively, indicating that the analysed volume, for these feature sizes, is just about adequate to describe these important properties. This analysis is presented in Table 13 and Figure 84.

Volume Fraction		0.1	0.3	0.5	0.7	0.9	1.0
Porosity (%)		25.7	29.9	31.5	32.3	33.1	33.3
Tortuosity Factor	*Direction*						
Pore	*X*	8.9	7.1	6.6	5.2	5.0	5.1
	Y	11.7	6.9	5.6	4.9	4.4	4.4
	Z	5.4	5.7	6.9	6.8	6.3	6.3

Table 13: Values from Pore RVE analysis of Sample 1Va$_F$ *raw segmentation*

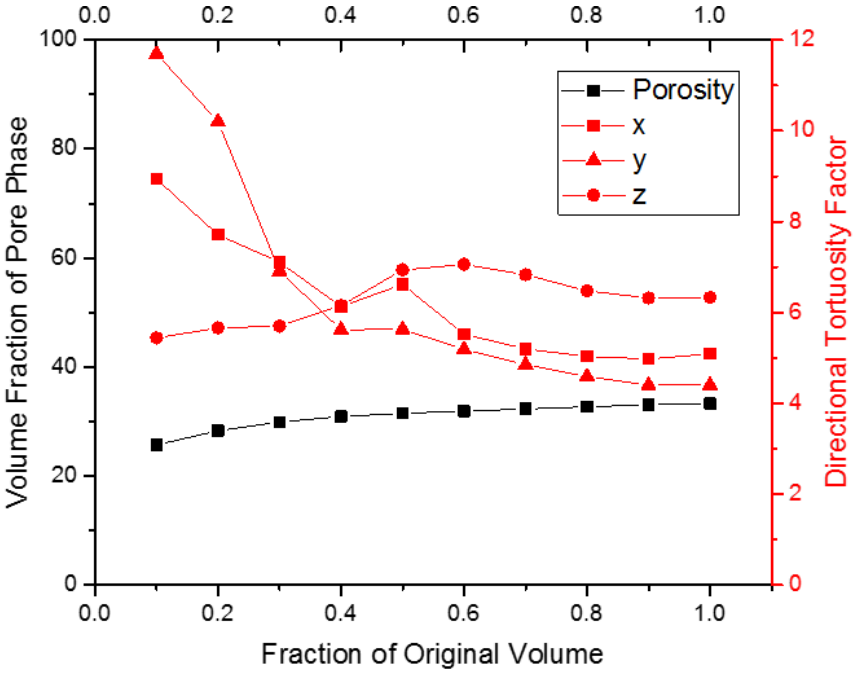

Figure 84: Plot displaying the Pore RVE analysis of the raw Sample 1Va$_F$ *data*

This analysis confirms that the volumes analysed by the FIB-SEM slice-and-view approach were too small to yield accurate metrics and highlight the greater ease with which a larger, more representative volume can be investigated by lab-based X-ray nano-CT.

This RVE analysis illustrates the need for volumes of ca. 5000 µm^3 for these microstructures containing features with characteristic sizes of 1 - 2 µm, which is a larger

volume than for most previously investigated SOFC electrode microstructures [175] and therefore highlights the importance of maximising the use of the X-ray FOV.

5.6.3.1.2 Sample 1Vb$_F$

Sample 1Vb$_F$ was also segmented from an extracted filtered (Unsharp Masking) sub-volume, comprising 270 × 270 × 405 voxels, with a voxel dimension of 63.1 nm, giving a total sampled volume of approximately 7,400 µm^3. The segmentation was performed using a combination of grayscale and watershed thresholding, along with manual adjustment at boundaries as before (Figure 85). Length, area and volume metrics were calculated as described above, giving rise to the values presented in Table 14. These are then compared with the metrics extracted from the same-sized volume of *Sample 1B$_F$* which underwent the same processing and analysis procedures (same volume and filtering), shown in Table 16.

Phase	Volume (µm^3)	Phase Fraction (%)	VSSA (µm^{-1})	Interface	VSIA (µm^{-1})	ρ_{TPB} (µm^{-2})
Pore	2403	32.4%	1.0	**Pore-Nickel**	0.6	**Active: 2.8**
Nickel	2688	36.2%	1.4	**Nickel-YSZ**	0.8	
YSZ	2329	31.4%	1.2	**YSZ-Pore**	0.4	
Total	7420	100.0%	-	**Pore-Nickel-YSZ**	-	**Total: 3.4**

Table 14: Estimated Sample 1Vb$_F$ *volume, area and length metrics (filtered)*

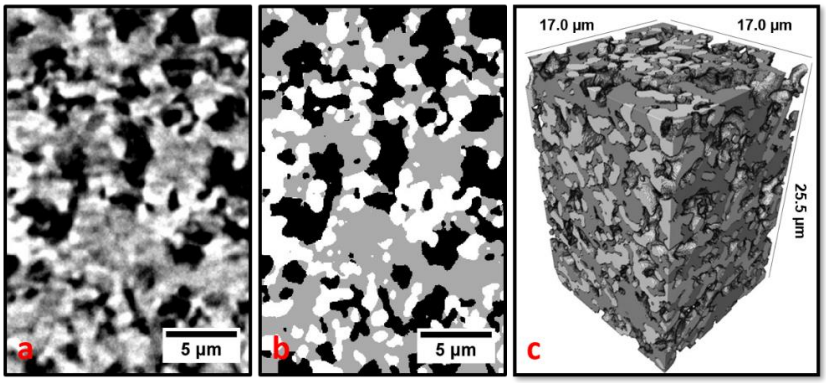

Figure 85: Raw slice from Sample 1Vb$_F$*; b) Corresponding segmented image showing the three phases; c) 3D reconstruction of full volume (transparent = pore, grey = nickel, white = YSZ)*

Phase	Direction			Standard Deviation
	X-	***Y-***	***Z-***	**(Anisotropy)**
Pore	4.9	4.3	6.2	0.8 (15% of average)
Nickel	2.8	2.8	3.4	0.3 (9% of average)
YSZ	8.1	6.5	7.3	0.6 (9% of average)

Table 15: Tortuosity Factor values from Sample 1Vb$_F$ *filtered segmentation*

Representative flux volumes for the pore phase from *Sample 1Vb$_F$* are shown in Figure 86**.**

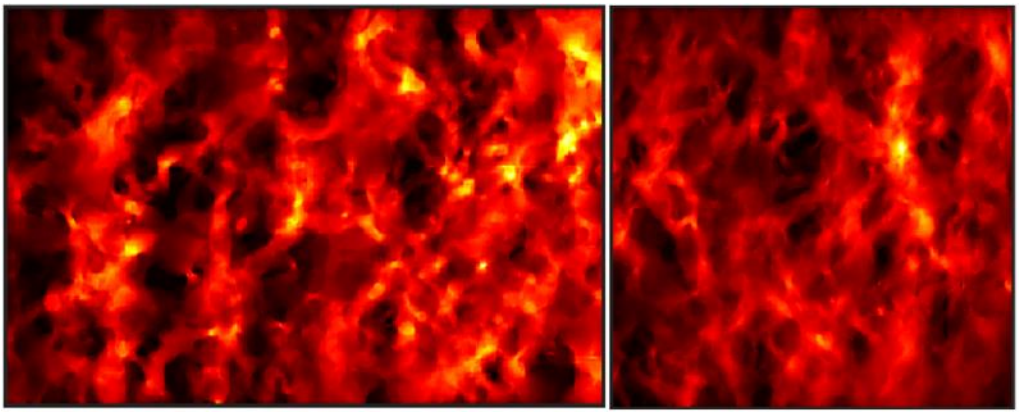

Figure 86: 2D a) X-; and b) Y-projected Flux Maps for Pore phase of (filtered) Sample $1Vb_F$

	Sample $1Va_F$ (filtered)	Sample $1Vb_F$ (filtered)	Difference (|a-b| / AVG(a:b))
Volume Fraction (%):			
Pore	31.5%	32.4%	2.8%
Nickel	34.8%	36.2%	3.9%
YSZ	33.7%	31.4%	7.1%
VSSA (μm^{-1})			
Pore	0.9	1.0	11.4%
Nickel	1.2	1.4	12.8%
YSZ	1.2	1.2	1.6%
VSIA (μm^{-1})			
Pore-Nickel	0.5	0.6	10.7%
Nickel-YSZ	0.8	0.8	6.1%
YSZ-Pore	0.4	0.4	4.7%
Total TPB Density (μm^{-2})	2.7	3.4	22.0%
Active TPB Density (μm^{-2})	2.4	2.8	14.5%
% Active TPB	89.7%	83.1%	7.6%
Pore Tortuosity Factor:			
X	4.6	4.9	5.7%
Y	5.1	4.3	17.3%
Z	6.9	6.2	10.8%
Nickel Tortuosity Factor:			
X	3.7	2.8	29.1%
Y	3.2	2.8	14.5%
Z	3.8	3.4	11.5%
YSZ Tortuosity Factor:			
X	3.9	8.1	70.7%
Y	4.4	6.5	38.3%
Z	4.2	7.3	53.5%

Table 16: Comparison of estimated metrics between (filtered) Sample $1Va_F$ *and* Sample $1Vb_F$

The volume fractions from the two sub-samples are in broad agreement; in absolute terms, the percentages vary by no more than 2.3% (7.1% proportionally) which is likely to be a confluence of the microstructural variation in manufacture and the error in segmentation. In both cases, the nickel phase fraction is larger than the other phases. In terms of VSSA, the trend is the same, with nickel being slightly 'rougher' than the other

phases. For the VSIAs, there is good agreement, with the same trend apparent, adding validity to this approach.

For the simple metrics, the greatest disagreement comes in the absolute values of the TPB densities (total ~22% difference, active ~15 % difference). As this 1D interface requires contact between all three phases, it is unsurprising that this metric shows the greatest deviation across sub-samples. Interestingly, the %Active TPB is much closer in value, approximately 8% different. In terms of tortuosity factor, the pore networks represent the least change, at an average of 11% over all directions. The solid networks show greater deviation between sub-sample, and most notably, the YSZ network appears significantly more tortuous in *Sample 1Vb$_F$* than *1Va$_F$* (τ_x is 8.1 versus 3.9, respectively). This greater deviation for YSZ is another indicator that it is this network (both its fine structure and the nature of its connectivity) that is either the most heterogeneous, most difficult to reliably segment, or both.

RVE analysis was similarly conducted for *Sample 1Vb$_F$*, the results of which are shown in Table 17 and Figure 87.

Volume Fraction		**0.1**	**0.3**	**0.5**	**0.7**	**0.9**	**1.0**
Porosity (%)		26.9	30.9	32.0	32.0	32.2	32.4
Tortuosity Factor	*Direction*						
	X-	10.7	5.6	4.9	5.0	4.9	4.9
	Y-	7.9	4.8	4.7	4.7	4.4	4.3
	Z-	6.5	5.9	5.6	6.0	6.1	6.2

Table 17: Values from RVE analysis of Sample 1Vb$_F$ *segmentation*

Using a tolerance of 4%, the RVE analysis of porosity shows that, as with *Sample 1Va$_F$*, a volume dimension, *x = 0.7*, is required to be representative of the pore volume, representing a total volume of ~4,800 µm^3. For tortuosity factor, *x = 0.5, 0.9 and 0.7* for the X-, Y- and Z-directions, respectively, indicating that representative volume elements must be considered specific not only to a metric but to its directional aspect, too.

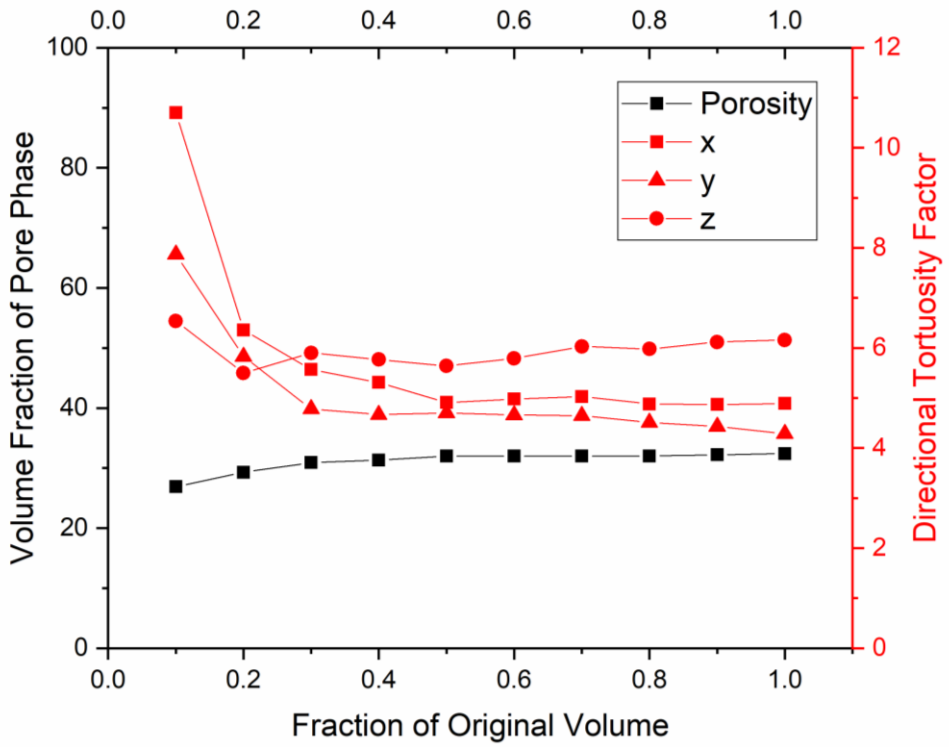

Figure 87: Plot displaying the Pore RVE analysis of the Sample $1Vb_F$ *data*

5.6.3.2 Sample 2 (with electrolyte)

5.6.3.2.1 Sample $2Va_F$

Sample $2Va_L$ did not display sufficient solid-phase contrast for ternary segmentation. However, once it was FIB-milled to approximately 18 µm in width, the AFL microstructure in *Sample* $2Va_F$ appeared to become adequately resolvable. The solid-phase contrast was greater but was not optimised, hence *Sample* $2Vb_F$ was machined to an even thinner pillar (14 µm). However, there was a limit to how thin the pillar ought to be milled as it had become clear that a representative volume for the ASL was >4000 μm^3. As the AFL features were finer, it was likely that a smaller volume would suffice, but as the layer is only 10 µm in thickness, approaching 10 µm lateral dimensions results in a limited volume of 1000 μm^3. It is worth noting that work by Villanova *et al.* proposed a ~13 µm-diameter pillar sufficient to deliver representative results from holotomographic imaging [198].

Sample $2Va_F$ was segmented from the extracted, filtered (Unsharp Masking) sub-volume, comprising 128 × 128 × 128 voxels from the AFL. Similarly, these voxels had a dimension of 63.1 nm, giving a total sampled volume of approximately 530 μm^3.

The segmentation was performed as described for *Sample 1Vb$_F$*, as was the metrics extraction (Table 18).

Phase	Volume (μm^3)	Phase Fraction (%)	VSSA (μm^{-1})	Interface	VSIA (μm^{-1})	ρ_{TPB} (μm^{-2})
Pore	96	18.2	0.9	**Pore-Nickel**	0.7	**Active: 1.1**
Nickel	229	43.5	1.8	**Nickel-YSZ**	1.1	
YSZ	202	38.3	1.3	**YSZ-Pore**	0.2	
Total	527	100.0	-	**Pore-Nickel-YSZ**	-	**Total: 2.8**

Table 18: Estimated Sample 2Va$_F$ *volume, area and length metrics (filtered)*

As expected for an AFL, the porosity is significantly lower than for the ASLs investigated in previous samples. This is by design, as large pores for mass transport are less crucial here, wherein most, if not all, electrochemical reactions take place. In the AFL it is important to maximise the TPB density and ensure sufficient access to the nickel surface for the gas phase. In this respect, the pore-nickel interface is not hugely greater than that seen in the ASLs. However, as can be seen in Figure 88, the segmentation does not appear optimal, and there may be some features that are being obscured by the lack of solid-phase contrast in some places. Moreover, although the total TPB agrees with the ASL values well, one might expect this value to be higher given the finer microstructure. Significantly, the active TPB density is very low, representing only 38% of the total TPB length. It is for this reason that another sample was fabricated with a slightly narrower fine pillar, to further increase the signal-to-noise ratio and better produce solid-phase contrast for a more reliable ternary segmentation of the AFL.

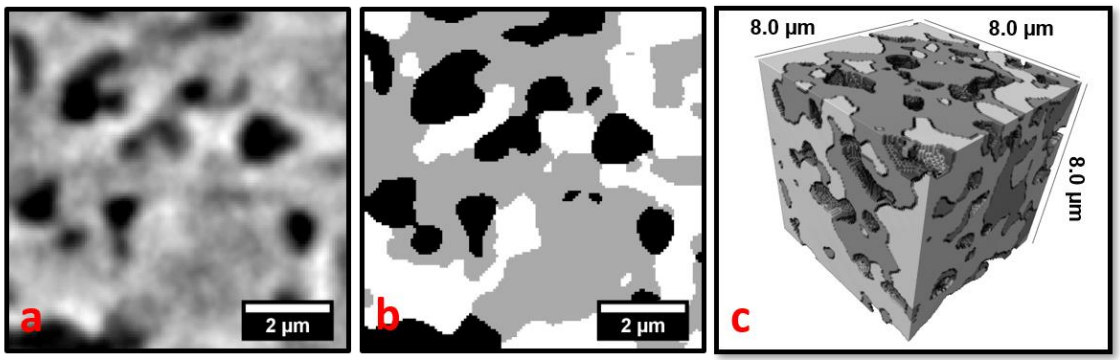

Figure 88: a) Raw slice from Sample 2Va$_F$*; b) Corresponding segmented image; c) 3D volume rendering (transparent = pore, grey = nickel, white = YSZ)*

Tortuosity calculations were performed on the porous phase, whose volume fraction was noticeably reduced versus the ASL (~18% versus ~32%, respectively) and

thus had few percolated pathways. The results are shown in Table 19**,** along with total projected flux maps in the X- and Y-directions in Figure 89.

Phase	Direction			Standard Deviation
	X-	***Y-***	***Z-***	**(Anisotropy)**
Pore	49.1	33.4	∞	-
Nickel	2.3	2.3	2.1	0.12 (5% of average)
YSZ	3.5	3.4	2.9	0.32 (10% of average

Table 19: Tortuosity Factor values from Sample $2Va_F$ *segmentation*

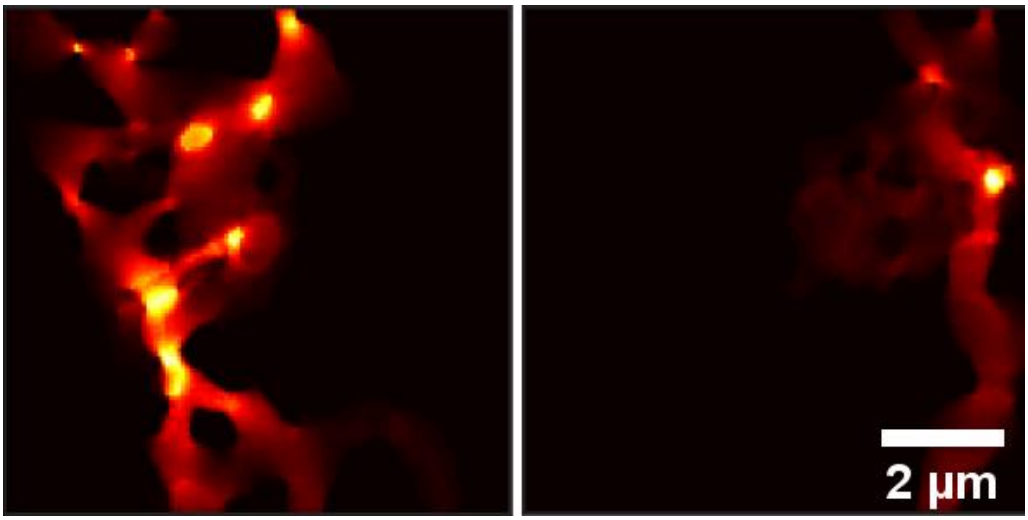

Figure 89: 2D a) X-; and b) Y-projected Flux Maps for Pore phase of Sample $2Va_F$

As the infinite tortuosity factor in the Z-direction shows, for the sub-volume investigated, the porous phase does not percolate from its interface with the ASL to its interface with the electrolyte. In theory, this may be limiting the TPB volumetric density throughout the active layer, as regions close to the electrolyte may be without connected porosity. More investigation would be needed to see where the disconnection occurs, whether this is a segmentation error or a real phenomenon. The low %Active TPB value is likely the result of the poor percolation of the porous phase.

5.6.3.2.2 Sample $2Vb_F$

Sample $2Vb_F$ displayed very clear solid-phase contrast alongside clearly segmentable porosity. It was segmented from the extracted, filtered (Unsharp Masking) sub-volume as before, comprising 128 × 128 × 128 voxels from the AFL. Similarly, these voxels had a dimension of 63.1 nm, giving a total sampled volume of approximately 530 μm^3. The segmentation was performed *via* an improved method which will be covered in detail in **Chapter 6**, utilising machine-learning based freeware alongside

Avizo. The extracted metrics are shown in Table 20 and an example slice along with its corresponding ternary segmentation and volume rendering can be seen in Figure 90.

Phase	Volume (μm^3)	Phase Fraction (%)	VSSA (μm^{-1})	Interface	VSIA (μm^{-1})	ρ_{TPB} (μm^{-2})
Pore	96	18.2	0.9	**Pore-Nickel**	0.6	**Active: 2.7**
Nickel	227	43.2	1.7	**Nickel-YSZ**	1.3	
YSZ	204	38.6	1.6	**YSZ-Pore**	0.5	
Total	527	100.0		**Pore-Nickel-YSZ**		**Total: 4.1**

Table 20: Estimated Sample $2Vb_F$ *volume, area and length metrics (filtered)*

The phase fractions are in very good agreement with those extracted from *Sample* $2Va_F$ and the VSSA values are also close, bar the value for 8YSZ (1.34 versus 1.62 for $2Va_F$ versus $2Vb_F$). Comparing the orthoslices from Figure 90 a) and b), it is clear that the latter presents much clearer contrast between solid phases. The segmentation of the latter appears more reliable by eye when inspecting each 2D slice, and it is thought the high YSZ surface value reflects the fine details of the YSZ microstructure picked up in the case of the 14-µm pillar. The total and active TPB densities are much higher than for *Sample* $2A_F$ (Total: 4.08 versus 2.63; Active: 2.82 versus 1.08) and represents 67% of the total TPB length as opposed to 38%: a value more aligned with literature values for AFL microstructures [181].

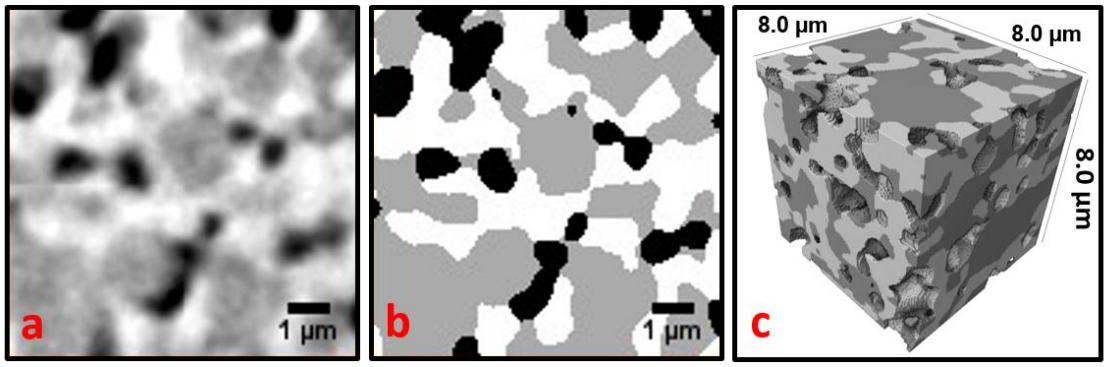

Figure 90: a) Raw slice from Sample $2Vb_F$*; b) Corresponding segmented image; c) 3D volume rendering (transparent = pore, grey = nickel, white = YSZ)*

Tortuosity factor analysis was conducted as before, giving the values in Table 21 and the flux maps in Figure 91. An RVE analysis was run on the pore phase fraction and pore tortuosity factor, with the results presented both in Table 21 and Figure 91. Some values are missing due to a lack of percolation for the investigated sub-volume.

Phase	Direction			Standard Deviation
	X-	*Y-*	*Z-*	(Anisotropy)
Pore	22.3	∞	24.9	-
Nickel	2.5	2.5	2.8	0.19 (7% of average)
YSZ	2.8	3.0	2.6	0.17 (6% of average)

Table 21: Tortuosity Factor values from Sample $2Vb_F$ *segmentation*

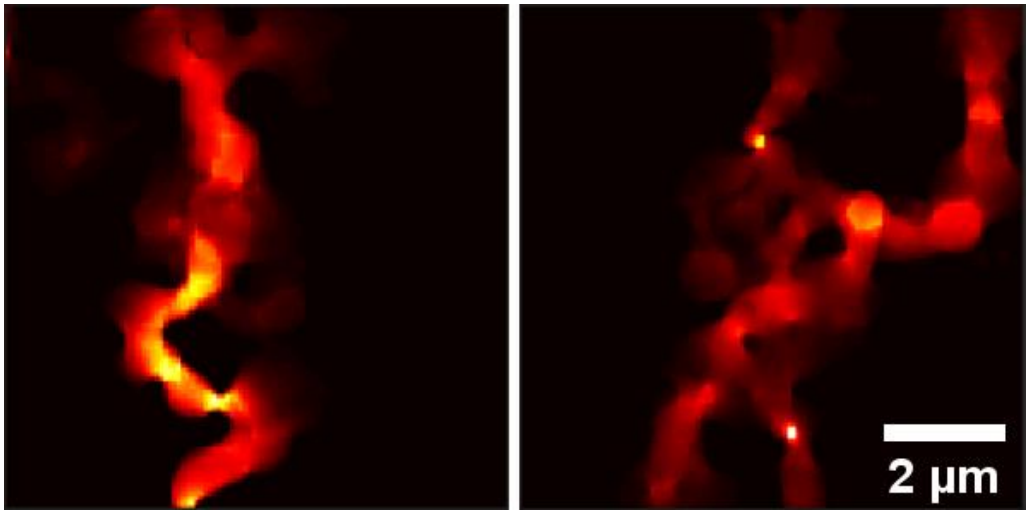

Figure 91: 2D a) X-; and b) Y-projected Flux Maps for Pore phase of Sample $2Vb_F$

Volume Fraction		0.1	0.3	0.5	0.7	0.9	1.0
Porosity (%)		23.0	18.2	17.1	17.6	18.1	18.2
Tortuosity Factor	*Direction*						
	X-	4.9	13.4	24.6	19.9	21.6	22.3
	Y-	-	-	-	42.6	-	∞
	Z-	4.7	-	-	241	26.8	24.9

Table 22: Values from RVE analysis of Sample $2Vb_F$ *segmentation*

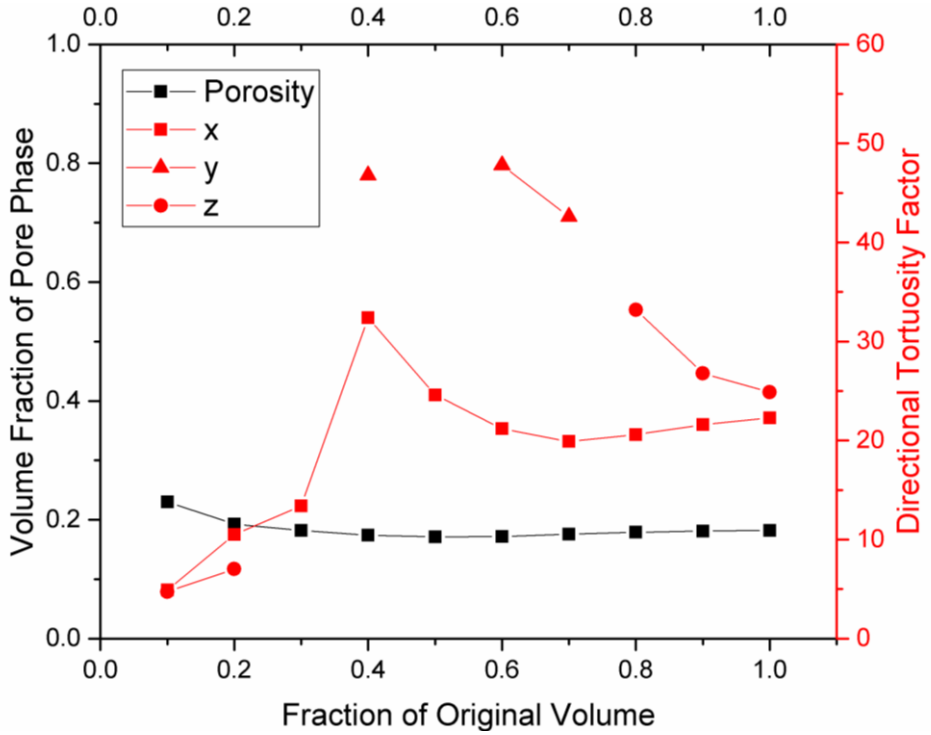

Figure 92: Plot displaying the Pore RVE analysis of the Sample $2Vb_F$ *data*

The Ni and YSZ phases have tortuosity values similar to those found in the literature for Ni-YSZ AFLs [183]. However, the porous network in this region of the AFL, like in that found in *Sample 2Va$_F$*, is highly tortuous. Both samples contain a direction in which there is no contiguous network between one set of planes of the sampled cube for the pore phase. In this case, the direction is in Y-, as opposed to Z-, the latter of which would be more detrimental to electrochemical behaviour as it is likely to reduce the proportion of active TPB lengths in the vicinity of the electrode/electrolyte interface. It is worth noting that this may be the reason for the erroneously low active TPB for *Sample 2Va$_F$*. For *Sample 2Vb$_F$*, the lack of Y-direction percolation may be an indication that the volume is not large enough or that the channels have some degree of anisotropy, with a preponderance towards the Z-direction for gas transport in and out of the cell. However, the latter explanation is not supported by percolation at the same full volume for the X-direction (see Figure 92).

The RVE analysis shows that for measuring the pore phase fraction, a small volume is sufficient; approximately ~370 µm^3 appears to be enough at 2% tolerance or ~100 µm^3 at 4% tolerance. However, when inspecting the directional tortuosity factors, larger volumes are needed. Taking a 4% tolerance, for instance, shows that to be representative in the X-direction requires a volume dimension of *x = 0.9* (~475 µm^3) and the full sampled volume is not large enough to be representative in the Z-direction (nor Y- as it is non-percolating). However, application of the same analysis on the Ni and YSZ phases, with larger volume fractions and less tortuous networks, shows that again phase fraction is accounted for well by volumes as small as ~100 µm^3, and tortuosity factor RVEs are highly anisotropic (see Table 23).

Phase	***Direction***			***Comment***
	X-	*Y-*	*Z-*	
Pore	0.9	No percolation	**>1.0**	Volume too small
Nickel	0.2	**0.9**	0.7	Volume just sufficient
YSZ	0.6	0.4	0.7	Volume sufficient

Table 23: RVE dimensions required on a 4% tolerance level for directional tortuosity factors from Sample 1Vb$_F$

This analysis shows that a smaller volume is required to extract representative phase fraction data for the smaller (finer) features of the AFL than for the ASL

(~100-370 μm^3 vs ~5000 μm^3). However, with regard to tortuosity factor, it appears that it depends on which phase and its connectivity, and thus heterogeneity. For the pore phase in this case, the volume required needs to be larger, although it has been shown to be sufficient for both of the solid phases. This work highlights the importance of specifying the exact metric in question when establishing a representative volume element; in terms of phase, property and direction.

5.7 Conclusions

This chapter has catalogued the successful development of a laser-based preparation technique to fabricate samples of appropriate size and geometry for use in X-ray nano-CT investigations of SOFC anodes. The technique widens the scope of recent work in the same group [190] that illustrated that lab-based X-ray nano-CT can provide access to useful three-phase segmentation of Ni-YSZ cermets. The key to achieving the necessary solid-phase contrast is utilising high exposure times, minimising the number of projections to keep the scan times reasonable, and ensuring the sample is cylindrical and most importantly about 15-25 µm in thickness (depending on the microstructure of interest).

This work has underscored the importance of balancing sample size to achieve representative volumes for the corresponding microstructure with the need to ensure high signal-to-noise ratio and therefore maximisation of solid-phase contrast. It has been recognised that this technique can provide three-dimensional information about both the coarser ASL and the finer ASL, the latter of which requires a smaller volume to be representative of the finer details. This is fortunate because to attain the necessary transmission to give suitable signal-to-noise within sensible scan times, the pillars have to be slightly thinner, due to the lower porosity. However, it is noteworthy that the assessed “representativeness” depends on the metric in question, and this should be borne in mind when considering sample preparation and the reliability of extracted properties.

Moreover, some error analysis was conducted with respect to repeating the same analysis with two samples prepared from the same batch and separately by comparing

the extracted metrics from a raw and filtered segmentation of the same sample. The level of error attributable to microstructural variation between samples appears to be approximately 5 - 15%, depending on the metric in question, in order of $error_{volume} < error_{area} < error_{length.}$ When applying a common filter, the segmented results adjust by approximately the same amount, with an average error of approximately 10.4% (versus 10.3% for sample variation). However, the analysis of the filter application only takes into account the use of one filter and only one duplicate is used in both comparisons, so more investigation is needed to confirm that the average error entailed in both cases is truly of the order of 10%. Moreover, it was noted that the application of the filter had a specified effect on delineating the YSZ phase. As an addition to these preliminary error analysis studies, it is recommended that a calibrant is used to provide a more robust comparison between the imaged object and its segmented reconstruction.

It was confirmed that the finer AFL structure could be resolved by lab-based X-ray nano-CT, which had not been previously achieved. This required a particularly fine pillar, accessible by laser micro-machining to ~30 µm, before FIB-milling to approximately 14 µm. Moreover, the microstructure was recognisably different from that of the coarser ASL. In particular, the porosity in the AFL was lower (with a higher solid fraction), although the Ni:8YSZ ratios were approximately equal (~1.1 vol. ratio) in the anodes investigated. For the final sample, a mixture of machine-learning (see **Chapter 3** and **6**) and ordinary threshold segmentation techniques were used. The resulting three-phase segmentation proved to be representative for all phase fractions and all directional tortuosity factors, except for the highly tortuous, low-volume pore phase.

Chapter 6: *Ex-situ* annealing of SOFC anodes

This chapter focuses on using the laser-micromachining procedure developed in **Chapter 5** to produce geometrically optimised pillars as samples to be subjected to lab-based annealing-imaging cycles, in order to probe microstructural evolution on the nanoscale. The first section provides a brief overview of the procedures used to form the sample pillars relevant to this chapter, and the second section outlines the annealing and imaging conditions used. The results section examines the impact of annealing on the anode microstructure, highlighting important considerations with regards to external nickel agglomerates, segmentation procedures and techniques for following the changes. Simple global metrics are extracted as before, alongside the development of more advanced local metrics, including the use of chord length distributions and a local thickness algorithm.

6.1 Samples

Two planar Ni-8YSZ anode-supported cells (ASC), each comprising a fine AFL, a coarse ASL, and a thin dense 8YSZ electrolyte, were supplied by Forschungszentrum Jülich (Jülich, Germany). No cathode layer had been deposited on either electrolyte. One of the ASCs corresponds to *Sample 2* from **Chapter 5** and the other was nominally the same.

6.1.1 Reduction

Two ASCs were sectioned into small pieces (12 x 12 mm) by laser micro-machining before being reduced in a Carbolite GHA 12/300 tube furnace (Carbolite Gero, UK) with 4% H_2 / 96% N_2 forming gas, flowing through the system at 300 ml/min. Inside an Alsint (Carbolite) ceramic tube, the samples were placed in an alumina crucible and positioned in the hot-zone of the furnace. The furnace tube was evacuated by a rotary pump, forming gas was introduced to refill the system and once this was completed three times, the flow rate was set, and the first sample was heated at a ramp rate of 5 °C/min to 800 °C, before dwelling for 4 h. For the second sample, the procedure was altered to probe its effect on the reduced microstructure: the ramp rate

was kept at 5 °C/min but reduction was performed at 700 °C for 0.5 h. In both cases, the furnace contents were allowed to cool passively to below 300 °C before the gas was switched to pure N_2. All temperature readings were monitored by a K-type thermocouple (Omega Engineering, UK) located close to the sample.

A reduced piece from the first ASC was examined by XRD to verify that complete reduction had taken place. This was undertaken by removal of a small section from a reduced piece, before grinding it with a pestle and mortar and placing the resulting powder on the stage inside the instrument. The XRD acquisition and analysis was performed as detailed in **Chapter 3**. The resulting spectra exhibited no NiO peaks, indicating that the sample was fully reduced (Figure 93). Small peaks at approximately 28.5° and 31.5° were assigned to monoclinic ZrO_2 also present in small concentrations.

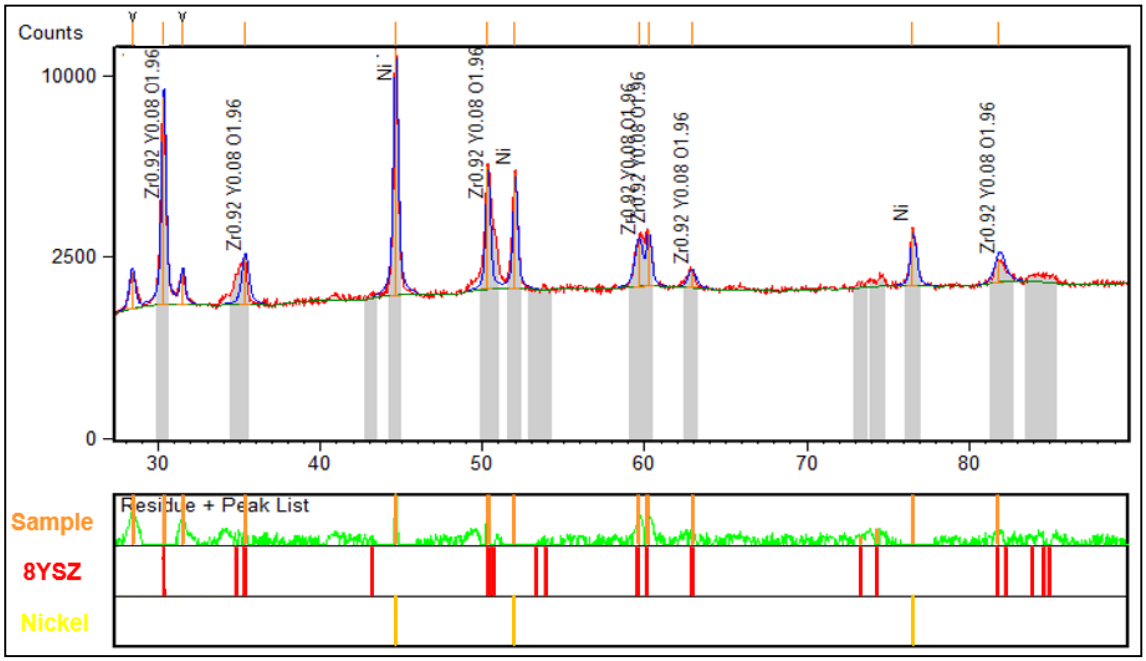

Figure 93: XRD analysis indicates lack of NiO peaks after reduction at 800 °C

6.1.2 Sample Preparation

As detailed in **Chapter 5**, coarse pillars were removed from each of two ASC pieces by laser micro-machining. The coarse pillars each measured approximately 3 mm in diameter and in all cases were affixed atop a short Al_2O_3 tube of similar diameter using high-temperature Ceramabond 685-N cement (Aremco Products, US) – details of this procedure have been discussed elsewhere [191]. In each case, a tiered structure with a fine pillar at the top was laser-milled at moderately low laser power (0.4 W) with ultimate

dimensions of approximately 30-40 µm. FIB-milling (see **Chapters 3** and **5**) was subsequently used to reduce the upper-most portion of the fine pillar to approximately 10-20 µm in diameter and ranging in height from 100 to 200 µm. Two of the samples prepared in this way were examined in **Chapter 5**, namely *Sample 2Va$_F$* (18 µm) and *Sample 2Vb$_F$* (14 µm)**.** A third pillar was produced from the second ASC but following the same procedure, which will be known hereafter as *Sample 2Vc$_F$*. and measured 14 µm in diameter. The details of the coarse and fine laser milling procedures were outlined previously [305], and the alternative mounting set-up is shown below in Figure 94 a). This procedure was conducted with three separate reduced tokens in total (2 from one ASC and 1 from the other ASC), giving three Ni/YSZ pillars (similar to that shown in Figure 94 c) and d)) ready for annealing treatments.

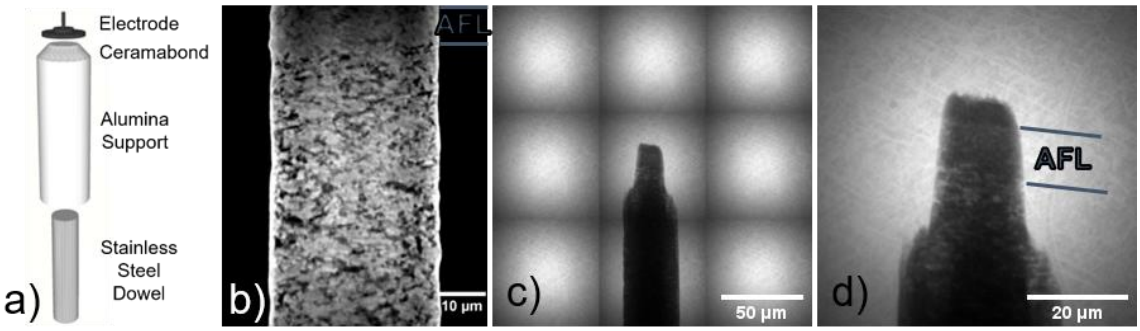

Figure 94: a) Schematic of electrode-ceramic mounting; b) XZ-orthoslice of fine pillar after laser milling; c) Radiograph mosaic of finer pillar after FIB milling; d) Radiograph showing FIB milled area, illustrating different densities of electrolyte, AFL and ASL

6.2 Annealing-Imaging Cycles

6.2.1 Annealing

The annealing procedure consisted of heating at 1150 °C, 700 °C or 900 °C under a dry atmosphere of forming gas (4% H_2 96% N_2) in a Carbolite GHA 12/300 tube furnace at a flow rate of 300 ml/min. The first temperature (1150 °C) was chosen as it is higher than that used in typical SOFC operation so would accelerate changes, but had also been used successfully in the literature in recent synchrotron X-ray nano-CT studies [183]. This temperature was also the maximum working temperature achievable within the readily accessible tube furnace used in this thesis. The next temperature investigated, 700 °C, was selected to be much lower than the first to try to avoid the large nickel agglomerates observed to form on the outside of the pillars, precluding reliable

metrics analysis. 900 °C was subsequently investigated as the changes seen at 700 °C appeared negligible, and thus as an attempt to access changes that would be measurable above image processing errors. A dry atmosphere was chosen to avoid potential complications that may arise from nickel loss, as reported previously [304][115].

The samples were positioned upright in small recesses CNC-machined into a bespoke holder made from pyrophyllite (Ceramic Substrates & Components Ltd, UK), which had been fired according to the manufacturer's guidelines. The samples were held this way both to ensure their exposure to the reducing atmosphere and to avoid pillar breakage. As noted in **Chapter 3**, a K-type, Inconel-sheathed thermocouple was used to monitor the temperature near the sample. In each case, after sample preparation was complete, X-ray nano-CT imaging was conducted to capture the *virgin* microstructure. Subsequently, each sample was exposed to its first annealing period of 4 h in the furnace. Once the sample had cooled passively (~4 h), the sample was transported to the X-ray nano-CT instrument and imaged again. Thereafter, the intention was to repeat this annealing-imaging process twice more, giving a heating profile similar to that shown in Figure 95, and yielding 4 data points per temperature investigated.

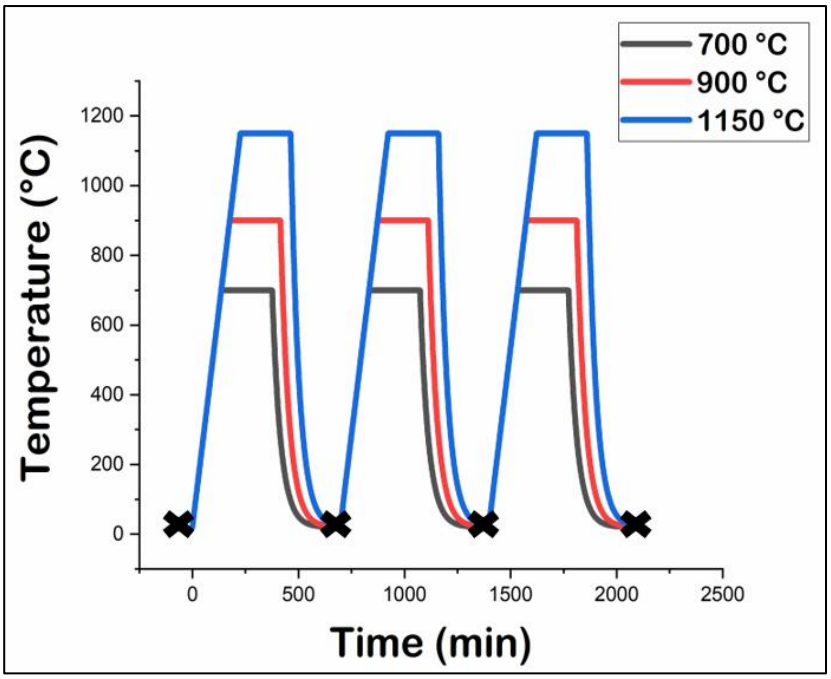

Figure 95: Schematic profile for planned imaging-annealing cycles (X = XCT imaging)

Due to issues encountered in the highest temperature case (see **Section 6.3.1.1**), only one annealing-imaging cycle was conducted after initial imaging

for 1150 °C. The data was found to be unsatisfactory for further analysis, both from a contrast perspective and due to loss of nickel from the internal AFL microstructure.

6.2.2 X-ray nano-CT acquisition

All imaging was carried out using the Zeiss Xradia 810 Ultra lab-based X-ray nano-CT, details about which are found in **Section 3.2.5.** X-ray acquisition was performed with conditions outlined in Table 24. In all cases, X-ray imaging was performed in LFOV mode such that the voxel dimension for all tomograms was 63.1 nm, giving a spatial resolution of approximately 165 nm [280], measured according to the principles outlined in [157]. The samples are denoted as previously stated, with information about the time and temperature of annealing appended in the form "_temperature_time" where temperature is given in °*C* and time in *h*.

Sample	Temperature / °C	Annealing time / h	AFL Diameter / µm	Projection Number	Exposure Time / s
2Va$_{F}$	-	0	18	2201	64
2Aa$_{F_1150_4}$	1150	4	18	1601	64
2Vb$_{F}$	-	0	14	1101	64
2Ab$_{F_700_4}$	700	4	14	1101	64
2Ab$_{F_700_8}$	700	8	14	1101	64
2Ab$_{F_700_12}$	700	12	14	1101	64
2Vc$_{F}$	-	0	14	1201	72
2Ac$_{F_900_4}$	900	4	14	1101	72
2Ac$_{F_900_8}$	900	8	14	1201	72
2Ac$_{F_900_12}$	900	12	14	1201	72

Table 24: Imaging parameters for samples exposed to annealing-imaging cycles

A long scan (~40 h) was performed on the first virgin sample (*Sample 2Va$_{F}$)* due to the availability of the instrument but it was found that this long duration negatively affected scan quality. The slight blurring that resulted was attributed to sample drift throughout the scan, possibly due to temperature variations from the stage or the outside environment. Nonetheless, the scan provided usable data (see **Section 6.3.1.1**), and the second scan reduced the number of projections to shorten the scan time. All scans in the 700 °C regime were conducted with the optimised parameters from work displayed in **Chapter 5**. Although the final fabricated pillar was similar in diameter, attempts were made to increase the overall signal-to-noise ratio by raising the exposure time to 72 s, to

further improve the reliability of three-phase segmentation of the Ni-YSZ AFL, without raising the scan time excessively.

6.3 Results & Discussion

6.3.1 Tomograms

All reconstructed scans are presented in this section for qualitative analysis. The first pillar inspected was *Sample 2Va$_F$* which was annealed for 4 h at 1150 °C and imaged again, resulting in the tomogram denoted as *Sample 2Aa$_{F_1150_4}$*. The other two samples, *Sample 2b$_F$* and *2c$_F$* are presented thereafter.

6.3.1.1 1150 °C

The first virgin sample (*Sample 2Va$_F$*) was scanned with high numbers of projections (2201) in an effort to ensure a high-quality reconstruction. However, the long duration of the scan led to a slight blurring of the tomogram, as seen in Figure 96 a). With the larger diameter of 18 µm, it is also clear that although there is evidence of two phases, the solid-phase contrast is not optimal, and as seen in **Chapter 5**, three-phase segmentation is likely to be highly erroneous. Nevertheless, the solid-pore contrast may be sufficient to extract a porous network and after annealing, the number of projections was lowered to prevent blurring in the second tomogram. A registered XZ-orthoslice of the annealed sample (*Sample 2Aa$_{F_1150_4}$*) is shown in Figure 96 b).

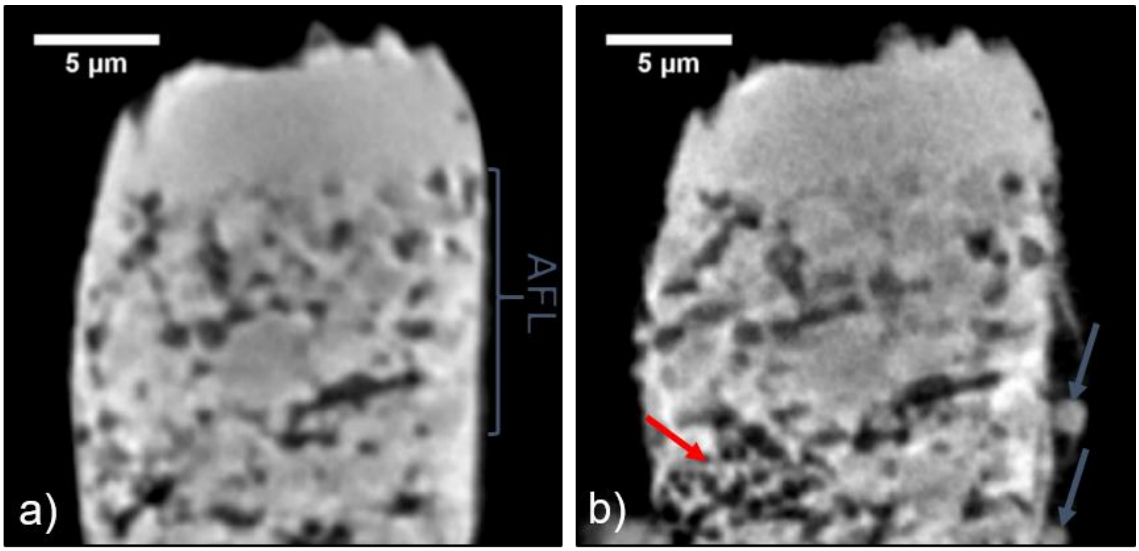

Figure 96: Registered pillar tomograms from 1150 °C regime, showing Electrolyte, AFL and ASL, a) virgin b) after 4 h anneal (*long scan)*

Some clear changes between samples are evident from the single registered slices presented in Figure 96. The first qualitative change to note is the appearance of

small nickel agglomerates on the exterior surfaces of the pillar (blue arrows). Moreover, there is a clear section of the pillar, towards the AFL-ASL interface, where a significant depletion of nickel can be seen (red arrow). However, to better visualise the impact of the short high-temperature anneal, radiographs of the annealed pillar are shown in Figure 97.

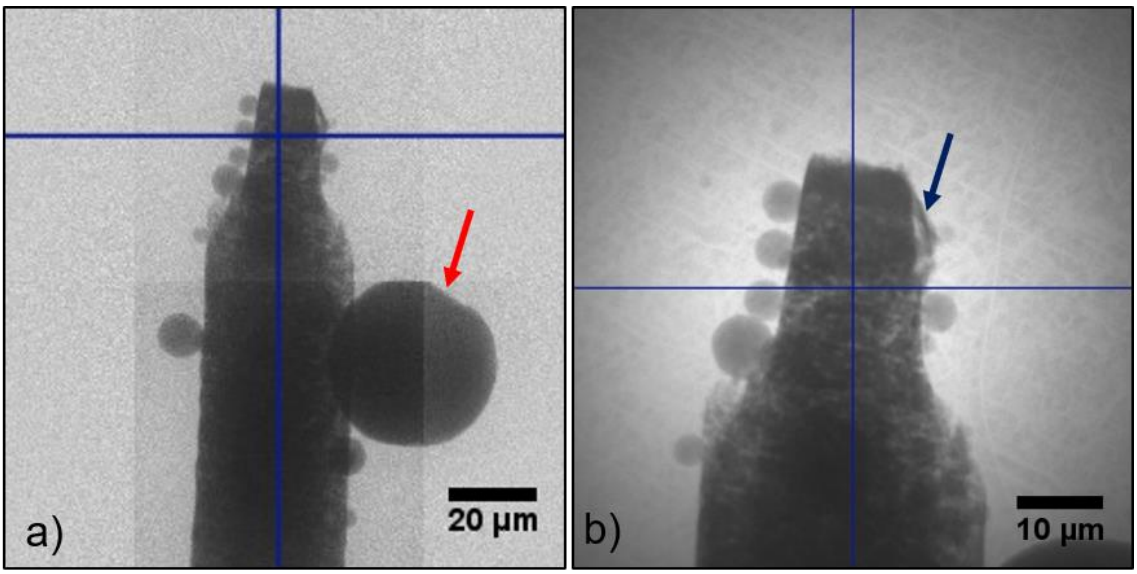

Figure 97: a) Mosaic of radiographs of Sample 2Aa$_{F_1150_4}$, showing large nickel agglomerates on exterior of pillar b) Single radiograph highlighting spherical nature of nickel agglomerates and their "egress" from constraining wall (blue arrow)

The exterior of the annealed pillar was covered in variously sized nickel agglomerates, as confirmed by SEM-EDX analysis. The diameters of the agglomerates varied, with the largest approximately 40 µm in diameter (red arrow), and several in the 5 – 10 µm range. The appearance of these large nickel agglomerates had been mentioned in brief in the literature before [315] and appears to result from a net flow of nickel from inside the electrode pillar to the outside, likely driven by the lowering of surface free energy. The depletion region seen in Figure 96 b) (red arrow) is an example of the microstructure left behind once the mobile nickel phase has agglomerated at one of the pillar surface nucleation sites.

Additionally, it was observed that a laser-damaged region, not removed during FIB-milling, was broken open by the agglomeration of nickel as indicated in Figure 97 b) (blue arrow). This phenomenon gives a qualitative understanding of the driving force behind the nickel coarsening process and highlights the need to remove all the

laser-affected zones around the sample pillars to better represent real anode-edge behaviour. 27 external nickel agglomerates from the top exterior of the pillar were segmented by simple thresholding giving rise to a distribution as shown in the volume rendering in Figure 98.

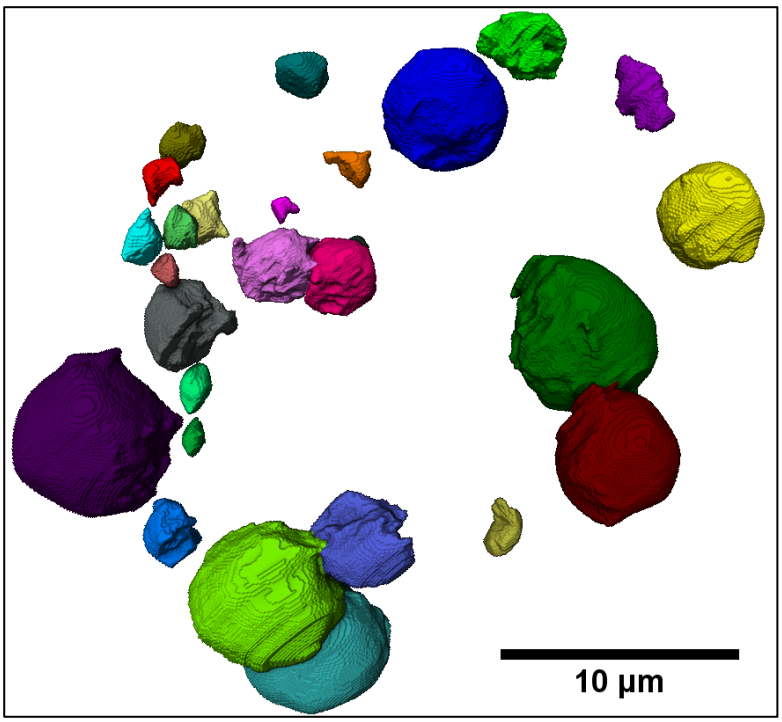

Figure 98: Volume rendering of a selection of nickel agglomerates found at the top of the exterior of annealed pillar, Sample $2Aa_{F\_1150\_4}$

A total of ~600 µm^3 of nickel was observed to form the agglomerates on the top outer edges of the milled pillar after 4 h annealing at 1150 °C. Given that the AFL has a maximum volume of ~2,500 µm^3, and nickel constitutes approximately 33% of this volume, the exuded nickel is approximately the three-quarters of the nickel volume available from the AFL. As appreciable amounts of nickel was observed to remain in the AFL, it is clear that a portion of the nickel agglomerate material came from the ASL beneath. Taking the average particle radius in the AFL as approximately 1 µm and assuming perfect sphericity, this would correspond to the disappearance, from the internal microstructure, of roughly 140 individual particles, and renders the ASL and AFL in the sampled volume unusable directly for microstructural evolution analysis. By voxel counting, the volumes and surface areas of each of the agglomerates were extracted and the equivalent particle radius (sphere) and sphericity were measured. The results are summarised in Table 25**.**

Metric	Min	Max	Mean	Standard Deviation
Volume (μm³)	0.4	128.0	21.9	34.1
Equivalent Radius (μm)	0.5	3.1	1.3	0.8
Surface Area (μm²)	3.2	133.0	33.2	36.8
Sphericity	0.7	1.0	0.9	0.1

Table 25: Extracted volume and surface area metrics from nickel agglomerates at top of Sample $2Aa_{F\_1150\_4}$ *pillar*

If all the agglomerates are modelled as spheres, the average equivalent radius is 1.3 μm ± 0.8 μm and the sphericity is 0.9 ± 0.1. Given that a sphericity of 1 is a perfect sphere, there is a reasonably narrow distribution of high sphericity in this case, which fits well with the observed spherical objects seen in Figure 98**.**

6.3.1.2 700 °C

To avoid the formation of large agglomerates which obscure the true internal changes in the AFL of the electrode pillar, a much lower temperature was selected (700 °C) for the second annealing regime. 4 registered XZ-orthoslices of the electrolyte-AFL-ASL section of each pillar are shown in Figure 99 displaying the minor microstructural evolution occurring after 4 h of annealing in each case.

Qualitatively, it is worth noting the almost complete cleavage of the nickel particle from the YSZ electrolyte, between the virgin and annealed (4 h) samples (red arrows). Although only minor change occurred thereafter, the morphology of this particle did appear to continue to evolve. This observation is consistent with the de-wetting behaviour reported previously [101][200].

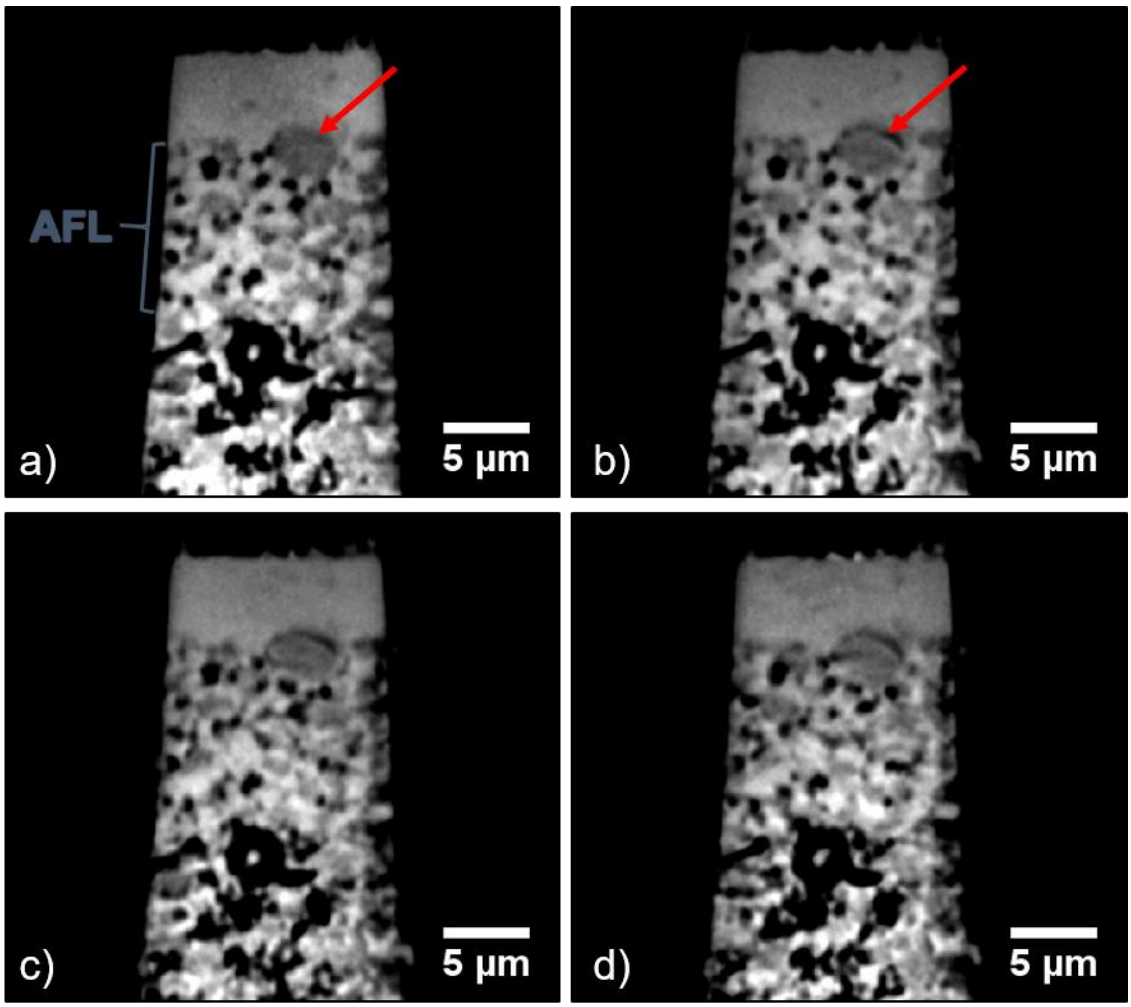

Figure 99: Registered pillar tomograms from 700 °C regime, showing Electrolyte, AFL and ASL, a) virgin; *b) after 4 h annealing; c) after 8 h annealing; d) after 12 h annealing*

Major nickel agglomerates on the exterior of the sample pillar were avoided at this lower annealing temperature, although some surface mobility was detectable, as shown in the full tomograms shown side-by-side in Figure 100.

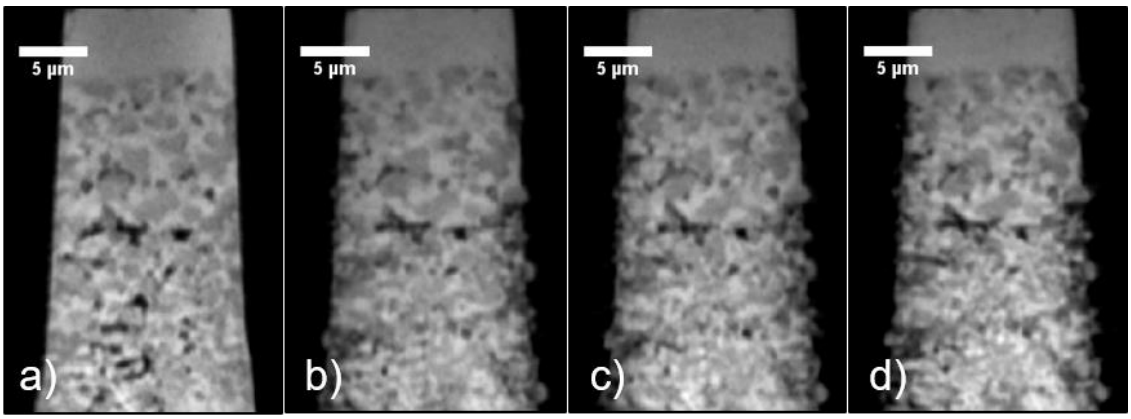

Figure 100: Registered pillar tomograms from 700 °C regime, illustrating the minor surface mobility at this lower temperature a) virgin*; b) after 4 h annealing; c) after 8 h annealing; d) after 12 h annealing*

6.3.1.3 900 °C

To both avoid large nickel agglomerates and effect sufficient microstructural evolution for unambiguous analysis, an intermediate temperature of 900 °C was chosen for the final temperature regime. It should be noted that the initial microstructure (*Sample 2Vc$_F$*) has a distinctly different morphology from that reduced at the higher temperature and longer time (*Sample 2Vb$_F$*). This is likely due to the inherent coarsening/densification of nickel that occurs during the reduction dwell time: here, internal porosity is retained and is clearly visible and useful for image registration purposes. 4 registered XZ-orthoslices of the Electrolyte-AFL-ASL section of each pillar are shown in Figure 101 displaying significant microstructural evolution occurring after 4 h of annealing in each case.

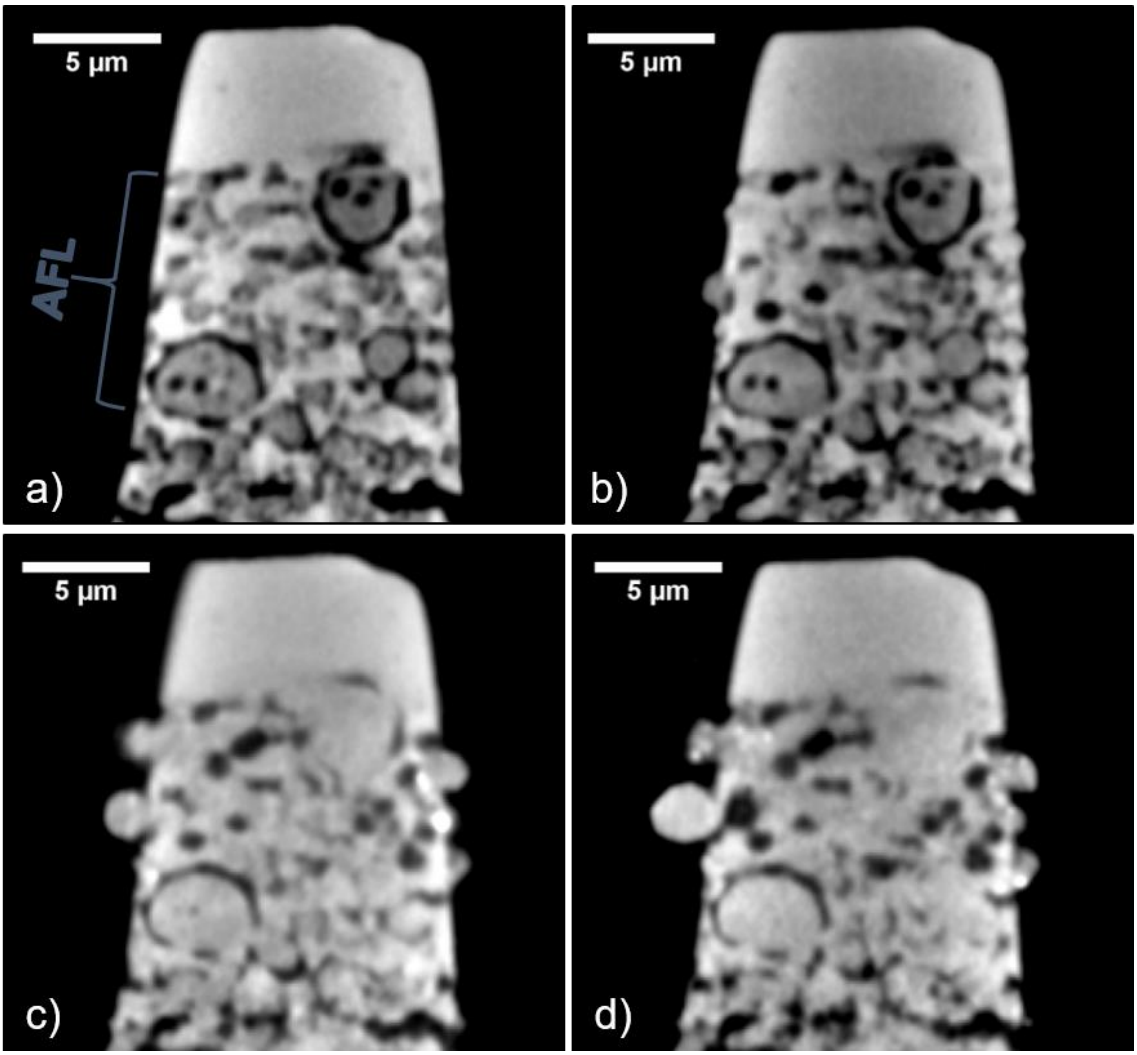

Figure 101: Registered pillar tomograms from 900 °C regime, showing Electrolyte, AFL and ASL, a) virgin b) after 4 h anneal, c) after 8 h anneal, d) after 12 h anneal

However, as is evident from Figure 101, it appears that the final two tomograms represent a loss in solid-phase contrast. It also appears, on first impression, that since numerous particles appeared to have grown (cavity size is seen to reduce), that this morphological change would be in keeping with oxidation of nickel to nickel (II) oxide, which is usually accompanied by a ~70% volume expansion. However, on oxidation, the density, ρ, of the particles should be reduced from ~8.9 to ~6.7 gcm^{-3}, which would manifest in a darker grayscale value given that the average electron density would also be reduced. It is possible that solid-phase contrast was lost due to uncontrolled instrument parameters, as it has been previously observed that the same exposure time for the same sample can give rise to greater or lesser solid-phase contrast. Alternatively, contamination of the nickel phase by denser materials, such as a small amount of gold used during sample preparation, may help explain the change in contrast.

6.3.2 Image Processing

6.3.2.1 Standard Segmentation

The reconstructed volumes were imported into Avizo and in the first instance these volumes were registered using the “Register Images” module which computes a transformation to register two image data sets (all tomograms relative to the starting tomogram), using an iterative optimization algorithm, by starting at a coarse resampling of the dataset, and proceeding to finer resolutions, by means of a “mutual information” approach [302]. From these full registered datasets, the largest cubic volume from the AFL was extracted, avoiding the outer surfaces. This procedure was followed to both avoid ambiguities between real pore space and air external to the pillar and to prevent inclusion of any growing nickel agglomerates nucleated on the outer surfaces. Standard segmentation procedures, including simple thresholding and the watershed algorithm, could then be applied to the cubic AFL regions.

6.3.2.2 Advanced (Iterative) Segmentation

The fidelity of segmentation when processing X-ray CT data is crucial. In the 1150 °C regime, the three-phases, although distinguishable by eye, are not easily segmentable, and only a binary segmentation is undertaken here. By visual inspection,

the three phases are clearly defined for both the 700 and 900 °C regimes, but unfortunately simple grayscale thresholding procedures or more complex seeding/watershed procedures did not give rise to reliable segmentations of the two solid phases. On the other hand, a more facile binary segmentation can be made as the pore-solid boundaries are well-defined, thus permitting access to monitoring of the porous network.

For the more difficult ternary segmentation, a multi-software iterative procedure was developed, using python-based machine-learning freeware, Ilastik [262], (Ilastik, University of Heidelberg, Germany) alongside, Avizo. Balancing time and accuracy, the procedure outlined in Figure 102 was followed to ensure reliable comparison between tomograms, particularly key when inspecting small changes at modest (700 °C) annealing temperatures. This involved the key step of using the final ternary segmentation from one dataset as the training dataset for the initial Ilastik segmentation of the next dataset.

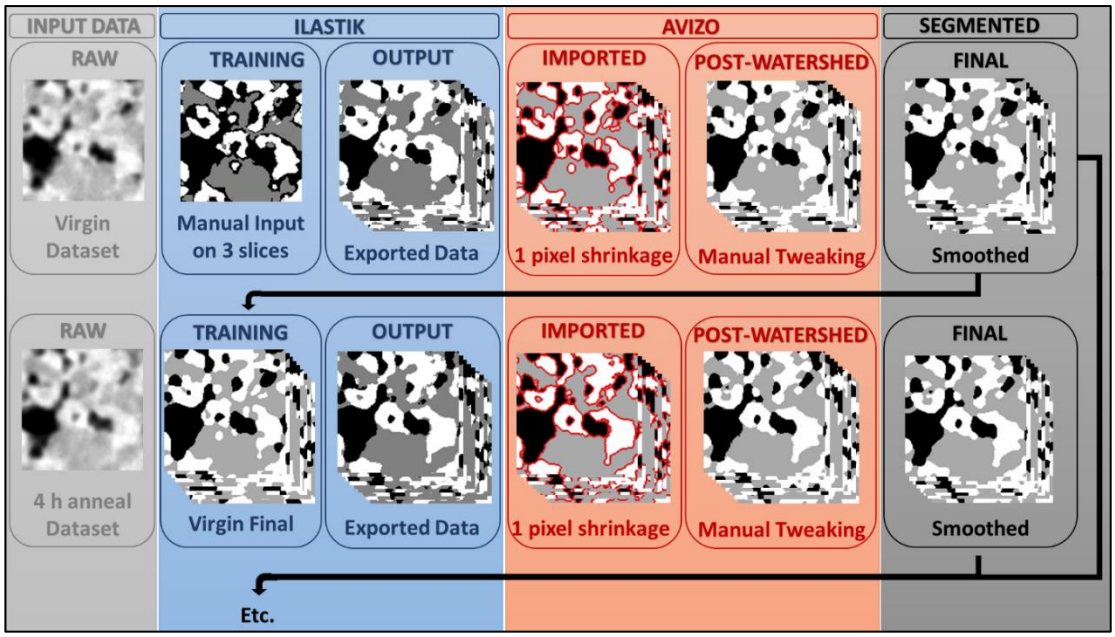

Figure 102: Schematic of iterative segmentation approach: a) initial manual training on virgin dataset; b) shrinking each phase of the output; c) watershed segmentation; d) minor manual tweaking and smoothing; e) use result as Ilastik input for the next dataset

6.3.3 Image Analysis

6.3.3.1 Simple global metrics

A raw sub-volume was extracted from the AFL of *Sample 2Va$_F$*, comprising 160 × 160 × 128 voxels, with a voxel dimension of 63.1 nm, giving a total sampled

volume of ~825 µm^3. Using simple thresholding and 2 h manual tweaking at ambiguous interfaces, a binary segmentation from the virgin sample pillar was achieved, and an example orthoslice, and its overlaid segmentation, is shown in Figure 103.

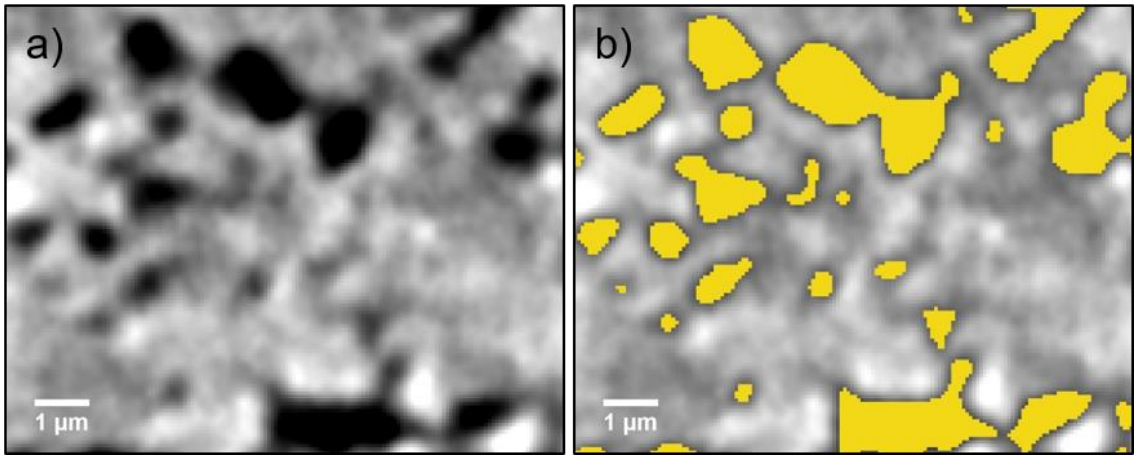

Figure 103: a) YZ-orthoslice from Sample 2Va$_F$*; b) Binary segmentation overlaid on YZ-orthoslice*

Simple metrics analysis gave the results shown in Table 26, including tortuosity factor analysis. It was found that in two directions (X- and Z-) there was no percolation.

Phase	Volume (µm^3)	Phase Fraction (%)	Interfacial Area Pore-Solid (µm^2)	VSIA (µm^{-1}) Pore-Solid	Tortuosity Factor		
					X-	Y-	Z-
Pore	136.6	16.6	745.0	0.90	∞	26.6	∞
Solid	686.9	83.4			1.1	1.1	1.2

Table 26: Simple metrics extracted from AFL region of Sample 2Va$_F$

Continuous pore size distribution (cPSD) analysis was undertaken on the segmented phase, according to the method outlined in **Chapter 3**. The results are displayed in Figure 104. The r50 value extracted from these results was 353 nm, giving an estimate of the average "pore diameter" of approximately 700 nm.

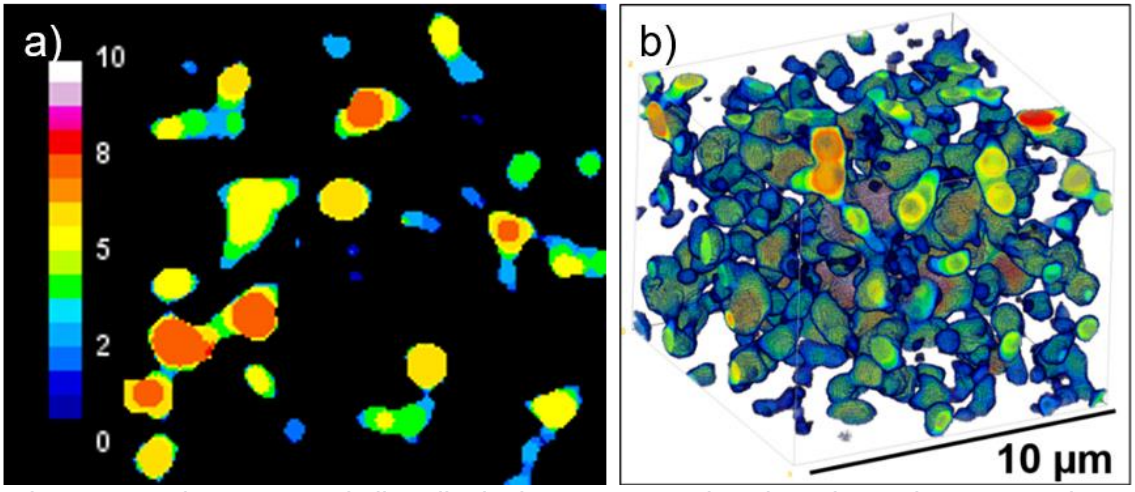

Figure 104: a) Segmented slice displaying cPSD results where legend corresponds to radius in pixels (63.1 nm each); b) 3D volume rendering of the same

Given the major loss of nickel from the interior volume of the AFL, and the poor solid-phase contrast given by this slightly wider pillar, segmentation of the aged pillar is not considered reliable and is not included here.

A raw sub-volume was extracted from the AFL of the slightly thinner *Sample 2Vb$_F$* pillar, comprising 128 × 128 × 128 voxels, with a voxel dimension of 63.1 nm, giving a total sampled volume of ~525 µm^3. In the 700 °C regime, only minor evolution in the microstructure was observed across a total of 12 h of annealing. Firstly, the porous network was segmented from each tomogram using a combination of Avizo and Ilastik, and an example slice with its corresponding smoothed segmented slice is presented in Figure 105.

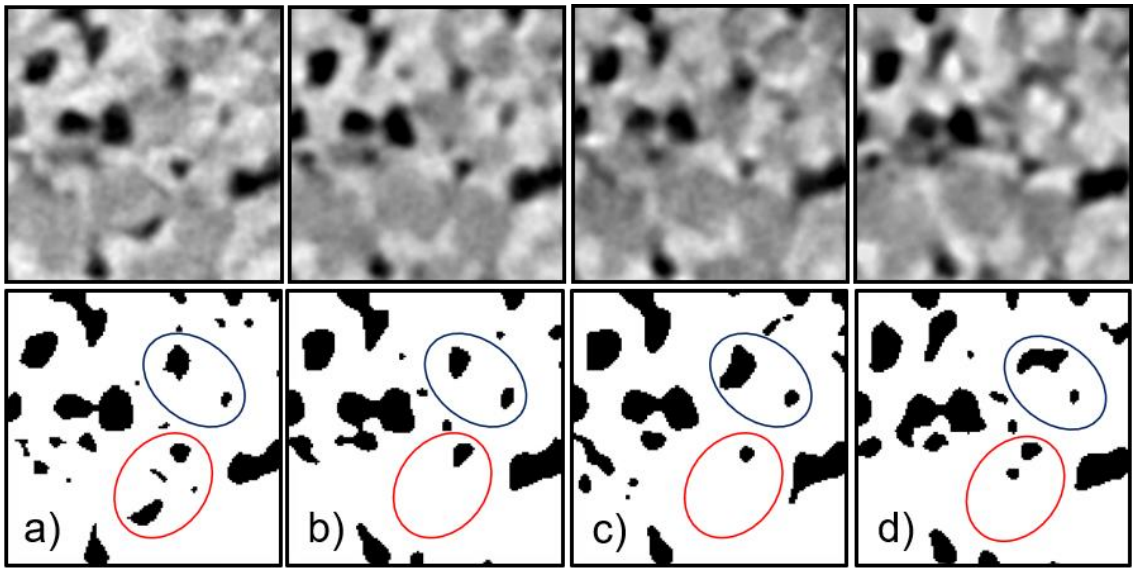

Figure 105: XY-orthoslices from each tomogram in the 700 °C regime: a) 0 h; b) 4 h c) 8 h; d) 12 h; with their corresponding binary Avizo/Ilastik segmentation (porosity in black). Some minor changes are highlighted in blue and red circles

The simple metrics extracted from the binary segmentations are given in Table 27.

Metric	0 h		4 h		8 h		12 h	
	Pore	Solid	Pore	Solid	Pore	Solid	Pore	Solid
Vol. Fraction (%)	13.1	86.9	13.9	86.1	14.1	85.9	14.7	85.3
Pore VSSA (µm^{-2})	0.9		0.8		0.9		0.9	
Tortuosity Factor								
x	39.4	1.1	16.5	1.1	14.8	1.1	20.5	1.1
y	∞	1.1	∞	1.1	118.5	1.1	∞	1.1
z	∞	1.1	∞	1.1	23.1	1.1	∞	1.2
Percolation (%)								
x	56	100	58	100	65	100	57	100
y	0	100	0	100	65	100	0	100
z	0	100	0	100	65	100	0	100

Table 27: Simple binary metrics from Ilastik segmentation of Sample 2b$_F$

Using the machine-learning approach (Ilastik), with an initial training set from using Avizo to place seeds in each phase, gave a binary segmentation that appeared to adequately capture the porous network, by visual observation of the individual slices, as shown in Figure 105. Comparing the extracted porosity from *Sample 2Vb$_F$* with that from *Sample 2Va$_F$* (13.1% versus 16.6%) showed broad agreement, and the volume-specific surface area showed excellent agreement (0.9 versus 0.9 μm^{-2}). The former discrepancy may have come from the inclusion of a very large pore in the larger *Sample 2Vb$_F$* volume, which is shown in Figure 106, which constituted 30.8 μm^3 or 3.7% of the total volume.

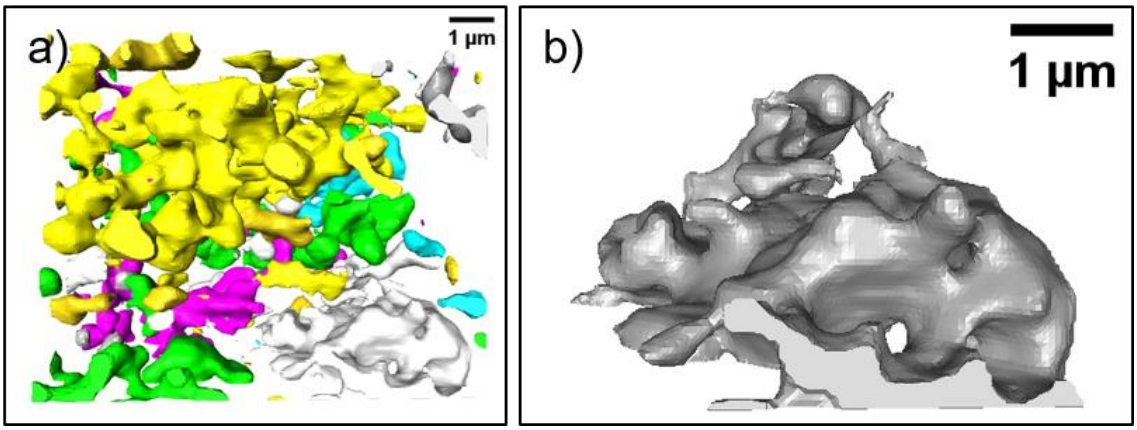

Figure 106: a) Surface rendering of all pore networks from Sample 2Va$_F$*, b) Surface rendering of suspect pore, likely to be an artefact of the AFL-ASL interface*

This was likely due to the imperfect delineation between AFL and ASL, such that a larger "ASL-like" pore had been included in the analysis. Substitution of this volume by a porous solid (at the level seen in *Sample 2Vb$_F$*) returned an overall corrected porosity of 13.3%, which matched well (13.1%). Continuous pore size distribution (cPSD) analysis gave an r50 value of 325 nm which represented only a 4% discrepancy with *Sample 2Va$_F$* (325 nm versus 353 nm).

The average porosity measured across all 4 binary segmentations was 14.0% ± 0.7%. The values for each of the consecutive time steps did not suggest a significant porosity change (see Figure 107). In fact, the source of this variation more likely stemmed from the compound errors of image acquisition (very low), image processing (low) and image segmentation (medium). Alternatively, as it had already been seen that nickel has a propensity to migrate towards the edges of the pillar, the small porosity

increase may have been real, but further experiments would be required to confirm this, as the changes were subtle and likely conflated with other experimental errors.

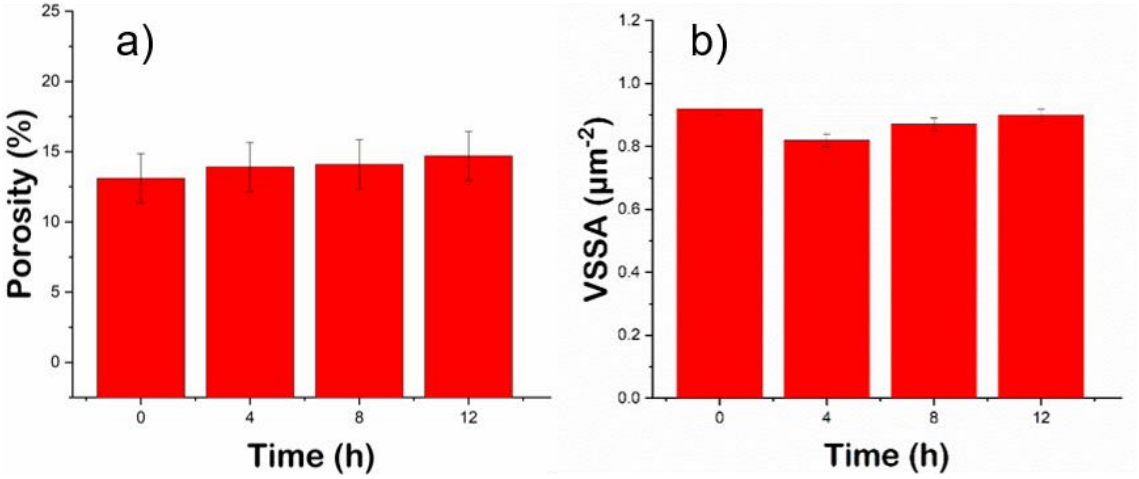

Figure 107: Plot of Sample 2b a) *porosity & b) VSSA$_{Pore}$ over 12 h annealing at 700 °C*

The changes in VSSA did not show a monotonic trend but were significant according to the estimated VSSA segmentation error (± 0.02 µm^{-1}) and may have been suggestive of subtle changes as a result of the mobile nickel network. There was an initial drop in VSSA in the very early stages (0-4 h) and then a slow increase in VSSA as annealing continued. This may be indicative of two mechanisms at play, one at a very short timescale and one at a longer timescale. Potentially, the initial reorganisation of the microstructure might incur a loss in VSSA$_{Pore}$ as high surface energy features are highly mobile. Subsequently, a longer-term ageing mechanism, wherein nickel mobility accumulates to give rise to more elongated pores, could manifest as a shallow incline in VSSA$_{Pore}$ over a longer time span.

The tortuosity factor was very sensitive to these small changes in porosity, as evidenced by the values given in Table 27**,** and shown in Figure 108. In the X-direction, the volume remained percolated at all time steps, and the tortuosity value dropped from a high value (0 – 4h), marginally decreased at 8 h and then rose again at 12 h. This initial behaviour is consistent with a reorganisation of the microstructure such that mass transport is initially improved. The subsequent behaviour might have been expected to follow a trend of becoming steadily more tortuous, but the 8 h value appeared lower than anticipated. However, tortuosity factor is highly sensitive to connectivity, and both the Y- and Z- directions, which did not percolate at the other time steps, did give finite

tortuosity factors (were percolated) at 8 h. This was suggestive that a vital new connection had been made, which was subsequently lost by 12 h. Overall, due to the subtlety of the changes in this microstructure, annealed at the conservative temperature of 700 °C, these observations are somewhat speculative and further analysis would be required to support these claims.

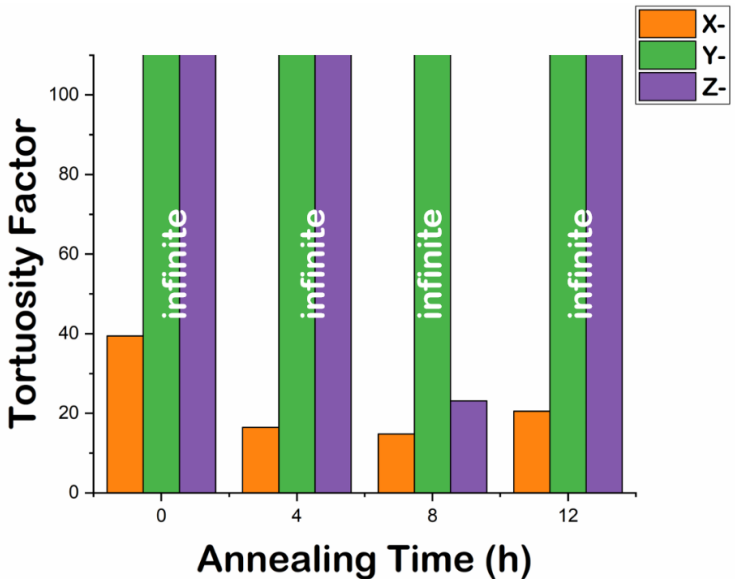

Figure 108: Plot tracking the evolution of pore tortuosity factor as a function of annealing time under the 700 °C regime

As it is known that there are pores below the detection limit of the instrument, there is a strong likelihood that there was porosity encapsulated within the dark regions that remained assigned to the solid phase. RVE analysis was undertaken based on the binarised images and the results for the porous phase for each time step are shown in Table 28-Table 31 and Figure 109**.**

Volume Fraction		**0.1**	**0.3**	**0.5**	**0.7**	**0.9**	**1**
Porosity		0.19	0.16	0.15	0.14	0.13	0.13
Tortuosity Factor	*Direction*						
Pore	*X-*	12.9	40.3	29.5	38.2	38.1	39.4
	Y-	7.1	19.8	24.7	36.9	43.3	-
	Z-	9.1	18.8	23.7	-	-	-

Table 28: Values from Pore RVE analysis of Sample 2Vb$_F$ *Ilastik segmentation*

Volume Fraction		**0.1**	**0.3**	**0.5**	**0.7**	**0.9**	**1**
Porosity		0.23	0.18	0.16	0.15	0.14	0.14
Tortuosity Factor	*Direction*						
Pore	*X-*	5.7	10.9	11.6	15.4	15.9	16.5
	Y-	6.8	11.4	-	-	-	-
	Z-	4.1	8.0	13.6	-	-	-

Table 29: Values from Pore RVE analysis of Sample 2Ab$_{F_700_4}$ *Ilastik segmentation*

Volume Fraction		0.1	0.3	0.5	0.7	0.9	1
Porosity		0.22	0.18	0.16	0.15	0.14	0.14
Tortuosity Factor	*Direction*						
Pore	*X-*	11.6	6.9	7.1	10.0	13.6	14.8
	Y-	5.0	18.7	106.0	109.0	115.0	119
	Z-	5.8	7.0	11.9	31.4	34.6	23.1

Table 30: Values from Pore RVE analysis of Sample $2Ab_{F\_700\_8}$ *Ilastik segmentation*

Volume Fraction		0.1	0.3	0.5	0.7	0.9	1
Porosity		0.21	0.17	0.15	0.15	0.15	0.15
Tortuosity Factor	*Direction*						
Pore	*X-*	6.9	10.4	10.8	12.9	17.9	20.5
	Y-	8.0	14.4	-	-	-	-
	Z-	7.6	10.5	18.7	-	-	-

Table 31: Values from Pore RVE analysis of Sample $2Ab_{F\_700\_12}$ *Ilastik segmentation*

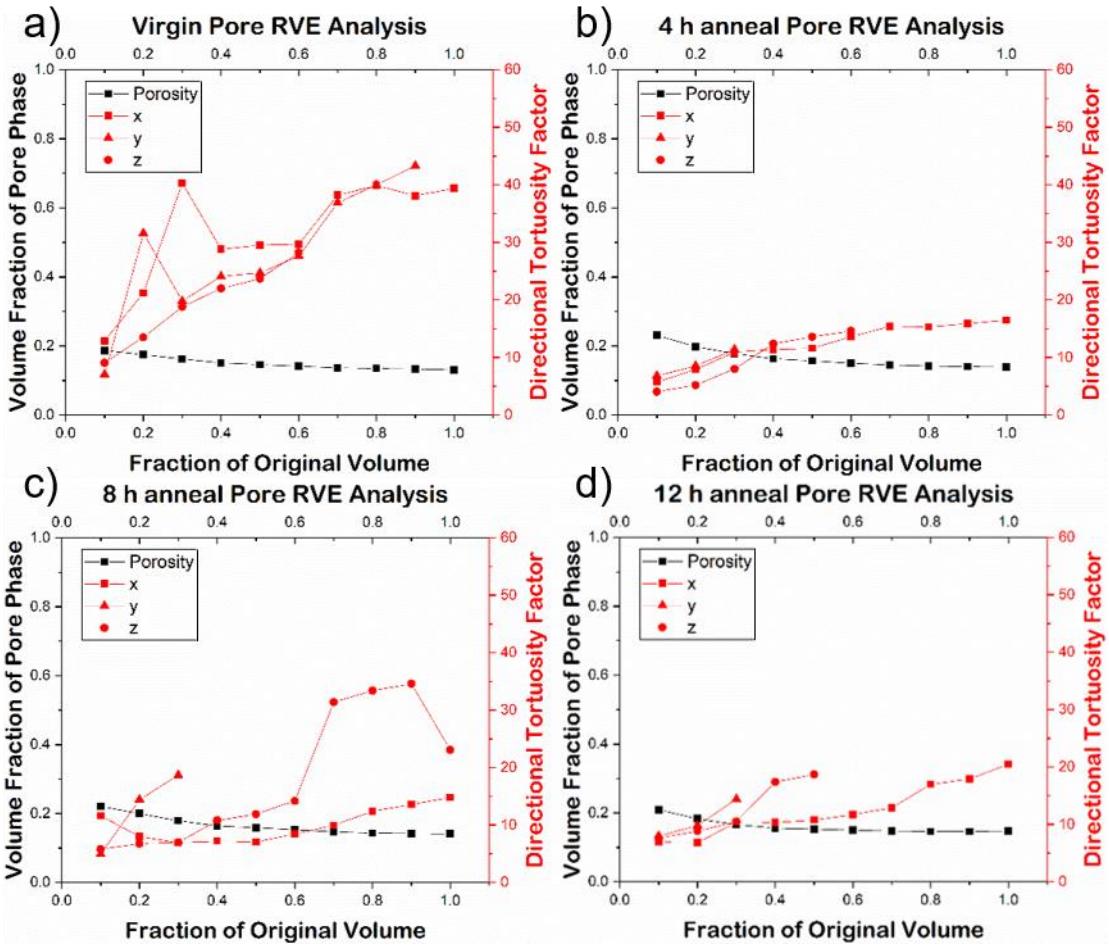

Figure 109: Plots displaying the Ilastik Pore RVE analysis of Sample 2b *data: a) 0 h; b) 4 h; c) 8 h; d) 12 h*

From RVE analysis, the full volume was shown to be sufficient to represent the phase fraction for the pore phase, for all timesteps the value is approximately constant, according to 10% steps in volume dimension, falling only slightly with the last 4 h of

annealing (12 h anneal). Given a 4% tolerance (see **Chapter 4**), the following volumes were shown to be sufficient to represent the pore phase fraction:

Sample	$2Vb_F$	$2Ab_{F\_700\_4}$	$2Ab_{F\_700\_8}$	$2Ab_{F\_700\_}$
Fractional Dimension	0.8	0.8	0.8	0.6
Representative Volume	~420 μm^3	~420 μm^3	~420 μm^3	~320 μm^3

Table 32: RVE sizes for porosity, for various timesteps of 700 °C annealing regime

However, the volume investigated was not sufficient to capture a representative value for tortuosity factor – only the X-direction of *Sample* $2Ab_{F\_700\_4}$ converged to give a value within a 4% tolerance level (at $x = 0.9$, ~480 μm^3). For this sparsely distributed phase, it is important to note that the extracted tortuosity values are unlikely to be representative.

On comparison with the ASL pore tortuosity values extracted in **Chapter 5** (ca. 4-7), the pores in the AFL investigated here were more tortuous (ca. 15-40 in the fully percolated direction). This is consistent with the finer microstructure of the anode functional layer. However, the degree to which this constrictivity can be tolerated in the electrochemically active region is not clear from this analysis.

Next, a ternary segmentation was conducted using the iterative procedure outlined in **Section 6.3.2.2**. The first step was to provide an initial training set for the ternary segmentation of *Sample* $2Vb_F$ which was achieved using the binary segmentation plus conservative grayscale thresholding for the distinction of Ni from YSZ in Avizo. This allowed for Ilastik to allocate the unsegmented voxels based on the training data, which provided, after minor morphological operations, the ternary segmented image shown in Figure 110 a). This image was then used as a training dataset for the subsequent segmentation of *Sample* $2Ab_{F\_700\_4}$ which is shown in Figure 110 b). This was repeated for the two other time steps and the extracted three-phase simple metrics are displayed in Table 33 - Table 36. It is worth noting there is still visible discrepancy, but the segmentation is improved versus the segmentation conducted purely in Avizo.

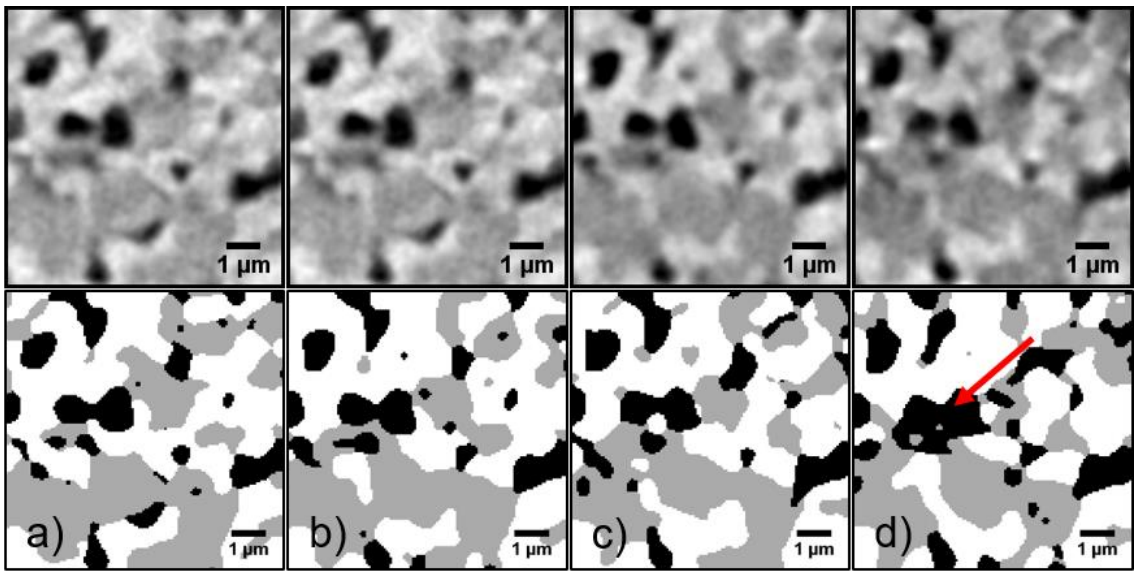

Figure 110: Raw and segmented XY-orthoslice from a) virgin*; b) 4 h anneal; c) 8 h anneal; and d) 12 h anneal samples, where black is pore, grey is nickel, white is YSZ*

Phase	Volume (μm^3)	Phase Fraction (%)	VSSA (μm^{-1})	Interface	VSIA (μm^{-1})	ρ_{TPB} (μm^{-2})
Pore	75.2	14.2	0.9	**Pore-Nickel**	0.4	**Active: 2.4**
Nickel	199.2	37.7	1.6	**Nickel-YSZ**	1.2	
YSZ	253.8	48.1	1.6	**YSZ-Pore**	0.5	
Total	528.2	100.0	-	**Pore-Nickel-YSZ**	-	**Total: 3.9**

Table 33: Estimated ternary metrics from Ilastik segmentation of Sample $2Vb_F$

Phase	Volume (μm^3)	Phase Fraction (%)	VSSA (μm^{-1})	Interface	VSIA (μm^{-1})	ρ_{TPB} (μm^{-2})
Pore	76.1	14.4	0.9	**Pore-Nickel**	0.4	**Active: 1.9**
Nickel	180.4	34.2	1.5	**Nickel-YSZ**	1.1	
YSZ	271.1	51.4	1.6	**YSZ-Pore**	0.5	
Total	528.2	100.0	-	**Pore-Nickel-YSZ**	-	**Total: 3.8**

Table 34: Estimated ternary metrics from Ilastik segmentation of Sample $2Ab_{F\_700\_4}$

Phase	Volume (μm^3)	Phase Fraction (%)	VSSA (μm^{-1})	Interface	VSIA (μm^{-1})	ρ_{TPB} (μm^{-2})
Pore	81.7	15.5	1.0	**Pore-Nickel**	0.5	**Active: 3.2**
Nickel	176.5	33.4	1.7	**Nickel-YSZ**	1.2	
8YSZ	270.0	51.1	1.7	**YSZ-Pore**	0.5	
Total	528.2	100.0	-	**Pore-Nickel-YSZ**	-	**Total: 4.7**

Table 35: Estimated ternary metrics from Ilastik segmentation of Sample $2Ab_{F\_700\_8}$

Phase	Volume (μm^3)	Phase Fraction (%)	VSSA (μm^{-1})	Interface	VSIA (μm^{-1})	ρ_{TPB} (μm^{-2})
Pore	102.4	19.4	1.2	**Pore-Nickel**	0.7	**Active: 3.6**
Nickel	199.4	37.8	1.9	**Nickel-YSZ**	1.2	
8YSZ	226.4	42.9	1.7	**YSZ-Pore**	0.5	
Total	528.2	100.0	-	**Pore-Nickel-YSZ**	-	**Total: 5.0**

Table 36: Estimated ternary metrics from Ilastik segmentation of Sample $2Ab_{F\_700\_12}$

Using this approach, the segmentation procedure was straightforward and required little manual allocation of voxels to phases. However, small changes in the acquisition or processing of the image may give rise to erroneous results when training datasets are only applied to other tomograms, and do not constitute training on the

dataset in question. In this case (700 °C regime), the final segmentation of the *Sample 2Ab$_{F_700_12}$* appeared to over-segment the pore phase, both by visual comparison (see red arrow in Figure 110 d)) with the processed image and by volume analysis. It is worth emphasising that although the above ternary segmentations (Figure 110) resemble the raw images, there are clear limitations due to the limited solid-phase contrast. For such minor microstructural changes, the segmentation procedure may not give rise to sufficiently accurate metrics for conclusive analysis.

On comparing the pore phase fractions output from the ternary segmentation for each sample, with those output from the binary segmentation, however, the discrepancy was low. Excluding the erroneous result for *Sample 2Ab$_{F_700_12}$*, the deviation was within 5% and the value from the ternary segmentation the *Sample 2Vb$_F$* (14.2%) was between the upper and lower bounds set by the binary segmentation of the same and that of *Sample 2Va$_F$* [13.1%, 16.6%]. The volume fraction and VSSA evolution is shown in Figure 111.

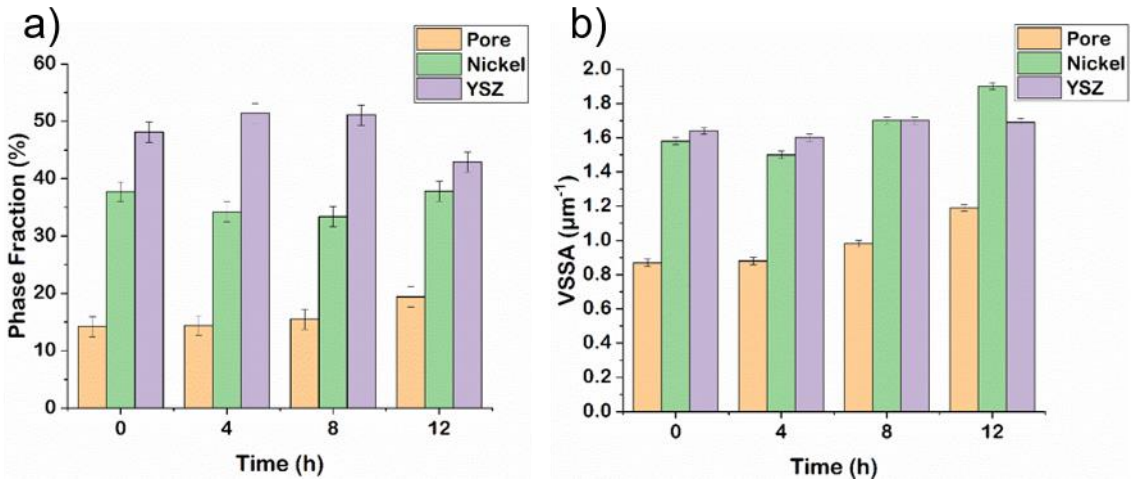

Figure 111: Plots displaying the evolution of a) phase fraction and b) VSSA with time under the 700 °C regime, plotted with errors from previous segmentation comparisons

Barring the erroneously segmented 12 h annealing result, the YSZ volume fraction was more or less constant at approximately 50% ± 2%, with nickel changing only slightly throughout annealing. However, due to the very subtle changes at this temperature, clear monotonic trends in particular metrics were not forthcoming, and the variation seen in Figure 111 is thought to be due to the composite errors associated with acquisition, processing and segmentation. Similarly, the VSSA values did not change

dramatically, apart from for the final sample, which is thought to be due to the significantly increased segmentation error. The evolution of VSIA and TPB density (total, active and %Active) are shown in Figure 112. It is worth underlining that although these results illustrate a procedure that can be used to monitor microstructural evolution for Ni-YSZ AFLs using lab-based X-ray nano-CT instruments, the very minor microstructural evolution which occurs over 12 h at 700 °C renders the results suggestive rather than conclusive.

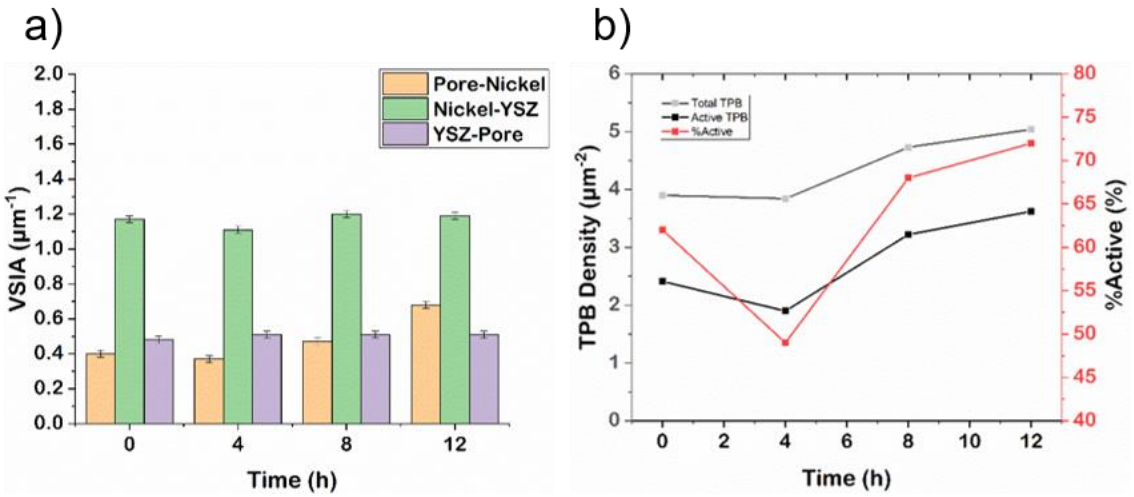

Figure 112: Plots displaying the evolution of a) VSIA and b) TPB density with time under the 700 °C regime (latter has unknown errors)

The extracted absolute TPB values were similar in magnitude to the values reported in the literature [294][316]. Interestingly, the total TPB remained constant over the first 4 h, whereas the active TPB dropped, which could be caused by very minor microstructural changes leading to disconnections in one or more of the three vital networks. However, the general trend after this initial behaviour was to increase both in total and active TPB, showing an increased proportion in active TPB at the same time. This could help to explain the initial performance increase observed in the literature [84][317][105]. However, due to the low annealing temperature, these microstructural changes are very subtle and thus this analysis is particularly susceptible to segmentation error. For that reason, a higher temperature was selected, between 700 and 1150 °C for the final annealing-imaging series.

As in the 700 °C regime, a raw sub-volume was extracted from the AFL of *Sample 2Vc$_F$* (900 °C regime), comprising 128 × 128 × 128 voxels, with a voxel

dimension of 63.1 nm, giving a total sampled volume of ~525 μm^3. As noted in **Section 6.3.1.3**, solid-phase contrast was lost in the final two tomograms, which will be discussed in a later section. However, a binary segmentation was performed using Avizo and Ilastik, the results of which are shown in Figure 113.

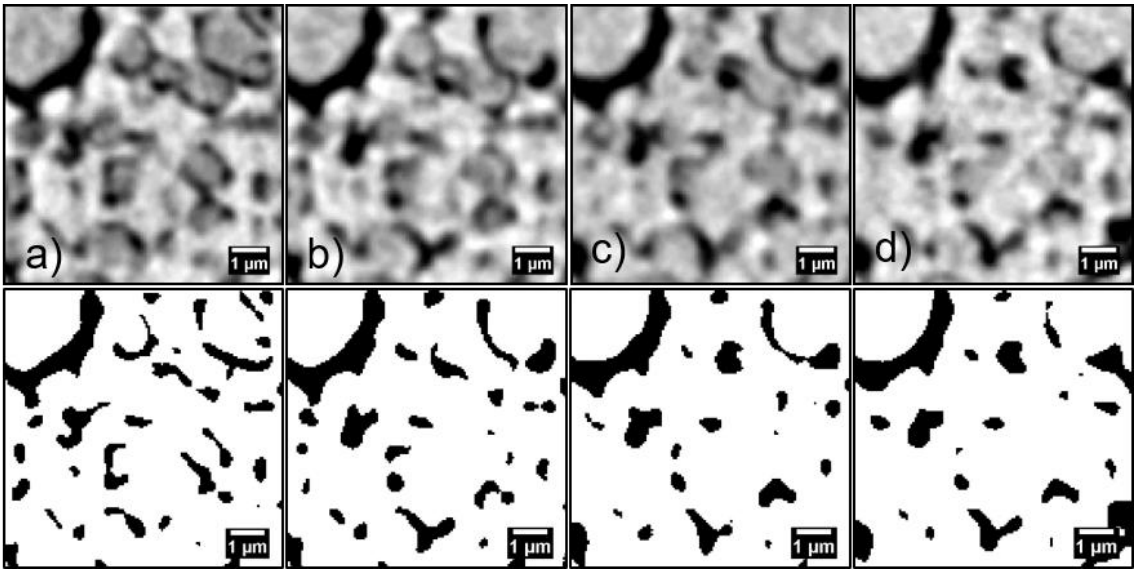

Figure 113: XY-orthoslices from each tomogram in the 900 °C regime: a) 0 h; b) 4 h c) 8 h; d) 12 h; with their corresponding binary Avizo/Ilastik segmentation (porosity in black)

The simple metrics extracted from the binary segmentations are given in Table 37.

Metric	0 h		4 h		8 h		12 h	
	Pore	Solid	Pore	Solid	Pore	Solid	Pore	Solid
Vol. Fraction (%)	13.8	86.2	14.0	86.0	11.9	88.1	11.6	88.4
Pore VSSA (μm^{-2})	1.2		1.1		0.9		0.8	
Tortuosity Factor								
x	65.5	1.2	183.2	1.2	∞	1.1	∞	1.1
y	32.0	1.2	30.2	1.2	∞	1.2	∞	1.1
z	84.8	1.2	53.6	1.2	∞	1.1	∞	1.1
Percolation (%)								
x	74.4	100.0	57.9	100.0	0	100.0	0	100.0
y	74.4	100.0	57.9	100.0	0	100.0	0	100.0
z	74.4	100.0	57.9	100.0	0	100.0	0	100.0

Table 37: Simple binary metrics from Ilastik segmentation of Sample $2c_F$

By comparison, the extracted porosity from *Sample 2Vc$_F$* compared most favourably with that extracted from *Sample 2Vb$_F$* (13.8% versus 13.1%), showing excellent agreement and suggesting the higher porosity value from *Sample 2Va$_F$* was erroneously high due to over-segmentation of the pore phase. However, the $VSSA_{Pore}$ for the virgin sample subjected to 900 °C annealing was found to be significantly higher than the $VSSA_{Pore}$ values (1.2 μm^{-1} versus 0.9 μm^{-1}) from either of the previous samples

and reflected the different morphology observable in Figure 113. Continuous pore size distribution (cPSD) analysis gave an r50 value of 213 nm which represented a 40% reduction with respect to *Sample 2Va$_F$ (*353 nm) and a 34% reduction compared with *Sample 2Vb$_F$* (325 nm). This smaller size of the pores was in keeping with the visibly different microstructure, wherein the pores appeared to more closely represent voids left by the reduction of nickel (II) oxide to nickel than in the previous microstructures investigated.

A distinct change was observed between 4 and 8 h, which was observed simultaneously as the loss of solid-phase contrast in the tomograms. This change corresponded to a drop in porosity and volume-specific surface area. The overall evolution of both metrics is shown in Figure 114, wherein the error shown for phase fraction and VSSA are ±0.6% and ±0.05 μm^{-1} given the extracted results from a segmentation of *Sample 2Vc$_F$* purely using Avizo, which provided an estimate of the segmentation error.

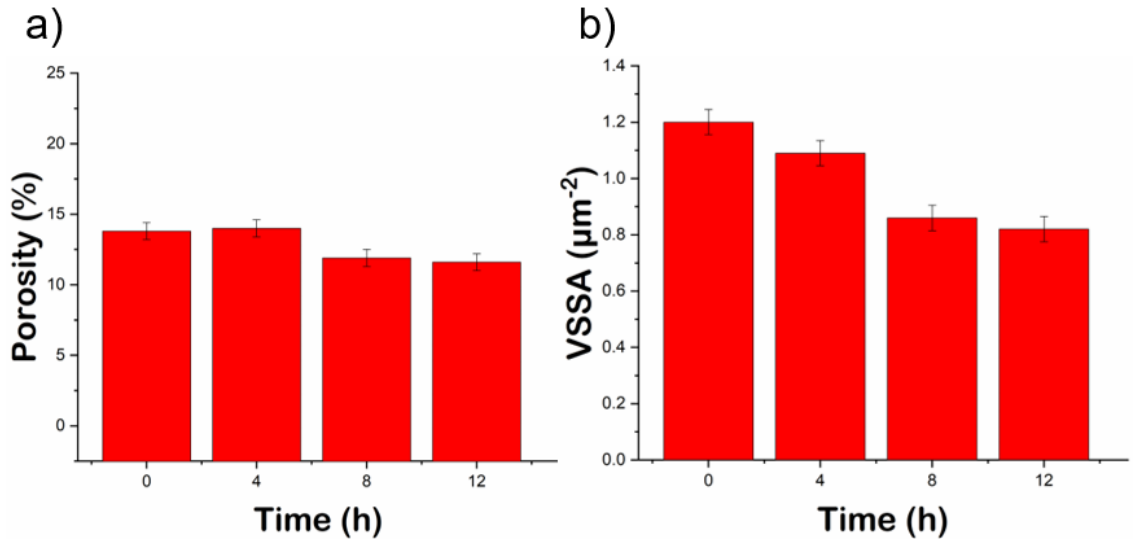

Figure 114: Plot of Sample 2c *a) porosity & b) VSSA$_{Pore}$ over 12 h annealing at 900 °C*

The apparent volume increase of the nickel particles between 4 and 8 h resulted in a significant loss of porosity. The difference between 0 and 4 h, however, was within the estimated segmentation error. VSSA$_{Pore}$ appeared to decline between 0 and 4 h, however, a drop representing a loss of ~9% in surface area. This “coarsening” of the porous network matches well the same surface area reduction seen in the first 4 h under the 700 °C regime, which involved a ~11% loss in surface area. A very significant loss in

surface area was also observed over the 4 – 8 h period, concomitant with the loss of porosity. Most starkly, connectivity was adversely affected by annealing; percolation dropped from ~74% to ~58% in the first 4 h, and after this point, with the volume expansion of the nickel phase, percolation was entirely lost in all directions of the sampled volume. It should be noted, however, that the tortuosity factors extracted from *Sample 2Ac$_{900_4}$* were not all higher than in the virgin sample – in fact, the X-direction increases, the Y-direction remains approximately constant and Z-direction decreases, indicating a complex evolution of connected porous pathways with the evolution of the nickel network.

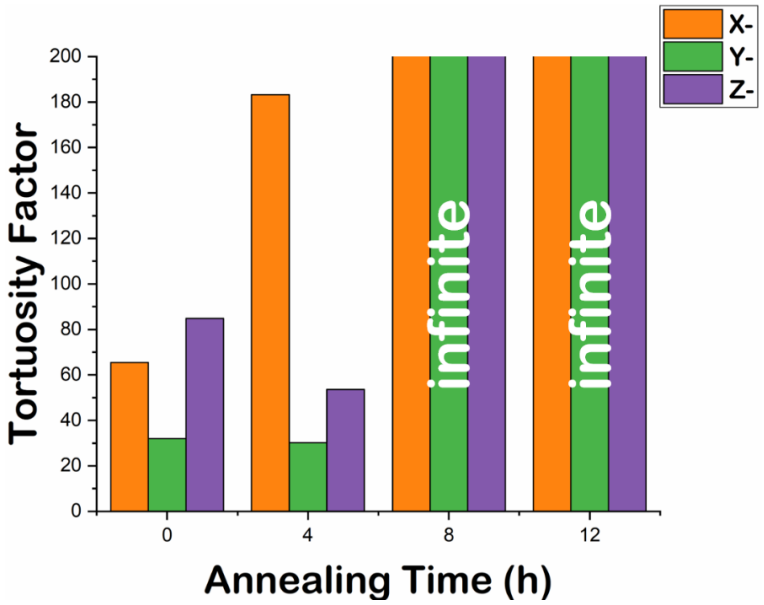

Figure 115: Plot tracking the evolution of pore tortuosity factor as a function of annealing time under the 900 °C regime

RVE analysis was undertaken based on the binarised images and the results for the porous phase for each time step are shown in Table 38 **-** Table 41. Since, in most cases, the porous network was found to not percolate for the 8 h and 12 h anneal samples, these figures are omitted and only the 0 and 4 h anneal samples are shown in Figure 116**.**

Volume Fraction		**0.1**	**0.3**	**0.5**	**0.7**	**0.9**	**1**
Porosity		0.13	0.13	0.13	0.13	0.14	0.14
Tortuosity Factor	*Direction*						
Pore	*X*	11.4	16.9	46.0	52.7	62.7	65.5
	Y	38.8	24.7	22.0	23.5	26.0	32.0
	Z	11.7	31.9	55.9	68.1	79.6	84.8

Table 38: Values from Pore RVE analysis of Sample 2Vc$_F$ *Ilastik segmentation*

Volume Fraction		0.1	0.3	0.5	0.7	0.9	1
Porosity		0.13	0.13	0.13	0.14	0.14	0.14
Tortuosity Factor	*Direction*						
Pore	*X*	16.7	70.7	-	178.0	178.0	183.0
	Y	12.4	35.6	36.1	32.6	31.1	30.2
	Z	9.2	18.2	29.7	42.7	51.2	53.5

Table 39: Values from Pore RVE analysis of Sample $2Ac_{F\_900\_4}$ *Ilastik segmentation*

Volume Fraction		0.1	0.3	0.5	0.7	0.9	1
Porosity		0.11	-	0.11	0.11	-	-
Tortuosity Factor	*Direction*						
Pore	*X*	17.3	-	-	-	-	-
	Y	35.4	-	78.6	107.0	-	-
	Z	-	-	-	-	-	-

Table 40: Values from Pore RVE analysis of Sample $2Ac_{F\_900\_8}$ *Ilastik segmentation*

Volume Fraction		0.1	0.3	0.5	0.7	0.9	1
Porosity		0.11	0.11	0.10	-	-	-
Tortuosity Factor	*Direction*						
Pore	*X*	-	-	-	-	-	-
	Y	32.4	54.5	71.2	-	-	-
	Z	14.1	-	-	-	-	-

Table 41: Values from Pore RVE analysis of Sample $2Ac_{F\_900\_12}$ *Ilastik segmentation*

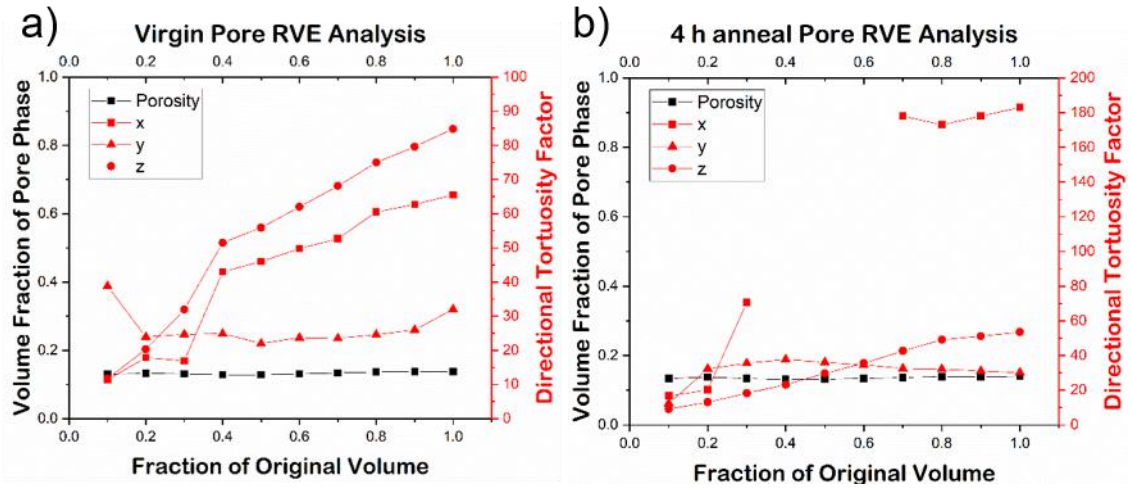

Figure 116: Plots displaying the Ilastik Pore RVE analysis of Sample 2c *data for the a) 0 h and 4 b) h annealing timesteps*

The analysis showed that, as was the case for the 700 °C regime, the sampled volume was large enough to capture a representative element for the measurement of pore phase fraction. This occurred at x = 0.8 for both the 0 and 4 h timesteps, indicating again that ~420 μm^3 was sufficient as an RVE for this metric. However, in assessing the more sensitive tortuosity factor, it was clear that a larger volume is required. Using a 4% tolerance, no direction reached convergence in the 0 h pore network, whereas both the

X- and Y-directions pass below the threshold at x = 0.9 (although without further expansion possible, this is difficult to confirm).

Due to the reduction in solid-phase contrast, a ternary segmentation was only performed for the first two datasets (0 and 4 h anneal), an XY-orthoslice from each of the resulting segmented tomograms is shown in Figure 117. The three-phase simple metrics are displayed in Table 42 and Table 43.

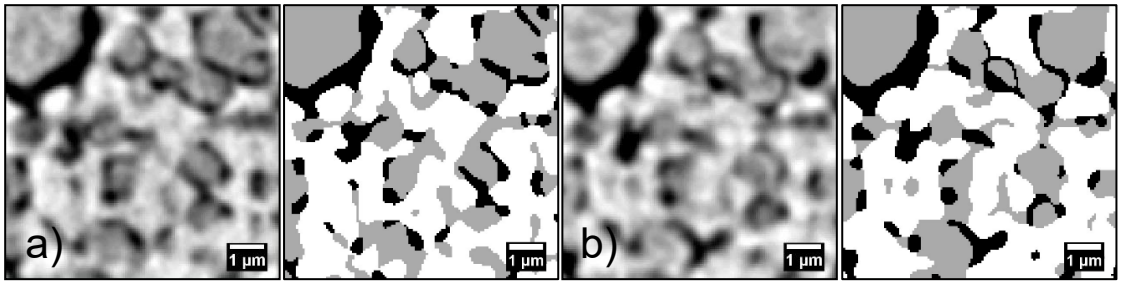

Figure 117: XY-orthoslices from tomograms in the 900 °C regime: a) 0 h and b) 4 h, with their corresponding ternary Ilastik segmentations, where black is pore, grey is nickel, white is YSZ

Phase	Volume (μm^3)	Phase Fraction (%)	VSSA (μm^{-1})	Interface	VSIA (μm^{-1})	ρ_{TPB} (μm^{-2})
Pore	72.8	13.8	1.2	**Pore-Nickel**	0.7	**Active: 2.5**
Nickel	173.5	32.8	1.8	**Nickel-YSZ**	1.2	
YSZ	281.9	53.4	1.6	**YSZ-Pore**	0.5	
Total	528.2	100.0	-	**Pore-Nickel-YSZ**	-	**Total: 5.5**

Table 42: Estimated ternary metrics from Ilastik segmentation of Sample $2Vc_F$

Phase	Volume (μm^3)	Phase Fraction (%)	VSSA (μm^{-1})	Interface	VSIA (μm^{-1})	ρ_{TPB} (μm^{-2})
Pore	73.0	13.8	1.1	**Pore-Nickel**	0.7	**Active: 2.4**
Nickel	175.3	33.2	2.0	**Nickel-YSZ**	1.3	
8YSZ	279.9	53.0	1.7	**YSZ-Pore**	0.4	
Total	528.2	100.0	-	**Pore-Nickel-YSZ**	-	**Total: 5.1**

Table 43: Estimated ternary metrics from Ilastik segmentation of Sample $2Ac_{F\_900\_4}$

The phase fractions remained effectively unchanged after the 4 h anneal, with a maximum discrepancy of 1.2%. However, $VSSA_{Ni}$ was observed to significantly change; it rose by 12.5%. This result is somewhat at odds with the longer-term observations of nickel coarsening which would give rise to a decrease in VSSA, but on the other hand, it is in keeping with the hypothesis that very early-stage reorganisation is of a different character and may in fact give rise to a short period of activation. The $VSSA_{YSZ}$ remained unchanged, which is in keeping with the YSZ backbone being little affected by short-term annealing at 900 °C. The VSIA values suggested a loss of YSZ-pore interface in exchange for greater interfacial contact between nickel and YSZ. Again, this is at odds

with the de-wetting behaviour seen at long times, but instead implies a different nature to the very early-stage microstructural evolution.

The TPB densities were similar to previously reported values, as in the 700 °C regime. However, the total TPB densities were higher here, whereas the active TPB densities were of approximately the same magnitude, giving rise to lower %Active TPB values for the *virgin* and *annealed* samples in the 900 °C regime than for the 700 °C regime. This illustrates the impact of the reduction procedure on the initial microstructure and hence the degree of percolation of the three-phases and highlights the importance of choosing the optimal processing conditions, as well as composition and PSD for the constituent materials. Although the total TPB density dropped between the *virgin* and *annealed* samples (-8%), the active TPB was essentially unchanged and so the %Active TPB actually increased after annealing (44% to 48%). Again, this is not the behaviour expected from general coarsening behaviour, but instead may represent initial reorganisation that might counteract some of the tendency towards fewer interfacial contact points. Moreover, it is worth noting that at 72 s, the solid-phase contrast appears to be somewhat improved and the resultant ternary segmentation appears to better capture the microstructure observed from the raw data than in the 700 °C (64 s) case.

6.3.3.2 Advanced Geometrical Metrics

Due to the subtlety of the changes observed in the 700 °C regime (*Sample 2Vb$_F$)*, and the minor changes in global metrics, a more local approach was developed. This method is detailed in **Chapter 3**, so only a brief description is given here. Firstly, chord length measurements are made, in each direction, on each phase, to probe the changing shape/anisotropy of the networks under investigation (Figure 118 – Figure 121).

The pore chord distribution for the virgin sample peaked at approximately 630 - 690 nm, which agrees excellently with the cPSD analysis (radius = 325 nm) in **Section 6.3.3.1**. The chord length associated with this peak remained unchanged throughout annealing, for all directions, apart from a small dip in the Y-direction for the 12 h anneal sample. At the same time, there was an increase at larger chord lengths associated with this timestep, potentially representing a coalescence of smaller pores

into larger ones. However, it is worth noting that the Y-direction at 12 h was non-percolating, such that an increase in connectivity does not always lead to an increase in percolation. Aside from the peak at 630 - 690 nm, there was an indication of a second small peak at approximately 2 µm, which was present throughout.

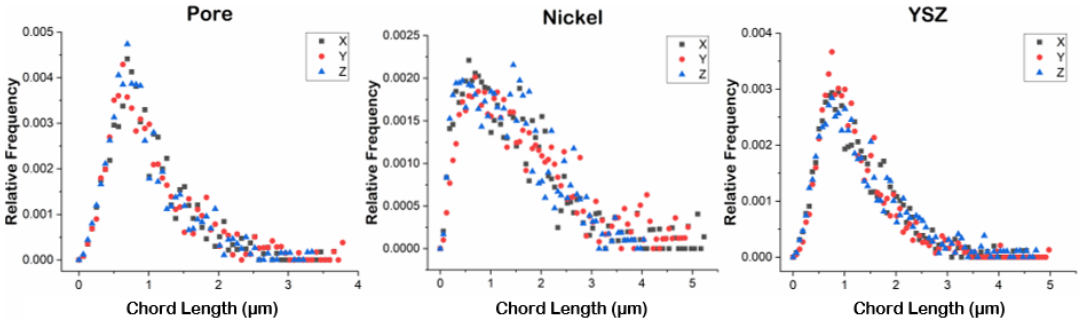

Figure 118: Chord-length distributions for Sample $2Vb_F$ *for all three phases (pores, nickel and YSZ), in all three directions (x-, y- and z-)*

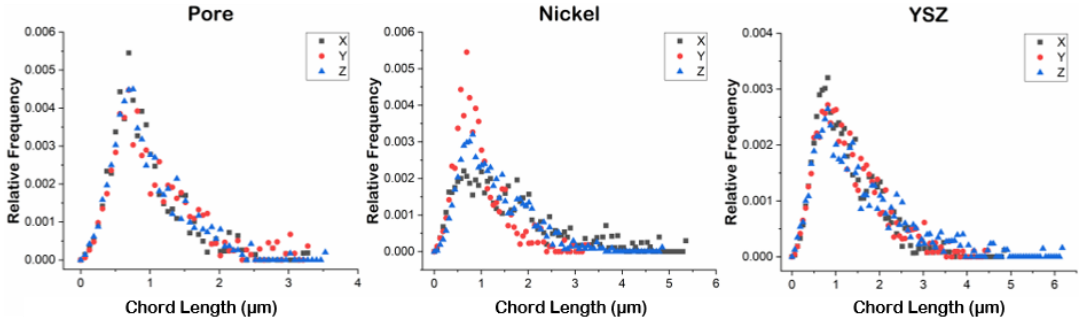

Figure 119: Chord-length distributions for Sample $2Ab_{F\_700\_4}$ *for all three phases (pores, nickel and YSZ), in all three directions (x-, y- and z-)*

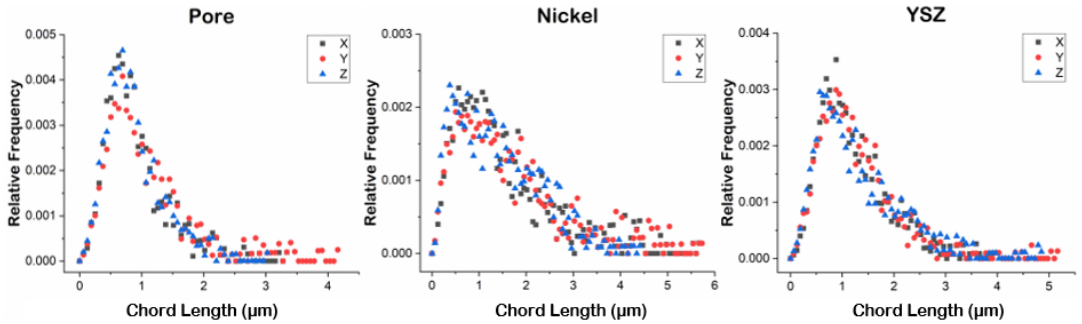

Figure 120: Chord-length distributions for Sample $2Ab_{F\_700\_8}$ *for all three phases (pores, nickel and YSZ), in all three directions (x-, y- and z-)*

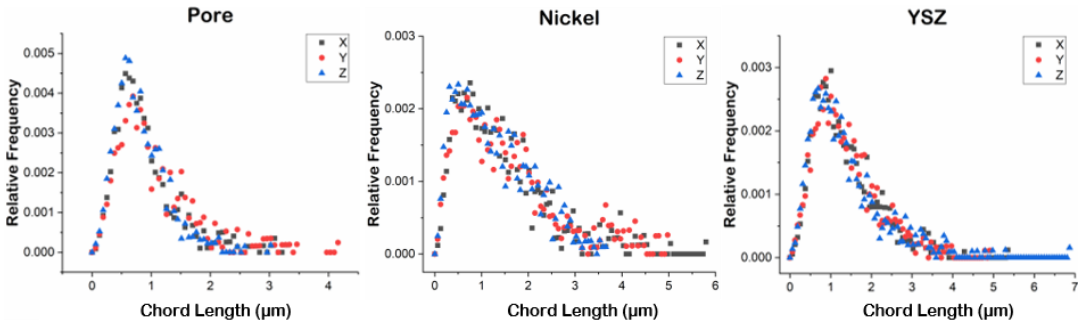

Figure 121: Chord-length distributions for Sample $2Ab_{F\_700\_12}$ *for all three phases (pores, nickel and YSZ), in all three directions (x-, y- and z-)*

The nickel network appeared to be quite different from the pore and YSZ networks. The clearest difference was the anisotropy represented by a significantly different distribution of feature size in each direction. The anisotropy (measured as the standard deviation) was on average 21%, as opposed to 8% and 12% for pores and YSZ, respectively. Most notably, there was a distinct distribution for the 4 h timestep, with a large average elongation in the Y-direction, which disappeared in the latter two timesteps. On average, the nickel particle size increased slightly in the first 4 h, and then decreased significantly between 4 and 8 h, and by a lesser extent between 8 and 12 h. A clear monotonic trend was not observed, and this behaviour is not thought to be characteristic of the longer-term coarsening phenomenon previously reported.

As an alternative measure of anisotropy, the largest feature (the upper cut-off chord length) in each direction and for each phase was compared. In the YSZ case, the ratio of the largest feature in the Z-direction to the average in the X- and Y-directions was approximately constant, deviating from unity by only ±9%. In the pore and nickel cases, however, this ratio was 0.86 on average, implying some oblate character to the particles and pores. Overall, the pore network appeared to change only marginally; the distribution broadened slightly, but a high level of isotropy was retained throughout. The nickel distribution narrowed, its peak increased first before decreasing for the two following timesteps and was highly anisotropic throughout. Finally, the YSZ chord length distribution remained largely unchanged with only small changes observable in the Z-direction.

Subsequently, the sizes of each of the three phase networks of the 4 tomograms were investigated by the local thickness algorithm described in **Chapter 3**. The characteristic sizes of these networks were represented in histogram form. Figure 122 **-** Figure 125 display example slices representing each of the three phases, next to which the corresponding histogram for the entire phase is given.

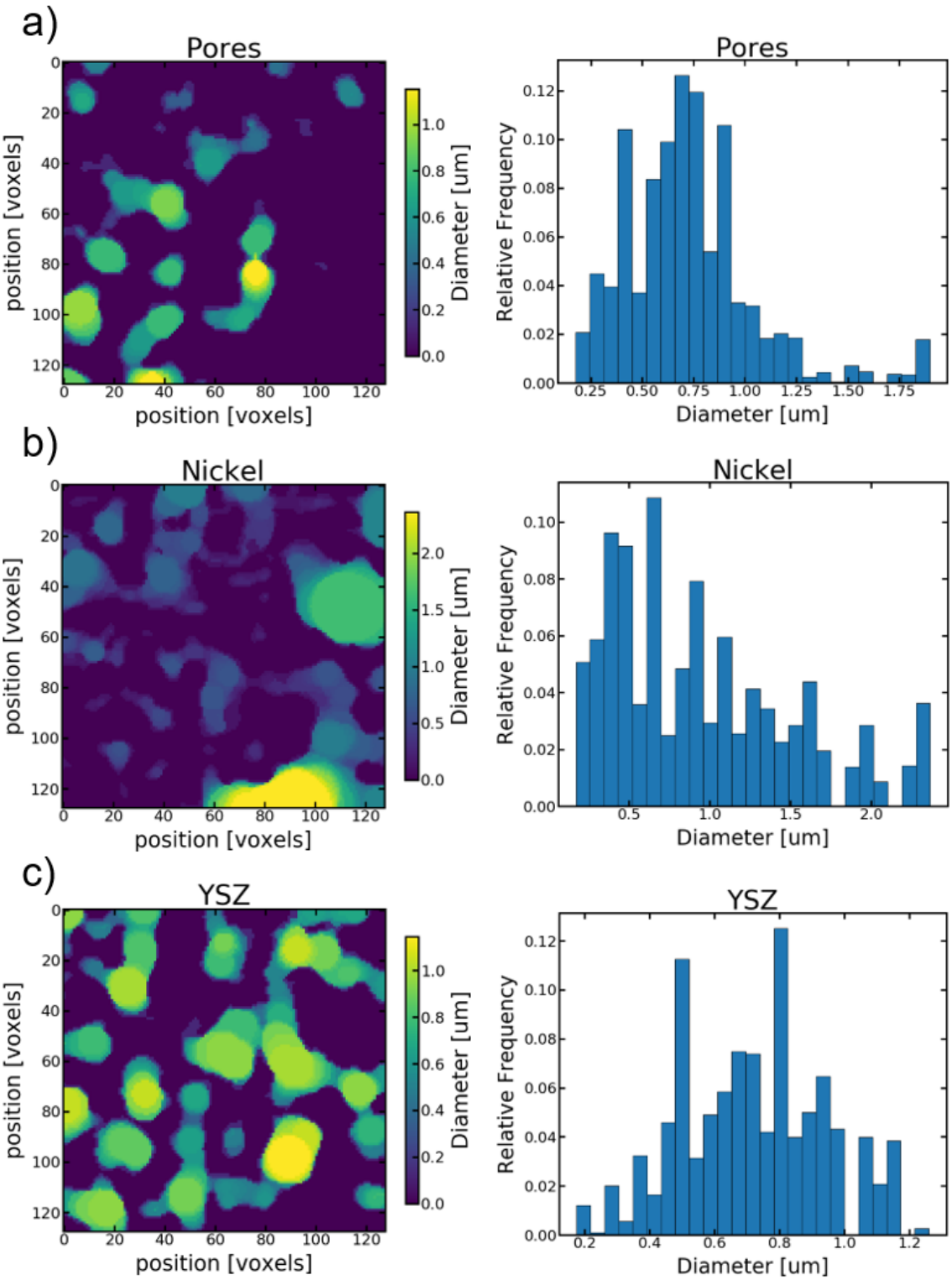

Figure 122: Local metrics for 700 °C regime, showing example slices from local thickness measurements and the histograms for the entire a) pore; b) nickel; and c) YSZ phases for Sample $2Vb_F$

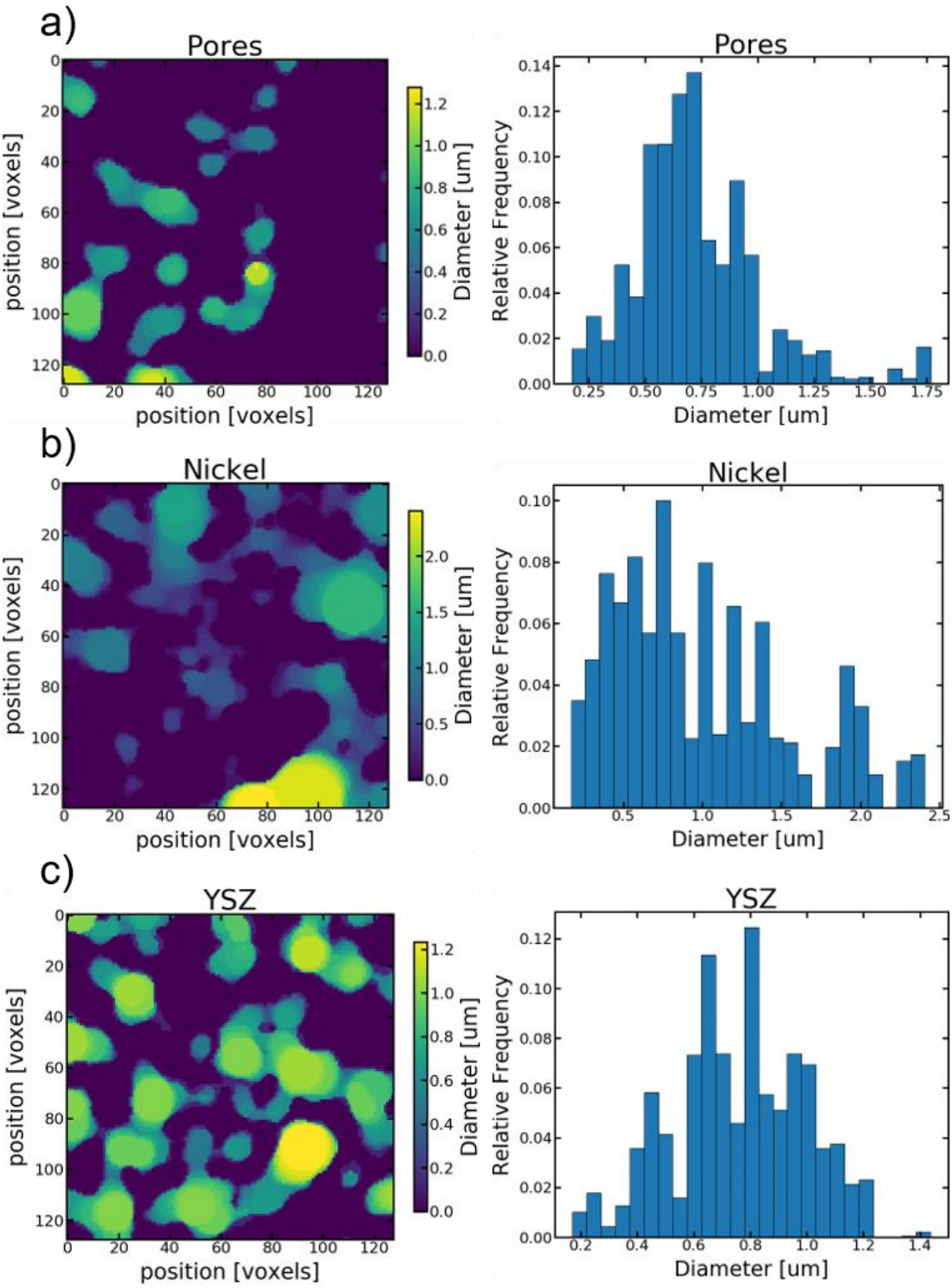

Figure 123: Local metrics for 700 °C regime, showing example slices from local thickness measurements and the histograms for the entire a) pore; b) nickel; and c) YSZ phases for Sample $2Ab_{F\_700\_4}$

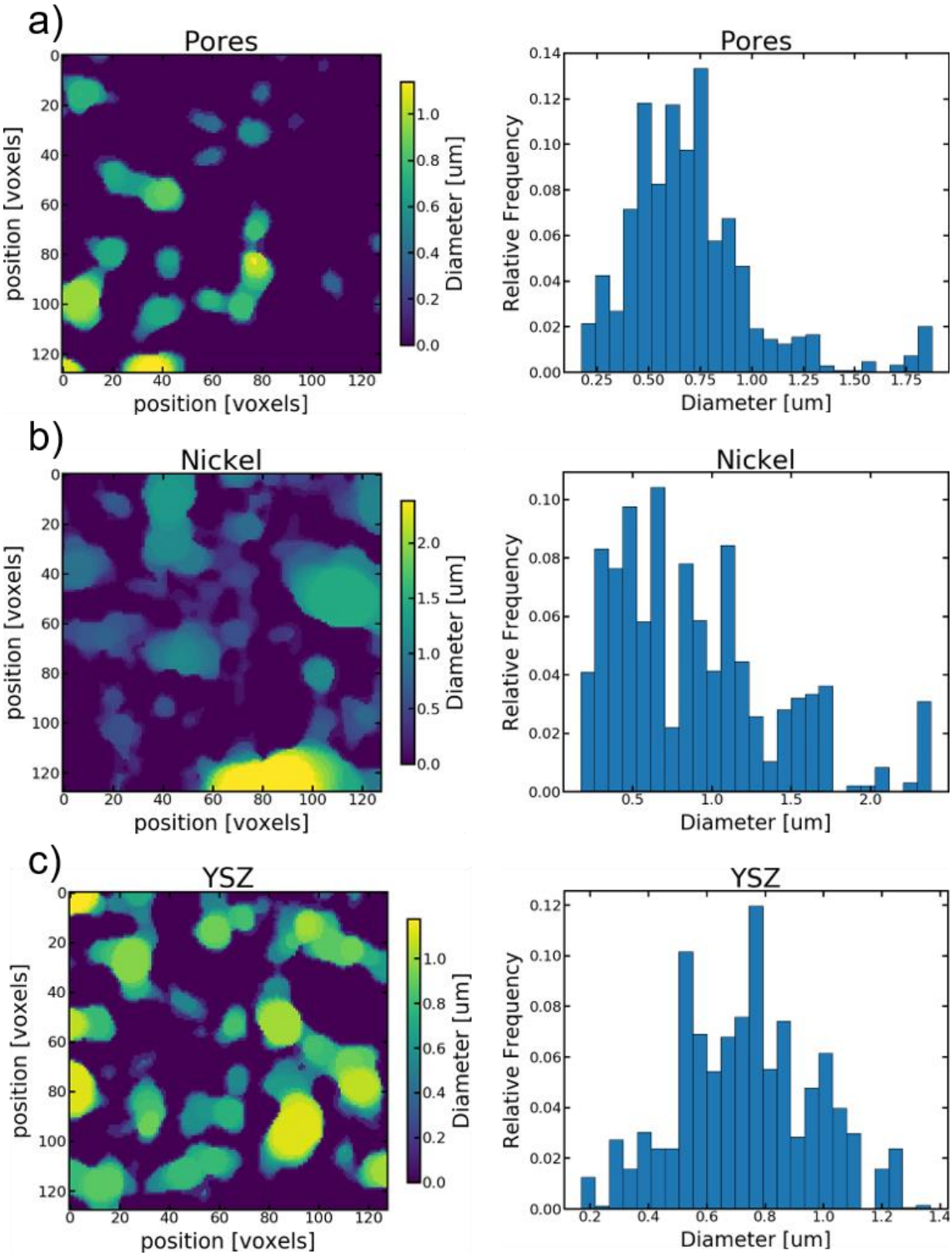

Figure 124: Local metrics for 700 °C regime, showing example slices from local thickness measurements and the histograms for the entire a) pore; b) nickel; and c) YSZ phases for Sample $2Ab_{F\_700\_8}$

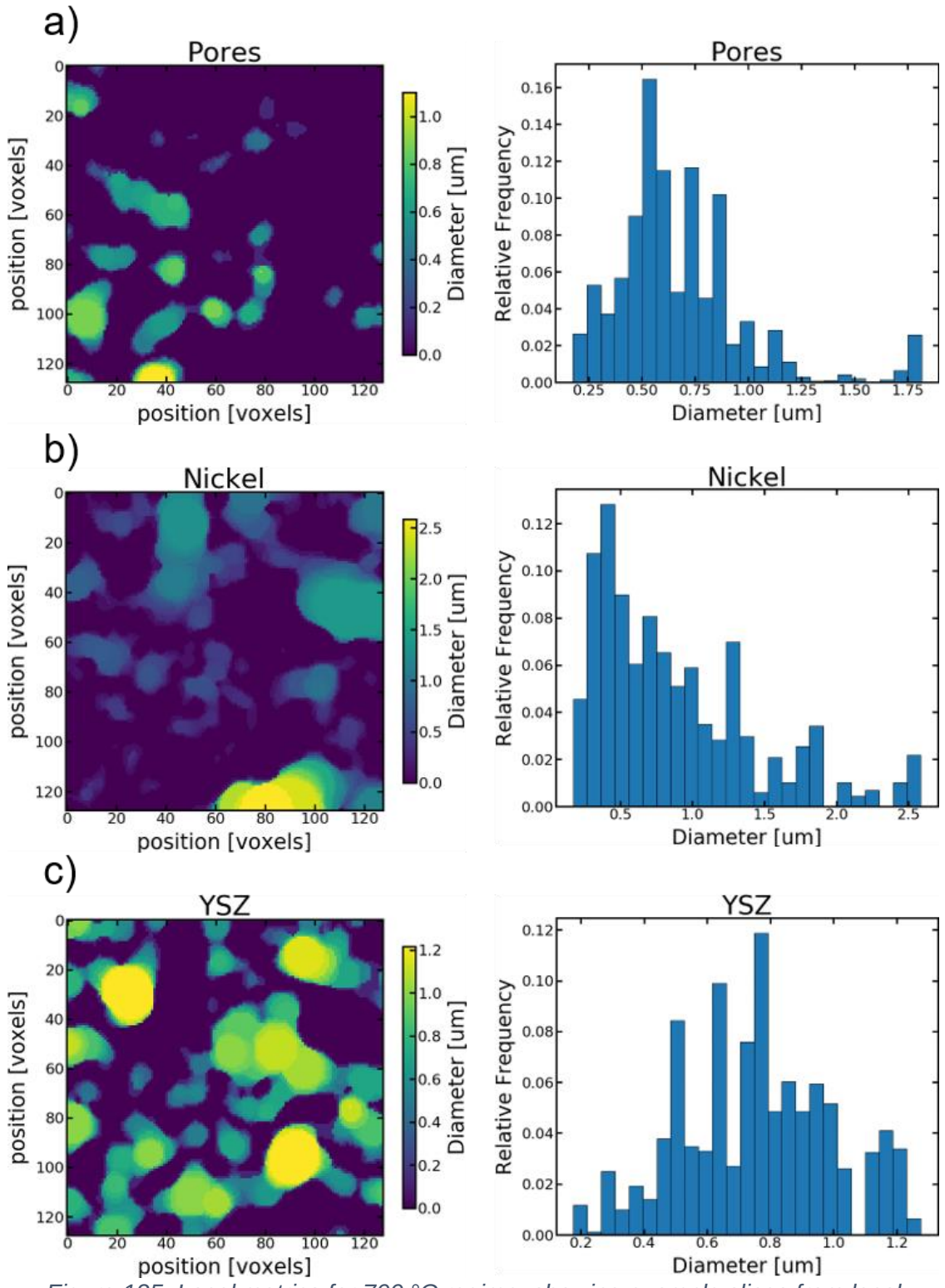

Figure 125: Local metrics for 700 °C regime, showing example slices from local thickness measurements and the histograms for the entire a) pore; b) nickel; and c) YSZ phases for Sample $2Ab_{F\_700\_12}$

Small changes can be observed across both the registered slices and the corresponding histograms. For the pore, nickel and YSZ phases, the evolution of feature radius can be more easily visualised by inspection of the changes shown in Figure 126**,** Figure 127 and Figure 128, respectively.

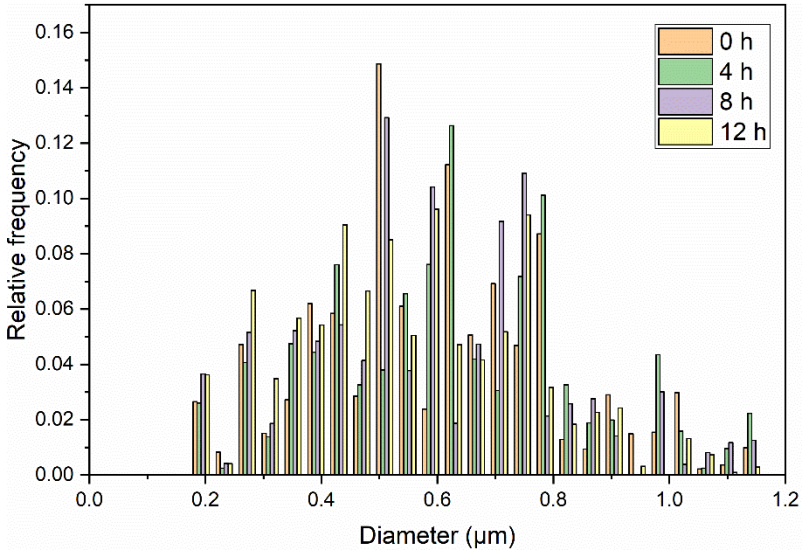

Figure 126: Histogram showing evolution of the radius of pore "objects" under the 700 °C

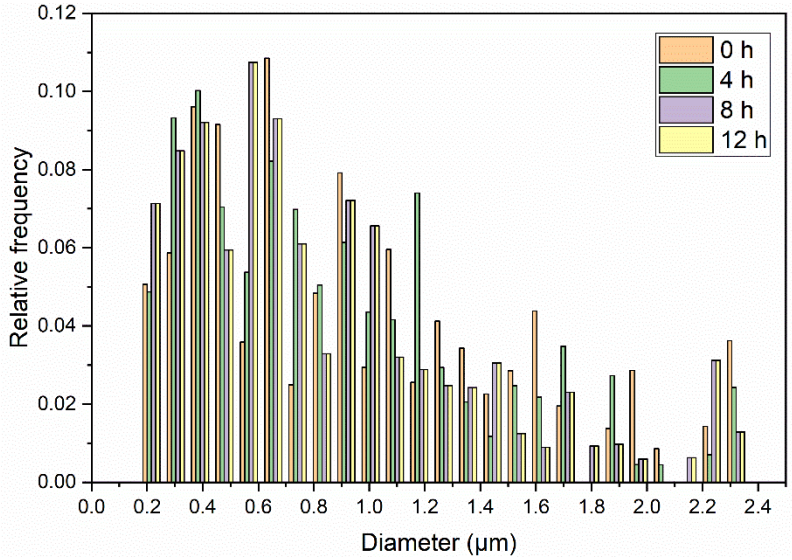

Figure 127: Histogram showing evolution of the radius of nickel "objects" under the 700 °C

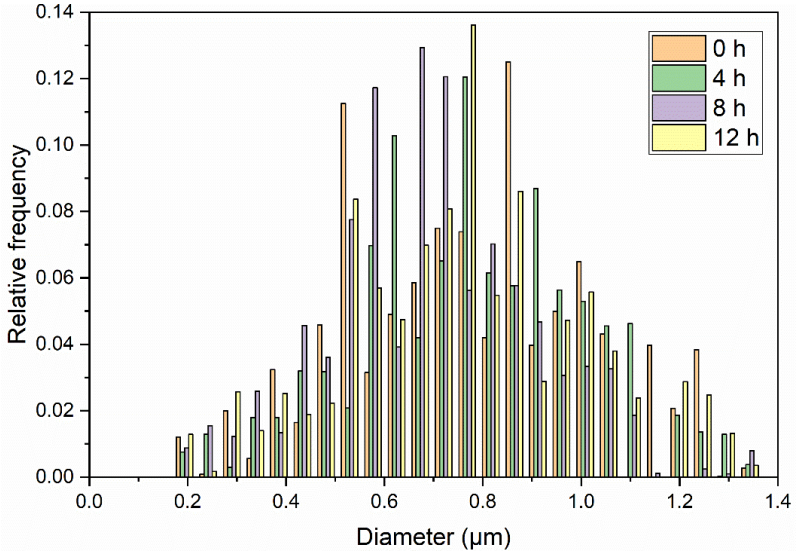

Figure 128: Histogram showing evolution of the radius of YSZ "objects" under the 700 °C

It was evident that the distributions were different for each phase (positive skew for nickel and approaching normal distributions for pore and YSZ). The changes throughout annealing were subtle and each distribution type broadly remained. The major changes extracted for each phase and for each timestep are specified below.

For the pore phase, during the first 4 h, the largest peak increases were at ~590 and 980 nm and the largest peak decreases appeared at ~510 and 710 nm. This may indicate the connection of some 510-nm-features and the slight growth of some as a result of nickel mobility. Between 4 and 8 h, the most prominent changes were drops in features measuring approximately 630 and 790 nm, with significant rises in features measuring ~510 and 710 nm in diameter. This result may imply that certain networks which were joined in the first 4 h of annealing were then subsequently broken with further reorganisation of the mobile metal, highlighting the complex local evolution which is not easy to predict from global metrics. In the final 4 hours of annealing, again there was a reversal in changes for features of ~510 and 710 nm in diameter, with the largest increases now at ~430 and 630 nm.

For nickel, the first 4 h anneal led to the appearance of more features with diameters of approximately 740 and 1180 nm, at the expense of features measuring ~2000 nm, which may indicate the separation of nickel structures. There was also a sizeable increase for 300-nm-features and loss of 650-nm-features, which may or may not be linked. In the following 4 h, the major changes centred on increases at ~570 and 2230 nm and decreases at ~830 and 1180 nm. This appears to suggest that some networks joined up in this annealing step, which might lead to an effective increase in electronic conductivity across the AFL. In the final annealing step, the large object(s) appeared to break up again, with the largest peak decline at ~2230 nm, as well as a continuation of a decline at ~1710 nm. The largest growths were at ~480 and 390 nm, also supporting the hypothesis that large networks were disconnected in this step. Although this would require further experimental validation, the initial findings potentially corroborate the hypothesis that more than one mechanism is at play during early-stage microstructural evolution, whereby nickel networks may break up or reconnect as

opposed to following a monotonic trend. As a result, electronic pathways from reaction sites may vary accordingly, leading to changes in ohmic polarisation.

For the YSZ phase during the first 4 h of annealing, the objects that grow the most were ~620 and 910 nm. Those that shrink the most were approximately 860 and 530 nm. Subsequently, for the second 4 h period, these values were ~670 and 530 nm for the largest increases and ~620 and 770 nm for the largest decreases. This may indicate connections and disconnections for the features at 530 and 620 nm over the first 8 hours of annealing. Finally, after the full 12 h of annealing, there was clear growth at high object diameter. The greatest growth was found for ~1200 µm, most likely a connection re-established that was lost at 8 h (see Figure 128). The YSZ skeleton appeared to evolve, despite the low temperature and times used. This may represent the mobile nickel affecting the ceramic backbone, potentially subtle coarsening of the YSZ microstructure or could be due to segmentation errors.

By summing all peak increases, and comparing across the timesteps, the amount of change between “before” and “after” an anneal step appears to be least for the final 4 h of heating, for all phases. However, as the confidence in this segmentation is low, a direct conclusion from this cannot be drawn. The results are suggestive, accompanied by the simple metrics, that there are multiple mechanisms at play – or simply that the Ostwald ripening coarsening mechanism cannot describe this initial pattern of behaviour. Further analysis is required to verify a trend at longer times, and fortunately this is readily accessible by this *ex-situ* lab-based methodology.

Similarly, the local advanced metrics approach was applied to the virgin and 4 h annealed ternary segmentations from the 900 °C regime. Figure 129 and Figure 130 display the chord length distribution results.

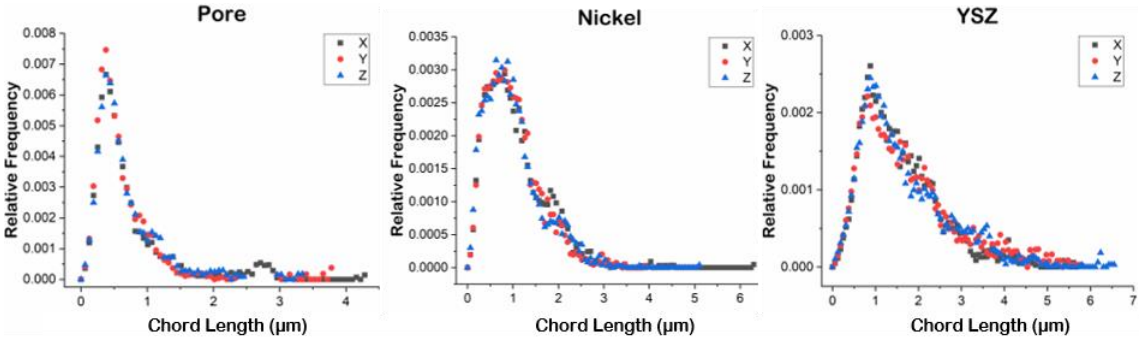

Figure 129: Chord-length distributions for Sample $2Vc_F$ *for all three phases (pores, nickel and YSZ), in all three directions (x-, y- and z-)*

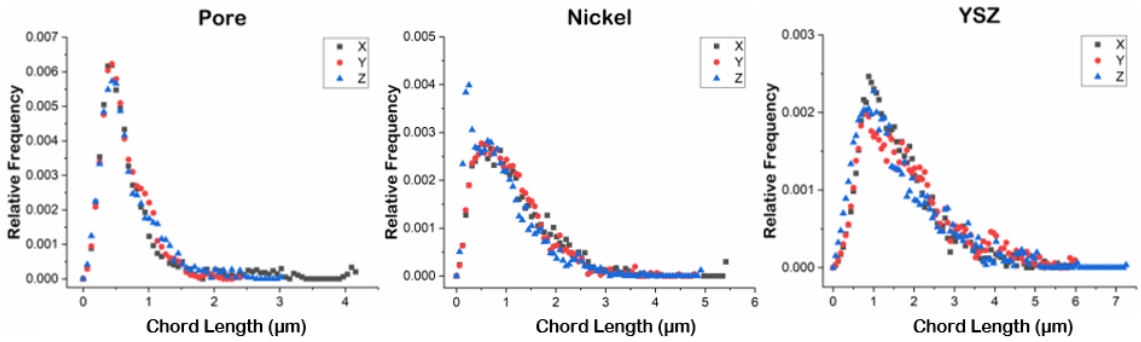

Figure 130: Chord-length distributions for Sample $2Ac_{F\_900\_4}$ *for all three phases (pores, nickel and YSZ), in all three directions (x-, y- and z-)*

The chord length distribution for YSZ appeared broadly unchanged after annealing for 4 h at 900 °C: the peak remains at ~900 nm with a wide distribution and a slight increase at larger chord length. The peak of the pore chord length distribution moved marginally to larger diameters after the anneal, with a slight broadening of the distribution and a noticeable decrease in features of approximately 2.5-3 µm and an increase in features with a diameter on the order of 1 µm. By far, the greatest changes were identifiable in the nickel phase. The most substantial change was the appearance of a peak in the Z-direction at very low diameters (250 nm). Since there were not peaks in the X- and Y-directions, and no peaks at shorter lengths, this implies an appreciable proportion of "flattened" features, which were greater in length in the lateral plane than in their Z-height. This could be due to the effect of gravity – as the nickel phase becomes semi-molten, there may be a "flattening" effect leading to oblate nickel features. However, more analysis would be required to support this hypothesis.

As before, each of the three phase networks of the 2 tomograms was broken into individual objects using a local thickness algorithm. The characteristic sizes of each of

the objects was represented in histogram form. Figure 131 and Figure 132 display example slices representing those objects for each of the three phases, underneath which the corresponding histogram for all the 3D objects is given.

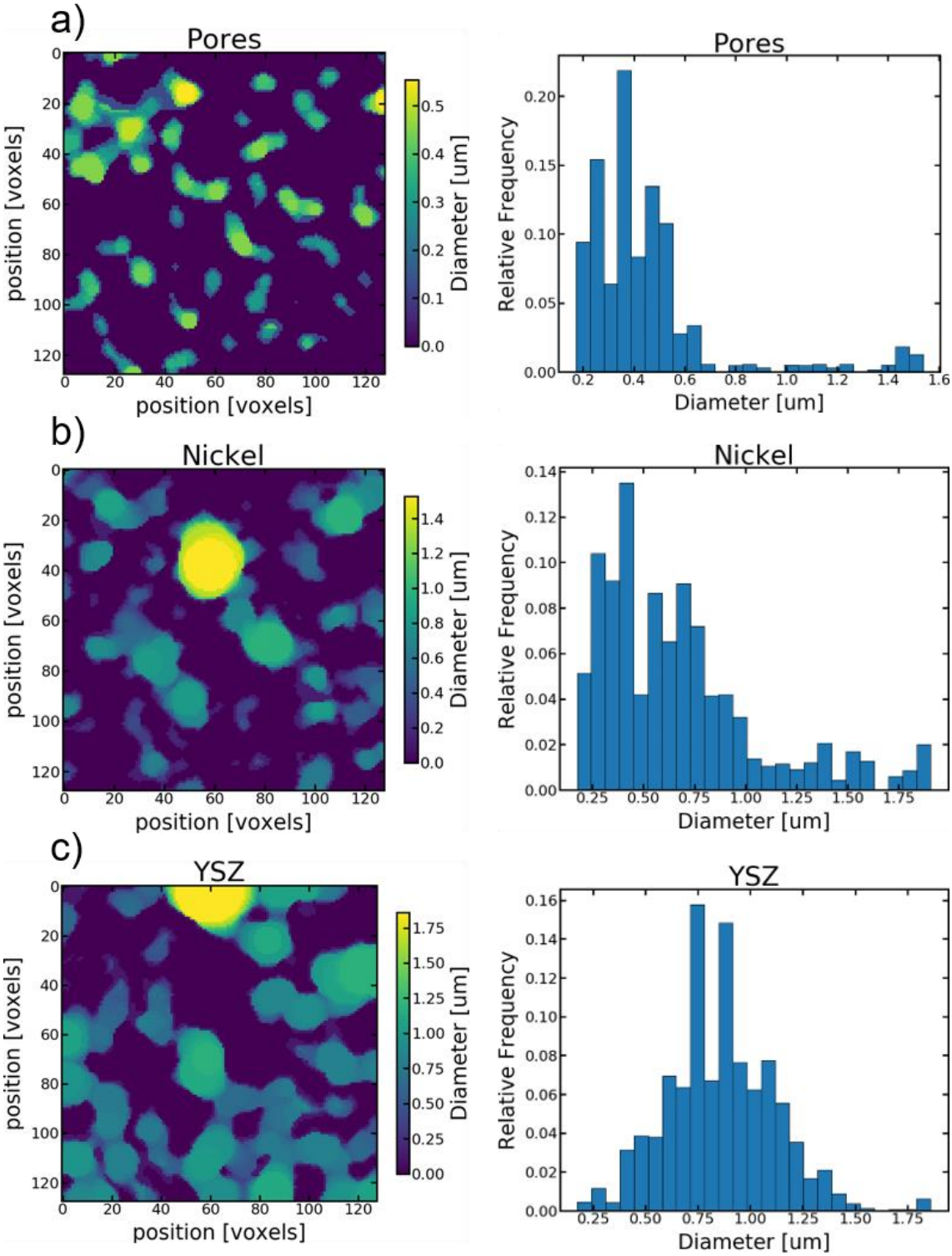

Figure 131: Local metrics for 900 °C regime, showing example slices from local thickness measurements and the histograms for the entire a) pore; b) nickel; and c) YSZ phases for Sample $2Vc_F$

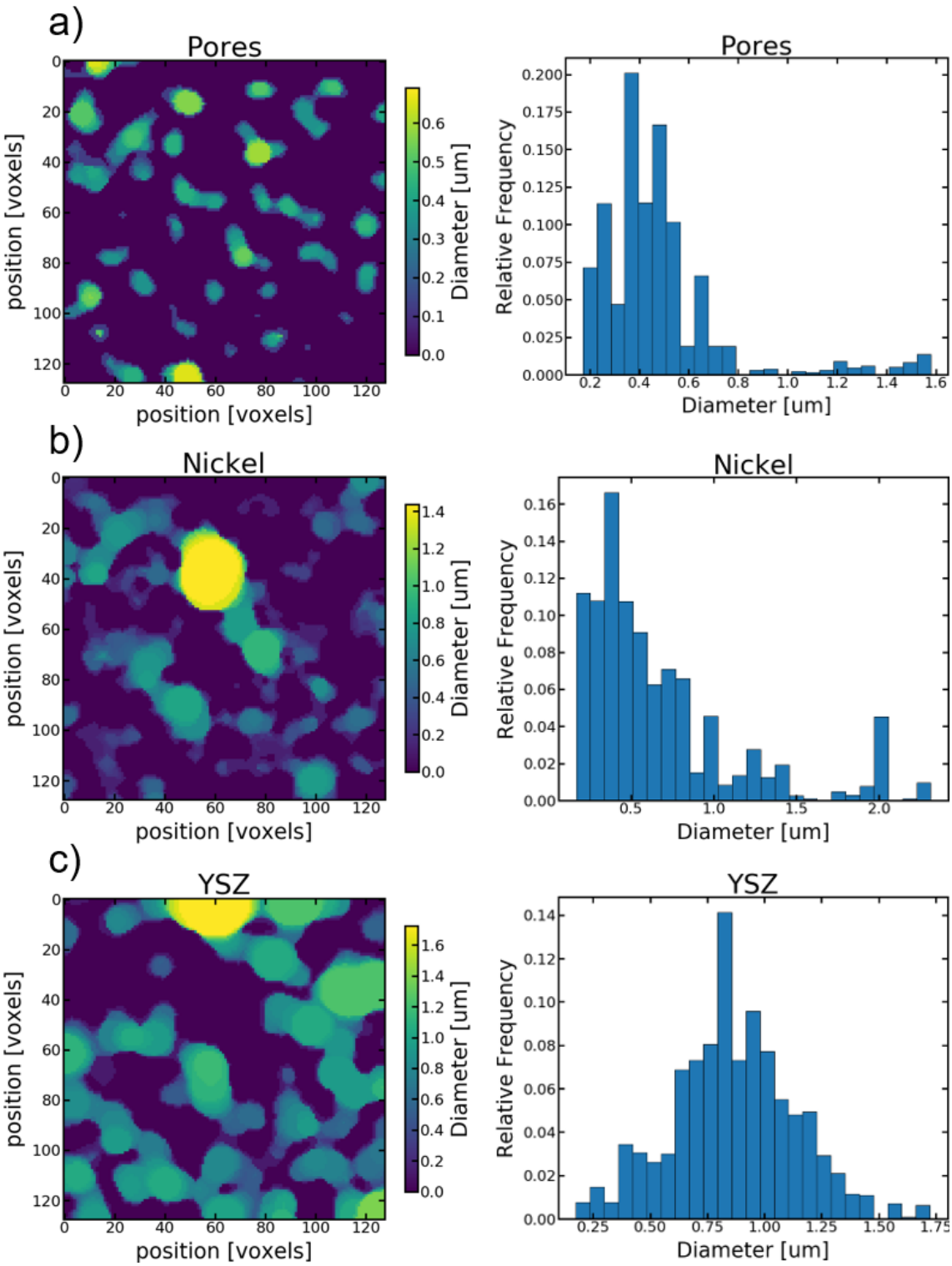

Figure 132: Local metrics for 900 °C regime, showing example slices from local thickness measurements and the histograms for the entire a) pore; b) nickel; and c) YSZ phases for Sample $2Ac_{F\_900\_4}$

To best visualise the changes in each of the phase networks, between the virgin and aged samples, the histograms for each phase have been plotted in turn, as shown in Figure 133**,** Figure 134 and Figure 135.

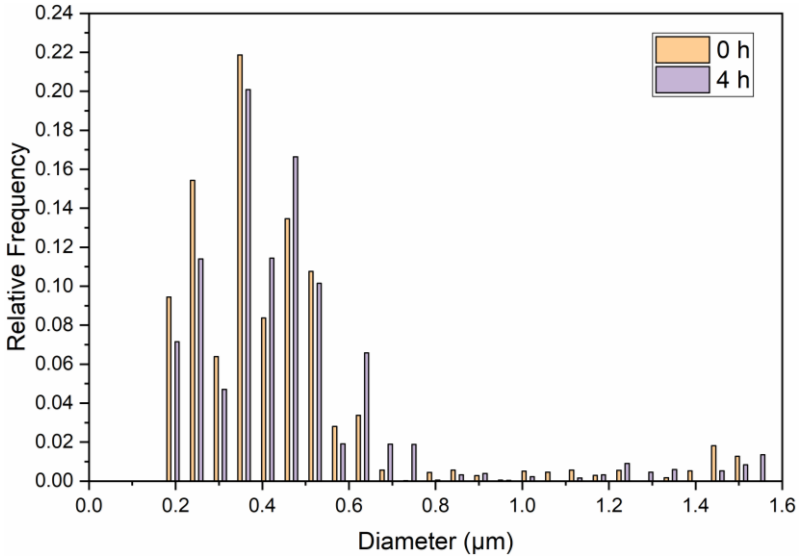

Figure 133: Histogram showing evolution of the radius of pore "objects" under the 900 °C

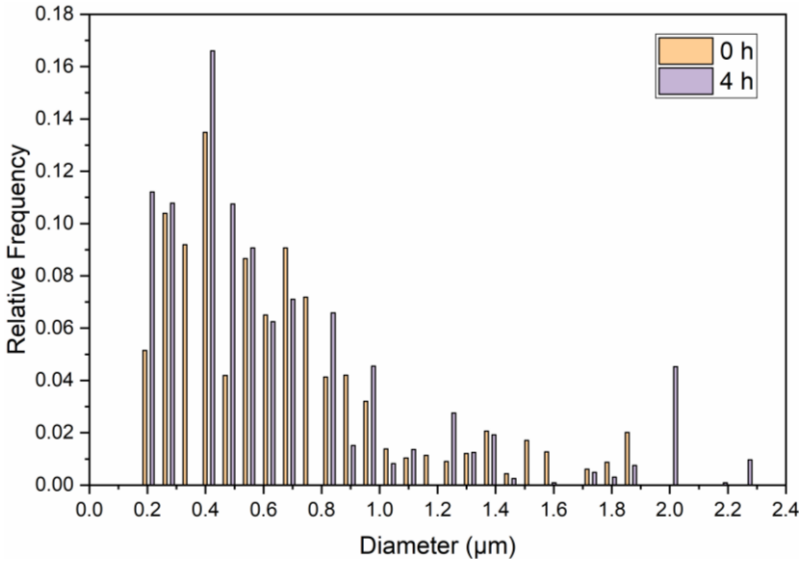

Figure 134: Histogram showing evolution of the radius of nickel "objects" under the 900 °C

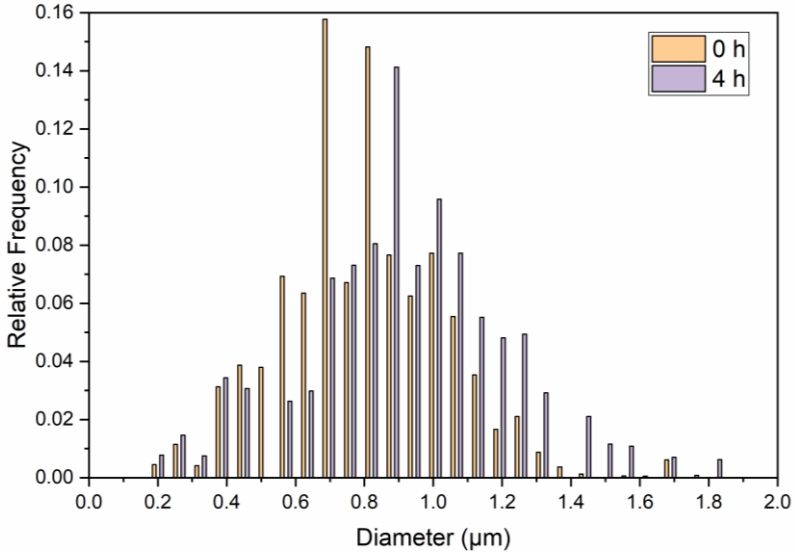

Figure 135: Histogram showing evolution of the radius of YSZ "objects" under the 900 °C

Each distribution was different, but on the whole, there was a positive skew for pore and nickel phases and approaching normal distributions for YSZ. The changes throughout annealing were subtle and each distribution type broadly remained. The major changes extracted for each phase are specified below.

For the pore phase in the 900 °C regime, the changes that were apparent from this analysis were minor and smaller in magnitude than the changes in nickel (or YSZ, to a lesser extent). The largest peak rise was at ~640 nm, whereas the largest decline was at ~250 nm. Generally, there appeared to be a shift towards slightly larger diameters (r50 changes from approximately 350 nm to 400 nm), as illustrated by the drop in the first 4 peaks. The distribution above 800 nm remained broadly unchanged.

For nickel, the largest increases occurred at ~350 and 210 nm, with the most significant decreases occurring at ~900 and 1530 nm. At the same time, there was a clear shift at the upper end of the nickel feature size distribution with the appearance of features of sizes > 2.0 µm. The feature of greatest size shifted upwards from ~1.9 µm to 2.3 µm, which is potentially due to the connection of some of the midrange networks. This illustrates an odd manifestation of an increase in both small and large features at the expense of midsize networks, and possibly points to two competing mechanisms of nickel mobility. Tentatively, the increase at high diameter might have been ascribed to the Ostwald ripening phenomenon, in which very small features are transported to larger features, causing the latter to grow modestly and the proportion of small features to drop. However, the increase in small features, and growth of large features at the expense of intermediate-size features is not in keeping with this mechanism. Moreover, to capture this mechanism might require successful segmentation of very small features, only 3-4 pixels in size. To gain a better understanding of the mode of nickel transport, further investigation with a technique with improved resolution would be recommended to inspect appearance/disappearance of very small features.

In the case of YSZ, this analysis displayed less change in diameter distribution than for nickel, illustrating that at this temperature and for a short annealing time of 4 h, the YSZ network is less mobile. However, there still appeared to be some change, such

as mild coarsening behaviour, which manifested as a modal peak shift from ~700 to 900 nm, a drop in most peaks below 900 nm and a growth in most after 900 nm.

6.3.4 Simulation (Cellular Automata)

Initial work using the Cellular Automata (CA) model was carried out to understand the major nickel agglomeration phenomenon observed when annealing at the high temperature of 1150 °C for 4 h (*Sample 2Va$_F$* and *Sample 2Aa$_{F_1150_4}$*). First, a simple tubular channel with a uniform diameter was modelled and the nickel evolution was compared with a tubular channel with a larger opening at the external surface. The simulated results are shown in Figure 136.

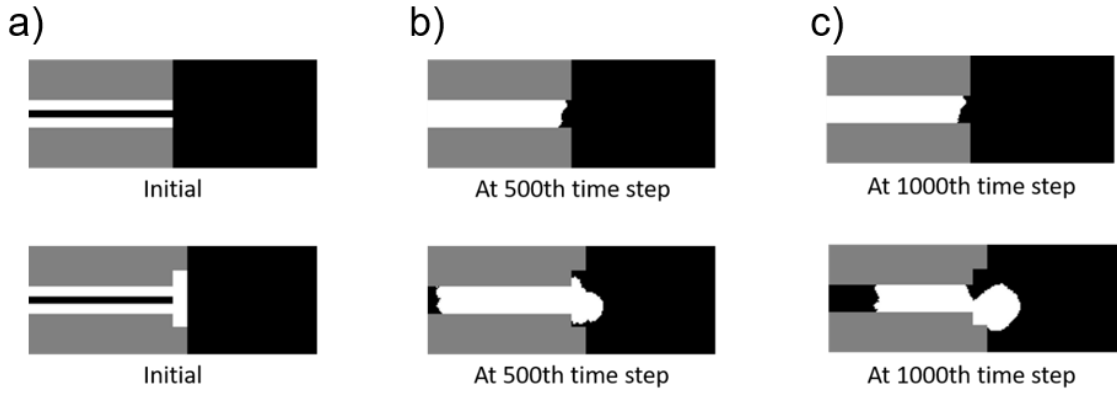

Figure 136: 2D slice from 3D simulation of two model systems a) tube with opening; b) tube with larger opening at external surface, where pore = black, YSZ = grey, nickel = white

Running the CA simulation for many timesteps illustrated that if nickel is inside a uniformly sized channel, agglomeration tends to occur inside the channel, but nickel is not driven to the external surface. This suggests there is no net driving force to lead to nickel exiting the channel, whereas having a larger opening clearly leads to a nucleation point whereby a spherical nickel agglomerate is seen to grow. Much like liquid capillarity effects, the larger channel draws the “molten-like” nickel out, giving rise to external agglomerates seen in **Section 6.3.1.1**. This process was repeated with a real initial structure from a X-ray nano-CT tomogram and the results are shown in Figure 137 for a simulation with a wetting angle of 125° (close to the 117° reported by Tsoga *et al.* [101]). The system was set-up to mimic the X-ray nano-CT pillar geometry, wherein 5 out of the 6 faces of the cube were “exposed” to the atmosphere and the lower face was set with

a mirror boundary condition to model the remaining pillar below the simulated microstructure.

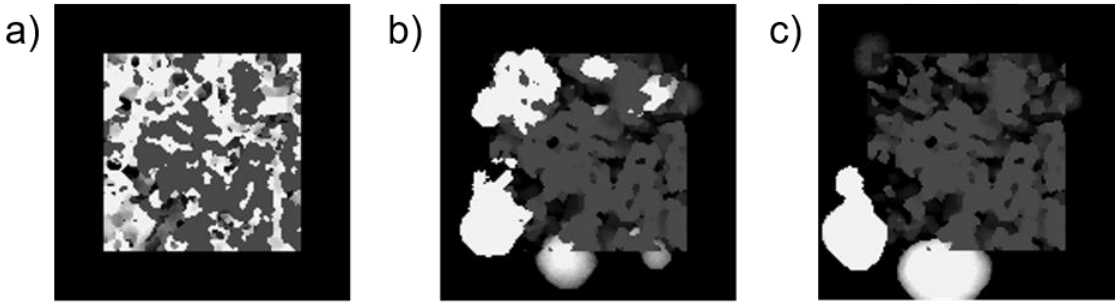

Figure 137: 3D simulation of real system, with a wetting angle of 125°, wherein the initial microstructure was a ternary segmentation of an XCT reconstruction of an ASL, showing a) the initial microstructure and after b) 500 and c) 1000 time steps

This simulation clearly demonstrates the likelihood of observing external nickel agglomerates on the pillar surface as a result of sufficient annealing time at a suitably high temperature, given the poor wetting characteristics of Ni and YSZ. This theoretical approach confirmed that a humid atmosphere and vaporisation-condensation were not a pre-requisite for establishing the decoration of large nickel spheres, as surface diffusion was the only mechanism invoked. Moreover, the simulation provided evidence that the experimental results gathered need not result from contamination by other sources of nickel and that such large agglomerates can grow by surface diffusion with a sufficiently high temperature. The preparation of pillars to match the FOV of typical X-ray nano-CT configurations lends itself to an appreciable degree of open space accessible to pore networks truncated during sample fabrication. As a consequence, the selection of annealing temperatures and times for practical investigations is vital to ensure validity of subsequent microstructural analysis.

6.3.5 Digital Volume Correlation (DVC)

The raw sub-volumes were exported to DVC software, DaVis, ready for comparison (see **Section 3.4.3** for details). Calculations were performed on the unsegmented (grayscale) images, based on input parameters given as a guideline by the software developers, based on the numbers of voxels, voxel dimension, feature size and separation for the images in question. The initial input parameters were: FFT pre-shift window: 64; and a total of 3 steps: i) 32 voxel sub-volume, 75% overlap, peak

search of 8, 8 × 8 × 8 binning, 1 pass; ii) 16 voxel sub-volume, 75% overlap, Peak search of 4, 4 × 4 × 4 binning, 1 pass; iii) 8 voxel sub-volume, 75% overlap, Peak search of 2, no binning, 2 passes. An example of the outputs given by the DVC software is presented in Figure 138, which shows an XY-orthoslice for each timestep and the three corresponding displacement vector fields.

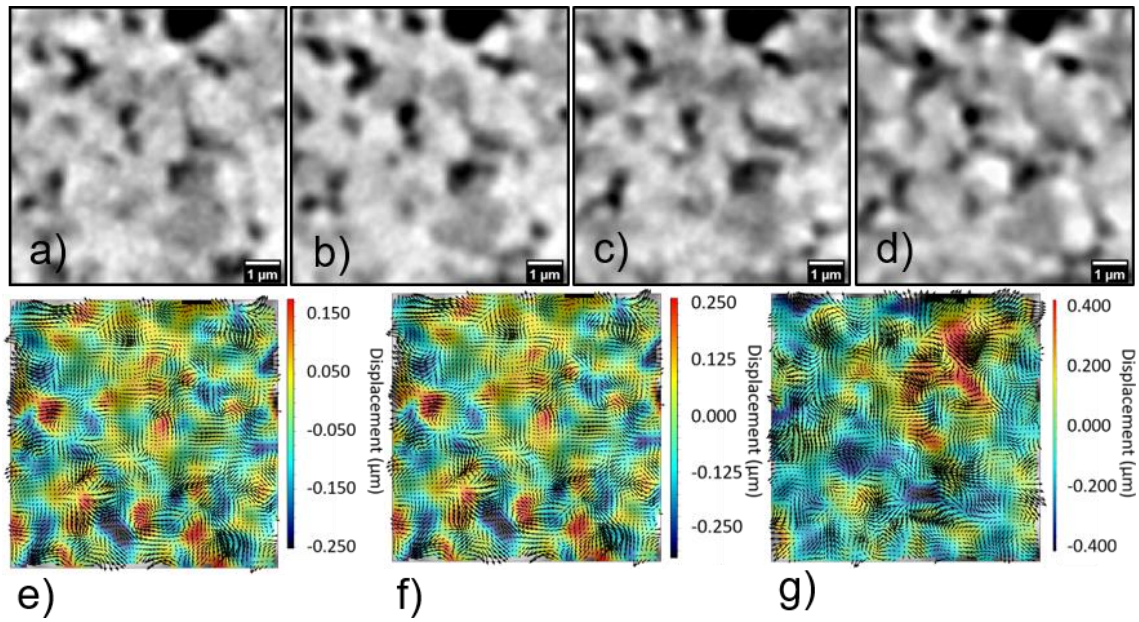

Figure 138: Example raw XY-slices from a) 0 h; b) 4 h; c) 8h; and d) 12 h tomograms with corresponding displacement vector fields between each consecutive pair, e) 0-4 h; f) 4-8 h; and g) 8-12 h (magnitude of Z displacement by colour and direction of overall displacement by arrow)

As a qualitative assessment of the sample regions at which microstructural change is concentrated, the slice corresponding to the "starting" image containing the greatest Z-displacement was selected for each consecutive pair. Figure 139 displays the original slice, followed by the displacement vector field, followed by the corresponding slice in the "deformed" volume.

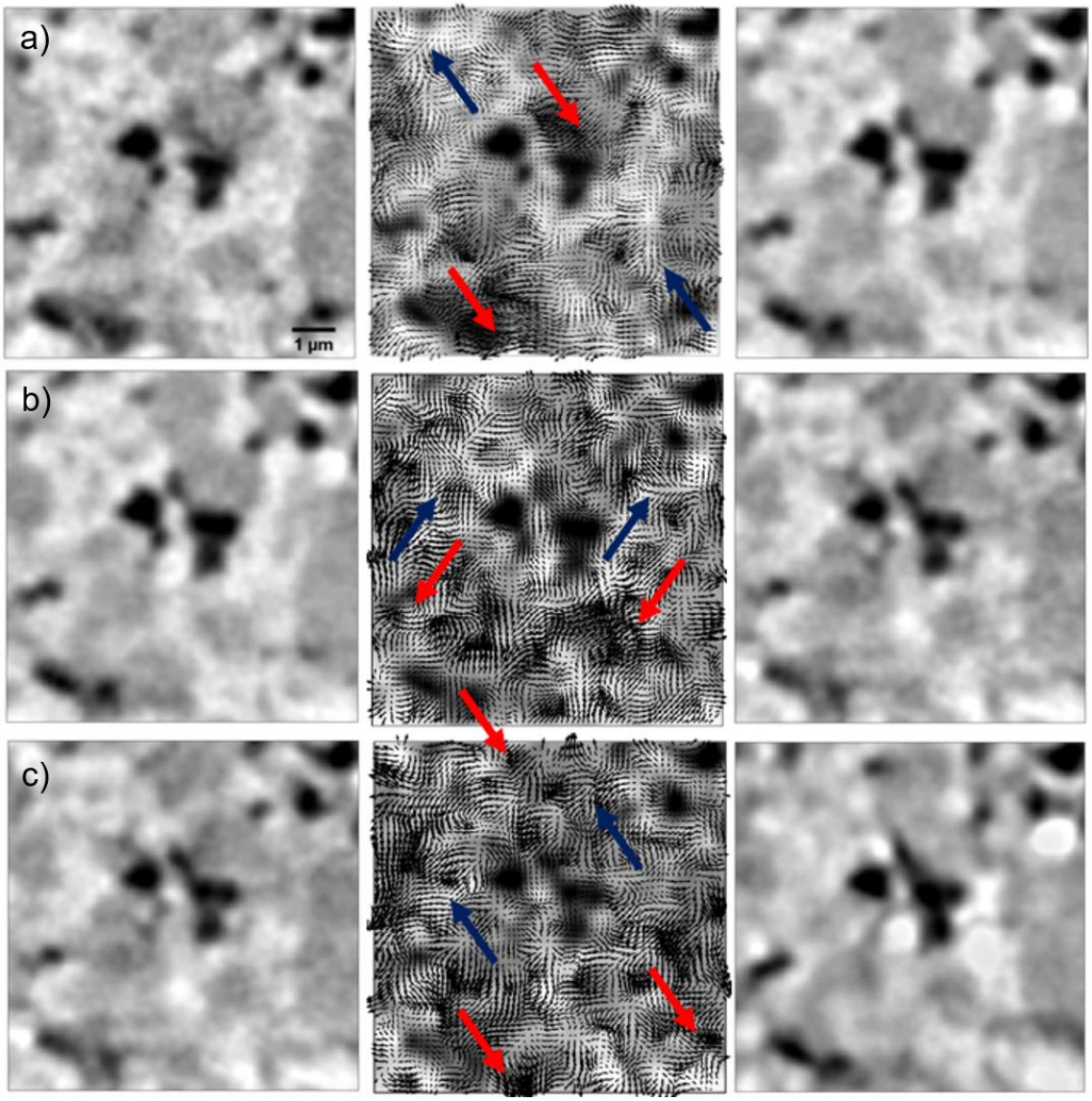

Figure 139: Example XY-orthoslice from before, before overlaid with DVC displacement vector field and after for a) 0 and 4 h; b) 4 h and 8 h; and c) 8 h and 12 h, at 700 °C

From each of the vector fields, a high concentration of displacement vectors can be seen in areas where porosity is replaced by nickel or vice versa, as highlighted by the red arrows. However, there are also regions which appear to represent movement of YSZ, as highlighted by the dark blue arrows. This is likely to be due to processing errors as YSZ is not thought to be mobile at this modest temperature.

In order to quantify the degree of microstructural change across the tomography series, the strain in each of the three orthogonal directions (E_{XX}, E_{YY}, E_{ZZ}) was processed and the total strain magnitude for each DVC sub-unit for every tomographic pair was computed. A plot of the distribution of strain magnitudes between each tomographic pair is shown in Figure 140.

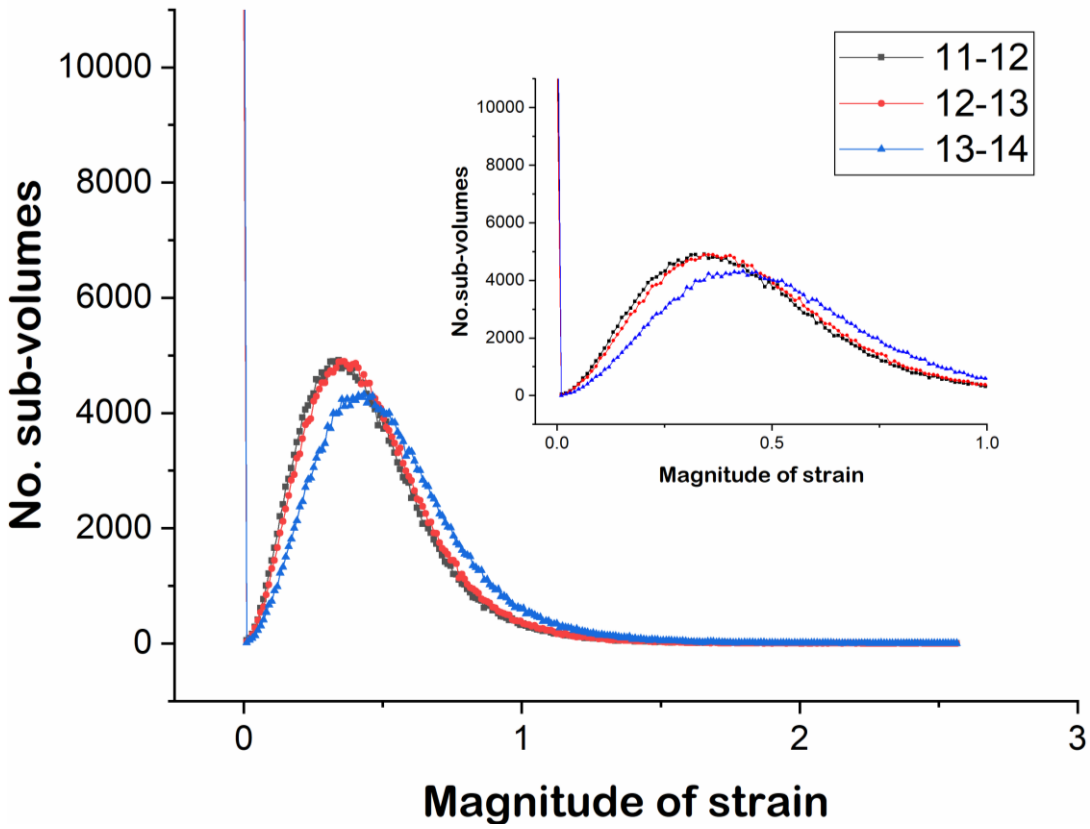

Figure 140: Plot of the distribution of strain magnitude of all DVC sub-units for 700 °C regime, with a magnified inset

The distributions for the first two 4-h anneals are very similar, with peaks at 0.32 and 0.35 µm whereas the distribution for the final dataset appears significantly different, with a slight broadening and increase in modal strain magnitude to 0.43 µm. The fact that the 12 h anneal appears slightly different may suggest that the discrepancies discussed earlier were not solely attributable to segmentation. Possibly there is more change in this step, or possibly the raw data collection was somehow compromised, leading the iterative segmentation approach to give erroneous results. These results demonstrate that on average, at 700 °C, strain magnitudes of approximately 0.3 – 0.4 are expected.

The DVC procedure was repeated with the first two raw sub-volumes from the 900 °C regime, with the same initial input parameters. An example of the output given by the DVC software is presented in Figure 141, which shows an XY-orthoslice for each timestep and the corresponding displacement vector slice.

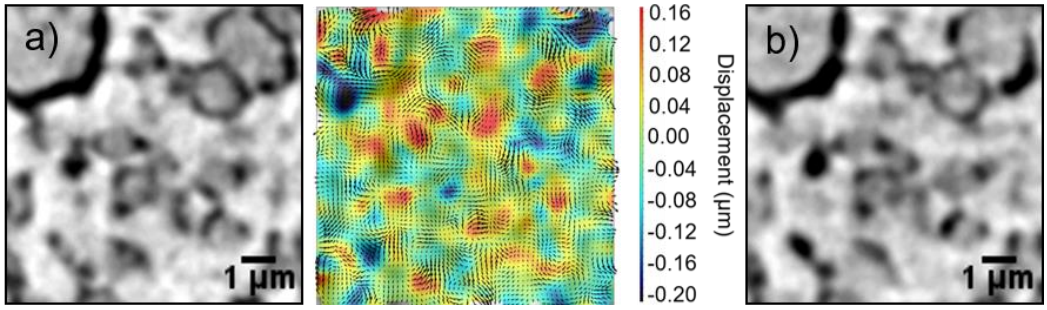

Figure 141: Example raw XY-slices from tomograms at a) 0 h and b) 4 h, with corresponding displacement vector field between (magnitude of z displacement by colour and direction of overall displacement by arrow)

Despite the higher temperature there is not a large increase in maximum Z-displacement; on viewing all vector slices from the displacement vector field, the maximum Z-displacement was approximately the same as for the 700 °C.

As a qualitative assessment of the sample regions at which microstructural change is concentrated, the slice containing the greatest Z-displacement was selected for this tomographic pair. Figure 142 displays the original slice, followed by the displacement vector field overlaid, followed by the corresponding slice in the “deformed” volume.

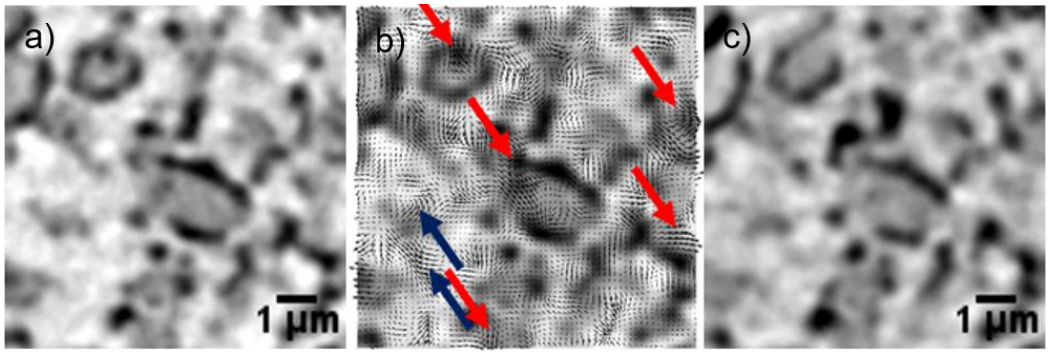

Figure 142: Example XY-orthoslice from a) before; b) before overlaid with DVC displacement vector field and c) after 4 h anneal at 900 °C

Although there are some displacement vectors which appear to represent movement of YSZ, as highlighted by the dark blue arrows, these are generally less concentrated and of smaller magnitude than those corresponding to the changes in nickel and pore networks, as highlighted by the red arrows. The datasets here appear to be more amenable to analysis by DVC which can pinpoint regions of local nickel mobility. When total magnitude of strain is calculated for the transformation, its distribution peak lies at a lower value of 0.22 µm, but with far more sub-volumes presenting movement, giving a taller, narrower distribution as shown in Figure 143.

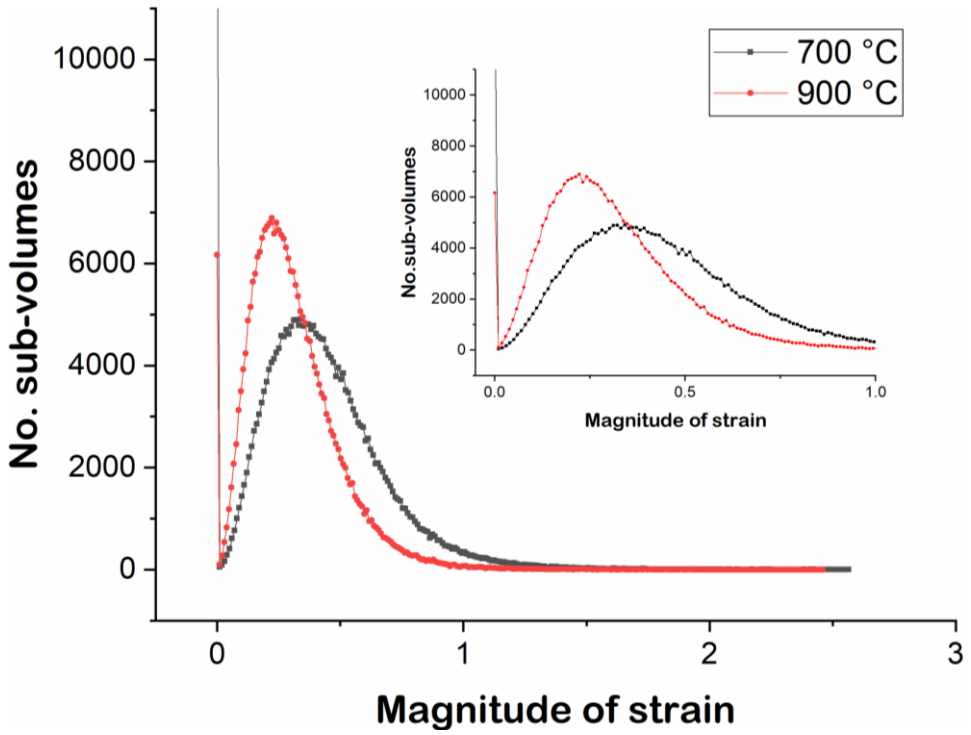

Figure 143: Comparative plot of the strain magnitudes of all DVC sub-units for the first 4 h annealing under the 700 °C and 900 °C regime, with a magnified inset

This result suggests that, at least for the mechanisms dominating microstructural evolution in the first 4 h, the higher temperature does not necessarily correlate to greater displacement (and therefore strain) but potentially invokes a greater number of regions of movement, however, more experiments would be required to support this hypothesis.

6.4 Conclusions

A methodology has been developed to track nanoscale microstructural evolution in Ni-YSZ AFLs by use of a robust laser-preparation route and annealing-imaging cycles that utilise high-resolution, lab-based X-ray nano-CT. When the imaging parameters are optimised, the procedure produces high-quality tomograms amenable to three-phase segmentation for the subsequent extraction of useful metrics such as surface areas, tortuosity factors and triple-phase boundary densities. By imaging the same microstructure after repeated annealing, sample-to-sample variations are avoided, such that observations and measured property changes could, in theory, be used to track genuine microstructural change and infer its effects on electrochemical performance. To address the various phenomena identified through this study, a variety of techniques were employed. Segmentation of tomographic information was performed with traditional thresholding and watershed methods, alongside the implementation of machine-learning

approaches and importantly, an iterative combination of the two. From the segmented data, several tools were employed to try to capture subtle to severe changes: voxel counting for phase fraction and interfacial areas; matrix algorithms for TPB density calculations; alongside chord length and local thickness measurements to measure PSD and better capture geometrical changes in pore and particle networks. Moreover, a diffusive-flux simulation was utilised for tortuosity factor estimation; a cellular automata simulation was used to probe the likelihood of external nickel agglomeration and DVC calculations were employed to monitor displacements and strains across annealing steps, without incurring segmentation errors. Key conclusions from conducting annealing under the three heating regimes are given in the following paragraphs.

To achieve solid-phase contrast that is amenable to ternary segmentation, a pillar diameter of 18 µm is too large and reducing the pillar diameter to 14 µm corresponds to a significant improvement, in accordance with theoretical estimations based on X-ray attenuation coefficients. An improved ternary segmentation is achieved when exposure time is increased from 64 to 72 s, whilst keeping scans below 30 h is necessary to avoid blurring. Despite the allure of accelerated testing, 1150 °C is too high a temperature as it leads to significant numbers of external nickel agglomerates (totalling ~600 μm^3 after 4 h), which depletes the internal microstructure of Ni. At short times (0 – 12 h), 700 °C proves arguably too low a temperature – although there is little issue with external agglomerates, microstructural change is too subtle to be unambiguously resolved given acquisition and processing errors. Nevertheless, at these times, 900 °C appears to be an appropriate temperature that produces far fewer nickel agglomerates than 1150 °C, but appreciable microstructural evolution for detection by these protocols.

For the highest temperature inspected (1150 °C), cellular automata studies corroborated that, both in a model and a real system, the nucleation of external nickel agglomerates is to be expected and is driven by capillarity effects and the presence of more open structures at the pillar edges. Surface diffusion alone is sufficient to describe this phenomenon. Even in the lowest temperature regime (700 °C), de-wetting behaviour is observed between nickel particles and ceramic electrolyte at the anode-electrolyte

interface. Comparing the virgin samples from both regimes, similarly reduced, the pore networks appear to be very similar, with very similar VSSA and r50 values in the AFL. However, by limiting the reduction time (and lowering its temperature), a different cermet morphology is produced in the virgin sample of the 900 °C regime, with more elongated pores and nickel particles with resolvable internal porosity. The virgin pore chord length distributions for the 700 °C and 900 °C regimes peak at 630 – 690 nm and 400 – 460 nm, respectively, which favourably match the r50 values of 325 nm and 212 nm from cPSD measurements and the local thickness histogram peaks at ~660 nm and 400 nm, providing corroborative evidence of the impact of reduction on the pore network.

Although imperfect, the use of an iterative approach to ternary segmentation produces improved results versus simple thresholding or even watershed methods. It must be noted, however, that the procedure as outlined is susceptible to changes in imaging conditions across tomographic time steps, as the training dataset for the previous sample is used in each case. Since the segmentability of the 700 °C regime samples was low, the lack of monotonic trends in VSSA, tortuosity factors and TPB densities is not surprising. The significant drop in VSSA after 4 h of annealing is suggestive of an early-stage rearrangement, but this requires greater scrutiny to be conclusive. With improved segmentability, the 900 °C regime demonstrated a similar drop as seen in the 700 °C regime during the first 4 h, adding weight to this initial reorganisation, which may occur as a result of relaxation from an initial high-energy state after sample preparation, or a true early-stage microstructural change inherent to SOFC electrode operation. The improved solid-phase contrast was achieved without significant losses in data quality from stage/temperature shifts, and the iterative segmentation approach for the 900 °C regime gave the most visually convincing segmentations of this work. Moreover, the pore phase fraction and $VSSA_{Pore}$ outputs match those from the binary segmentation excellently (0.2% and 4% discrepancies, respectively). The total TPB densities are higher in the 900 °C regime but active TPB density is much lower to begin with, likely a result of the different pore morphology. The total TPB density remains relatively constant during the first 4 h (-8%), similar to the behaviour in the 700 °C regime

(-2%). However, the active TPB density remains effectively unchanged (-1%) unlike the significant drop in the first 4 h in the 700 °C case (-20%). These results highlight the importance of initial microstructure on both performance and durability. RVE analysis suggests ~320-420 μm^3 is sufficient to represent the (low) pore phase fraction in both cases, but shows the sampled volumes are not sufficient to capture a representative value for the pore tortuosity, suggesting the AFL pore phase should be studied with larger-diameter pillars where solid-pore contrast suffices for binary segmentation.

DVC analysis suggests that at 700 °C, average strain magnitudes of approximately 0.3-0.4 are expected, but that at 900 °C, a smaller average strain magnitude of approximately 0.2 is expected. However, a significantly higher number of sub-volumes are shown to be displaced in this instance, such that more features will likely evolve in the same timeframe at the higher temperature, but by a lesser extent. If segmentability is suitably high, the range of metrics previously demonstrated may be implemented to inspect microstructural evolution, but DVC may also offer a useful corroborative tool, bypassing possible segmentation issues.

The results in this chapter suggest that there may be multiple mechanisms behind the early microstructural evolution of an SOFC AFL, with differing time constants and whose behaviour is only beginning to be characterised in these short studies. This hypothesis is in accordance with literature suggestions that a short activation period is often observed when running a cell [115], and that initial TPB rises are possible if new pores open up [105] to provide a more percolated pathway for the electrochemical reaction. However, it is at odds with the conclusions drawn by Tanasini *et al.* that initial cell activation is unlinked to early microstructural changes in electrodes. Nonetheless, these studies also demonstrate the unique advantages of utilising lab-based X-ray nano-CT to routinely inspect the same microstructure repeatedly to probe important microstructural developments in state-of-the-art Ni-YSZ AFLs, and highlight the importance of considering the metric, direction and timestep, as well as the tolerance, when performing RVE analysis of extracted properties.

Chapter 7: *In-situ* annealing of SOFC anodes

As an extension of the *ex-situ* work carried out between a lab-based X-ray nano-CT instrument and a lab-based tube furnace (see **Chapter 6**), further work was carried out at the Swiss Light Source (SLS) (Paul Scherrer Institut, Villigen, Switzerland) to perform *in-situ* experiments with synchrotron radiation and direct laser heating. The aim of these experiments was to monitor very early-stage microstructural changes by taking high spatial resolution (162.5 nm voxel dimension) tomographies with very high temporal resolution (full tomogram generated in minutes) as samples were heated by laser in a forming gas environment.

7.1 Samples

Cells from two different suppliers were investigated in this work; anode-supported half-cells from Forschungszentrum Jülich (Jülich, Germany) and anode-supported cells from SOFCMAN (Ningbo City, China) wherein pillar samples from the latter cells were fabricated to exclude cathode materials. Both sample sets were composed initially of 8YSZ electrolytes and NiO/YSZ cermet anodes before reduction.

For all samples, an initial reduction step was performed in a lab-based tube furnace to form an electroactive nickel network and provide the porosity required for adequate gas transport (as per the reduction in volume from NiO to metallic Ni). This reduction step consisted of a 5 °C/min ramp to 800 °C, under 4% H_2/balance N_2, a dwell for 4 h and passive cooling to room temperature.

A wide array of samples was prepared before access was provided to the TOMCAT beamline at SLS, due to the unpredictability of the laser heating regime and sample stability. For both sample types, various preparation routes were followed, as summarised in Table 44. Two examples, an alumina tube and platelet geometry, are shown in Figure 144.

Supplier	Geometry	Pillar Formation	Code
Jülich	Alumina Tube	Reduced as electrode	J011-01,02,03,04,05,06
	Nickel Cylinder		J111-01,02
	Platelet		J021-01,02,03,04,05
SOFCMAN	Alumina Tube	Reduced as pillar	S010-01,02,03
		Reduced as electrode	S011-01,02
	Platelet	Reduced as pillar	S021-01,02,03

Table 44: List of prepared samples for in-situ synchrotron experiments

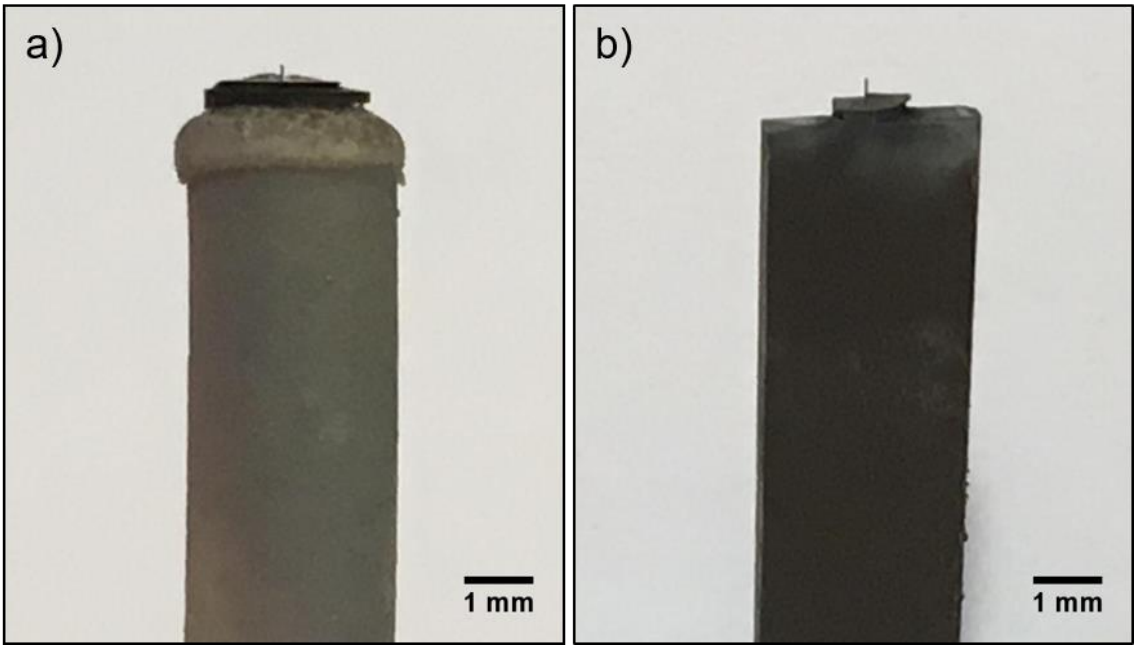

Figure 144: a) Electrode mounted on alumina tube; b) Fine pillar machined from the edge of a macroscopic electrode

The rationale behind different geometries stemmed partly from the availability of certain equipment at the beamline. At TOMCAT, a laser-based heating system had recently been developed which was capable of heating certain materials to temperatures approaching 1700 °C [238]. Details of the two-diode-laser set-up is given in **Section 7.2.1.1**; importantly the pyrometer used to regulate the laser power, affording a particular temperature, had a spot size of 1 × 1 mm. As the pillars to be examined had dimensions at least an order of magnitude smaller, a separate base with larger dimensions was needed if a pyrometer reading was to be reliably obtained. For this reason, some sample electrode pillars were affixed to small nickel cylinders (3 – 5 mm in diameter) with a small amount of Ceramabond (Aremco, New York, USA) and some were milled as a protrusion from a larger electrode piece (“Platelet”, 3 mm in diameter). These geometries provided a base to be heated and for the temperature to be reliably monitored by pyrometer reading, although this indirect laser heating would make the

actual temperature of the imaged pillar difficult to predict precisely. Alternatively, the typical ceramic mounting geometry used in the *ex-situ* lab-based experiments in **Chapter 6** was also envisaged, but with the need to calibrate laser power without the pyrometer, potentially by direct heating of a thermocouple.

7.2 Synchrotron Radiation

The synchrotron studies featured in this thesis were all performed at the X02DA beamline (also known as TOMCAT) in SLS at the Paul Scherrer Institut (PSI), which offers fast, non-destructive, high resolution, high brilliance, high coherence X-ray capabilities. The TOMCAT beamline receives synchrotron light from a 2.9 Tesla superbend, giving rise to a peak beam energy of 11.1 keV, yielding high fluxes for hard X-rays [252].

7.2.1 Experimental Set-up

7.2.1.1 Laser-heating

The laser set-up used in all cases was that provided by the TOMCAT beamline scientists and is described thoroughly in [238]. The system comprises two Class 4 diode lasers which operate at near-infrared (NIR) wavelengths with a maximum power output of 150 W each. At 40 mm from the sample, the spot size is nominally 200 × 1000 μm (XY) and is created by the interaction of the two lasers spaced almost 180 ° apart, except for a small deviation to avoid self-illumination. Two Class 2 visible light lasers are used for alignment, two beam blockers are used to catch the parts of the beam not absorbed by the sample, and a non-contact pyrometer is the primary mode of temperature regulation (see Figure 145). The pyrometer filters out the Class 4 laser and can measure temperatures to an accuracy of 0.1 K given the correct emissivity value of the material being measured. However, the pyrometer spot size is nominally 1 × 1 mm, which posed a challenge for the Ni/YSZ pillar samples of dimensions at least an order of magnitude smaller. Normally samples are contained within an alumina, quartz or boron nitride sample holder, although this was also impractical in this case, due to the fine, fragile pillar of interest.

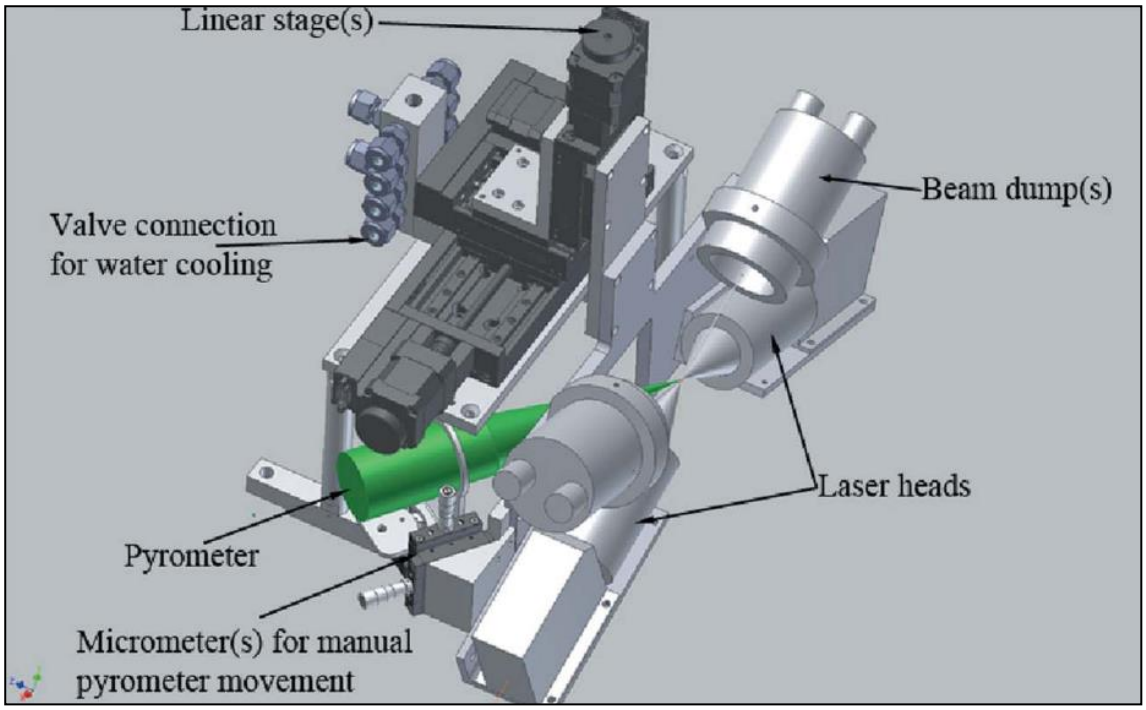

Figure 145: 3D drawing of synchrotron laser set-up used in in-situ *experiments, reproduced with permission of the International Union of Crystallography from [238]*

7.2.1.2 Testing

First, the indirect heating of a Ni/YSZ sample affixed atop a nickel cylinder by Ceramabond (J111-01) was performed in air due to the ease of set-up. As expected, initial testing led to the oxidation of the nickel cylinder (at least its surface), observed by green film formation. Although not ideal, this lowered the reflectivity of the heated surface and the oxidised cylinder was amenable to heating to higher temperatures than the unoxidized cylinder, for the same laser power. More significantly, the adhesion between the cylinder and the electrode did not withstand the thermal gradients induced in the system and delamination occurred at higher temperatures (> 500 °C).

Further testing under pure N_2 and forming gas (0.5% H_2 in N_2) retained the nickel cylinder in metallic form; Figure 146 shows a glowing nickel cylinder heated to approximately 900 °C. However, when nickel cylinders affixed with coarse electrodes were heated, large thermal gradients were observed between two thermocouple readings: one directly adjacent to the point of laser heating on the cylinder; and one atop the bulk electrode. Due to the poor thermal conduction properties of the ceramic-based glue, along with the high reflectivity of the metal surface, achieving suitably high temperatures at the electrode pillar by indirect heating was not deemed possible. At very

high laser powers, delamination compounded these issues. For these reasons, an alternative temperature calibration methodology was pursued.

Figure 146: Photograph of nickel pillar heated to 900 °C, emitting visible light due to incandescence

7.2.1.3 Temperature Calibration

Direct heating was applied to the electrode pillar in all following tests and scans. Identifying the temperature of the sample afforded by a particular laser power remained an issue since the pyrometer reading was unreliable due to its large spot size. Instead, indirect calibration using a Reckmann K-type thermocouple was employed. The thermocouple was placed in the laser path, and its extension connected to a data logger (Picolog, Pico Technology, Cambridge, UK), in turn connected to a laptop. Alignment of the laser spot with the end of the thermocouple was achieved by selecting a fixed low laser power and incrementally moving the laser until a maximum temperature was found. Once this was achieved, the laser power was gradually increased, and the temperature logged as a function of the power (Figure 147). The thermocouple used was composed predominantly of nickel metal and therefore acted as a proxy for the Ni/YSZ cylinder. However, it should be noted that the lack of ceramic and porosity in the thermocouple hot junction does render this temperature reading somewhat of an approximation. Fortunately, the inclusion of air (porosity) and the inclusion of YSZ (Ceramic), relative to the thermocouple, are likely to have compensatory effects due to their respective thermal properties. This calibration was repeated with the inclusion of 500 ml/min flow of 0.5%

H_2 / balance N_2 forming gas. In order to reach similar temperatures as without gas flow, the laser power had to be increased by approximately 2 A.

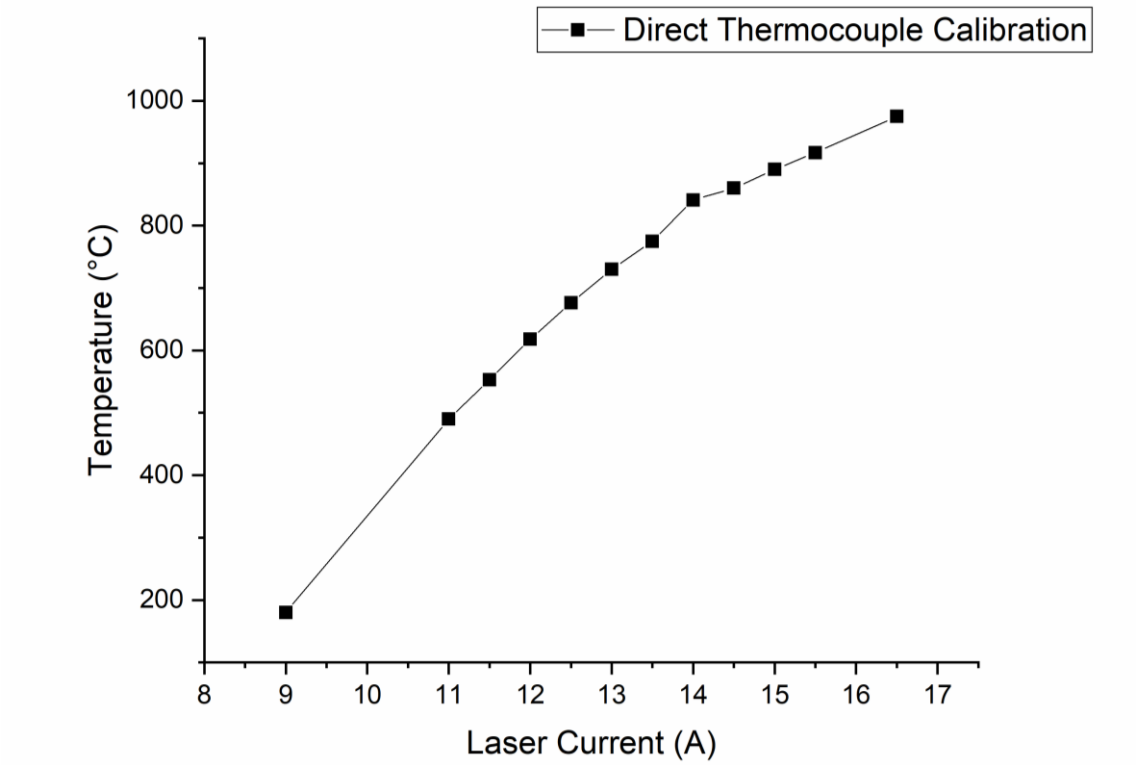

Figure 147: Plot of temperature calibration data taken from aligning laser spot directly with thermocouple hot junction, without gas flow. To attain these temperatures with 500 ml/min flow of forming gas, an extra 2 A were required

7.2.1.4 Gas injection

To prevent oxidation of the metallic nickel in the electrode pillar, it was required that the immediate vicinity was low pO_2 or that the pillar be surrounded by a reducing atmosphere. Although a nitrogen blanket in initial tests prevented oxidation at intermediate temperatures, a small amount of NiO (green colouration) was observed at high temperatures so a reducing environment was favoured. Due to the high temperatures envisaged in the experiment (up to 1000 °C), and to keep the hydrogen level below the lower explosive limit (LEL) for this high temperature, a special formulation of 0.5 % H_2 (balance N_2) was used in all beamtime experiments. To allow for free rotation of the sample stage and avoid any bulky furnace enclosures which may prevent the detector from being brought close to the pillar, top-down gas injection was chosen, whereby the forming gas flooded the sample pillar from directly above, with a steady flow to displace any air from the vicinity of the sample. The success of the forming gas

envelope was judged by the colour of the pillar and/or its surrounding electrode base (grey for nickel, green for nickel (II) oxide).

7.2.2 Imaging

7.2.2.1 Set-up

The number of optical elements along the beam path at the TOMCAT beamline is minimised to avoid deterioration of the beam profile [252], and the set-up may facilitate both white beam and monochromatic options. For the latter set-up, a double crystal multilayer monochromator is mounted at approximately 7 m from the source, and the vertical dimension of the beam can be manipulated by moving the end-station along the path such that a collimating mirror is not necessary. The sample stage allows for the centring of the sample with 100 nm-precision and is air-bearing for highly precise rotation. The detection system comprises a 40 × magnification lens, a LSO:LySO 20 um scintillator (X-rays converted to visible light) and a CMOS (sCMOS) - PCO.edge 5.5 camera. The general layout of the imaging set-up (without the laser system in place) is shown in Figure 148.

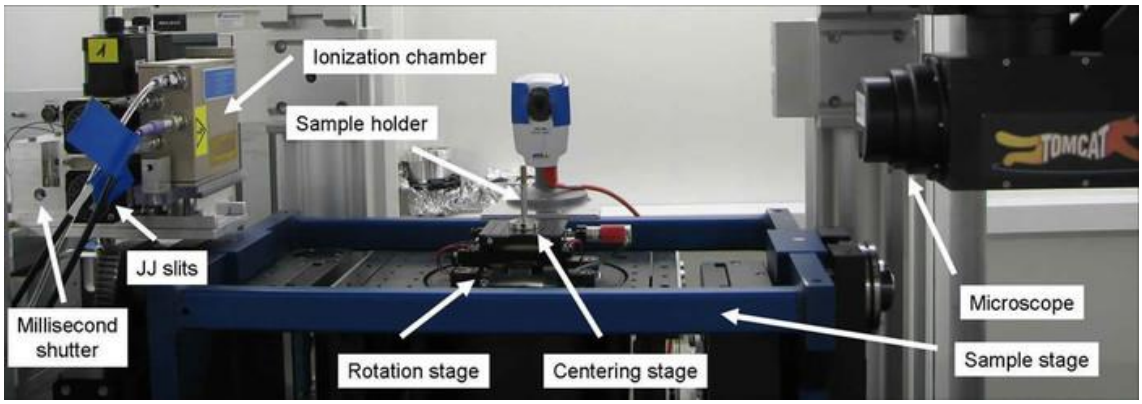

Figure 148: Layout of end-station imaging set-up (without the laser system in place)

Initial testing was carried out to explore the parameter space which encompasses: X-ray energy, exposure time, number of projections and reference corrections.

7.2.2.2 Beam Energy

From the X-ray attenuation coefficients of Ni and 8YSZ, an optimal X-ray beam energy range could be identified. The Ni K-edge at 8.333 keV [318] and the effective 8YSZ edge at approximately 18 keV (Zr K-edge at 17.998 keV [318]) gave an operating window of approximately 9 – 17 keV, see Figure 149.

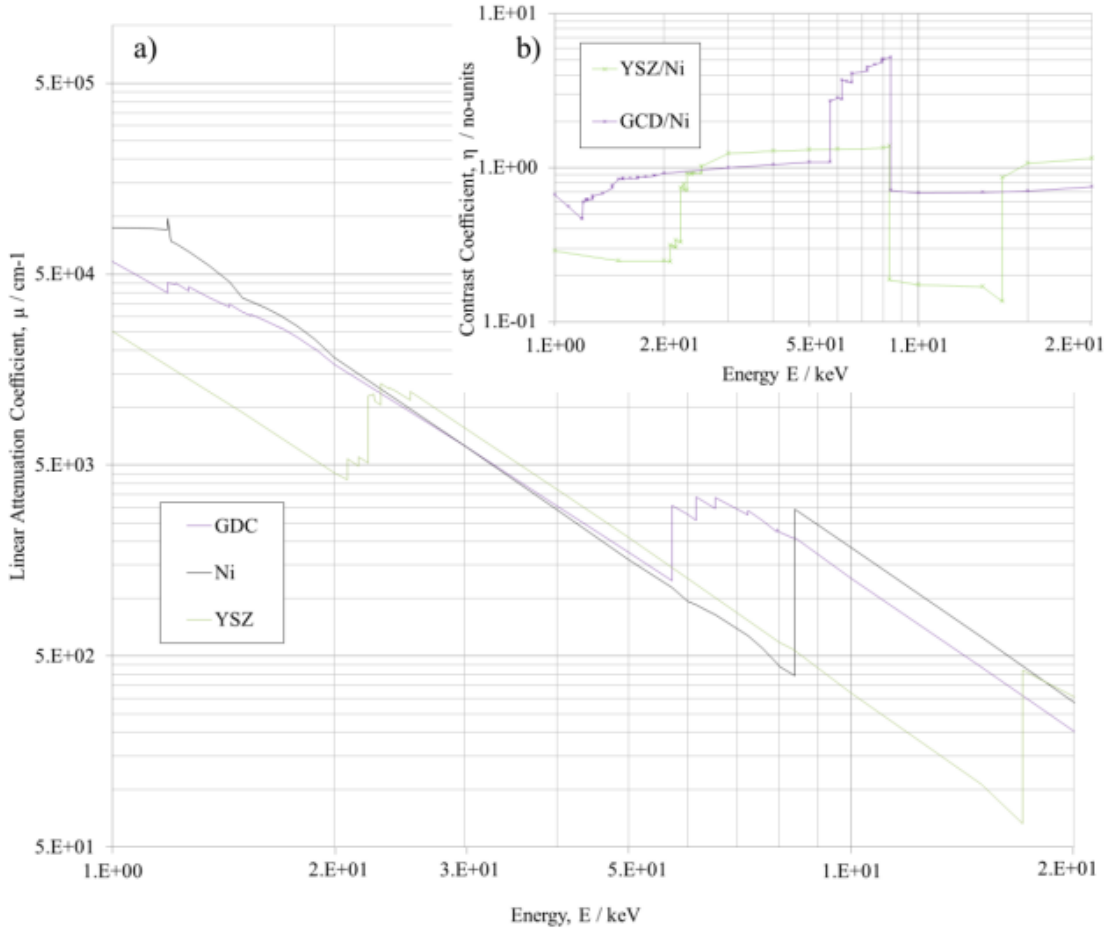

Figure 149: Plots of a) attenuation coefficients of Ni and 8YSZ and inset; b) their ratio as a proxy for segmentability in resulting tomograms, reproduced from [309]

The flux at the X02DA beamline was highest in the 15-18 keV range and initial scans were conducted at 16 keV and compared with scans conducted at 17 keV; 18 keV was not used to ensure the K-edge was avoided. Marginal improvement was found in Ni-YSZ contrast on changing from 16 to 17 keV, which was henceforth used for all scans. An example of a radiograph and a tomograph from an early scan of a Jülich sample at 17 keV is shown in Figure 150. In Figure 150 b)**,** black represents void (porous space or air surrounding sample), grey represents YSZ and white is nickel. It is clear for this type of sample that the electrolyte and AFL can be identified, although the finer microstructure of the AFL is not resolvable.

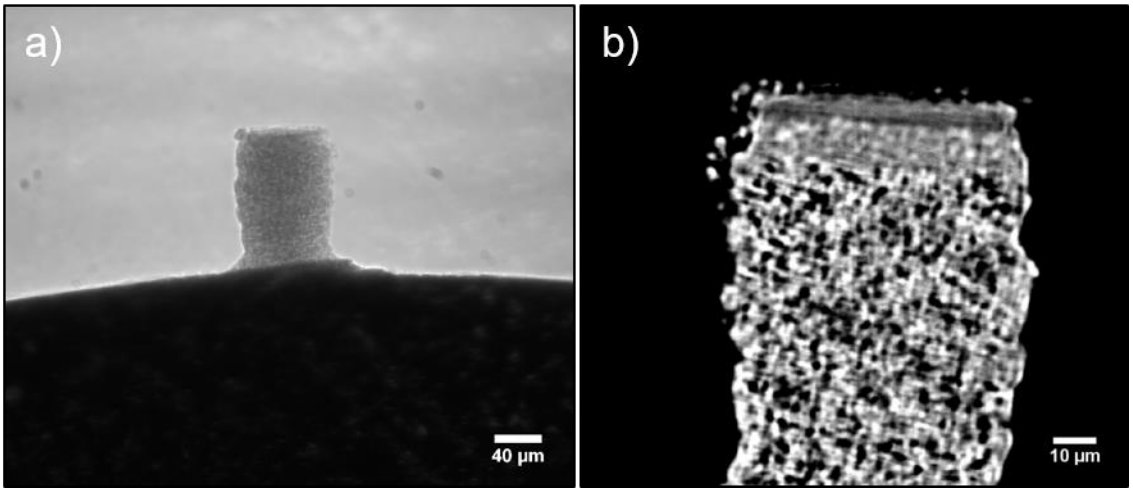

Figure 150: a) Uncorrected radiograph of J011-06; b) XZ-orthoslice from J011-06 tomogram

7.2.2.3 Exposure Time

The beamline set-up is designed for taking high temporal resolution measurements and due to the high brilliance of synchrotron radiation, very short exposure times are necessary in order to produce an image with adequate signal-to-noise ratio. 100, 200 and 280 ms were explored as possible exposure times, wherein 280 ms was found to give the highest data quality and solid phase contrast. However, to achieve high temporal resolution and not capture a blur of microstructural evolution, this relatively 'long' exposure time necessitated a reduction in projection number, in order to give a usable tomogram time.

7.2.2.4 Projection Number

1201 and 501 projections were explored as possible projection numbers, as standard long and short scan lengths, respectively. Although 1201 projections gave a marginally improved image of unheated samples, the time taken for a full tomogram, at 280 ms, was between 5 and 6 minutes, whereas 501 projections meant a full tomogram could be produced in less than 2.5 minutes and gave no significant artefacts by virtue of the sample occupying a very small fraction of the detector width. Given the limited spatial resolution and *in-situ* constant heating set-up, the play-off between the long and short scan regimes was explored. On the one hand, the long scan may provide the added image quality required for feature recognition but similarly maintaining a short tomogram time may avoid the blurring of any changes happening during acquisition. 501 projections were used for most scans, but 1201 was also used for one tomographic series.

7.2.2.5 X-ray CT scan parameters

All scans reported in the **Section 7.4** were conducted with a beam energy of 17 keV, 280 ms exposure time, and used a LSO:LySO 20 µm scintillator, coupled with a PCO.Edge 5.5 detector. The details of each reported scan are given in Table 45.

Scan No.	Sample	Heating Regime	Proj. No.	Comment
1	J011-06	1000 °C, after 20 min	501	One aged tomogram
2	S011-02	-	501	Solid-phase contrast test
3	S010-01	800 °C, every 10 min	1201	Seven tomographies taken
4	S010-02	1040 °C, every 21/25 min	501	Seven tomographies taken

Table 45: List of in-situ *synchrotron scans with their respective heating regimes*

7.3 Data Processing

7.3.1 Reconstruction

All scans were reconstructed using the "*Gridrec"* algorithm [319], developed at SLS by TOMCAT beamline scientists, which is an alternative to the standard FBP algorithm. The algorithm is "highly optimized for conventional CPU technology", thus avoiding the need for specialised understanding of GPU architectures. *Gridrec* is based on a Fourier Transform method, wherein a series of 1D Fourier transforms of a series of projection images at varying angles yields a 2D Fourier space object, which upon a 2D inverse Fourier transform gives rise to a reconstructed slice [319]. To overcome interpolation issues encountered in the Fourier domain, a gridding method for resampling the Fourier space from polar to Cartesian co-ordinates [320] is implemented.

7.3.2 Data Import/Export

For the calculation of basic metrics, the 3D tiff of each tomogram was imported into Avizo before subsequent image filtering, as described in the relevant sections below. For DVC calculations, the data was first imported into Avizo, converted to 8-bit datasets and exported as a 3D .raw file for import into the DaVis (LaVision, Germany) software.

7.4 Results & Discussion

7.4.1 Initial Test (J011-06, 1000 °C)

7.4.1.1 Acquisition & Registration

The first sample imaged before and after heat treatment was J011-06, a Jülich sample fixed atop a ceramic tube with cured Ceramabond. The sample constituted a fine pillar with a diameter of approximately 60 µm, composed of a thin electrolyte, a thin AFL,

and mostly an ASL (Figure 151). After registration of the two volumes, *virgin* and *aged*, a sub-volume was extracted from the interior of the ASL, before another registration step. The X-, Y- and Z- transformations performed as a result of the second registration step were all less than one pixel in distance (< 0.1625 µm), with angular changes no more than 0.15 °. The edges were cropped to delete extraneous surfaces, giving a sub-volume of 185 × 168 × 390 voxels. XY-orthoslices of the two registered datasets are shown in Figure 152 for direct visual comparison of the evolution captured after 20 min of heating at approximately 1000 °C. Some retained features are highlighted (blue arrows) to support the successful registration of the tomograms.

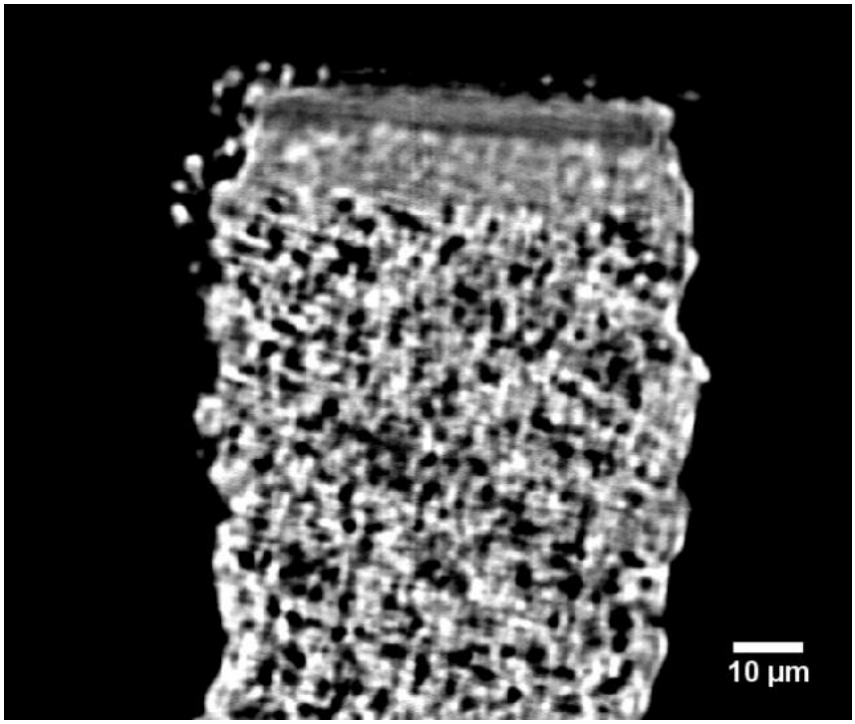

Figure 151: XZ-orthoslice from J011-06 tomogram

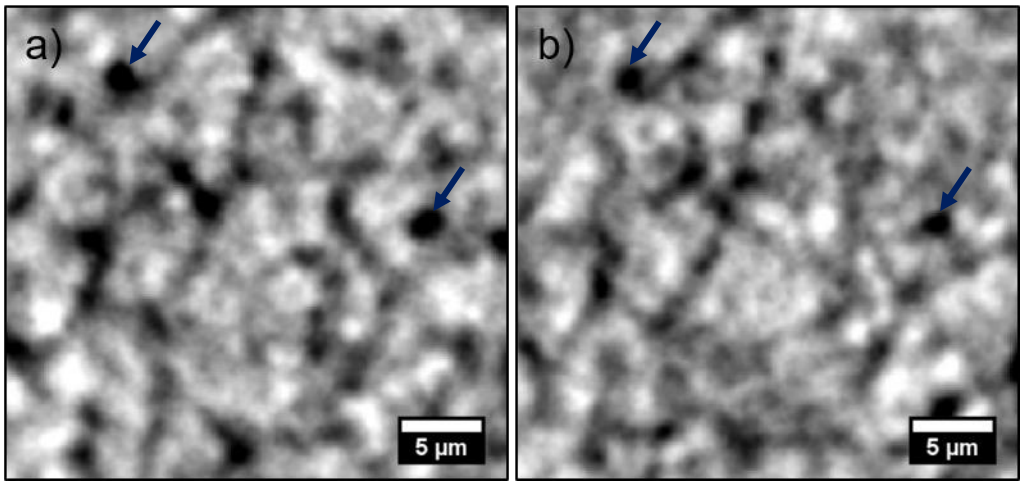

Figure 152: a) Raw XY-orthoslice from virgin J011-06; b) Raw XY-orthoslice from aged J011-06

From the tomograms, it is observable that three phases are present: white is nickel; grey is YSZ and black is pore (air), from the attenuation coefficients (Figure 149). The solid phases appear reversed relative to lab-based work at 5.4 keV due to the higher energy beam (17 keV) used at the beamline and the X-ray attenuation behaviour of the solid materials. However, since the smallest voxel dimension accessible with the laser set-up at the beamline was 162.5 nm, there appears to be some “partial voluming” issues, whereby the resolution is insufficient to readily separate the solid phases, and many voxels individually represent a weighted average of the attenuation properties of more than one phase. Nonetheless, the porous phase is easily distinguishable from the solid phases and hence a binary segmentation was conducted after processing.

7.4.1.2 Filtering

To increase the contrast between pore and solid phases, an “Unsharp Masking” filter was employed, which is commonly used to sharpen edges without incurring more noise. This filter first applies a Gaussian denoising, and blends the result to the original image, but only in areas of high gradient (edges), by use of a mask based on an original gradient image. The result of the application of this filter is shown in Figure 153, which displays an XY-orthoslice of the virgin sample, from a) original dataset (full histogram); b) original dataset (histogram adjusted); c) filtered dataset (full histogram); d) filtered dataset (histogram adjusted).

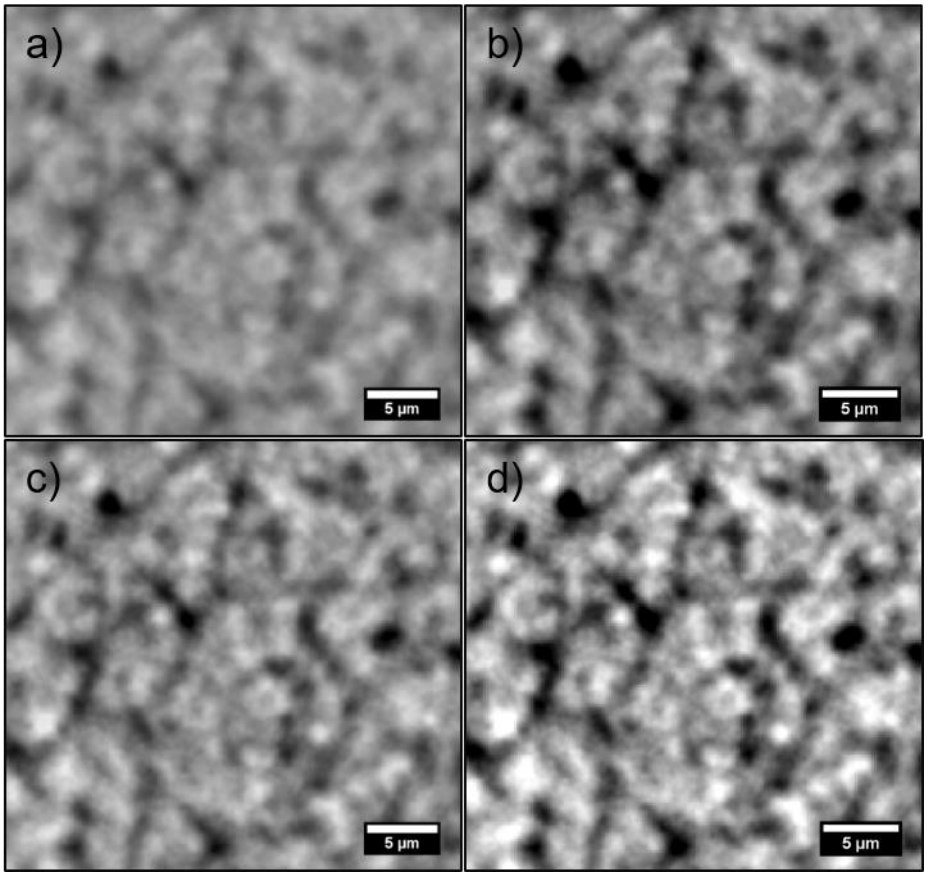

Figure 153: XY-orthoslice from virgin J011-06 a) pre-filter, full histogram; b) pre-filter, histogram adjusted; c) post-filter, full histogram; d) post-filter, histogram adjusted

7.4.1.3 Segmentation

Given the high contrast at the solid-pore interfaces, a standard watershed segmentation approach was used to efficiently separate pores from solids; first seeds were placed in the pore volume whereby there was high confidence that these voxels indeed belonged to the pore phase. The same was repeated for voxels clearly identifiable as “solids”, leaving a selection of interim voxels unassigned, and the watershed algorithm was run to grow from the seeds to their local basin peaks. A single XY-orthoslice of the filtered data and the corresponding binary segmentations are shown in Figure 154. (N.B. the contrast has been artificially increased to accentuate the difference between solid and pores).

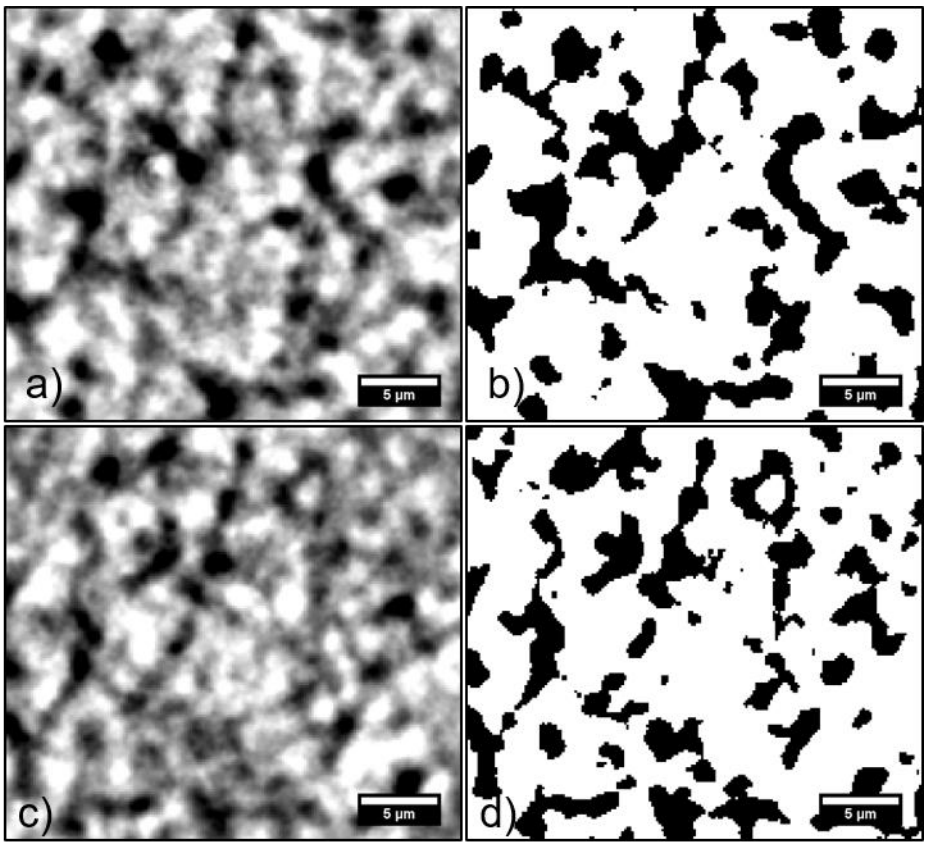

Figure 154: XY-orthoslice from J011-06 a) virgin filtered data; b) virgin binary segmentation; c) aged filtered data; d) aged binary segmentation

7.4.1.4 Analysis

The total analysed volume was approximately 52,000 μm^3, which is large compared with most 3D reconstructions in the literature [175]. By standard voxel counting methods, volume fractions and VSSAs were calculated for the virgin and aged samples and the results are shown in Table 46.

	Virgin		Aged	
Phase	**Pore**	**Solid**	**Pore**	**Solid**
Volume Fraction (%)	23.3	76.7	23.8	76.2
VSIA (μm^{-1}) (unsmoothed)	0.7		0.7	
VSIA (μm^{-1}) (smoothed)	0.6		0.7	

Table 46: Basic metrics extracted for J011-06 virgin and aged tomograms

The pore volume fraction appears unchanged within experimental and analytical error (only 2% proportional increase) although the surface area of the binary interface appears to have increased somewhat. The change represents an increase of 7-8% towards greater surface area and may be due to an effective roughening due to nickel movement during this early-stage rearrangement. From Figure 154, it is clear that there has been substantial microstructural change between the acquisition of the two tomograms, even though the global metrics indicated only a small degree of surface area

change. To verify this apparent visual change was not due to misregistration, a similar registration step was performed on the binarised volumes, and on comparison of the two, no transformational corrections were suggested. On misaligning by a given transformation, followed by a re-registration, the resulting transformational correction needed was the opposite of the misalignment co-ordinates, to the nearest voxel, suggesting the volumes are well-registered.

To visualise the changes, a composite segmentation approach was followed, wherein voxels were allocated to particular labels based on their identity in the virgin and aged samples. Voxels which were pores in the virgin sample but changed to solids, are labelled red, those which remain pores are yellow and those which were solids but are newly formed pores in the aged sample are green. A slice from this volume is shown in Figure 155 for clarity. Analysis of these volumes showed that approximately 57% of the original pore volume was still present after the 20 min anneal, and 43% changed (with a discrepancy between absolute pore volumes measured of only 0.45%).

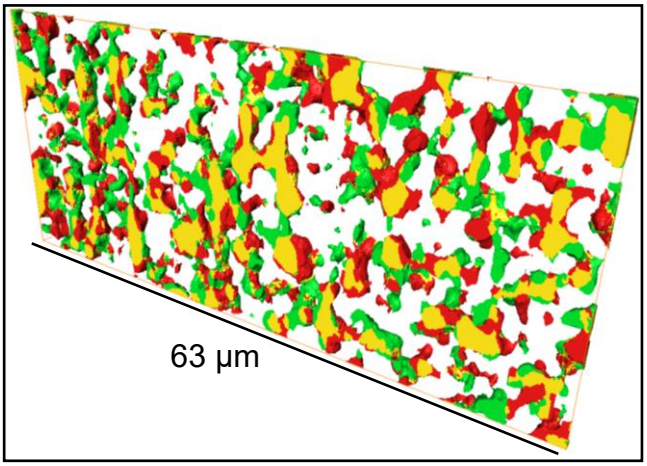

Figure 155: Surface rendering slice of composite segmentation: red = pore volume lost; yellow = pore volume unchanged, green = new pore volume gained

From observation of many slices, it is evident that the majority of old pores and new pores are “connected” to each other or the unchanged pore space which remains after the annealing step. As the proposed principal mechanism of porosity change is movement of nickel, porosity should not appear or disappear from “unconnected” regions, unless a densification mechanism is at play.

Tortuosity factor analysis was undertaken to identify any changes in the impediment to gas transport through the porous network. As can be seen from Table 47, small decreases in tortuosity factor are accompanied by a small increase in the proportion of the pore volume that is percolated (in all directions).

Tortuosity Factor (direction)	Virgin		Aged	
	Pore	Solid	Pore	Solid
X-	9.8	1.3	8.4	1.3
Y-	6.3	1.2	5.1	1.2
Z-	14.0	1.3	9.3	1.3
Percolation (%)	96.7	100.0	98.7	100.0

Table 47: Pore network metrics extracted from J011-06 virgin *and* aged *tomograms*

This result suggests that in very early-stage microstructural re-arrangement, there is scope for an improvement in gas transport and potentially, an increase in the available active TPBs [105]. The former would suggest a reduction in mass transport polarisation losses (likely recognisable only at high current loads) and a decrease in activation polarisation losses if new active TPBs are effectively created. However, the observations from this experiment correspond to the ASL, thus the inferences drawn which relate to TPB creation and pore connection are not necessarily transferrable to the electrochemically active AFL, and only indicate the potential for these changes. RVE analysis was performed using the approach set out in **Section 3.4.2.3**. and yielded the results shown in Figure 156 and detailed in Table 48.

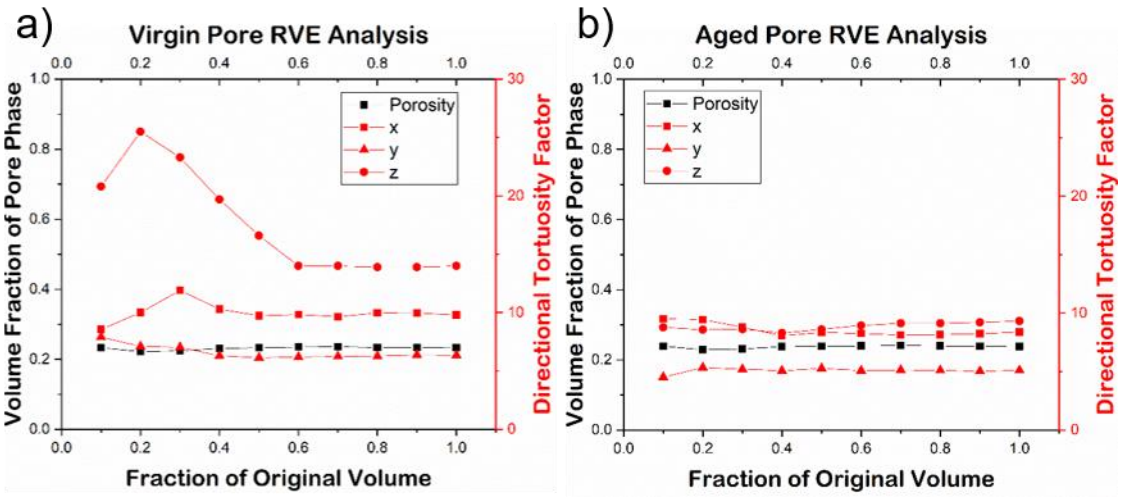

Figure 156: Plots of RVE analysis of J011-06 pore phase in a) virgin *and b)* aged *samples*

J011-06								
Virgin					Aged			
		Tortuosity Factor				Tortuosity Factor		
x	**Volume fraction**	**X-**	**Y-**	**Z-**	**Volume fraction**	**X-**	**Y-**	**Z-**
0.1	0.23	8.6	7.9	20.8	0.24	9.5	4.5	8.8
0.2	0.22	10.0	7.1	25.5	0.23	9.5	5.3	8.6
0.3	0.22	11.9	7.0	23.3	0.23	8.8	5.2	8.6
0.4	0.23	10.3	6.3	19.7	0.24	8.1	5.1	8.3
0.5	0.23	9.7	6.1	16.6	0.24	8.4	5.3	8.6
0.6	0.24	9.8	6.2	14.0	0.24	8.3	5.1	9.0
0.7	0.24	9.7	6.3	14.0	0.24	8.1	5.1	9.1
0.8	0.23	10.0	6.3	13.9	0.24	8.2	5.1	9.1
0.9	0.23	10.0	6.4	13.9	0.24	8.2	5.0	9.2
1.0	0.23	9.8	6.3	14.0	0.24	8.4	5.1	9.3

Table 48: List of RVE analysis values as a function of sample dimension (x)

The volume fraction behaviour with changing sample volume is almost identical between the *virgin* and *aged* samples. Throughout the entire range, this metric deviates a maximum of 4.1% (*virgin*) and 3.5% (*aged*) from the full volume (x=1.0) value, and these deviations all remain less than 2% after x = 0.3 – 0.4. This corresponds to an RVE of between approximately 15,000 μm^3 and 20,000 μm^3, based on volume fraction and a stringent tolerance of 2%.

For tortuosity factor, there is greater variation at small volumes in the virgin sample versus the aged sample, particularly in the X- and Z-directions. A clear plateau is observable starting at x = 0.6 for the Z-direction tortuosity factor of the virgin sample, implying an RVE of approximately 31,000 μm^3 based on this metric alone. This plateau falls earlier for the X- and Y- directions, at x = 0.5. Tortuosity factor is often more sensitive to analysis volume size, and if the same stringent 2% tolerance level is used, RVEs are reached generally at higher values of x (Figure 156). For the virgin sample: x = 0.5, 0.7, 0.6 (X-, Y-, Z-) and for the aged sample: x =0.9, 0.6, 0.7 (X-, Y-, Z-). If, however, the tolerance is increased only slightly, to 4% (see **Chapter 5**) to account for the greater acceptable variability, the numbers become: virgin: x = 0.5, 0.4, 0.6 (X-, Y-, Z-) aged: x = 0.4, 0.3, 0.6 (X-, Y-, Z-). On average, this changes the implied RVE volume dimension from 0.6 to 0.5 and 0.7 to 0.4, for the *virgin* and *aged* samples, respectively.

This analysis highlights both the importance of choosing a suitable metric and the significance of selecting an appropriate tolerance level when conducting RVE analysis.

7.4.1.5 Digital Volume Correlation (DVC)

The same sub-volume was exported to DVC software, DaVis, ready for comparison (see **Section 3.4.3** for details). An initial calculation was performed on the unsegmented (grayscale) images, based on input parameters given as a guideline by the software developers, based on the numbers of voxels, voxel dimension, feature size and separation for the images in question. The initial input parameters were: FFT pre-shift window: 64; and a total of 3 steps: i) 32 voxel sub-volume, 75% overlap, peak search of 8, 8 × 8 × 8 binning, 1 pass; ii) 32 voxel sub-volume, 75% overlap, Peak search of 4, 4 × 4 × 4 binning, 1 pass; iii) 16 voxel sub-volume, 75% overlap, Peak search of 2, no binning, 2 passes. An example of the outputs given by the DVC software is presented in Figure 157. The first image is a single XY-orthoslice from the *virgin* tomogram, the middle image represents the direction of displacement for each sub-volume by arrow and its magnitude by colour and the third image is the same single XY-orthoslice from the *aged* tomogram, after the 20 min anneal at approximately 1000 °C.

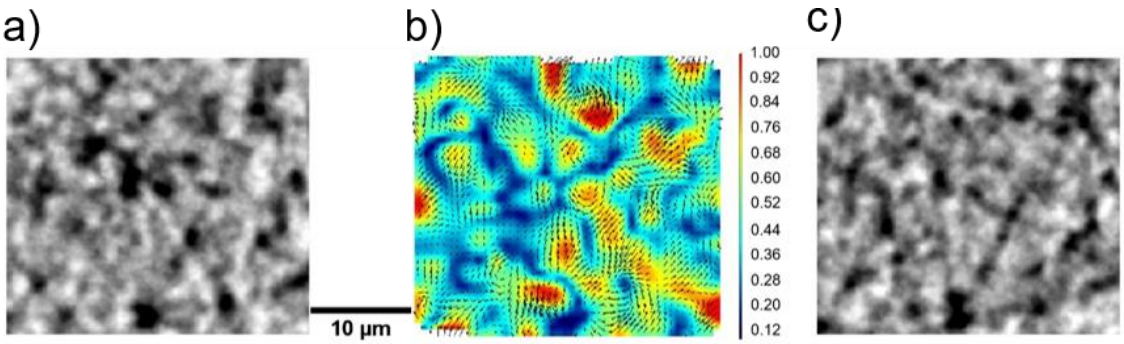

Figure 157: Example XY-slices a) from virgin *tomogram; b) from DVC calculation (magnitude of Z displacement by colour (µm) and direction of overall displacement by arrow); c) from* aged *tomogram, for J011-06*

As a qualitative assessment of the sample regions at which microstructural change is concentrated, a single slice which contained the regions of maximal displacement was overlaid on the *virgin* and *aged* tomographic slices, which is shown in Figure 158 and Figure 159, respectively.

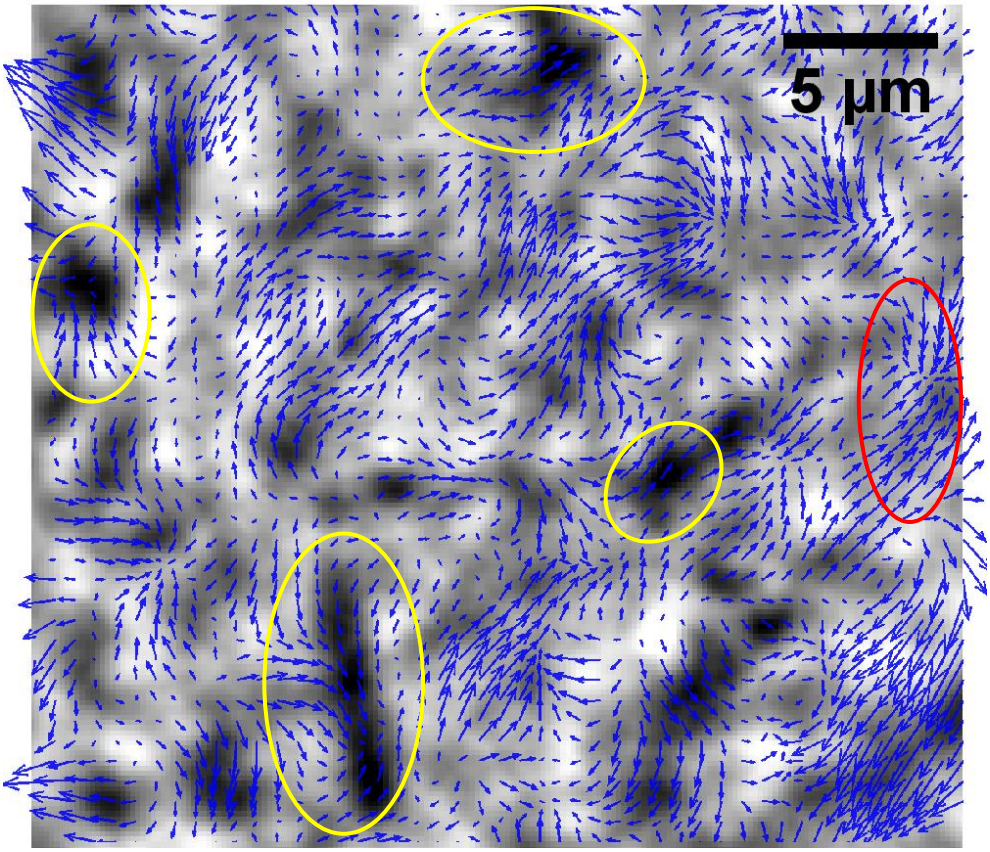

Figure 158: Overlay of displacement vectors for slice with region of highest displacement vectors (top left and bottom right), on virgin *image*

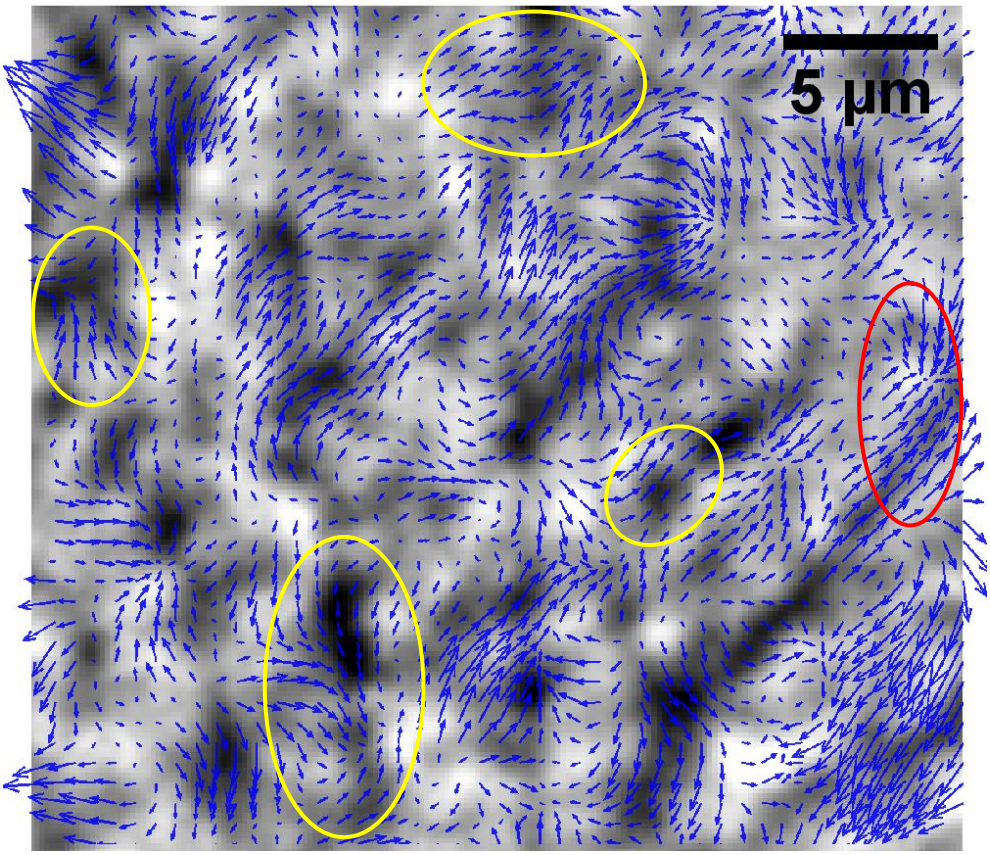

Figure 159: Overlay of displacement vectors for slice with region of highest displacement vectors, on aged *image*

Upon inspection, a number of features are apparent. Firstly, as highlighted by the red ovals, the displacement vectors identify mass transport that gives rise to a clearer centre of nickel (white/high grayscale) that was less apparent in the *virgin* image, giving support to the use of DVC for tracking nickel mobility. Moreover, as highlighted by the yellow ovals, there are multiple examples of movement detected into locations of porosity in the *virgin* image, whereby these are at least partially filled with solid material in the *aged* image.

A semi-quantitative analysis was subsequently performed, analysing the 5 slices from the displacement vector field which contained the greatest displacement magnitudes and focussing on the 6 areas of greatest displacement in each slice. The maximum displacement vector magnitude, its correlation value and the nature of the movement identified in that region was recorded in Table 49. Due to viewing single 2D slices at any one time, the observations vary depending upon whether the suspected relocation of the nickel is in the same plane. When this is the case, it is denoted "relocation"*, otherwise, the change may be: an increase/decrease in size of an existing high or low grayscale feature (Ni or pore growth/shrinkage) *or* the loss/creation of a high or low grayscale feature (Ni or pore appearance/disappearance). Ni features are neither lost or created in reality, but no evidence of their presence in the plane of inspection is present in the *aged* or *virgin* slice, respectively. It is worth noting that this analysis could be further conducted in a 3D manner, observing slices before and after the slice of interest, but this approach would be far more time-consuming.

Vector slice no.	Image slice no.	Maximum displacement (µm)	Correlation value	Nature of region change
91	365	1.86	0.70	Ni shrinkage (at volume edge)
		1.58	0.76	Ni relocation* (at volume edge)
		1.48	0.74	Ni relocation* (towards volume edge)
		1.12	0.74	Pore disappearance (interior)
		1.02	0.80	Pore disappearance (interior)
		1.01	0.66	Pore appearance (at volume edge)
51	205	1.58	0.59	Ni appearance (at volume edge)
		1.12	0.81	Pore appearance (interior)
		1.05	0.62	Ni appearance (interior)
		1.05	0.69	Pore appearance (at pore edge)
		0.99	0.90	Ni growth (interior)
		0.97	0.50	Ni disappearance (interior)
65	261	1.40	0.64	Ni shrinkage (at volume edge)
		1.26	0.84	Pore disappearance (at volume edge)
		1.22	0.68	Ni appearance (at volume vertex)
		1.12	0.56	Ni relocation* (interior)
		0.93	0.53	Ni disappearance (at volume edge)
		0.74	0.68	Ni relocation* (interior)
19	76	1.35	0.65	Pore appearance (at volume edge)
		1.33	0.63	Pore appearance (at volume edge)
		1.20	0.75	Ni relocation* (at volume edge)
		1.18	0.63	Ni relocation* (at volume edge)
		1.17	0.75	Ni appearance (at volume edge)
		1.03	0.76	Ni appearance (at volume edge)
43	173	1.23	0.69	Pore growth (at volume edge)
		1.14	0.80	Ni appearance (at volume edge)
		1.10	0.53	Pore appearance (at volume edge)
		1.01	0.89	Ni growth (at volume vertex)
		0.88	0.82	Pore disappearance (interior)
		0.88	0.63	Pore growth (at volume edge)
Average		**1.14**	**0.70**	-

**Suspected visualisation of in-plane nickel movement*

Table 49: Maximum displacement and correlation values for regions of greatest displacement across five XY-slices from J011-06 displacement vector field

From this 2D analysis of the regions of greatest displacement magnitude, on average, during the 20 min of annealing at approximately 1000 °C, the most mobile features moved by approximately 1.1 µm, with a typical correlation value of around 0.7. Identifying the areas of greatest displacement, allows for a 3D inspection of the movement of particular features, as shown in Figure 160, which displays the movement of the highest grayscale features from the region with 1.12 µm maximal displacement from DVC slice 65. This was produced by segmenting sub-volumes (48 × 48 × 48 voxels) containing these points of high displacement which was achieved by applying an

Unsharp Masking filter and subsequently segmenting the highest grayscale features with a simple threshold at 250 (maximum grayscale ~350) chosen by visual observation to capture areas highly likely to represent nickel clusters/particles. Features at the border of the extracted volume were excluded, and the largest feature left in the interior was selected for observation.

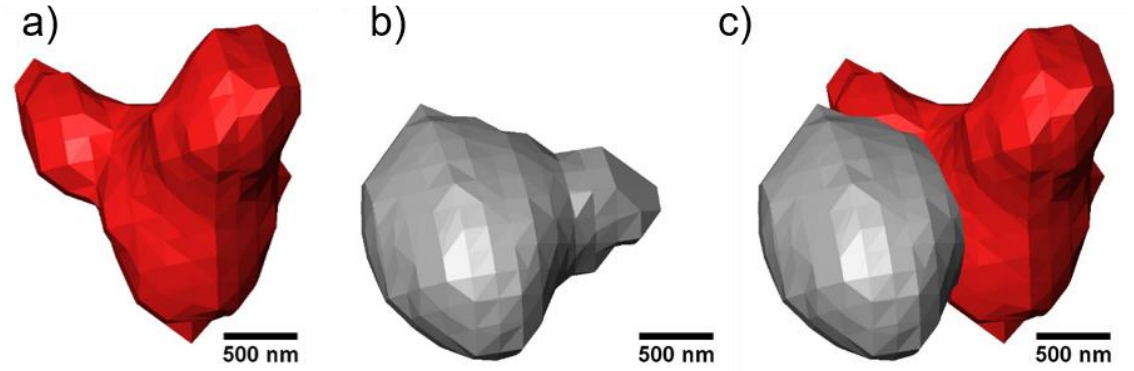

Figure 160: 3D surface renderings of likely Ni features a) before anneal; b) after anneal; c) both overlaid

Although this arbitrary thresholding was necessary due to imperfect delineation between Ni and YSZ, the corresponding "likely Ni" features are not equivalent in volume; the former measures ~ 2.4 μm^3 and the latter 2.2 μm^3. Nonetheless, it does display the morphological change in which a more complex, higher surface area feature (4.6 μm^{-1}), essentially coarsens, leading to a lower volume-specific surface area (4.1 μm^{-1}) at the same time as becoming visually more spherical.

The output displacement vectors, d, were processed to give rise to the strain vectors, E_{ii}, where $i = x, y$ *or* z, and this quantity represents the i^{th} component of the strain of each correlation window (approximately 4 × 4 × 4 voxels each). This is calculated by finding the derivative of the i^{th} component of the displacement vector, $d_{(i)}$, with respect to the correlation window dimension, L. A 3D representation of each of these strain fields is presented in Figure 161.

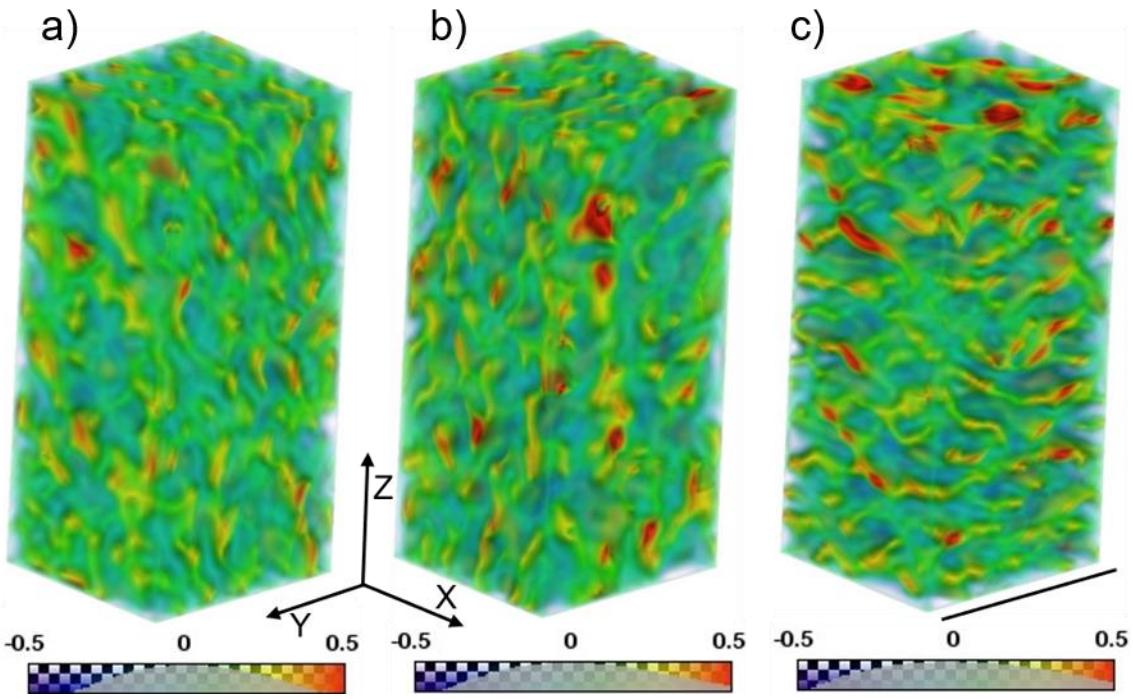

Figure 161: Three-dimensional strain maps for a) Exx; b) Eyy; *and c)* Ezz *calculated from the displacement vectors for the change of J011-06 sample, black line represents ~27 µm*

There is on average little to no net strain in one particular direction along a single axis and the strain is relatively isotropic; the histograms for the Y- and Z- directions are almost identical, with slightly less strain in the X-direction. The magnitude of the strain vector at every sub-volume can be calculated by the following equation (Equation *7-1*):

$$|E| = \sqrt{({E_{xx}}^2 + {E_{yy}}^2 + {E_{zz}}^2)} \quad 7\text{-}1$$

The result highlights the areas in the microstructure that show small or large changes, independent of direction. The result is presented alone and overlaid on the virgin (reference) pore volume in Figure 162.

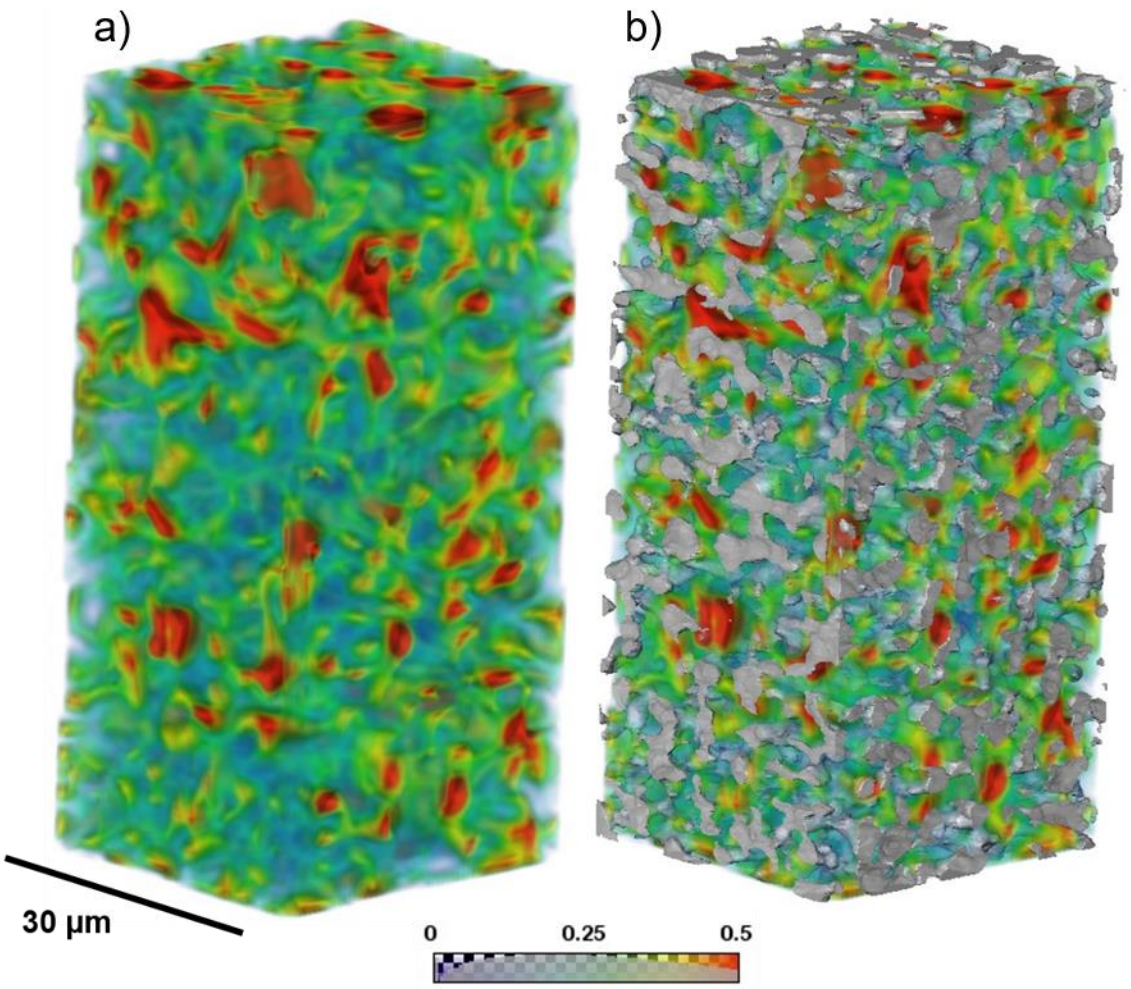

Figure 162: Strain magnitude map, a) without and b) with overlaid pore network from virgin *J011-06 sample, with same orientation as above*

It appears that the maximal strain regions are found predominantly at the interfaces between the solid and pore volume. To interpret these results, it is important to consider how the DVC software calculates the displacement vectors from which the above strain magnitude map comes. The algorithms involved in the calculation depend upon texture at the level of the sub-volumes chosen. Due to the scaling of the data, the pore phase central regions are often filled with multiple voxels with zero grayscale, such that pore grayscale “texture” is more concentrated at the edges of the pore network. On the other hand, the phase which is thought to be most mobile is the nickel phase, the brightest phase, but the histogram of the input data was not saturated, so texture is likely present throughout the entirety of that phase. As a result, it is predicted that the algorithm will better correlate the movement of nickel (or at least high grayscale values) than it will correlate the movement of pore space, by virtue of the movement on solids. This is

advantageous for the purposes of tracking nickel movement, so partial masking of the pore phase might be considered to potentially aid in the monitoring of solid movement.

7.4.2 Second Test (S011-02)

7.4.2.1 Acquisition

As the microstructure in the SOFCMAN samples was nominally slightly coarser than in the Jülich samples, and spatial resolution appeared to be limiting good image quality for the first sample, the second sample imaged was an SOFCMAN sample, again fixed on a ceramic tube with cured Ceramabond. The sample was a fine pillar with a width of 40-50 µm (but with an irregular geometry) and was composed of a thin electrolyte and an ASL; an AFL could not be clearly detected from the tomogram but may be present (Figure 163).

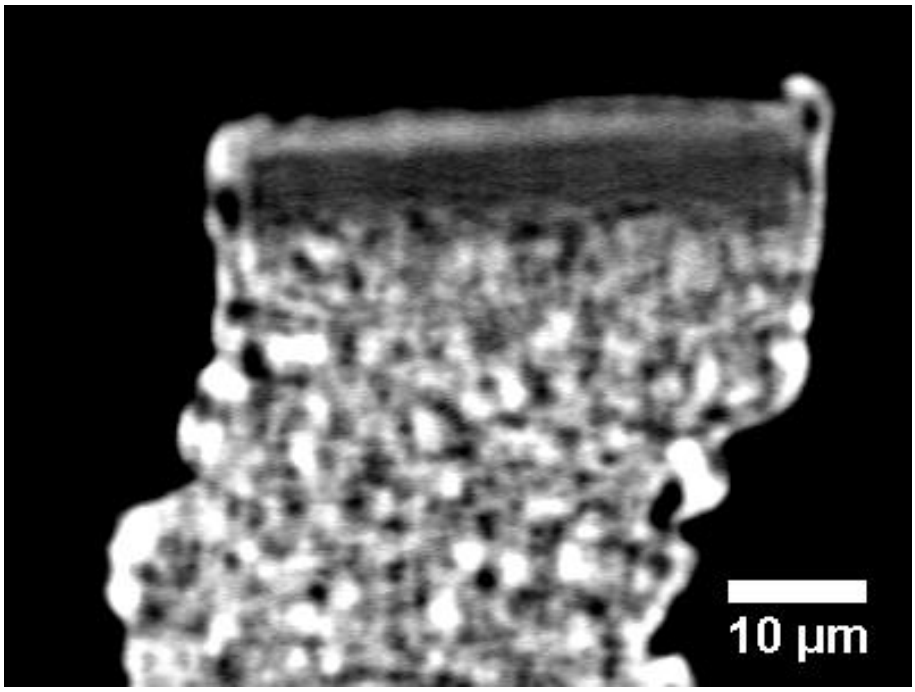

Figure 163: Single XZ-orthoslice from tomogram of S011-02

The edges were cropped to delete extraneous surfaces, giving a sub-volume of 116 × 111 × 148 voxels. This is considerably shorter in the Z-direction than for J011-02 as the sample pillar was shorter. Nonetheless, a volume of approximately 8,200 µm^3 was sampled, which remains large compared with that achievable on lab-based systems.

7.4.2.2 Filtering

Again, an “Unsharp Masking” filter was employed, to increase the solid-pore demarcation. The result of the application of this filter is shown in Figure 164, which

displays an XY-orthoslice of the sample, from a) original dataset (full histogram); b) original dataset (histogram adjusted); c) filtered dataset (full histogram); d) filtered dataset (histogram adjusted).

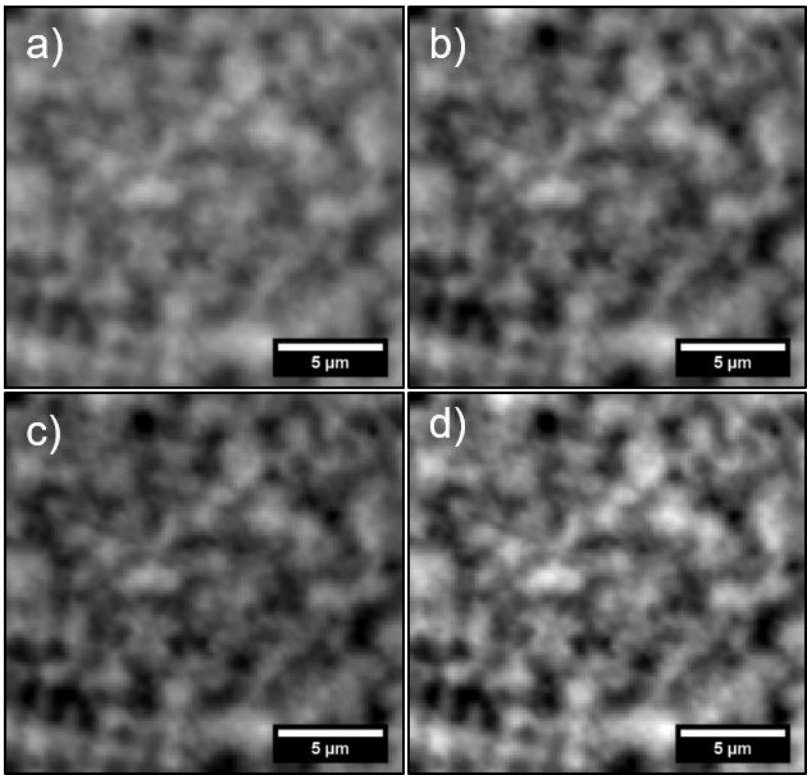

Figure 164: XY-orthoslice from S011-02 a) pre-filter, full histogram; b) pre-filter, histogram adjusted; c) post-filter, full histogram; d) post-filter, histogram adjusted

7.4.2.3 Segmentation

A simple watershed algorithm was used to perform a binary segmentation (Figure 165) on this initial microstructure, the raw image of which has been adjusted to accentuate the differences in attenuation of the three materials (pore = black, YSZ = grey, nickel = white). In Figure 164 b), the black regions represent porosity.

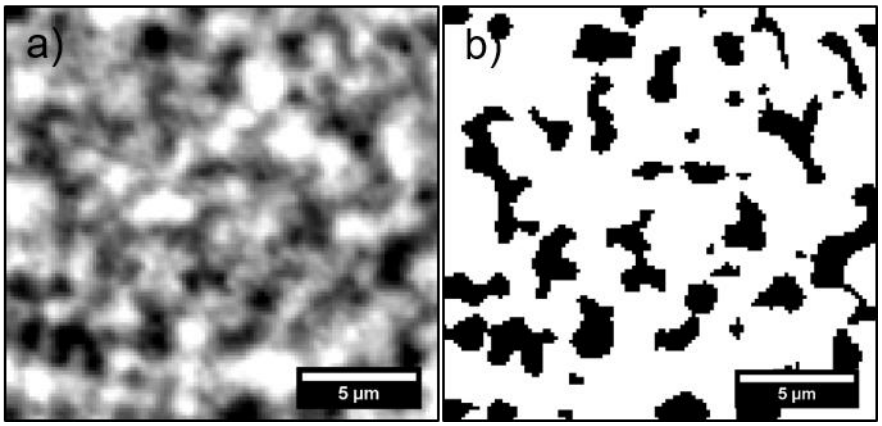

Figure 165: XY-orthoslice from S011-02 a) virgin *filtered data b)* virgin *binary segmentation*

7.4.2.4 Analysis

By standard voxel counting methods, volume fractions and volume-specific surface areas (VSSA) were calculated for the binarised sample and the results are shown in Table 50**.**

	S011-02	
Phase	**Pore**	**Solid**
Volume Fraction (%)	32.9	67.1
VSIA (μm^{-1}) (unsmoothed)	0.95	
VSIA (μm^{-1}) (smoothed)	0.84	

Table 50: Basic metrics extracted from S011-02 tomogram

This second investigated microstructure was from a different supplier and may have had distinct processing conditions in its manufacture; the volume fractions and surface areas were shown to be different (33% versus 23% porosity and a $VSSA_{Pore}$ approximately 50% greater (~0.9 versus ~0.6). The tomogram appeared to give marginally improved solid-phase contrast and sharper delineation of features. Henceforth, only SOFCMAN samples were investigated.

As the microstructure was different, RVE analysis was again applied so that the required volume for representativeness specifically for SOFCMAN sampling could be ascertained. The results are shown in Figure 166 and Table 51.

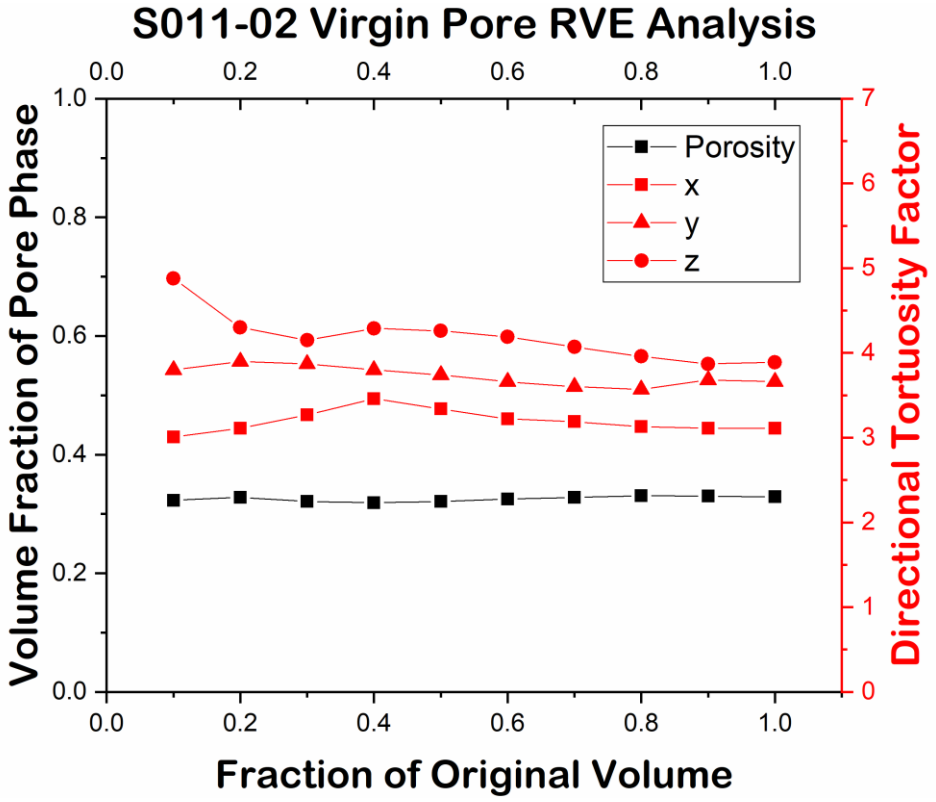

Figure 166: Plot of RVE analysis of the virgin S011-02 pore phase

S011-02				
		Tortuosity Factor		
x	Volume fraction	X-	Y-	Z-
0.1	0.32	3.0	3.8	4.9
0.2	0.33	3.1	3.9	4.3
0.3	0.32	3.3	3.9	4.2
0.4	0.32	3.5	3.8	4.3
0.5	0.32	3.3	3.7	4.3
0.6	0.33	3.2	3.7	4.2
0.7	0.33	3.2	3.6	4.1
0.8	0.33	3.1	3.6	4.0
0.9	0.33	3.1	3.7	3.9
1.0	0.33	3.1	3.7	3.9

Table 51: List of RVE analysis values as a function of sample dimension for S011-02

With a 2% tolerance, pore volume fraction becomes representative at x = 0.6 which represents approximately 4,900 μm^3. Throughout the entire range, this metric deviates a maximum of 3.0% from the full volume (x=1.0) value. Applying the less stringent tolerance of 4% to tortuosity factor gives RVE at x = 0.6, 0.4 and 0.8 for the X-, Y- and Z-directions, respectively. The largest of these suggests a volume of ~6,500 μm^3 should be sufficient to represent this microstructure. The tortuosity factors are lower than those found for the AFL in **Chapter 6**, which is in accordance with the ASL being engineered for mass transport and the AFL maximising TPB density.

7.4.2.5 Annealing

Unfortunately, due to improper placement of a monitoring thermocouple, and the use of high laser power, the annealing of this sample had to be halted as smoke was observed emanating from the vicinity of the sample. After switching to a pure N_2 stream, shutting off the laser and closing the X-ray shutter, the sample was inspected for damage. The sheathing of the thermocouple was seen to have burnt and had to be replaced by a new thermocouple. As it was not clear if any debris had contaminated the sample, the sample was exchanged for another SOFCMAN sample (with nominally the same microstructure).

7.4.3 1st Tomography Series (S010-01, 800 °C)

7.4.3.1 Acquisition & Registration

For the first tomography series, sample S010-01 was imaged, which was fabricated from an SOFCMAN cell and had a pillar diameter of ~35 µm (Figure 167). Moreover, the sample had been reduced as a pillar after it was formed from NiO/YSZ, potentially mitigating any small amounts of NiO re-introduced by the laser micro-machining step. The sample was composed of a thin electrolyte and an ASL – whether an AFL was present was not identifiable from the tomograms. 1201 projections were used in an attempt to maximise image quality.

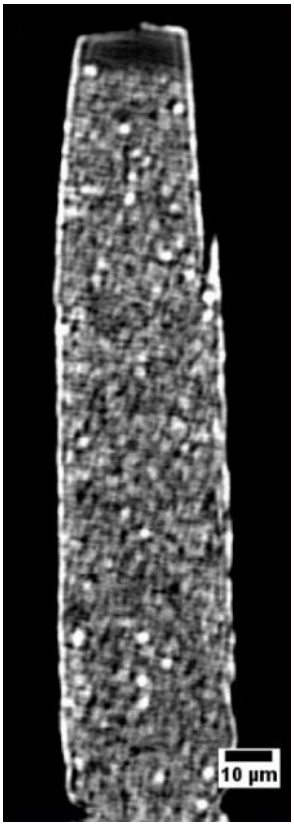

Figure 167: Single XZ-orthoslice from full tomogram of S010-01

Registration was performed as stated previously and repeated to ensure satisfactory alignment. The edges were cropped, giving sub-volumes of 120 × 120 × 390 voxels, totalling ~24,000 µm^3.

7.4.3.2 Filtering

To maximise the grayscale gradient at the pore-solid interface, an Unsharp Masking filter was applied. The result of this filter is shown in Figure 168, which displays an XY-orthoslice from the *virgin* sample, from a) the original dataset and b) the filtered dataset.

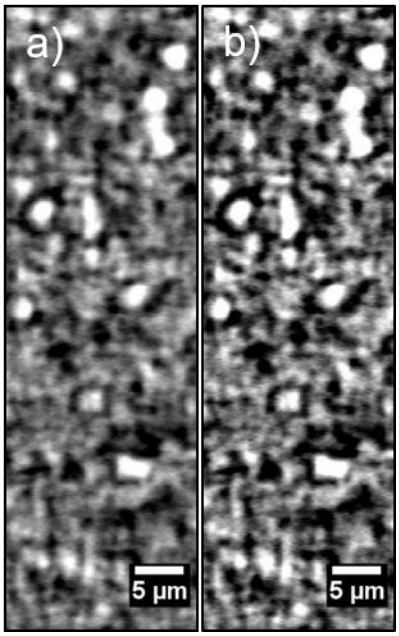

Figure 168: YZ-orthoslice from S010-01 a) pre-filter and b) post-filter

7.4.3.3 Segmentation

An XZ-orthoslice from each of 7 consecutive tomograms taken with a time spacing of ~10 min is shown in Figure 169, alongside their corresponding binary segmented slice.

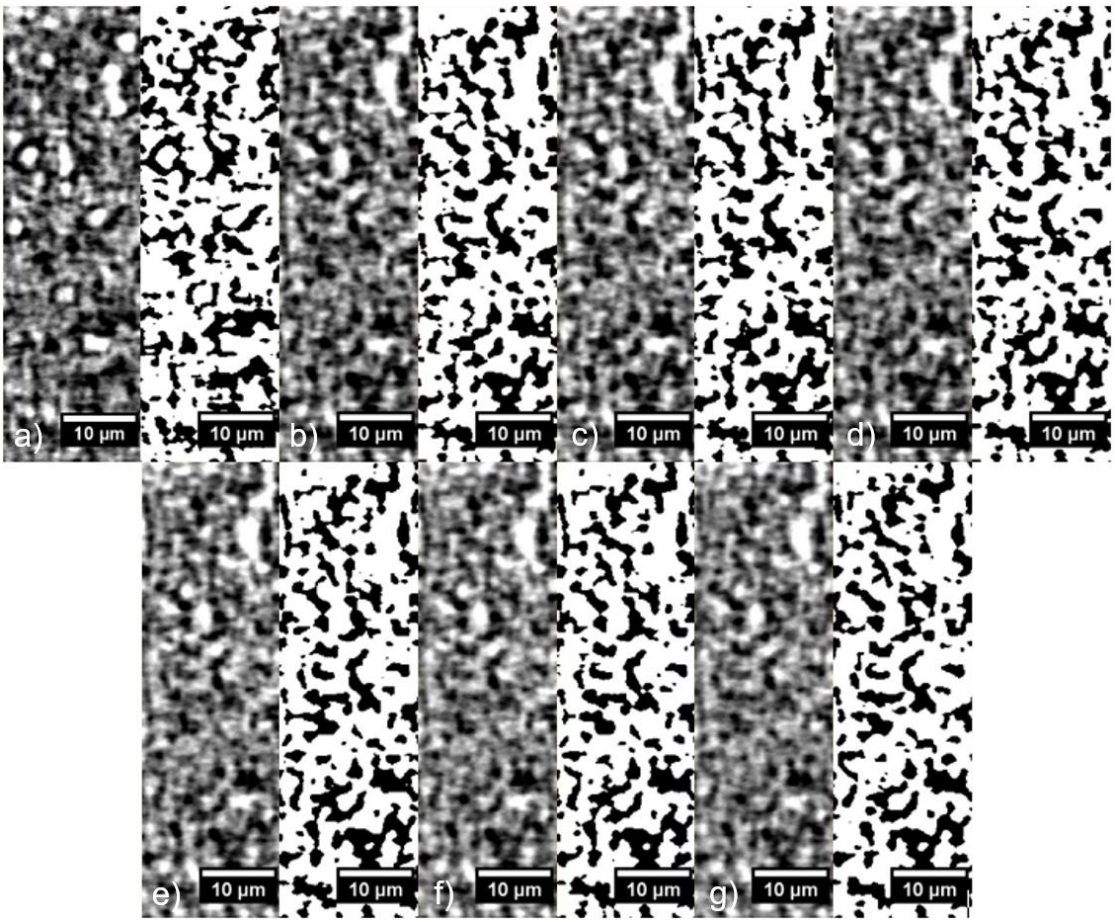

Figure 169: YZ-orthoslices and their binary segmented slices from tomography series S010-01, at a) 0; b) 10; c) 20; d) 30; e) 40; f) 50; and g) 60 min anneal at 800 °C

3D volume renderings of the binary segmentations (pore phase) are presented in Figure 170, where it is clear that the greatest change occurs in the first 10-min anneal.

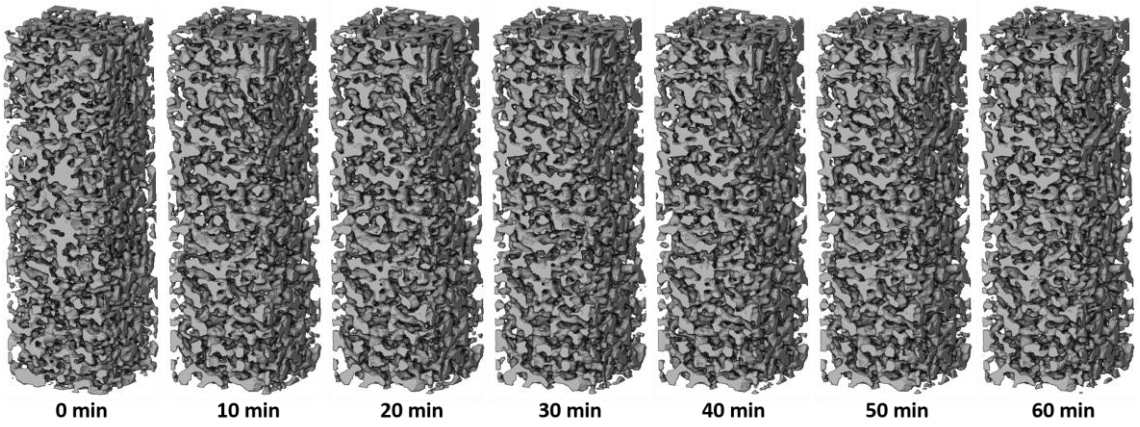

Figure 170: Pore phase volume renderings for every 10 min of annealing at 800 °C

7.4.3.4 Analysis

Volume fractions and VSSAs were calculated for the binary segmentations of each of the samples. The pore volume fraction presented is from the unsmoothed simple thresholding of the filtered data, and its corresponding VSSA is given alongside a VSSA calculated from a smoothed binarisation (Table 52 and Figure 171).

Time (min)	0	10	20	30	40	50	60
Volume Fraction (%)	33.3	32.9	33.0	33.5	33.7	33.3	33.2
VSIA (μm^{-1}) (unsmoothed)	1.1	0.9	0.9	0.9	0.9	0.9	0.9
VSIA (μm^{-1}) (smoothed)	0.9	0.8	0.8	0.8	0.9	0.8	0.8

Table 52: Simple pore metrics from consecutive binarised segmentations for S010-01

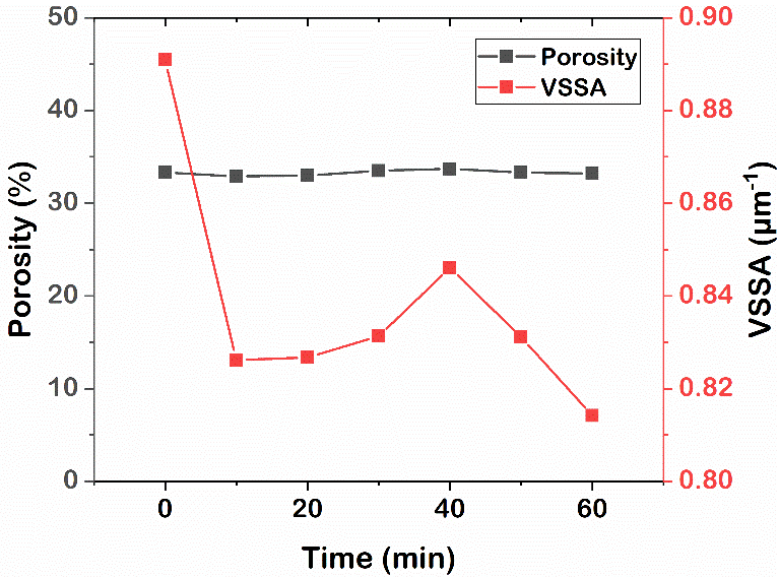

Figure 171: Evolution of porosity and smoothed pore VSSA for S010-01

The variation in porosity is small, with a maximum relative deviation from the average of 1.3%, which suggests a constant porosity with small segmentation error. However, there is a drop in VSSA between the first and second tomogram (10-min anneal at 800 °C), which accompanies the clearest observable change in microstructure, though its significance is difficult to gauge given the inherent difficulty of error estimation. The behaviour of the subsequent samples does not show a clear monotonic trend but shows less variation than the magnitude of change during the first timestep. This may suggest an initial reorganisation of microstructure that involves a coarsening of the pore phase, followed by a second mechanism in which nickel transport gives rise to a change in the pore network without coarsening. Analysis of more samples is needed to test this hypothesis.

7.4.3.5 Digital Volume Correlation (DVC)

Registered but unfiltered tomograms were used as inputs for DVC analysis. Displacements were measured with respect to each pair of consecutive tomograms, and the vectors generated are differentials relative only to the tomogram immediately before the one in question. The initial input parameters for comparison of the *virgin* and *aged* (1 timestep = 10 min) samples were: FFT pre-shift window: 64; and a total of 3 steps: i) 32 voxel sub-volume, 75% overlap, peak search of 8, 8 × 8 × 8 binning, 1 pass; ii) 16 voxel sub-volume, 75% overlap, Peak search of 4, 4 × 4 × 4 binning, 1 pass; iii) 8 voxel sub-volume, 75% overlap, Peak search of 2, no binning, 2 passes. This calculation used a slightly finer sub-volume window for the intermediate and final passes as computational times had been reasonably low when applied to J011-06 at a slightly coarser level. An example of the outputs given by the DVC software is presented in Figure 172. The first image is a single XY-orthoslice from the virgin tomogram, the middle image represents the direction of displacement for each DVC sub-unit by arrow and its magnitude by colour and the third image is the same single XY-orthoslice from the aged tomogram, after the 10 min anneal at approximately 800 °C.

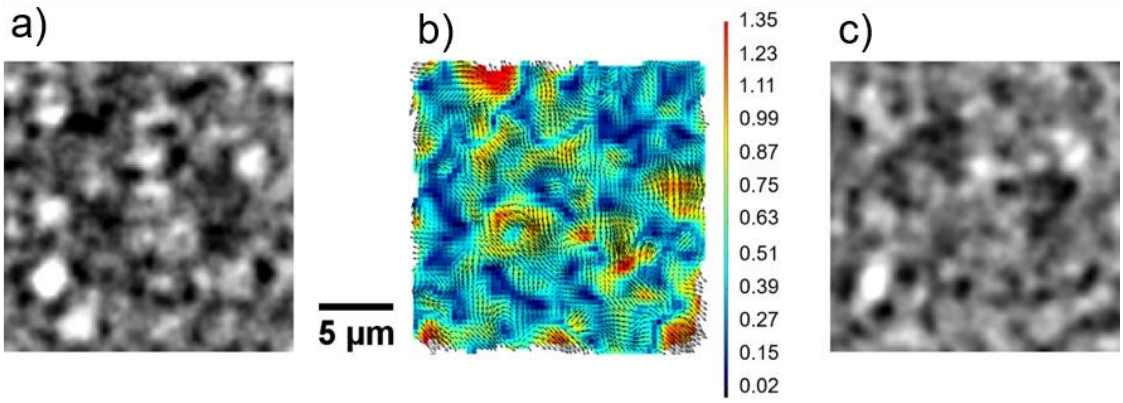

Figure 172: Example XY-slices a) from virgin *tomogram; b) from DVC calculation (magnitude of z displacement by colour (µm) and direction of overall displacement by arrow); c) from 10 min tomogram, for S010-01*

From Figure 172 it can be observed that the tomogram taken after 10 minutes of heating at 800 °C is blurrier than that taken of the virgin sample. This blurriness is also present in the consecutive tomograms and may be due to microstructural change occurring on the timescale of the tomographic scan. This is likely to be due to the increase in scan duration (from ~2 to ~6 minutes) as a result of the greater number of projections used, where the loss of temporal resolution outweighs any increase in spatial resolution. Nonetheless, clear evolution is observed between the first and second scans, with vastly reduced alteration detectable thereafter (see Figure 169 and Figure 170).

In order to quantify the degree of microstructural change across the tomography series, the displacement vectors between each consecutive pair of tomograms was calculated and the strain in each of the three orthogonal directions (E_{XX}, E_{YY}, E_{ZZ}) for each pair was processed. The total strain magnitude for each DVC sub-unit for every tomographic pair was computed as given in Equation *7-1*. A plot of the distribution of strain magnitudes for each tomogram is shown in Figure 173.

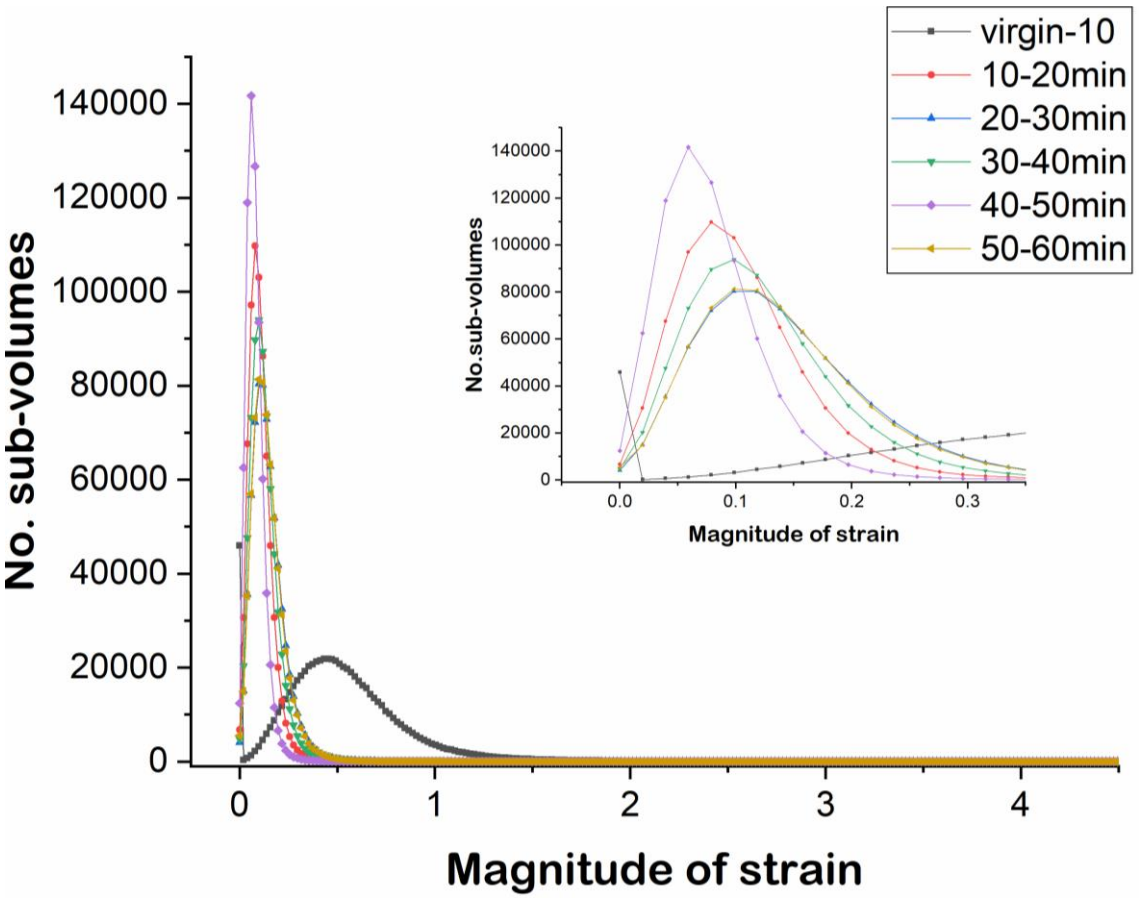

Figure 173: Plot of the distribution of strain magnitude of all DVC sub-units for S010-01 with a magnified inset

The maximum strain magnitude begins at the high value of 5.03 and drops precipitously to 0.99 for the second 10-min anneal and varies between 1.18 and 0.97 thereafter. Moreover, the distribution and modal value for the first 10-min anneal is clearly different from the distributions thereafter. The modal value for the first 10-min anneal occurs at 0.43 and drops to values between 0.059 – 0.099 afterwards, without displaying a monotonic trend. These results suggest a different character of the reorganisation happening in the first anneal, with a greater degree of average and maximal strain. The results also suggest that at 800 °C, 10 min of annealing produces an average of ~ 0.08 strain.

7.4.4 2nd Tomography Series (S010-02, 1040 °C)

7.4.4.1 Acquisition & Registration

For the second tomography series, sample S010-02 was imaged due to its coarse SOFCMAN microstructure and thinner pillar width (30 µm) (Figure 174). The sample had been reduced as a pillar after it was formed from NiO/YSZ and was fixed on a ceramic tube with Ceramabond. The sample was composed of a thin electrolyte and

an ASL – whether an AFL was present was not identifiable from the tomograms. Heating at the higher temperature of 1040 °C was employed, alongside longer timesteps between tomograms, in an attempt to capture changes that may be due to a separate mechanism from the hypothesised reorganisation at very short times. 501 projections were used to avoid the blurriness issues seen with S010-01.

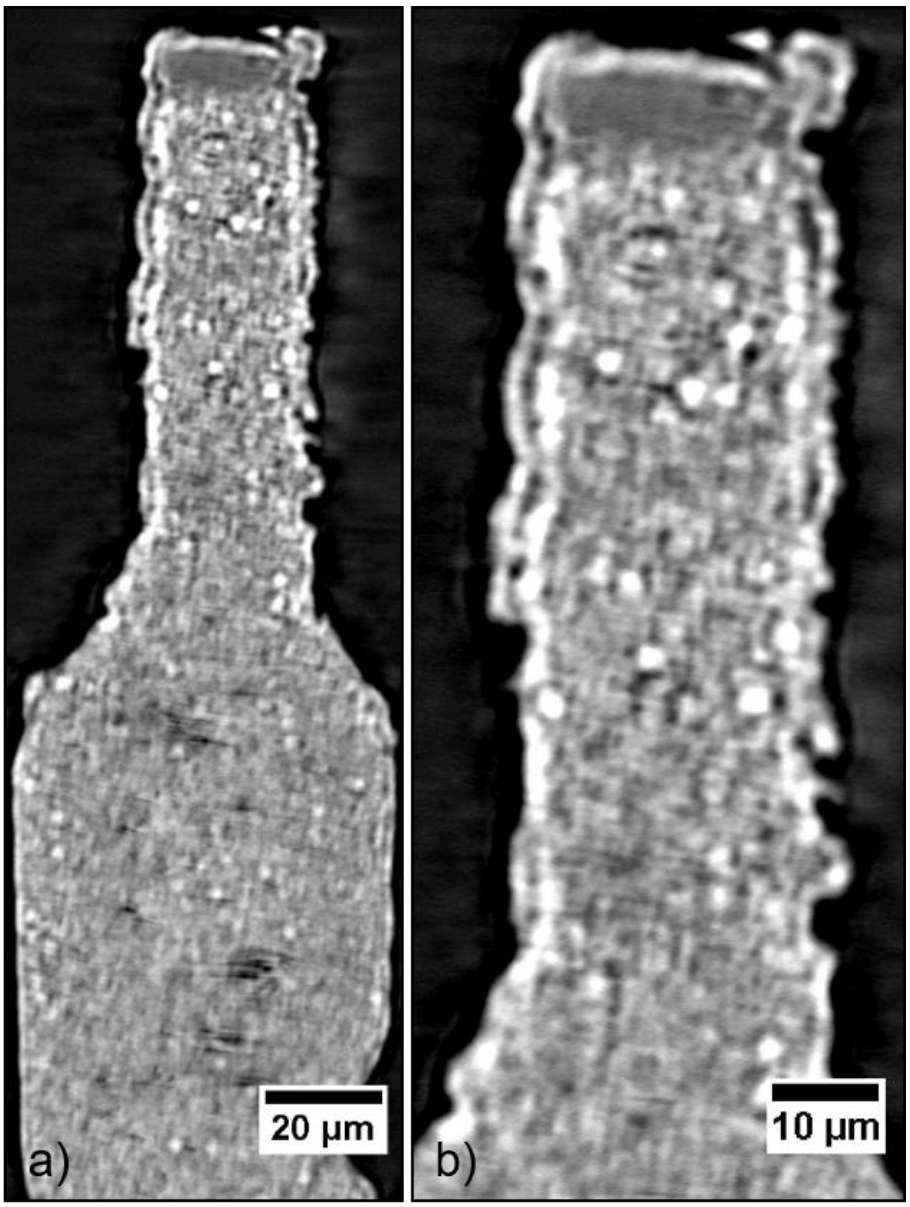

Figure 174: a) Single XZ-orthoslice from full tomogram of S010-02; b) Zoomed in XZ-orthoslice from thin area of interest

Registration was performed in Avizo, as described previously. The edges were cropped, giving sub-volumes of 66 × 86 × 390 voxels, totalling ~9,500 µm^3. An example XZ-orthoslice from the consecutive registered sub-volumes from each tomogram is shown in Figure 175.

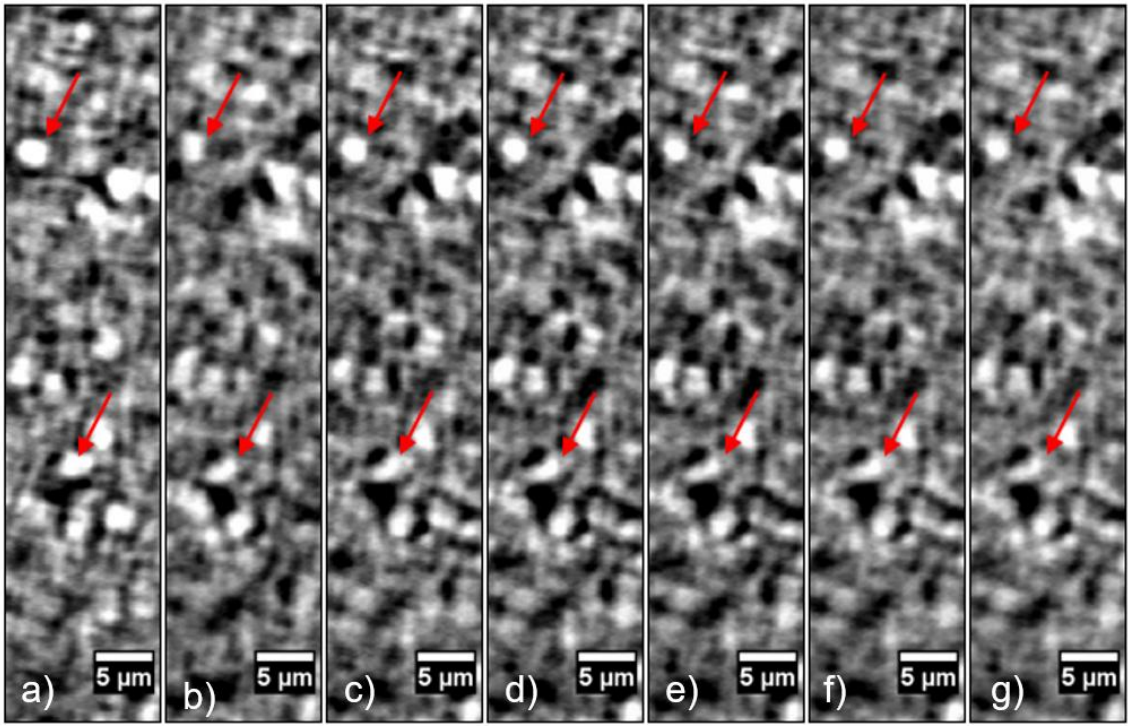

Figure 175: Raw XZ-orthoslices from registered S010-02 tomograms

Minor changes are observable by eye (see red arrows in Figure 175). The largest apparent changes, however, visibly occur between the *virgin* tomogram and the first *aged* tomogram, and between the first and second *aged* tomograms. This suggests that to capture important early-stage microstructural change, the timescale of interest is of the order of minutes, as opposed to hours. This microstructural change may represent an inherent early-stage coarsening mechanism, the relaxation from a non-equilibrium state due to the high-temperature laser-preparation route or significant evolution during laser ramping. The changes between the subsequent time steps are not as significant and detection by normal metric extraction is not facile, since the segmentation error is likely to be greater than the microstructural change.

7.4.4.2 Filtering

To maximise the grayscale gradient at the edges between solids and pores, an Unsharp Masking filter was applied. The result of the application of this filter is shown in Figure 176, which displays an XY-orthoslice of the sample, from a) the original dataset and b) the filtered dataset.

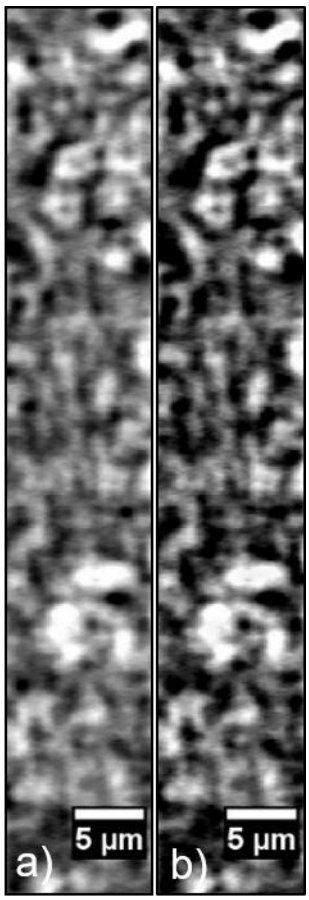

Figure 176: Raw YZ-orthoslices from a) without and b) with the application of the Unsharp Masking filter

7.4.4.3 Segmentation

A binary segmentation of each tomogram was performed in Avizo using simple thresholding, an orthoslice of which is shown in Figure 177 and the basic global metrics extracted are presented in Table 53.

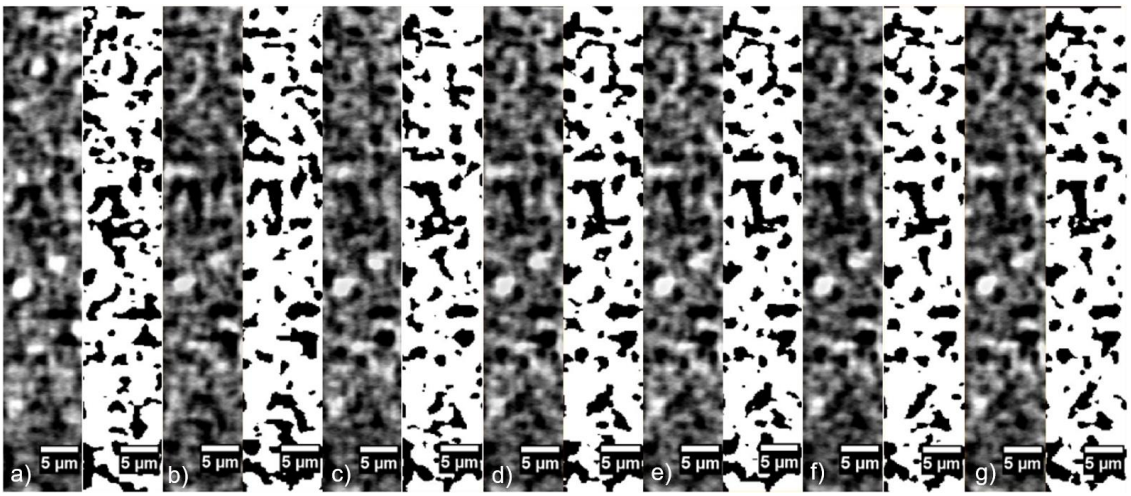

Figure 177: Raw XZ-orthoslices and their corresponding binary segmentation for timesteps: a) 0 min; b) 21 min; c) 46 min; d) 71 min; e) 96 min; f) 106 min; g) 116 min

7.4.4.4 Analysis

Volume fractions and VSSAs were calculated for the binary segmentations of each of the samples. The volume fraction presented is from the unsmoothed simple thresholding of the filtered data, and its corresponding VSSA is given alongside a VSSA calculated from a smoothed binarisation (Table 53 and Figure 178).

Time (min)	0	21	46	71	96	106	116
Volume Fraction (%)	33.5	32.6	31.7	32.7	31.6	33.2	33.4
VSIA (μm^{-1}) (unsmoothed)	1.0	0.9	0.9	0.9	0.9	0.9	0.9
VSIA (μm^{-1}) (smoothed)	0.9	0.8	0.8	0.8	0.8	0.8	0.8

Table 53: Simple pore metrics from consecutive binarised segmentations for S010-02

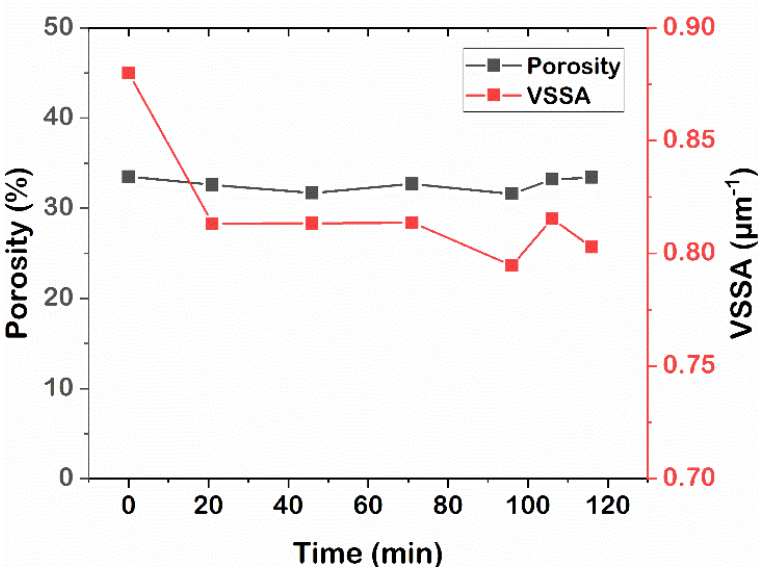

Figure 178: Evolution of porosity and smoothed $VSSA_{Pore}$ for S010-02

The porosity across each of the tomograms varied by less than any previously used estimate of the segmentation error and there is no significant evidence of a change in porosity during annealing over two hours. However, there is a significant drop in $VSSA_{Pore}$ between the first tomogram and that imaged after 21 min of annealing at approximately 1040 °C. After this change, there was a clear plateau, with variation in the last three data points which is of a smaller magnitude and likely due to segmentation error. This would need to be replicated for substantiation, however. Nonetheless, this initial analysis implies very early-stage microstructural evolution, on the order of minutes. To avoid segmentation errors, DVC can be used instead, with its sub-pixel resolution, to define the changes between tomograms.

7.4.4.5 Digital Volume Correlation (DVC)

Registered but unfiltered tomograms were used as inputs for DVC analysis. Displacements were measured with respect to each pair of consecutive tomograms, and the vectors generated are differentials relative only to the tomogram immediately before the one in question. The initial input parameters for comparison of the virgin and aged (1 timestep = 21 min) samples were: FFT pre-shift window: 64; and a total of 3 steps: i) 32 voxel sub-volume, 75% overlap, peak search of 8, 8 × 8 × 8 binning, 1 pass; ii) 16 voxel sub-volume, 75% overlap, Peak search of 4, 4 × 4 × 4 binning, 1 pass; iii) 8 voxel sub-volume, 75% overlap, Peak search of 2, no binning, 2 passes. This calculation also used a slightly finer sub-volume window for the intermediate and final passes than for J011-06, as explained in **Section 7.4.3.5**. An example of the outputs given by the DVC software is presented in Figure 179. The first image is a single XY-orthoslice from the *virgin* tomogram, the middle image represents the direction of displacement for each sub-volume by arrow and its magnitude by colour and the third image is the same single XY-orthoslice from the *aged* tomogram, after the 21 min anneal at approximately 1040 °C.

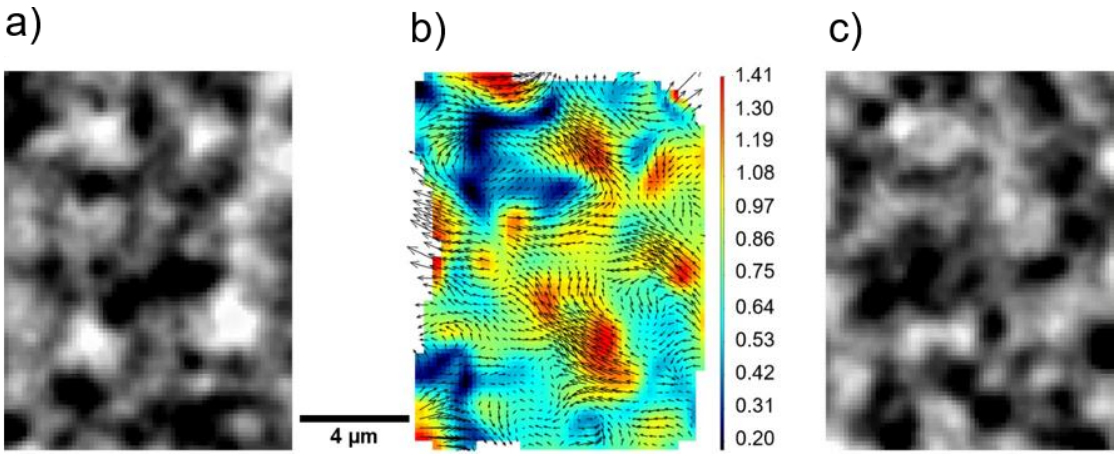

Figure 179: Example XY-slices a) from virgin tomogram; b) from DVC calculation (magnitude of Z displacement by colour (µm) and direction of overall displacement by arrow); c) from 21 min tomogram, for S010-02

In order to quantify the degree of microstructural change across the tomography series, the strain in each of the three orthogonal directions (E_{XX}, E_{YY}, E_{ZZ}) was processed and the total strain magnitude for each DVC sub-unit for every tomographic pair was

computed. A plot of the distribution of strain magnitudes for each tomographic pair is shown in Figure 180.

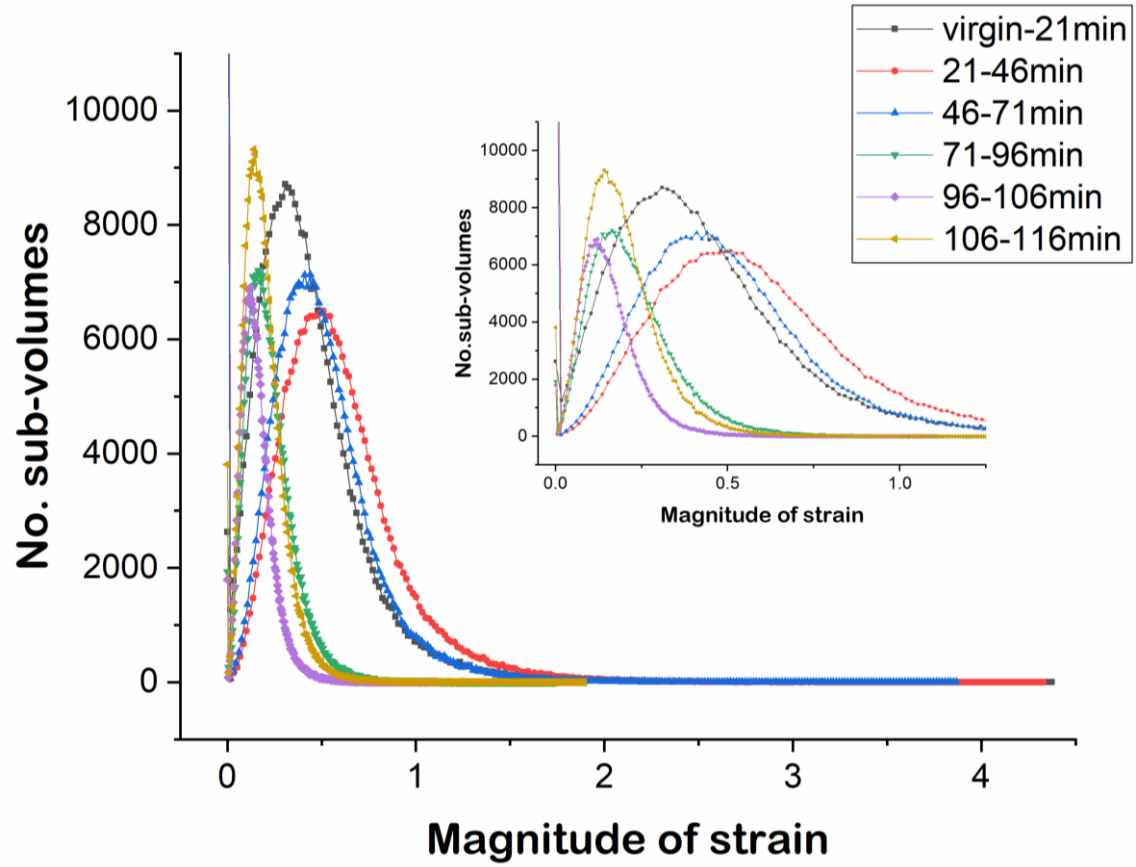

Figure 180: Plot of the distribution of strain magnitude of all DVC sub-units for S010-02 with a magnified inset

The maximum strain magnitude across the entirety of the sample decreases with each timestep, most notably between 71 and 96 minutes. The general distribution displays complex behaviour. The strain magnitude distribution after the first 21 minutes is broad, with only 1% of the DVC sub-units displaying zero strain, which is consistent with the sample relaxing from a high-energy state in which movement is not necessarily constrained to the nickel/pore matrix. The modal strain magnitude is ~0.31 for this timestep. The following timestep displays, on average, greater strain, with a modal strain magnitude of ~0.51, but a narrower distribution with many more sub-units registering zero strain (11%). This value is lower than the approximate composition of 33% of YSZ, illustrating possibly that the sub-optimal spatial resolution confounds the boundaries between pore and nickel with an immobile YSZ phase, there exists some mobility in the YSZ phase at 1040 °C [187], or a combination thereof. This high number of 'static'

sub-units is retained by the third timestep, with a slightly narrower distribution and a peak at 0.44, whereas it returns to a much lower value (~1%) for all timesteps thereafter. From 71 min to 116 min, the peak strain magnitude varies very little, with values of 0.12-0.16. The reason for which the number of DVC sub-units with non-zero strain changes from 1%, to 11% and back to just 1% is not clear.

7.5 Conclusion

Two SOFC anode microstructures have been successfully imaged at a synchrotron beamline, with high spatial and temporal resolution, whilst being heated *in-situ* by laser under a reducing atmosphere. It was found that there are several challenges to overcome when aiming to capture microstructural evolution on the nanoscale. Firstly, it is important to match the characteristic microstructural feature size to the spatial resolution afforded by the voxel dimension of the imaging set-up; here it was shown that although sub-optimal, a noticeable improvement in three-phase distinction between pore, nickel and YSZ was achieved when switching to a coarser ASL microstructure. Alternatively, a beamline with a smaller voxel dimension might be chosen, however, none exist with the same capability of in-line *in-situ* laser heating.

Secondly, scan time and temporal resolution must be matched to the rate of change and the time constant of the mechanism of change, respectively. It was shown that taking a single tomography lasting approximately 6 minutes (1201 projections) leads to blurring of the microstructure whereas reducing this to 501 projections and a scan time close to 2 minutes gives sharper images. This could be accomplished due to the relative narrowness of the sample pillar with respect to the detector width, avoiding artefacts and giving access to faster tomographies with reduced projections. Moreover, the time-lapse duration has an impact on what degree of microstructural change is imaged and therefore detectable, with the first *aged* tomograms of both series demonstrating that rapid rearrangement remained uninspected.

Thirdly, the tomographic series highlighted that rapid re-organisation appears to occur during the first minutes of heating, possibly suggestive of an unavoidable SOFC anode phenomenon at very short times, or as an artefact of the sample preparation route

(residual stress relief) or laser-heating set-up. This supports the conclusions drawn from the *ex-situ* experiments in **Chapter 6**, whereby the largest proportion of microstructural evolution was completed in the first timestep (4 h). This work goes further to suggest that some key changes are mainly concentrated at even shorter times, on the order of minutes.

Nonetheless, small changes were observed across later tomograms, albeit difficult to capture in simple global metrics analysis, other than a clear decline in VSSA between the *virgin* and first *aged* tomogram. The use of DVC techniques to monitor the changes provided deeper insight. DVC was utilised to concentrate on specific regions of high strain, allowing the investigation of microstructural changes of particular features that demonstrated local coarsening. Moreover, work at 1000 °C on the Jülich sample suggested that over 20 minutes of heating, the regions of greatest movement displayed displacement magnitudes of up to ~2 μm and the maximum and average strains were calculated to be 1.00 and 0.19, respectively. Later work at 800 °C on an SOFCMAN sample also suggested a maximum strain of approximately 0.97-1.18 but a lower average strain of ~0.08. Further work on another SOFCMAN sample at 1040 °C suggested average strain values of ~0.5, which is substantially larger than that seen in the Jülich sample at a similar temperature. These experiments demonstrate the potential to conduct highly insightful investigations into the complex high-temperature evolution for a range of SOFC microstructures at various temperatures.

Chapter 8: Overview

This chapter collates the work conducted as part of this thesis to distil conclusions from the experiments in **Chapters 4 - 7**. Moreover, a proposal of follow-on experiments and approaches is given in **Section 8.2** to provide direction and suggestions for further investigation.

8.1 Conclusions

The broad aim of this thesis was to gain a valuable understanding of microstructural evolution that occurs in SOFC anode materials during annealing, on multiple timescales. As part of this investigation, the suitability of the chosen tomographic technique was to be considered alongside the detailed inspection of the entire workflow: from sample preparation, through image acquisition, to processing and data analysis. In accessing relevant metrics from this process, the objective was to probe the impact of high-temperature operation on performance-related changes in cermet microstructure.

This thesis has shown that lab-based X-ray nano-CT is a suitable analytical technique for the monitoring of 4D (3D plus time) microstructural evolution of traditional HT-SOFC Ni-YSZ cermet anodes undergoing high-temperature annealing in a reducing atmosphere. Below are conclusions drawn from each of the Results chapters (**Chapter 4 - 7**) which support this overarching statement, as well as highlighting its limitations and extending this work into the domain of *in-situ* synchrotron experiments.

8.1.1 FIB-SEM slice-and-view of virgin & aged SOFC anodes

At low accelerating voltages, FIB-SEM slice-and-view tomography provides high resolution images that are potentially more amenable to three-phase segmentation than those from X-ray computed tomography. The work in **Chapter 4** illustrates that this technique can be used to characterise fundamental changes, particularly in the pore and nickel networks, which occur with long-term high-temperature operation. The changes in nickel morphology, from a highly connected, well-dispersed network, to a disconnected array of coarsened, spheroid nickel agglomerates after 1,500 h of humid annealing can be visualised and the corresponding 3D virtual reconstructions lend themselves to the

extraction of metrics underpinning property-microstructure relationships. However, due to the destructive nature of this technique, any quantitative assessments of microstructure evolution are limited by the natural variation between the initial microstructures of the two separately investigated samples. Although the spatial resolution is appropriate for the investigation of typical feature sizes in state-of-the-art anodes, and adequate solid-phase contrast is accessible, incomplete epoxy-impregnation of samples and issues with channelling contrast can in fact lead to ambiguity in the allocation of voxels to the correct phases. Even more significantly, during the slice-and-view process, several issues may be encountered that prevent the acquisition of large usable volumes, such as shadowing, curtaining and re-deposition of sputtered material, such that a RVE is not always forthcoming. Although larger volumes have been achieved, this laborious technique, with the potential for irregular or inhibited milling, is not facile. As a result, non-destructive X-ray nano-CT was proposed as an alternative, and its advantages and disadvantages have been explored in detail.

8.1.2 Laser-preparation for X-ray nano-CT

Rather than crude mechanical methods, or relying solely on slow FIB-milling, a robust laser-based technique has been developed to provide samples of appropriate size and geometry for the small FOVs typically found in X-ray nano-CT instruments. The laser micro-machining tool provides a suitably fast and accurate route to achieving cylindrical samples of Ni-YSZ of diameters down to approximately 30 µm, which is ideal for the subsequent distinction of pores from solids. In order to achieve adequate solid-phase contrast for further three-phase segmentation, a final FIB-milling step to achieve the refining and diameter reduction of the sample pillar can be performed in 2-3 hours. Additionally, the necessary solid-phase contrast requires high exposure times (64 – 72 s) and low numbers of projections (1101-1201) to avoid sample-drift-induced blurring. By fabricating cylindrical samples, X-ray path length differences and therefore contrast discrepancies are significantly reduced and full use of the FOV for the selected diameter is made. This procedure can provide useful 3D reconstructions of both the ASL and the finer AFL, but their requirements are different. When inspecting the ASL, for example, a

larger volume is required to represent the coarser features, however, this is in keeping with the diminished interest in assessing the TPB (as electrochemistry predominantly occurs in the AFL) and thus larger diameter (ca. 30 µm) pillars may be inspected and adequate solid-pore contrast still achieved. In reconstructing the finer AFL microstructure, a smaller diameter (ca. 14 µm) pillar is required for distinguishing nickel and YSZ, but fortunately the finer features thus demand a smaller volume for representativeness, at least for solid phase fractions.

Microstructural variation errors between samples is estimated to be approximately 5-15%, depending on the metric in question, in the order: $error_{volume} < error_{area} < error_{length,}$ illustrating the significance of a non-destructive technique over FIB-SEM slice-and-view. The three-phase segmentation of the sample used for future annealing studies is shown to be representative for all phase fractions and all directional tortuosity factors except for the highly tortuous, low-volume pore phase. This suggests that RVE analysis should be considered both metric- and phase-specific.

8.1.3 Ex-situ annealing of SOFC anodes

Lab-based *ex-situ* annealing-imaging cycles, relying on the sample preparation route investigated in **Chapter 5**, have been shown to be successful in capturing microstructural evolution in the AFL of state-of-the-art Ni-YSZ anodes. The same exact microstructure can be probed repeatedly between high-temperature treatments conducted in a tube furnace, to track real changes in the three interpenetrating networks. Valuable metrics such as phase fractions, surface/interfacial areas, tortuosity factors, PSDs and TPB densities can be extracted at each timestep for comparison.

When inspecting a shorter time-scale than that examined in **Chapter 4**, the selection of a suitable annealing temperature is key to avoiding either too little, or too much microstructural evolution. Over a 12-hour annealing duration, 700 °C provides too little change to be reliably tracked, over and above the inherent acquisition and processing errors. Nevertheless, very high temperatures that may be envisaged as “accelerated test” conditions are also not ideal as they invoke such substantial changes

as to disqualify the internal volume from reasonable analysis. In particular, at 1150 °C, large nickel agglomerates nucleate on the exterior of the prepared sample pillar to such an extent that the nickel source reservoir likely extends into the ASL and certainly renders the internal volume erroneously devoid of the metallic phase. The most promising results come from an intermediate annealing temperature of 900 °C wherein microstructual change is appreciable but the external nickel agglomeration phenomenon is far less pronounced.

Scan times must be kept below 30 h to prevent critical loss of data quality; the pillar diameter should be <15 µm for good solid-phase contrast; and exposure times need to be upwards of 60 s for adequate signal-to-noise. Projection number can be lowered to 1101 with the retention of sufficiently good image quality for segmentation and a resolution of 63.1 nm is sufficient to capture the particulate size in the AFL of state-of-the-art Ni-YSZ anodes.

Conducting this process at 900 °C, with pillars of ~14 µm in diameter, yields data with adequate contrast and data quality that an iterative segmentation approach with watershed and machine-based learning algorithms can provide ternary segmentations that match the raw data by eye. The evolution of metrics does not, however, match the typical behaviour associated with one dominant nickel coarsening degradation route, and in fact several observed changes imply a more complex pattern of microstructural evolution that could manifest as minor improvements in electrochemical performance.

Key qualitative observations in conducting these experiments include the visible de-wetting of the metal from the ceramic and both connections and disconnections in networks signalled by fluctuating percolation levels. Several specific quantitative observations can also be captured which show that VSSAs and tortuosity factors do not display monotonic trends within the first 12 h of annealing, but there is similar behaviour in the first 4 h for both annealing at 700 and 900 °C whereby the pore network becomes coarser and more tortuous. RVE analysis shows that a volume of ~420 μm^3 is adequate to represent the pore phase fraction under both regimes but that tortuosity factor requires a larger volume. Both the reduction regime and the annealing temperature may have an

effect on the evolution of total and active TPB density values. For instance, the active TPB density drops in the first 4 h at 700 °C whereas it is constant and the total TPB density drops for the first 4 h at 900 °C. However, the %Active TPB in the virgin samples was much lower for the morphology produced by reduction at lower temperature and shorter time. More experiments would be required to inspect the impact of this initial microstructure on the subsequent changes seen to total and active TPB densities.

Another notable result of reducing the sample at lower temperature and for a shorter time is that the morphology is visually different, giving rise to internal nickel porosity which persisted under 4 h of annealing at 900 °C. However, the unexplained changes in the latter half of this heating regime, both in terms of a loss of solid-phase contrast and a small porosity decrease, make it difficult to assess the reasons why the internal porosity is lost after 8 h.

Some crucial insight was gained regarding the processing and analysis of sequential tomographic datasets. When conducting RVE analysis, selection of the metric, its direction (if applicable), as well as the timestep are vital, such that morphological evolution can alter the volume required to provide a representative value for a given parameter, with a fixed tolerance. Moreover, when working with X-ray nano-CT data, a composite approach using traditional watershed and novel machine-learning algorithms improves the robustness to inherent noise in acquired data.

8.1.4 In-situ annealing of SOFC anodes

Achieving high spatial and temporal resolution, *in-situ* laser heating of two SOFC anodes has been used to capture 4D microstructural evolution under a high-temperature, reducing atmosphere at a synchrotron beamline. The coarser SOFCMAN microstructure is more amenable to analysis than the Jülich microstructure investigated in **Chapter 6** as the laser/imaging set-up at TOMCAT limits the voxel dimension to 162.5 nm. Reduction of projections (to 501) retains adequate image quality while minimising the blurring induced by microstructural change at elevated temperatures occurring during acquisition. An exposure time of 280 ms at an energy of 17 keV gives solid-phase contrast while conducting a single tomography in just over two minutes.

When imaging the ASL of these anodes, the non-optimal voxel dimension leads to some “partial volume” effects which make unambiguous three-phase segmentation challenging. However, DVC can be employed to great effect and can be used on the raw data to extract quantitative strain maps and pinpoint regions of greatest displacement for further investigation. On inspecting tomographic series, the largest changes have been shown to occur within the first timestep (10 or 20 min), suggesting that very early-stage reorganisation takes place, requiring an even faster acquisition set-up to resolve. This initial microstructural evolution may be a result of sample fabrication, an artefact of the laser heating set-up, or an inherent part of the changes that occur upon primary operation of SOFC anodes. Nonetheless, this result narrows the time window in which the majority of early-stage microstructural evolution occurs, from 4 h (**Chapter 6**) to 10 min (**Chapter 7**). Displacement magnitudes averaging ~500 nm and up to maxima of ~2 µm were observed for work at ~1000 °C, highlighting the extent of change possible on the timescale of tens of minutes.

The major findings from this thesis were achievable by the development of a robust workflow, from sample preparation, through annealing and X-ray nano-CT imaging, to image processing and analysis. *Via* said workflow, observations of the same exact Ni-YSZ microstructure of a cermet SOFC anode could be made which allowed for qualitative and quantitative conclusions to be drawn. In particular, it was shown that there is likely a number of phenomena involved in this type of microstructural evolution, both on a very short timescale (on the order of minutes) and potentially other mechanisms occurring *before* the more pronounced long-term nickel coarsening process dominates these changes. This observation may help explain initial activation behaviour reported in the literature but also demands further investigation at these short timescales to better elucidate SOFC anode microstructural evolution. The hope is that this workflow and these observations will provide routes to reliable feedback loops in the development of better performing and longer-lasting SOFCs and focus some research efforts on the fundamental microstructural organisation occurring at high-temperature on start-up.

8.2 Future Work

8.2.1 FIB-SEM slice-and-view of virgin & aged SOFC anodes

To overcome the limitations posed by the small analysed volumes, future work in this vein should focus on improving reliable routes to accessing larger volumes. One of the most striking limitations in this study was the re-deposition of material on the FOI, obscuring the microstructure and preventing the requisite extension into the third dimension necessary for achieving a near-cubic sample volume. There are two particular strategies that could be followed to improve on the current investigations; greater area and depth of milled trenches or by following a FIB lift-out approach [133]. The former is more technically straightforward and only requires more time in the sample preparation procedure, whereas the latter is likely to yield even better results but requires a FIB instrument with the appropriate micromanipulator stage (tungsten probe) installed. To improve the data quality, fiducial marks could be utilised so as to provide a more reliable reference point for slice registration and determination of slice thickness.

The results in **Chapter 4** derived from the more readily accessible ASL. However, many works focus on the reaction volume in which the electrochemical reactions take place, since it is thought that the majority of activity happens within 10-20 µm of the electrode-electrolyte interface [65][322][19][323]. This suggests that further analysis should be undertaken of the AFL, as opposed to the ASL. One of the strong advantages of this FIB-SEM technique is its high resolution which ought to capture the necessary details of the finer microstructure in the AFL – however, as it is a destructive procedure, differences between one anodes' AFL microstructure and the next may preclude the drawing of clear conclusions.

8.2.2 Laser-preparation for X-ray nano-CT

To extend the work related to the sample preparation technique, it would be valuable to conduct more experiments to verify repeatability. Although robustness of the laser-preparation and FIB-milling stages is proven, the validity of the segmented data as a result of the specific pillar geometry fabricated could be tested further. This may be

achieved either by the use of a calibrant (known structure), by correlating with another technique (such as FIB-SEM slice-and-view) of a pillar already imaged by X-ray nano-CT or possibly by producing and imaging more samples and conducting a wider-ranging statistical analysis.

The laser-preparation technique may also be applied to the other typical anode cermet microstructures, such as the common IT-SOFC materials set Ni-CGO, in order to investigate nickel agglomeration with a different ceramic and at lower, operationally relevant temperatures. Given the work at 700 °C and assuming similar behaviour, longer times would be recommended for initial investigations to provide appreciable microstructural change for detection. The approach is also applicable to the investigation of cathode microstructures composed of ceramics, although the optimisation of the laser milling and X-ray nano-CT procedures would be required.

8.2.3 Ex-situ annealing of SOFC anodes

Given the RVE analysis of the fine pillars, a recommendation for further work is to follow a protocol of inspecting larger-diameter pillars (~30 µm) for binary segmentation and inspection of the pore network and smaller-diameter pillars (~14 µm) for investigation of ternary segmentation and investigation of the solid phases and their interfaces. This could be achieved with the same pillar, with a wider diameter ASL and thinner AFL or alternatively with an interim laser step if the *virgin* AFL pore network is of interest. With the procedure developed, it would also be worthwhile extending the timeframe to several tens of hours and beyond, and investigating the impact of a change of temperature around the intermediate mark of 900 °C.

For further support of the impact of the microstructural evolution on SOFC anode performance, electrochemical experiments such as EIS and measuring *j-V* curves could be performed on half- or full cells undergoing the same annealing processes in the tube furnace. Although this would not overcome issues of microstructural variation, evidence could be provided to support microstructure-property relationships of interest.

The technique also allows for other investigations to take place, as noted in the previous section on different materials sets, or with Ni-YSZ but with relevance to a host

of other well-known degradation mechanisms, such as thermal cycling, redox cycling or even particular poisoning mechanisms thought to provoke microstructural rearrangement. This work could be extended to compare the longer-term microstructural evolution behaviour on different cermet morphologies brought about by various reducing conditions. Additionally, high-resolution work could be carried out on even thinner pillars, likely at the expense of a representative volume, but nonetheless to uncover features below the current spatial resolution limit.

8.2.4 In-situ annealing of SOFC anodes

One possible route for future work at the synchrotron beamline would be to perform experiments at even higher temporal resolution to investigate the initial rearrangement in more detail. To maintain good solid-phase contrast, the diameter of the investigated pillars could be reduced further, alongside the number of projections taken per tomography and the exposure time. Although this data may be amenable to DVC calculations, achieving reliable three-phase segmentation is mainly hindered by the limited voxel dimension. To achieve this high level of spatial resolution, with the capability of *in-situ* heating whilst imaging, perhaps a ptychographic approach might be followed. Nevertheless, scan times and blurring of microstructural changes under heating would have to be reconsidered with this alternative time-consuming set-up.

Publications & Conferences

Primary Publications

Bailey, J.J., Heenan, T.M.M., Finegan, D.P., Lu, X., Daemi, S.R., Iacoviello, F., Backeberg, N.R., Taiwo, O.O., Brett, D.J.L., Atkinson, A. and Shearing, P.R., 2017. Laser-preparation of geometrically optimised samples for X-ray nano-CT. *Journal of microscopy*, *267*(3), pp.384-396.

Secondary Publications

1. Meyer, Q., Ashton, S., Boillat, P., Cochet, M., Engebretsen, E., Finegan, D.P., Lu, X., Bailey, J.J., Mansor, N., Abdulaziz, R. and Taiwo, O.O., 2016. Effect of gas diffusion layer properties on water distribution across air-cooled, open-cathode polymer electrolyte fuel cells: A combined ex-situ X-ray tomography and in-operando neutron imaging study. *Electrochimica Acta*, 211, pp.478-487.

2. Finegan, D.P., Darcy, E., Keyser, M., Tjaden, B., Heenan, T.M., Jervis, R., Bailey, J.J., Malik, R., Vo, N.T., Magdysyuk, O.V. and Atwood, R., 2017. Characterising thermal runaway within lithium-ion cells by inducing and monitoring internal short circuits. *Energy & Environmental Science*, 10(6), pp.1377-1388.

3. Heenan, T.M., Bailey, J.J., Lu, X., Robinson, J.B., Iacoviello, F., Finegan, D.P., Brett, D.J.L. and Shearing, P.R., 2017. Three-Phase Segmentation of Solid Oxide Fuel Cell Anode Materials Using Lab Based X-ray Nano-Computed Tomography. *Fuel Cells*, 17(1), pp.75-82

4. Heenan, T.M., Robinson, J.B., Lu, X., Bailey, J.J., Brett, D.J. and Shearing, P.R., 2017. Analyzing the mechanical performance of solid oxide fuel cells at interfacial anode/electrolyte regions using sub-micron resolution 3D X-ray computed tomography. *ECS Transactions*, 78(1), pp.2317-2321.

5. Lu, X., Li, T., Taiwo, O.O., Bailey, J., Heenan, T., Li, K., Brett, D.J.L. and Shearing, P.R., 2017, June. Study of the tortuosity factors at multi-scale for a novel-structured SOFC anode. *Journal of Physics: Conference Series* (Vol. 849, No. 1, p. 012020). IOP Publishing.

6. Meyer, Q., Mansor, N., Iacoviello, F., Cullen, P.L., Jervis, R., Finegan, D., Tan, C., Bailey, J., Shearing, P.R. and Brett, D.J.L., 2017. Investigation of hot-pressed polymer electrolyte fuel cell assemblies via X-ray computed tomography. *Electrochimica Acta*, 242, pp.125-136.

7. Marchesini, S., McGilvery, C.M., Bailey, J. and Petit, C., 2017. Template-Free Synthesis of Highly Porous Boron Nitride: Insights into Pore Network Design and Impact on Gas Sorption. *ACS nano*, 11(10), pp.10003-10011.

8. Bharath, V.J., Jervis, J.R., Bailey, J.J., Engebretsen, E., Neville, T.P., Millichamp, J., Mason, T., Shearing, P.R., Brown, R.J.C., Manos, G. and Brett, D.J.L., 2017. Effect of humidity on the interaction of CO2 with alkaline anion exchange membranes probed using the quartz crystal microbalance. *International Journal of Hydrogen Energy*, 42(38), pp.24301-24307.

9. Lu, X., Heenan, T.M., Bailey, J.J., Li, T., Li, K., Brett, D.J. and Shearing, P.R., 2017. Correlation between triple phase boundary and the microstructure of Solid Oxide Fuel Cell anodes: The role of composition, porosity and Ni densification. *Journal of Power Sources*, 365, pp.210-219.

10. Finegan, D.P., Darcy, E., Keyser, M., Tjaden, B., Heenan, T.M., Jervis, R., Bailey, J.J., Vo, N.T., Magdysyuk, O.V., Drakopoulos, M. and Di Michiel, M., 2018. Identifying the Cause of Rupture of Li-Ion Batteries during Thermal Runaway. *Advanced Science*, 5(1), p.1700369.

11. Heenan, T.M., Lu, X., Finegan, D.P., Robinson, J., Iacoviello, F., Bailey, J.J., Brett, D.J.L. and Shearing, P.R., 2018. Evaluating microstructure evolution in an SOFC electrode using digital volume correlation. *Sustainable Energy & Fuels*, 2, pp.2625-2635.

12. Heenan, T.M.M., Robinson, J.B., Lu, X., Tjaden, B., Cervellino, A., Bailey, J.J., Brett, D.J.L. and Shearing, P.R., 2018. Understanding the thermo-mechanical behaviour of solid oxide fuel cell anodes using synchrotron X-ray diffraction. *Solid State Ionics*, 314, pp.156-164.

13. Johnson, T.F., Bailey, J.J., Iacoviello, F., Welsh, J.H., Levison, P.R., Shearing, P.R. and Bracewell, D.G., 2018. Three-dimensional characterisation of chromatography bead internal structure using X-ray computed tomography and focused ion beam microscopy. *Journal of Chromatography A*, 1566, pp.79-88.

14. Cho, J.I.S., Neville, T.P., Trogadas, P., Bailey, J., Shearing, P., Brett, D.J.L. and Coppens, M.O., 2018. Capillaries for water management in polymer electrolyte membrane fuel cells. *International Journal of Hydrogen Energy*, 43(48), pp.21949-21958.

Conferences

H2FC Supergen – University of Bath, 2015

Poster: “Characterisation of Microstructural Evolution in Solid Oxide Fuel Cell Anodes”

STFC Early Career Researchers Conference (ECRC) – Abingdon, 2016

Talk: “Characterisation of Microstructural Evolution in Solid Oxide Fuel Cell Anodes”

XRM2016 – Oxford University, 2016

Poster: “Three-dimensional correlative imaging: a comparison between X-ray computed tomography and FIB-SEM slice-and-view in the study of SOFC Anodes”

H2FC Supergen – Ulster University, 2016

Talk: “4-Dimensional X-ray nano-computed tomographic imaging of SOFC Anodes: Monitoring microstructural evolution at the nanoscale”

IC3D – Imperial College London, 2017

Poster: “3D Imaging of Solid Oxide Fuel Cell Materials”

QMUL-UCL Energy Materials and Devices Hub – Queen Mary University London, 2017

Talk: “Tomography of SOFC Anode Materials: Electrons vs X-rays”

References

[1] IPCC, “Climate Change 2014 Synthesis Report Summary Chapter for Policymakers,” *IPCC*, p. 31, 2014.

[2] UNFCCC, “Paris Agreement,” *Conf. Parties its twenty-first Sess.*, p. 32, December 2015.

[3] U. Nations, “The Sustainable Development Goals Report,” pp. 1–56, 2018.

[4] CCAC, “Annual Report,” 2016.

[5] WHO, “WHO Global Ambient Air Quality Database (update 2018).” [Online]. Available: http://www.who.int/airpollution/data/cities/en/.

[6] World Health Organization, “Burden of disease from ambient air pollution for 2016 Description of method,” vol. 2017, p. 6, May 2018.

[7] HEI, “State of Global Air / 2017 WHO,” 2017.

[8] United Nations Department of Economic and Social Affairs Population Division, “World Population Prospects The 2017 Revision Key Findings and Advance Tables,” *World Popul. Prospect. 2017*, pp. 1–46, 2017.

[9] I. E. Agency, “World Energy Balances,” 2017.

[10] U.S. EPA, “Inventory of U.S. Greenhouse Gas Emissions and Sinks,” 2018.

[11] B. British Petroleum, “Statistical review of world energy,” p. 21, 2018.

[12] Parliament of the United Kingdom, “Climate Change Act 2008,” *HM Gov.*, pp. 1-103, 2008.

[13] National Grid, “Future Energy Scenarios,” p. 133, July 2018.

[14] H. Ibrahim, A. Ilinca, and J. Perron, “Energy storage systems — Characteristics and comparisons,” vol. 12, pp. 1221–1250, 2008.

[15] A. Z. Weber, M. M. Mench, J. P. Meyers, P. N. Ross, J. T. Gostick, and Q. Liu, “Redox flow batteries: A review,” *J. Appl. Electrochem.*, vol. 41, no. 10, pp. 1137–1164, 2011.

[16] A. Scipioni, A. Manzardo, and J. Ren, *Hydrogen Economy: Supply Chain, Life Cycle Analysis and Energy Transition for Sustainability*. 2017.

[17] R. O’Hayre, S.-W. Cha, W. Colella, and F. B. Prinz, *Fuel Cell Fundamentals*. John Wiley & Sons, Inc., 2009.

[18] B. C. Steele and A. Heinzel, “Materials for fuel-cell technologies.,” *Nature*, vol. 414, no. November, pp. 345–352, 2001.

[19] M. Brown, S. Primdahl, and M. Mogensen, “Structure/Performance Relations for Ni/Yttria-Stabilized Zirconia Anodes for Solid Oxide Fuel Cells,” *J. Electrochem. Soc.*, vol. 147, no. 2, p. 475, 2000.

[20] K. Huang and S. C. Singhal, “Cathode-supported tubular solid oxide fuel cell technology: A critical review,” *J. Power Sources*, vol. 237, pp. 84–97, Sep. 2013.

[21] K. Huang and J. B. Goodenough, *Solid Oxide Fuel Cell Technology: Principles, Performance and Operations*. Woodhead Publishing, 2009.

[22] J. Park *et al.*, “Atomic layer deposition of yttria-stabilized zirconia thin films for enhanced reactivity and stability of solid oxide fuel cells,” *Energy*, vol. 116, pp. 170–176, 2016.

[23] N. Q. Duan, D. Yan, B. Chi, J. Pu, and L. Jian, “High performance anode-supported tubular solid oxide fuel cells fabricated by a novel slurry-casting method,” *Sci. Rep.*, vol. 5, pp. 5–8, 2015.

[24] S. M. Jamil, M. H. D. Othman, M. a. Rahman, J. Jaafar, a. F. Ismail, and K. Li, “Recent fabrication techniques for micro-tubular solid oxide fuel cell support: A review,” *J. Eur. Ceram. Soc.*, vol. 35, no. 1, pp. 1–22, Jan. 2015.

[25] S. Suthirakun, G. Xiao, S. C. Ammal, F. Chen, H.-C. zur Loye, and A. Heyden, “Rational design of mixed ionic and electronic conducting perovskite oxides for solid oxide fuel cell anode materials: A case study for doped $SrTiO_3$,” *J. Power Sources*, vol. 245, pp. 875–885, Jan. 2014.

[26] J. Wan, J. Goodenough, and J. Zhu, “$Nd_{2-x}La_xNiO_{4+\delta}$, a mixed ionic/electronic conductor with interstitial oxygen, as a cathode material,” *Solid State Ionics*, vol. 178, no. 3–4, pp. 281–286, Feb. 2007.

[27] S. Badwal, S. Giddey, A. Kulkarni, and C. Munnings, “Review of progress in high temperature solid oxide fuel cells,” *J. Aust. Cer. Soc*, vol. 50, pp. 23–37, 2014.

[28] D. J. L. Brett, A. Atkinson, N. P. Brandon, and S. J. Skinner, “Intermediate temperature solid oxide fuel cells.,” *Chem. Soc. Rev.*, vol. 37, no. 8, pp. 1568-78, Aug. 2008.

[29] F. Zhao and a Virkar, “Dependence of polarization in anode-supported solid oxide fuel cells on various cell parameters,” *J. Power Sources*, vol. 141, no. 1, pp. 79–95, Feb. 2005.

[30] N. Mahato, A. Banerjee, A. Gupta, S. Omar, and K. Balani, “Progress in Material Selection for Solid Oxide Fuel Cell Technology: A Review,” *Prog. Mater. Sci.*, vol. 72, pp. 141–337, 2015.

[31] M. Mogensen, D. Lybye, N. Bonanos, P. V. Hendriksen, and F. W. Poulsen, “Factors controlling the oxide ion conductivity of fluorite and perovskite structured oxides,” *Solid State Ionics*, vol. 174, no. 1–4, pp. 279–286, 2004.

[32] E. Ivers-Tiffée, A. Weber, and D. Herbstritt, “Materials and technologies for SOFC-components,” *J. Eur. Ceram. …*, vol. 21, pp. 1805–1811, 2001.

[33] H. C. of the Netherlands, “Zirconium and Zirconium Compounds,” *Ullmann’s Encycl. Ind. Chem.*, no. 2000, pp. 111–172, 2000.

[34] O. Yamamoto *et al.*, “Zirconia based oxide ion conductors for solid oxide fuel cells,” *Ionics (Kiel).*, vol. 4, no. 5–6, pp. 403–408, 1998.

[35] I. Kosacki, H. U. Anderson, Y. Mizutani, and K. Ukai, “Nonstoichiometry and electrical transport in Sc-doped zirconia,” vol. 153, pp. 431–438, 2002.

[36] M. Mogensen, K. V. Jensen, M. J. Jorgensen, and S. Primdahl, “Progress in understanding SOFC electrodes,” in *Solid State Ionics*, 2002, vol. 150, no. 1–2, pp. 123–129.

[37] J. W. Fergus, “Electrolytes for solid oxide fuel cells,” *J. Power Sources*, vol. 162, no. 1, pp. 30–40, Nov. 2006.

[38] Z. GAO, L. V. Mogni, E. C. Miller, J. G. Railsback, and S. Barnett, “A Perspective On Low-Temperature Solid Oxide Fuel Cells,” *Energy Environ. Sci.*, 2016.

[39] R. D. Shannon, “Revised effective ionic radii in halides and chalcogenides,” *Acta Cryst.*, no. A32, p. 751, 1976.

[40] C. Sun, R. Hui, and J. Roller, “Cathode materials for solid oxide fuel cells: A review,” *J. Solid State Electrochem.*, vol. 14, no. 7, pp. 1125–1144, 2010.

[41] S. P. Jiang, Development of lanthanum strontium manganite perovskite cathode materials of solid oxide fuel cells: A review, *J. Mat. Sci.*, vol. 43, no. 21. 2008.

[42] Z. Yang, M. Guo, N. Wang, C. Ma, J. Wang, and M. Han, “A short review of cathode poisoning and corrosion in solid oxide fuel cell,” *Int. J. Hydrogen Energy*, vol. 42, no. 39, pp. 24948–24959, 2017.

[43] A. V. Nikonov, K. A. Kuterbekov, K. Z. Bekmyrza, and N. B. Pavzderin, “A brief review of conductivity and thermal expansion of perovskite-related oxides for SOFC cathode,” *Eurasian J. Phys. Funct. Mater.*, vol. 2, no. 3, pp. 274–292, 2018.

[44] S. P. Jiang and S. H. Chan, “A review of anode materials development in solid oxide fuel cells,” *J. Mater. Sci.*, vol. 39, no. 14, pp. 4405–4439, Jul. 2004.

[45] N. Q. Minh and T. Takahashi, *Science and Technology of Ceramic Fuel Cells*. Elsevier, 1995.

[46] N. Q. Minh, “Ceramic Fuel Cells,” *J. Am. Ceram. Soc.* vol. 76, no. 3, pp. 563-588, 1993.

[47] T. Setoguchi, K. Okamoto, K. Eguchi, and H. Arai, “Effects of anode material and fuel on anodic reaction of solid oxide fuel cells,” *J. Electrochem. Soc.*, vol. 139, no. 10, pp. 2875–2880, 1992.

[48] B. Steele, “Fuel-cell technology: Running on natural gas,” *Nature*, vol. 400, no. August, pp. 619–621, 1999.

[49] J. Kuhn and O. Kesler, “Carbon deposition thresholds on nickel-based solid oxide fuel cell anodes I. Fuel utilization,” *J. Power Sources*, vol. 277, pp. 443-454, 2015.

[50] M. Mori, “Thermal Expansion of Nickel-Zirconia Anodes in Solid Oxide Fuel Cells during Fabrication and Operation,” *J. Electrochem. Soc.*, vol. 145, no. 4, p. 1374, 1998.

[51] H. Hayashi, T. Saitou, N. Maruyama, H. Inaba, K. Kawamura, and M. Mori, “Thermal expansion coefficient of yttria stabilized zirconia for various yttria contents,” *Solid State Ionics*, vol. 176, no. 5–6, pp. 613–619, 2005.

[52] H. Spacil, “Electrical device including nickel-containing stabilized zirconia electrode,” 3,503,809, 1970.

[53] J. H. Koh, Y. S. Yoo, J. W. Park, and H. C. Lim, “Carbon deposition and cell performance of Ni-YSZ anode support SOFC with methane fuel,” *Solid State Ionics*, vol. 149, pp. 157–166, 2002.

[54] K. L. Choy, “Chemical vapour deposition of coatings,” *Prog. Mater. Sci.*, vol. 48, no. 2, pp. 57–170, 2003.

[55] U. B. Pal, “Electrochemical vapor deposition of solid oxide films,” *Solid State Ionics*, vol. 52, no. 1–3, pp. 227–233, 1992.

[56] Z. Ogumi, T. Ioroi, Y. Uchimoto, and Z. -i Takehara, “Novel Method for Preparing Nickel/YSZ Cermet by a Vapor-Phase Process,” *J. Am. Ceram. Soc.*, vol. 78, no. 3, pp. 593–598, 1995.

[57] P. Charpentier., P. Fragnaud, D. M. Schleich, and C. Lunot, “Thin Film Solid Oxide Fuel Cells,” *Ionics (Kiel).*, vol. 2, pp. 312–318, 1996.

[58] K. L. Choy, “Fabrication of ceramic coatings using flame assisted vapour deposition,” in *Br. Ceram. Proc.*, no. 54, pp. 65–74, 1994

[59] F. Kokai, K. Amano, H. Ota, and F. Umemura, “XeCl laser ablation of yttria stabilized zirconia - Etch depth and characterization of ablated surfaces,” *Appl. Phys. A Solids Surfaces*, vol. 54, no. 4, pp. 340–342, 1992.

[60] K. Mehta, X. U. Ren, and A. V. Virkar, “Two-layer fuel cell electrolyte structure by sol-gel processing,” *J. Sol-Gel Sci. Technol.*, vol. 11, no. 2, pp. 203–207, 1998.

[61] J. Will, A. Mitterdorfer, C. Kleinlogel, D. Perednis, and L. J. Gauckler, “Fabrication of thin electrolytes for second-generation solid oxide fuel cells,” *Solid State Ionics*, vol. 131, no. 1, pp. 79–96, 2000.

[62] T. Fukui, S. Ohara, M. Naito, and K. Nogi, “Performance and stability of SOFC anode fabricated from NiO/YSZ composite particles,” *J. Eur. Ceram. Soc.*, vol. 23, no. 15, pp. 2963–2967, 2003.

[63] D. Simwonis, H. Thülen, F. J. Dias, A. Naoumidis, and D. Stöver, “Properties of Ni/YSZ porous cermets for SOFC anode substrates prepared by tape casting and coat-mix process,” *J. Mater. Process. Technol.*, vol. 92–93, pp. 107–111, 1999.

[64] M. Cassidy, G. Lindsay, and K. Kendall, “The reduction of nickel-zirconia cermet anodes and the effects on supported thin electrolytes,” *J. Power Sources*, vol. 61, no. 1–2, pp. 189–192, 1996.

[65] N. Nakagawa, “Evaluation of the Effective Reaction Zone at Ni(NiO)/Zirconia Anode by Using an Electrode with a Novel Structure,” *J. Electrochem. Soc.*, vol. 142, no. 10, p. 3474, 1995.

[66] G. S. A. M. Theunissen, a. J. a Winnubst, and a. J. Burggraaf, “Surface and grain boundary analysis of doped zirconia ceramics studied by AES and XPS,” *J. Mater. Sci.*, vol. 27, pp. 5057–5066, 1992.

[67] K. Vels Jensen, S. Primdahl, I. Chorkendorff, and M. Mogensen, “Microstructural and chemical changes at the Ni/YSZ interface,” *Solid State Ionics*, vol. 144, no. 3–4, pp. 197–209, 2001.

[68] Y. Liu, “Effects of impurities on microstructure in Ni/YSZ–YSZ half-cells for SOFC,” *Solid State Ionics*, vol. 161, no. 1–2, pp. 1–10, Jul. 2003.

[69] Y. Matsuzaki and I. Yasuda, “The poisoning effect of sulfur-containing impurity gas on a SOFC anode: Part I. Dependence on temperature, time, and impurity concentration,” vol. 132, pp. 261–269, 2000.

[70] A. L. Dicks, “Hydrogen generation from natural gas for the fuel cell systems of tomorrow,” *J. Power Sources*, vol. 61, no. 1–2, pp. 113–124, 1996.

[71] C. M. Finnerty, N. J. Coe, R. H. Cunningham, and R. M. Ormerod, “Carbon formation on and deactivation of nickel-based/zirconia anodes in solid oxide fuel cells running on methane,” *Catal. Today*, vol. 46, no. 2–3, pp. 137–145, Nov. 1998.

[72] E. P. Murray, T. Tsai, and S. a. Barnett, “A direct-methane fuel cell with a ceria-based anode,” *Nature*, vol. 400, pp. 649–651, 1999.

[73] S. P. S. Shaikh, A. Muchtar, and M. R. Somalu, “A review on the selection of anode materials for solid-oxide fuel cells,” *Renew. Sustain. Energy Rev.*, vol. 51, pp. 1–8, 2015.

[74] D. D. Macdonald and A. C. Khandkar, “High temperature electrode materials and characterization,” in *D. D. Macdonald, and A. C. Khandkar, symposium held May, 1991 in Washington, DC, 304*, p. 32, 1991.

[75] S. Primdahl and M. Mogensen, “Durability and thermal cycling of Ni / YSZ cermet anodes for solid oxide fuel cells,” *J. Appl. Electrochem.*, vol. 30, pp. 247-257, 2000.

[76] T. M. M. Heenan, J. B. Robinson, X. Lu, J. J. Bailey, D. J. L. Brett, and P. R. Shearing, “Analyzing the Mechanical Performance of Solid Oxide Fuel Cells at Interfacial Anode/Electrolyte Regions using Sub-Micron Resolution 3D X-Ray Computed Tomography,” vol. 78, no. 1, pp. 2317–2321, 2017.

[77] D. Sarantaridis and a. Atkinson, “Redox Cycling of Ni-Based Solid Oxide Fuel Cell Anodes: A Review,” *Fuel Cells*, vol. 7, no. 3, pp. 246–258, Jun. 2007.

[78] B. Song, E. Ruiz-Trejo, A. Bertei, and N. P. Brandon, “Quantification of the degradation of Ni-YSZ anodes upon redox cycling,” *J. Power Sources*, vol. 374, no. October 2017, pp. 61–68, 2018.

[79] A. Faes *et al.*, “RedOx study of anode-supported solid oxide fuel cell,” *J. Power Sources*, vol. 193, no. 1, pp. 55–64, 2009.

[80] J. Laurencin, G. Delette, O. Sicardy, S. Rosini, and F. Lefebvre-Joud, “Impact of ‘redox’ cycles on performances of solid oxide fuel cells: Case of the electrolyte supported cells,” *J. Power Sources*, vol. 195, no. 9, pp. 2747–2753, 2010.

[81] D. Simwonis, “Nickel coarsening in annealed Ni/8YSZ anode substrates for solid oxide fuel cells,” *Solid State Ionics*, vol. 132, no. 3–4. pp. 241–251, 2000.

[82] D. W. Dees, T. D. Claar, and D. C. Fee, “Conductivity of Porous Ni / ZrO2-Y203 Cermets,” *J. Electrochem. Soc.*, vol. 134, no. 9, pp. 2141–2146, 1987.

[83] D. Stauffer and A. Aharony, “Introduction to percolation theory.” CRC Press, 1994.

[84] T. Kawada, “Characteristics of Slurry-Coated Nickel Zirconia Cermet Anodes for Solid Oxide Fuel Cells,” *J. Electrochem. Soc.*, vol. 137, no. 10, p. 3042, 1990.

[85] S. . Aruna, M. Muthuraman, and K. . Patil, “Synthesis and properties of Ni-YSZ cermet: anode material for solid oxide fuel cells,” *Solid State Ionics*, vol. 111, no. 1–2, pp. 45–51, 1998.

[86] S. Sunde, “Calculation of Conductivity and Polarization Resistance of Composite SOFC Electrodes from Random Resistor Networks,” *J. Electrochem. Soc.*, vol. 142, no. 4, pp. L50–L52, 1995.

[87] C.-H. Lee, C.-H. Lee, H.-Y. Lee, and S. M. Oh, “Microstructure and anodic properties of Ni/YSZ cermets in solid oxide fuel cells,” *Solid State Ionics*, vol. 98, no. 1–2, pp. 39–48, 1997.

[88] S. C. Singhal and M. Dokiya, “Solid Oxide Fuel Cells (SOFC VI),” in *Proceedings of the Sixth International Symposium*, 1999, pp. 503–512.

[89] J. H. Lee, H. Moon, H. W. Lee, J. Kim, J. D. Kim, and K. H. Yoon, “Quantitative analysis of microstructure and its related electrical property of SOFC anode, Ni-YSZ cermet,” *Solid State Ionics*, vol. 148, no. 1–2, pp. 15–26, 2002.

[90] T. L. Heath, *The Works of Archimedes*, vol. 53, no. 9. Cambridge University Press, 1897.

[91] S. Jiang, “Sintering behavior of Ni/Y_2O_3-ZrO_2 cermet electrodes of solid oxide fuel cells,” *J. Mater. Sci.*, vol. 8, pp. 3775–3782, 2003.

[92] H. Itoh, “Configurational and Electrical Behavior of Ni-YSZ Cermet with Novel Microstructure for Solid Oxide Fuel Cell Anodes,” *Journal of The Electrochemical Society*, vol. 144, no. 2. p. 641, 1997.

[93] A. Faes, A. Hessler-Wyser, D. Presvytes, C. G. Vayenas, and J. Van herle, “Nickel/Zirconia Anode Degradation and Triple Phase Boundary Quantification from Microstructural Analysis,” *Fuel Cells*, vol. 9, no. 6, pp. 841–851, Dec. 2009.

[94] Y. Suzue, N. Shikazono, and N. Kasagi, “Micro modeling of solid oxide fuel cell anode based on stochastic reconstruction,” *J. Power Sources*, vol. 184, pp. 52-59, 2008.

[95] Y. Guan *et al.*, “Lattice-Boltzmann modeling of gas transport in Ni-Yttria-stabilized zirconia anodes during thermal cycling based on X-ray computed tomography,” *Electrochim. Acta*, vol. 121, pp. 386–393, 2014.

[96] S. Succi, M. Sbragaglia, and S. Ubertini, “Lattice boltzmann method,” *Scholarpedia*, vol. 5.5, p. 9507, 2010.

[97] S. Primdahl, B. F. Sørensen, and M. Mogensen, “Effect of Nickel Oxide/Yttria-Stabilized Zirconia Anode Precursor Sintering Temperature on the Properties of Solid Oxide Fuel Cells,” *J. Am. Ceram. Soc.*, vol. 83, no. 3, pp. 489–494, 2004.

[98] T. Shirakawa, S. Matsuda, and A. Fukushima, “Characterization of NiO/YSZ electrode by temperature-programmed reduction,” in *Proceedings of the Third International Symposium on Solid Oxide Fuel Cells (SOFC-III)*, 1993, vol. 1, pp. 464–472.

[99] C. W. Tanner, K.-Z. Fung, and A. V. Virkar, “The Effect of Porous Composite Electrode Structure on Solid Oxide Fuel Cell Performance,” *J. Electrochem. Soc.*, no. 1, pp. 21–30, 1997.

[100] J. Winkler, “Geometric Requirements of Solid Electrolyte Cells with a Reference Electrode,” *J. Electrochem. Soc.*, vol. 145, no. 4, p. 1184, 1998.

[101] A. Tsoga, A. Naoumidis, and P. Nikolopoulos, “Wettability and interfacial reactions in the systems and Ni/Ti-TiO_2/YSZ,” *Acta Mater.*, vol. 44, no. 9, pp. 3679–3692, Sep. 1996.

[102] T. Huhtamäki and X. Tian, “Surface-wetting characterization using contact-angle measurements,” *Nat. Protoc.*, vol. 13, no. July, pp. 1521–1538, 2018.

[103] D. Skarmoutsos, A. Tsoga, A. Naoumidis, and P. Nikolopoulos, “5 mol% TiO_2-doped Ni-YSZ anode cermets for solid oxide fuel cells,” *Solid State Ionics*, vol. 135, no. 1–4, pp. 439–444, 2000.

[104] J. Mizusaki, “Preparation of Nickel Pattern Electrodes on YSZ and Their Electrochemical Properties in H_2-H_2O Atmospheres,” *J. Electrochem. Soc.*, vol. 141, no. 8, p. 2129, 1994.

[105] A. Ioselevich, A. A. Kornyshev, and W. Lehnert, “Degradation of Solid Oxide Fuel Cell Anodes Due to Sintering of Metal Particles: Correlated Percolation Model,” *J. Electrochem. Soc.*, vol. 144, no. 9, pp. 3010–3019, 1997.

[106] N. Nakagawa, K. Nakajima, M. Sato, and K. Kato, “Contribution of the internal active three-phase zone of Ni-zirconia cermet anodes on the electrode performance of SOFCs,” *J. Electrochem. Soc.*, vol. 146, no. 4, pp. 1290–1295, 1999.

[107] J. Divisek and R. Wilkenhöner, “Structure investigations of SOFC anode cermets Part I : Porosity investigations,” *J. Appl. Electrochem.*, vol. 29, no. 2, pp. 153-163, 1999.

[108] H. J. G. Gundersen and E. B. Jensen, “Particle sizes and their distributions estimated from line- and point-sampled intercepts. Including graphical unfolding,” *J. Microsc.*, vol. 131, no. 3, pp. 291–310, 1983.

[109] T. Norby, O. J. Velle, H. Leth-Olsen, R. Tunold, S. C. Singhal, and H. Iwahara, “Reaction resistance in relation to three phase boundary length of Ni-YSZ electrodes,” vol. 93–4, pp. 473–478, 1993.

[110] M. Poulsen, FW, Bentzen, JJ, Jacobsen, T, Skou, E & Østergård, *High temperature electrochemical behaviour of fast ion and mixed conductors*. 1993.

[111] L. B. Valdes, “Resistivity Measurements on Germanium for Transistors,” *Proc. I.R.E.*, pp. 420–427, 1954.

[112] J. Mizusaki, K. Waragai, S. Tsuchiya, H. Tagawa, Y. Arai, and Y. Kuwayama, “Simple Mathematical Model for the Electrical Conductivity of Highly Porous Ceramics,” *J. Am. Ceram. Soc.*, vol. 79, no. 1, pp. 109–113, 1996.

[113] R. Vassen, D. Simwonis, and D. Stöver, “Modelling of the agglomeration of Ni-particles in anodes of solid oxide fuel cells,” *J. Mater. Sci.*, vol. 6, pp. 147–151, 2001.

[114] D. Simwonis, F. Tietz, and D. Stover, “Nickel coarsening in annealed Ni / 8YSZ anode substrates for solid oxide fuel cells,” *Solid State Ionics*, vol. 132, pp. 241-251, 2000.

[115] A. Hagen, R. Barfod, P. V. Hendriksen, Y.-L. Liu, and S. Ramousse, “Degradation of Anode Supported SOFCs as a Function of Temperature and Current Load,” *J. Electrochem. Soc.*, vol. 153, no. 6, p. A1165, 2006.

[116] Y. Jiang and A. V. Virkar, “Fuel Composition and Diluent Effect on Gas Transport and Performance of Anode-Supported SOFCs,” *J. Electrochem. Soc.*, vol. 150, no. 7, p. A942, 2003.

[117] M. Division, “The Theory of Ostwald Ripening,” vol. 38, pp. 231–252, 1985.

[118] P. Tanasini *et al.*, “Experimental and Theoretical Investigation of Degradation Mechanisms by Particle Coarsening in SOFC Electrodes,” *Fuel Cells*, vol. 9, no. 5, pp. 740–752, Oct. 2009.

[119] J. Geyer, H. Kohlmueller, H. Landes, and R. Stuebner, “Investigations into the kinetics of the Ni-YSZ-Cermet-Anode of a Solid Oxide Fuel Cell,” in *Proceedings - Electrochemical Society*, vol. 40, pp. 585–594, 1997.

[120] S. Koch *et al.*, “Solid oxide fuel cell performance under severe operating conditions,” *Fuel Cells*, no. 2, pp. 130–136, 2006.

[121] H. Xiao, T. L. Reitz, and M. A. Rottmayer, “Polarization measurements of anode-supported solid oxide fuel cells studied by incorporation of a reference electrode,” *J. Power Sources*, vol. 183, no. 1, pp. 49–54, 2008.

[122] Z. D. Gostovic, J. R. Smith, D. P. Kundinger, K. S. Jones, and E. D. Wachsman, “Three-dimensional reconstruction of porous LSCF cathodes,” *Electrochem. Solid-State Lett.*, vol. 10, no. 12, pp. B214–B217, 2007.

[123] J. Wilson *et al.*, “Three Dimensional Reconstruction of Solid Oxide Fuel Cell Electrodes Using Focused Ion Beam - Scanning Electron Microscopy,” *ECS Trans.*, vol. 7, no. Suppl 2, pp. 1879–1887, 2007.

[124] V. M. Janardhanan, V. Heuveline, and O. Deutschmann, “Three-phase boundary length in solid-oxide fuel cells: A mathematical model,” *J. Power Sources*, vol. 178, no. 1, pp. 368–372, 2008.

[125] T. Matsui, R. Kishida, J.-Y. Kim, H. Muroyama, and K. Eguchi, “Performance Deterioration of Ni–YSZ Anode Induced by Electrochemically Generated Steam in Solid Oxide Fuel Cells,” *J. Electrochem. Soc.*, vol. 157, no. 5, p. B776, 2010.

[126] H. Iwai *et al.*, “Quantification of SOFC anode microstructure based on dual beam FIB-SEM technique,” *J. Power Sources*, vol. 195, no. 4, pp. 955–961, Feb. 2010.

[127] N. Vivet *et al.*, “Effect of Ni content in SOFC Ni-YSZ cermets: A three-dimensional study by FIB-SEM tomography,” *J. Power Sources*, vol. 196, no. 23, pp. 9989–9997, 2011.

[128] K. Thyden, “Microstructural characterization of SOFC Ni–YSZ anode composites by low-voltage scanning electron microscopy,” *Solid State Ionics*, vol. 178, no. 39–40, pp. 1984–1989, Mar. 2008.

[129] O. O. Taiwo *et al.*, “Comparison of three-dimensional analysis and stereological techniques for quantifying lithium-ion battery electrode microstructures.,” *J. Microsc.*, vol. 263(3), Mar. 2016.

[130] K. Matsuzaki, D. Kannoa, H. Teshimaa, N. Shikazonoa, and N. Kasagia, “Three-Dimensional Numerical Simulation of Ni-YSZ Anode Polarization Using Reconstructed Microstructure from FIB-SEM Images,” *ECS Trans.*, vol. 25, no. 2, pp. 1829–1836, 2009.

[131] J. R. Wilson, M. Gameiro, K. Mischaikow, W. Kalies, P. W. Voorhees, and S. a Barnett, “Three-dimensional analysis of solid oxide fuel cell Ni-YSZ anode interconnectivity.,” *Microsc. Microanal.*, vol. 15, pp. 71–77, 2009.

[132] J. R. Wilson *et al.*, “Three-dimensional reconstruction of a solid-oxide fuel-cell anode.,” *Nat. Mater.*, vol. 5, no. 7, pp. 541–4, Jul. 2006.

[133] P. R. Shearing, J. I. Golbert, R. J. Chater, and N. P. Brandon, “3D reconstruction of SOFC anodes using a focused ion beam lift-out technique,” *Chem. Eng. Sci.*, vol. 64, no. 17, pp. 3928–3933, Sep. 2009.

[134] J. Golbert, C. S. Adjiman, and N. P. Brandon, “Microstructural Modeling of Solid Oxide Fuel Cell Anodes,” *Ind. Eng. Chem. Res.*, vol. 47, pp. 7693–7699, 2008.

[135] P. R. Shearing, Q. Cai, J. I. Golbert, V. Yufit, C. S. Adjiman, and N. P. Brandon, “Microstructural analysis of a solid oxide fuel cell anode using focused ion beam techniques coupled with electrochemical simulation,” *J. Power Sources*, vol. 195, no. 15, pp. 4804–4810, Aug. 2010.

[136] A. Bieberle, L. P. Meier, and L. J. Gauckler, “The Electrochemistry of Ni Pattern Anodes Used as Solid Oxide Fuel Cell Model Electrodes,” *J. Electrochem. Soc.*, vol. 148, no. 6, p. A646, 2001.

[137] N. Shikazono, D. Kanno, K. Matsuzaki, H. Teshima, S. Sumino, and N. Kasagi, “Numerical Assessment of SOFC Anode Polarization Based on Three-Dimensional Model Microstructure Reconstructed from FIB-SEM Images,” *J. Electrochem. Soc.*, vol. 157, no. 5, p. B665, 2010.

[138] D. Kanno, N. Shikazono, N. Takagi, K. Matsuzaki, and N. Kasagi, “Evaluation of SOFC anode polarization simulation using three-dimensional microstructures reconstructed by FIB tomography,” *Electrochim. Acta*, vol. 56, no. 11, pp. 4015-4021, 2011.

[139] R. Krishna and J. A. Wesselingh, “The Maxwell-Stefan approach to mass transfer,” *Chem. Eng. Sci.*, vol. 52, no. 6, pp. 861–911, 1997.

[140] B. De Boer, *SOFC anode: hydrogen oxidation at porous nickel and nickel/YSZ cermet electrodes*, vol. 4, no. 31. 2001.

[141] M. Kishimoto, H. Iwai, M. Saito, and H. Yoshida, “Quantitative evaluation of solid oxide fuel cell porous anode microstructure based on focused ion beam and scanning electron microscope technique and prediction of anode overpotentials,” *J. Power Sources*, vol. 196, no. 10, pp. 4555–4563, 2011.

[142] L. Holzer, B. Münch, B. Iwanschitz, M. Cantoni, T. Hocker, and T. Graule, “Quantitative relationships between composition, particle size, triple phase boundary length and surface area in nickel-cermet anodes for Solid Oxide Fuel Cells,” *J. Power Sources*, vol. 196, no. 17, pp. 7076–7089, 2011.

[143] J. Joos, M. Ender, I. Rotscholl, N. H. Menzler, and E. Ivers-Tiffée, “Quantification of double-layer Ni/YSZ fuel cell anodes from focused ion beam tomography data,” *J. Power Sources*, vol. 246, pp. 819–830, 2014.

[144] J. Hoshen and R. Kopelman, “Percolation and cluster distribution. I. Cluster multiple labeling technique and critical concentration algorithm,” *Phys. Rev. B*, vol. 14, no. 8, pp. 3438–3445, 1976.

[145] N. Vivet *et al.*, “3D Microstructural characterization of a solid oxide fuel cell anode reconstructed by focused ion beam tomography,” *J. Power Sources*, vol. 196, no. 18, pp. 7541–7549, Sep. 2011.

[146] M. Kishimoto, H. Iwai, M. Saito, and H. Yoshida, “Quantitative Evaluation of Transport Properties of SOFC Porous Anode by Random Walk Process,” in *ECS Transactions*, 2009, vol. 25, no. 2, pp. 1887–1896.

[147] N. Epstein, “On tortuosity and the tortuosity factor in flow and diffusion through porous media,” *Chem. Eng. Sci.*, vol. 44, no. 3, pp. 777–779, 1989.

[148] L. Holzer *et al.*, “Microstructure degradation of cermet anodes for solid oxide fuel cells: Quantification of nickel grain growth in dry and in humid atmospheres,” *J. Power Sources*, vol. 196, no. 3, pp. 1279–1294, Feb. 2011.

[149] P. W. Voorhees, “The Theory of Ostwald Ripening,” *J. Stat. Phys.*, vol. 38, pp. 231–252, 1985.

[150] G. C. Kuczynski, “Measurement of self-diffusion of silver without radioactive tracers,” *J. Appl. Phys.*, vol. 21, no. 7, pp. 632–635, 1950.

[151] B. Münch and L. Holzer, “Contradicting Geometrical Concepts in Pore Size Analysis Attained with Electron Microscopy and Mercury Intrusion,” *J. Am. Ceram. Soc.*, vol. 91, no. 12, pp. 4059–4067, 2008.

[152] J. S. Cronin, J. R. Wilson, and S. a. Barnett, “Impact of pore microstructure evolution on polarization resistance of Ni-Yttria-stabilized zirconia fuel cell anodes,” *J. Power Sources*, vol. 196, no. 5, pp. 2640–2643, Mar. 2011.

[153] T. Matsui *et al.*, “Anode microstructural change upon long-term operation for the cathode-supported tubular-type SOFC,” *Solid State Ionics*, vol. 225, pp. 50–54, 2012.

[154] Z. Jiao, G. Lee, N. Shikazono, and N. Kasagi, “Quantitative Study on the Correlation Between Solid Oxide Fuel Cell Ni-YSZ Composite Anode Performance and Sintering Temperature Based on Three-dimensional Reconstruction,” *J. Electrochem. Soc.*, vol. 159, no. 7, pp. F278–F286, 2012.

[155] S. Linderoth, N. Bonanos, K. V. Jensen, and J. B. Bilde-Sørensen, “Effect of NiO-to-Ni Transformation on Conductivity and Structure of Yttria-Stabilized ZrO2,” *J. Am. Ceram. Soc.*, vol. 84, no. 11, pp. 2652–2656, 2001.

[156] Y. H. Lee, H. Muroyama, T. Matsui, and K. Eguchi, “Degradation of nickel-yttria-stabilized zirconia anode in solid oxide fuel cells under changing temperature and humidity conditions,” *J. Power Sources*, vol. 262, pp. 451–456, 2014.

[157] A. Tkachuk, F. Duewer, H. Cui, M. Feser, S. Wang, and W. Yun, “X-ray computed tomography in Zernike phase contrast mode at 8 keV with 50-nm resolution using Cu rotating anode X-ray source,” *Zeitschrift fur Krist.*, vol. 222, no. 11, pp. 650–655, 2007.

[158] J. R. Izzo *et al.*, “Non-destructive Reconstruction and Analysis of SOFC Anodes Using X-ray Computed Tomography at Sub-50 nm Resolution,” *J. Electrochem. Soc.*, vol. 155, no. 5, p. B504, 2008.

[159] A. S. Joshi, K. N. Grew, J. R. Izzo, A. A. Peracchio, and W. K. S. Chiu, “Lattice Boltzmann Modeling of Three-Dimensional, Multicomponent Mass Diffusion in a Solid Oxide Fuel Cell Anode,” *J. Fuel Cell Sci. Technol.*, vol. 7, no. 1, p. 011006, 2010.

[160] P. R. Shearing, J. Gelb, and N. Brandon, “Characterization of SOFC Electrode Microstructure Using Nano-Scale X-ray Computed Tomography and Focused Ion Beam Techniques: a Comparative Study,” *ECS Trans.* , vol. 19, no. 17, pp. 51–57, 2009.

[161] P. R. Shearing, J. Gelb, and N. P. Brandon, “X-ray nano computerised tomography of SOFC electrodes using a focused ion beam sample-preparation technique,” *J. Eur. Ceram. Soc.*, vol. 30, no. 8, pp. 1809–1814, Jun. 2010.

[162] P. R. Shearing, J. Gelb, J. Yi, W.-K. Lee, M. Drakopolous, and N. P. Brandon, “Analysis of triple phase contact in Ni–YSZ microstructures using non-destructive X-ray tomography with synchrotron radiation,” *Electrochem. commun.*, vol. 12, no. 8, pp. 1021–1024, Aug. 2010.

[163] K. N. Grew *et al.*, “Nondestructive Nanoscale 3D Elemental Mapping and Analysis of a Solid Oxide Fuel Cell Anode,” *J. Electrochem. Soc.*, vol. 157, no. 6, p. B783, 2010.

[164] K. N. Grew, A. A. Peracchio, and W. K. S. Chiu, “Characterization and analysis methods for the examination of the heterogeneous solid oxide fuel cell electrode microstructure. Part 2: Quantitative measurement of the microstructure and contributions to transport losses,” *J. Power Sources*, vol. 195, no. 24, pp. 7943-7958, 2010.

[165] T. X. Ho, P. Kosinski, A. C. Hoffmann, and A. Vik, “Effects of heat sources on the performance of a planar solid oxide fuel cell,” *Int. J. Hydrogen Energy*, vol. 35, no. 9, pp. 4276–4284, 2010.

[166] Y. Guan *et al.*, “Analysis of the three-dimensional microstructure of a solid-oxide fuel cell anode using nano X-ray tomography,” *J. Power Sources*, vol. 196, no. 4, pp. 1915–1919, 2011.

[167] D. P. Bentz and E. J. Garboczi, “Percolation of Phases in a Three-Dimensional Cement Paste Microstructural Model,” vol. 21, pp. 325–344, 1991.

[168] Y. C. Karen Chen-Wiegart, J. S. Cronin, Q. Yuan, K. J. Yakal-Kremski, S. A. Barnett, and J. Wang, “3D Non-destructive morphological analysis of a solid oxide fuel cell anode using full-field X-ray nano-tomography,” *J. Power Sources*, vol. 218, pp. 348–351, 2012.

[169] J. Laurencin, R. Quey, G. Delette, H. Suhonen, P. Cloetens, and P. Bleuet, “Characterisation of Solid Oxide Fuel Cell Ni-8YSZ substrate by synchrotron X-ray nano-tomography: From 3D reconstruction to microstructure quantification,” *J. Power Sources*, vol. 198, pp. 182–189, 2012.

[170] J. R. Wilson *et al.*, “Effect of composition of $La_{0.8}Sr_{0.2}MnO_3$-Y_2O_3-stabilized ZrO_2 cathodes. Correlating three-dimensional microstructure and polarization resistance,” *J. Power Sources*, vol. 195, no. 7, pp. 1829–1840, 2010.

[171] J. S. Cronin, J. R. Wilson, and S. Barnett, “Impact of pore microstructure evolution on polarization resistance of Ni-Yttria-stabilized zirconia fuel cell anodes,” *J. Power Sources*, vol. 196, no. 5, pp. 2640–2643, Mar. 2011.

[172] C. Metcalfe, O. Kesler, T. Rivard, F. Gitzhofer, and N. Abatzoglou, “Connected Three-Phase Boundary Length Evaluation in Modeled Sintered Composite Solid Oxide Fuel Cell Electrodes,” *J. Electrochem. Soc.*, vol. 157, no. 9, p. B1326, 2010.

[173] P. Cloetens *et al.*, “Holotomography: Quantitative phase tomography with micrometer resolution using hard synchrotron radiation x rays,” *Appl. Phys. Lett.*, vol. 75, no. 19, pp. 2912–2914, 1999.

[174] J. Joos, T. Carraro, A. Weber, and E. Ivers-Tiffée, “Reconstruction of porous electrodes by FIB/SEM for detailed microstructure modeling,” *J. Power Sources*, vol. 196, no. 17, pp. 7302–7307, 2011.

[175] J. Joos, M. Ender, T. Carraro, A. Weber, and E. Ivers-Tiffée, “Representative volume element size for accurate solid oxide fuel cell cathode reconstructions from focused ion beam tomography data,” *Electrochim. Acta*, vol. 82, pp. 268-276, 2012.

[176] J. S. Cronin, Y. K. Chen-Wiegart, J. Wang, and S. a. Barnett, “Three-dimensional reconstruction and analysis of an entire solid oxide fuel cell by full-field transmission X-ray microscopy,” *J. Power Sources*, vol. 233, pp. 174-179, 2013.

[177] G. Nelson *et al.*, “X-ray Imaging and Analysis of 3D Microstructural Changes in Aged Ni-YSZ Anode,” *ECS Trans.*, vol. 35, no. 1, pp. 1323–1327, 2011.

[178] Y. Guan *et al.*, “Quantitative analysis of micro structural and conductivity evolution of Ni-YSZ anodes during thermal cycling based on nano-computed tomography,” *J. Power Sources*, vol. 196, no. 24, pp. 10601–10605, 2011.

[179] G. J. Nelson *et al.*, “Three-dimensional microstructural changes in the Ni-YSZ solid oxide fuel cell anode during operation,” *Acta Mater.*, vol. 60, no. 8, pp. 3491–3500, 2012.

[180] C. F. J. Wu and M. S. Hamada, *Experiments: planning, analysis, and optimization*. Wiley, 2009.

[181] K. Yakal-Kremski, J. S. Cronin, Y.-C. K. Chen-Wiegart, J. Wang, and S. a. Barnett, “Studies of Solid Oxide Fuel Cell Electrode Evolution Using 3D Tomography,” *Fuel Cells*, vol. 13, no. 4, pp. 449–454, Aug. 2013.

[182] D. Kennouche, Y. -c. K. Chen-Wiegart, J. S. Cronin, J. Wang, and S. A. Barnett, “Three-Dimensional Microstructural Evolution of Ni- Yttria-Stabilized Zirconia Solid Oxide Fuel Cell Anodes At Elevated Temperatures,” *J. Electrochem. Soc.*, vol. 160, no. 11, pp. F1293–F1304, 2013.

[183] D. Kennouche, Y. K. Chen-Wiegart, C. Riscoe, J. Wang, and S. A. Barnett, “Combined electrochemical and X-ray tomography study of the high temperature evolution of Nickel – Yttria Stabilized Zirconia solid oxide fuel cell anodes,” *J. Power Sources*, vol. 307, pp. 604–612, 2016.

[184] P. R. Shearing *et al.*, “Using Synchrotron X-Ray Nano-CT to Characterize SOFC Electrode Microstructures in Three-Dimensions at Operating Temperature,” *Electrochem. Solid-State Lett.*, vol. 14, no. 10, p. B117, 2011.

[185] P. R. Shearing, R. S. Bradley, J. Gelb, F. Tariq, P. J. Withers, and N. P. Brandon, “Exploring microstructural changes associated with oxidation in Ni-YSZ SOFC electrodes using high resolution X-ray computed tomography,” *Solid State Ionics*, vol. 216, pp. 69–72, 2012.

[186] F. Tariq, M. Kishimoto, S. J. Cooper, P. R. Shearing, and N. P. Brandon, “Advanced 3D Imaging and Analysis of SOFC Electrodes,” *ECS Trans.*, vol. 57, no. 1, pp. 2553–2562, 2013.

[187] D. Kennouche *et al.*, “[187]es,” *Acta Mater.*, vol. 103, pp. 204-210, 2016.

[188] E. B. Gulsoy, J. P. Simmons, and M. De Graef, “Application of joint histogram and mutual information to registration and data fusion problems in serial sectioning microstructure studies,” *Scr. Mater.*, vol. 60, no. 6, pp. 381–384, 2009.

[189] Y. K. Chen-wiegart, D. Kennouche, J. S. Cronin, S. A. Barnett, and J. Wang, “Effect of Ni content on the morphological evolution of Ni-YSZ solid oxide fuel cell electrodes,” vol. 108, p. 083903, 2016.

[190] T. M. M. Heenan *et al.*, “Three-Phase Segmentation of Solid Oxide Fuel Cell Anode Materials Using Lab Based X-ray Nano-Computed Tomography,” *Fuel Cells*, vol. 17, no. 1, pp. 75–82, 2017.

[191] T. M. M. Heenan *et al.*, “4D Nano-Tomography of Electrochemical Energy Devices using Lab-based X-ray Computed Tomography,” *Nano Energy*, vol. 47, pp. 556-565, 2018.

[192] T. M. M. Heenan, X. Lu, J. B. Robinson, F. Iacoviello, D. J. L. Brett, and P. R. Shearing, “Thermally Driven SOFC Degradation in 4D: Part I. Microscale,” *J. Electrochem. Soc.*, vol. 165, no. 11, pp. F932–F941, 2018.

[193] A. Ioselevich, A. A. Kornyshev, and W. Lehnert, “Statistical geometry of reaction space in porous cermet anodes based on ion-conducting electrolytes patterns of degradation,” *Solid State Ionics*, vol. 124, no. 3, pp. 221–237, 1999.

[194] H. N. Chapman, “Phase-retrieval X-ray microscopy by Wigner-distribution deconvolution,” *Ultramicroscopy*, vol. 66, no. 3–4, pp. 153–172, 1996.

[195] J. M. Rodenburg *et al.*, “Hard-X-ray lensless imaging of extended objects,” *Phys. Rev. Lett.*, vol. 98, no. 3, pp. 1–4, 2007.

[196] H. M. L. Faulkner and J. M. Rodenburg, “Movable aperture lensless transmission microscopy: A novel phase retrieval algorithm,” *Phys. Rev. Lett.*, vol. 93, no. 2, pp. 023903-1, 2004.

[197] M. Stockmar *et al.*, “X-ray nanotomography using near-field ptychography,” *Opt. Express*, vol. 23, no. 10, p. 12720, 2015.

[198] V. Julie *et al.*, “3D phase mapping of solid oxide fuel cell YSZ/Ni cermet at the nanoscale by holographic X-ray nanotomography,” *J. Power Sources*, vol. 243, pp. 841–849, 2013.

[199] S. De Angelis *et al.*, “Ex-situ tracking solid oxide cell electrode microstructural evolution in a redox cycle by high resolution ptychographic nanotomography,” *J. Power Sources*, vol. 360, pp. 520–527, 2017.

[200] S. De Angelis, P. S. Jørgensen, E. H. R. Tsai, M. Holler, K. Kreka, and J. R. Bowen, “Three dimensional characterization of nickel coarsening in solid oxide cells via ex-situ ptychographic nano-tomography,” *J. Power Sources*, vol. 383, pp. 72–79, 2018.

[201] P. J. Besl and N. D. McKay, “Method for registration of 3-D shapes,” April 1992, pp. 586–606, 1992.

[202] M. . Phaneuf, “Applications of focused ion beam microscopy to materials science specimens,” *Micron*, vol. 30, no. 3, pp. 277–288, Jun. 1999.

[203] M. Peña-Fernández, A. H. Barber, G. W. Blunn, and G. Tozzi, “Optimisation of digital volume correlation computation in SR-microCT images of trabecular bone and bone-biomaterial systems,” *J. Microsc.*, pp. 1–16, 2018.

[204] G. Parravano, “The Reduction of Nickel Oxide by Hydrogen,” *J. Am. Chem. Soc.*, vol. 74, no. 5, pp. 1194–1198, 1952.

[205] B. Delmon and A. Roman, “Kinetic Study of the Reduction of Nickel Oxide near its Antiferromagnetic-Paramagnetic Transition,” 1972.

[206] F. Tietz, F. J. Dias, D. Simwonis, and D. Stöver, “Evaluation of commercial nickel oxide powders for components in solid oxide fuel cells,” *J. Eur. Ceram. Soc.*, vol. 20, pp. 1023–1034, 2000.

[207] J. J. Haslam, A. Q. Pham, B. W. Chung, J. F. DiCarlo, and R. S. Glass, “Effects of the use of pore formers on performance of an anode supported solid oxide fuel cell,” *J. Am. Ceram. Soc.*, vol. 88, pp. 513–518, 2005.

[208] Z. Jiao, A. Ueno, Y. Suzuki, and N. Shikazono, “Study on the influences of reduction temperature on nickel-yttria-stabilized zirconia solid oxide fuel cell anode using nickel oxide-film electrode,” *J. Power Sources*, vol. 328, pp. 377-384, 2016.

[209] T. E. Everhart and R. F. M. Thornley, “Wide-band detector for micro-microampere low-energy electron currents,” *J. Sci. Instrum.*, vol. 37, no. 7, p. 246, 1960.

[210] L. A. Giannuzzi, *Introduction To Focused Ion Beam Instrument*. 2005.

[211] N. Yao, *Focused ion beam systems: basics and applications*. 2007.

[212] J. R. Wilson *et al.*, “Quantitative three-dimensional microstructure of a solid oxide fuel cell cathode,” *Electrochem. commun.*, vol. 11, no. 5, pp. 1052–1056, May 2009.

[213] J. R. Wilson, J. S. Cronin, and S. A. Barnett, “Linking the microstructure , performance and durability of Ni-yttria-stabilized zirconia solid oxide fuel cell anodes using three-dimensional focused ion beam – scanning electron microscopy imaging,” *Scr. Mater.*, vol. 65, no. 2, pp. 67–72, 2011.

[214] G. Kapun and M. Gaberscek, “Microstructural evaluation of Ni-SDC cermet from a representative 2D image and / or a 3D reconstruction based on a stack of images,” November 2017.

[215] A. Zekri, M. Knipper, J. Parisi, and T. Plaggenborg, “Microstructure degradation of Ni/CGO anodes for solid oxide fuel cells after long operation time using 3D reconstructions by FIB tomography,” *Phys. Chem. Chem. Phys.*, vol. 19, no. 21, pp. 13767–13777, 2017.

[216] D. O. Kennouche, “The Evolution of Solid Oxide Fuel Cell Nickel-Yttria Stabilized Zirconia Anodes Studied Using Electrochemical and Three-Dimensional Microstructural Characterizations,” 2015.

[217] J. Schindelin *et al.*, “Fiji: An open-source platform for biological-image analysis,” *Nat. Methods*, vol. 9, no. 7, pp. 676–682, 2012.

[218] L. Holzer, F. Indutnyi, P. Gasser, B. Münch, and M. Wegmann, “Three-dimensional analysis of porous $BaTiO_3$ ceramics using FIB nanotomography,” *J. Microsc.*, vol. 216, no. April, pp. 84–95, 2004.

[219] T. Shimura, Z. Jiao, and N. Shikazono, “Dependence of solid oxide fuel cell electrode microstructure parameters on focused ion beam Scanning electron microscopy resolution,” *Int. J. Hydrogen Energy*, vol. 41, no. 47, pp. 22373-22380, 2016.

[220] W. C. Röntgen, “Über eine neue Art von Strahlen,” *Ann. Phys.*, vol. 300, no. 1, pp. 1–11, 1898.

[221] C. Oilund, *The Radon Transform*. Springer Science, 2007.

[222] J. Radon, “Ueber die Bestimmung von Funktionen durch ihre Integralwere laengs gewisser Mannigfaltigkeiten,” *Berichte ueber die Verhandlungen der Koeniglich Saechsischen Gesellschaft der Wissenschaften zu Leipzig. Math. Klasse*, no. 69, pp. 262–277, 1917.

[223] W. A. Kalender, “X-ray computed tomography,” *Phys. Med. Biol.*, vol. 51, no. 13, pp. R29–R43, 2006.

[224] S. Carmignato, W. Dewulf, and R. Leach, *Industrial X-ray computed tomography*. 2017.

[225] R. Bracewell, “Strip Integration in Radio Astronomy,” *Aust. J. Phys.*, vol. 9, no. 2, p. 198, 1956.

[226] W. H. Oldendorf, “Isolated Flying Spot Detection of Radiodensity Dis-Continuities-Displaying the Internal Structural Pattern of a Complex Object,” *Ire Trans. Biomed. Electron.*, vol. 8, no. 1, pp. 68–72, 1961.

[227] D. E. Kuhl and R. Q. Edwards, “Image Separation Radioisotope Scanning,” *JAMA J. Am. Med. Assoc.*, vol. 184, no. 4, p. 187, 1963.

[228] A. M. Cormack, “Representation of a function by its line integrals, with some radiological applications. II,” *J. Appl. Phys.*, vol. 35, no. 10, pp. 2908–2913, 1964.

[229] R. N. Bracewell and A. C. Riddle, “Inversion of fan-beam scans in radio astronomy,” *Astrophys. J.*, vol. 150, pp. 427–434, 1967.

[230] G. N. Hounsfield, “Computerized transverse axial scanning (tomography): Part 1. Description of system,” *Br. J. Radiol.*, vol. 46, no. 552, 1973.

[231] L. A. Shepp, B. F. Logan, and M. Hill, “The Fourier Reconstruction of a Head Section,” vol. NS-21, 1974.

[232] L. Salvo *et al.*, “X-ray micro-tomography an attractive characterisation technique in materials science,” *Nucl. Instruments Methods Phys. Res. Sect. B Beam Interact. with Mater. Atoms*, vol. 200, pp. 273–286, 2003.

[233] J. Baruchel *et al.*, “Advances in synchrotron radiation microtomography,” *Scr. Mater.*, vol. 55, no. 1 SPEC. ISS., pp. 41–46, 2006.

[234] A. Diaz, P. Trtik, M. Guizar-Sicairos, A. Menzel, P. Thibault, and O. Bunk, “Quantitative x-ray phase nanotomography,” *Phys. Rev. B*, vol. 85, pp. 1–4, 2012.

[235] W. D. Coolidge, “A powerful röntgen ray tube with a pure electron discharge,” *Phys. Rev.*, vol. 2, no. 6, pp. 409–430, 1913.

[236] P. Chebotayev *et al.*, *Topics in Applied Physics*, Volume 13. New York, Berlin, Heidelberg: Springer-Verlag, 1979.

[237] J. Hsieh, *Computed Tomography: Principles, Design, Artifacts, and Recent Advances*. 2015.

[238] J. L. Fife, M. Rappaz, M. Pistone, T. Celcer, G. Mikuljan, and M. Stampanoni, "Development of a laser-based heating system for in situ synchrotron-based X-ray tomographic microscopy," *J. Synchrotron Radiat.*, vol. 19, no. 3, pp. 352-358, 2012.

[239] F. R. Elder, A. M. Gurewitsch, R. V Langmuir, and H. C. Pollock, "Radiation from Electrons in a Synchrotron," 1947.

[240] M. Benfatto and C. Meneghini, *Synchrotron Radiation*. 2015.

[241] C. Su, Y. Wu, W. Wang, Y. Zheng, R. Ran, and Z. Shao, "Assessment of nickel cermets and $La_{0.8}Sr_{0.2}Sc_{0.2}Mn_{0.8}O_3$ as solid-oxide fuel cell anodes operating on carbon monoxide fuel," *J. Power Sources*, vol. 195, no. 5, pp. 1333–1343, March 2010.

[242] K. Andersen, "Neutron Imaging and Applications," *Source*, pp. 31–45, 2009.

[243] A. Kesner, "3D Image reconstruction," *Department of Radiology, University of Colorado*, 2016. .

[244] P. Cahill and L. M. Blau, "The preliminary application of a matrix inversion method for radionuclide imaging.," *J. Nucl. Med. Off. Publ. Soc. Nucl. Med.*, vol. 11, no. 10, pp. 613–615, 1970.

[245] P. Metherall, D. C. Barber, R. H. Smallwood, and B. H. Brown, "Three-dimensional electrical impedance tomography," *Nature*, vol. 380, no. 6574, pp. 509–512, 1996.

[246] R. Gordon, R. Bender, and G. T. Herman, "Algebraic Reconstruction Techniques (ART) for three-dimensional electron microscopy and X-ray photography," *J. Theor. Biol.*, vol. 29, no. 3, pp. 471–481, 1970.

[247] U. Imaging, "a Superior Implementation of the Art Algorithm," vol. 94, pp. 81–94, 1984.

[248] A. H. Andersen, "Algebraic Reconstruction in CT from Limited Views," *IEEE Trans. Med. Imaging*, vol. 8, no. 1, pp. 50–55, 1989.

[249] G. N. Ramchandran and A. V Lakshminarayan, "Three-Dimensional Reconstruction From Radiograph and Electron Micrographs: Application of Convolution Methods Instead of Fourier Transforms," *Proc. Natl. Acad. Sc. US*, vol. 68, no. 9, pp. 2236–2240, 1971.

[250] Y. Wei, G. Wang, and J. Hsieh, "An intuitive discussion on the ideal ramp filter in computed tomography (I)," *Comput. Math. with Appl.*, vol. 49, no. 5–6, pp. 731-740, 2005.

[251] G. L. Zeng, "Revisit of the Ramp Filter," *IEEE Trans. Nucl. Sci.*, vol. 62, no. 1, pp. 131–136, 2015.

[252] M. Stampanoni *et al.*, "Trends in synchrotron-based tomographic imaging: the SLS experience," *Dev. X-Ray Tomogr. V*, vol. 6318, p. 63180M–63180M–14, 2006.

[253] M. Lee, *X-Ray Diffraction for Materials Research*. 2016.

[254] I. Hargittai, “Symmetry in Crystallography,” *Acta Crystallogr. Sect. A Found. Crystallogr.*, vol. 54, no. 6, pp. 697–706, Nov. 1998.

[255] G. S. Girolami, *X-ray crystallography*. 2016.

[256] W. H. Miller, *A treatise on crystallography*. For J. & JJ Deighton, 1839.

[257] B. B. Baker and E. T. Copson, *The mathematical theory of Huygens’ principle*, vol. 329. American Mathematical Soc., 2003.

[258] P. Th, U. E. Ruttimann, M. Unser, and S. Member, “A Pyramid Approach to Subpixel Registration Based on Intensity,” vol. 7, no. 1, pp. 27–41, 1998.

[259] A. Buades and B. Coll, “A non-local algorithm for image denoising,” *Comput. Vis. Pattern*, vol. 2, no. 0, pp. 60–65, 2005.

[260] N. Kwok and H. Shi, “Design of unsharp masking filter kernel and gain using particle swarm optimization,” *Proc. - 2014 7th Int. Congr. Image Signal Process. CISP 2014*, pp. 217–222, 2014.

[261] T. F. Scientific, “Avizo Software 9 User ’s Guide,” vol. 9. pp. 1–915, 2018.

[262] C. Sommer, C. Straehle, U. Köthe, and F. A. Hamprecht, “Ilastik: Interactive Learning and Segmentation Toolkit,” pp. 230–233, 2011.

[263] A. Kan, “Machine learning applications in cell image analysis,” *Immunol. Cell Biol.*, vol. 95, no. 6, pp. 525–530, 2017.

[264] M. Kishimoto, Y. Kawakami, Y. Otani, H. Iwai, and H. Yoshida, “Improved controllability of wet infiltration technique for fabrication of solid oxide fuel cell anodes,” *Scr. Mater.*, vol. 140, pp. 5–8, 2017.

[265] J. A. Taillon, C. Pellegrinelli, Y. L. Huang, E. D. Wachsman, and L. G. Salamanca-Riba, “Improving microstructural quantification in FIB/SEM nanotomography,” *Ultramicroscopy*, vol. 184, pp. 24–38, 2018.

[266] I. Cousin, P. Levitz, and A. Bruand, “Three-dimensional analysis of a loamy-clay soil using pore and solid chord distributions,” *Eur. J. Soil Sci.*, vol. 47, no. 4, pp. 439–452, 1996.

[267] P. Levitz, “Off-lattice reconstruction of porous media: Critical evaluation, geometrical confinement and molecular transport,” *Adv. Colloid Interface Sci.*, vol. 76–77, pp. 71–106, 1998.

[268] R. S. Maier, R. S. Bernard, and D. W. Grunau, “Boundary conditions for the lattice Boltzmann method,” *Phys. Fluids*, vol. 8, no. 7, pp. 1788–1801, 1996.

[269] I. Ginzburg, “Multiple-relaxation-time lattice Boltzmann,” pp. 437–451, 2002.

[270] B. Münch, P. Gasser, L. Holzer, and R. Flatt, “FIB-nanotomography of particulate systems - Part II: Particle recognition and effect of boundary truncation,” *J. Am. Ceram. Soc.*, vol. 89, no. 8, pp. 2586–2595, 2006.

[271] J. T. Gostick, “Versatile and efficient pore network extraction method using marker-based watershed segmentation,” *Phys. Rev. E*, vol. 96, no. 2, pp. 1–15, 2017.

[272] M. D. R. Kok, R. Jervis, D. Brett, P. R. Shearing, and J. T. Gostick, “Insights into the Effect of Structural Heterogeneity in Carbonized Electrospun Fibrous Mats for Flow Battery Electrodes by X-Ray Tomography,” *Small*, vol. 1703616, p. 1703616, 2018.

[273] F. Zhao, Y. Jiang, G. Y. Lin, and A. V Virkar, “The Effect of Electrode Microstructure,” *Electrochem. Soc. Proc. vol. 2001-16*, pp. 501–510, 2001.

[274] J. R. Smith *et al.*, “Evaluation of the relationship between cathode microstructure and electrochemical behavior for SOFCs,” *Solid State Ionics*, vol. 180, no. 1, pp. 90–98, 2009.

[275] J. R. Wilson and S. a. Barnett, “Solid Oxide Fuel Cell Ni–YSZ Anodes: Effect of Composition on Microstructure and Performance,” *Electrochem. Solid-State Lett.*, vol. 11, no. 10, p. B181, 2008.

[276] L. C. R. Schneider, C. L. Martin, Y. Bultel, L. Dessemond, and D. Bouvard, “Percolation effects in functionally graded SOFC electrodes,” *Electrochim. Acta*, vol. 52, no. 9, pp. 3190–3198, 2007.

[277] A. Ali, X. Wen, K. Nandakumar, J. Luo, and K. T. Chuang, “Geometrical modeling of microstructure of solid oxide fuel cell composite electrodes,” *J. Power Sources*, vol. 185, no. 2, pp. 961–966, 2008.

[278] B. Kenney, M. Valdmanis, C. Baker, J. G. Pharoah, and K. Karan, “Computation of TPB length, surface area and pore size from numerical reconstruction of composite solid oxide fuel cell electrodes,” *J. Power Sources*, vol. 189, no. 2, pp. 1051–1059, 2009.

[279] O. Pecho, A. Mai, B. Münch, T. Hocker, R. Flatt, and L. Holzer, “3D Microstructure Effects in Ni-YSZ Anodes: Influence of TPB Lengths on the Electrochemical Performance,” *Materials (Basel).*, vol. 8, no. 10, pp. 7129–7144, Oct. 2015.

[280] X. Lu *et al.*, “Correlation between triple phase boundary and the microstructure of Solid Oxide Fuel Cell anodes: The role of composition, porosity and Ni densification,” *J. Power Sources*, vol. 365, pp. 210–219, 2017.

[281] S. J. Cooper, A. Bertei, P. R. Shearing, J. A. Kilner, and N. P. Brandon, “TauFactor: An open-source application for calculating tortuosity factors from tomographic data,” *SoftwareX*, vol. 5, pp. 203–210, 2016.

[282] M. D. R. Kok *et al.*, “Mass transfer in fibrous media with varying anisotropy for flow battery electrodes: Direct numerical simulations with 3D X-ray computed tomography,” *Chem. Eng. Sci.*, 2018.

[283] R. Hill, “Elastic properties of reinforced solids: Some theoretical principles,” *J. Mech. Phys. Solids*, vol. 11, no. 5, pp. 357–372, 1963.

[284] K. N. Grew, A. A. Peracchio, A. S. Joshi, J. R. Izzo, and W. K. S. Chiu, “Characterization and analysis methods for the examination of the heterogeneous solid oxide fuel cell electrode microstructure. Part 1: Volumetric measurements of the heterogeneous structure,” *J. Power Sources*, vol. 195, no. 24, pp. 7930–7942, 2010.

[285] Z. Yan, S. Hara, Y. Kim, and N. Shikazono, “Homogeneity and representativeness analyses of solid oxide fuel cell cathode microstructures,” *Int. J. Hydrogen Energy*, pp. 1–13, 2017.

[286] LaVision, “Digital Volume Correlation (DVC),” vol. C, p. 2014, 2014.

[287] A. Wheeler, “Reaction rates and selectivity in catalyst pores.,” *Catalysis*, vol. 2, pp. 105–165, 1955.

[288] B. Tjaden, S. J. Cooper, D. J. Brett, D. Kramer, and P. R. Shearing, “On the origin and application of the Bruggeman correlation for analysing transport phenomena in electrochemical systems,” *Curr. Opin. Chem. Eng.*, vol. 12, pp. 44–51, 2016.

[289] B. Tjaden, D. J. L. Brett, and P. R. Shearing, “Tortuosity in electrochemical devices: a review of calculation approaches,” *Int. Mater. Rev.*, vol. 63, no. 2, pp. 47–67, 2018.

[290] J. van Brakel and P. M. Heertjes, “Analysis of diffusion in macroporous media in terms of a porosity, a tortuosity and a constrictivity factor,” *Int. J. Heat Mass Transf.*, vol. 17, no. 9, pp. 1093–1103, 1974.

[291] L. Holzer *et al.*, “The influence of constrictivity on the effective transport properties of porous layers in electrolysis and fuel cells,” *J. Mater. Sci.*, vol. 48, no. 7, pp. 2934–2952, 2013.

[292] W. He *et al.*, “Gas transport in porous electrodes of solid oxide fuel cells: A review on diffusion and diffusivity measurement,” *J. Power Sources*, vol. 237, pp. 64–73, 2013.

[293] X. Lu *et al.*, “3D Characterization of Diffusivities and Its Impact on Mass Flux and Concentration Overpotential in SOFC Anode,” *J. Electrochem. Soc.*, 2017.

[294] J. R. Wilson *et al.*, “Three-dimensional reconstruction of a solid-oxide fuel-cell anode.,” *Nat. Mater.*, vol. 5, no. 7, pp. 541–4, Jul. 2006.

[295] S. J. Cooper, A. Bertei, P. R. Shearing, J. A. Kilner, and N. P. Brandon., “TauFactor: An open-source application for calculating tortuosity factors from tomographic data.,” *SoftwareX*, 2016.

[296] X. Wang and A. Atkinson, “Modeling Microstructure Evolution of Ni Cermet Using a Cellular Automaton Approach,” *J. Electrochem. Soc.*, vol. 161, no. 5, pp. F605–F614, Mar. 2014.

[297] X. Wang, “Modelling and understanding materials microstructure evolution driven by interface energy,” *Comput. Mater. Sci.*, vol. 107, pp. 1–7, 2015.

[298] X. Wang and A. Atkinson, “Combining densification and coarsening in a Cellular Automata-Monte-Carlo simulation of sintering: Methodology and calibration,” *Comput. Mater. Sci.*, vol. 143, pp. 338–349, 2018.

[299] X. Wang and a. Atkinson, “Modeling Microstructure Evolution of Ni Cermet Using a Cellular Automaton Approach,” *J. Electrochem. Soc.*, vol. 161, no. 5, pp. F605–F614, Mar. 2014.

[300] N. P. B. B. Song, A. Bertei, X. Wang, S.J. Cooper, E. Ruiz-Trejo, R. Chowdhury, R. Podor, “In-situ imaging and microstructural-electrochemical quantification of Ni dewetting in novel 2D Ni-YSZ electrodes for solid oxide fuel cells,” 2018.

[301] W. S. Rasband, “ImageJ.” U. S. National Institutes of Health, Bethesda, Maryland, USA.

[302] T. F. Scientific, “Avizo Software 9 User ’s Guide,” vol. 9, pp. 1–915, 2018.

[303] S.-S. Liu, A. Takayama, S. Matsumura, and M. Koyama, “Image contrast enhancement of Ni/YSZ anode during the slice-and-view process in FIB-SEM,” *J. Microsc.*, 2015.

[304] A. Gubner, H. Landes, J. Metzger, H. Seeg, and R. Stübner, “Investigations into the degradation of the cermet anode of a solid oxide fuel cells,” *Solid Oxide Fuel Cells V*, 1997, vol. 97, no. 18, pp. 844–850.

[305] J. J. Bailey *et al.*, “Laser-preparation of geometrically optimised samples for X-ray nano-CT,” *J. Microsc.*, vol. 267, no. 3, pp. 384–396, 2017.

[306] F. Kharfi, “Mathematics and Physics of Computed Tomography (CT): Demonstrations and Practical Examples,” *Imaging Radioanal. Tech. Interdiscip. Res. - Fundam. Cut. Edge Appl.*, pp. 82–106, 2013.

[307] E. Maire and P. J. Withers, “Quantitative X-ray tomography,” *Int. Mater. Rev.*, vol. 59, no. 1, pp. 1–43, Jan. 2014.

[308] D. Kennouche *et al.*, “Observing the microstructural evolution of Ni-Yttria-stabilized zirconia solid oxide fuel cell anodes,” *Acta Mater.*, vol. 103, pp. 204–210, 2016.

[309] Heenan, T.M.M., Brett, D.J.L., Shearing, P.R., “X-ray attenuation properties of commonly employed solid oxide fuel cell materials X-ray attenuation properties of commonly employed solid oxide fuel cell materials,” *J. Phys. Conf. Ser.*, vol. 849, 2017.

[310] J. Banhart, “Advanced Tomographic Methods in Materials Research and Engineering,” *New York Oxford Univ. Press*, 2008.

[311] F. Natterer, “The Mathematics of Computerized Tomography (Philadelphia, PA: SIAM),” 2001.

[312] C. Lanczos, “Trigonometric interpolation of empirical and analytical functions,” *J. Math. Phys.*, vol. 17, no. 1–4, pp. 123–199, 1938.

[313] A. Polesel, G. Ramponi, and V. J. Mathews, “Image enhancement via adaptive unsharp masking,” *IEEE Trans. Image Proc.*, vol. 9, no. 3, pp. 505–510, 2000.

[314] S. J. Cooper, A. Bertei, P. R. Shearing, J. A. Kilner, and N. P. Brandon, “TauFactor: An open-source application for calculating tortuosity factors from tomographic data,” *SoftwareX*, vol. 5, pp. 203–210, 2016.

[315] D. Kennouche *et al.*, “Observing the microstructural evolution of Ni-Yttria-stabilized zirconia solid oxide fuel cell anodes,” *Acta Mater.*, vol. 103, pp. 204–210, 2016.

[316] K. T. Lee, N. J. Vito, and E. D. Wachsman, “Comprehensive quantification of Ni-Gd0.1Ce0.9O 1.95 anode functional layer microstructures by three-dimensional reconstruction using a FIB/SEM dual beam system,” *J. Power Sources*, vol. 228, pp. 220–228, 2013.

[317] T. Iwata, “Characterization of Ni-YSZ Anode Degradation for Substrate-Type Solid Oxide Fuel Cells,” *Journal of The Electrochemical Society*, vol. 143, no. 5. p. 1521, 1996.

[318] J. H. Hubbell and S. M. Seltzer, “Tables of X-Ray Mass Attenuation Coefficients and Mass Energy-Absorption Coefficients,” *Radiation Physics Division, PML, NIST*, 1996. .

[319] F. Marone and M. Stampanoni, “Regridding reconstruction algorithm for real-time tomographic imaging,” *J. Synchrotron Radiat.*, vol. 19, no. 6, pp. 1029-1037, 2012.

[320] B. A. Dowd *et al.*, “Developments in synchrotron x-ray computed microtomography at the National Synchrotron Light Source,” no. September 1999, pp. 224–236, 1999.

[321] S. Primdahl and M. Mogensen, “Oxidation of Hydrogen on Ni/Yttria-Stabilized Zirconia Cermet Anodes,” *J. Electrochem. Soc.*, vol. 144, no. 10, pp. 3409-3419, 1997.

[322] K. Miyawaki, M. Kishimoto, H. Iwai, M. Saito, and H. Yoshida, “Comprehensive understanding of the active thickness in solid oxide fuel cell anodes using experimental, numerical and semi-analytical approach,” *J. Power Sources*, vol. 267, pp. 503–514, 2014.

[323] J. Banhart, *Advanced tomographic methods in materials research and engineering*. Oxford University Press, 2008.

Appendices

11.1 Mathematical Treatment of FBP

A mathematical treatment of the FBP, simplified from work by Kuba and Herman [324], and adjusted to the coordinate system used in **Section 3.2.5.4**, is given below:

Rotated coordinate system (Figure 52):

$$s = -x\sin\theta + y\cos\theta$$

$$t = \quad x\cos\theta + y\sin\theta$$

Eliminating *s* and re-writing Equation *3-3* in terms of *t* and *θ*:

$$[Rf](t,\theta) = \int_{-\infty}^{\infty} f(x,y)ds$$

The task is to find the inverse of the Radon transform, such that when given a function, g(t,θ), one can apply said function to return f(t,θ), the function of the property of interest. This can be thought of as, given g(t,θ), find the function f(x,y) such that:

$$[Rf](t,\theta) = \mathrm{g}(t,\theta) \qquad \text{for } -\infty < t < \infty \text{ and } 0 < \theta < \pi$$

Other transforms are required to produce the inverse Radon transform, including: the back-projection transform, *B*, the normal and inverse versions of the 1D Fourier Transform, F_s, and 2D Fourier Transform, F_2.

Back-projection: $[B\mathrm{f}](x,y) = \int_0^{\pi} \mathrm{g}(x\cos\theta + y\sin\theta, \theta)d\theta$

1D FT: $[F_s\mathrm{g}](t,\theta) = \int_{-\infty}^{\infty} \mathrm{g}(t,\theta)\, exp(-2\pi itT)\, dt$

1D Inv. FT: $\left[{F_s}^{-1}\mathrm{g}\right](t,\theta) = \int_{-\infty}^{\infty} \mathrm{g}(T,\theta)\, exp(2\pi itT)\, dT$

2D FT: $[F_2\mathrm{g}](X,Y) = \int_{-\infty}^{\infty}\int_{-\infty}^{\infty} \mathrm{f}(x,y)\, exp(-2\pi i(xX+yY)\, dxdy$

2D Inv. FT: $\left[{F_s}^{-1}\mathrm{g}\right](x,y) = \int_{-\infty}^{\infty}\int_{-\infty}^{\infty} \mathrm{f}(X,Y)\, exp(2\pi i(xX+yY)\, dXdY$

If the 2D inverse FT is expressed in polar coordinates:

$$\left[{F_2}^{-1}g\right](x,y) = \int_0^{\pi}\int_{-\infty}^{\infty} f(T\cos\theta, T\sin\theta)\, exp(2\pi i(x\cos\theta + y\sin\theta)T)|T|dTd\theta$$

Given that the 1D convolution of functions $g_1(t,\theta)$ and $g_2(t,\theta)$ can be defined by:

$$[g_1 * g_2](t,\theta) = \int_{-\infty}^{\infty} g_1(\sigma,\theta)g_2(t-\sigma,\theta)d\theta \qquad 11\text{-}1$$

And the fact that the convolution theorem holds that:

$$F_s(\mathrm{g}_1 * \mathrm{g}_2) = F_s\mathrm{g}_1 \cdot F_s\mathrm{g}_2$$

$$F_s{}^{-1}(\mathrm{g}_1 \cdot \mathrm{g}_2) = F_s{}^{-1}\mathrm{g}_1 * F_s{}^{-1}\mathrm{g}_2$$

This means the Fourier slice theorem (providing a connection between the Fourier Transform and the Radon Transform) is given by:

$$[F_sRf](t,\theta) = [F_2f](Tcos\theta, Tsin\theta)$$

Given that the 2D inverse FT of the 2D FT transform of a function, returns the function:

$$\mathrm{f}(x,y) = [F_2^{-1}F_2\mathrm{f}](x,y)$$

Employing Equation *3-5* and Equation *3-7*:

$$\mathrm{f}(x,y) = \int_0^{\pi}\int_{-\infty}^{\infty}[F_2\mathrm{f}](Tcos\theta, Tsin\theta)\exp(2\pi i(xcos\theta + ysin\theta)T)|T|dTd\theta$$

$$\mathrm{f}(x,y) = \int_0^{\pi}(\int_{-\infty}^{\infty}[F_sR\mathrm{f}](T,\theta)\,|T|exp(2\pi i(xcos\theta + ysin\theta)T)dT)d\theta$$

$$\mathrm{f}(x,y) = \int_0^{\pi}(\int_{-\infty}^{\infty}(abs(T,\theta)[F_sR\mathrm{f}](T,\theta)\,exp(2\pi i(xcos\theta + ysin\theta)T)dT)d\theta$$

The inner integral is the 1D inverse FT of the product abs.F_s*R*f, and using *B*:

$$\mathrm{f}(x,y) = \int_0^{\pi}[F_s^{-1}(abs\cdot F_sR\mathrm{f})](xcos\theta + ycos\theta\,,\theta)d\theta$$

$$f(x,y) = [BF_s^{-1}(abs\cdot F_sRf](x,y)$$

Since this reconstruction formula (Equation *3-8*) can be used to regain an expression for f(x,y) from its Radon transform *R*f, the inverse Radon transform is given by:

$$\boldsymbol{R^{-1}g = BF_s^{-1}[abs.F_sg]}$$

where abs is a function of two variables and is defined as |T| and:

$$abs.F_s\mathrm{g}(T,\theta) = |T||F_s|\mathrm{g}(T,\theta)$$

11.2 Mathematical Treatment of DVC

The 1D procedure outlined in **Section 3.4.3.1** can be readily extended to 2 or 3 dimensions, the latter of which is known as digital *volume* correlation (DVC). The type of DVC implemented in this thesis is known as Direct Correlation (DC) as it involves *directly* summing the products of voxel grayscale values of the initial and deformed volumes to construct the 3D correlation map [286].

In three dimensions, the correlation coefficient C at a point (x_0, y_0, z_0) for volumes *A* and *B*, with a window size of $N \times N \times N$, and shifts of *dx, dy*, and *dz*, is given Equation *3-18:*

$$C(dx, dy, dz) = \sum_{(i,j,k)=(x_0,y_0,z_0)}^{(i,j,k)<(x_0+N,y_0+N,z_0+N)} A(i,j,k)B(i+dx, j+dy, k+dz) \quad 11\text{-}2$$

where A(i,j,k) is the gray-scale value of the voxel at position (i, j, k) in volume A etc.

Normalising and re-defining the arithmetic means in 3D gives Equation *3-19* [286]:

$$< A > = \sum_{i,j,k} \frac{A(i,j,k)}{N^3} \text{ and } < B > = \sum_{i,j,k} \frac{B(i+dx,j+dy,k+dz)}{N^3}$$

$$C_{norm}(dx, dy, dz) = \sum_{(i,j,k)} \frac{(A(i,j,k)-<A>)(B(i+dx,j+dy,k+dz)-<B>)}{\sqrt{\sum_{(i,j,k)}(A(i,j,k)-<A>)^2}\sqrt{\sum_{i,j,k}(B(i+dx,j+dy,k+dz)-<B>)^2}}$$

11-3

The computational cost to perform this type of calculation depends on the window size chosen and particularly on the cube of the search radius such that it is important to minimise this latter value, particularly when processing large volumes. It is also worth noting that an initial step, using FFT-based methods, is used to find large shifts. In the software used in this thesis, a coarse FFT step is used to create an initial predictor displacement field from which DC methods then proceed [286].